Sourav Sarkar
Helmut Satz
Bikash Sinha
Editors

LECTURE NOTES IN PHYSICS 785

The Physics of the Quark-Gluon Plasma

Introductory Lectures

Springer

Lecture Notes in Physics

The Lecture Notes in Physics

The series Lecture Notes in Physics (LNP), founded in 1969, reports new developments in physics research and teaching – quickly and informally, but with a high quality and the explicit aim to summarize and communicate current knowledge in an accessible way. Books published in this series are conceived as bridging material between advanced graduate textbooks and the forefront of research and to serve three purposes:

- to be a compact and modern up-to-date source of reference on a well-defined topic
- to serve as an accessible introduction to the field to postgraduate students and nonspecialist researchers from related areas
- to be a source of advanced teaching material for specialized seminars, courses and schools

Both monographs and multi-author volumes will be considered for publication. Edited volumes should, however, consist of a very limited number of contributions only. Proceedings will not be considered for LNP.

Volumes published in LNP are disseminated both in print and in electronic formats, the electronic archive being available at springerlink.com. The series content is indexed, abstracted and referenced by many abstracting and information services, bibliographic networks, subscription agencies, library networks, and consortia.

Proposals should be sent to a member of the Editorial Board, or directly to the managing editor at Springer:

Christian Caron
Springer Heidelberg
Physics Editorial Department I
Tiergartenstrasse 17
69121 Heidelberg / Germany
christian.caron@springer.com

S. Sarkar
H. Satz
B. Sinha (Eds.)

The Physics of the Quark-Gluon Plasma

Introductory Lectures

Springer

Sourav Sarkar
Variable Energy Cyclotron Centre (VECC)
Bidhan Nagar
Kolkata-700064
Sector 1 Block AF
India

Helmut Satz
Universität Bielefeld
Fak. Physik
Universitätsstr. 25
33615 Bielefeld
Germany
satz@physik.uni-bielefeld.de
reder@physik.uni-bielefeld.de
h.satz@cern.ch

Bikash Sinha
Variable Energy Cyclotron Centre (VECC)
Bidhan Nagar
Kolkata-700064
Sector 1 Block AF
India

Sarkar, S., Satz, H., Sinha, B. (Eds.), *The Physics of the Quark-Gluon Plasma: Introductory Lectures*, Lect. Notes Phys. 785 (Springer, Berlin Heidelberg 2010), DOI 10.1007/978-3-642-02286-9

Lecture Notes in Physics ISSN 0075-8450 e-ISSN 1616-6361
ISBN 978-3-642-02285-2 e-ISBN 978-3-642-02286-9
DOI 10.1007/978-3-642-02286-9
Springer Heidelberg Dordrecht London New York

Library of Congress Control Number: 2009938884

Cover design: Integra Software Services Pvt. Ltd., Pondicherry

Printed on acid-free paper

Springer is part of Springer Science+Business Media (www.springer.com)

Preface

The study of strongly interacting matter has over the past 30 years become one of the major areas of high-energy physics. Pioneering theoretical work in statistical quantum chromodynamics leads to the advent of a vigorous experimental program, using heavy-ion collisions to create small droplets of a medium whose energy density surpasses all previously investigated ranges. This in turn triggered new approaches in theory, addressing innovative aspects from hydrodynamics to parton saturation and gravity models. Never before have creative theoretical ideas and ingenious experiments worked so well in a complimentary and tandem mode. The exciting perspectives of all these developments have brought numerous young research workers into the game. The future of the field clearly depends on the competence and the enthusiasm of these young experimentalists and theorists beginning their research on high-energy nuclear collisions.

This was the justification for organizing in February of 2008 a large-scale school on the topic in Jaipur, India, a charming Rajasthan city filled with cultural heritage. The fact that the Quark Matter conference was going to be held here soon afterward provided good opportunity to convene a school introducing to young physicists in particular the more recent developments in the field, those not yet covered by excellent textbooks available on this topic. The lectures at the school were to be held by leading international experts on the different topics, and as can be seen, we indeed succeeded in attracting scientists who combine expertise with pedagogical capabilities.

The essential aspects and concepts of high-energy heavy-ion collisions to be addressed at the school were

- QCD Thermodynamics
- Global Features
- Hydrodynamics and Flow
- Electromagnetic Probes
- Jet Production
- Quarkonium Production
- Saturation and Color Glass Condensate
- Gravity–QCD Relations

For each of these topics, general survey lectures introduced the main ideas, presented the current state of the theoretical understanding, and summarized the basic experimental results obtained so far.

The planning of the school met with excellent resonance among young physicists worldwide. Almost 100 students from many countries attended, listened, and, as these lecture notes bear witness of, participated. We had decided the written version of the lectures would be prepared by each lecturer together with two to three students, who volunteered for this task. Furthermore, this idea fell on fruitful ground, and both students and lecturers profited from the collaboration in preparing the different chapters.

It is a particular pleasure to one of us (B.S.) that these lectures are published by Springer Verlag, who had already published the lectures at the first school on the QGP in India. That was held many years ago, 1989 in Puri, and it was to a large extent responsible for creating the great and active present community of research workers in India.

We have received generous funding from the Variable Energy Cyclotron Centre, Kolkata, the Centre for Advanced Research and Education of the Saha Institute of Nuclear Physics, Kolkata, the Board of Research in Nuclear Science, the Department of Atomic Energy, Government of India, and the Institute of Physics, Bhubaneswar. For all this support, we are very grateful.

Bielefeld, Kolkata
February 2009

Sourav Sarkar
Helmut Satz
Bikash Sinha

Contents

The Thermodynamics of Quarks and Gluons

Helmut Satz

Abstract This is an introduction to the study of strongly interacting matter. We survey its different possible states and discuss the transition from hadronic matter to a plasma of deconfined quarks and gluons. Following this, we summarize the results provided by lattice QCD finite temperature and density and then investigate the nature of the deconfinement transition. Finally we give a schematic overview of possible ways to study the properties of the quark–gluon plasma.

1 Prelude

The fundamental questions of physics appear on two levels, the microscopic and macroscopic. We begin by asking the following questions:

- What are the ultimate constituents of matter?
- What are the basic forces between these constituents?
  Given the basic building blocks and their interactions, we want to know
- What are the possible states of matter?
- How do transitions between these states take place?

How far have we advanced today in our understanding of these different aspects?

According to our present state of knowledge, the ultimate constituents are quarks, leptons, gluons, photons, intermediate vector bosons ($Z/W^{\pm}$) and Higgs bosons – in a conservative count (no antiparticles, etc.), 16 in all, with gravitation not yet in the game.

Their interactions were originally classified as strong, electromagnetic, weak and gravitation, leaving a more general scheme as a challenge. The first unification brought electroweak theory, the second combined this with strong interactions to the standard model. The origin of all the different basic constituents, as well as the role of gravitation, is still open, waiting for the theory of everything (TOE).

H. Satz (✉)
Fakultät für Physik, Universität Bielefeld, Universitätsstrasse 25, D-33615 Bielefeld, Germany,
satz@physik.uni-bielefeld.de

Satz, H.: *The Thermodynamics of Quarks and Gluons*. Lect. Notes Phys. **785**, 1–21 (2010)
DOI 10.1007/978-3-642-02286-9_1

In ancient times, the basic states of matter were earth, water, air and fire; today we have solids, liquids, gases and plasmas. In addition, now there is a multitude of others: insulators, conductors and superconductors, fluids and superfluids, ferromagnets, spin glasses, gelatines and many more. And the question of the possible states of matter brings us a new kind of physics; the knowledge of the elementary constituents and their interactions in general does not predict the structure of the possible complex states of many constituents.

The study of complex systems becomes even more general, less dependent on the microstructure, when we ask for the transitions between the different states. We have phase transitions, depending on the singular behaviour of the partition function determined by the respective dynamics, as well as clustering and percolation transitions, determined by the connectivity aspects of the system. But we then find that scaling and renormalization concepts lead to a universal description of critical phenomena, and critical exponents define universality classes which contain quite different interaction forms.

When we study strongly interacting matter, we are therefore led to aspects which are relevant not only to QCD but also to the understanding of complex systems in general.

2 States of Strongly Interacting Matter

What happens to strongly interacting matter in the limit of high temperatures and densities? This question has fascinated physicists ever since the discovery of the strong force and the multiple hadron production it leads to. Let us look at some of the features that have emerged over the years.

- Hadrons have an intrinsic size, with a radius $r_h \simeq 1$ fm, and hence a hadron needs a space of volume $V_h \simeq (4\pi/3) r_h^3$ in order to exist. This suggests a limiting density n_c of hadronic matter [1], with $n_c = 1/V_h \simeq 1.5\, n_0$, where $n_0 \simeq 0.17$ fm^{-3} denotes the density of normal nuclear matter.
- Hadronic interactions provide abundant resonance production, and the resulting number $\rho(m)$ of hadron species increases exponentially as a function of the resonance mass m, $\rho(m) \sim \exp(bm)$. Such a form for $\rho(m)$ appeared first in the statistical bootstrap model, based on self-similar resonance formation or decay [2, 3]. It was then also obtained in the more dynamical dual resonance approach [3, 4]. In hadron thermodynamics, the exponential increase in the resonance degeneracy results in an upper limit for the temperature of hadronic matter, $T_c = 1/b \simeq 150$–200 MeV [2, 3].
- What happens beyond T_c? In QCD, hadrons are dimensionful colour-neutral bound states of more basic pointlike coloured quarks and gluons. Hadronic matter, consisting of colourless constituents of hadronic dimensions, can therefore turn at high temperatures and/or densities into a quark–gluon plasma of pointlike coloured quarks and gluons as constituents [6]. This deconfinement

transition leads to a colour-conducting state and thus is the QCD counterpart of the insulator–conductor transition in atomic matter [7].

- A shift in the effective constituent mass is a second transition phenomenon expected from the behaviour of atomic matter. At $T = 0$, in vacuum, quarks dress themselves with gluons to form the constituent quarks that make up hadrons. As a result, the bare quark mass $m_q \sim 0$ is replaced by a constituent quark mass $M_q \sim 300$ MeV. In a hot medium, this dressing melts and $M_q \to 0$. Since the QCD Lagrangian for $m_q = 0$ is chirally symmetric, $M_q \neq 0$ implies spontaneous chiral symmetry breaking. The melting $M_q \to 0$ thus corresponds to chiral symmetry restoration. We shall see later on that in QCD, as in atomic physics, the shift of the constituent mass coincides with the onset of conductivity.
- A third type of transition would set in if the attractive interaction between quarks leads in the deconfined phase to the formation of coloured bosonic diquark pairs, the Cooper pairs of QCD. These diquarks can then condense at low temperature to form a colour superconductor. Heating will dissociate the diquark pairs and turn the colour superconductor into a normal colour conductor.

Using the baryochemical potential μ as a measure for the baryon density of the system, we thus expect the phase diagram of QCD to have the schematic form shown in Fig. 1. Given QCD as the fundamental theory of strong interactions, we can use the QCD Lagrangian as dynamics input to derive the resulting thermodynamics of strongly interacting matter. For vanishing baryochemical potential, $\mu = 0$, this can be evaluated with the help of the lattice regularization, leading to finite-temperature lattice QCD.

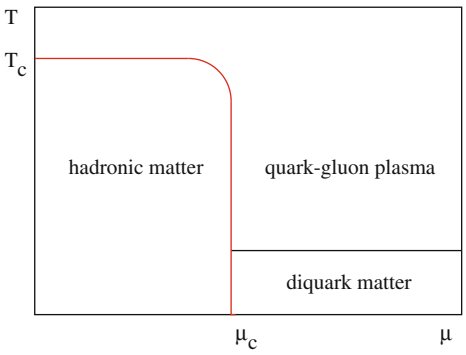

Fig. 1 The phase diagram of QCD

3 From Hadrons to Quarks and Gluons

Before turning to the results from lattice QCD, we illustrate the transition from hadronic matter to quark–gluon plasma by a very simple model. For an ideal gas of massless pions, the pressure as a function of the temperature is given by the Stefan–Boltzmann form

$$P_\pi = 3\frac{\pi^2}{90}T^4, \tag{1}$$

where the factor 3 accounts for the three charge states of the pion. The corresponding form for an ideal quark–gluon plasma with two flavours and three colours is

$$P_{qg} = \left\{2 \times 8 + \frac{7}{8}(3 \times 2 \times 2 \times 2)\right\}\frac{\pi^2}{90}T^4 - B = 37\frac{\pi^2}{90}T^4 - B. \tag{2}$$

In Eq. (2), the first temperature term in the curly brackets accounts for the two spin and eight colour degrees of freedom of the gluons, the second for the three colour, two flavour, two spin and two particle–antiparticle degrees of freedom of the quarks, with 7/8 to obtain the correct statistics. The bag pressure B takes into account the difference between the physical vacuum and the ground state for quarks and gluons in a medium.

Since in thermodynamics, a system chooses the state of lowest free energy and hence highest pressure, we compare in Fig. 2a the temperature behaviour of Eqs. (1) and (2). Our simple model thus leads to a two-phase picture of strongly interacting matter, with a hadronic phase up to

$$T_c = \left(\frac{45}{17\pi^2}\right)^{1/4} B^{1/4} \simeq 0.72\, B^{1/4} \tag{3}$$

and a quark gluon plasma above this critical temperature. From hadron spectroscopy, the bag pressure is given by $B^{1/4} \simeq 0.2$ GeV, so that we obtain

$$T_c \simeq 150 \text{ MeV} \tag{4}$$

as the deconfinement temperature. In the next section we shall find this simple estimate to be remarkably close to the value obtained in lattice QCD.

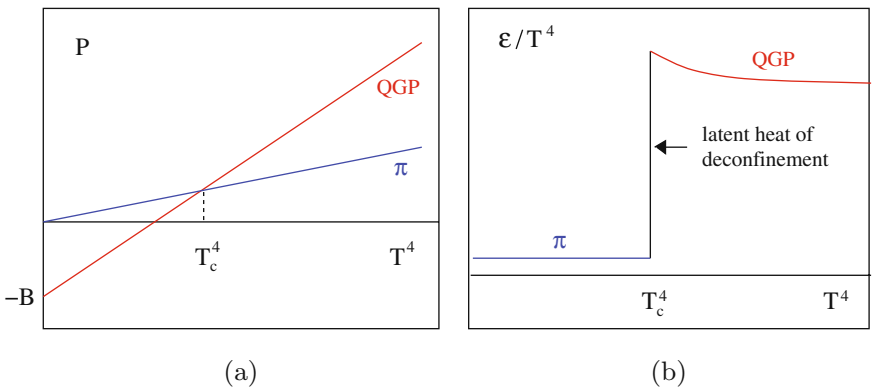

Fig. 2 Pressure and energy density in a two-phase ideal gas model

The energy densities of the two phases of our model are given by

$$\epsilon_\pi = \frac{\pi^2}{10} T^4 \tag{5}$$

and

$$\epsilon_{qg} = 37 \frac{\pi^2}{30} T^4 + B. \tag{6}$$

By construction, the transition is first order, and the resulting temperature dependence is shown in Fig. 2b. At T_c, the energy density increases abruptly by the latent heat of deconfinement. We note that even though both phases consist of massless non-interacting constituents, the dimensionless "interaction measure"

$$\frac{\epsilon - 3P}{T^4} = \frac{4B}{T^4} \tag{7}$$

does not vanish in the quark–gluon plasma, due to the (non-perturbative) difference between physical vacuum and in-medium QCD ground state [8].

4 Finite-Temperature Lattice QCD

We now want to show that the conceptual considerations of the last section indeed follow from strong interaction thermodynamics as based on QCD as the input dynamics. QCD is defined by the Lagrangian

$$\mathcal{L} \;=\; -\frac{1}{4} F^a_{\mu\nu} F_a^{\mu\nu} \;-\; \sum_f \bar{\psi}^f_\alpha (i\gamma^\mu \partial_\mu + m_f - g\gamma^\mu A_\mu)^{\alpha\beta} \psi^f_\beta \,, \tag{8}$$

with

$$F^a_{\mu\nu} \;=\; \partial_\mu A^a_\nu - \partial_\nu A^a_\mu - g f^a_{bc} A^b_\mu A^c_\nu \,. \tag{9}$$

Here A^a_μ denotes the gluon field of colour a ($a = 1, 2, \ldots, 8$) and ψ^f_α the quark field of colour α ($\alpha = 1, 2, 3$) and flavour f; the input ('bare') quark masses are given by m_f. With the dynamics thus determined, the corresponding thermodynamics is obtained from the partition function, which is most suitably expressed as a functional path integral,

$$Z(T, V) = \int dA\, d\psi\, d\bar{\psi}\; \exp\left(- \int_V d^3x \int_0^{1/T} d\tau\; \mathcal{L}(A, \psi, \bar{\psi}) \right), \tag{10}$$

since this form involves directly the Lagrangian density defining the theory. The spatial integration in the exponent of Eq. (10) is performed over the entire spatial volume V of the system; in the thermodynamic limit it becomes infinite. The time component x_0 is "rotated" to become purely imaginary, $\tau = ix_0$, thus turning the Minkowski manifold, on which the fields A and ψ are originally defined, into a Euclidean space. The integration over τ in Eq. (10) runs over a finite slice whose thickness is determined by the temperature of the system.

¿From $Z(T, V)$, all thermodynamical observables can be calculated in the usual fashion. Thus

$$\epsilon = (T^2/V)\left(\frac{\partial \ln Z}{\partial T}\right)_V \tag{11}$$

gives the energy density, and

$$P = T\left(\frac{\partial \ln Z}{\partial V}\right)_T \tag{12}$$

the pressure. For the study of critical behaviour, long-range correlations and multi-particle interactions are of crucial importance; hence perturbation theory cannot be used. The necessary non-perturbative regularization scheme is provided by the lattice formulation of QCD [9]; it leads to a form which can be evaluated numerically by computer simulation [10].

The calculational methods and techniques of finite-temperature lattice QCD form a challenging subject on its own, which certainly surpasses the scope of this survey. We therefore restrict ourselves here to a summary of the main results obtained so far; for more details, we refer to excellent recent surveys and reviews [11–15].

The first variable considered in finite-temperature lattice QCD is the deconfinement measure provided by the Polyakov loop [16–18]

$$L(T) \sim \lim_{r\to\infty} \exp\{-V(r)/T\}, \tag{13}$$

where $V(r)$ is the potential between a static quark–antiquark pair separated by a distance r. In pure gauge theory, without light quarks, $V(r) \sim \sigma r$, where σ is the string tension; hence here $V(\infty) = \infty$, so that $L = 0$. In a deconfined medium, colour screening among the gluons leads to a melting of the string, which makes $V(r)$ finite at large r; hence now L does not vanish. It thus becomes an "order parameter" like the magnetization in the Ising model: for the temperature range $0 \leq T \leq T_c$, we have $L = 0$ and hence confinement, while for $T_c < T$ we have $L > 0$ and deconfinement. The temperature T_c at which L becomes finite thus defines the onset of deconfinement.

In the large quark mass limit, QCD reduces to pure $SU(3)$ gauge theory, which is invariant under a global Z_3 symmetry. The Polyakov loop provides a measure of the state of the system under this symmetry: it vanishes for Z_3 symmetric states and becomes finite when Z_3 is spontaneously broken. Hence the critical behaviour of

$SU(3)$ gauge theory is in the same universality class as that of Z_3 spin theory (the three-state Potts model): both are due to the spontaneous symmetry breaking of a global Z_3 symmetry [19].

For finite quark mass m_q, $V(r)$ remains finite for $r \to \infty$, since the "string" between the two colour charges "breaks" when the corresponding potential energy becomes equal to the mass M_h of the lowest hadron; beyond this point, it becomes energetically more favourable to produce an additional hadron. Hence now L no longer vanishes in the confined phase but only becomes exponentially small there,

$$L(T) \sim \exp\{-M_h/T\}; \tag{14}$$

here M_h is of the order of the ρ-mass, so that $L \sim 10^{-2}$, rather than zero. Deconfinement is thus indeed much like the insulator–conductor transition, for which the order parameter, the conductivity $\sigma(T)$, also does not really vanish for $T > 0$, but with $\sigma(T) \sim \exp\{-\Delta E/T\}$ is only exponentially small, since thermal ionization (with ionization energy ΔE) produces a small number of unbound electrons even in the insulator phase.

Figure 3a shows recent lattice results for $L(T)$ and the corresponding susceptibility $\chi_L(T) \sim \langle L^2\rangle - \langle L\rangle^2$ [20]. The calculations were performed for the case of two flavours of light quarks, using a current quark mass about four times larger than that needed for the physical pion mass. We note that $L(T)$ undergoes the expected sudden increase from a small confinement to a much larger deconfinement value. The sharp peak of $\chi_L(T)$ defines quite well the transition temperature T_c, which we shall shortly specify in physical units.

The next quantity to consider is the effective quark mass; it is measured by the expectation value of the corresponding term in the Lagrangian, $\langle\bar{\psi}\psi\rangle(T)$. In the limit of vanishing current quark mass, the Lagrangian becomes chirally symmetric

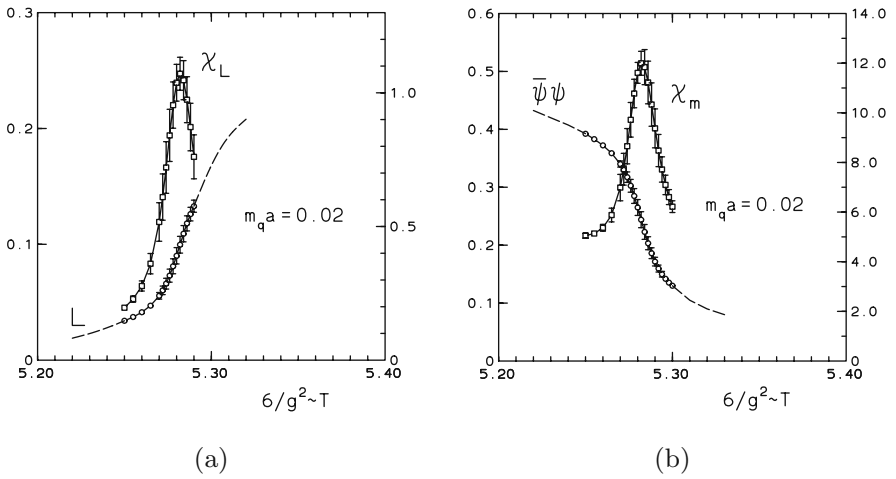

Fig. 3 Polyakov loop and chiral condensate in two-flavour QCD [20]

and $\langle\bar{\psi}\psi\rangle(T)$ the corresponding order parameter. In the confined phase, with effective constituent quark masses $M_q \simeq 0.3$ GeV, this chiral symmetry is spontaneously broken, while in the deconfined phase, at high enough temperature, we expect its restoration. In the real world, with finite pion and hence finite current quark mass, this symmetry is also only approximate, since $\langle\bar{\psi}\psi\rangle(T)$ now never vanishes at finite T.

The behaviour of $\langle\bar{\psi}\psi\rangle(T)$ and the corresponding susceptibility $\chi_m \sim \partial\langle\bar{\psi}\psi\rangle/\partial m_q$ are shown in Fig. 3b [20], calculated for the same case as above in Fig. 3a. We note here the expected sudden drop of the effective quark mass and the associated sharp peak in the susceptibility. The temperature at which this occurs coincides with that obtained through the deconfinement measure. We therefore conclude that at vanishing baryon number density, quark deconfinement and the shift from constituent to current quark mass coincide.

We thus obtain for $\mu_B = 0$ a rather well-defined phase structure, consisting of a confined phase for $T < T_c$, with $L(T) \simeq 0$ and $\langle\bar{\psi}\psi\rangle(T) \neq 0$, and a deconfined phase for $T > T_c$ with $L(T) \neq 0$ and $\langle\bar{\psi}\psi\rangle(T) \simeq 0$. The underlying symmetries associated to the critical behaviour at $T = T_c$, the Z_3 symmetry of deconfinement and the chiral symmetry of the quark mass shift, become exact in the limits $m_q \to \infty$ and $m_q \to 0$, respectively. In the real world, both symmetries are only approximate; nevertheless, we see from Fig. 3 that both associated measures retain an almost critical behaviour.

Next we come to the behaviour of energy density ϵ and pressure P at deconfinement [21, 22]. In Fig. 4, it is seen that ϵ/T^4 changes quite abruptly at the above critical temperature T_c, increasing from a low hadronic value to the one slightly below that expected for an ideal gas of massless quarks and gluons [23].

Besides the sudden increase at deconfinement, there are two further points to note. In the region $T_c < T < 2\ T_c$, there still remain strong interaction effects. As seen in Fig. 5, the "interaction measure" $\Delta = (\epsilon - 3P)/T^4$ remains sizeable and does not vanish, as it would for an ideal gas of massless constituents. In the simple

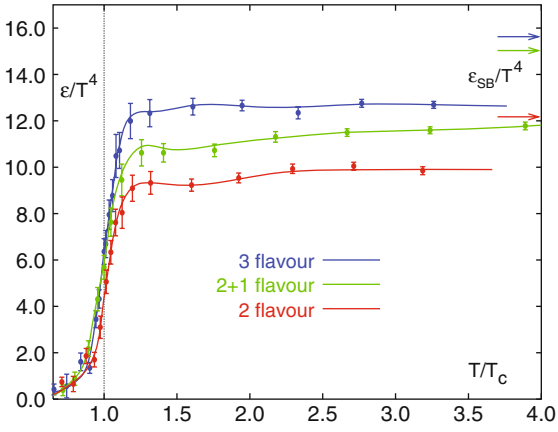

Fig. 4 Energy density vs. temperature [23]

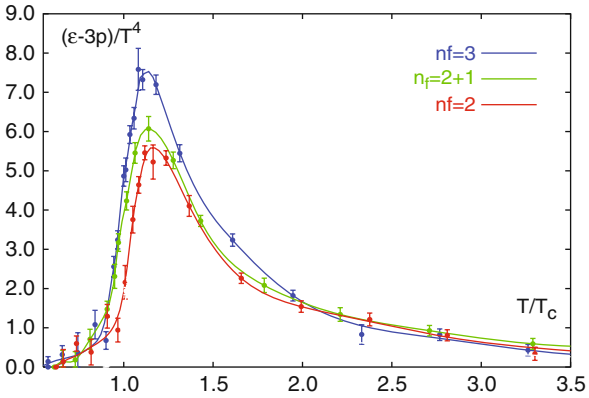

Fig. 5 Interaction measure vs. temperature [23]

model of the previous section, such an effect arose due to the bag pressure, and in actual QCD, one can also interpret it in such a fashion [8]. It has also been considered in terms of a gradual onset of deconfinement starting from high momenta [24], and most recently as a possible consequence of coloured "resonance" states [25]. The second point to note is that the thermodynamic observables remain about 10% below their Stefan–Boltzmann values (marked "SB" in Fig. 4) even at very high temperatures, where the interaction measure becomes very small. Such deviations from ideal gas behaviour can be expressed to a large extent in terms of effective "thermal" masses $m_{\rm th}$ of quarks and gluons, with $m_{\rm th} \simeq g(T)\ T$ [26–28]. Maintaining the next-to-leading order term in mass in the Stefan–Boltzmann form gives for the pressure

$$P = c\,T^4\left[1 - a\left(\frac{m_{\rm th}}{T}\right)^2\right] = c\ T^4[1 - a\ g^2(T)] \tag{15}$$

and for the energy density

$$\begin{aligned}\epsilon &= 3cT^4\left[1 - \frac{a}{3}\left(\frac{m_{\rm th}}{T}\right)^2 - \frac{2a}{3}\left(\frac{m_{\rm th}}{T}\right)\left(\frac{dm_{\rm th}}{dT}\right)\right] \\ &= 3cT^4\left[1 - a\,g^2(T) - \frac{2a\,m_{\rm th}}{3}\left(\frac{dg}{dT}\right)\right],\end{aligned} \tag{16}$$

where c and a are colour- and flavour-dependent positive constants. Since $g(T) \sim 1/\log T$, the deviations of P and ϵ from the massless Stefan–Boltzmann form vanish as $(\log\ T)^{-2}$, while the interaction measure

$$\Delta \sim \frac{1}{(\log\ T)^3} \tag{17}$$

decreases more rapidly by one power of $\log\ T$.

Finally we turn to the value of the transition temperature. Since QCD (in the limit of massless quarks) does not contain any dimensional parameters, T_c can only be obtained in physical units by expressing it in terms of some other known observables which can also be calculated on the lattice, such as the ρ-mass, the proton mass or the string tension. In the continuum limit, all different ways should lead to the same result. Within the present accuracy, they define the uncertainty so far still inherent in the lattice evaluation of QCD. Using the ρ-mass to fix the scale leads to $T_c \simeq 0.15$ GeV, while the string tension still allows values as large as $T_c \simeq 0.20$ GeV. Very recently, fine structure charmonium calculations (the mass splitting between J/ψ, χ_c and ψ') have been used to fix the dimensional scale, leading to [29–31] $T_c \simeq 190 \pm 10$ MeV. In any case, energy densities of some 1–2 GeV/fm^3 are needed in order to produce a medium of deconfined quarks and gluons.

In summary, finite-temperature lattice QCD at vanishing baryon density shows

- that there is a transition leading to colour deconfinement coincident with chiral symmetry restoration at $T_c \simeq 0.15$–0.20 GeV;
- that this transition is accompanied by a sudden increase in the energy density (the "latent heat of deconfinement") from a small hadronic value to a much larger value, about 10% below that of an ideal quark–gluon plasma.

In the following section, we want to address in more detail the nature of the critical behaviour encountered at the transition.

5 The Nature of the Transition

We begin with the behaviour for vanishing baryon density ($\mu = 0$) and come to $\mu \neq 0$ at the end. Consider the case of three quark species, u, d, s.

- In the limit $m_q \to \infty$ for all quark species, we recover pure $SU(3)$ gauge theory, with a deconfinement phase transition provided by spontaneous Z_3 breaking. It is first order, as is the case for the corresponding spin system, the three-state Potts model.
- For $m_q \to 0$ for all quark masses, the Lagrangian becomes chirally symmetric, so that we have a phase transition corresponding to chiral symmetry restoration. In the case of three massless quarks, the transition is also of first order.
- For $0 < m_q < \infty$, there is neither spontaneous Z_3 breaking nor chiral symmetry restoration. Hence in general, there is no singular behaviour, apart from the transient disappearance of the first-order discontinuities on a line of second-order transitions. Beyond this, there is no genuine phase transition, but only a "rapid cross-over" from confinement to deconfinement. The overall behaviour is summarized in Fig. 6.
- As already implicitly noted above, both "order parameters" $L(T)$ and $\chi(T)$ nevertheless show a sharp temperature variation for all values of m_q, so that it is in fact possible to define quite well a common cross-over point T_c.

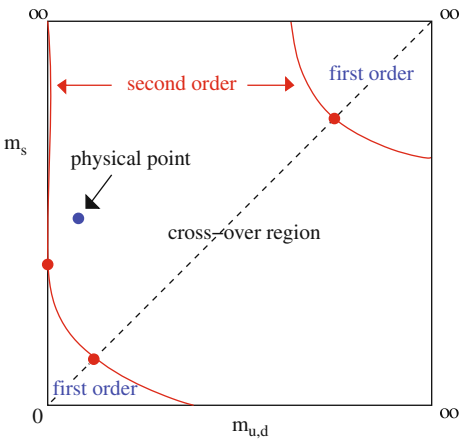

Fig. 6 The nature of thermal critical behaviour in QCD

- The nature of the transition thus depends quite sensitively on the number of flavours N_f and the quark mass values: it can be a genuine phase transition (first order or continuous), or just a rapid cross-over. The case realized in nature, the "physical point", corresponds to small u, d masses and a larger s-quark mass. It is fairly certain today that this point falls into the cross-over region.
- Finally we consider briefly the case of finite baryon density, $\mu \neq 0$, so that the number of baryons exceeds that of antibaryons. Here the conventional computer algorithms of lattice QCD break down, and hence new calculation methods have to be developed. First such attempts (reweighting [32], analytic continuation [33], power series [34]) suggest for two light quark flavours the phase diagram shown in Fig. 7. It shows non-singularity in a region between $0 \leq \mu < \mu_t$, a tricritical point at μ_t and beyond this a first-order transition. Recent lattice calculations provide some support for such behaviour; as shown in Fig. 8, the baryon density fluctuations appear to diverge for some critical value of the baryochemical potential [34].

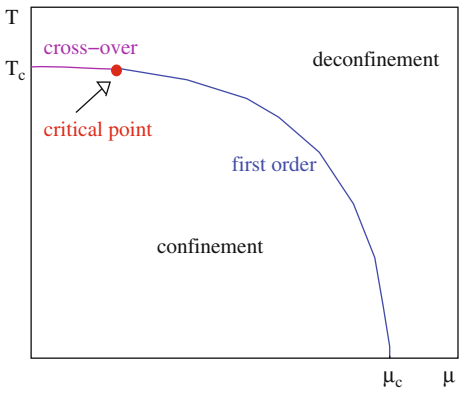

Fig. 7 Phase structure in terms of the baryon density

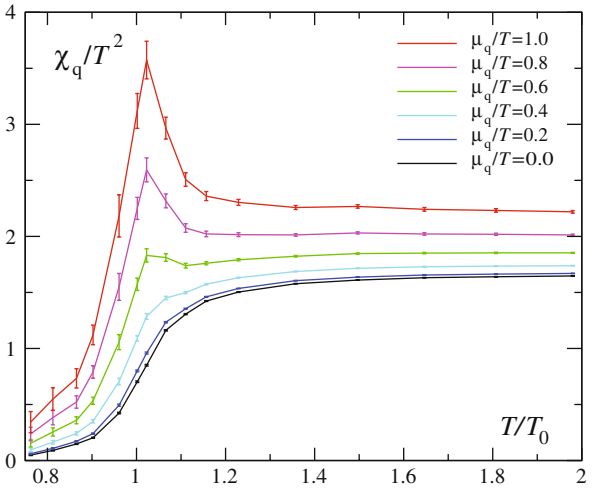

Fig. 8 Baryon number susceptibility χ_q vs. temperature

The critical behaviour for strongly interacting matter at low or vanishing baryon density, describing the onset of confinement in the early universe and in high-energy nuclear collisions, thus occurs in the rather enigmatic form of a "rapid cross-over". There is no thermal singularity and hence, in a strict sense, there are neither distinct states of matter nor phase transitions between them. So what does the often mentioned experimental search for a "new state of matter" really mean? How can a new state appear without a phase transition? Is there a more general way to define and distinguish different states of bulk media? After all, in statistical QCD one does find that thermodynamic observables – energy and entropy densities, pressure as well as the "order parameters" $L(T)$ and $\chi(T)$ – continue to change rapidly and thus define a rather clear transition line in the entire cross-over region. Why is this so, what is the mechanism which causes such a transition?

In closing this section, we consider a speculative answer to this rather fundamental question [35–37]. The traditional phase transitions, such as the freezing of water or the magnetization of iron, are due to symmetry breaking and the resulting singularities of the partition function. But there are other "transitions", such as making pudding or boiling an egg, where one also has two clearly different states but no singularities in the partition function. Such "liquid–gel" transitions are generally treated in terms of cluster formation and percolation [38]. They also correspond to critical behaviour, but the quantities that diverge are geometric (cluster size) and cannot be obtained from the partition function.

The simplest example of this phenomenon is provided by two-dimensional disk percolation, something poetically called "lilies on a pond" (see Fig. 9). More formally, One distributes small disks of area $a = \pi r^2$ randomly on a large surface $A = \pi R^2$, $R \gg r$, with overlap allowed. With an increasing number of disks, clusters begin to form. If the large surface were water and the small disks floating

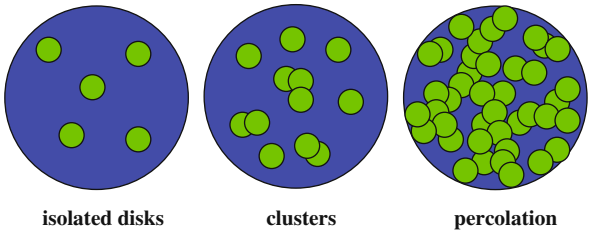

Fig. 9 Lilies on a pond

water lilies, how many lilies are needed for a cluster to connect the opposite sides, so that an ant could walk across the pond without getting its feet wet? Given N disks, the disk density is $n = N/A$. Clearly, the average cluster $S(n)$ size will increase with n. The striking feature is that it does so in a very sudden way (see Fig. 10); as n approaches some "critical value" n_c, $S(n)$ suddenly becomes large enough to span the pond. In fact, in the limit $N \to \infty$ and $A \to \infty$ at constant n, both $S(n)$ and $dS(n)/dn$ diverge for $n \to n_c$: we have percolation as a geometric form of critical behaviour.

The critical density for the onset of percolation has been determined (numerically) for a variety of different systems. In two dimensions, disks percolate at $n_c \simeq 1.13/(\pi r^2)$, i.e. when we have a little more than one disk per unit area. Because of overlap, at this point only 68% of space is covered by disks, 32% remain empty. Nevertheless, when our ant can walk across, a ship can no longer cross the pond, and vice versa. This is a special feature of two dimensions (the "fence effect"), and no longer holds for $d > 2$.

In three dimensions, the corresponding problem is one of overlapping spheres in a large volume. Here the critical density for the percolating spheres becomes $n_c \simeq 0.34/[(4\pi/3)r^3]$, with r denoting the radius of the little spheres now taking the place of the small disks we had in two dimensions. At the critical point in three dimensions, however, only 29% of space is covered by overlapping spheres, while 71% remains empty, and here both spheres and empty space form infinite connected networks. If we continue to increase the density of spheres, we reach a second critical point at $\bar{n}_c \simeq 1.24/[(4\pi/3)r^3]$, at which the vacuum stops to form an infinite

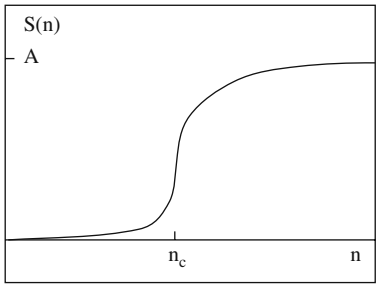

Fig. 10 Cluster size $S(n)$ vs. density n

network: Now 71% of space is covered by spheres, and for $n > \bar{n}_c$, only isolated vacuum bubbles remain.

Let us then consider hadrons of intrinsic size $V_h = (4\pi/3)r_h^3$, with $r_h \simeq 0.8$ fm. In three-dimensional space, the formation of a connected large-scale cluster first occurs at the density

$$n_c = \frac{0.34}{V_h} \simeq 0.16 \text{ fm}^{-3}. \tag{18}$$

This point specifies the onset of hadronic matter, in contrast to a gas of hadrons, and it indeed correctly reproduces the density of normal nuclear matter. However, at this density the vacuum as connected medium also still exists (see Fig. 11a).

To prevent infinite connecting vacuum clusters, a much higher hadron density is needed, as we saw above. Measured in hadronic size units, the vacuum disappears for

$$\bar{n}_c = \frac{1.24}{V_h} \simeq 0.56 \text{ fm}^{-3}, \tag{19}$$

schematically illustrated in Fig. 11b. If we assume that at this point, the medium is of an ideal gas of all known hadrons and hadronic resonances, then we can calculate the temperature of the gas at the density $\bar{n}_c$: $n_{\text{res}}(T_c) = \bar{n}_c$ implies $T_c \simeq 170$ MeV, which agrees quite well with the value of the deconfinement temperature found in lattice QCD for $\mu = 0$.

We can thus use percolation to define the states of hadronic matter. At low density, we have a hadron gas, which at the percolation point n_c turns into connected hadronic matter. When this becomes so dense that only isolated vacuum bubbles survive, at $\bar{n}_c$, it turns into a quark–gluon plasma. This approach provides the correct values both for the density of standard nuclear matter and for the deconfinement transition temperature.

Such considerations may in fact well be of a more general nature than the problem of states and transitions in strong interaction physics. The question of

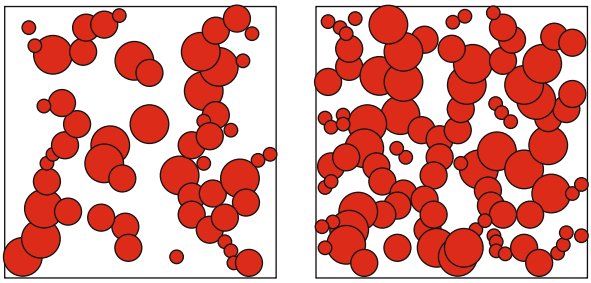

(a) (b)

Fig. 11 Hadron and vacuum percolation thresholds

whether symmetry or connectivity (cluster formation) determines the different states of many-body systems has intrigued theorists in statistical physics for a long time [39, 40]. The lesson learned from spin systems appears to be that cluster formation and the associated critical behaviour are the more general features, which under certain conditions can also lead to thermal criticality, i.e. singular behaviour of the partition function.

6 Probing the Quark–Gluon Plasma

We thus find that at sufficiently high temperatures and/or densities, strongly interacting matter will be in a new state, consisting of deconfined quarks and gluons. How can we probe the properties of this state, how can we study its features as a function of temperature and density? We want to address this question here in the sense of Einstein, who told us to make things as simple as possible, but not simpler. So let us start with a theorist's experimental set-up, consisting of a volume of unknown strongly interacting matter and a Bunsen burner to heat it up and thus increase its energy density.

There are a number of methods we can use to study the unknown matter in our container:

- hadron radiation,
- electromagnetic radiation,
- dissociation of a passing quarkonium beam,
- energy loss of a passing hard jet.

All methods will be dealt with in detail during the course of this school. Here we just want to have a brief first look.

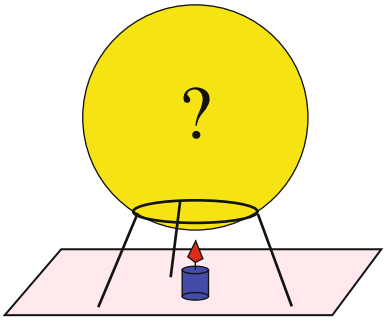

First of all, we note that the unknown medium radiates, since its temperature is (by assumption) much higher than that of its environment. Hadron radiation means that we study the emission of hadrons consisting of light (u, d, s) quarks; their size is given by the typical hadronic scale of about 1 fm $\simeq$ 1/(200 MeV). Since they cannot exist inside a deconfined medium, they are formed at the transition surface between the QGP and the physical vacuum. The physics of this surface is independent of the

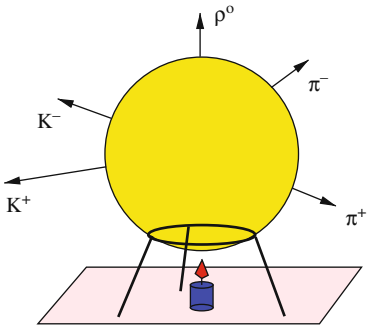

Fig. 12 Hadron radiation

interior – the transition from deconfinement to confinement occurs at a temperature $T \simeq 160$–180 MeV, no matter how hot the QGP initially was or still is in the interior of our volume. This is similar to having hot water vapour inside a glass container kept in a cool outside environment: at the surface, the vapour will condense into liquid, at a temperature of 100°C – no matter how hot it is in the middle. As a result, studying soft hadron production in high-energy collisions will provide us with information about the hadronization transition, but not about the hot QGP. The striking observation that the relative hadron abundances in all high-energy collisions are the same, from e^+e^- annihilation to hadron–hadron and heavy-ion interactions, and that they correspond to those of an ideal resonance gas at $T \simeq 170$ MeV, is a direct consequence of this fact [2, 3, 41–45].

Hadron radiation, as we have pictured it here, is oversimplified from the point of view of heavy-ion interactions. In the case of static thermal radiation, at the point of hadronization all information about the earlier stages of the medium is lost, as we had noted above. If, however, the early medium has a very high energy density and can expand freely, i.e. is not constrained by the walls of a container, then this expansion will lead to a global hydrodynamic flow [46–48], giving an additional overall boost in momentum to the produced hadrons: they will experience a "radial flow" depending on the initial energy density (see Fig. 13). Moreover, if the initial conditions were not spherically symmetric, as is in fact the cases in peripheral heavy-ion collisions, the difference in pressure in different spatial directions will lead to a further "directed" or "elliptic" flow. Since both forms of flow thus do depend on the initial conditions, flow studies of hadron spectra can, at least in principle, provide information about the earlier, pre-hadronic stages.

The unknown hot medium also radiates electromagnetically, i.e. it emits photons and dileptons (e^+e^- or $\mu^+\mu^-$ pairs) [49, 50]. These are formed either by the interaction of quarks and/or gluons, or by quark–antiquark annihilation. Since the photons and leptons interact only electromagnetically, they will, once they are formed, leave the medium without any further modification. Hence their spectra provide information about the state of the medium at the place or the time they were formed, and this can be in its deep interior or at very early stages of its evolution. Photons

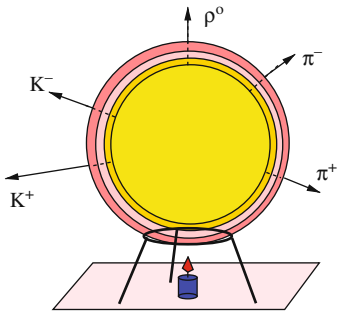

Fig. 13 Radial flow and hadron radiation

and dileptons thus do provide a possible probe of the hot QGP. The only problem is that they can be formed anywhere and at any time, even at the cool surface or by the emitted hadrons. The task in making them a viable tool is therefore the identification of the hot "thermal" radiation indeed emitted by the QGP.

Both electromagnetic and hadronic radiations are emitted by the medium itself, and they provide some information about the state of the medium at the time of emission. Another possible approach is to test the medium with an outside probe, and here we have two so far quite successful examples, quarkonia and jets.

Quarkonia are a special kind of hadrons, bound states of a heavy (c or b) quark and its antiquark. For the ground states J/ψ and Υ the binding energies are around 0.6 and 1.2 GeV, respectively, and thus much larger than the typical hadronic scale $\Lambda \sim 0.2$ GeV; as a consequence, they are also much smaller, with radii of about 0.1 and 0.2 fm. It is therefore expected that they can survive in a quark–gluon plasma through some range of temperatures above T_c, and this is in fact confirmed by lattice studies [51, 52].

The higher excited quarkonium states are less tightly bound and hence larger, although their binding energies are in general still larger, their radii still smaller, than those of the usual light quark hadrons. Take the charmonium spectrum as example:

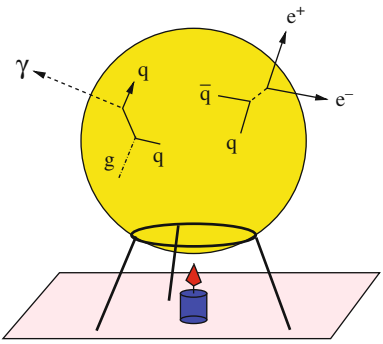

Fig. 14 Electromagnetic radiation

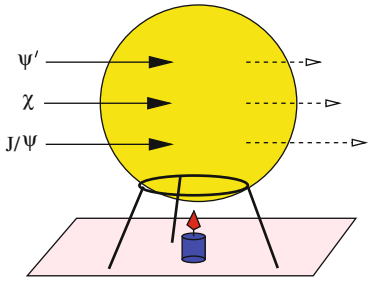

Fig. 15 Charmonium suppression

the radius of the J/ψ(1S) is about 0.2 fm, that of the χ_c(1P) about 0.3 fm, and that of the ψ'(2S) 0.4 fm. Since deconfinement is related to colour screening, the crucial quantity for dissociation of a bound state is the relation of binding to screening radius. We therefore expect that the different charmonium states have different "melting temperatures" in a quark–gluon plasma. Hence the spectral analysis of in-medium quarkonium dissociation should provide a QGP thermometer [53].

As probe, we then shoot beams of specific charmonia (J/ψ, χ_c, ψ') into our medium sample and check which comes out on the other side (Fig. 15). If all three survive, we have an upper limit on the temperature, and by checking at just what temperature the ψ', the χ_c and the J/ψ are dissociated, we have a way of specifying the temperature of the medium [54], as illustrated in Fig. 16.

Another possible probe is to shoot an energetic parton, quark or gluon, into our medium to be tested. How much energy it loses when it comes out on the other side will tell us something about the density of the medium [55–58]. In particular, the density increases by an order of magnitude or more in the course of the deconfinement transition, and so the energy loss of a fast passing colour charge is expected to increase correspondingly (Fig. 17). Moreover, for quarks, the amount of jet quenching is predicted to depend on the mass of the quarks.

In using quarkonia and jets as tools, we have so far considered a simplified situation, in which we test a given medium with distinct external probes. In heavy-ion collisions, we have to create the probe in the same collision in which we create

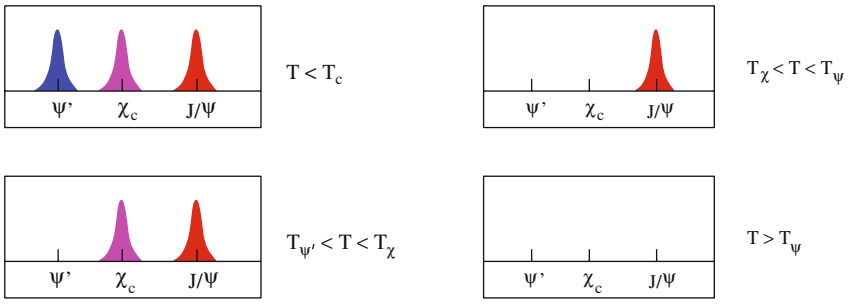

Fig. 16 Charmonia as thermometer

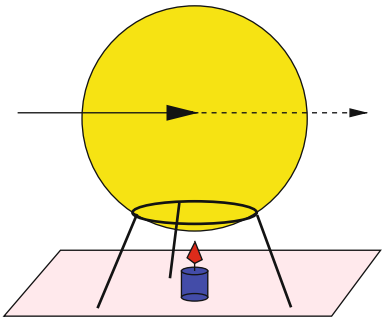

Fig. 17 Jet quenching

the medium. Quarkonia and jets (as well as open charm/beauty and very energetic dileptons and photons) constitute so-called hard probes, whose production occurs at the very early stages of the collision, before the medium is formed; they are therefore indeed present when it appears. Moreover, their production involves large energy/momentum scales and can be calculated by perturbative QCD techniques and tested in pp/pA collisions, so that behaviour and strength of such outside "beams" or "colour charges" are indeed quite well known.

7 Summary

We have shown that strong interaction thermodynamics leads to a well-defined transition from hadronic matter to a plasma of deconfined quarks and gluons. For vanishing baryon number density, the transition leads to simultaneous deconfinement and chiral symmetry restoration at $T_c \simeq 160$–$190\,\mathrm{MeV}$. At this point, the energy density increases by an order of magnitude through the latent heat of deconfinement.

The properties of the new medium above T_c, the quark–gluon plasma, can be studied through hard probes (quarkonium and open charm/beauty production, jet quenching) and electromagnetic radiation (photons and dileptons). Information about transition aspects is provided by light hadron radiation; through hydrodynamic flow, this can also shed light on pre-hadronic features.

References

1. I. Ya. Pomeranchuk: Doklady Akad. Nauk. SSSR **78** (1951) 2
2. R. Hagedorn: Nuovo Cim. Suppl. **3**, 147 (1965) 2, 16
3. R. Hagedorn: Nuovo Cim. **56A**, 1027 (1968) 2, 16
4. K. Bardakci and S. Mandelstam: Phys. Rev. **184**, 1640 (1969) 2
5. S. Fubini and G. Veneziano: Nuovo Cim. **64A**, 811 (1969)
6. N. Cabbibbo and G. Parisi: Phys. Lett. **59B**, 67 (1975) 2
7. H. Satz: Fortschr. Phys. **33**, 259 (1985) 3
8. M. Asakawa and T. Hatsuda: Nucl. Phys. **A 610**, 470c (1996) 5, 9
9. K. Wilson: Phys. Rev. **D 10**, 2445 (1974) 6

10. M. Creutz: Phys. Rev. **D 21**, 2308 (1980) 6
11. I. Montvay and G. Münster: *Quantum Fields on a Lattice*, Cambridge University Press, Cambridge (1994) (for textbooks, surveys and further literature) 6
12. H.J. Rothe: *Lattice Gauge Theory*, Lecture Notes in Physics, vol. 59. World Scienfic, Singapore (1997) (for textbooks, surveys and further literature)
13. F. Karsch: *Lattice QCD at High Temperature and Density*. In: W. Plessas and L. Mathelitsch (eds.) Lecture Notes in Physics, vol. 583, pp. 209–249, Springer, Berlin Heidelberg New York (2002) (for textbooks, surveys and further literature)
14. F. Karsch and E. Laermann: Thermodynamics and In-Medium Hadron Properties from Lattice QCD. In: R.C. Hwa and X.-N. Wang (eds.) *Quark-Gluon Plasma 3*, pp. 1–59, World Scientific, Singapore (2004) (for textbooks, surveys and further literature)
15. F. Karsch: arXiv[hep-lat] 0711.0661 and 0711.0656 (for textbooks, surveys and further literature) 6
16. L.D. McLerran and B. Svetitsky: Phys. Lett. **98B**, 195 (1981) 6
17. L.D. McLerran and B. Svetitsky: Phys. Rev. **D 24**, 450 (1981)
18. J. Kuti, J. Polónyi and K. Szlachányi: Phys. Lett. **98B**, 199 (1981) 6
19. B. Svetitsky and L.G. Yaffe: Nucl. Phys. **B 210** [FS6], 423 (1982) 7
20. F. Karsch and E. Laermann: Phys. Rev. **D 50**, 6954 (1994) 7, 8
21. J. Engels et al.: Phys. Lett. **101B**, 89 (1981) 8
22. J. Engels et al.: Nucl. Phys. **B 205**, 545 (1982) 8
23. F. Karsch, E. Laermann and A. Peikert: Phys. Lett. **B 478**, 447 (2000) 8, 9
24. J. Engels et al.: Z. Phys. **C 42**, 341 (1989) 9
25. E. Shuryak and I. Zahed: Phys. Rev. **C 70**, 021901 (2004) 9
26. J. Engels et al.: Z. Phys. **C 42**, 341 (1989) 9
27. V. Goloviznin and H. Satz: Z. Phys. **C 57**, 671 (1993)
28. F. Karsch, A. Patkos and P. Petreczky: Phys. Lett. **B 401**, 69 (1997) 9
29. C. Aubin et al. [MILC Collaboration]: Phys. Rev. **D 70**, 094505 (2004) 10
30. A. Gray et al.: Phys. Rev. **D 72**, 0894507 (2005)
31. M. Cheng et al.: arXiv:hep-lat/0608013 10
32. Z. Fodor and S. Katz: JHEP **0203**, 014 (2002) 11
33. M.-P. Lombardo: Phys. Rev. **D 67**, 014505 (2003) 11
34. C.R. Allton et al.: Phys. Rev. **D 68**, 014507 (2003) 11
35. G. Baym: Physica **96A**, 131 (1979) 12
36. T. Çelik, F. Karsch and H. Satz: Phys. Lett. **97B**, 128 (1980)
37. H. Satz: Nucl. Phys. **A 642**, 130c (1998) 12
38. D. Stauffer and A. Aharony: *Introduction to Percolation Theory* Taylor and Francis, London (1994) 12
39. C.M. Fortuin and P.W. Kasteleyn: J. Physical Soc. Japan **26**(Suppl.), 11 (1969) 15
40. C.M. Fortuin and P.W. Kasteleyn: Physica **57**, 536 (1972) 15
41. J. Cleymans and H. Satz: Z. Phys. **C 57**, 135 (1993) 16
42. K. Redlich et al.: Nucl. Phys. **A 566**, 391 (1994)
43. P. Braun-Munzinger et al.: Phys. Lett. **B 344**, 43 (1995)
44. F. Becattini: Z. Phys. **C 69**, 485 (1996)
45. F. Becattini and U. Heinz: Z. Phys. **C 76**, 268 (1997) 16
46. L.D. Landau: Izv. Akad. Nauk Ser. Fiz. **17**, 51 (1953) 16
47. J.-P. Blaizot and J.-Y. Ollitrault: Title. In: R.C. Hwa (ed.) *Quark-Gluon Plasma 2*, World Scientific, Singapore (1990)
48. U. Heinz, P.F. Kolb and J. Sollfrank, Phys. Rev. **C 62**, 054909 (2000) 16
49. E.V. Shuryak: Phys. Rep. **61**, 71 (1980) 16
50. K. Kajantie and H.I. Miettinen: Z. Phys. **C 9**, 341 (1981) 16
51. S. Datta et al.: Phys. Rev. **D 69**, 094507 (2004) 17
52. G. Aarts et al.: Phys. Rev. **D 67**, 0945413 (2007) (literature given there) 17
53. T. Matsui and H. Satz: Phys. Lett. **B 178**, 416 (1986) 18

54. F. Karsch and H. Satz: Z. Phys. **C 51**, 209 (1991) 18
55. J.D. Bjorken: Fermilab-Pub-82/59-THY (1982) (Erratum) 18
56. M. Gyulassy and X.-N. Wang: Nucl. Phys. **B 420**, 583 (1994)
57. R. Baier et al.: Phys. Lett. **B 345**, 277 (1995)
58. B.G. Zakharov: JETP Lett. **63**, 952 (1996) 18

Global Properties of Nucleus–Nucleus Collisions

Michael Kliemant, Raghunath Sahoo, Tim Schuster, and Reinhard Stock

1 Introduction

QCD as a theory of extended, strongly interacting matter is familiar from big bang evolution which, within the time interval from electro-weak decoupling (10^{-12} s) to hadron formation (5×10^{-6} s), is dominated by the expansion of quark–gluon matter, a color conducting plasma that is deconfined. In the 1970s deconfinement was predicted [1–5] to arise from the newly discovered "asymptotic freedom" property of QCD; i.e., the plasma was expected to be a solution of perturbative QCD at asymptotically high square momentum transfer Q^2, or temperature T. Thus the quark–gluon plasma (QGP) was seen as a dilute gas of weakly coupled partons. This picture may well hold true at temperatures in the GeV to TeV range. However, it was also known since R. Hagedorns work [6] that hadronic matter features a phase boundary at a very much lower temperature, $T(H) = 170\,\mathrm{MeV}$. As it was tempting to identify this temperature with that of the cosmological hadronization transition, thus suggesting $T(H) = T(\mathrm{crit})$, the QGP state must extend downward to such a low temperature, with $Q^2 \ll 1\,\mathrm{GeV}^2$, and far into the non-perturbative sector of QCD, and very far from asymptotic freedom. The fact that, therefore, the confinement–deconfinement physics of QCD, occurring at the parton–hadron phase boundary, had to be explained in terms other than a dilute perturbative parton gas was largely ignored until rather recently, when laboratory experiments concerning the QGP had reached maturity.

In order to recreate matter at the corresponding high energy density in the terrestrial laboratory, one collides heavy nuclei (also called "heavy ions") at ultra-

M. Kliemant (✉)
Goethe-Universität Frankfurt, Germany, kliemant@ikf.uni-frankfurt.de

R. Sahoo
SUBATECH-Ecole des Mines de Nantes, France, raghu@subatech.in2p3.fr

T. Schuster
Goethe-Universität Frankfurt, Germany, schuster@ikf.uni-frankfurt.de

R. Stock
Goethe-Universität Frankfurt, Germany, stock@ikf.uni-frankfurt.de

Kliemant, M. et al.: *Global Properties of Nucleus–Nucleus Collisions*. Lect. Notes Phys. **785**, 23–103 (2010)
DOI 10.1007/978-3-642-02286-9_2

relativistic energies. Quantum chromodynamics predicts [2–4, 7–10] a phase transformation to occur between deconfined quarks and confined hadrons. At near-zero net baryon density (corresponding to big bang conditions) non-perturbative Lattice QCD places this transition at an energy density of about 1 GeV/fm^3, and at a critical temperature, $T_{\mathrm{crit}} \approx 170$ MeV [10–15]. The ultimate goal of the physics with ultra-relativistic heavy ions is to locate this transition, elaborate its properties, and gain insight into the detailed nature of the deconfined QGP phase that should exist above. What is meant by the term "ultrarelativistic" is defined by the requirement that the reaction dynamics reaches or exceeds the critical density $\epsilon \approx 1\,\mathrm{GeV/fm^3}$. Required beam energies turn out [14, 15] to be $\sqrt{s} \geq 10$ GeV, and various experimental programs have been carried out or are being prepared at the CERN SPS (up to about 20 GeV), at the BNL RHIC collider (up to 200 GeV) and finally reaching up to 5.5 TeV at the LHC of CERN.

QCD confinement–deconfinement is of course not limited to the domain that is relevant to cosmological expansion dynamics, at very small excess of baryon over anti-baryon number density and, thus, near zero baryo-chemical potential μ_B. In fact, modern QCD suggests [16–19] a detailed phase diagram of QCD matter and its states, in the plane of T and baryo-chemical potential μ_B. For a map of the QCD matter phase diagram we are thus employing the terminology of the grand canonical Gibbs ensemble that describes an extended volume V of partonic or hadronic matter at temperature T. In it, total particle number is not conserved at relativistic energy, due to particle production–annihilation processes occurring at the microscopic level. However, the probability distributions (partition functions) describing the particle species abundances have to respect the presence of certain, to be conserved net quantum numbers (i), notably nonzero net baryon number and zero net strangeness and charm. Their global conservation is achieved by a thermodynamic trick, adding to the system Lagrangian a so-called Lagrange multiplier term, for each of such quantum number conservation tasks. This procedure enters a "chemical potential" μ_i that modifies the partition function via an extra term $\exp(-\mu_i/T)$ occurring in the phase space integral (see Section 4 for detail). It modifies the canonical "punishment factor" $\exp(-E/T)$, where E is the total particle energy in vacuum, to arrive at an analogous grand canonical factor for the extended medium of $\exp(-E/T - \mu_i/T)$. This concept is of prime importance for a description of the state of matter created in heavy ion collisions, where net-baryon number (valence quarks) carrying objects are considered – extended "fireballs" of QCD matter. The same applies to the matter in the interior of neutron stars. The corresponding conservation of net baryon number is introduced into the grand canonical statistical model of QCD matter via the "baryo-chemical potential" μ_B.

We employ this terminology to draw a phase diagram of QCD matter in Fig. 1, in the variables T and μ_B. Note that μ_B is high at low energies of collisions creating a matter fireball. In a head-on collision of two mass 200 nuclei at $\sqrt{s} = 15$ GeV the fireball contains about equal numbers of newly created quark–antiquark pairs (of zero net baryon number) and of initial valence quarks. The accommodation of the latter, into created hadronic species, thus requires a formidable redistribution task of net baryon number, reflecting a high value of μ_B. Conversely, at LHC energy

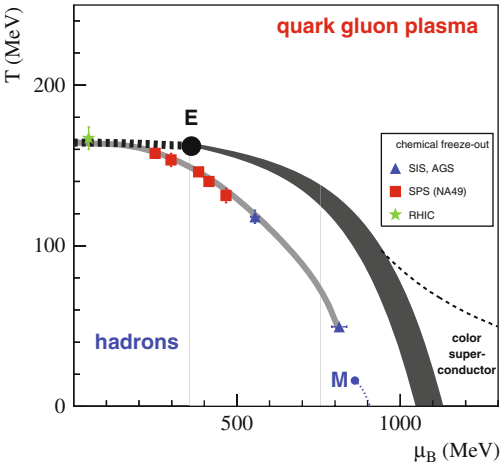

Fig. 1 Sketch of the QCD matter phase diagram in the plane of temperature T and baryo-chemical potential μ_B. The parton–hadron phase transition line from lattice QCD [14–19] ends in a critical point E. A cross over transition occurs at smaller μ_B. Also shown are the points of hadrochemical freeze-out from the grand canonical statistical model

($\sqrt{s} = 5.5$ TeV in Pb+Pb collisions), the initial valence quarks constitute a mere 5% fraction of the total quark density, correspondingly requiring a small value of μ_B. In the extreme, big bang matter evolves toward hadronization (at $T = 170$ MeV) featuring a quark over antiquark density excess of 10^{-9} only, resulting in $\mu_B \approx 0$.

Note that the limits of existence of the hadronic phase are reached not only by temperature increase, to the so-called Hagedorn value T_H (which coincides with $T_{\rm crit}$ at $\mu_B \to 0$), but also by density increase to $\varrho > (5-10)\,\varrho_0$: "cold compression" beyond the nuclear matter ground state baryon density ϱ_0 of about $0.16\,\mathrm{B/fm^3}$. We are talking about the deep interior sections of neutron stars or about neutron star mergers [20–22]. A sketch of the present view of the QCD phase diagram [16–19] is given in Fig. 1. It is dominated by the parton–hadron phase transition line that interpolates smoothly between the extremes of predominant matter heating (high T, low μ_B) and predominant matter compression ($T \to 0$, $\mu_B > 1$ GeV). Onward from the latter conditions, the transition is expected to be of first order [23] until the critical point of QCD matter is reached at $200 \le \mu_B(E) \le 500$ MeV. The relatively large position uncertainty reflects the preliminary character of Lattice QCD calculations at finite μ_B [16–19]. Onward from the critical point, E, the phase transformation at lower μ_B is a cross over [19]. However, the position of the critical point in the phase diagram is still hypothetical in nature.

We note, however, that these estimates represent a major recent advance of QCD lattice theory which was, for two decades, believed to be restricted to the $\mu_B = 0$ situation. Onward from the critical point, toward lower μ_B, the phase transformation should acquire the properties of a rapid cross over [24], thus also including the case of primordial cosmological expansion. This would finally rule out former ideas,

based on the picture of a violent first-order "explosive" cosmological hadronization phase transition, that might have caused nonhomogeneous conditions, prevailing during early nucleo-synthesis [25, 26], and fluctuations of global matter distribution density that could have served as seedlings of galactic cluster formation [27]. However, it needs to be stressed that the conjectured order of phase transformation, occurring along the parton–hadron phase boundary line, has not been unambiguously confirmed by experiment, as of now.

On the other hand, the *position* of the QCD phase boundary at low μ_B has, in fact, been located by the hadronization points in the T, μ_B planes that are also illustrated in Fig. 1. They are obtained from statistical model analysis [28] of the various hadron multiplicities created in nucleus–nucleus collisions, which results in a $[T,\ \mu_B]$ determination at each incident energy, which ranges from SIS via AGS and SPS to RHIC energies, i.e., $3 \leq \sqrt{s} \leq 200\,\mathrm{GeV}$. Toward low μ_B these hadronic freeze-out points merge with the lattice QCD parton–hadron coexistence line: hadron formation coincides with hadronic species freeze-out. These points also indicate the μ_B domain of the phase diagram which is accessible to relativistic nuclear collisions. The domain at $\mu_B \geq 1.5\,\mathrm{GeV}$ which is predicted to be in a further new phase of QCD featuring color-flavor locking and color superconductivity [29, 30] will probably be accessible only to astrophysical observation.

One may wonder how states and phases of matter in thermodynamical equilibrium – as implied by a description in grand canonical variables – can be sampled via the dynamical evolution of relativistic nuclear collisions. Employing heavy nuclei, $A \approx 200$, as projectiles/targets or in colliding beams (RHIC, LHC), transverse dimensions of the primordial interaction volume do not exceed about $8\,fm$, and strong interaction ceases after about $20\,fm/c$. We note, for now, that the time and dimension scale of primordial perturbative QCD interaction at the microscopic partonic level amounts to subfractions of $1\,fm/c$, the latter scale, however, being representative of non-perturbative processes (confinement, "string" formation, etc.). The A+A fireball size thus exceeds, by far, the elementary non-perturbative scale. An equilibrium quark–gluon plasma represents an extended non-perturbative QCD object, and the question whether its relaxation time scale can be provided by the expansion time scale of an A+A collision needs careful examination. Reassuringly, however, the hadrons that are supposedly created from such a preceding non-perturbative QGP phase at top SPS and RHIC energies do in fact exhibit perfect hydrodynamic and hadrochemical equilibrium, the derived $[T,\ \mu_B]$ values [28] thus legitimately appearing in the phase diagram, Fig. 1.

In the present book we will order the physics observables to be treated, with regard to their origin from successive stages that characterize the overall dynamical evolution of a relativistic nucleus–nucleus collision. In rough outline this evolution can be seen to proceed in three major steps. An initial period of matter compression and heating occurs in the course of interpenetration of the projectile and target baryon density distributions. Inelastic processes occurring at the microscopic level convert initial beam longitudinal energy to new internal and transverse degrees of freedom, by breaking up the initial baryon structure functions. Their partons thus acquire virtual mass, populating transverse phase space in the course of inelastic

perturbative QCD shower multiplication. This stage should be far from thermal equilibrium, initially. However, in step 2, inelastic interaction between the two arising parton fields (opposing each other in longitudinal phase space) should lead to a pile-up of partonic energy density centered at mid-rapidity (the longitudinal coordinate of the overall center of mass). Due to this mutual stopping down of the initial target and projectile parton fragmentation showers, and from the concurrent decrease of parton virtuality (with decreasing average square momentum transfer Q^2), there results a slowdown of the time scales governing the dynamical evolution. Equilibrium could be approached here, the system "lands" on the T, μ plane of Fig. 1, at temperatures of about 300 and 200 MeV at top RHIC and top SPS energies, respectively. The third step, system expansion and decay, thus occurs from well above the QCD parton–hadron boundary line. Hadrons and hadronic resonances then form, which decouple swiftly from further inelastic transmutation so that their yield ratios become stationary ("frozen-out"). A final expansion period dilutes the system to a degree such that strong interaction ceases all together.

It is important to note that the above description, in terms of successive global stages of evolution, is only valid at very high energy, e.g., at and above top RHIC energy of $\sqrt{s} = 200\,\text{GeV}$. At this energy the target–projectile interpenetration time $2R/\gamma = 0.12\,\text{fm}/c$, and thus the interpenetration phase is over when the supposed next phase (perturbative QCD shower formation at the partonic level by primordial, "hard" parton scattering) settles, at about $0.25\,\text{fm}/c$. "Hard" observables (heavy flavor production, jets, high-p_T hadrons) all originate from this primordial interaction phase. On the other hand it is important to realize that at top SPS energy, $\sqrt{s} = 17.3\,\text{GeV}$, global interpenetration takes as long as $1.5\,\text{fm}/c$, much longer than microscopic shower formation time. There is thus no global, distinguishable phase of hard QCD mechanisms: they are convoluted with the much longer interpenetration time. During that it is thus impossible to consider a global physics of the interaction volume, or any equilibrium. Thus we can think of the dynamical evolution in terms of global "states" of the system's dynamical evolution (such as local or global equilibrium) only after about 2–3 fm/c, just before bulk hadronization sets in. Whereas at RHIC, and even more ideally so at the LHC, the total interaction volume is "synchronized" at times below $0.5\,\text{fm}/c$, such that a hydrodynamic description becomes possible: we can expect that "flow" of partons sets in at this time, characterized by extremely high parton density. The dynamics at such early time can thus be accessed in well-defined variables (e.g., elliptic flow or jet quenching).

In order to verify in detail this qualitative overall model, and to ascertain the existence (and to study the properties) of the different states of QCD that are populated in sequence, one seeks observable physics quantities that convey information imprinted during distinct stages of the dynamical evolution and "freezing-out" without significant obliteration by subsequent stages. Ordered in sequence of their formation in the course of the dynamics, the most relevant such observables are briefly characterized below:

1. Suppression of J/Ψ and Y production by Debye screening in the QGP. These vector mesons result from primordial, pQCD production of $c\overline{c}$ and $b\overline{b}$ pairs

that would hadronize unimpeded in elementary collisions but are broken up if immersed into a npQCD deconfined QGP, at certain characteristic temperature thresholds.

2. Suppression of di-jets which arise from primordial $q\overline{q}$ pair production fragmenting into partonic showers (jets) in vacuum but being attenuated by QGP-medium-induced gluonic bremsstrahlung: jet quenching in A+A collisions.

   a) A variant of this: *any* primordial hard parton suffers a high, specific loss of energy when traversing a deconfined medium: high p_T suppression in A+A collisions.

3. Hydrodynamic collective motion develops with the onset of (local) thermal equilibrium. It is created by partonic pressure gradients that reflect the initial collisional impact geometry via non-isotropies in particle emission called "directed" and "elliptic" flow. The latter reveals properties of the QGP, seen here as an ideal partonic fluid.

   a) Radial hydrodynamical expansion flow ("Hubble expansion") is a variant of the above that occurs in central, head-on collisions with cylinder symmetry, as a consequence of an isentropic expansion. It should be sensitive to the mixed-phase conditions characteristic of a first-order parton–hadron phase transition.

4. Hadronic "chemical" freeze-out fixes the abundance ratios of the hadronic species into an equilibrium distribution. Occuring very close to, or at hadronization, it reveals the dynamical evolution path in the $[T, \mu_B]$ plane and determines the critical temperature and density of QCD. The yield distributions in A+A collisions show a dramatic strangeness enhancement effect, characteristic of an extended QCD medium.
5. Fluctuations, from one collision event to another (and even within a single given event), can be quantified in A+A collisions due to the high charged hadron multiplicity density (of up to 600 per rapidity unit at top RHIC energy). Such event-by-event (ebye) fluctuations of pion rapidity density and mean transverse momentum (event "temperature"), as well as event-wise fluctuations of the strange to non-strange hadron abundance ratio (may) reflect the existence and position of the conjectured critical point of QCD (Fig. 1).
6. Two particle Bose–Einstein correlations are the analog of the Hanbury-Brown, Twiss (HBT) effect of quantum optics. They result from the last interaction experienced by mesons, i.e., from the global decoupling stage. Owing to a near-isentropic hadronic expansion they reveal information on the overall space–time development of the "fireball" evolution.

In an overall view the first group of observables (1–2a) is anchored in established pQCD physics that is well known from theoretical and experimental analysis of elementary collisions (e^+e^- annihilation, pp and $p\overline{p}$ data). In fact, the first generation of high Q^2 baryon collisions, occurring at the microscopic level in A+A collisions, should closely resemble such processes. However, their primary partonic

products do not escape into pQCD vacuum but get attenuated by interaction with the concurrently developing extended high-density medium , thus serving as diagnostic tracer probes of that state. The remaining observables capture snapshots of the bulk matter medium itself. After initial equilibration we may confront elliptic flow data with QCD during the corresponding partonic phase of the dynamical evolution employing thermodynamic [31] and hydrodynamic [32–35] models of a high-temperature parton plasma. The hydro-model stays applicable well into the hadronic phase. Hadron formation (confinement) occurs in between these phases (at about 5 microseconds time in the cosmological evolution). In fact relativistic nuclear collision data may help to finally pin down the mechanism(s) of this fascinating QCD process [36–40] as we can vary the conditions of its occurrence, along the parton–hadron phase separation line of Fig. 1, by proper choice of collisional energy $\sqrt{s}$, and system size A, while maintaining the overall conditions of an extended imbedding medium of high energy density within which various patterns [16–19, 23, 24] of the hadronization phase transition may establish. The remaining physics observables (3a, 5, and 6 above) essentially provide for auxiliary information about the bulk matter system as it traverses (and emerges from) the hadronization stage, with special emphasis placed on manifestations of the conjectured critical point.

The observables from 1 to 4 above will all be treated, in detail, in this book. We shall focus here on the bulk matter expansion processes of the primordially formed collisional volume, as reflected globally in the population patterns of transverse and longitudinal (rapidity) phase space (Sect. 3), and on the transition from partons to hadrons and on hadronic hadro-chemical decoupling, resulting in the observed abundance systematics of the hadronic species (Section 4). These Sections will be preceded by a detailed recapitulation of relativistic kinematics, notably rapidity, to which we shall turn now.

2 Relativistic Kinematics

2.1 Description of Nucleus–Nucleus Collisions in Terms of Light-Cone Variables

In relativistic nucleus–nucleus collisions, it is convenient to use kinematic variables which take simple forms under Lorentz transformations for the change of frame of reference. A few of them are the light-cone variables x_+ and x_-, the rapidity and pseudorapidity variables, y and η. A particle is characterized by its 4-momentum, $p_\mu = (E, \mathbf{p})$. In fixed-target and collider experiments where the beam(s) define reference frames, boosted along their direction, it is important to express the 4-momentum in terms of more practical kinematic variables.

Figure 2 shows the collision of two Lorentz contracted nuclei approaching each other with velocities nearly equal to the velocity of light. The vertical axis represents the time direction with the lower half representing time before the collision and

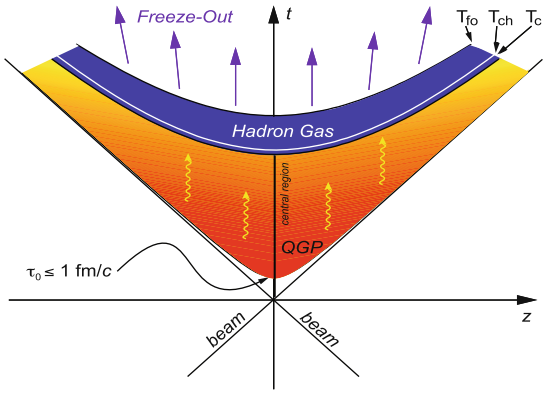

Fig. 2 Description of heavy-ion collisions in one space (z) and one time (t) dimension

the upper half time after the collision. The horizontal axis represents the spatial direction. Both the nuclei collide at $(t, z) = (0, 0)$ and then the created fireball expands in time going through various processes till the created particles freeze-out and reach the detectors. The lines where $t^2 - z^2 = 0$ (note that $\sqrt{t^2 - z^2} \equiv \tau$, τ being the proper time of the particle) along the path of the colliding nuclei define the light-cone. The upper part of the light cone, where $t^2 - z^2 > 0$, is the time-like region. In nucleus–nucleus collisions, particle production occurs in the upper half of the (t, z)-plane within the light cone. The region outside the light-cone for which $t^2 - z^2 < 0$ is called space-like region. The space-time rapidity is defined as

$$\eta_s = \frac{1}{2} \ln\left(\frac{t+z}{t-z}\right). \tag{1}$$

It could be seen that η_s is not defined in the space-like region. It takes the value of positive and negative infinities along the beam directions for which $t = \pm z$, respectively. A particle is "light like" along the beam direction. Inside the light cone which is time like, η_s is properly defined.

For a particle with 4-momentum p $(p_0, \mathbf{p}_T, p_z)$, the light-cone momenta are defined by

$$p_+ = p_0 + p_z, \tag{2}$$
$$p_- = p_0 - p_z, \tag{3}$$

p_+ is called "forward light-cone momentum" and p_- is called "backward light-cone momentum."

For a particle traveling along the beam direction has higher value of forward light-cone momentum and that traveling opposite to the beam direction has lower value of forward light-cone momentum. The advantages of using light-cone variables to study particle production are the following.

1. The forward light-cone momentum of any particle in one frame is related to the forward light-cone momentum of the same particle in another boosted Lorentz frame by a constant factor.
2. Hence, if a daughter particle c is fragmenting from a parent particle b, then the ratio of the forward light-cone momentum of c relative to that of b is independent of the Lorentz frame.
   Define

$$x_+ = \frac{p_0^c + p_z^c}{p_0^b + p_z^b} = \frac{c_+}{b_+}. \tag{4}$$

   The forward light-cone variable x_+ is always positive because c_+ cannot be greater than b_+. Hence the upper limit of x_+ is 1. x_+ is Lorentz invariant.
3. The Lorentz invariance of x_+ provides a tool to measure the momentum of any particle in the scale of the momentum of any reference particle.

2.2 The Rapidity Variable

The coordinates along the beam line (conventionally along the z-axis) is called *longitudinal* and perpendicular to it is called *transverse* (x–y). The 3-momentum can be decomposed into the longitudinal (p_z) and the transverse ($\mathbf{p}_T$), $\mathbf{p}_T$ being a vector quantity which is invariant under a Lorentz boost along the longitudinal direction. The variable rapidity "y" is defined by

$$y = \frac{1}{2} \ln \left(\frac{E + p_z}{E - p_z} \right). \tag{5}$$

It is a dimensionless quantity related to the ratio of forward light cone to backward light-cone momentum. The rapidity changes by an additive constant under longitudinal Lorentz boosts.

For a free particle which is on the mass shell (for which $E^2 = p^2 + m^2$), the 4-momentum has only three degrees of freedom and can be represented by (y, $\mathbf{p}_T$). (E, $\mathbf{p}_T$) could be expressed in terms of (y, $\mathbf{p}_T$) as

$$E = m_T \cosh y, \tag{6}$$

$$p_z = m_T \sinh y, \tag{7}$$

m_T being the transverse mass which is defined as

$$m_T^2 = m^2 + \mathbf{p}_T^2. \tag{8}$$

The advantage of rapidity variable is that the shape of the rapidity distribution remains unchanged under a longitudinal Lorentz boost. When we go from CMS

to LS, the rapidity distribution is the same, with the y-scale shifted by an amount equal to y_{cm}. This is shown below.

2.2.1 Rapidity of Center of Mass in the Laboratory System

The total energy in the CMS system is $E_{\mathrm{cm}} = \sqrt{s}$. The energy and momentum of the CMS in the LS are $\gamma_{\mathrm{cm}}\sqrt{s}$ and $\beta_{\mathrm{cm}}\gamma_{\mathrm{cm}}\sqrt{s}$, respectively. The rapidity of the CMS in the LS is

$$\begin{aligned} y_{\mathrm{cm}} &= \frac{1}{2}\,\ln\left[\frac{\gamma_{\mathrm{cm}}\sqrt{s}+\beta_{\mathrm{cm}}\gamma_{\mathrm{cm}}\sqrt{s}}{\gamma_{\mathrm{cm}}\sqrt{s}-\beta_{\mathrm{cm}}\gamma_{\mathrm{cm}}\sqrt{s}}\right] \\ &= \frac{1}{2}\,\ln\left[\frac{1+\beta_{\mathrm{cm}}}{1-\beta_{\mathrm{cm}}}\right]. \end{aligned} \tag{9}$$

It is a constant for a particular Lorentz transformation.

2.2.2 Relationship Between Rapidity of a Particle in LS and Rapidity in CMS

The rapidities of a particle in the LS and CMS of the collision are, respectively, $y = \frac{1}{2}\,\ln\left(\frac{E+p_z}{E-p_z}\right)$ and $y^* = \frac{1}{2}\,\ln\left(\frac{E^*+p_z^*}{E^*-p_z^*}\right)$. Inverse Lorentz transformations on E and p_z give

$$\begin{aligned} y &= \frac{1}{2}\,\ln\left[\frac{\gamma\left(E^*+\beta p_z^*\right)+\gamma\left(\beta E^*+p_z^*\right)}{\gamma\left(E^*+\beta p_z^*\right)-\gamma\left(\beta E^*+p_z^*\right)}\right] \\ &= \frac{1}{2}\,\ln\left[\frac{E^*+p_z^*}{E^*-p_z^*}\right]+\frac{1}{2}\,\ln\left[\frac{1+\beta}{1-\beta}\right], \end{aligned} \tag{10}$$

$$\Rightarrow y = y^* + y_{\mathrm{cm}}. \tag{11}$$

Hence the rapidity of a particle in the laboratory system is equal to the sum of the rapidity of the particle in the center of mass system and the rapidity of the center of mass in the laboratory system. It can also be stated that the rapidity of a particle in a moving (boosted) frame is equal to the rapidity in its own rest frame minus the rapidity of the moving frame. In the nonrelativistic limit, this is like the subtraction of velocity of the moving frame. However, this is not surprising because, nonrelativistically, the rapidity y is equal to longitudinal velocity β. Rapidity is a relativistic measure of the velocity. This simple property of the rapidity variable under Lorentz transformation makes it a suitable choice to describe the dynamics of relativistic particles.

2.2.3 Relationship Between Rapidity and Velocity

Consider a particle traveling in z-direction with a longitudinal velocity β. The energy E and the longitudinal momentum p_z of the particle are

$$E = \gamma m, \tag{12}$$

$$p_z = \gamma \beta m, \tag{13}$$

where m is the rest mass of the particle. Hence the rapidity of the particle traveling in z-direction with velocity β is

$$\begin{aligned} y_\beta &= \frac{1}{2}\ln\left[\frac{E+p_z}{E-p_z}\right] = \frac{1}{2}\ln\left[\frac{\gamma m+\gamma\beta m}{\gamma m-\gamma\beta m}\right] \\ &= \frac{1}{2}\ln\left[\frac{1+\beta}{1-\beta}\right]. \end{aligned} \tag{14}$$

Note here that y_β is independent of particle mass. In the nonrelativistic limit when β is small, expanding y_β in terms of β leads to

$$y_\beta = \beta + O(\beta^3). \tag{15}$$

Thus the rapidity of the particle is the relativistic realization of its velocity.

2.2.4 Beam Rapidity

We know,
$E = m_T \cosh y$, $p_z = m_T \sinh y$, and $m_T^2 = m^2 + \mathbf{p}_T^2$.
For the beam particles, $p_T = 0$.
Hence, $E = m_b \cosh y_b$ and $p_z = m_b \sinh y_b$,
where m_b and y_b are the rest mass and rapidity of the beam particles.

$$\begin{aligned} y_b &= \cosh^{-1}(E/m_b) \\ &= \cosh^{-1}\left[\frac{\sqrt{s_{NN}}}{2\,m_n}\right], \end{aligned} \tag{16}$$

and

$$y_b = \sinh^{-1}(p_z/m_b). \tag{17}$$

Here m_n is the mass of the nucleon. Note that the beam energy $E = \sqrt{s_{NN}}/2$.

Example 1. For the nucleon–nucleon center of mass energy $\sqrt{s_{NN}} = 9.1$ GeV, the beam rapidity $y_b = \cosh^{-1}\left(\frac{9.1}{2\times 0.938}\right) = 2.26$.
For p+p collisions with lab momentum 100 GeV/c,
$y_b = \sinh^{-1}\left(\frac{p_z}{m_b}\right) = \sinh^{-1}\left(\frac{100}{0.938}\right) = 5.36$
and for Pb+Pb collisions at SPS with lab energy 158 AGeV, $y_b = 2.92$.

2.2.5 Rapidity of the CMS in Terms of Projectile and Target Rapidities

Let us consider the beam particle "b" and the target particle "a." $b_z = m_T \sinh\ y_b = m_b \sinh\ y_b$. This is because p_T of beam particles is zero. Hence

$$y_b = \sinh^{-1}\ (b_z/m_b). \tag{18}$$

The energy of the beam particle in the laboratory frame is
$b_0 = m_T \cosh\ y_b = m_b \cosh\ y_b$.
Assuming target particle a has longitudinal momentum a_z, its rapidity in the laboratory frame is given by

$$y_a = \sinh^{-1}\ (a_z/m_a) \tag{19}$$

and its energy

$$a_0 = m_a \cosh\ y_a. \tag{20}$$

The CMS is obtained by boosting the LS by a velocity of the center of mass frame $\beta_{\rm cm}$ such that the longitudinal momenta of the beam particle b_z^* and of the target particle a_z^* are equal and opposite. Hence $\beta_{\rm cm}$ satisfies the condition,
$a_z^* = \gamma_{\rm cm}(a_z - \beta_{\rm cm}a_0) = -b_z^* = -\gamma_{\rm cm}(b_z - \beta_{\rm cm}b_0)$, where $\gamma_{\rm cm} = \frac{1}{\sqrt{1-\beta_{\rm cm}^2}}$.
Hence,

$$\beta_{\rm cm} = \frac{a_z + b_z}{a_0 + b_0}. \tag{21}$$

We know the rapidity of the center of mass is

$$y_{\rm cm} = \frac{1}{2}\ \ln\left[\frac{1+\beta_{\rm cm}}{1-\beta_{\rm cm}}\right]. \tag{22}$$

Using Eqs. (21) and (22), we get

$$y_{\rm cm} = \frac{1}{2}\ \ln\left[\frac{a_0 + a_z + b_0 + b_z}{a_0 - a_z + b_0 - b_z}\right]. \tag{23}$$

Writing energies and momenta in terms of rapidity variables in the LS,

$$\begin{aligned} y_{\rm cm} &= \frac{1}{2}\ \ln\left[\frac{m_a\ \cosh\ y_a + m_a\ \sinh\ y_a + m_b\ \cosh\ y_b + m_b\ \sinh\ y_b}{m_a\ \cosh\ y_a - m_a\ \sinh\ y_a + m_b\ \cosh\ y_b - m_b\ \sinh\ y_b}\right] \\ &= \frac{1}{2}(y_a + y_b)\ +\ \frac{1}{2}\ \ln\left[\frac{m_a\ e^{y_a} + m_b\ e^{y_b}}{m_a\ e^{y_b} + m_b\ e^{y_a}}\right]. \end{aligned} \tag{24}$$

For a symmetric collision (for $m_a = m_b$),

$$y_{\mathrm{cm}} = \frac{1}{2}(y_a + y_b). \tag{25}$$

Rapidities of a and b in the CMS are

$$y_a^* = y_a - y_{\mathrm{cm}} = -\frac{1}{2}(y_b - y_a), \tag{26}$$

$$y_b^* = y_b - y_{\mathrm{cm}} = \frac{1}{2}(y_b - y_a). \tag{27}$$

Given the incident energy, the rapidity of projectile particles and the rapidity of the target particles can thus be determined. The greater is the incident energy, the greater is the separation between the projectile and the target rapidity.
Central Rapidity The region of rapidity mid-way between the projectile and target rapidities is called central rapidity.

Example 2. In p+p collisions at a laboratory momentum of 100 GeV/c, beam rapidity $y_b = 5.36$, target rapidity $y_a = 0$, and the central rapidity ≈ 2.7.

2.2.6 Mid-rapidity in Fixed-Target and Collider Experiments

In fixed-target experiments (LS), $y_{\mathrm{target}} = 0$.
$y_{\mathrm{lab}} = y_{\mathrm{target}} + y_{\mathrm{projectile}} = y_{\mathrm{beam}}$. Hence mid-rapidity in fixed-target experiment is given by,

$$y_{\mathrm{mid}}^{\mathrm{LS}} = y_{\mathrm{beam}}/2. \tag{28}$$

In collider experiments (center of mass system),
$y_{\mathrm{projectile}} = -y_{\mathrm{target}} = y_{\mathrm{CMS}} = y_{\mathrm{beam}}/2$.
Hence, mid-rapidity in CMS system is given by

$$y_{\mathrm{mid}}^{\mathrm{CMS}} = (y_{\mathrm{projectile}} + y_{\mathrm{target}})/2 = 0. \tag{29}$$

This is valid for a symmetric energy collider. The rapidity difference is given by $y_{\mathrm{projectile}} - y_{\mathrm{target}} = 2y_{\mathrm{CMS}}$ and this increases with energy for a collider as y increases with energy.

2.2.7 Light-Cone Variables and Rapidity

Consider a particle having rapidity y and the beam rapidity y_b. The particle has forward light-cone variable x_+ with respect to the beam particle,

$$x_+ = \frac{p_0^c + p_z^c}{p_0^b + p_z^b} = \frac{m_T^c}{m^b} e^{y - y_b}, \tag{30}$$

where m_T^c is the transverse mass of c. Note that the transverse momentum of the beam particle is zero. Hence,

$$y = y_b + \ln\ x_+ + \ln\left(\frac{m_b}{m_T^c}\right). \tag{31}$$

Similarly, relative to the target particle a with a target rapidity y_a, the backward light-cone variable of the detected particle c is x_-. x_- is related to y by

$$x_- = \frac{m_T^c}{m^b} e^{y_a - y} \tag{32}$$

and conversely

$$y = y_a - \ln\ x_- - \ln\left(\frac{m_a}{m_T^c}\right). \tag{33}$$

In general, the rapidity of a particle is related to its light-cone momenta by

$$y = \frac{1}{2}\ \ln\left(\frac{p_+}{p_-}\right). \tag{34}$$

Note that in situations where there is a frequent need to work with boosts along z-direction, it is better to use $(y, \mathbf{p}_T)$ for a particle rather than using it is 3-momentum because of the simple transformation rules for y and $\mathbf{p}_T$ under Lorentz boosts.

2.3 The Pseudorapidity Variable

Let us assume that a particle is emitted at an angle θ relative to the beam axis. Then its rapidity can be written as $y = \frac{1}{2}\ \ln\left(\frac{E+P_L}{E-P_L}\right) = \frac{1}{2}\ \ln\left[\frac{\sqrt{m^2+p^2}+p\ \cos\ \theta}{\sqrt{m^2+p^2}-p\ \cos\ \theta}\right]$. At very high energy, $p \gg m$ and hence

$$y = \frac{1}{2}\ \ln\left[\frac{p + p\ \cos\ \theta}{p - p\ \cos\ \theta}\right] = -\ln\ \tan\ \theta/2 \equiv \eta, \tag{35}$$

η is called the pseudorapidity. Hence at very high energy,

$$y \approx \eta = -\ln \tan \theta/2. \tag{36}$$

In terms of the momentum, η can be rewritten as

$$\eta = \frac{1}{2} \ln \left[\frac{|\mathbf{p}| + p_z}{|\mathbf{p}| - p_z} \right]. \tag{37}$$

θ is the only quantity to be measured for the determination of pseudorapidity, independent of any particle identification mechanism. Pseudorapidity is defined for any value of mass, momentum, and energy of the collision. This also could be measured with or without momentum information which needs a magnetic field.

2.3.1 Change of Variables from (y, $\mathbf{p}_T$) to (η, $\mathbf{p}_T$)

By Eq. (37),

$$e^{\eta} = \sqrt{\frac{|\mathbf{p}| + p_z}{|\mathbf{p}| - p_z}}, \tag{38}$$

$$e^{-\eta} = \sqrt{\frac{|\mathbf{p}| - p_z}{|\mathbf{p}| + p_z}}. \tag{39}$$

Adding both of the equations, we get

$$|\mathbf{p}| = p_T \cosh \eta. \tag{40}$$

$\mathbf{p}_T = \sqrt{|\mathbf{p}|^2 - p_z^2}$. By subtracting the above equations, we get

$$p_z = p_T \sinh \eta. \tag{41}$$

Using these equations in the definition of rapidity, we get

$$y = \frac{1}{2} \ln \left[\frac{\sqrt{p_T^2 \cosh^2 \eta + m^2} + p_T \sinh \eta}{\sqrt{p_T^2 \cosh^2 \eta + m^2} - p_T \sinh \eta} \right]. \tag{42}$$

Similarly η could be expressed in terms of y as

$$\eta = \frac{1}{2} \ln \left[\frac{\sqrt{m_T^2 \cosh^2 y - m^2} + m_T \sinh y}{\sqrt{m_T^2 \cosh^2 y - m^2} - m_T \sinh y} \right]. \tag{43}$$

The distribution of particles as a function of rapidity is related to the distribution as a function of pseudorapidity by the formula

$$\frac{dN}{d\eta d\mathbf{p}_T} = \sqrt{1 - \frac{m^2}{m_T^2 \cosh^2 y}} \frac{dN}{dyd\mathbf{p}_T}. \tag{44}$$

In the region $y \gg 0$, the pseudorapidity distribution ($dN/d\eta$) and the rapidity distribution (dN/dy) which are essentially the $\mathbf{p}_T$-integrated values of $\frac{dN}{d\eta d\mathbf{p}_T}$ and $\frac{dN}{dyd\mathbf{p}_T}$, respectively, are approximately the same. In the region $y \approx 0$, there is a small "*depression*" in $dN/d\eta$ distribution compared to dN/dy distribution due to the above transformation. At very high energies where dN/dy has a mid-rapidity plateau, this transformation gives a small dip in $dN/d\eta$ around $\eta \approx 0$ (see Fig. 3). However, for a massless particle like photon, the dip in $dN/d\eta$ is not expected (which is clear from the above equation). Independent of the frame of reference where η is measured, the difference in the maximum magnitude of $dN/d\eta$ appears due to the above transformation. In the CMS, the maximum of the distribution is located at $y \approx \eta \approx 0$ and the η-distribution is suppressed by a factor $\sqrt{1 - m^2/ < m_T^2 >}$ with reference to the rapidity distribution. In the laboratory frame, however, the maximum is located around half of the beam rapidity $\eta \approx y_b/2$ and the suppression factor is $\sqrt{1 - m^2/ < m_T^2 > \cosh^2 (y_b/2)}$, which is about unity. Given the fact that the shape of the rapidity distribution is independent of frame of reference, the peak value of the pseudorapidity distribution in the CMS frame is lower than its value in LS. This suppression factor at SPS energies is $\sim 0.8-0.9$.

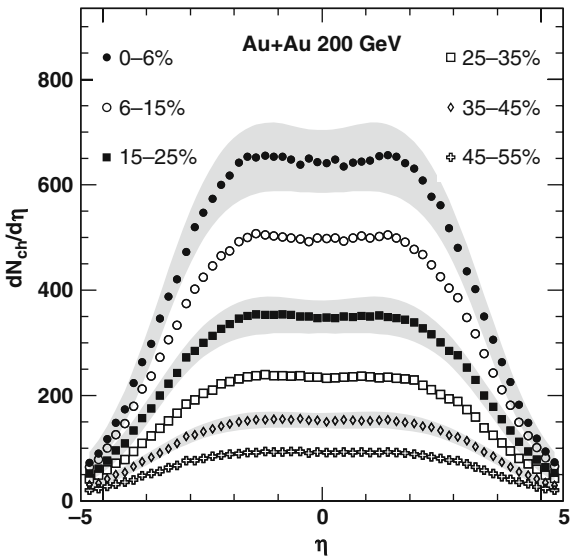

Fig. 3 The mid-rapidity $dN_{ch}/d\eta$ for Au+Au collisions at $\sqrt{s_{NN}} = 200$ GeV [41]

2.4 The Invariant Yield

First we show $\frac{d^3p}{E}$ is Lorentz invariant. The differential of Lorentz boost in longitudinal direction is given by

$$dp_z^* \;=\; \gamma\,(dp_z - \beta dE)\,. \tag{45}$$

Taking the derivative of the equation $E^2 \;=\; p^2 + m^2$, we get

$$E dE \;=\; p_z dp_z. \tag{46}$$

Using Eqs. (45) and (46) we get

$$\begin{aligned} dp_z^* &= \gamma\left(dp_z - \beta\frac{p_z dp_z}{E}\right) \\ &= \frac{dp_z}{E}\,E^*. \end{aligned} \tag{47}$$

As $\mathbf{p}_T$ is Lorentz invariant, multiplying $\mathbf{p}_T$ on both the sides and rearranging gives

$$\frac{d^3p^*}{E^*} \;=\; \frac{d^2\mathbf{p}_T\;dp_z}{E} \;=\; \frac{d^3p}{E}. \tag{48}$$

In terms of experimentally measurable quantities, $\frac{d^3p}{E}$ could be expressed as

$$\begin{aligned} \frac{d^3p}{E} &= d\mathbf{p}_T\;dy \\ &= p_T dp_T d\phi dy \qquad (49) \\ &= m_T dm_T d\phi dy. \qquad (50) \end{aligned}$$

The Lorentz invariant differential cross-section $\frac{Ed^3\sigma}{dp^3} \;=\; \frac{Ed^3N}{dp^3}$ is the invariant yield. In terms of experimentally measurable quantities this could be expressed as

$$\begin{aligned} \frac{Ed^3\sigma}{dp^3} &= \frac{1}{m_T}\,\frac{d^3N}{dm_T d\phi dy} \\ &= \frac{1}{2\pi\;m_T}\,\frac{d^2N}{dm_T dy} \\ &= \frac{1}{2\pi\;p_T}\,\frac{d^2N}{dp_T dy}. \end{aligned} \tag{51}$$

To measure the invariant yields of identified particles Eq. (51) is used experimentally.

2.5 Inclusive Production of Particles and the Feynman Scaling Variable x_F

A reaction of type
beam + target $\longrightarrow$ A + anything,
where A is called an "inclusive reaction." The cross-section for particle production could be written separately as functions of $\mathbf{p}_T$ and p_L as follows:

$$\sigma \;=\; f(\mathbf{p}_T)g(p_L). \tag{52}$$

This factorization is empirical and convenient because each of these factors has simple parameterizations which fit well to experimental data.

Similarly the differential cross-section could be expressed by

$$\frac{d^3\sigma}{dp^3} \;=\; \frac{d^2\sigma}{\mathbf{p}_T^2}\,\frac{d\sigma}{dp_L}. \tag{53}$$

Define the variable

$$x_F = \frac{p_L^*}{p_L^*(\max)} \tag{54}$$

$$= \frac{2p_L^*}{\sqrt{s}}. \tag{55}$$

x_F is called the *Feynman scaling variable*: longitudinal component of the cross-section when measured in CMS of the collision, would scale, i.e., would not depend on the energy $\sqrt{s}$. Instead of $\frac{d\sigma}{dp_L^*}$, $\frac{d\sigma}{dx_F}$ is measured which would not depend on energy of the reaction, $\sqrt{s}$. This Feynman's assumption is valid approximately.

The differential cross-section for the inclusive production of a particle is then written as

$$\frac{d^3\sigma}{dx_F d^2\mathbf{p}_T} \;=\; F(s,\; x_F,\; \mathbf{p}_T). \tag{56}$$

Feynman's assumption that at high energies the function $F(s,\; x_F,\; \mathbf{p}_T)$ becomes asymptotically independent of the energy means
$\lim_{s\to\infty} F(s,\; x_F,\; \mathbf{p}_T) \;= F(x_F,\; \mathbf{p}_T) \;=\; f(\mathbf{p}_T)\; g(x_F)$.

2.6 The $\mathbf{p}_T$-Distribution

The distribution of particles as a function of $\mathbf{p}_T$ is called $\mathbf{p}_T$-distribution. Mathematically,

$$\frac{dN}{d\mathbf{p}_T} = \frac{dN}{2\pi\ |\mathbf{p}_T| d|\mathbf{p}_T|}, \tag{57}$$

where dN is the number of particles in a particular $\mathbf{p}_T$-bin. People usually plot $\frac{dN}{p_T dp_T}$ as a function of p_T taking out the factor $1/2\pi$ which is a constant. Here p_T is a scalar quantity. The low-p_T part of the p_T-spectrum is well described by an exponential function having thermal origin. However, to describe the whole range of the p_T, one uses the Levy function which has an exponential part to describe low-p_T and a power law function to describe the high-p_T part which is dominated by hard scatterings (high momentum transfer at early times of the collision). The inverse slope parameter of p_T-spectra is called the effective temperature (T_{eff}), which has a thermal contribution because of the random kinetic motion of the produced particles and a contribution from the collective motion of the particles. This will be described in detail in the section of freeze-out properties and how to determine the chemical and kinetic freeze-out temperatures experimentally.

The most important parameter is then the mean p_T which carries the information of the effective temperature of the system. Experimentally, $\langle p_T \rangle$ is studied as a function of $\frac{dN_{ch}}{d\eta}$ which is the measure of the entropy density of the system. This is like studying the temperature as a function of entropy to see the signal of phase transition. The phase transition is of first order if a plateau is observed in the spectrum signaling the existence of latent heat of the system. This was first proposed by Van Hove [42].

The average of any quantity A following a particular probability distribution $f(A)$ can be written as

$$\langle A \rangle = \frac{\int A\ f(A)\, dA}{\int f(A)\, dA}. \tag{58}$$

Similarly,

$$\begin{aligned}\langle p_T \rangle &= \frac{\int_0^\infty p_T\ (\frac{dN}{dp_T})\, dp_T}{\int_0^\infty (\frac{dN}{dp_T})\, dp_T} \\ &= \frac{\int_0^\infty p_T\ dp_T\ \ p_T(\frac{dN}{p_T dp_T})}{\int_0^\infty p_T\ dp_T(\frac{dN}{p_T dp_T})} \\ &= \frac{\int_0^\infty p_T\ dp_T\ \ p_T\ f(p_T)}{\int_0^\infty p_T\ dp_T f(p_T)},\end{aligned} \tag{59}$$

where $2\pi\ p_T\ dp_T$ is the phase space factor and the p_T-distribution function is given by

$$f(p_T) = \frac{dN}{d\mathbf{p}_T} = \frac{dN}{p_T dp_T}. \tag{60}$$

Example 3. Experimental data on p_T-spectra are sometimes fitted to the exponential Boltzmann-type function given by

$$f(p_T) \;=\; \frac{1}{p_T}\frac{dN}{dp_T} \;\simeq\; C\, e^{-m_T/T_{\rm eff}}. \tag{61}$$

The $\langle m_T \rangle$ could be obtained by

$$\begin{aligned}\langle m_T \rangle &= \frac{\int_0^\infty p_T\, dp_T\, m_T\ \exp(-m_T/T_{\rm eff})}{\int_0^\infty p_T\, dp_T\ \exp(-m_T/T_{\rm eff})} \\ &= \frac{2T_{\rm eff}^2 + 2m_0 T_{\rm eff} + m_0^2}{m_0 + T_{\rm eff}},\end{aligned} \tag{62}$$

where m_0 is the rest mass of the particle. It can be seen from the above expression that for a massless particle

$$\langle m_T \rangle \;=\; \langle p_T \rangle \;=\; 2T_{\rm eff}. \tag{63}$$

This also satisfies the principle of equipartition of energy which is expected for a massless Boltzmann gas in equilibrium.

However, in experiments the higher limit of p_T is a finite quantity. In that case the integration will involve an incomplete gamma function.

2.7 Energy in CMS and LS

2.7.1 For Symmetric Collisions ($A + A$)

Consider the collision of two particles. In LS, the projectile with momentum $\mathbf{p}_1$, energy E_1, and mass m_1 collides with a particle of mass m_2 at rest. The 4-momenta of the particles are

$p_1 \;=\; (E_1, \mathbf{p}_1), \qquad p_2 \;=\; (m_2, \mathbf{0})$.

In CMS, the momenta of both the particles are equal and opposite, the 4-momenta are

$p_1^* \;=\; (E_1^*, \mathbf{p}_1^*), \qquad p_2^* \;=\; (E_2^*, -\mathbf{p}_1^*)$.

The total 4-momentum of the system is a conserved quantity in the collision.

In CMS,

$(p_1 + p_2)^2 \;=\; (E_1 + E_2)^2 - (\mathbf{p}_1 + \mathbf{p}_2)^2$

$\;=\; (E_1 + E_2)^2 \;=\; E_{\rm cm}^2 \;\equiv\; s$.

$\sqrt{s}$ is the total energy in the CMS which is the invariant mass of the CMS.

In LS,

$(p_1 + p_2)^2 \;=\; m_1^2 + m_2^2 + 2E_1 m_2$.

Hence

$$E_{\rm cm} \;=\; \sqrt{s} \;=\; \sqrt{m_1^2 + m_2^2 + 2E_{\rm proj} m_2}, \tag{64}$$

where $E_1 = E_{\text{proj}}$, the projectile energy in LS. Hence it is evident here that the CM frame with an invariant mass $\sqrt{s}$ moves in the laboratory in the direction of $\mathbf{p}_1$ with a velocity corresponding to
Lorentz factor,

$$\gamma_{\text{cm}} = \frac{E_1 + m_2}{\sqrt{s}} \tag{65}$$

$$\Rightarrow \sqrt{s} = \frac{E_{\text{lab}}}{\gamma_{\text{cm}}}, \tag{66}$$

this is because $E = \gamma m$ and

$$y_{\text{cm}} = \cosh^{-1} \gamma_{\text{cm}}. \tag{67}$$

Note 1. We know

$$s = E_{\text{cm}}^2 = m_1^2 + m_2^2 + 2(E_1 + E_2 + \mathbf{p}_1.\mathbf{p}_2). \tag{68}$$

For a head-on collision with $m_1,\ m_2 \ll E_1, E_2$,

$$E_{\text{cm}}^2 \simeq 4E_1E_2. \tag{69}$$

For two beams crossing at an angle θ,

$$E_{\text{cm}}^2 = 2E_1E_2(1 + \cos\ \theta). \tag{70}$$

The CM energy available in a collider with equal energies (E) for new particle production rises linearly with E, i.e.,

$$E_{\text{cm}} \simeq 2E. \tag{71}$$

For a fixed-target experiment the CM energy rises as the square root of the incident energy

$$E_{\text{cm}} \simeq \sqrt{2m_2E_1}. \tag{72}$$

Hence the highest energy available for new particle production is achieved at collider experiments. For example, at SPS fixed-target experiment to achieve a CM energy of 17.3 AGeV the required incident beam energy is 158 AGeV.

Note 2. Most of the times the energy of the collision is expressed in terms of nucleon–nucleon center of mass energy. In the nucleon–nucleon CM frame, two nuclei approach each other with the same boost factor γ. The nucleon–nucleon CM is denoted by $\sqrt{s_{NN}}$ and is related to the total CM energy by

$$\sqrt{s} \;=\; A\,\sqrt{s_{NN}}. \tag{73}$$

This is for a symmetric collision with number of nucleons in each nuclei as A. The colliding nucleons approach each other with energy $\sqrt{s_{NN}}/2$ and with equal and opposite momenta. The rapidity of the nucleon–nucleon center of mass is $y_{NN} = 0$ and taking $m_1 = m_2 = m_N$, the projectile and target nucleons are at equal and opposite rapidities.

$$y_{\text{proj}} \;=\; -\,y_{\text{target}} \;=\; \cosh^{-1}\,\frac{\sqrt{s_{NN}}}{2m_N} \;=\; y_{\text{beam}}. \tag{74}$$

Note 3. Lorentz factor

$$\begin{aligned}\gamma &= \frac{E}{M} = \frac{\sqrt{s}}{2A\,m_N} \\ &= \frac{A\,\sqrt{s_{NN}}}{2A\,m_N} = \frac{\sqrt{s_{NN}}}{2\,m_N} \\ &= \frac{E^{\text{CMS}}_{\text{beam}}}{m_N},\end{aligned} \tag{75}$$

where E and M are energy and mass in CMS, respectively. Assuming mass of the nucleon $m_N \sim 1$ GeV, the Lorentz factor is of the order of beam energy in CMS for a symmetric collision.

2.7.2 For Asymmetric Collisions ($A + B$)

During the early phase of relativistic nuclear collision research, the projectile mass was limited by accelerator-technical conditions (^{38}Ar at the Bevalac, ^{28}Si at the AGS, ^{32}S at the SPS). Nevertheless, collisions with mass ≈ 200 nuclear targets were investigated. Analysis of such collisions is faced with the problem of determining an "effective" center of mass frame, to be evaluated from the numbers of projectile and target participant nucleons, respectively. Their ratio – and thus the effective CM rapidity – depends on impact parameter. Moreover, this effective CM frame refers to soft hadron production only whereas hard processes are still referred to the frame of nucleon–nucleon collisions. The light projectile on heavy target kinematics is described in [43].

2.8 Luminosity

The luminosity is an important parameter in collision experiments. The reaction rate in a collider is given by

$$R \;=\; \sigma L, \tag{76}$$

where

$\sigma \equiv$ interaction cross-section,
$L \equiv$ luminosity (in $\mathrm{cm}^{-2}\mathrm{s}^{-1}$)

$$L = fn\,\frac{N_1 N_2}{A}, \tag{77}$$

where

$f \equiv$ revolution frequency,
$N_1,\ N_2 \equiv$ number of particles in each bunch,
$n \equiv$ number of bunches in one beam in the storage ring,
$A \equiv$ cross-sectional area of the beams,
L is larger if the beams have small cross-sectional area.

2.9 Collision Centrality

In a collision of two nuclei, the impact parameter (b) can carry values from 0 to $R_1 + R_2$, where R_1 and R_2 are the diameters of the two nuclei. When $b = 0$, it is called *head-on collision*. When collisions with $0 \leq b \leq (R_1 + R_2)$ are allowed, it is called *minimum-bias collision*. In heavy-ion collisions, initial geometric quantities such as impact parameter and the collision geometry cannot be directly measured experimentally. Contrarily, it is however possible to relate the particle multiplicity, transverse energy, and the number of spectactor nucleons (measured by a "zero-degree calorimeter" ZDC) to the centrality of the collisions.

It is straightforward to assume that on the average,

1) the energy released in a collision is proportional to the number of nucleons participating in the collisions,
2) the particle multiplicity is proportional to the participating nucleon number.

Hence the particle multiplicity is proportional to the energy released in the collision. One can measure the particle multiplicity distribution or the transverse energy (E_T) distribution for minimum-bias collisions. Here the high values of particle multiplicity or E_T correspond to central collisions and lower values correspond to more peripheral collisions. Hence the minimum-bias E_T or multiplicity distribution could be used for centrality determination in a collision experiment. Figure 4 shows the minimum-bias multiplicity (N_{ch}) distribution used for the selection of collision centrality. The minimum-bias yield has been cut into successive intervals starting from the maximum value of N_{ch}. The first 5% of the high N_{ch} events correspond to top 5% central collisions. The correlation of centrality and the impact parameter with the number of participating nucleons has also been elaborated, in detail, by Glauber-type Monte Carlo calculations employing Woods–Saxon nuclear density distributions.

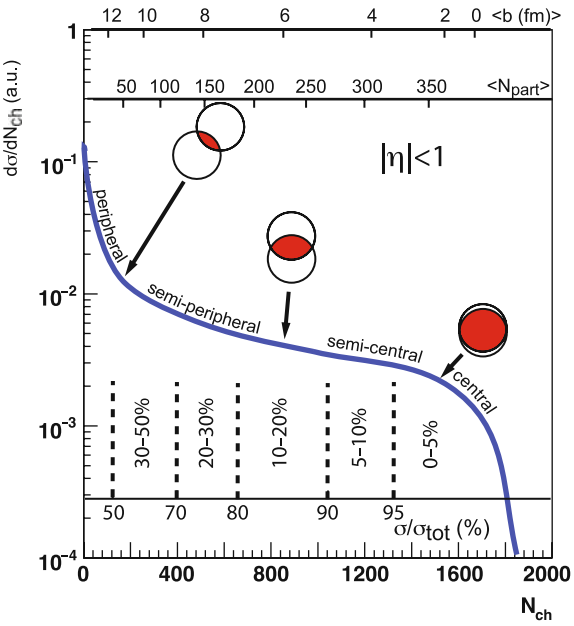

Fig. 4 A cartoon showing the centrality definition from the final-state particle multiplicity and its correlation with the impact parameter (b) and the number of participating nucleons (N_{part}) in the collisions

2.10 Number of Participants and Number of Binary Collisions

Experimentally there is no direct way to estimate the number of participating nucleons (N_{part}) and the number of binary collisions (N_{bin}) in any event, for a given impact parameter. The Glauber model calculation is performed to estimate the above two quantities as a function of the impact parameter. The Glauber model treats a nucleus–nucleus collision as a superposition of many independent nucleon–nucleon ($N-N$) collisions. This model depends on the nuclear density profile(Woods–Saxon) and the non-diffractive inelastic $N + N$ cross-sections. The Woods–Saxon distribution is given by

$$\rho(r) \;=\; \frac{\rho_0}{1+\exp(\frac{r-r_0}{c})}, \tag{78}$$

where r is the radial distance from the center of the nucleus, r_0 is the mean radius of the nucleus, c is the skin depth of the nucleus and ρ_0 is the nuclear density constant. The parameters r_0 and c are measured in electron–nucleus scattering experiments. ρ_0 is determined from the overall normalization condition

$$\int \rho(r)\, d^3r \;=\; A, \tag{79}$$

where A is the mass number of the nucleus.

There are two separate implementations of Glauber approach: optical and Monte Carlo (MC). In the optical Glauber approach, N_{part} and N_{bin} are estimated by an analytic integration of overlapping Woods–Saxon distributions.

The MC Glauber calculation proceeds in two steps. First the nucleon position in each nucleus is determined stochastically. Then the two nuclei are "collided," assuming the nucleons travel in a straight line along the beam axis (this is called eikonal approximation). The position of each nucleon in the nucleus is determined according to a probability density function which is typically taken to be uniform in azimuth and polar angles. The radial probability function is modeled from the nuclear charge densities extracted from electron scattering experiments. A minimum inter-nucleon separation is assumed between the positions of nucleons in a nucleus, which is the characteristic length of the repulsive nucleon–nucleon force. Two colliding nuclei are simulated by distributing A nucleons of nucleus A and B nucleons of nucleus B in three-dimensional coordinate system according to their nuclear density distribution. A random impact parameter b is chosen from the distribution $d\sigma/db = 2\pi b$. A nucleus–nucleus collision is treated as a sequence of independent nucleon–nucleon collisions with a collision taking place if their distance D in the transverse plane satisfies

$$D < \sqrt{\sigma_{\text{inel}}^{NN}/\pi}, \tag{80}$$

where $\sigma_{\text{inel}}^{NN}$ is the total inelastic nucleon–nucleon cross-section. An arbitrary number of such nucleus–nucleus collisions are performed by the Monte Carlo and the resulting distributions of $d\sigma/N_{\text{part}}$ and $d\sigma/N_{\text{bin}}$, $d\sigma/db$ are determined. Here N_{part} is defined as the total number of nucleons that underwent at least one interaction and N_{bin} is the total number of interactions in an event. These histograms are binned according to fractions of the total cross-sections. This determines the mean values of N_{part} and N_{bin} for each centrality class. The systematic uncertainties in these values are estimated by varying the Wood–Saxon parameters, by varying the value of $\sigma_{\text{inel}}^{NN}$, and from the uncertainty in the determination of total nucleus–nucleus cross-section. These sources of uncertainties are treated as fully correlated in the final systematic uncertainty in the above measured variables.

When certain cross-sections scale with number of participants, those are said to be associated with "soft" processes: small momentum transfer processes. The low-p_T hadron production which accounts for almost 95% of the bulk hadron multiplicity comes in the "soft processes." These soft processes are described by phenomenological non-perturbative models. Whereas, in "hard" QCD processes like jets, charmonia, other heavy flavor and processes associated with high-p_T phenomena, the cross-section scales with the number of primordial target/projectile parton collisions. This is estimated in the above Glauber formalism as the total number of inelastic participant–participant collisions. For the hard processes the interaction is at partonic level with large momentum transfer and is governed by pQCD. N_{coll} is always higher than N_{part}: When N_{part} grows like A, N_{coll} grows like $A^{4/3}$.

Sometimes, to study the contribution of soft and hard processes to any cross section, one takes a two-component model like

$$\text{cross section} \;=\; (1-f)\,N_{\text{part}} \;+\; f\,N_{\text{coll}}, \tag{81}$$

where f is the fractional contribution from hard processes.

3 Bulk Hadron Production in A+A Collisions

We will now take an overall look at bulk hadron production in nucleus–nucleus collisions. In view of the high total cm energies involved at, e.g., top SPS ($E_{cm}^{tot} \approx 3.3\,\text{TeV}$) and top RHIC (38 TeV) energies, in central Pb+Pb (SPS) and Au+Au (RHIC) collisions, one can expect an extraordinarily high spatial density of produced particles. The average number of produced particles at SPS energies is $\approx$ 1600 while at RHIC multiplicities of ≈ 4000 are reached. Thus, as an overall idea of analysis, one will try to relate the observed flow of energy into transverse and longitudinal phase space and particle species to the high energy density contained in the primordial interaction volume, thus to infer about its contained matter.

Most of the particles under investigation correspond to "thermal" pions (p_T up to 2 GeV) and, in general, such thermal hadrons make up for about 95% of the observed multiplicity: the bulk of hadron production. Their distributions in phase space will be illustrated in the subsections below. This will lead to a first insight into the overall reaction dynamics, and also set the stage for consideration of the rare signals, imbedded in this thermal bulk production: direct photons, jets, heavy flavors, which are the subject of later chapters in this volume.

3.1 Particle Multiplicity and Transverse Energy Density

Particle production can be assessed globally by the total created transverse energy, the overall result of the collisional creation of *transverse* momentum p_T, or transverse mass $\left(m_T = \sqrt{p_T^2 + m_0^2}\right)$, at the microscopic level. Figure 5 shows the distribution of total transverse energy $E_T = \sum_i E(\theta_i) \cdot \sin\theta$ resulting from a calorimetric measurement of energy flow into calorimeter cells centered at angle θ_i relative to the beam [44], for ^{32}S+^{197}Au collisions at $\sqrt{s} = 20\,\text{GeV}$, and for ^{208}Pb+^{208}Pb collisions at $\sqrt{s} = 17.3\,\text{GeV}$.

The shape is characteristic of the impact parameter probability distribution (for equal size spheres in the Pb+Pb case). The turnoff at $E_T = 520\,\text{GeV}$ indicates the point where geometry runs out of steam, i.e., where $b \to 0$, a configuration generally referred to as a "central collision." The adjacent shoulder results from genuine event-by-event fluctuations of the actual number of participant nucleons from target and projectile (recall the diffuse Woods–Saxon nuclear density profiles),

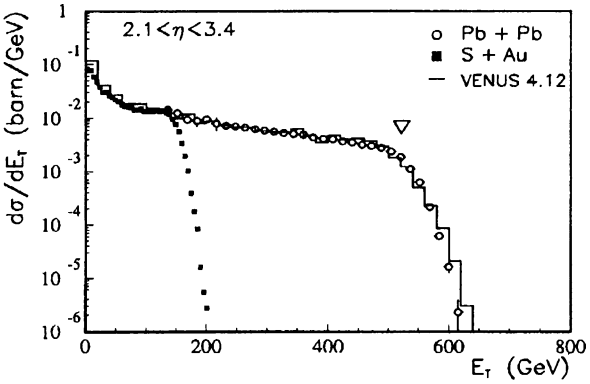

Fig. 5 Minimum bias distribution of total transverse energy in Pb+Pb collisions at $\sqrt{s} = 17.3\,\text{GeV}$, and S+Au collisions at $\sqrt{s} = 20\,\text{GeV}$, in the rapidity interval $2.1 < y < 3.4$, from [44]

and from experimental factors like calorimeter resolution and limited acceptance. The latter covers 1.3 units of pseudorapidity and contains mid-rapidity $\eta_{\text{mid}} = 2.9$. Re-normalizing [44] to $\Delta\,\eta = 1$ leads to $dE_T/d\eta(\text{mid}) = 400\,\text{GeV}$, in agreement with the corresponding WA80 result [45]. Also, the total transverse energy of central Pb+Pb collisions at $\sqrt{s} = 17.3\,\text{GeV}$ turns out to be about 1.2 TeV. As the definition of a central collision, indicated in Fig. 5, can be shown [46] to correspond to an average nucleon participant number of $N_{\text{part}} = 370$ one finds an average total transverse energy per nucleon pair, of $E_T/\langle 0.5\,N_{\text{part}}\rangle = 6.5\,\text{GeV}$. After proper consideration of the baryon pair rest mass (not contained in the calorimetric E_T response but in the corresponding $\sqrt{s}$) one concludes [44] that the observed total E_T corresponds to about 0.6 $E_T^{\max}$, the maximal E_T derived from a situation of "complete stopping" in which the incident $\sqrt{s}$ gets fully transformed into internal excitation of a single, ideal isotropic fireball located at mid-rapidity. The remaining fraction of $E_T^{\max}$ thus stays in longitudinal motion, reflecting the onset, at SPS energy, of a transition from a central fireball to a longitudinally extended "fire-tube," i.e., a cylindrical volume of high primordial energy density. In the limit of much higher $\sqrt{s}$ one may extrapolate to the idealization of a boost-invariant primordial interaction volume, introduced by Bjorken [47].

We shall show below (Sect. 3.2) that the charged particle rapidity distributions, from top SPS to top RHIC energies, do in fact substantiate a development toward a boost-invariant situation. One may thus employ the Bjorken model for an estimate of the primordial spatial energy density ϵ, related to the energy density in rapidity space via the relation [47]

$$\epsilon(\tau_0) = \frac{1}{\pi R^2}\,\frac{1}{\tau_0}\,\frac{dE_T}{dy}, \tag{82}$$

where the initially produced collision volume is considered as a cylinder of length $dz = \tau_0 dy$ and transverse radius $R \propto A^{1/3}$. Inserting for πR^2 the longitudinally projected overlap area of Pb nuclei colliding near head-on ("centrally"), and assuming that the evolution of primordial pQCD shower multiplication (i.e., the energy transformation into internal degrees of freedom) proceeds at a time scale $\tau_0 \leq 1\,\mathrm{fm/c}$, the above average transverse energy density of $dE_T/dy = 400\,\mathrm{GeV}$ at top SPS energy [44, 45] leads to the estimate

$$\epsilon(\tau_0 = 1\,\mathrm{fm}) = 3.0 \pm 0.6\,\mathrm{GeV/fm^3}, \tag{83}$$

thus exceeding, by far, the estimate of the critical energy density ϵ_0 obtained from lattice QCD (see below), of about $1.0\,\mathrm{GeV/fm^3}$. Increasing the collision energy to $\sqrt{s} = 200\,\mathrm{GeV}$ for Au+Au at RHIC, and keeping the same formation time, $\tau_0 = 1\,\mathrm{fm/c}$ (a conservative estimate as we shall show in Sect. 3.4), the Bjorken estimate grows to $\epsilon \approx 6.0 \pm 1\,\mathrm{GeV/fm^3}$. This statement is based on the increase in charged particle multiplicity density at mid-rapidity with $\sqrt{s}$, as illustrated in Fig. 6. From top SPS to top RHIC energy [48] the density per participant nucleon pair almost doubles. However, at $\sqrt{s} = 200\,\mathrm{GeV}$ the formation or thermalization time τ_0, employed in the Bjorken model [47], was argued [49, 50] to be shorter by a factor of about 4. We will return to such estimates of τ_0 in Sect. 3.5 but note, for now, that the above choice of $\tau_0 = 1\,\mathrm{fm/c}$ represents a conservative upper limit at RHIC energy.

These Bjorken-estimates of spatial transverse energy density are confronted in Fig. 7 with lattice QCD results obtained for three dynamical light quark flavors [53, 54], and for zero baryo-chemical potential (as is realistic for RHIC energy and beyond but still remains a fair approximation at top SPS energy where $\mu_B \approx 250\,\mathrm{MeV}$). The energy density of an ideal, relativistic parton gas scales with the fourth power of the temperature,

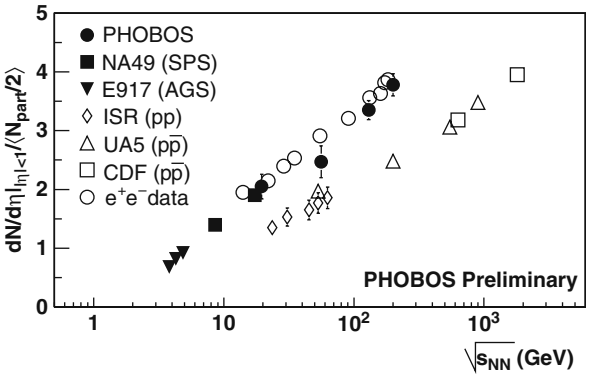

Fig. 6 Charged hadron rapidity density at mid-rapidity vs. $\sqrt{s}$, compiled from e^+e^-, pp, $p\overline{p}$, and A+A collisions [51, 52]

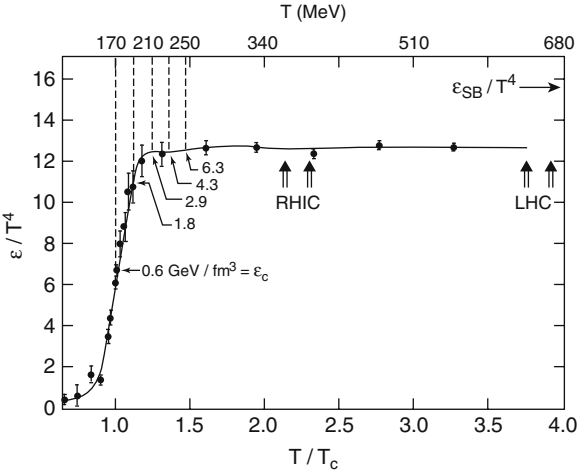

Fig. 7 Lattice QCD results at zero baryon potential for energy density ϵ/T^4 vs. T/T_c with three light quark flavors, compared to the Stefan–Boltzmann limit ϵ_{SB} of an ideal quark–gluon gas [53, 54]

$$\epsilon = gT^4, \tag{84}$$

where g is related to the number of degrees of freedom. For an ideal gluon gas, $g = 16\,\pi^2/30$; in an interacting system the effective g is smaller. The results of Fig. 7 show, in fact, that the Stefan–Boltzmann limit ϵ_{SB} is not reached, due to non-perturbative effects, even at four times the critical temperature $T_c = 170\,\text{MeV}$. The density $\epsilon/T^4 = g$ is seen to ascend steeply, within the interval $T_c \pm 25\,\text{MeV}$. At T_c the critical QCD energy density $\epsilon = 0.6 - 1.0\,\text{GeV/fm}^3$. Relating the thermal energy density with the Bjorken estimates discussed above, one arrives at an estimate of the initial temperatures reached in nucleus–nucleus collisions, thus implying thermal partonic equilibrium to be accomplished at time scale τ_0 (see Sect. 3.5). For the SPS, RHIC and LHC energy domains this gives an initial temperature in the range $190 \leq T^{\text{SPS}} \leq 220\,\text{MeV}$, $220 \leq T^{\text{RHIC}} \leq 400\,\text{MeV}$ (assuming [49, 50] that τ_0 decreases to about 0.3 fm/c here), and $T^{\text{LHC}} \geq 600\,\text{MeV}$, respectively. From such estimates one tends to conclude that the immediate vicinity of the phase transformation is sampled at SPS energy, whereas the dynamical evolution at RHIC and LHC energies dives deeply into the "quark–gluon plasma" domain of QCD. We shall return to a more critical discussion of such assertions in Sect. 3.5.

One further aspect of the mid-rapidity charged particle densities per participant pair requires attention: the comparison with data from elementary collisions. Figure 6 shows a compilation of pp, $p\overline{p}$, and e^+e^- data covering the range from ISR to LEP and Tevatron energies.

The data from e^+e^- represent dN_{ch}/dy, the rapidity density along the event thrust axis, calculated assuming the pion mass [55] (the difference between dN/dy

and $dN/d\eta$ can be ignored here). Remarkably, they superimpose with the central A+A collision data, whereas pp and $p\overline{p}$ show similar slope but amount to only about 60% of the AA and e^+e^- values. This difference between e^+e^- annihilation to hadrons, and pp or $p\overline{p}$ hadro-production has been ascribed [56, 57] to the characteristic leading particle effect of minimum-bias hadron–hadron collisions which is absent in e^+e^-. It thus appears to be reduced in AA collisions due to subsequent interaction of the leading parton with the oncoming thickness of the remaining target/projectile density distribution. This naturally leads to the scaling of total particle production with N_{part} that is illustrated in Fig. 8, for three RHIC energies and minimum-bias Au+Au collisions; the close agreement with e^+e^- annihilation data is obvious again. One might conclude that, analogously, the participating nucleons get "annihilated" at high $\sqrt{s}$, their net quantum number content being spread out over phase space (as we shall show in the next section).

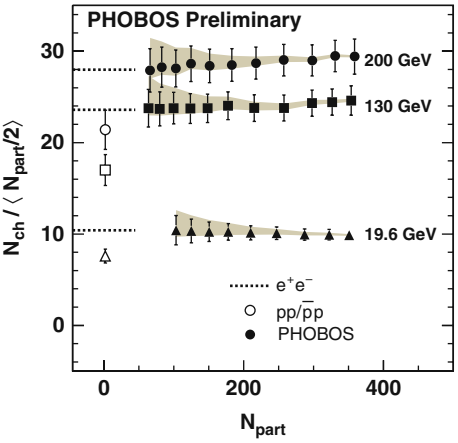

Fig. 8 The total number of charged hadrons per participant pair shown as a function of N_{part} in Au+Au collisions at three RHIC energies [37]

3.2 Rapidity Distributions

Particle production number in A+A collisions depends globally on $\sqrt{s}$ and collision centrality, and differentially on p_T and rapidity y, for each particle species i. Integrating over p_T results in the rapidity distribution dN_i/dy. Particle rapidity $y = \sinh^{-1} p_L/M_T$ (where $M_T = \sqrt{m^2 + p_T^2}$) requires mass identification. If that is unknown one employs pseudorapidity ($\eta = -\ln[\tan(\theta/2)]$) instead. This is also chosen if the joint rapidity distribution of several unresolved particle species is considered: notably the charged hadron distribution. We show two examples in Fig. 9. The left panel illustrates charged particle production in $p\overline{p}$ collisions studied by UA1 at $\sqrt{s} = 540\,\text{GeV}$ [58]. Whereas the minimum-bias distribution (dots)

exhibits the required symmetry about the center of mass coordinate, $\eta = 0$, the rapidity distribution corresponding to events in which a W boson was produced (histogram) features, both, a higher average charged particle yield and an asymmetric shape. The former effect can be seen to reflect the expectation that the W production rate increases with the "centrality" of $p\overline{p}$ collisions, involving more primordial partons as the collisional overlap of the partonic density profiles gets larger, thus also increasing the overall, softer hadro-production rate. The asymmetry should result from a detector bias favoring W identification at negative rapidity: The transverse W energy of about 100 GeV would *locally* deplete the energy store available for associated soft production. If correct, this interpretation suggests that the wide rapidity gap between target and projectile, arising at such high $\sqrt{s}$, of width $\Delta y \approx 2 \ln(2\gamma_{\mathrm{CM}})$, makes it possible to define local sub-intervals of rapidity within which the species composition of produced particles varies.

The right panel of Fig. 9 shows charged particle pseudorapidity density distributions for Au+Au collisions at $\sqrt{s} = 130$ GeV measured by RHIC experiment PHOBOS [42] at three different collision centralities, from "central" (the 6% highest charged particle multiplicity events) to semi-peripheral (the corresponding 35–45% cut). We will turn to centrality selection in more detail below. Let us first remark that the slight dip at mid-rapidity and, moreover, the distribution shape in general are common to $p\overline{p}$ and Au+Au. This is also the case for e^+e^- annihilation as is shown in Fig. 10 which compares the ALEPH rapidity distribution along the mean p_T ("thrust") axis of jet production in e^+e^- at $\sqrt{s} = 200$ GeV [55] with the scaled PHOBOS–RHIC distribution of central Au+Au at the same $\sqrt{s}$ [51, 52]. Note that

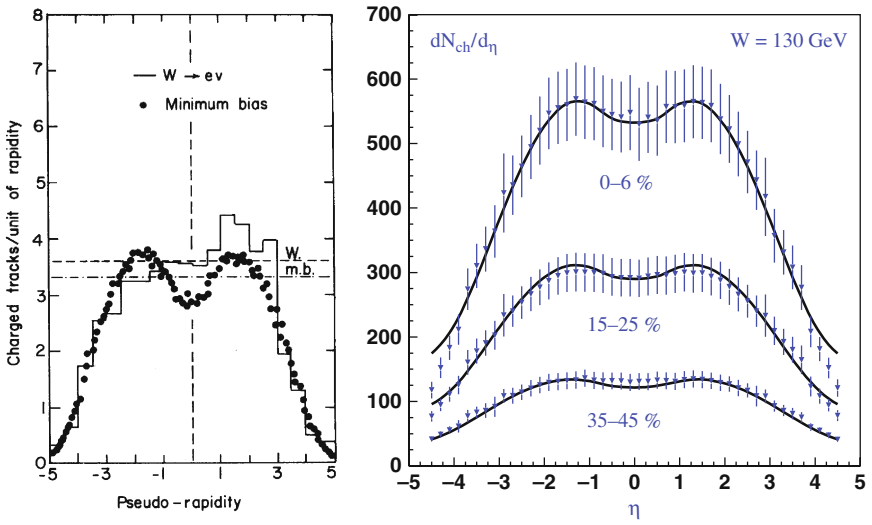

Fig. 9 *Left panel*: charged particle pseudorapidity distribution in $p\overline{p}$ collisions at $\sqrt{s} = 540$ GeV [58]. *Right panel*: same in RHIC Au+Au collisions at $\sqrt{s} = 130$ GeV at different centralities [59]. *Closed lines* represent fits with the color glass condensate model [60]

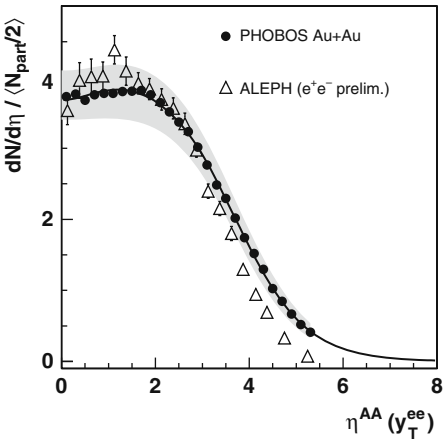

Fig. 10 Pseudorapidity distribution of charged hadrons produced in central Au+Au collisions at $\sqrt{s} = 200\,\text{GeV}$ compared with e^+e^- data at similar energy. The former data normalized by $N_{\text{part}}/2$. From ref. [51, 52]

the mid-rapidity values contained in Figs. 9 and 10 have been employed already in Fig. 6, which showed the overall $\sqrt{s}$ dependence of mid-rapidity charged particle production. What we concluded there was a perfect scaling of A+A with e^+e^- data at $\sqrt{s} \geq 20\,\text{GeV}$ and a 40% suppression of the corresponding pp, $p\overline{p}$ yields. We see here that this observation holds, semi-quantitatively, for the entire rapidity distributions. These are not ideally boost invariant at the energies considered here, but one sees in $dN_{ch}/d\eta$ a relatively smooth "plateau" region extending over $\mid \eta \mid \leq 2.0$.

The production spectrum of charged hadrons is, by far, dominated by soft pions ($p_T \leq 1\,\text{GeV/c}$) which contribute about 85% of the total yield, in both elementary and nuclear collisions. The evolution of the π^- rapidity distribution with $\sqrt{s}$ is illustrated in Fig. 11 for central Au+Au and Pb+Pb collisions from AGS via SPS to RHIC energy, $2.7 \leq \sqrt{s} \leq 200\,\text{GeV}$ [61].

At lower $\sqrt{s}$ the distributions are well described by single Gaussian fits [61] with $\sigma(y)$ nearly linearly proportional to the total rapidity gap $\Delta y \propto \ln\sqrt{s}$ as shown in the right-hand panel of Fig. 11. Also illustrated is the prediction of the schematic hydrodynamical model proposed by Landau [62, 63],

$$\sigma^2 \propto \ln\left(\frac{\sqrt{s}}{2m_p}\right) \tag{85}$$

which pictures hadron production in high $\sqrt{s}$ pp collisions to proceed via a dynamics of initial complete "stopping down" of the reactants matter/energy content in a mid-rapidity fireball that would then expand via one-dimensional ideal hydrodynamics. Remarkably, this model that has always been considered a wildly extremal proposal falls rather close to the lower $\sqrt{s}$ data for central A+A collisions, but as longitudinal phase space widens approaching boost invariance we expect that the

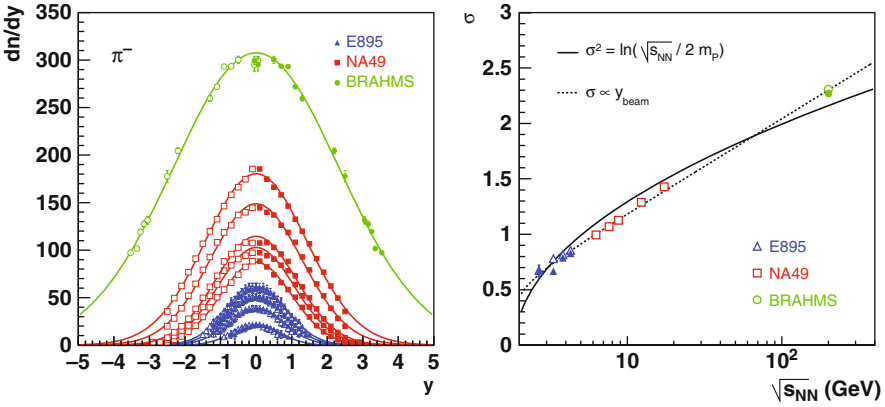

Fig. 11 *Left panel*: negative pion rapidity distributions in central Au+Au and Pb+Pb collisions from AGS via SPS to RHIC energies [61]. *Right panel*: the Gaussian rapidity width of pions vs. $\sqrt{s}$, confronted by Landau model predictions (*solid line*) [61]

(non-Gaussian) width of the rapidity distribution grows linearly with the rapidity gap Δy. LHC data will finally confirm this expectation, but Figs. 9–11 clearly show the advent of boost invariance, already at $\sqrt{s} = 200\,\text{GeV}$.

A short didactic aside: At low $\sqrt{s}$ the total rapidity gap $\Delta y = 2{-}3$ does closely resemble the total rapidity width obtained for a thermal pion velocity distribution at temperature $T = 120{-}150\,\text{MeV}$, of a single mid-rapidity fireball, the y-distribution of which represents the longitudinal component according to the relation [28]

$$\frac{dN}{dy} \propto (m^2 T + \frac{2mT^2}{\text{cosh}y} + \frac{2T^2}{\text{cosh}^2 y}) \exp[-m \cdot \text{cosh}y/T], \tag{86}$$

where m is the pion mass. *Any* model of preferentially longitudinal expansion of the pion-emitting source, away from a trivial single central "completely stopped" fireball, can be significantly tested only once $\Delta y > 3$ which occurs upward from SPS energy. The agreement of the Landau model prediction with the data in Fig. 11 is thus fortuitous, below $\sqrt{s} \approx 10\,\text{GeV}$, as *any* created fireball occupies the entire rapidity gap with pions.

The Landau model offers an extreme view of the mechanism of "stopping," by which the initial longitudinal energy of the projectile partons or nucleons is inelastically transferred to produced particles and redistributed in transverse and longitudinal phase space, of which we saw the total transverse fraction in Fig. 5. Obviously e^+e^- annihilation to hadrons represents the extreme stopping situation. Hadronic and nuclear collisions offer the possibility to analyze the final distribution in phase space of their nonzero net quantum numbers, notably net baryon number. Figure 12 shows the net-proton rapidity distribution (i.e., the proton rapidity distribution subtracted by the antiproton distribution) for central Pb+Pb/Au+Au collisions at AGS ($\sqrt{s} = 5.5\,\text{GeV}$), SPS ($\sqrt{s} \leq 17.3\,\text{GeV}$), and RHIC ($\sqrt{s} = 200\,\text{GeV}$)

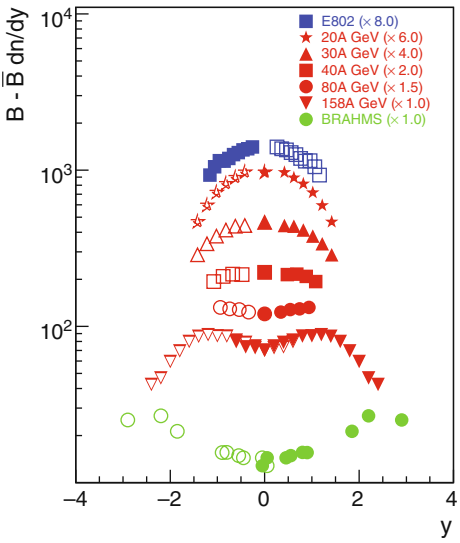

Fig. 12 Net proton rapidity distributions in central Au+Au/Pb+Pb collisions at AGS, SPS, and RHIC energies [64, 65]

[64]. With increasing energy we see a central (but non-Gaussian) peak developing into a double-hump structure that widens toward RHIC leaving a plateau about mid-rapidity. The RHIC-BRAHMS experiment acceptance for p, $\overline{p}$ identification does unfortunately not reach up to the beam fragmentation domain at $y_p = 5.4$ (nor does any other RHIC experiment) but only to $y \approx 3.2$, with the consequence that the major fraction of p^{net} is not accounted for. However, the mid-rapidity region is by no means net baryon free. At SPS energy the NA49 acceptance covers the major part of the total rapidity gap, and we observe in detail a net p distribution shifted down from $y_p = 2.9$ by an average rapidity shift [64] of $\langle \delta y \rangle = 1.7$. From Fig. 12 we infer that $\langle \delta y \rangle$ cannot scale linearly with $y_p \approx \ln(2\gamma_{\text{CM}}) \approx \ln \sqrt{s}$ forever – as it does up to top SPS energy where $\langle \delta y \rangle = 0.58\ y_p$ [64]. Because extrapolating this relation to $\sqrt{s} = 200\,\text{GeV}$ would result in $\langle \delta y \rangle = 3.1$ and with $y_p \approx 5.4$, at this energy we would expect to observe a major fraction of net proton yield in the vicinity of $y = 2.3$ which is not the case. A saturation must thus occur in the $\langle \delta y \rangle$ vs. $\sqrt{s}$ dependence.

The redistribution of net baryon density over longitudinal phase space is, of course, only partially captured by the net proton yield, but a recent study [65] has shown that proper inclusion of neutron[1] and hyperon production data at SPS and RHIC energies scales up, of course, the dN/dy distributions of Fig. 12 but leaves the peculiarities of their shapes essentially unchanged. As the net baryon rapidity

[1] Neutrons are not directly measured in the SPS and RHIC experiments, but their production rate, relative to protons, reflects in the ratio of tritium to ^{3}He production measured by NA49 [65], applying the isospin mirror symmetry of the corresponding nuclear wave functions.

density distribution should resemble the final valence quark distribution, the Landau model is ruled out as the valence quarks are seen to be streaming from their initial position at beam rapidity toward mid-rapidity (not vice versa). It is remarkable, however, to see that some fraction gets transported very far, during the primordial partonic nonequilibrium phase. We shall turn to its theoretical description in Sect. 3.4 but note, for now, that pp collisions studied at the CERN ISR [66] lead to a qualitatively similar net baryon rapidity distribution, albeit characterized by a smaller $\langle \delta y \rangle$.

The data described above suggest that the stopping mechanism universally resides in the primordial, first generation of collisions at the microscopic level. The rapidity distributions of charged particle multiplicity, transverse energy, and valence quarks exhibit qualitatively similar shapes (which also evolve similarly with $\sqrt{s}$) in pp, $p\overline{p}$, e^+e^- reactions, on the one hand, and in central or semi-peripheral collisions of $A \approx 200$ nuclei, on the other. Comparing in detail we formulate a nuclear modification factor for the bulk hadron rapidity distributions,

$$R_y^{\mathrm{AA}} \equiv \frac{dN^{ch}/dy\,(y) \quad \text{in } A+A}{0.5\,N_{\mathrm{part}}\; dN^{ch}/dy \quad \text{in } pp}, \tag{87}$$

where $N_{\mathrm{part}} < 2A$ is the mean number of "participating nucleons" (which undergo at least one inelastic collision with another nucleon) which increases with collision centrality. For identical nuclei colliding $\left\langle N_{\mathrm{part}}^{\mathrm{proj}} \right\rangle \simeq \left\langle N_{\mathrm{part}}^{\mathrm{targ}} \right\rangle$ and thus $0.5\,N_{\mathrm{part}}$ gives the number of opposing nucleon pairs. $R^{\mathrm{AA}} = 1$ if each such "opposing" pair contributes the same fraction to the total A+A yield as is produced in minimum-bias pp at similar $\sqrt{s}$. From Figs. 6 to 8 we infer that for $|\,\eta\,| < 1$, $R^{\mathrm{AA}} = 1.5$ at top RHIC energy, and for the pseudorapidity-integrated total N^{ch} we find $R^{\mathrm{AA}} = 1.36$, in central Au+Au collisions. AA collisions thus provide for a higher stopping power than pp (which is also reflected in the higher rapidity shift $\langle \delta y \rangle$ of Fig. 12). The observation that their stopping power resembles the e^+e^- inelasticity suggests a substantially reduced leading particle effect in central collisions of heavy nuclei. This might not be surprising. In a Glauber view of successive minimum-bias nucleon collisions occurring during interpenetration, each participating nucleon is struck $\nu > 3$ times on average, which might saturate the possible inelasticity, removing the leading fragment.

This view naturally leads to the scaling of the total particle production in nuclear collisions with N_{part}, as seen clearly in Fig. 8, reminiscent of the "wounded nucleon model" [67] but with the scaling factor determined by e^+e^- rather than pp [68]. Overall we conclude from the still rather close similarity between nuclear and elementary collisions that the mechanisms of longitudinal phase space population occur primordially, during interpenetration which is over after 0.15 fm/c at RHIC and after 1.5 fm/c at SPS energy. That is, it is the primordial nonequilibrium pQCD shower evolution that accounts for stopping, and its time extent should be a lower limit to the formation time τ_0 employed in the Bjorken model [47], Eq. (82). Equilibration at the partonic level might begin at $t > \tau_0$ only (the development toward

a quark–gluon–plasma phase) but the primordial parton redistribution processes set the stage for this phase, and control the relaxation time scales involved in equilibration [69] (more about this in Sect. 3.5). We infer the existence of a saturation scale [70] controlling the total inelasticity: With ever higher reactant thickness, proportional to $A^{1/3}$, one does not get a total rapidity or energy density proportional to $A^{4/3}$ (the number of "successive binary collisions") but to $A^{1.08}$ only [71]. Note that the lines shown in Fig. 9 (right panel) refer to such a saturation theory: the color glass condensate (CGC) model [60] developed by McLerran and Venugopalan. The success of these models demonstrates that "successive binary baryon scattering" is not an appropriate picture at high $\sqrt{s}$. One can free the partons from the nucleonic parton density distributions only *once*, and their corresponding transverse areal density sets the stage for the ensuing QCD parton shower evolution [70]. Moreover, an additional saturation effect appears to modify this evolution at high transverse areal parton density (see Sect. 3.4).

3.3 Dependence on System Size

We have discussed above a first attempt toward a variable (N_{part}) that scales the system size dependence in A+A collisions. Note that one can vary the size either by centrally colliding a sequence of nuclei, $A_1 + A_1$, $A_2 + A_2$, etc., or by selecting different windows in N_{part} out of minimum-bias collision ensembles obtained for heavy nuclei for which BNL employs ^{197}Au and CERN ^{208}Pb. The third alternative, scattering a relatively light projectile, such as ^{32}S, from increasing A nuclear targets has been employed initially both at the AGS and at the SPS but got disfavored in view of numerous disadvantages, of both experimental (the need to measure the entire rapidity distribution, i.e., lab momenta from about 0.3 to 100 GeV/c, with uniform efficiency) and theoretical nature (different density distributions of projectile and target; occurrence of an "effective" center of mass, different for hard and soft collisions, and depending on impact parameter).

The determination of N_{part} is of central interest, and thus we need to look at technicalities, briefly. The approximate linear scaling with N_{part} that we observed in the total transverse energy and the total charged particle number (Figs. 5 and 8) is a reflection of the primordial redistribution of partons and energy. Whereas all observable properties that refer to the system evolution at later times, which are of interest as potential signals from the equilibrium, QCD plasma "matter" phase, have different specific dependences on N_{part}, be it suppressions (high-p_T signals, jets, quarkonia production) or enhancements (collective hydrodynamic flow, strangeness production). N_{part} thus emerges as a suitable common reference scale.

N_{part} captures the number of potentially directly hit nucleons. It is estimated from an eikonal straight trajectory Glauber model as applied to the overlap region arising, in dependence of impact parameter b, from the superposition along beam direction of the two initial Woods–Saxon density distributions of the interacting nuclei. To account for the dilute surfaces of these distributions (within which the intersect-

ing nucleons might not find an interaction partner) each incident nucleon trajectory gets equipped with a transverse radius that represents the total inelastic NN cross section at the corresponding $\sqrt{s}$. The formalism is imbedded into a Monte Carlo simulation (for detail see [72]) starting from random microscopic nucleon positions within the transversely projected initial Woods–Saxon density profiles. Overlapping cross-sectional tubes of target and projectile nucleons are counted as a participant nucleon pair. Owing to the statistics of nucleon initial position sampling each considered impact parameter geometry thus results in a probability distribution of derived $N_{\rm part}$. Its width σ defines the resolution $\Delta(b)$ of impact parameter b determination within this scheme via the relation

$$\frac{1}{\Delta\,(b)}\,\sigma\,(b) \approx \frac{d\left\langle N_{\rm part}\,(b)\right\rangle}{db} \tag{88}$$

which, at A=200, leads to the expectation to determine b with about 1.5 fm resolution [72], by measuring $N_{\rm part}$.

How to measure $N_{\rm part}$? In fixed-target experiments one can calorimetrically count all particles with beam momentum per nucleon and superimposed Fermi momentum distributions of nucleons, i.e., one looks for particles in the beam fragmentation domain $y_{\rm beam} \pm 0.5,\ \ p_T \leq 0.25\,{\rm GeV/c}$. These are identified as spectator nucleons, and $N_{\rm part}^{\rm proj} = A - N_{\rm spec}^{\rm proj}$. For identical nuclear collision systems $\left\langle N_{\rm part}^{\rm proj}\right\rangle = \left\langle N_{\rm part}^{\rm targ}\right\rangle$, and thus $N_{\rm part}$ gets approximated by $2\ N_{\rm part}^{\rm proj}$. This scheme was employed in the CERN experiments NA49 and WA80 and generalized [73] in a way that is illustrated in Fig. 13.

The top panel shows the minimum-bias distribution of total energy registered in a forward calorimeter that covers the beam fragment domain in Pb+Pb collisions at lab energy of 158 GeV per projectile nucleon, $\sqrt{s} = 17.3\,{\rm GeV}$. The energy spectrum extends from about 3 TeV which corresponds to about 20 projectile spectators (indicating a "central" collision), to about 32 TeV which is close to the total beam energy and thus corresponds to extremely peripheral collisions. Note that the shape of this forward energy spectrum is the mirror image of the minimum-bias transverse energy distribution of Fig. 5, both recorded by NA49. From both figures we see that the *ideal* head-on, $b \to 0$ collision cannot be selected from these (or any other) data, owing to the facts that $b = 0$ carries zero geometrical weight and the diffuse Woods–Saxon nuclear density profiles lead to a fluctuation of participant nucleon number at given finite b. Thus the $N_{\rm part}$ fluctuation at finite-weight impact parameters overshadows the genuinely small contribution of near-zero impact parameters. Selecting "central" collisions, either by an online trigger cut on minimal forward energy or maximal total transverse energy or charged particle rapidity density, or by corresponding off-line selection, one thus faces a compromise between event statistics and selectivity for impact parameters near zero. In the example of Fig. 13 these considerations suggest a cut at about 8 TeV which selects the 5% most inelastic events, from among the overall minimum-bias distribution, then to be labeled as "central" collisions. This selection corresponds to a soft cutoff at $b \leq 3$ fm.

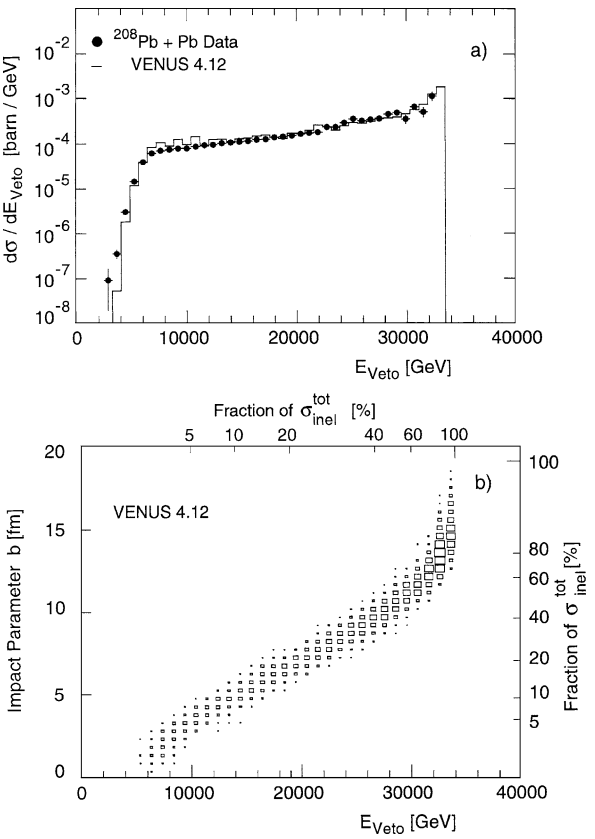

Fig. 13 (a) Energy spectrum of the forward calorimeter in Pb+Pb collisions at 158*A* GeV; (b) impact parameter and fraction of total inelastic cross section related to forward energy from the VENUS model [73, 74]

The selectivity of this, or of other less stringent cuts on collision centrality, is then established by comparison to a Glauber or cascade model. The bottom panel of Fig. 13 employs the VENUS hadron/string cascade model [74] which starts from a Monte Carlo position sampling of the nucleons imbedded in Woods–Saxon nuclear density profiles but (unlike in a Glauber scheme with straight trajectory overlap projection) following the cascade of inelastic hadron/string multiplication, again by Monte Carlo sampling. It reproduces the forward energy data reasonably well and one can thus read off the average impact parameter and participant nucleon number corresponding to any desired cut on the percent fraction of the total minimum-bias cross section. Moreover, it is clear that this procedure can also be based on the total minimum-bias transverse energy distribution, Fig. 5, which is the mirror image of the forward energy distribution in Fig. 13, or on the total, and even the mid-rapidity charged particle density (Fig. 8). The latter method is employed by the RHIC experiments STAR and PHENIX.

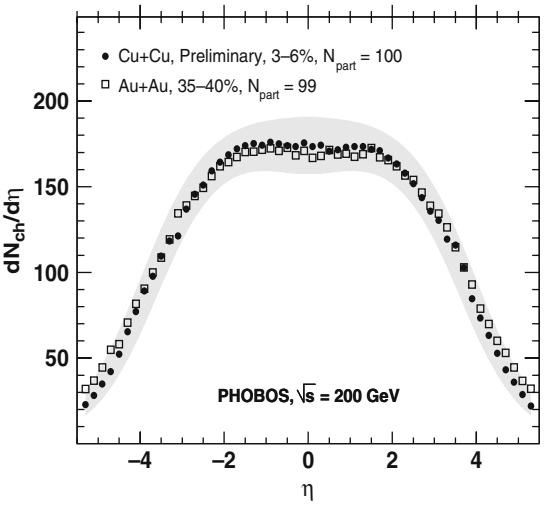

Fig. 14 Charged hadron pseudorapidity distributions in Cu+Cu and Au+Au collisions at $\sqrt{s} =$ 200 GeV, with similar $N_{\text{part}} \approx 100$ [59]

How well this machinery works is illustrated in Fig. 14 by RHIC–PHOBOS results at $\sqrt{s} = 200\,\text{GeV}$ [59]. The charged particle pseudorapidity density distributions are shown for central (3–6% highest N_{ch} cut) Cu+Cu collisions, with $\langle N_{\text{part}} \rangle = 100$, and semi-peripheral Au+Au collisions selecting the cut window (35–40%) such that the same $\langle N_{\text{part}} \rangle$ emerges. The distributions are nearly identical. In extrapolation to $N_{\text{part}} = 2$ one would expect to find agreement between min. bias p+p, and "super-peripheral" A+A collisions, at least at high energy where the nuclear Fermi momentum plays no large role. Figure 15 shows that this expectation is correct [75]. As it is technically difficult to select $N_{\text{part}} = 2$ from A=200 nuclei colliding, NA49 fragmented the incident SPS Pb beam to study $^{12}\text{C} + ^{12}\text{C}$ and $^{28}\text{Si} + ^{28}\text{Si}$ collisions [73]. These systems are isospin symmetric, and Fig. 15 thus plots $0.5\left(\langle \pi^+ \rangle + \langle \pi^- \rangle\right) / \langle N_W \rangle$ including p+p where $N_W = 2$ by definition. We see that the pion multiplicity of A+A collisions interpolates to the p+p data point.

Note that NA49 employs the term "wounded nucleon" number (N_W) to count the nucleons that underwent at least one inelastic nucleon–nucleon collision. This is what the RHIC experiments (that follow a Glauber model) call N_{part} whereas NA49 reserves this term for nucleons that underwent *any* inelastic collision. Thus N_W in Fig. 15 has the same definition as N_{part} in Figs. 6, 8, 10, and 14. We see that a smooth increase joins the p+p data, via the light A+A central collisions, to a saturation setting in with semi-peripheral Pb+Pb collisions, the overall, relative increase amounting to about 40% (as we saw in Fig. 6).

There is nothing like an $N_{\text{part}}^{1/3}$ increase (the thickness of the reactants) observed here, pointing to the saturation mechanism(s) mentioned in the previous section, which are seen from Fig. 15 to dampen the initial, fast increase once the primordial interaction volume contains about 80 nucleons. In the Glauber model view of successive collisions (to which we attach only symbolical significance at high $\sqrt{s}$)

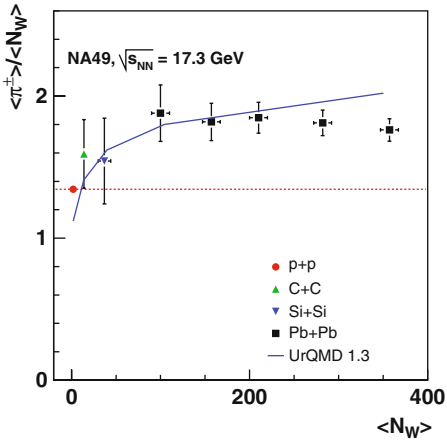

Fig. 15 Charged pion multiplicity normalized by N_W vs. centrality in p+p, C+C, Si+Si, and Pb+Pb collisions at $\sqrt{s} = 17.3\,\text{GeV}$ [73, 75]

this volume corresponds to $\langle \nu \rangle \approx 3$, and within the terminology of such models we might thus argue, intuitively, that the initial *geometrical* cross section, attached to the nucleon structure function as a whole, has disappeared at $\langle \nu \rangle \approx 3$, all constituent partons being freed.

3.4 Gluon Saturation in A+A Collisions

We will now take a closer look at the saturation phenomena of high-energy QCD scattering and apply results obtained for deep inelastic electron–proton reactions to nuclear collisions, a procedure that relies on a universality of high energy scattering. This arises at high $\sqrt{s}$, and at relatively low momentum transfer squared Q^2 (the condition governing bulk charged particle production near mid-rapidity at RHIC, where Feynman $x \approx 0.01$ and $Q^2 \leq 5\,\text{GeV}^2$). Universality comes about as the transverse resolution becomes higher and higher, with Q^2, so that within the small area tested by the collision there is no difference whether the partons sampled there belong to the transverse gluon and quark density projection of any hadron species, or even of a nucleus. And saturation arises once the areal transverse parton density exceeds the resolution, leading to interfering QCD sub-amplitudes that do not reflect in the total cross section in a manner similar to the mere summation of separate[2], resolved color charges [60, 69–71, 76–80].

The ideas of saturation and universality are motivated by HERA deep inelastic scattering (DIS) data [81] on the gluon distribution function shown in Fig. 16 (left side). The gluon rapidity density, $xG(x, Q^2) = \frac{dN^{\text{gluon}}}{dy}$, rises rapidly as a function of

[2] Note that QCD considers interactions only of single charges or charge–anticharge pairs.

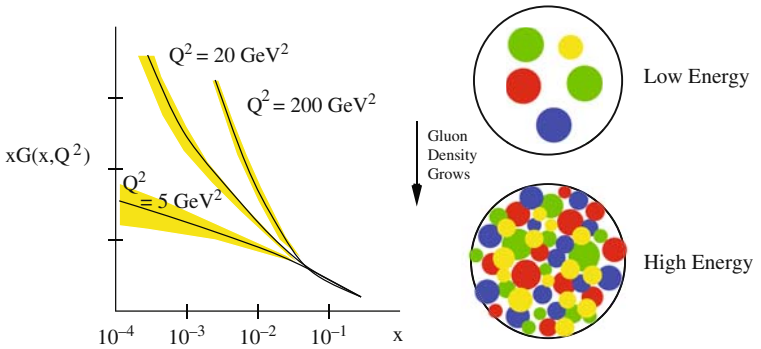

Fig. 16 (*left*) The HERA data for the gluon distribution function as a function of fractional momentum x and square momentum transfer Q^2 [81]. (*right*) Saturation of gluons in a hadron; a head on view as x decreases [84]

decreasing fractional momentum, x, or increasing resolution, Q^2. The origin of this rise in the gluon density is, ultimately, the non-abelian nature of QCD. Due to the intrinsic nonlinearity of QCD [78–80], gluon showers generate more gluon showers, producing an avalanche toward small x. As a consequence of this exponential growth, the spatial density of gluons (per unit transverse area per unit rapidity) of any hadron or nucleus must increase as x decreases [76, 77]. This follows because the transverse size, as seen via the total cross section, rises more slowly toward higher energy than the number of gluons. This is illustrated in Fig. 16 (right side). In a head-on view of a hadronic projectile more and more partons (mostly gluons) appear as x decreases. This picture reflects a representation of the hadron in the "infinite momentum frame" where it has a large light-cone longitudinal momentum $P^+ \gg M$. In this frame one can describe the hadron wave function as a collection of constituents carrying a fraction $p^+ = xP^+$, $0 \leq x < 1$, of the total longitudinal momentum [82] ("light-cone quantization" method [83]). In DIS at large $\sqrt{s}$ and Q^2 one measures the quark distributions dN_q/dx at small x, deriving from this the gluon distributions $xG(x, Q^2)$ of Fig. 16.

It is useful [84] to consider the rapidity distribution implied by the parton distributions in this picture. Defining $y = y_{\text{hadron}} - \ln(1/x)$ as the rapidity of the potentially struck parton, the invariant rapidity distribution results as

$$dN/dy = x\, dN/dx = xG(x, Q^2). \tag{89}$$

At high Q^2 the measured quark and gluon structure functions are thus simply related to the number of partons per unit rapidity, resolved in the hadronic wave function.

The above textbook-level [83, 84] recapitulation leads, however, to an important application: the dN/dy distribution of constituent partons of a hadron (or nucleus), determined by the DIS experiments, is similar to the rapidity distribution of produced particles in hadron–hadron or A+A collisions as we expect the initial gluon rapidity density to be represented in the finally observed, produced hadrons, at high

$\sqrt{s}$. Due to the longitudinal boost invariance of the rapidity distribution, we can apply the above conclusions to hadron–hadron or A+A collisions at high $\sqrt{s}$, by replacing the infinite momentum frame hadron rapidity by the center of mass frame projectile rapidity, $y_{\rm proj}$, while retaining the result that the rapidity density of potentially interacting partons grows with increasing distance from $y_{\rm proj}$ like

$$\Delta y \equiv y_{\rm proj} - y = \ln(1/x). \tag{90}$$

At RHIC energy, $\sqrt{s} = 200\,\text{GeV}$, Δy at mid-rapidity thus corresponds to $x < 10^{-2}$ (well into the domain of growing structure function gluon density, Fig. 16), and the two intersecting partonic transverse density distributions thus attempt to resolve each other given the densely packed situation that is depicted in the lower circle of Fig. 16 (right panel). At given Q^2 (which is modest, $Q^2 \leq 5\,\text{GeV}^2$, for bulk hadron production at mid-rapidity) the packing density at mid-rapidity will increase toward higher $\sqrt{s}$ as

$$\Delta y^{\text{mid-rap}} \approx \ln(\sqrt{s}/M), \text{ i.e., } 1/x \approx \sqrt{s}/M, \tag{91}$$

thus sampling smaller x domains in Fig. 16 according to Eq. (90). It will further increase in proceeding from hadronic to nuclear reaction partners A+A. Will it be in proportion to $A^{4/3}$? We know from the previous sections (3.2 and 3.3) that this is not the case, the data indicating an increase with $A^{1.08}$. This observation is, in fact caused by the parton saturation effect, to which we turn now.

For given transverse resolution Q^2 and increasing $1/x$, the parton density of Fig. 16 becomes so large that one cannot neglect their mutual interactions any longer. One expects such interactions to produce "*shadowing*," a decrease of the scattering cross section relative to incoherent independent scattering [78–80]. As an effect of such shadowed interactions there occurs [84] a *saturation* [60, 69–71, 76–80, 84] of the cross section at each given Q^2, slowing the increase with $1/x$ to become logarithmic once $1/x$ exceeds a certain critical value $x_s(Q^2)$. Conversely, for fixed x, saturation occurs for transverse momenta below some critical $Q^2(x)$,

$$Q_s^2(x) = \alpha_s N_c \, \frac{1}{\pi R^2} \, \frac{dN}{dy}, \tag{92}$$

where dN/dy is the x-dependent gluon density (at $y = y_{\rm proj} - \ln(1/x)$). Q_s^2 is called the *saturation scale*. In Eq. (92) πR^2 is the hadron area (in transverse projection), and $\alpha_s N_c$ is the color charge squared of a single gluon. More intuitively, $Q_s^2(x)$ defines an inversely proportional resolution area $F_s(x)$ and at each x we have to choose $F_s(x)$ such that the ratio of total area πR^2 to $F_s(x)$ (the number of resolved areal pixels) equals the number of single gluon charge sources featured by the total hadron area. As a consequence the saturation scale $Q_s^2(x)$ defines a critical areal resolution, with two different types of QCD scattering theory defined, at each x, for $Q^2 > Q_s^2$ and $Q^2 < Q_s^2$, respectively [70, 76, 77, 84].

As one expects a soft transition between such theories, to occur along the transition line implied by $Q_s^2(x)$, the two types of QCD scattering are best studied with processes featuring typical Q^2 well above, or below $Q_s^2(x)$. Jet production at $\sqrt{s} \geq 200\,\mathrm{GeV}$ in $p\overline{p}$ or AA collisions with typical Q^2 above about $10^3\,\mathrm{GeV}^2$ clearly falls into the former class, to be described, e.g., by perturbative QCD DGLAP evolution of partonic showers [85, 86]. The acronym DGLAP refers to the inventors of the perturbative QCD evolution of parton scattering with the "running" strong coupling constant $\alpha_s(Q^2)$, Dokshitzer, Gribov, Levine, Altarelli, and Parisi. On the other hand, mid-rapidity bulk hadron production at the upcoming CERN LHC facility ($\sqrt{s} = 14\,\mathrm{TeV}$ for pp, and $5.5\,\mathrm{TeV}$ for A+A), with typical $Q^2 \leq 5\,\mathrm{GeV}^2$ at $x \leq 10^{-3}$, will present a clear case for QCD saturation physics, as formulated, e.g., in the "color glass condensate (CGC)" formalism developed by McLerran, Venugopalan, and collaborators [60, 76, 77, 84, 87]. This model develops a classical gluon field theory for the limiting case of a high areal occupation number density, i.e., for the conceivable limit of the situation depicted in Fig. 16 (right-hand panel) where the amalgamating small x gluons would overlap completely, within any finite resolution area at modest Q^2. Classical field theory captures, by construction, the effects of color charge coherence, absent in DGLAP parton cascade evolution theories [84]. This model appears to work well already at $\sqrt{s}$ as "low" as at RHIC, as far as small Q^2 bulk charged particle production is concerned. We have illustrated this by the CGC model fits [60] to the PHOBOS charged particle rapidity distributions, shown in Fig. 9.

Conversely, QCD processes falling in the transition region between such limiting conditions, such that typical $Q^2 \approx Q_s^2(x)$, should present observables that are functions of the ratio between the transferred momentum Q^2 and the appropriate saturation scale, expressed by $Q_s^2(x)$. As Q^2 defines the effective transverse sampling area, and $Q_s^2(x)$ the characteristic areal size at which saturation is expected to set in, a characteristic behavior of cross sections, namely that they are universal functions of Q^2/Q_s^2, is called "*geometric scaling*." The HERA ep scattering data obey this scaling law closely [88, 89], and the idea arises to apply the universality principle that we mentioned above: at small enough x, all hadrons or nuclei are similar, their specific properties only coming in via the appropriate saturation scales $Q_s^2(x, h)$ or $Q_s^2(x, A)$. Knowing the latter for RHIC conditions we will understand the systematics of charged particle production illustrated in the previous section and thus also be able to extrapolate toward LHC conditions in pp and AA collisions.

All data for the virtual photo-absorption cross section $\sigma^{\gamma p}(x, Q^2)$ in deep inelastic ep scattering with $x \leq 0.01$ (which is also the RHIC mid-rapidity x-domain) have been found [88, 89] to lie on a single curve when plotted against Q^2/Q_s^2, with

$$Q_s^2(x) \sim \left(\frac{x_0}{x}\right)^{\lambda} 1\,\mathrm{GeV}^2 \tag{93}$$

with $\lambda \simeq 0.3$ and $x_0 \simeq 10^{-4}$. This scaling [90, 91] with $\tau = Q^2/Q_s^2$ is shown in Fig. 17 (top panel) to interpolate all data. A chain of arguments, proposed by Armesto, Salgado, and Wiedemann [71], connect a fit to these data with photo-

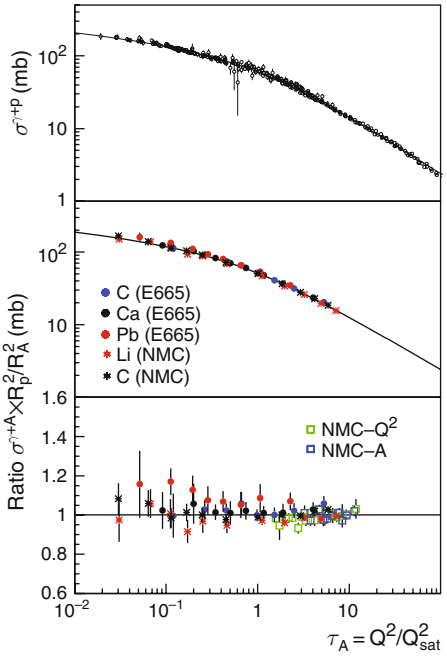

Fig. 17 (*top*) Geometric scaling of the virtual photo-absorption cross section $\sigma^{\gamma p}$ on protons; (*middle*) cross sections for nuclei normalized according to Eq. (94); (*bottom*) the ratio of $\sigma^{\gamma A}$ to a fit of $\sigma^{\gamma p}$ (see [71] for data reference)

absorption data for (virtual) photon–A interactions [92, 93] via the geometrical scaling ansatz

$$\frac{\sigma^{\gamma A}(\tau_A)}{\pi R_A^2} = \frac{\sigma^{\gamma p}(\tau_p = \tau_A)}{\pi R_p^2}, \tag{94}$$

assuming that the scale in the nucleus grows with the ratio of the transverse parton densities, raised to the power $1/\delta$ (a free parameter),

$$Q_{s,A}^2 = Q_{s,p}^2 \left(\frac{A\pi R_p^2}{\pi R_A^2}\right)^{1/\delta}, \quad \tau_A = \tau_h \left(\frac{\pi R_A^2}{A\pi R_h^2}\right)^{1/\delta}. \tag{95}$$

Figure 17 (middle and bottom panels) shows their fit to the nuclear photo-absorption data which fixes $\delta = 0.79$ and $\pi R_p^2 = 1.57\,\mathrm{fm}^2$ (see ref. [71] for detail). The essential step in transforming these findings to the case of A+A collisions is then taken by the empirical ansatz

$$\frac{dN^{AA}}{dy} \text{ (at } y \simeq 0) \propto Q_{s,A}^2(x)\pi R_A^2 \tag{96}$$

by which the mid-rapidity parton (gluon) density dN/dy in Eq. (92) gets related to the charged particle mid-rapidity density at $y \approx 0$ [78, 94], measured in nucleus–nucleus collisions. Replacing, further, the total nucleon number 2A in a collision of identical nuclei of mass A by the number N_{part} of participating nucleons, the final result is [71]

$$\frac{1}{N_{\rm part}} \frac{dN^{AA}}{dy} \text{ (at } y \approx 0) = N_0 \left(\sqrt{s}\right)^{\lambda} N_{\rm part}^{\alpha}, \tag{97}$$

where the exponent $\alpha \equiv (1-\delta)/3\delta = 0.089$ and $N_0 = 0.47$. The exponent α is *far* smaller than 1/3, a value that represents the thickness of the reactants, and would be our naive guess in a picture of "successive" independent nucleon participant collisions, whose average number $\langle \nu \rangle \propto (N_{\rm part}/2)^{1/3}$. The observational fact (see Fig. 15) that $\alpha < 1/3$ for mid-rapidity low Q^2 bulk hadron production in A+A collisions illustrates the importance of the QCD saturation effect. This is shown [71] in Fig. 18 where Eq. (97) is applied to the RHIC–PHOBOS data for mid-rapidity charged particle rapidity density per participant pair, in Au+Au collisions at $\sqrt{s} = 19.6$, 130, and 200 GeV [95, 96], also including a *prediction* for LHC energy. Note that the *factorization of energy and centrality dependence*,

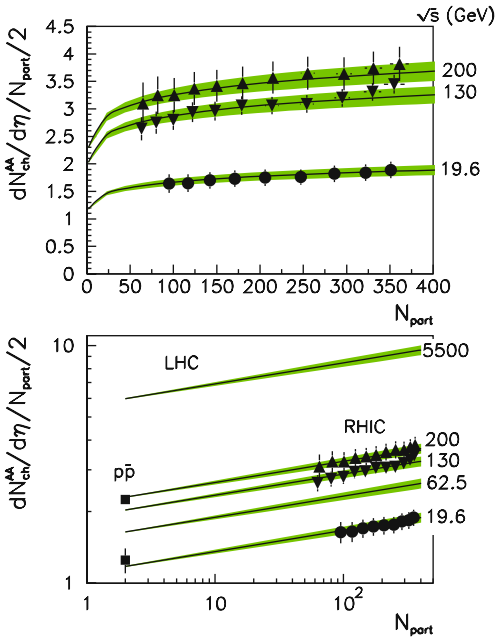

Fig. 18 Saturation model fit [71] applied to RHIC charged hadron multiplicity data at mid-rapidity normalized by number of participant pairs, at various energies [95, 96]. Also shown is an extrapolation to $p\overline{p}$ data and a prediction for minimum-bias Pb+Pb collisions at LHC energy, $\sqrt{s} = 5500$ GeV

implied by the RHIC data [59], is well captured by Eq. (92) and the resulting fits in Fig. 18. Furthermore, the steeper slope, predicted for $N_{\rm part} \leq 60$ (not covered by the employed data set), interpolates to the corresponding pp and $p\overline{p}$ data, at $N_{\rm part} = 2$. It resembles the pattern observed in the NA49 data (Fig. 15) for small $N_{\rm part}$ collisions of light A+A systems, at $\sqrt{s} = 17-20\,\text{GeV}$, and may be seen to reflect the onset of QCD saturation. Finally we note that the conclusions of the above, partially heuristic approach [71], represented by Eqs. (94–97), have been backed up by the CGC theory of McLerran and Venugopalan [60, 76, 77, 84], predictions of which we have illustrated in Fig. 9.

Bulk hadron production in AA collisions at high $\sqrt{s}$ can be related, via the assumption of universality of high-energy QCD scattering, to the phenomenon of geometric scaling first observed in HERA deep inelastic ep cross sections. The underlying feature is a QCD saturation effect arising from the diverging areal parton density, as confronted with the limited areal resolution Q^2, inherent in the considered scattering process. The "saturation scale" $Q_s^2(x, A)$ captures the condition that a single partonic charge source within the transverse partonic density profile can just be resolved by a sufficiently high Q^2. Bulk hadron production in A+A collisions falls below this scale.

3.5 Transverse Phase Space: Equilibrium and the QGP State

At RHIC energy, $\sqrt{s} = 200\,\text{GeV}$, the Au+Au collision reactants are longitudinally contracted discs. At a nuclear radius $R \approx A^{1/3}\,\text{fm}$ and Lorentz $\gamma \approx 100$ their primordial interpenetration phase ends at time $\tau_0 \leq 0.15\,\text{fm/c}$. This time scale is absent in e^+e^- annihilation at similar $\sqrt{s}$ where $\tau_0 \approx 0.1\,\text{fm/c}$ marks the end of the primordial pQCD partonic shower evolution [97] during which the initially created $q\overline{q}$ pair, of "virtually" $Q = \sqrt{s}/2$ each, multiplies in the course of the QCD DGLAP evolution in perturbative vacuum, giving rise to daughter partons of far lower virtuality, of a few GeV. In A+A collisions this shower era should last longer, due to the interpenetrational spread of primordial collision time. It should be over by about 0.25 fm/c. The shower partons in e^+e^- annihilation stay localized within back-to-back cone geometry reflecting the directions of the primordial quark pair. The eventually observed "jet" signal, created by an initial Q^2 of order $10^4\,\text{GeV}^2$, is established by then. Upon a slow-down of the dynamical evolution time scale to $\tau \approx 1\,\text{fm/c}$ the shower partons fragment further, acquiring transverse momentum and yet lower virtuality, then to enter a non-perturbative QCD phase of color neutralization during which hadron-like singlet parton clusters are formed. Their net initial pQCD virtuality, in pQCD vacuum, is recast in terms of non-perturbative vacuum hadron mass. The evolution ends with on-shell, observed jet hadrons after about 3 fm/c of overall reaction time.

Remarkably, even in this somehow most elementary process of QCD evolution, an aspect of equilibrium formation is observed, not in the narrowly focussed final di-jet momentum topology but in the relative production rates of the various created

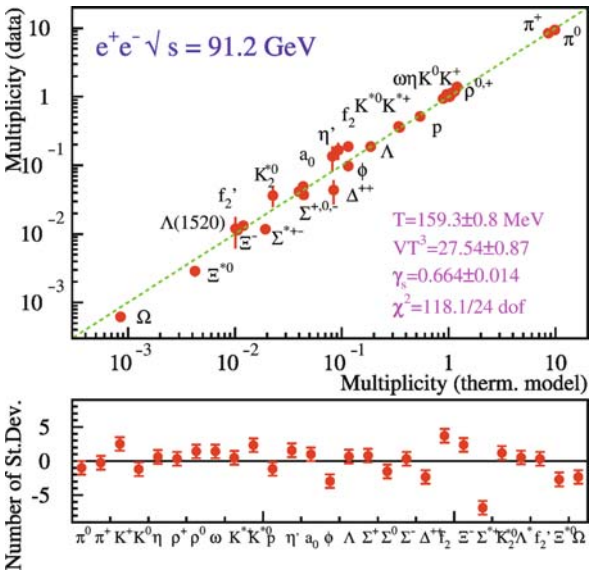

Fig. 19 Hadron multiplicities in LEP e^+e^- annihilation at $\sqrt{s} = 91.2\,\text{GeV}$ confronted with the predictions of the canonical statistical hadronization model [98]

hadronic species. This so-called hadrochemical equilibrium among the hadronic species is documented in Fig. 19. The hadron multiplicities per e^+e^- annihilation event at $\sqrt{s} = 91.2\,\text{GeV}$ [6] are confronted with a Hagedorn [6] canonical statistical Gibbs ensemble prediction [98] which reveals that the apparent species equilibrium was fixed at a temperature of $T = 165\,\text{MeV}$, which turns out to be the universal hadronization temperature of all elementary and nuclear collisions at high $\sqrt{s}$ (Hagedorns limiting temperature of the hadronic phase of matter). We shall return to this topic in Sect. 4 but note, for now, that reactions with as few as 20 charged particles exhibit such statistical equilibrium properties.

What happens with parton (and hadron) dynamics in A+A collisions after τ_0? There will not be a QCD evolution in vacuum as the transverse radius of the interacting system is large. It may grow to about twice the nuclear radius, i.e., to about 15 fm before interactions cease; i.e., the system needs about 15 fm/c to decouple. This simple fact is the key to our expectation that the expansive evolution of the initial high energy density deposited in a cylinder of considerable diameter (about 10 fm) may create certain equilibrium properties that allow us to treat the contained particles and energy in terms of thermodynamic phases of matter, such as a partonic QGP liquid, or a hadronic liquid or gas. Such that the expansion dynamics makes contact to the phase diagram illustrated in Fig. 1. This expectation turns out to be justified as we shall describe in Sect. 4. What results for the evolution after τ_0 in a central A+A collision is sketched in Fig. 2 by means of a schematic two-dimensional light-cone diagram, which is entered by the two reactant nuclei along $\pm z = t$ trajectories where z is the beam direction and Lorentz contraction has been taken to an extreme,

such that there occurs an idealized $t = z = 0$ interaction "point." Toward positive t the light-cone proper time profiles of progressing parton–hadron matter evolution are illustrated. The first profile illustrated here corresponds to the end of shower formation time τ_0. From our above discussion of the e^+e^- annihilation process one obtains a first estimate, $\tau_0 \geq 0.25\,\mathrm{fm/c}$ (including interpenetration time of 0.15 fm/c at RHIC) which refers to processes of very high $Q^2 \geq 10^3\,\mathrm{GeV}^2$, far above the saturation scale Q_s^2 discussed in the previous section. The latter scale has to be taken into account for low p_T hadron production.

It is the specific resolution scale Q^2 of a QCD subprocess, as enveloped in the overall collision dynamics of two slabs of given transverse partonic structure function density, that determines which fraction of the constituent partons enters interaction. In the simple case of extremely high Q^2 processes the answer is that all constituents are resolved. However, at modest Q^2 (dominating bulk hadron production) the characteristic QCD saturation scale $Q_s^2(x)$ gains prominence, defined such that processes with $Q^2 < Q_s^2$ do not exploit the initial transverse parton densities at the level of independent single constituent color field sources (see Eq. 92). For such processes the proper formation time scale, τ_0, is of the order of the inverse saturation momentum [69], $1/Q_s \sim 0.2\,\mathrm{fm/c}$ at $\sqrt{s} = 200\,\mathrm{GeV}$. The first profile of the time evolution, sketched in Fig. 2, should correspond to proper time $t = \tau_0 = 0.25\,\mathrm{fm/c}$ at RHIC energy. At top SPS energy, $\sqrt{s} = 17.3\,\mathrm{GeV}$, we cannot refer to such detailed QCD considerations. A pragmatic approach suggests to take the interpenetration time, at $\gamma \approx 8.5$, for guidance concerning the formation time, which thus results as $\tau_0 \approx 1.5\,\mathrm{fm/c}$.

In summary of the above considerations we assume that the initial partonic color sources, as contained in the structure functions (Fig. 16), are spread out in longitudinal phase space after light-cone proper time $t = \tau_0 \approx 0.25\,\mathrm{fm/c}$, at top RHIC energy, and after $\tau_0 \approx 1.4\,\mathrm{fm/c}$ at top SPS energy. No significant transverse expansion has occurred at this early stage, in a central collision of $A \approx 200$ nuclei with transverse diameter of about 12 fm. The Bjorken estimate [47] of initial energy density ϵ (Eq. 82) refers to exactly this condition, after formation time τ_0. In order to account for the finite longitudinal source size and interpenetration time, at RHIC, we finally put the average $\tau_0 \approx 0.3\,\mathrm{fm}$, at $\sqrt{s} = 200\,\mathrm{GeV}$, indicating the "initialization time" after which all partons that have been resolved from the structure functions are engaged in shower multiplication. As is apparent from Fig. 2, this time scale is Lorentz dilated for partons with a large longitudinal momentum, or rapidity. This means that the slow particles are produced first toward the center of the collision region and the fast (large rapidity) particles are produced later, away from the collision region. This Bjorken "inside-out" correlation [47] between coordinate and momentum space is similar to the Hubble expansion pattern in cosmology: more distant galaxies have higher outward velocities. Analogously, the matter created in A+A collisions at high $\sqrt{s}$ is born expanding, however, with the difference that the Hubble flow is initially one dimensional along the collision axis. This pattern will continue, at $\sqrt{s} = 200\,\mathrm{GeV}$, until the system begins to feel the effects of finite size in the transverse direction which will occur at some time t_0 in the vicinity of 1 fm/c. However, the tight correlation between position and momentum initially imprinted

on the system will survive all further expansive evolution of the initial "fire-tube", and is well recovered in the expansion pattern of the finally released hadrons of modest p_T as we shall show when discussing radial flow (see Sect. 3.6).

In order to proceed to a more quantitative description of the primordial dynamics (that occurs onward from τ_0 for as long the time period of predominantly longitudinal expansion might extend), we return to the Bjorken estimate of energy density, corresponding to this picture [47], as implied by Eq. (82), which we now recast as

$$\epsilon = \left(\frac{dN_h}{dy}\right)\left\langle E_h^T\right\rangle(\pi\ R_A^2\ t_0)^{-1}, \tag{98}$$

where the first term is the (average) total hadron multiplicity per unit rapidity which, multiplied with the average hadron transverse energy, equals the total transverse energy recorded in the calorimetric study shown in Fig. 5, as employed in Eq. (82). The quantity R_A is, strictly speaking, *not* the radius parameter of the spherical Woods–Saxon nuclear density profile but the *rms* of the reactant overlap profiles as projected onto the transverse plane (and thus slightly smaller than $R_A \approx A^{1/3}$ fm). Employing $A^{1/3}$ here (as is done throughout) leads to a conservative estimate of ϵ, a minor concern. However, the basic assumption in Eq. (98) is to identify the primordial transverse energy "radiation," of an interactional cylindric source of radius R_A and length t_0 (where $\tau_0 \leq t_0 \leq 1$ fm/c, not Lorentz dilated at mid-rapidity), with the finally emerging bulk hadronic transverse energy. We justify this assumption by the two observations, made above, that

1. the bulk hadron multiplicity density per unit rapidity $\frac{dN_h}{dy}$ resembles the parton density, primordially released at saturation scale τ_0 (Figs. 9 and 18) at $\sqrt{s} = 200$ GeV, and that
2. the global emission pattern of bulk hadrons (in rapidity and p_T) closely reflects the initial correlation between coordinate and momentum space, characteristic of a primordial period of a predominantly longitudinal expansion, as implied in the Bjorken model.

Both these observations are surprising, at first sight. The Bjorken model was conceived for elementary hadron collisions where the expansion proceeds into vacuum, i.e., directly toward observation. Figure 2 proposes that, to the contrary, primordially produced partons have to transform through further, successive stages of partonic and hadronic matter, at decreasing but still substantial energy density, in central A+A collisions. The very fact of high energy density, with implied short mean free path of the constituent particles, invites a hydrodynamic description of the expansive evolution. With initial conditions fixed between τ_0 and t_0, an ensuing three-dimensional hydrodynamic expansion would preserve the primordial Bjorken-type correlation between position and momentum space, up to lower density conditions and, thus, close to the emission of the eventually observed hadrons. We thus feel justified to employ Eq. (82) or 98 for the initial conditions at RHIC, obtaining [69, 98]

$$6\,\mathrm{GeV/fm^3} \leq \epsilon \leq 20\,\mathrm{GeV/fm^3} \tag{99}$$

for the interval $0.3\,\mathrm{fm/c} \leq t_0 \leq 1\,\mathrm{fm/c}$, in central Au+Au collisions at $y \approx 0$ and $\sqrt{s} = 200\,\mathrm{GeV}$. The energy density at top SPS energy, $\sqrt{s} = 17.3\,\mathrm{GeV}$, can similarly be estimated [44, 45] to amount to about $3\,\mathrm{GeV/fm^3}$ at a t_0 of 1 fm/c but we cannot identify conditions at $\tau_0 < t_0$ in this case as the mere interpenetration of two Pb nuclei takes 1.4 fm/c. Thus the commonly accepted $t_0 = 1\,\mathrm{fm/c}$ may lead to a high estimate. An application of the parton–hadron transport model of Ellis and Geiger [99–101] to this collision finds $\epsilon = 3.3\,\mathrm{GeV/fm^3}$ at $t = 1\,\mathrm{fm/c}$. A primordial energy density of about $3\,\mathrm{GeV/fm^3}$ is 20 times $\rho_0 \approx 0.15\,\mathrm{GeV/fm^3}$, the average energy density of ground state nuclear matter, and it also exceeds, by far, the critical QCD energy density of $0.6 \leq \epsilon_c \leq 1\,\mathrm{GeV/fm^3}$ according to lattice QCD [53, 54]. The initial dynamics thus clearly proceeds in a deconfined QCD system also at top SPS energy, and similarly so with strikingly higher energy density, at RHIC, where time scales below 1 fm/c can be resolved.

However, now in order to clarify the key question as to whether and when conditions of partonic dynamical equilibrium may arise under such initial conditions, we need estimates both of the proper relaxation time scale (which will, obviously, depend on energy density and related collision frequency) and of the expansion time scale as governed by the overall evolution of the collision volume. Only if $\tau(relax.) < \tau(expans.)$ one may conclude that the "deconfined partonic system" can be identified with a "deconfined QGP *state* of QCD matter" as described, e.g., by lattice QCD and implied in the phase diagram of QCD matter suggested in Fig. 1.

For guidance concerning the overall time order of the system evolution we consider information [102] obtained from Bose–Einstein correlation analysis of pion pair emission in momentum space. Note that pions should be emitted at *any* stage of the evolution, after formation time, from the surface regions of the evolving "fire-tube." Bulk emission of pions occurs, of course, after hadronization (the latest stages illustrated in the evolution sketch given in Fig. 2). The dynamical pion source expansion models by Heinz [103] and Sinyukov [104] elaborate a Gaussian emission time profile, with mean τ_f (the decoupling time) and width $\Delta\tau$ (the duration of emission).

Figure 20 shows an application of this analysis to central Pb+Pb collision negative pion pair correlation data obtained by NA49 at top SPS energy, $\sqrt{s} = 17.3\,\mathrm{GeV}$ [105], where $\tau_f \approx 8\,\mathrm{fm/c}$ and $\Delta\tau \approx 4\,\mathrm{fm/c}$ (note that $\tau = 0$ in Fig. 20 corresponds, not to interaction time $t = 0$ but to $t \approx 1.4\,\mathrm{fm/c}$, the end of the interpenetration phase). We see, first of all, that the overall dynamical evolution of a central Pb+Pb collision at $\sqrt{s} = 17.3\,\mathrm{GeV}$ is ending at about 15 fm/c; the proper time defines the position of the last, decoupling profile illustrated in Fig. 2, for the SPS collisions considered here. While the details of Fig. 20 will turn out to be relevant to our later discussion of hadronization (Sect. 4) and hadronic expansion, we are concerned here with the average proper time at which the partonic phase ends. After consideration of the duration widths of these latter expansion phases [100–102] one arrives at an estimate for the average time, spent before hadronization, of $\Delta t = 3{-}4\,\mathrm{fm/c}$, again in agreement with the parton cascade model mentioned above [100, 101]. This model also leads to the conclusion that parton thermal equilibrium is, at least, closely approached locally in these central Pb+Pb collisions as far as mid-rapidity

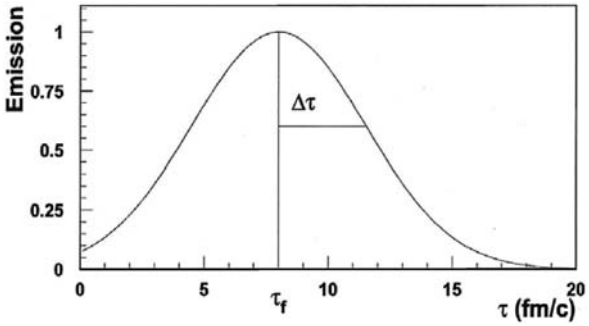

Fig. 20 Time profile of pion decoupling rate from the fireball in a central Pb+Pb collision with $\tau = 0$, the end of the formation phase. Bose–Einstein correlation of $\pi^-\pi^-$pairs yields an average Gaussian decoupling profile with $\tau_f = 8\,\mathrm{fm/c}$ and duration of emission parameter $\Delta\tau = 4\,\mathrm{fm/c}$ [102, 103]

hadron production is concerned (at forward–backward rapidity the cascade rescattering processes do not suffice, however).

This finding agrees with earlier predictions of $\tau_{\mathrm{relax}} = 1{-}2\,\mathrm{fm/c}$ at top SPS energy [106]. However, we note that all such calculations employ perturbative QCD methods, implying the paradoxical consequence that equilibrium is closely approached toward *the end* of the partonic phase, at such low $\sqrt{s}$, i.e., in a QGP state at about $T = 200\,\mathrm{MeV}$ which is, by definition, of non-perturbative nature. We shall return to the question of partonic equilibrium attainment at SPS energy in the discussion of the hadronization process in nuclear collisions (Sect. 4).

Equilibrium conditions should set in earlier at top RHIC energy. As transverse partonic expansion should set in after the proper time interval $0.3\,\mathrm{fm/c} \leq t_0 \leq 1\,\mathrm{fm/c}$ (which is now resolved by the early dynamics, unlike at top SPS energy), we take guidance from the Bjorken estimate of primordial energy density which is based on transverse energy production *data*. Conservatively interpreting the result in Eq. (99) we conclude that ϵ is about four times higher than that at $\sqrt{s} = 17.3\,\mathrm{GeV}$ in the above proper time interval. As the binary partonic collision frequency scales with the square of the density ρ (related to the energy density ϵ via the relation $\epsilon = \langle E \rangle\, \rho = T\rho$), and is inversely proportional to the relaxation time τ_{relax}, we expect

$$\tau_{\mathrm{relax}} \propto (1/\rho)^2 \approx (T/\epsilon)^2 \tag{100}$$

which implies that $\tau_{\mathrm{relax}}(\mathrm{RHIC}) \approx 0.25\ \tau_{\mathrm{relax}}(\mathrm{SPS}) \approx 0.5\,\mathrm{fm/c}$ if we employ the estimate $T(\mathrm{RHIC}) = 2T(\mathrm{SPS})$. This crude estimate is, however, confirmed by the parton transport model of Molar and Gyulassy [107, 108].

Partonic equilibration at $\sqrt{s} = 200\,\mathrm{GeV}$ should thus set in at a time scale commensurate to the (slightly smaller) formation time scale, at which the to-be participant partons are resolved from the initial nucleon structure functions and enter shower multiplication. Extrapolating to the conditions expected at LHC energy ($\sqrt{s} = 5.5\,\mathrm{TeV}$ for A+A collisions), where the initial parton density of the structure

functions in Fig. 16 is even higher ($x \approx 10^{-3}$ at mid-rapidity), and so is the initial energy density, we may expect conditions at which the resolved partons are almost "born into equilibrium."

Early dynamical local equilibrium at RHIC is required to understand the observations concerning elliptic flow. This term refers to a collective anisotropic azimuthal emission pattern of bulk hadrons in semi-peripheral collisions, a hydrodynamical phenomenon that originates from the initial geometrical non-isotropy of the primordial interaction zone [109–111]. A detailed hydrodynamic model analysis of the corresponding elliptic flow signal at RHIC [112, 113] leads to the conclusion that local equilibrium (a prerequisite to the hydrodynamic description) sets in at $t_0 \approx 0.5\,\mathrm{fm/c}$. This conclusion agrees with the estimate via Eq. (100) above, based on Bjorken energy density and corresponding parton collision frequency.

We note that the concept of a hydrodynamic evolution appears to be, almost necessarily ingrained in the physics of a system born into (Hubble-type) expansion, with a primordial correlation between coordinate and momentum space, and at extreme initial parton density at which the partonic mean free path length λ is close to the overall spatial resolution resulting from the saturation scale, i.e., $\lambda \approx 1/Q_s$.

The above considerations suggest that a quark–gluon plasma state should be created early in the expansion dynamics at $\sqrt{s} = 200\,\mathrm{GeV}$, at about $T = 300\,\mathrm{MeV}$, that expands hydrodynamically until hadronization is reached, at $T \approx 165-170\,\mathrm{MeV}$. Its manifestations will be considered in Sect. 4. At the lower SPS energy, up to 17.3 GeV, we can conclude, with some caution, that a deconfined hadronic matter system should exist at $T \approx 200\,\mathrm{MeV}$, in the closer vicinity of the hadronization transition. It may closely resemble the QGP state of lattice QCD, near T_c.

3.6 Bulk Hadron Transverse Spectra and Radial Expansion Flow

In this section we analyze bulk hadron transverse momentum spectra obtained at SPS and RHIC energies, confronting the data with predictions of the hydrodynamical model of collective expansion matter flow that we have suggested in the previous section, to arise, almost necessarily, from the primordial Hubble-type coupling between coordinate and momentum space that prevails at the onset of the dynamical evolution in A+A collisions at high $\sqrt{s}$. As all hadronic transverse momentum spectra initially follow an approximately exponential fall-off (see below), the bulk hadronic output is represented by thermal transverse spectra at $p_T \leq 2\,\mathrm{GeV/c}$.

Furthermore, we shall focus here on mid-rapidity production in near-central A+A collisions, because hydrodynamic models refer to an initialization period characterized by Bjorken-type longitudinal boost invariance, which we have seen in Figs. 9 and 11 to be restricted to a relatively narrow interval centered at mid-rapidity. Central collisions are selected to exploit the azimuthal symmetry of emission, in an ideal impact parameter $b \to 0$ geometry. We thus select the predominant, relevant hydrodynamic "radial flow" expansion mode from, among other, azimuthally oriented (directed) flow patterns that arise once this cylindrical symmetry (with respect to the beam direction) is broken in finite impact parameter geometries.

In order to define, quantitatively, the flow phenomena mentioned above, we rewrite the invariant cross section for production of hadron species i in terms of transverse momentum, rapidity, impact parameter b, and azimuthal emission angle φ_p (relative to the reaction plane),

$$\frac{dN_i(b)}{p_T dp_T dy d\varphi_p} = \frac{1}{2\pi} \frac{dN_i(b)}{p_T dp_T dy} \left[1 + 2v_1^i(p_T, b)\cos\varphi_p + 2v_2^i(p_T, b)\cos(2\varphi_p) + \ldots\right], \quad (101)$$

where we have expanded the dependence on φ_p into a Fourier series. Due to reflection symmetry with respect to the reaction plane in collisions of identical nuclei, only cosine terms appear. Restricting to mid-rapidity production all odd harmonics vanish, in particular the "directed flow" coefficient v_1^i, and we have dropped the y-dependence in the flow coefficients v_1^i and v_2^i. The latter quantifies the amount of "elliptic flow" as discussed above. In the following, we will restrict to central collisions which we shall idealize as near-zero impact parameter processes governed by cylinder symmetry, whence all azimuthal dependence (expressed by the $v_1^i,\ v_2^i, \ldots$ terms) vanishes, and the invariant cross section reduces to the first term in Eq. (101), which by definition also corresponds to all measurements in which the orientation of the reaction plane is not observed.

Typical transverse momentum spectra of the latter type are shown in Fig. 21, for charged hadron production in Au+Au collisions at $\sqrt{s} = 200\,\text{GeV}$, exhibiting

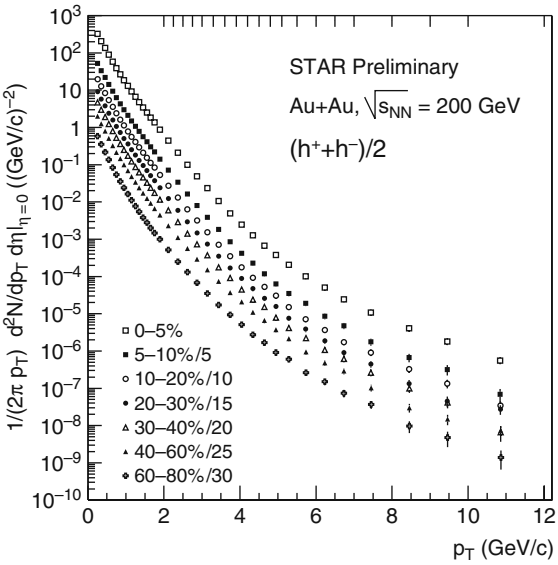

Fig. 21 Transverse momentum spectra of charged hadrons in Au+Au collisions at $\sqrt{s} = 200\,\text{GeV}$, in dependence of collision centrality [114] (offset as indicated), featuring transition from exponential to power law shape

mid-rapidity data at various collision centralities [114]. We observe a clear-cut transition, from bulk hadron emission at $p_T \leq 2\,\mathrm{GeV/c}$ featuring a near-exponential cross section (i.e., a thermal spectrum), to a high-p_T power law spectral pattern. Within the context of our previous discussion (Sect. 3.4) we tentatively identify the low p_T region with the QCD physics near saturation scale. Hadron production at $p_T \rightarrow 10\,\mathrm{GeV/c}$ should, on the other hand, be the consequence of primordial leading parton fragmentation originating from "hard," high-Q^2 perturbative QCD processes.

We thus identify bulk hadron production at low p_T as the emergence of the initial parton saturation conditions that give rise to high energy density and small equilibration time scale, leading to a hydrodynamical bulk matter expansion evolution. Conversely, the initially produced hard partons, from high-Q^2 processes, are not thermalized into the bulk but traverse it, as tracers, while being attenuated by medium-induced rescattering and gluon radiation, the combined effects being reflected in the high p_T inclusive hadron yield, and in jet correlations of hadron emission. We cannot treat the latter physics observables in detail here, but will remain in the field of low p_T physics, related to hydrodynamical expansion modes, focussing on radially symmetric expansion.

In order to infer from the spectral shapes of the hadronic species about the expansion mechanism, we first transform to the transverse mass variable, $m_T = (p_T^2 + m^2)^{1/2}$, via

$$\frac{1}{2\pi}\,\frac{dN_i}{p_T dp_T dy} = \frac{1}{2\pi}\,\frac{dN_i}{m_T dm_T dy} \tag{102}$$

because it has been shown in p+p collisions [115] near RHIC energy that the m_T distributions of various hadronic species exhibit a universal pattern ("m_T scaling") at low m_T

$$\frac{1}{2\pi}\,\frac{dN_i}{m_T dm_T dy} = A_i\,\exp(-m_T^i/T) \tag{103}$$

with a universal inverse slope parameter T and a species-dependent normalization factor A. Hagedorn showed [116] that this scaling is characteristic of an adiabatic expansion of a fireball at temperature T. We recall that, on the other hand, an ideal hydrodynamical expansion is isentropic.

Figure 22 shows the $\sqrt{s}$ dependence of the average transverse kinetic energy $\langle m_T^i \rangle - m^i$ for pions, kaons, and protons observed at mid-rapidity in central Au+Au/Pb+Pb collisions [61]. Similarly, the inverse slope parameter T resulting from a fit of Eq. (103) to K^+ and K^- transverse mass spectra (at $p_T \leq 2\,\mathrm{GeV/c}$) is shown in Fig. 23, both for nuclear and p+p collisions [117, 118]. We see, first of all, that m_T scaling does not apply in A+A collisions, and that the kaon inverse slope parameter, $T \approx 230\,\mathrm{MeV}$ over the SPS energy regime, can not be identified with the fireball temperature at hadron formation which is $T_h \approx 165\,\mathrm{MeV}$ from Fig. 1. The latter is seen, however, to be well represented by the p+p spectral data

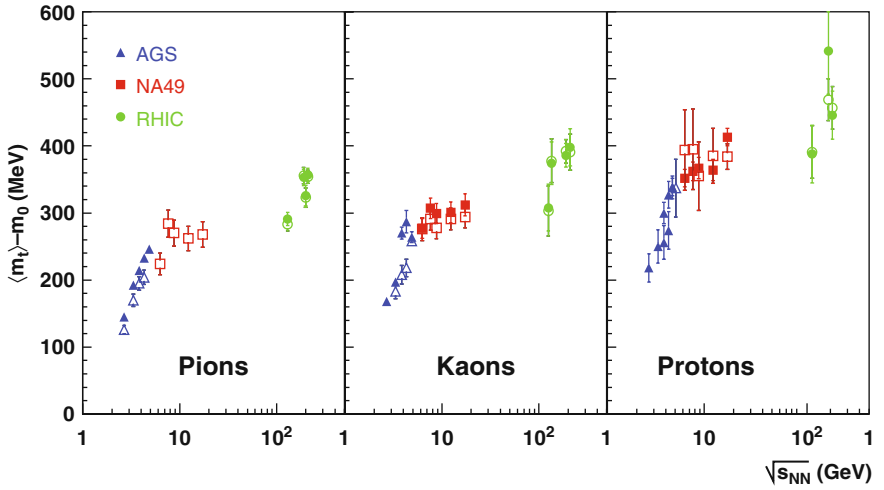

Fig. 22 The average transverse kinetic energy $\langle m_T \rangle - m_0$ for pions, kaons, and protons vs. $\sqrt{s}$ in central Au+Au/Pb+Pb collisions [61]. *Open symbols* represent negative hadrons

exhibited in the left panel of Fig. 23. There is, thus, not only thermal energy present in A+A transverse expansion but also hydrodynamical radial flow.

We note that the indications in Figs. 22 and 23, of a plateau in both $\langle m_T \rangle$ and T, extending over the domain of SPS energies, $6 \leq \sqrt{s} \leq 17\,\text{GeV}$, have not yet been explained by any fundamental expansive evolution model, including hydrodynamics. Within the framework of the latter model, this is a consequence of the *initialization problem* [119] which requires a detailed modeling, both of primordial energy density vs. equilibration time scale, and of the appropriate partonic matter equation of state (EOS) which relates expansion pressure to energy density. At top RHIC energy, this initialization of hydro-flow occurs, both, at a time scale $t_0 \approx 0.5\,\text{fm/c}$ which is far smaller than the time scale of eventual bulk hadronization ($t \approx 3\,\text{fm/c}$) and at a primordial energy density far in excess of the critical QCD confinement density. After initialization, the partonic plasma phase thus dominates the overall expansive evolution, over a time interval far exceeding the formation and relaxation time scales.

Thus, at RHIC energy, parton transport [107, 108] and relativistic hydrodynamic [112, 113, 119] models establish a well-developed expansion mode that survives the subsequent stages of hadronization and hadronic expansion. This is reflected in their success in describing elliptic flow. On the other hand, the hydrodynamical model far overestimates elliptic flow at SPS energy [119] at which, as we have shown in Sect. 3.5, the initialization period may not be well separated from the confinement (hadronization) stage. Thus, whereas the expansion evolution at $\sqrt{s} = 200\,\text{GeV}$ (occurring at near-zero baryo-chemical potential in Fig. 1) "races" across the parton–hadron phase boundary with fully established flow patterns, near $\mu_B = 0$ where lattice QCD predicts the phase transformation to be merely a soft cross over [24], the dynamics at $\sqrt{s} = 10{-}20\,\text{GeV}$ may originate from only slightly above,

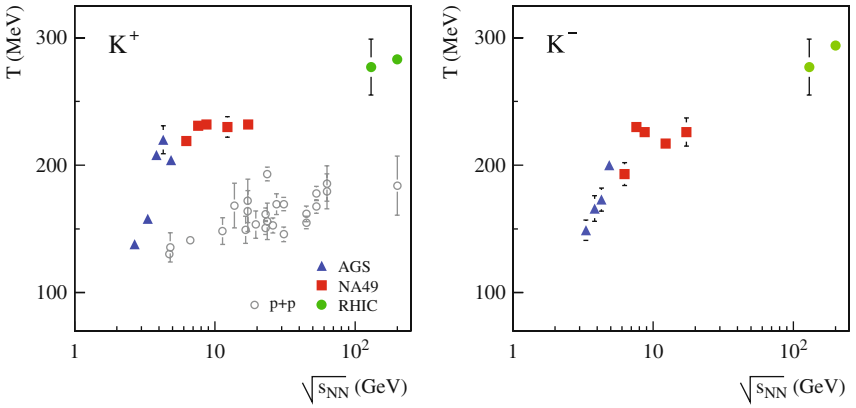

Fig. 23 The inverse slope parameter T of Eq. (103) for K^+ and K^- transverse mass spectra at $p_T < 2\,\text{GeV/c}$ and mid-rapidity in central A+A, and in minimum-bias p+p collisions [117, 118, 120]

or even at the phase boundary, thus sampling the domain $200 \leq \mu_B \leq 500\,\text{MeV}$ where the equation of state might exhibit a "softest point" [119]. The hydrodynamic model thus faces formidable uncertainties regarding initialization at SPS energy.

The plateau in Figs. 22 and 23 may be the consequence of the fact that not much flow is generated in, or transmitted from the partonic phase, at SPS energies, because it is initialized close to the phase boundary [117, 118] where the expected critical point [117, 118] (Fig. 1) and the corresponding adjacent first-order phase transition might focus [121] or stall [119] the expansion trajectory, such that the observed radial flow stems almost exclusively from the hadronic expansion phase. The SPS plateau, which we shall subsequently encounter in other bulk hadron variables (elliptic flow, HBT radii), might thus emerge as a consequence of the critical point or, in general, of the flatness of the parton–hadron coexistence line. RHIC dynamics, on the other hand, originates from far above this line.

Hadronic expansion is known to proceed isentropically [122]: commensurate to expansive volume increase the momentum space volume must decrease, from a random isotropic thermal distribution to a restricted momentum orientation preferentially perpendicular to the fireball surface, i.e., radial. The initial thermal energy, implied by the hadron formation temperature $T_H = 165\,\text{MeV}$, will thus fall down to a residual T_F at hadronic decoupling from the flow field ("thermal freeze-out") plus a radial transverse kinetic energy term $m_i \langle\beta_T\rangle^2$ where m_i is the mass of the considered hadron species and $\langle\beta_T\rangle$ the average radial velocity. We thus expect [123] for the slope of Eq. (103)

$$T = T_F + m_i \langle\beta_T\rangle^2\,,\ p_T \leq 2\,\text{GeV/c} \tag{104}$$

and

$$T = T_F \left(\frac{1 + \langle v_T \rangle}{1 - \langle v_T \rangle} \right)^{1/2}, \quad p_T \gg m_i, \tag{105}$$

the latter expression valid at p_T larger than hadron mass scale (T then is the "blue-shifted temperature" at decoupling [124] and $\langle v_T \rangle$ the average transverse velocity). The assumption that radial flow mostly originates from the hadronic expansion phase is underlined by the proportionality of flow energy to hadron mass (Eq. 104).

Figure 24 illustrates this proportionality, by a recent compilation [123] of RHIC results for central Au+Au collisions at $\sqrt{s} = 200\,\text{GeV}$, and SPS results for central Pb+Pb collisions at top SPS energy, $\sqrt{s} = 17.3\,\text{GeV}$. At the latter energy the slope parameter of the Φ meson is seen to be close to that of the similar mass baryons p and Λ, emphasizing the occurrence of m_i scaling as opposed to valence quark number scaling that we will encounter in RHIC elliptic flow data [111]. As is obvious from Fig. 24 the multi-strange hyperons and charmonia exhibit a slope saturation which is usually explained [123] as a consequence of their small total cross sections of rescattering from other hadrons, leading to an early decoupling from the bulk hadron radial flow field, such that $\langle \beta_T \rangle_\Omega < \langle \beta_T \rangle_p$.

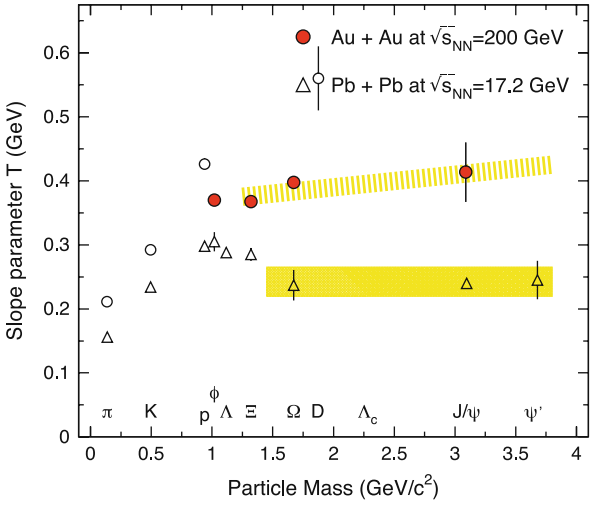

Fig. 24 Hadron slope parameters T at mid-rapidity as a function of mass. For Pb+Pb at $\sqrt{s} = 17.3\,\text{GeV}$ (*triangles*) and Au+Au at $\sqrt{s} = 200\,\text{GeV}$ (*circles*); from [123]

According to our observations with Eq. (104) a hydrodynamical ansatz for the transverse mass spectrum of hadrons should thus contain the variables "true temperature" T_F at decoupling from the flow field, and its average velocity $\langle \beta_T \rangle$, common to all hadrons. This is the case for the blast wave model [124] developed as an approximation to the full hydrodynamic formalism [119], assuming a common decoupling or "freeze-out" from flow, for all hadronic species, and a boost-invariant longitudinal expansion

$$\frac{dN_i}{m_T dm_T dy} = A_i\, m_T\, K_1\left(\frac{m_T \cosh\rho}{T_F}\right) I_0\left(\frac{p_T \sinh\rho}{T_F}\right), \tag{106}$$

where $\rho = \tanh^{-1}\beta_T$. In an extended version of this model a function is included that describes the radial profile of the transverse velocity field, $\beta_T(r) = \beta_T^{\max} r/R$, instead of employing a fixed β_T at decoupling [125]. Figure 25 shows [61] the resulting energy dependence of T_F and $\langle\beta_T\rangle$, for the same set of data as implied already in Figs. 22 and 23. The "true" decoupling temperature rises steeply at the AGS and less so at SPS energy (as does $\langle\beta_T\rangle$), to a value of about 95 MeV at top SPS energy, which is considerably lower than the chemical freeze-out temperature, $T_H = 165$ MeV, at which the hadronic species relative yield composition of the hadronic phase becomes stationary (see Sect. 4 and Fig. 1). Chemical decoupling thus occurs early, near the parton–hadron phase boundary, whereas hadronic radial flow ceases after significant further expansion and cooling, whence the surface radial velocity (its average value given by $\langle\beta_T\rangle$ in Fig. 25) approaches $\beta_T \approx 0.65$. Both data sets again exhibit an indication of saturation, over the interval toward top SPS energy: the SPS plateau. This supports our above conjecture that radial flow is, predominantly, a consequence of isentropic bulk hadronic expansion in this energy domain, which sets in at T_H. At RHIC energy, both parameters exhibit a further rise, suggesting that primordial partonic flow begins to contribute significantly to radial flow.

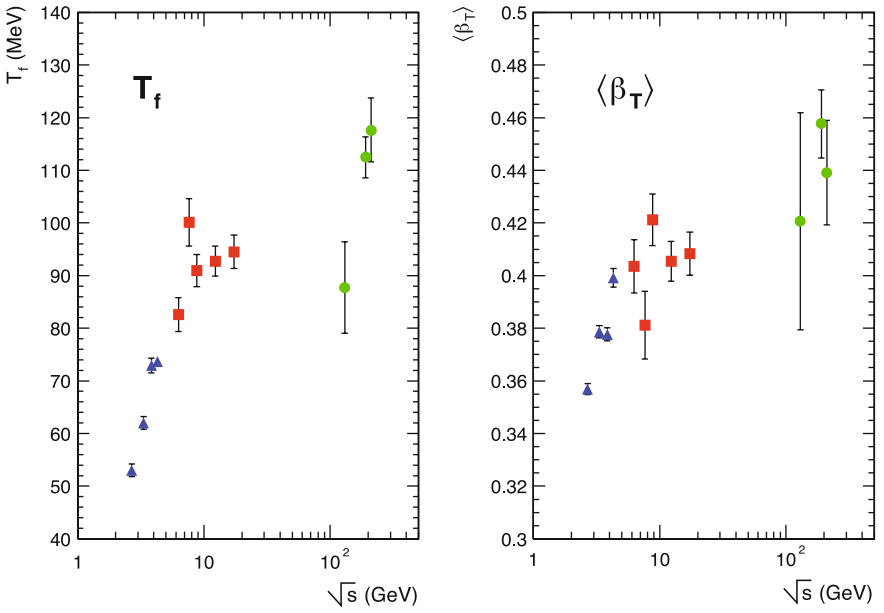

Fig. 25 Hadron decoupling temperature T_f, and average radial flow velocity $\langle\beta_T\rangle$ extracted from blast wave model (see Eq. 106) fits of m_T spectra vs. $\sqrt{s}$ [61]

In summary we conclude that hadronic hadrochemical freeze-out occurs near the parton–hadron boundary line of Fig. 1, at high $\sqrt{s}$. This fixes the hadronic species equilibrium distribution at $T = T_H$. Onward from hadronic freeze-out, the expanding system is out of equilibrium as far as its hadronic species composition is concerned. However, the momentum space distributions are subject to further change during the hadronic expansion phase, predominantly due to elastic scattering and development of radial flow. This process ends in final decoupling from strong interaction, at $T_f < T_H$. Analysis of p_T spectra exhibits a collective radial flow pattern at T_f, as characterized by a radial flow velocity β_T.

4 Hadronization and Hadronic Freeze-Out in A+A Collisions

Within the course of the global expansion of the primordial reaction volume, the local flow "cells" will hit the parton–hadron phase boundary as their energy density approaches $\epsilon_{\rm crit} \approx 1\,{\rm GeV/fm}^3$. Hadronization will thus occur, not at an instant over the entire interaction volume, but within a finite overall time interval [100, 101] that results from the spread of proper time at which individual cells or coherent clusters of such cells (as developed during expansion) arrive at the phase boundary. However, irrespective of such a local–temporal occurrence, the hadronization process (which is governed by non-perturbative QCD at the low Q^2 corresponding to bulk hadronization) universally results in a novel, *global* equilibrium property that concerns the relative abundance of produced hadrons and resonances. This so-called hadrochemical equilibrium state is directly observable, in contrast to the stages of primordial parton equilibration that are only indirectly assessed, via dynamical model studies.

This equilibrium population of species occurs in both elementary and nuclear collisions [126, 127]. We have seen in Fig. 19 a first illustration, by e^+e^- annihilation data at $\sqrt{s} = 91.2\,{\rm GeV}$ LEP energy, that are well reproduced by the partition functions of the statistical hadronization model (SHM) in its canonical form [98]. The derived hadronization temperature, $T_H = 165\,{\rm MeV}$, turns out to be universal to all elementary and nuclear collision processes at $\sqrt{s} \geq 20\,{\rm GeV}$, and it agrees with the limiting temperature predicted by Hagedorn [6] to occur in any multi-hadronic equilibrium system once the energy density approaches about $0.6\,{\rm GeV/fm}^3$. Thus, the upper limit of hadronic equilibrium density corresponds, closely, to the lower limit, $\epsilon_{\rm crit} = 0.6{-}1.0\,{\rm GeV/fm}^3$ of partonic equilibrium matter, according to lattice QCD [53, 54]. In elementary collisions only about 20 partons or hadrons participate: there should be no chance to approach thermodynamic equilibrium of species by rescattering cascades, neither in the partonic nor in the hadronic phase. The fact that, nevertheless, the hadron formation temperature T_H coincides with the Hagedorn limiting temperature and with the QCD confinement temperature is a consequence of the non-perturbative QCD hadronization process itself [99], which "gives birth" to hadrons/resonances in canonical equilibrium, at high $\sqrt{s}$, as we shall see below. This process also governs A+A collisions, but as it occurs here under conditions of

high energy density extended over considerable volume, the SHM description now requires a *grand* canonical ensemble, with important consequences for production of strange hadrons (strangeness enhancement).

The grand canonical order of hadron/resonance production in central A+A collisions, and its characteristic strangeness enhancement, shows that a state of extended matter that is quantum mechanically coherent must exist at hadronization [102, 103, 126, 127]. Whether or not it also reflects partonic equilibrium properties (including flavor equilibrium), that would allow us to claim the direct observation of a quark–gluon plasma state near T_c, cannot be decided on the basis of this observation alone, as the hadronization process somehow generates, by itself, the observed hadronic equilibrium. This conclusion, however, is still the subject of controversy [126, 127].

Two typical examples of grand canonical SHM application are illustrated in Figs. 26 and 27, the first showing total hadron multiplicities in central Pb+Pb collisions at $\sqrt{s} = 17.3\,\text{GeV}$ by NA49 [117, 118] confronted with SHM predictions by Becattini et al. [28]. This plot is similar to Fig. 19 in which e^+e^- annihilation to hadrons is confronted with an SHM prediction derived from the *canonical* ensemble [98]. Central Au+Au collision data at $\sqrt{s} = 200\,\text{GeV}$ from several RHIC experiments are compared to grand canonical model predictions by Braun-Munzinger et al. [128] in Fig. 27. The key model parameters T_H and the baryo-chemical potential μ_B result as 159 MeV (160 MeV) and 247 MeV (20 MeV) at $\sqrt{s} = 17.3\,(200)\,\text{GeV}$, respectively. The universality of the hadronization temperature is obvious from comparison of the present values with the results of the canonical procedure employed in e^+e^- annihilation to hadrons at $\sqrt{s} = 91.2\,\text{GeV}$ (Fig. 19), and in canonical SHM fits [129] to p+p collision data at $\sqrt{s} = 27.4\,\text{GeV}$ where $T_H = 159$ and 169 MeV, respectively.

Figures 26 and 27 illustrate two different approaches employed in grand canonical SHM application, the former addressing the values of the hadronic multiplicities as obtained in approximate full 4π acceptance (within limitations implied by detector performance), the latter employing a set of multiplicity *ratios* obtained in the vicinity of mid-rapidity as invited, at RHIC energy, by the limited acceptance of the STAR and PHENIX experiments. The latter approach is appropriate, clearly, in the limit of boost-invariant rapidity distributions where hadron production ratios would not depend on the choice of the observational rapidity interval. We have shown in Sect. 3.2 that such conditions do, in fact, set in at top RHIC energy, as referred to in Fig. 27. However, at low $\sqrt{s}$ the y-distributions are far from boost invariant, and the total rapidity gap Δy may become comparable, in the extreme case, to the natural rapidity widths of hadrons emitted in the idealized situation of a single, isotropically decaying fireball positioned at mid-rapidity. Its rapidity spectra, Eq. (86), resemble Gaussians with widths $\Gamma_i \approx 2.35\,(T/m_i)^{1/2}$ for hadron masses m_i. Clearly, the particle ratios $(dN_i/dy)/(dN_j/dy)$ then depend strongly on the position of the rapidity interval dy: away from $y = 0$ heavy hadrons will be strongly suppressed, and particle yields in narrow rapidity intervals are useless for a statistical model analysis unless it is known a priori that the radiator is a single stationary spherical fireball [130]. This is not the case toward top SPS energy (see

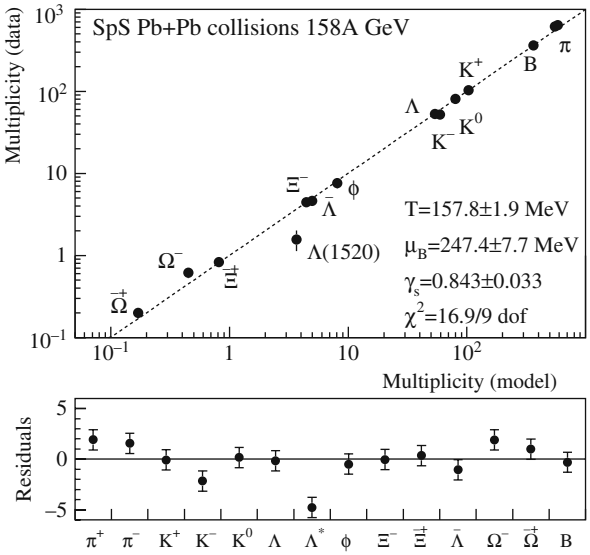

Fig. 26 Total hadron multiplicities in central Pb+Pb collisions at $\sqrt{s} = 17.3$ GeV [117, 118] vs. prediction of the grand canonical statistical hadronization model [28]

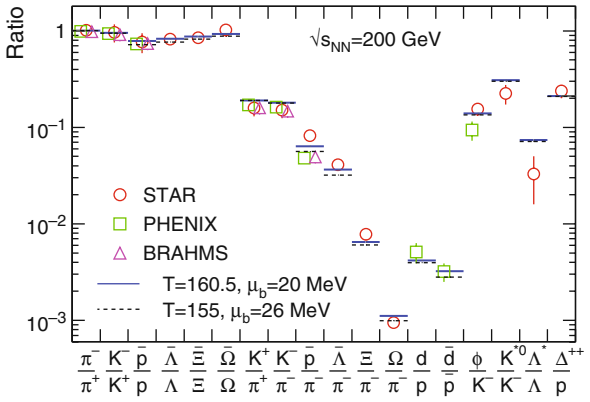

Fig. 27 Hadron multiplicity ratios at mid-rapidity in central Au+Au collisions at $\sqrt{s} = 200$ GeV from RHIC experiments STAR, PHENIX and BRAHMS, compared to predictions of the grand canonical statistical model [128]

Fig. 12), due to significant primordial longitudinal expansion of the hadron-emitting source. Given such conditions, the total multiplicity per collision event (the invariant yield divided by the total overall inelastic cross section) should be employed in the SHM analysis, as is exemplified in Fig. 26.

4.1 Hadronic Freeze-Out from Expansion Flow

The hadronic multiplicities result from integration of the invariant triple differential cross section over p_T and y. Instrumental, experiment-specific conditions tend to result in incomplete p_T and/or y acceptances. It is important to ascertain that the effects of hydrodynamic transverse and longitudinal flow do not blast a significant part of the total hadron yield to outside the acceptance, and that they, more generally, do not change the relative hadron yield composition, thus basically affecting the SHM analysis. To see that hadronization incorporates only the internal energy in the co-moving frame [130], we first assume that hadrochemical freeze-out occurs on a sharp hypersurface Σ and write the total yield of particle species i as

$$N_i = \int \frac{d^3p}{E} \int_\Sigma p^\mu d^3\sigma_\mu(x)\, f_i(x,\, p) = \int_\Sigma d^3\sigma_\mu(x) j_i^\mu(x), \tag{107}$$

where $d^3\sigma$ is the outward normal vector on the surface, and

$$j_i^\mu(x) = g_i \int d^4p 2\Theta(p^0)\delta(p^2 - m_i^2)\; p^\mu (\exp\left[p \cdot u(x) - \mu_i\right]/T \pm 1)^{-1} \tag{108}$$

is the grand canonical number current density of species i, μ_i the chemical potential, $u(x)$ the local flow velocity, and g_i the degeneracy factor. In thermal equilibrium it is given by

$$\begin{aligned} j_i^\mu(x) &= \rho_i(x) u^\mu(x) \;\text{ with} \\ \rho_i(x) &= u_\mu(x) j_i^\mu(x) = \int d^4p 2\Theta(p^0)\delta(p^2 - m_i^2)\; p \cdot u(x)\; f_i(p \cdot u(x); T; \mu_i) \\ &= \int d^3p'\; f_i(E_{p'}; T, \mu_i) = \rho_i(T, \mu_i). \end{aligned} \tag{109}$$

Here $E_{p'}$ is the energy in the local rest frame at point x. The total particle yield of species i is therefore

$$N_i = \rho_i(T, \mu_i) \int_\Sigma d^3\sigma_\mu(x) u^\mu(x) = \rho_i(T, \mu_i)\; V_\Sigma(u^\mu), \tag{110}$$

where only the total co-moving volume V_Σ of the freeze-out hypersurface Σ depends on the flow profile u^μ. V is thus a common total volume factor at hadronization (to be determined separately), and the flow pattern drops out from the yield distribution over species in 4π acceptance [130]. For nuclear collisions at SPS energies and below one thus should perform an SHM analysis of the total, 4π-integrated hadronic multiplicities, as was done in Fig. 26.

We note that the derivation above illustrates the termination problem of the hydrodynamic description of A+A collisions, the validity of which depends on conditions of a short mean free path, $\lambda < 1$ fm. A precise argumentation suggests

that two different free paths are relevant here, concerning hadron occupation number and hadron spectral freeze-out, respectively. As hadrochemical freeze-out occurs in the immediate vicinity of T_c (and $T_H \approx 160$–$165\,\mathrm{MeV}$ from Figs. 26 and 27), the hadron species distribution stays constant throughout the ensuing hadronic phase, i.e., the "chemical" mean free path abruptly becomes infinite at T_H, whereas elastic and resonant rescattering may well extend far into the hadronic phase, and so does collective pressure and flow. In fact we have seen in Sect. 3.6 that the decoupling from flow occurs at T_F as low as 90–100 MeV (Fig. 25). Thus the hydrodynamic evolution of high $\sqrt{s}$ collisions has to be, somehow artificially, stopped at the parton–hadron boundary in order to get the correct hadron multiplicities N_i, of Eqs. (107–110), which then stay frozen-out during the subsequent hadronic expansion.

The Eqs. (107–110) demonstrate the application of the Cooper–Frye prescription [131] for termination of the hydrodynamic evolution. The hyper-surface Σ describes the space–time location at which individual flow cells arrive at the freeze-out conditions, $\epsilon = \epsilon_c$ and $T = T_c$, of hadronization. At this point, the resulting hadron/resonance spectra (for species i) are then given by the Cooper–Frye formula

$$E\frac{dN_i}{d^3p} = \frac{dN_i}{dy p_T dp_T} = \frac{g_i}{(2\pi)^3}\int_\Sigma f_i(p\cdot u(x), x)\, p\cdot d^3\sigma(x), \tag{111}$$

where $p^\mu f_i d^3\sigma_\mu$ is the local flux of particle i with momentum p through the surface Σ. For the phase space distribution f in this formula one takes the local equilibrium distribution at hadronic species freeze-out from the grand canonical SHM

$$f_i(E, x) = [\exp\{(E_i - \mu_i(x))/T\} \pm 1]^{-1} \tag{112}$$

boosted with the local flow velocity $u^\mu(x)$ to the global reference frame by the substitution $E \to p\cdot u(x)$. Fixing $T = T_c$ (taken, e.g., from lattice QCD) the hadron multiplicities N_i then follow from Eq. (110), and one compares to experiment, as in Figs. 26 and 27. Now in order to follow the further evolution, throughout the hadronic rescattering phase, and to finally compare predictions of Eq. (111) to the observed flow data as represented by the various Fourier terms of Eq. (101) one has to re-initialize (with hadronic EOS) the expansion from $\Sigma(T_c = 165\,\mathrm{MeV})$ until final decoupling [119], at $T \approx 100\,\mathrm{MeV}$, thus describing e.g., radial and elliptic flows.

Alternatively, one might end the hydrodynamic description at $T = T_c$ and match the thus obtained phase space distribution of Eq. (111) to a microscopic hadron transport model of the hadronic expansion phase [112, 113, 132]. This procedure is illustrated in Fig. 28 by a UrQMD [133] calculation of Bass and Dumitru [134] for central Au+Au collisions at top RHIC energy. We select here the results concerning the survival of the hadronic multiplicities N_i throughout the dynamics of the hadronic expansion phase, which we have postulated above, based on the equality of the hadronization temperatures, $T_H \approx 160\,\mathrm{MeV}$, observed in e^+e^- annihilation (Fig. 19), where no hadronic expansion phase exists, and in central collisions of

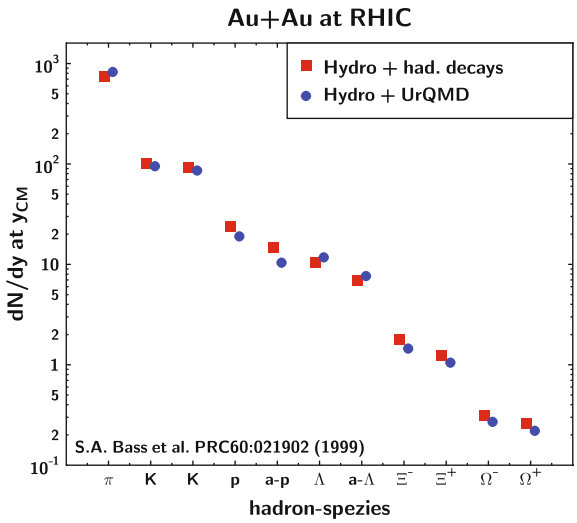

Fig. 28 Modification of mid-rapidity hadron multiplicities in central Au+Au collisions at $\sqrt{s} = 200\,\text{GeV}$ after chemical freeze-out at $T = T_c$. *Squares* show a hydrodynamic model prediction at $T = T_c$ (without further interaction); *circles* show the result of an attached UrQMD hadronic cascade expansion calculation [103]

$A \approx 200$ nuclei (Figs. 26 and 27). In fact, Fig. 28 shows that the $\{N_i\}$ observed at the end of the hadronic cascade evolution agree, closely, with the initial $\{N_i\}$ as derived from a Cooper–Frye procedure (Eq. 110) directly at hadronization. On the other hand, p_T spectra and radial flow observables change, drastically, during the hadronic cascade expansion phase.

The hadronic multiplicity distribution $\{N_i\}$, arising from the hadronization process at high $\sqrt{s}$, freezes out instantaneously also in A+A collisions and is thus preserved throughout the (isentropic) hadronic expansion phase. *It is thus directly measurable* and, moreover, its hadrochemical equilibrium features lend themselves to an analysis within the framework of Hagedorn-type statistical, grand canonical models. As we shall show below, the outcome of this analysis is contained in a $[T_H, \mu_B]$ parameter pair that reflects the conditions of QCD matter prevailing at hadronization, at each considered $\sqrt{s}$. In fact, the $[T, \mu]$ points resulting from the SHM analysis exhibited in Figs. 26 and 27 (at $\sqrt{s} = 17.3$ and 200 GeV, respectively) have been shown in the QCD matter phase diagram of Fig. 1 to approach, closely, the parton–hadron phase coexistence line predicted by lattice QCD. Thus, $T_H \approx T_c$ at high $\sqrt{s}$: hadrochemical freeze-out occurs in the immediate vicinity of QCD hadronization, thus providing for a location of the QCD phase boundary.

4.2 Grand Canonical Strangeness Enhancement

The statistical model analysis [28, 126–128] of the hadronization species distribution N_i in A+A collisions is based on the grand canonical partition function for species i,

$$\ln Z_i = \frac{g_i V}{6\pi^2 T} \int_0^\infty \frac{k^4 dk}{E_i(k) \exp\{(E_i(k) - \mu_i)/T\} \pm 1}, \tag{113}$$

where $E_i^2 = k^2 + m_i^2$, and $\mu_i \equiv \mu_B B_i + \mu_s S_i + \mu_I I_3^i$ is the total chemical potential for baryon number B, strangeness S, and isospin three-component I_3. Its role in Eq. (113) is to enforce, *on average* over the entire hadron source volume, the conservation of these quantum numbers. In fact, making use of overall strangeness neutrality ($\sum_i N_i S_i = 0$) as well as of conserved baryon number (participant Z+N) and isospin (participant (N–Z)/Z) one can reduce μ_i to a single effective potential μ_b. Hadronic freeze-out is thus captured in three parameters, T, V, and μ_b. The density of hadron/resonance species i then results as

$$n_i = \frac{T}{V} \frac{\delta}{\delta_\mu} \ln Z_i \tag{114}$$

which gives

$$N_i = V n_i = \frac{g_i V}{(2\pi)^2} \int_0^\infty \frac{k^2 dk}{\exp\{(E_i(k) - \mu_i)/T\} \pm 1}. \tag{115}$$

We see that the common freeze-out volume parameter is canceled if one considers hadron multiplicity ratios, N_i/N_j, as was done in Fig. 27. Integration over momentum yields the one-particle function

$$N_i = \frac{VTg_i}{2\pi^2} m_i^2 \sum_{n=1}^{\infty} \frac{(\pm 1)^{n+1}}{n} K_2\left(\frac{nm_i}{T}\right) \exp\left(\frac{n\mu_i}{T}\right), \tag{116}$$

where K_2 is the modified Bessel function. At high T the effects of Bose or Fermi statistics (represented by the ± 1 term in the denominators of Eqs. (113 and 115) may be ignored , finally leading to the Boltzmann approximation

$$N_i = \frac{VTgi}{2\pi^2} m_i^2 K_2\left(\frac{m_i}{T}\right) \exp\left(\frac{\mu_i}{T}\right) \tag{117}$$

which is the first term of Eq. (116). This approximation is employed throughout the SHM analysis. It describes the *primary* yield of hadron species i, directly at hadronization. The abundance of hadronic resonance states is obtained convoluting Eq. (115) with a relativistic Breit–Wigner distribution [28]. Finally, the overall multiplicity, to be compared to the data, is determined as the sum of the primary multiplicity (cf. Eq. 117) and the contributions arising from the unresolved decay of heavier hadrons and resonances

$$N_i^{\text{observed}} = N_i^{\text{primary}} + \sum_j Br(j \to i)\, N_j. \tag{118}$$

After having exposed the formal gear of grand canonical ensemble analysis we note that Eq. (117) permits a simple, first orientation concerning the relation of T to μ_B in A+A collisions by considering, e.g., the antiproton to proton production ratio. From Eq. (117) we infer the simple expression

$$N(\overline{p})/N(p) = \exp(-2\mu_B/T). \tag{119}$$

Taking the mid-rapidity value 0.8 for $\overline{p}/p$ (from Fig. 27) at top RHIC energy, and assuming that hadronization occurs directly at the QCD phase boundary, and hence $T \approx T_c \approx 165\,\text{MeV}$, we get $\mu_B \simeq 18\,\text{MeV}$ from Eq. (119), in close agreement with the result, $\mu_B = 20\,\text{MeV}$, obtained [128] from the full SHM analysis. Equation (119) illustrates the role played by μ_B in the grand canonical ensemble. It logarithmically depends on the ratio of newly created quark–antiquark pairs (the latter represented by the $\bar{p}$ yield), to the total number of quarks including the net baryon number-carrying valence quarks (represented by the p yield).

The most outstanding property of the hadronic multiplicities observed in central A+A collisions is the enhancement of all strange hadron species, by factors ranging from about 2 to 20, as compared to the corresponding production rates in elementary hadron–hadron (and e^+e^- annihilation) reactions at the same $\sqrt{s}$. That is, the nuclear collision modifies the relative strangeness output by a "nuclear modification factor," $R_s^{\text{AA}} = N_s^{\text{AA}}/0.5\,N_{\text{part}} \cdot N_s^{pp}$, which depends on $\sqrt{s}$ and N_{part} and features a hierarchy with regard to the strangeness number $s = 1$–3 of the considered species, $R_{s=1}^{\text{AA}} < R_{s=2}^{\text{AA}} < R_{s=3}^{\text{AA}}$. These properties are illustrated in Figs. 29 and 30. The former shows the ratio of total K^+ to positive pion multiplicities in central Au+Au/Pb+Pb collisions, from lower AGS to top RHIC energies, in comparison to corresponding ratios from minimum-bias p+p collisions [117, 118]. We have chosen this ratio, instead of $\langle K^+ \rangle / N_{\text{part}}$, because it reflects, rather directly, the "Wroblewski ratio" of produced strange to nonstrange quarks [126, 127], contained in the produced hadrons,

$$\lambda_s \equiv \frac{2(\langle s \rangle + \langle \overline{s} \rangle)}{\langle u \rangle + \langle d \rangle + \langle \overline{u} \rangle + \langle \overline{d} \rangle} \approx \begin{cases} 0.2 \text{ in pp} \\ 0.45 \text{ in AA.} \end{cases} \tag{120}$$

The low value of λ_s in pp (and all other elementary) collisions reflects a quark population far away from u, d, s flavor equilibrium, indicating *strangeness suppression* [129].

The so-called *strangeness enhancement* property of A+A collisions (obvious from Figs. 29 and 30) is, thus, seen as the removal of strangeness suppression; it is also referred to as a *strangeness saturation*, in SHM analysis [126–128], for the reason that $\lambda_s \approx 0.45$ corresponds to the grand canonical limit of strangeness production, implicit in the analysis illustrated in Figs. 26 and 27. The average $R_{s=1}^{\text{AA}}$ at $\sqrt{s} \geq 10\,\text{GeV}$ thus is about 2.2, both in the data of Fig. 29 and in the statistical model. It increases (Fig. 30) toward about 10 in $s = 3$ production of Ω hyperons.

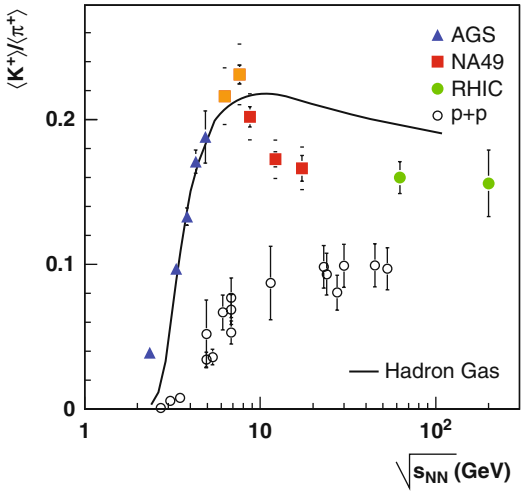

Fig. 29 The ratio of total K^+ to total π^+ multiplicity as a function of $\sqrt{s}$, in central Au+Au and Pb+Pb collisions and in p+p minimum-bias collisions [88]

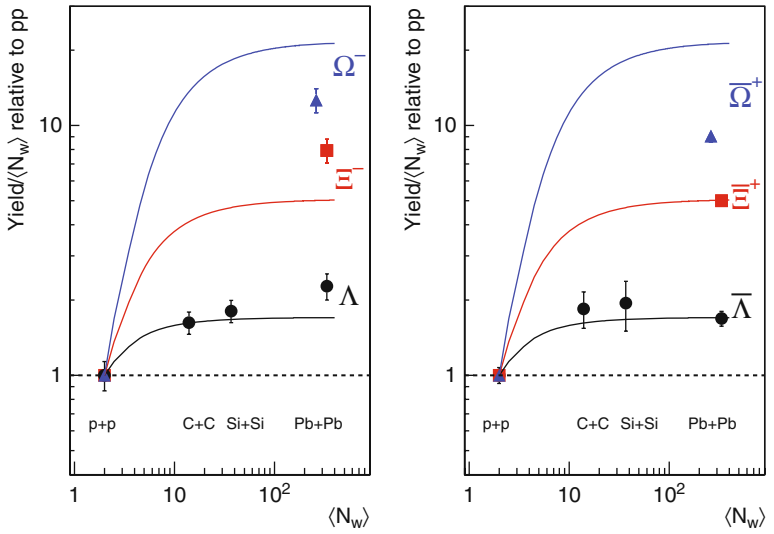

Fig. 30 The nuclear modification factors $R^{\mathrm{AA}}_{s=1,2,3}$ for hyperon and anti-hyperon production in nucleus–nucleus collisions at $\sqrt{s} = 17.3\,\mathrm{GeV}$, relative to the p+p reference at the same energy scaled by $N_W (= N_{\mathrm{part}})$. The NA49 data refer to total 4π yields [135]. *Closed lines* represent the inverse strangeness suppression factors from ref. [136], at this energy

In order to provide for a first guidance concerning the above facts and terminology regarding strangeness production, we propose an extremely naive argument, based on the empirical fact of a universal hadronization temperature (Figs. 19, 26, and 27) at high $\sqrt{s}$. Noting that $\langle s\rangle = \langle\overline{s}\rangle$ and $\langle u\rangle \approx \langle\overline{u}\rangle \approx \langle d\rangle \approx \langle\overline{d}\rangle$ in a QGP system at μ_b near zero, and $T = 165\,\mathrm{MeV}$, just prior to hadronization, $\lambda_s \approx \langle s\rangle / \langle u\rangle \approx \exp\{(m_u - m_s)/T\} = 0.45$ at $p_T \to 0$ if we take current quark masses, $m_s - m_u \approx 130\,\mathrm{MeV}$. That is, the value of λ_s in A+A collisions at high $\sqrt{s}$ resembles that of a grand canonical QGP at $\mu_b \to 0$, as was indeed shown in a three-flavor lattice QCD calculation [137] at $T \approx T_c$. On the contrary, a p+p collision features no QGP but a small fireball volume, at $T \approx T_c$, within which local strangeness neutrality, $\langle s\rangle = \langle\overline{s}\rangle$ has to be strictly enforced, implying a canonical treatment [129]. In our naive model the exponential penalty factor thus contains twice the strangeness quark mass in the exponent, λ_s in pp collisions $\approx \exp\{2(m_u - m_s)/T\} \approx 0.2$, in agreement with the observations concerning strangeness suppression, which are thus referred to as canonical suppression. In a further extension of our toy model, now ignoring the u, d masses in comparison to $m_s \approx 135\,\mathrm{MeV}$, we can estimate the hierarchy of hyperon enhancement in A+A collisions,

$$R_s^{\mathrm{AA}} \propto N_s^{\mathrm{AA}}/N_s^{pp} \cdot 0.5\, N_{\mathrm{part}} \approx \exp\{(-sm_s + 2sm_s)/T\} = 2.2,\ 5.1,\ 11.6 \quad (121)$$

for $s = 1$–3, respectively. Figure 30 shows that these estimates correspond well with the data [135] for R^{AA} derived in 4π acceptance for Λ, Ξ, and Ω as well as for their antiparticles, from central Pb+Pb collisions at $\sqrt{s} = 17.3\,\mathrm{GeV}$. The p+p reference data and C+C, Si+Si central collisions (obtained by fragmentation of the SPS Pb beam) refer to separate NA49 measurements at the same energy.

The above qualitative considerations suggest that the relative strangeness yields reflect a transition concerning the fireball volume (that is formed in the course of a preceding dynamical evolution) once it enters hadronization. Within the small volumes, featured by elementary collisions (see Sect. 4.3), phase space is severely reduced by the requirement of *local* quantum number conservation [129, 138] including, in particular, local strangeness neutrality. These constraints are seen to be removed in A+A collisions, in which extended volumes of high primordial energy density are formed. Entering the hadronization stage, after an evolution of expansive cooling, these extended volumes will decay to hadrons under conditions of global quantum mechanical coherence, resulting in quantum number conservation occurring, nonlocally, and *on average* over the entire decaying volume. This large coherent volume decay mode removes the restrictions, implied by local quantum number balancing. In the above naive model we have thus assumed that the hadronization of an omega hyperon in A+A collisions faces the phase space penalty factor of only three s quarks to be gathered, the corresponding three $\overline{s}$ quarks being taken care of elsewhere in the extended volume by global strangeness conservation. In the framework of the SHM this situation is represented by the grand canonical ensemble (Eqs. 115 and 117); the global chemical potential μ_b expresses quantum number conservation *on average*. Strict local conservation is represented by the canonical ensemble.

The grand canonical (GC) situation can be shown to be the large collision volume limit (with high multiplicities $\{N_i\}$) of the canonical (C) formulation [136, 139], with a continuous transition concerning the degree of canonical strangeness suppression [136]. To see this one starts from a system that is already in the GC limit with respect to baryon number and charge conservation whereas strangeness is treated canonically. Restricting to $s = 1$ and -1 the GC strange particle densities can be written (from Eq. (117) as

$$n^{GC}_{s=\pm1} = \frac{Z_{s=\pm1}}{V}\,\lambda_s^{\pm1} \tag{122}$$

with

$$Z_{s=\pm1} = \frac{V g_s}{2\pi^2}\, m_s^2\, K_2\left(\frac{m_s}{T}\right) \exp\left\{(B_s\mu_B + Q_s\mu_Q)/T\right\} \tag{123}$$

and a "fugacity factor" $\lambda_s^{\pm1} = \exp(\mu_s/T)$. The canonical strange particle density can be written as [136]

$$n_s^C = n_s^{GC} \cdot (\tilde{\lambda_s}) \tag{124}$$

with an effective fugacity factor

$$\tilde{\lambda_s} = \frac{S_{\pm1}}{\sqrt{S_1 S_{-1}}}\,\frac{I_1(x)}{I_0(x)}, \tag{125}$$

where $S_{\pm1} = \sum_{s=\pm1} Z_{s=\pm1}$ is the sum over all created hadrons and resonances with $s = \pm1$, the $I_n(x)$ are modified Bessel functions, and $x = 2\sqrt{S_1 S_{-1}}$ is proportional to the total fireball volume V. In the limit $x \approx V \to \infty$ the suppression factor $I_1(x)/I_0(x) \to 1$, and the ratio $S_{\pm1}/\sqrt{S_1 S_{-1}}$ corresponds exactly to the fugacity λ_s in the GC formulation (see Eq. 122). Thus the C and GC formulations are equivalent in this limit, and the canonical strangeness suppression effect disappears. Upon generalization to the complete strange hadron spectrum, with $s = \pm1, \pm2, \pm3$, the strangeness suppression factor results [136] as

$$\eta(s) = I_s(x)/I_0(x). \tag{126}$$

In particular for small x (volume), $\eta(s) \to (x/2)^s$, and one expects that the larger the strangeness content of the particle the smaller the suppression factor, and hence the larger the enhancement in going from elementary to central A+A collisions. This explains the hierarchy addressed in Eq. (121) and apparent from the data shown in Fig. 30. In fact, the curves shown in this figure represent the results obtained from Eq. (126), for $s = 1$–3 hyperon production at $\sqrt{s} = 17.3$ GeV [136]. They are seen to be in qualitative agreement with the data. However, the scarcity of data, existing at top SPS energy for total hyperon yields, obtained in 4π acceptance (recall the

arguments in Sect. 4.1) both for A+A and p+p collisions does not yet permit to cover the SHM strangeness saturation curves in detail, for $s > 1$.

This saturation is seen in Fig. 30, to set in already at modest system sizes, but sequentially so, for ascending hyperon strangeness. Note that SHM saturation is sequentially approached, from Eq. (126), with increasing fireball *volume* V. In order to make contact to the experimental size scaling with centrality, e.g., $N_{\rm part}$, the model of ref. [136], which is illustrated in Fig. 30, has converted the genuine volume scale to the $N_{\rm part}$ scale by assuming a universal eigenvolume of $7\,{\rm fm}^3$ per participant nucleon, i.e., $N_{\rm part} = 10$ really means a coherent fireball volume of $70\,{\rm fm}^3$, in Fig. 30. Within this definition, saturation of $s = 1$–3 sets in at fireball volumes at hadronization of about 60, 240, and $600\,{\rm fm}^3$, respectively: this is the *real* message of the SHM curves in Fig. 30.

The above direct translation of coherent fireball volume to participant number is problematic [140] as it assumes that all participating nucleons enter into a single primordially coherent fireball. This is, however, not the case [140] particularly in the relative small scattering systems that cover the initial steep increase in $\eta(s)$, where several local high-density clusters are formed, each containing a fraction of $N_{\rm part}$. This is revealed by a percolation model [140] of cluster overlap attached to a Glauber calculation of the collision/energy density. At each $N_{\rm part}$ an average cluster volume distribution results which can be transformed by Eq. (126) to an average $\{\eta(s, V)\}$ distribution whose weighted mean is the appropriate effective canonical suppression factor corresponding to $N_{\rm part}$. On the latter scale, the SHM suppression curve thus shifts to higher $N_{\rm part}$, as is shown in Fig. 31 for the K^+/π^+ ratio vs. $N_{\rm part}$, measured at mid-rapidity by PHENIX in Au+Au collisions at $\sqrt{s} = 200\,{\rm GeV}$, which is reproduced by the percolation model [140]. Also included is a prediction for Cu+Cu at this energy which rises more steeply on the common $N_{\rm part}$ scale because the collision and energy density reached in central Cu+Cu collisions, at $N_{\rm part} \approx 100$, exceed that in peripheral Au+Au collisions (at the same $N_{\rm part}$) which share a more prominent contribution from the dilute surface regions of the nuclear

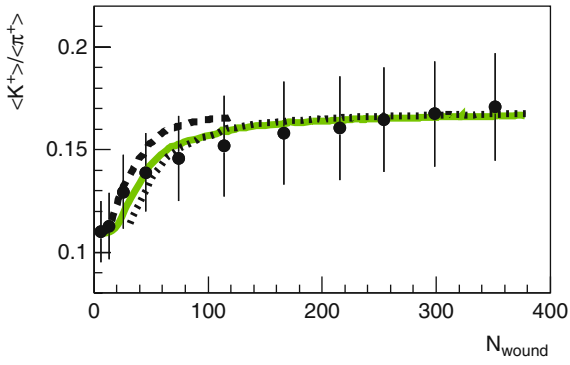

Fig. 31 The mid-rapidity K^+ to π^+ ratio vs. $N_{\rm part}$ in minimum-bias Au+Au collisions at $\sqrt{s} = 200\,{\rm GeV}$, compared to the percolation model [140] (*solid line*); a prediction of which for Cu+Cu at similar energy is given by the *long dashed line* (see text for detail)

density profile. We note, finally, that this deviation from universal N_{part} scaling does not contradict the observations of a perfect such scaling as far as overall charged particle multiplicity densities are concerned (recall Fig. 14) which are dominated by pions, not subject to size-dependent canonical suppression.

4.3 Origin of Hadrochemical Equilibrium

The statistical hadronization model (SHM) is *not* a model of the QCD confinement process leading to hadrons, which occurs once the dynamical cooling evolution of the system arrives at T_c. At this stage the partonic reaction volume, small in elementary collisions but extended in A+A collisions, will decay (by whatever elementary QCD process) to on-shell hadrons and resonances. This coherent quantum mechanical decay results in a de-coherent quasi-classical, primordial on-shell hadron–resonance population which, at the instant of its formation, lends itself to a quasi-classical Gibbs ensemble description. Its detailed modalities (canonical for small decaying systems, grand canonical for extended fireballs in A+A collisions), and its derived parameters $[T, \mu_B]$ merely recast the conditions, prevailing at hadronization. The success of SHM analysis thus implies that the QCD hadronization process ends in statistical equilibrium concerning the hadron–resonance species population.

In order to identify mechanisms in QCD hadronization that introduce the hadrochemical equilibrium we refer to jet hadronization in e^+e^- annihilation reactions, which we showed in Fig. 19 to be well described by the canonical SHM. In dijet formation at LEP energy, $\sqrt{s} = 92\,\text{GeV}$, we find a charged particle multiplicity of about 10 per jet, and we estimate that, likewise, about 10 primordial partons participate on either side of the back-to-back dijet [99]. There is thus no chance for either a partonic or hadronic, extensive rescattering toward chemical equilibrium. However, in the jet hadronization models developed by Amati and Veneziano [97], Webber [141], and Ellis and Geiger [99] the period of QCD DGLAP parton shower evolution (and of perturbative QCD, in general) ends with local color neutralization, by formation of spatial partonic singlet clusters. This QCD "color pre-confinement" [97] process reminds of a coalescence mechanism, in which the momenta and the initial virtual masses of the individual clustering partons get converted to internal, invariant virtual mass of color neutral, *spatially extended* objects. Their mass spectrum [141] extends from about 0.5 to 10 GeV. This cluster mass distribution, shown in Fig. 32, represents the first stochastic element in this hadronization model.

The clusters are then reinterpreted within non-perturbative QCD: their internal, initially perturbative QCD vacuum energy gets replaced by non-perturbative quark and gluon condensates, making the clusters appear like hadronic resonances. Their subsequent quantum mechanical decay to on-shell hadrons is governed by the phase space weights given by the hadron and resonance spectrum [99, 141]. That is, the clusters decay under "phase space dominance" [99], the outcome being a micro-canonical or a canonical hadron and resonance ensemble [98, 126, 127]. The

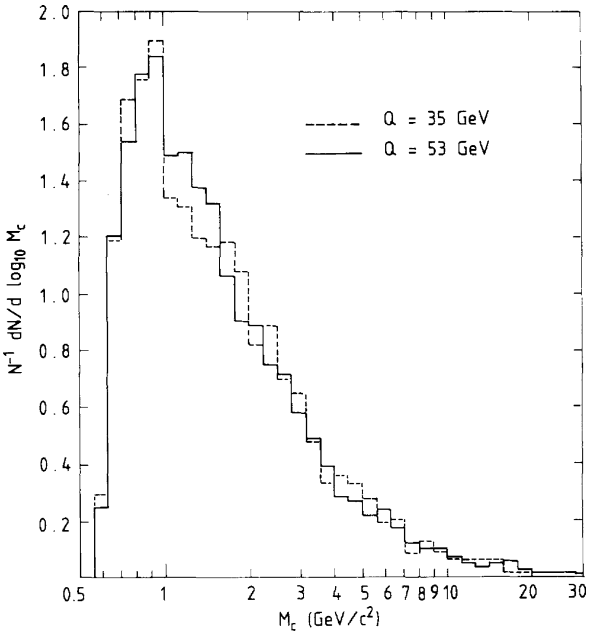

Fig. 32 Invariant mass spectrum of color neutralization clusters in the Veneziano–Webber hadronization model [97, 141]

apparent hadrochemical equilibrium thus is the consequence of QCD color neutralization to clusters, and their quantum mechanical decay under local quantum number conservation and phase space weights. We note that the alternative description of hadronization, by string decay [142], contains a quantum mechanical tunneling mechanism, leading to a similar phase space dominance [143, 144].

Hadronization in e^+e^- annihilation thus occurs from local clusters (or strings), isolated in vacuum, of different mass but similar energy density corresponding to QCD confinement. These clusters are boosted with respect to each other, but it was shown [145] that for a Lorentz invariant scalar, such as multiplicity, the contributions of each cluster (at similar T) can be represented by a single canonical system with volume equal to the sum of clusters. In the fit of Fig. 19 this volume sum amounts to about 25 fm^3 [98]; the individual cluster volumes are thus quite small, of magnitude a few fm^3 [99]. This implies maximum canonical strangeness suppression but may, in fact, require a micro-canonical treatment of strangeness [129], implying a further suppression. These MC effects are oftentimes included [146] in the canonical partition functions by an extra strangeness fugacity parameter $\gamma_s < 1$ which suppresses $s = 1$–3 in a hierarchical manner, $\langle N_i(s) \rangle \approx (\gamma_s)^{s_i}$. The fit of Fig. 19 requires $\gamma_s = 0.66$, a value typical of canonical multiplicity analysis in $p + p$, $p + \overline{p}$, and e^+e^- annihilation collisions [129] at $\sqrt{s} \geq 30\,\mathrm{GeV}$.

The above picture of hadrochemical equilibrium resulting from the combined stochastic features of QCD color neutralization by cluster formation and subse-

quent quantum mechanical decay to the on-shell hadron and resonance spectrum (under phase space governance) lends itself to a straightforward extension to A+A collisions. The essential new features, of grand canonical hadronization including strangeness enhancement, should result from the fact that extended space–time volumes of $\epsilon > \epsilon_{\rm crit}$ are formed in the course of primordial partonic shower evolution, an overlap effect increasing both with $\sqrt{s}$ and with the size of the primordial interaction volume. As the volume of the elementary hadronization clusters amounts to several fm^3 it is inevitable that the clusters coalesce, to form extended "super-cluster" volumes prior to hadronization [140]. As these super-clusters develop toward hadronization via non-perturbative QCD dynamics, it is *plausible* to assume an overall quantum mechanical coherence to arise over the entire extended volume, which will thus decay to hadrons under global quantum number conservation, the decay products thus modeled by the GC ensemble.

Our expectation that space–time coalescence of individual hadronization clusters will lead to a global, quantum mechanically coherent, extended super-cluster volume, which decays under phase space dominance, appears as an analogy to the dynamics and quantum mechanics governing low-energy nuclear fission from a preceding "compound nucleus" [147]. Note that the observation of a smooth transition from canonical strangeness suppression to grand canonical saturation (Figs. 30 and 31) lends further support to the above picture of a percolative growth [140] of the volume that is about to undergo hadronization.

An extended, coherent quark–gluon plasma state would, of course, represent an ideal example of such a volume [148] and, in fact, we could imagine that the spatial extension of the plasma state results from a percolative overlap of primordial zones of high energy density, which becomes more prominent with increasing $\sqrt{s}$ and $N_{\rm part}$. A QGP state preceding hadronization will thus lead to all the observed features. However, to be precise: The hadronizing QCD system of extended matter decaying quantum coherently could still be a nonequilibrium precursor of the ideal equilibrium QGP, because we have seen above that hadrochemical equilibrium also occurs in e^+e^- annihilation where no partonic equilibrium exists. It gets established in the course of hadronization, irrespective of the degree of equilibrium prevailing in the preceding partonic phase.

4.4 Hadronization vs. Rapidity and $\sqrt{s}$

We have argued in Sect. 4.1 that, at relatively low $\sqrt{s}$, the total rapidity gap Δy does not significantly exceed the natural thermal rapidity spreading width $\Gamma_i \approx 2.35\,(T/m_i)^{1/2}$ of a single, isotropically decaying fireball, centered at mid-rapidity and emitting hadrons of mass m_i [130]. However, this procedure involves an idealization because in the real Pb+Pb collision the intersecting dilute surface sections of the nuclear density profiles will lead to a significant contribution of single-scattering NN collisions, outside the central high-density fireball. The leading hadron properties of such "corona collisions" result in wider proper rapidity distributions, quite

different from those of the central fireball decay hadrons. Their contribution will thus be prominent near target/projectile rapidity and will feature a canonically suppressed strangeness. The one-fireball assumption, although inevitable at small Δy, does not quite resemble the physical reality. This may explain the need for an additional strangeness suppression factor in the GC one-particle partition function (Eq. 113) that has, unfortunately, also been labeled γ_s but expresses physics reasons quite different from the extra suppression factor that reflects micro-canonical phase space constraints in elementary collisions. It turns out that all GC analysis of central A+A collisions at low $\sqrt{s}$, and addressed to total 4π multiplicities, requires a γ_s of 0.7–0.85 [28]; in the fit of Fig. 26 $\gamma_s = 0.84$.

At RHIC, $\Delta y \approx 11 \gg \Gamma_i$, and such difficulties disappear: $\gamma_s \approx 1$ at mid-rapidity and, moreover, the wide gap permits an SHM analysis which is differential in y. Figure 33 shows the y-dependence of the ratios π^-/π^+, K^-/K^+, and $\overline{p}/p$ as obtained by BRAHMS [149] in central Au+Au collisions at $\sqrt{s} = 200\,\text{GeV}$. The figure shows a dramatic dependence of the $\overline{p}/p$ ratio, which reflects the local baryo-chemical potential according to Eq. (119). At $y_{CM} > 1$ the $\overline{p}/p$ ratio drops down steeply, to about 0.2 at $y \approx 3.5$, thus making close contact to the top SPS energy value obtained by NA49 [150]. The K^-/K^+ ratio follows a similar but weaker drop-off pattern, to about 0.65 again matching with the top SPS energy value of about 0.6 [151]. The deviation from unity of these ratios reflects the rapidity densities of initial valence u, d quarks, relative to the densities of newly created light, and strange quark–antiquark pairs, i.e., the y-distribution of the net baryon number density and of the related baryo-chemical potential of the GC ensemble. Thus, in analyzing successive bins of the rapidity distributions in Fig. 33, the major variation in the GC fit concerns the baryo-chemical potential μ_B(y) which increases from about 20 MeV (Fig. 27) at mid-rapidity to about 150 MeV at $y \geq 3$ while the hadronization temperature stays constant, at $T = 160\,\text{MeV}$. This interplay between

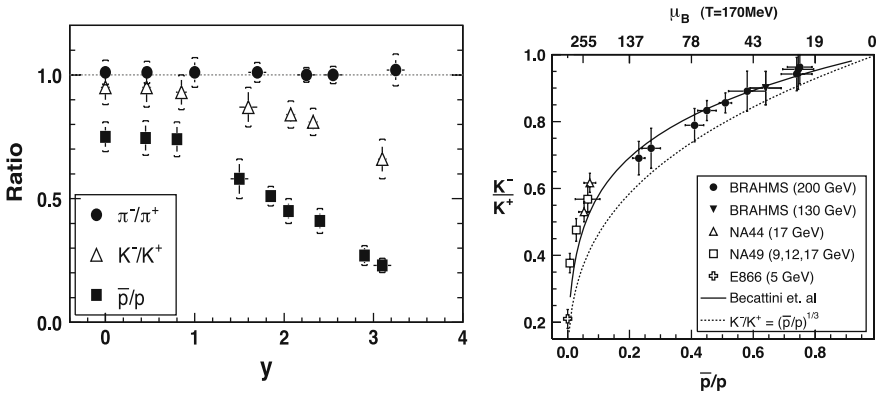

Fig. 33 (*left*) Anti-hadron to hadron ratios as a function of rapidity in central Au+Au collisions at $\sqrt{s} = 200\,\text{GeV}$. The *right panel* shows an interpretation of the correlation between $\overline{p}/p$ and K^-/K^+ in terms of baryo-chemical potential μ_B variation in the grand canonical statistical model. From [149]

K^-/K^+, $\overline{p}/p$, and μ_B is illustrated [149] in the right-hand panel of Fig. 33 and shown to be well accounted for by the GC statistical model [152].

These considerations imply that hadronization at RHIC (and LHC) energy occurs *local* in y-space and *late* in time. The density distribution of net baryon number results from the primordial pQCD shower evolution (c.f. Sect. 3.4) and is thus fixed at formation time, $t_0 \leq 0.5$ fm/c at RHIC. Hadronization of the bulk partonic matter occurs later, at $t \geq 3$ fm/c [100, 101, 112, 113], and transmits the local conditions in rapidity space by preserving the local net baryon quantum number density. Most importantly we conclude that hadronization occurs, not from a single longitudinally boosted fireball but from a succession of "super-clusters," of different partonic composition depending on y, and decaying at different time due to the Lorentz boost that increases with y, in an "inside–outside" pattern (c.f. Fig. 2). We are thus witnessing at hadronization a Hubble expanding system of local fireballs. The detailed implications of this picture have not been analyzed yet. Note that a central RHIC collision thus does not correspond to a single hadronization "point" in the $[T,\ \mu]$ plane of Fig. 1 but samples $\{T,\ \mu\}$ along the QCD parton–hadron coexistence line [153].

Throughout this section we have discussed hadronic freeze-out at high $\sqrt{s}$ only (top SPS to RHIC energy) because of the proximity of the chemical freeze-out parameters $[T,\ \mu_b]$ to the QCD phase boundary from lattice QCD, which suggests an overall picture of hadronization, to occur directly from a partonic cluster or super-cluster. Our discussion of the GC statistical hadronization model has been explicitly or implicitly based on the assumption that hadronic freeze-out coincides with hadronization. However, the GC model has also been applied successfully to hadrochemical freeze-out at $\sqrt{s}$ down to a few GeV [28, 126–128] where it is not expected that the dynamical evolution traverses the phase boundary at all, but grand canonical multiplicity distributions, and their characteristic strangeness enhancement pattern, are observed throughout. Toward lower $\sqrt{s}$, T decreases while μ_b increases, as is shown in Fig. 34 which presents a compilation of all reported freeze-out parameters [128].

These points have also been included in the phase diagram of Fig. 1 which shows that they are gradually branching away from the phase separation boundary line that could recently be predicted by lattice QCD once new methods had been developed to extend the theory to finite μ_B [16–18]. At $\sqrt{s} \geq 20$ GeV we see that

$$\epsilon_c(QCD) \approx \epsilon_H \approx \epsilon_{GC}, \tag{127}$$

where ϵ_{GC} is the freeze-out density inferred from GC analysis [28, 126–128].

In turn, the GC hadronic freeze-out points drop below the lattice QCD coexistence line at lower $\sqrt{s}$, implying that chemical freeze-out now occurs within the hadronic expansion phase. This requires a model of freeze-out, now governed by the properties of a high-density hadronic medium, upon expansive cooling and dilution. Holding on to the model of a quantum mechanical de-coherence decay to on-shell hadrons that we discussed in Sect. 4.3, we argue that an initial extended high-density hadronic fireball, given sufficient life-time at T smaller, but not far below T_c, could also be seen as a quantum mechanically coherent super-cluster, as governed by

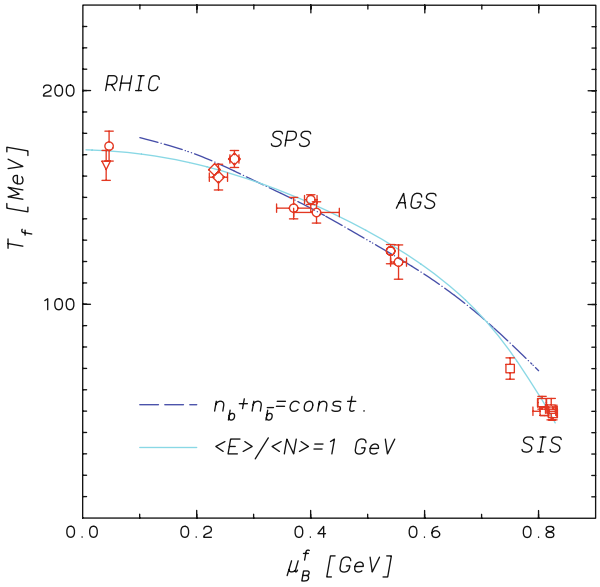

Fig. 34 Energy dependence of the hadrochemical freeze-out points obtained by grand canonical statistical model analysis in the plane $[T,\ \mu_B]$, with interpolating curve at fixed energy per particle of about 1 GeV [126, 127, 154]

effective mean fields [155]. In such a medium hadrons, at T near T_c, acquire effective masses and/or decay widths far off their corresponding properties in vacuum: they are off-shell, approaching conditions of QCD chiral symmetry restoration as $T \to T_c$ [156]. This symmetry is inherent in the elementary QCD Lagrangian, and "softly" broken within the light quark sector by the small nonzero current quark masses, but severely broken at $T \to 0$ by the high effective constituent quark masses that get dressed by non-perturbative QCD vacuum condensates. Pictorially speaking, hadrons gradually loose this dressing as $T \to T_c$ [157], introducing a change, away from in vacuum properties, in the hadronic mass and width spectrum. Such in-medium chiral restoration effects have, in fact, been observed in relativistic A+A collisions, by means of reconstructing the in-medium decay of the ρ vector meson to an observed e^+e^- pair [158].

A dense, high-T hadronic system, with mean-field-induced off-shell constituents is also, clearly, quantum mechanically coherent. At a certain characteristic density, $\epsilon < \epsilon_c$, and temperature $T < T_c$, as reached in the course of overall hadronic expansion, this extended medium will undergo a decoherence transition to classical on-shell hadrons. Its frozen-out hadronic multiplicity distribution should be, again, characterized by the phase space weights of a grand canonical ensemble at $T < T_c$. Theoretical studies of such a mean field hadronic expansion mode [159] have also shown that such mechanisms play essentially no role at $\sqrt{s} \geq 20\,\text{GeV}$ because the expanding system is already in rapid flow once it traverses the phase boundary, with an expansion time scale shorter than the formation time scale of mean field

phenomena. At lower energies, on the other hand, the system might not even dive into the deconfined phase but spend a comparatively long time in its direct vicinity, at the turning point between compression and re-expansion where all dynamical time constants are large, and the hadron density is high, such that the inelastic hadronic transmutation rate becomes high (particularly in collisions of more than two hadronic reactants, with reaction rates [160] proportional to ϵ^n), and sufficiently so for maintaining hadronic chemical equilibrium after it is first established at maximum hadron density, in low $\sqrt{s}$ systems that do not cross the phase boundary at all.

The GC freeze-out parameters $[T, \mu]$ at various $\sqrt{s}$ in Fig. 34 permit a smooth interpolation in the T, μ plane [153], which, in turn, allows for GC model predictions which are continuous in $\sqrt{s}$. Such a curve is shown in Fig. 29 compared to the 4π data points for the K^+/π^+ multiplicity ratio in central collisions Au+Au/Pb+Pb, at all $\sqrt{s}$ investigated thus far. It exhibits a smooth maximum, due to the interplay of T saturation and μ_B fall-off to zero but does not account for the sharp peak structure seen in the data at $\sqrt{s} \approx 7\,\text{GeV}$ and $\mu_B \approx 480\,\text{MeV}$. This behavior is not a peculiarity of the K^+ channel only; it also is reflected in an unusually high Wroblewski ratio (see Eq. 120) obtained at $\sqrt{s} = 7.6\,\text{GeV}$, of $\lambda_s = 0.60$ [28]. This sharp strangeness maximum is unexplained as of yet. It implies that hadron formation at this $\sqrt{s}$ reflects influences that are less prominent above and below, and most attempts to understand the effect [161–163] are centered at the assumption that at this particular $\sqrt{s}$ the overall bulk dynamics will settle directly at the phase boundary where, moreover, finite μ_B lattice theory also expects a QCD critical point [16–19]. This would cause a softest point to occur in the equation of state, i.e., a minimum in the relation of expansion pressure vs. energy density, slowing down the dynamical evolution [164–166] and thus increasing the sensitivity to expansion modes characteristic of a first-order phase transition [163], which occurs at $\mu_b \geq \mu_b^{\text{crit}}$. Such conditions may modify the K/π ratio (Fig. 29) [163].

It thus appears that the interval from top AGS to lower SPS energy, $5 \leq \sqrt{s} \leq 10\,\text{GeV}$, promises highly interesting information regarding the QCD phase diagram (Fig. 1) in the direct vicinity of the parton–hadron coexistence line. In particular, the physics of a critical point of QCD matter deserves further study. Observable consequences also comprise so-called critical fluctuations [167, 168] of multiplicity density, mean transverse momentum, and hadron-chemical composition [169], the latter in fact being observed near $\sqrt{s} = 7\,\text{GeV}$ in an event-by-event study of the K/π ratio in central Pb+Pb collisions [170].

References

1. J.C. Collins and M.J. Perry: Phys. Rev. Lett. **34**, 1353 (1975) 23
2. E.V. Shuryak: Phys. Rep. **61**, 71 (1980) 24
3. B. Müller: *The Physics of the Quark-Gluon-Plasma*, Lecture Notes in Physics, vol. 225, Springer, Heidelberg (1985)
4. L. McLerran: *The Physics of the Quark-Gluon Plasma*, Rev. Mod. Phys. **58** 1012 (1986) 24

5. S. Weinberg: *The First Three Minutes*, Basic Books, New York (1977) 23
6. R. Hagedorn: Suppl. Nuovo Cim. **3**, 147 (1965) 23, 69, 81
7. B.A. Freedman and L. McLerran: Phys. Rev. **D16**, 1169 (1977) 24
8. E.V. Shuryak: Zh. Eksp. Teor. Fiz. **74**, 408 (1978)
9. J.I. Kapusta: Nucl. Phys. **B148**, 461 (1979)
10. L. Susskind: Phys. Rev. **D20**, 2610 (1979) 24
11. J. Kuti, J. Polonyi and K. Szalachanyi: Phys. Lett. **B98**, 199 (1981)
12. J. Engels, F. Karsch, I. Montvay and H. Satz: Phys. Lett. **B101**, 89 (1981)
13. F.R. Brown, F.P. Butler, H. Chen, N.H. Christ, Z. Dong, W. Schaffer, L. I. Unger and A. Vaccarino: Phys. Rev. Lett. **65**, 2491 (1990)
14. F. Karsch: Nucl. Phys. **A590**, 372 (1995) 24, 25
15. R. Stock: hep-ph/9901415 24
16. Z. Fodor and S.D. Katz: JHEP **0203**, 014 (2002) 24, 25, 29, 97, 99
17. Ph. de Forcrand and O. Philipsen: Nucl. Phys. **B642**, 290 (2002)
18. C.R. Allton et al.: Phys. Rev. **D68**, 014507 (2003) 97
19. F. Karsch and E. Laermann: Thermodynamics and In-Medium Hadron Properties from Lattice QCD. In: R.C. Hwa and X.-N. Wang (eds.) *Quark-Gluon Plasma 3*, p. 1, World Scientific, Singapore (2004) 24, 25, 29, 99
20. S.L. Shapiro and S. Teukolsky: *Black Holes, White Dwarfs and Neutron Stars*, Wiley, New York, (1983) 25
21. F. Weber: *Pulsars as Astrophysical Laboratories*, Institute of Physics Publishing, Bristol (1999)
22. R. Oechslin, H.T. Janka and A. Marek: astro-ph/0611047 25
23. R. Rapp, T. Schäfer and E.V. Shuryak: Ann. Phys. **280**, 35 (2000) 25, 29
24. R.D. Pisarski and F. Wilczek: Phys. Rev. **D29**, 338 (1984) 25, 29, 77
25. E. Witten: Phys. Rev. **D30**, 272 (1984) 26
26. H. Kurki-Suonio, R.A. Matzner, K.A. Olive and D.N. Schramm: Astrophys. J. **353**, 406 (1990) 26
27. K. Kajantie and H. Kurki-Suonio, Phys. Rev. **D34**, 1719 (1986) 26
28. F. Becattini et al.: Phys. Rev. **C69**, 024905 (2004) 26, 55, 82, 83, 86, 87, 96, 97, 99
29. M.G. Alford, K. Rajagopal and F. Wilczek: Nucl. Phys. **B537**, 443 (1999) 26
30. D.H. Rischke: Prog. Part. Nucl. Phys. **52**, 197 (2004) 26
31. J.P. Blaizot, E. Iancu and A. Rebhan: In: R.C. Hwa and X.-N. Wang (eds.) *Quark-Gluon Plasma 3*, p. 60, World Scientific, Singapore (2004) 29
32. G. Baym, B.L. Friman, J.P. Blaizot, M. Soyeur and W. Czyz: Nucl. Phys. **A407**, 541 (1983) 29
33. H. Stöcker and W. Greiner: Phys. Rep. **137**, 277 (1986)
34. L.P. Csernai: *Introduction to Relativistic Heavy Ion Collisions*, Wiley, New York (1994)
35. P. Huovinen, P.F. Kolb and U. Heinz: Nucl. Phys. **A698**, 475 (2002) 29
36. N. Cabibbo and G. Parisi: Phys. Lett. **B59**, 67 (1975) 29
37. G. Veneziano: Nucl. Phys. **B159**, 213 (1979) 52
38. G. T'Hooft: Nucl. Phys. **B138**, 1 (1978)
39. G. T'Hooft: Nucl. Phys. **B190**, 455 (1981)
40. A. Di Giacomo: In: A. Molinari and L. Riccati (eds.) *Proceedings of the International School of Physics Enrico Fermi*, Course 43, p. 401, IOS Press, Amsterdam (2003) 29
41. B.B. Back et al.: The PHOBOS Perspectives on Discoveries at RHIC, Nucl. Phys. **A 757**, 28 (2005) 38
42. L. Van Hove: Phys. Lett. **B 118**, 138 (1982) 41, 53
43. J. Gosset et al.: Phys. Rev. **C 16**, 629 (1977) 44
44. T. Alber et al. [NA49 Collaboration]: Phys. Rev. Lett. **75**, 3814 (1995) 48, 49, 50, 72
45. M. Agarwal et al. [WA98 Collaboration]: Eur. Phys. J. **C18**, 651 (2001) 49, 50, 72
46. F. Karsch, E. Laermann and A. Peikert: Nucl. Phys. **B605**, 579 (2001) 49
47. J.D. Bjorken: Phys. Rev. **D27**, 140 (1983) 49, 50, 57, 70, 71
48. J. Adams et al. [STAR Collaboration]: Nucl. Phys. **A757**, 102 (2005) 50

49. K.J. Eskola, K. Kajantie, P. Ruuskanen and K. Tuominen: Nucl. Phys. **B570**, 379 (2000) 50, 51
50. E.V. Shuryak and L. Xiong: Phys. Rev. Lett. **70**, 2241 (1993) 50, 51
51. M.D. Baker et al. [PHOBOS Collaboration]: Nucl. Phys. **A715**, 65 (2003) 50, 53, 54
52. P.A. Steinberg et al. [PHOBOS Collaboration]: Nucl. Phys. **A715**, 490 (2003) 50, 53, 54
53. F. Karsch, E. Laerman and A. Peikert: Phys. Lett. **B478**, 447 (2000) 50, 51, 72, 81
54. S. Hands: Contemp. Phys. 42, 209 (2001) 50, 51, 72, 81
55. P. Abreu et al.: Phys. Lett. **B459**, 597 (1999) 51, 53
56. M. Basile et al.: Phys. Lett. **B92**, 367 (1980) 52
57. M. Basile et al.: Phys. Lett. **B95**, 311 (1980) 52
58. G. Panduri and C. Rubbia [UA1 Collaboration]: Nucl. Phys. **A418**, 117 (1984) 52, 53
59. G. Roland et al. [PHOBOS Collaboration]: Nucl. Phys. **A774**, 113 (2006) 53, 61, 68
60. J. Jalilian-Marian, J. Phys. **G30**, 751 (2004) 53, 58, 62, 64, 65, 68
61. Ch. Blume, J. Phys. **G31**, 57 (2005), and references therein 54, 55, 76, 77, 80
62. L.D. Landau: Izv. Akad. Nauk SSSR **17**, 52 (1953) 54
63. P. Carruthers and M. Duong-Van: Phys. Rev. **D8**, 859 (1973) 54
64. I.G. Baerden et al. [BRAHMS Collaboration]: Phys. Rev. Lett. **93**, 102301 (2004), and references to the other data therein 56
65. Ch. Blume et al. [NA49 Collaboration]: nucl-ex/0701042 56
66. P. Drijard et al.: Nucl. Phys. **B155**, 269 (1979) 57
67. A. Bialas, M. Bleszynski and W. Czyz: Nucl. Phys. **B111**, 461 (1976) 57
68. A. Bialas and W. Czyz: Acta Phys. Pol. **36**, 905 (2005) 57
69. M. Gyulassy and L. McLerran: Nucl. Phys. **A750**, 30 (2005) 58, 62, 64, 70, 71
70. A.H. Müller: Nucl. Phys. **A715**, 20 (2003), and references therein 58, 64
71. N. Armestro, C.A. Salgado and U.A. Wiedemann: Phys. Rev. Lett. **94**, 022002 (2005) 58, 62, 64, 65, 66, 67, 68
72. D. Kharzeev, E. Levin and M. Nardi: hep-ph/0408050 59
73. S. Afanasiev et al. [NA49 Collaboration]: Nucl. Instr. Meth. **A430**, 210 (1999) 59, 60, 61, 62
74. K. Werner: Phys. Rep. **232**, 87 (1993) 60
75. B. Lungwitz: [NA49 Collaboration]: Frankfurt Thesis (2004) 61, 62
76. L.D. McLerran and R. Venugopalan: Phys. Rev. **D49**, 2233 (1994) 62, 63, 64, 65, 68
77. L.D. McLerran and R. Venugopalan: Phys. Rev. **D49**, 3352 (1994) 63, 64, 65, 68
78. U.V. Gribov, E.M. Levin and M.G. Ryskin: Phys. Rep. **100**, 1 (1983) 63, 64, 67
79. A.H. Müller and J. Qiu: Nucl. Phys. **B268**, 427 (1986)
80. J.P. Blaizot and A.H. Müller: Nucl. Phys. **B289**, 847 (1987) 62, 63, 64
81. J. Breitweg et al.: Eur. Phys. J. **67**, 609 (1999), and references therein 62, 63
82. S.J. Brodsky, H.C. Pauli and S.S. Pinsky: Phys. Rep. **301**, 299 (1998) 63
83. R.K. Ellis, W.J. Stirling and B.R. Webber: *QCD and Collider Physics*, Cambridge Monographs (1996) 63
84. For a review see E. Iancu and R. Venugopalan: In: R.C. Hwa and X.-N. Wang (eds.) *Quark-Gluon Plasma 3*, p. 249, World Scientific, Singapore (2004) 63, 64, 65, 68
85. Y.L. Dokshitzer: Sov. Phys. JETP **46**, 641 (1977) 65
86. G. Altarelli and G. Parisi: Nucl. Phys. **B126**, 298 (1977) 65
87. D. Kharzeev, E. Levin and M. Nardi: hep-ph/0111315 65
88. A.M. Stasto, K. Golec-Biernat and J. Kwiecinski: Phys. Rev. Lett. **86**, 596 (2001) 65, 89
89. K. Golec-Biernat and M. Wüsthoff: Phys. Rev. **D59**, 3006 (1999) 65
90. C. Adloff et al.: Eur. Phys. J. **C21**, 33 (2001) 65
91. J. Breitweg et al.: Phys. Lett. **B487**, 53 (2000) 65
92. M.R. Adams et al.: Z. Phys. **C67**, 403 (1995) 66
93. M. Arneodo et al.: Nucl. Phys. **B481**, 3 and 23 (1996) 66
94. R. Baier, A.H. Müller and D. Schiff: hep-ph/0403201, and references therein 67
95. B.B. Back et al. [PHOBOS Collaboration]: Phys. Rev. **C65**, 061901 (2002) 67
96. B.B. Back et al. [PHOBOS Collaboration]: nuclex/0405027 67

97. D. Amati and G. Veneziano: Phys. Lett. **B83**, 87 (1979) 68, 93, 94
98. F. Becattini: Nucl. Phys. **A702**, 336 (2002) 69, 71, 81, 82, 93, 94
99. J. Ellis and K. Geiger: Phys. Rev. **D54**, 1967 (1996) 72, 81, 93, 94
100. K. Geiger and B. Müller: Nucl. Phys. **B369**, 600 (1992) 72, 81, 97
101. K. Geiger and D.K. Shrivastava: Nucl. Phys. **A661**, 592 (1999) 72, 81, 97
102. R. Stock: Phys. Lett. **B456**, 277 (1999) 72, 73, 82
103. U. Heinz: Nucl. Phys. **A610**, 264 (1996) 72, 73, 82, 86
104. Y.M. Sinyukov: Nucl. Phys. **A498**, 151 (1989) 72
105. H. Appelshäuser et al. [NA49 Collaboration]: Eur. Phys. J. **C2**, 611 (1998) 72
106. J. Rafelski and B. Müller: Phys. Rev. Lett. **48**, 1066 (1982) 73
107. D. Molnar and M. Gyulassy: Nucl. Phys. **A697**, 495 (2002) 73, 77
108. D. Molnar and M. Gyulassy: Nucl. Phys. **A698**, 379 (2002) 73, 77
109. S.A. Voloshin and A.M. Poskanzer: Phys. Lett. **B474**, 27 (2000) 74
110. S.A. Voloshin: Nucl. Phys. **A715**, 379 (2003)
111. R.A. Lacey and A. Taranenko: nucl-ex/0610029 74, 79
112. D. Teaney, J. Laurent and E.V. Shuryak: Nucl. Phys. **A698**, 479 (2002) 74, 77, 85, 97
113. D. Teaney, J. Laurent and E.V. Shuryak: nucl-th/0110037 74, 77, 85, 97
114. J.L. Klay et al. [STAR Collaboration]: Nucl. Phys. **A715**, 733 (2003) 75, 76
115. K. Alpgard et al.: Phys. Lett. **B107**, 310 (1981) 76
116. R. Hagedorn and J. Ranft: Nuovo Cim. Suppl. **6**, 169 (1968) 76
117. M. Gazdzicki et al. [NA49 Collaboration]: J. Phys. **G30**, 701 (2004) 76, 78, 82, 83, 88
118. M. Gazdzicki et al.: Braz. J. Phys. **34**, 322 (2004) 76, 78, 82, 83, 88
119. P.F. Kolb and U. Heinz: In: R.C. Hwa and X.-N. Wang (eds.) *Quark-Gluon Plasma 3*, p. 634, World Scientific, Singapore (2004), and references therein 77, 78, 79, 85
120. M. Kliemant, B. Lungwitz and M. Gazdzicki: Phys. Rev. **C 69**, 044903 (2004) 78
121. C. Nonaka and M. Asakawa: Phys. Rev. **C71**, 044904 (2005) 78
122. G. Bertsch and P. Cuguon: Phys. Rev. **C24**, 269 (1981) 78
123. N. Xu: J. Phys. **G32**, 123 (2006), and references therein 78, 79
124. E. Schnedermann, J. Sollfrank and U. Heinz: Phys. Rev. **C48**, 2462 (1993) 79
125. U. Wiedemann and U. Heinz: Phys. Rev. **C56**, 3265 (1997) 80
126. R. Stock: nucl-th/0703050 81, 82, 86, 88, 93, 97, 98
127. P. Braun-Munzinger, K. Redlich and J. Stachel: In: R.C. Hwa and X.-N. Wang (eds.) *Quark-Gluon Plasma 3*, p. 491, World Scientific, Singapore (2004) 81, 82, 88, 93, 98
128. A. Andronic, P. Braun-Munzinger and J. Stachel: nucl-th/0511071 82, 83, 86, 88, 97
129. F. Becattini and U. Heinz: Z. Phys. **C76**, 269 (1997) 82, 88, 90, 94
130. U. Heinz: nucl-th/9810056 82, 84, 95
131. F. Cooper and G. Frye: Phys. Rev. **D10**, 186 (1974) 85
132. H. Sorge: Z. Phys. **C67**, 479 (1995) 85
133. M. Bleicher et al.: J. Phys. **G25**, 1859 (1999) 85
134. S.A. Bass and A. Dimitru: Phys. Rev. **C61**, 064909 (2000) 85
135. M. Mitrovski et al. [NA49 Collaboration]: J. Phys. **G32**, 43 (2006) 89, 90
136. A. Tounsi and K. Redlich: J. Phys. **G28**, 2095 (2002) 89, 91, 92
137. R.V. Gavai and S. Gupta: J. Phys. **G30**, 1333 (2004) 90
138. E.V. Shuryak: Phys. Lett. **B42**, 357 (1972) 90
139. J. Rafelski and M. Danos: Phys. Lett. **B97**, 279 (1980) 91
140. C. Hoehne, F. Puehlhofer and R. Stock: Phys. Lett. **B640**, 96 (2006) 92, 95
141. B.R. Webber: Nucl. Phys. **B238**, 492 (1984) 93, 94
142. B. Andersson, G. Gustafsson, G. Ingelman and T. Sjöstrand: Phys. Rep. **97**, 33 (1983) 94
143. H. Satz: hep-ph/0612151 94
144. P. Castorina, D. Kharzeev and H. Satz: hepph/0704.1426 94
145. F. Becattini and G. Passaleva: Eur. Phys. J. **C23**, 551 (2002) 94
146. J. Rafelski, Phys. Lett. **B262**, 333 (1991) 94
147. W.S.C. Williams: *Nuclear and Particle Physics*, Oxford University Press, Oxford (1991) 95

148. B. Müller and J. Rafelski: Phys. Rev. Lett. **48**, 1066 (1982) 95
149. I.G. Baerden et al.: [BRAHMS Collaboration]: Phys. Rev. Lett. **90**, 102301 (2003) 96, 97
150. C. Alt et al. [NA49 Collaboration]: Phys. Rev. **C73**, 044910 (2006) 96
151. S.V. Afanasiev et al. [NA49 Collaboration], Phys. Rev. **C69**, 024902 (2004) 96
152. F. Becattini et al.: Phys. Rev. **C64**, 024901 (2001) 97
153. D. Röhrich: private communication 97, 99
154. P. Braun-Munzinger, J. Cleymans, H. Oeschler and K. Redlich: Nucl. Phys. **A697**, 902 (2002) 98
155. R. Rapp: J. Phys. **G31**, 217 (2005) 98
156. G.E. Brown and M. Rho: Phys. Rep. **269**, 333 (1996) 98
157. R. Rapp and J. Wambach: Adv. Nucl. Phys. **25**, 1 (2000) 98
158. S. Damjanovic et al. [NA60 Collaboration]: Nucl. Phys. **A774**, 715 (2006) 98
159. D. Zschiesche et al.: Nucl. Phys. **A681**, 34 (2001) 98
160. C. Greiner et al.: J. Phys. **G31**, 61 (2005) 99
161. M. Gazdzicki and M.I. Gorenstein: Acta Phys. Pol. **B30**, 2705 (1999) 99
162. R. Stock: J. Phys. **G30**, 633 (2004)
163. V. Koch, A. Majumder and J. Randrup: nucl-th/0509030 99
164. E.G. Nikonow, A.A. Shanenko and V.D. Toneev: Heavy Ion Phys. **8**, 89 (1998) 99
165. C.M. Hung and E.V. Shuryak: Phys. Rev. **C57**, 1891 (1998)
166. M. Bleicher: hep-ph/0509314 99
167. M. Stephanov, K. Rajagopal and E.V. Shuryak: Phys. Rev. Lett. **81**, 4816 (1998) 99
168. M. Stephanov, K. Rajagopal and E.V. Shuryak, Phys. Rev. **D60**, 114028 (1999) 99
169. V. Koch, A. Majumder and J. Randrup: nucl-th/0505052 99
170. Ch. Roland et al. [NA49 Collaboration]: J. Phys. **G30**, 1371 (2004) 99

Two Introductory Lectures on High-Energy QCD and Heavy-Ion Collisions

Debasish Banerjee, Jajati K. Nayak, and Raju Venugopalan

Abstract These introductory lectures present a broad overview of the physics of high parton densities in QCD and its application to our understanding of the early time dynamics in heavy-ion collisions.

1 Introduction

Quantum chromodynamics (QCD) is widely accepted as the fundamental theory describing the behavior of hadrons. In QCD, hadrons are composed of elementary quarks and gluons which are often together labeled partons. Quarks and gluons are never directly measured due to the confining property of the theory. However, their distributions inside a hadron can be probed precisely in deep inelastic scattering (DIS) experiments. It is seen from the H1 and ZEUS experiments at HERA that the structure functions of the gluons and the sea quarks, which to leading order in QCD are related to their number densities, grow very rapidly [1, 2] with decreasing values of a Lorentz invariant kinematic variable x_{Bj} introduced by Bjorken. Again, to the lowest order, this variable corresponds to the momentum fraction of the hadron's momentum carried by a parton. Small x physics is the regime of high energies in QCD and the physics of this regime exhibits many novel features that are not fully understood.

Small x physics is interesting for a variety of reasons. Even if the momentum transfer squared Q^2 are large such that, from asymptotic freedom, the QCD coupling

D. Banerjee (✉)
Department of Theoretical Physics, Tata Institute of Fundamental Research, Mumbai 400005, India, debasish@theory.tifr.res.in

J.K. Nayak
Theoretical Physics Division, Variable Energy Cyclotron Centre, Kolkata 700064, India, jajati-quark@veccal.ernet.in

R. Venugopalan
Brookhaven National Laboratory, Upton, NY 11973–5000, USA, raju@bnl.gov

Banerjee, D. et al.: *Two Introductory Lectures on High-Energy QCD and Heavy-Ion Collisions*. Lect. Notes Phys. **785**, 105–137 (2010)
DOI 10.1007/978-3-642-02286-9_3

constant α_s is small, the explosive growth in the number of partons with increasing energy makes the physics non-perturbative. The strongest electric and magnetic fields found in nature occur in this situation. The answer to a fundamental question in QCD – can we calculate the total number of particles produced in a strong interaction at asymptotically high energies – therefore requires that we understand the processes of particle creation in the presence of such strong color fields. Particle production in this context is important for understanding a variety of striking but little understood phenomena at high energies. These include, for instance, (i) limiting fragmentation [3–10], where the rapidity distributions of the produced hadrons turn out to be independent of energy around the fragmentation region but possess nontrivial features in the central rapidity region, (ii) the unusually large fraction of diffractive final states in DIS where no particles are produced in angular regions relative to the scattering plane called "rapidity gaps" [11, 12], and (iii) the phenomenon of "geometrical scaling," where cross sections appear to scale as a dimensionless function of the momentum transfer squared of the probe relative to a dimensionful dynamical scale in the hadron [13]. Small x physics is also of crucial importance in understanding the formation of bulk QCD matter in high-energy heavy-ion collisions and its possible thermalization to form a quark–gluon plasma (QGP). Finally, the hope is that understanding the properties of strong fields at small x will provide some insight into confinement in QCD and its role in high-energy scattering.

These questions can be addressed in a weak coupling effective field theory formalism [14, 15] which describes the properties of high-energy wavefunctions as a color glass condensate (CGC). In this approach, the degrees of freedom in the high-energy nuclear wavefunction are divided into static light cone color sources at large x and dynamical gauge fields at small x which are coupled to these static color sources. Because the scale between the two sorts of degrees of freedom is arbitrary, and because physics cannot depend on this scale, one obtains a renormalization group description in rapidity which arises from successively integrating out dynamical fields at one scale and absorbing them into color sources at the next.

Efforts to understand the rich non-perturbative phenomena of high-energy QCD are the subject of these lectures. The first lecture begins with DIS and describes high-energy scattering in DIS in the well-understood Bjorken limit and the much less understood Regge–Gribov limit of QCD. We show that parton saturation arises naturally in the latter limit. The effective field theory formalism of CGC, which incorporates the physics of parton saturation, is described next. We then discuss color dipole models that incorporate simply both the nonlinear dynamics of saturation and the linear dynamics of perturbative QCD in DIS and hadron scattering. In the second lecture, we apply the CGC approach to treat ab initio heavy-ion collisions at high energies. When two sheets of colored glass collide, they form bulk QCD matter called the glasma in heavy-ion collisions. We describe the properties of the glasma, probes of its dynamics and the possible fast thermalization of the glasma into a quark–gluon plasma.

2 Deep Inelastic Scattering

Deep inelastic scattering (DIS) involves the scattering of a high-energy lepton off a hadronic target in which the energy and momentum transfer of the lepton is measured experimentally. DIS is essentially a two-step process where the lepton emits a virtual photon in the first step which then interacts with the hadron in the second step. Depending on the energy transferred, the proton can break up and new particles are created. This provides a clean environment to study the structure of hadrons at high energies since one of the interaction vertices in the two-step process is completely known. The DIS process is schematically illustrated in Fig. 1. The cross section of the process is

$$\frac{d^2\sigma^{eh\to eX}}{dx\,dQ^2} = \frac{4\pi\alpha_{em}^2}{xQ^4}\left[(1-y+\frac{y^2}{2})F_2(x,Q^2) - \frac{y^2}{2}F_L(x,Q^2)\right]. \tag{1}$$

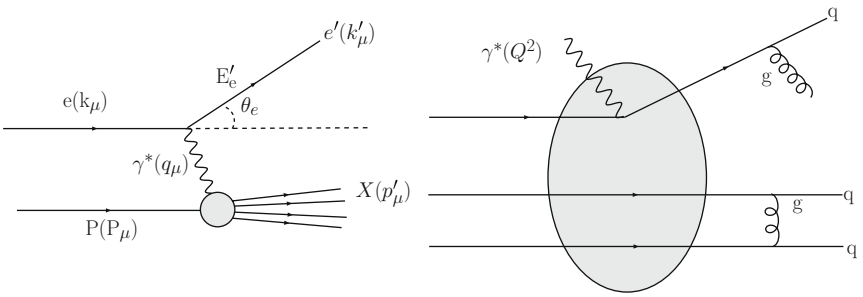

Fig. 1 *Left*. The general setup of DIS. *Right*. Inside the hadron via the parton model. In the impulse approximation the partons inside are non interacting on the interaction timescale of the virtual photon probe

Light cone coordinates : It is useful at this point to introduce light cone (LC) coordinates which are very useful to discuss high-energy scattering. Let z denote the longitudinal axis of collision. For an arbitrary four-vector $a^\mu = (a^t, a^x, a^y, a^z)$, the LC coordinates are defined as

$$a^+ \equiv \frac{a^t + a^z}{\sqrt{2}}, a^- \equiv \frac{a^t - a^z}{\sqrt{2}}, a_\perp \equiv (a^x, a^y). \tag{2}$$

In particular $x^+ = (t+z)/\sqrt{2}$ is the LC "time" and $x^- = (t-z)/\sqrt{2}$ is known as the LC "longitudinal coordinate."

Here e and h denote the initial electron and hadron state and X the final hadronic state. α_{em} is the usual QED coupling constant. The four vectors of the electron

and proton are shown in Fig. 1. If q^μ denotes the (space-like) four-momenta of the exchanged photon, then the energy transferred to the hadron is

$$Q^2 = -q^\mu q_\mu = -(k_\mu - k'_\mu)^2 = 4E_e E'_e \sin^2\left(\frac{\theta'_e}{2}\right). \tag{3}$$

The Q^2 is a measure of the resolution power of the probe. E_e and E'_e are the initial and final energies of the lepton and θ'_e is the lepton scattering angle in the center-of-mass (COM) frame. The variable y provides a measure of the inelasticity of the collision and is defined in the following frame-invariant way:

$$y = \frac{P.q}{P.k} = 1 - \frac{E'_e}{E_e}\cos^2\frac{\theta'_e}{2}. \tag{4}$$

The x here is the Bjorken variable x_{Bj} whose frame-invariant definition is

$$x_{\mathrm{Bj}} = \frac{Q^2}{2P.q}. \tag{5}$$

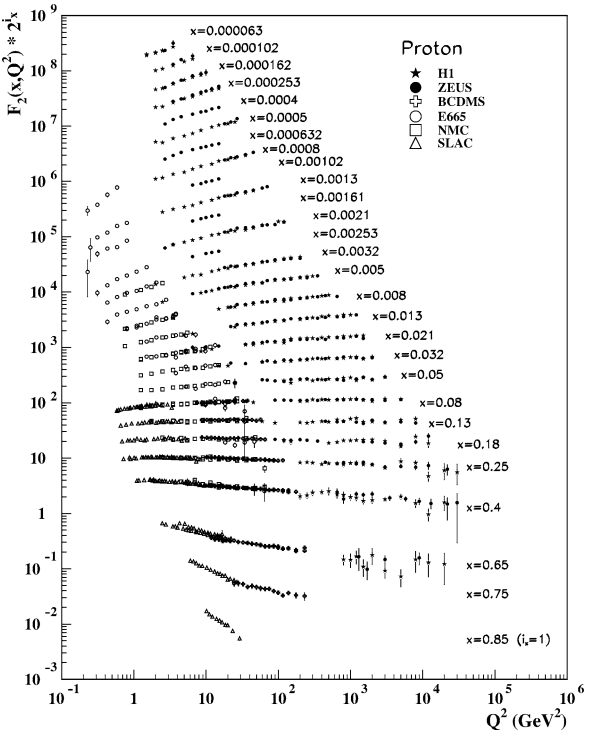

Fig. 2 Bjorken scaling: independence of structure functions vs Q^2 in proton. Courtesy PDG

At very high energies, we obtain $x_{\mathrm{Bj}} \sim Q^2/s$ for a fixed y. This clarifies why, for a fixed Q^2, small x physics is the physics of high energies in QCD. As we shall see shortly, x_{Bj} is related to the momentum fraction of the struck quark.

F_2 is the structure function that, at leading order in QCD, gives the quark + antiquark distributions in a proton, while the longitudinal structure function F_L is a measure of the gluon momentum distribution. These quantities can be independently extracted from the DIS cross section by varying x, Q^2, and the center of mass energy of the collision. The most striking feature observed in early DIS experiments was the flatness of the structure function F_2 over a wide range of Q^2 at which the experiments were first performed (see Fig. 2). The apparent scale invariance of the structure function gave the needed experimental support for the hypothesis of point-like, weakly interacting partons inside hadrons. The dynamical model that was formulated by Feynman [16–18] to understand these phenomena is called the parton model.

2.1 The Bjorken Limit, the Parton Model and pQCD

The Bjorken limit, in which the results of the DIS experiments were correctly interpreted, is attained when the center of mass energy $s \to \infty$ and the energy transferred in the collision $Q^2 \to \infty$ keeping the ratio $x_{\mathrm{Bj}} = Q^2/s =$ fixed. At these very high energies, the rest mass energy of the hadronic target M can be neglected compared to its longitudinal momentum P^+. In the parton model, formulated in the "infinite-momentum" frame, the hadron can be thought of as a collection of "quasi-free" partons which are nearly on-shell excitations carrying some fraction x_F of the total hadron momentum. Moreover the entire momentum of the hadron can be thought to be longitudinal. This picture is essentially true since the interactions between the partons are highly time dilated. In the "impulse approximation" when the virtual photon strikes a parton, the other partons form the spectators without interacting with the struck quark or among themselves (see Fig. 1). This demands

$$(x_F P + q)^2 = m_q^2 \simeq 0; \quad x_F \simeq \frac{Q^2}{2P.q} \equiv x_{\mathrm{Bj}}\,, \tag{6}$$

which confirms our interpretation of x_{Bj}.

The naive parton model also predicts F_L to be zero. This result is called the Callan–Gross relation and it provides strong evidence that the partons probed by the virtual photon are spin-1/2 objects. It was also realized that the hadron might also contain an infinite *sea* of light $q\overline{q}$ pairs, called appropriately *sea quarks*, as opposed to the *valence quarks* that carry the net baryon number of a hadron. However, it was experimentally found that, at a scale of O(1 GeV), the proposed valence and sea quark distributions could only account for about 50% of the total momentum in a proton. This necessitated the existence of other partons (*gluons*) which in turn explained the puzzle that F_L was not zero experimentally. With further experiments, it was also demonstrated that the Bjorken scaling was only approximately true and

there were scaling violations at lower x. This did not have an explanation within the naive parton model at all.

These experimental results set the stage for the formulation of the theory of strong interactions in terms of QCD which had quarks and gluons. Most important though, in tying all the pieces together, was the (Nobel) discovery of Gross, Wilczek, and Politzer that the theory had a β-function with negative sign – thereby indicating that the coupling asymptotically goes to zero at high Q^2. Perturbative QCD (pQCD) therefore showed that in the Bjorken limit the naive parton model is indeed a good approximation. It went further to give a quantitative explanation of the log scaling violations that were observed in the experiments. The key idea to the solution of this puzzle lay in the assumption of neglecting the transverse momentum of a quark. In fact, a quark can emit a gluon and acquire a large transverse momentum p_T, on timescales comparable with that of the probe, with a probability proportional to $\alpha_s dp_T^2/p_T^2$ at large p_T where α_s is the strong coupling constant. On integrating this till the kinematic limit of $p_T^2 \sim Q^2$, contributions proportional to $\alpha_s \ln Q^2$ are obtained which are precisely the scaling violations.

pQCD now has a host of machinery dedicated to precision physics. Tools such as the operator product expansion (OPE) are used to calculate many observables up to high orders in perturbation theory. Factorization theorems have been derived to separate out soft and hard dynamics in a systematic way; the former are parameterized as non-perturbative parton distribution functions while the latter can be computed order by order in perturbation theory. The factorization of hard and soft scales is manifest in a renormalization group treatment that requires that physics be independent of this scale. An important result is the Dokshitzer–Gribov–Lipatov–Altarelli–Parisi (DGLAP) [19–22] equation for the evolution of quark and gluon distribution functions as a function of Q^2 which made earlier work on the OPE accessible to straightforward experimental analysis. A consequence of DGLAP evolution is that, as shown in Fig. 3, the parton distributions increase rapidly at small-x as Q^2 increases. This means that as one probes finer and finer transverse resolution scales, more and more partons (which share the total hadron momentum) can be resolved within the hadron. However, albeit the number of partons increases with increasing Q^2, the phase space density – the number of partons/area/Q^2 – decreases and the proton becomes more and more dilute.

2.2 The Regge–Gribov Limit in QCD and Saturation

The DGLAP framework in pQCD has worked very well and explains many features of the HERA data very well. However, when pushed to lower Q^2, one begins to note increasingly unpleasant results. As shown in the right plot of Fig. 3, fits to data push the gluon distributions into negative territory. This also seems to afflict F_L, which must be a positive definite quantity as it is directly proportional to a cross section. Another feature of HERA data that the conventional pQCD approach needs further parameters to explain is the high fraction of diffractive events and the fact

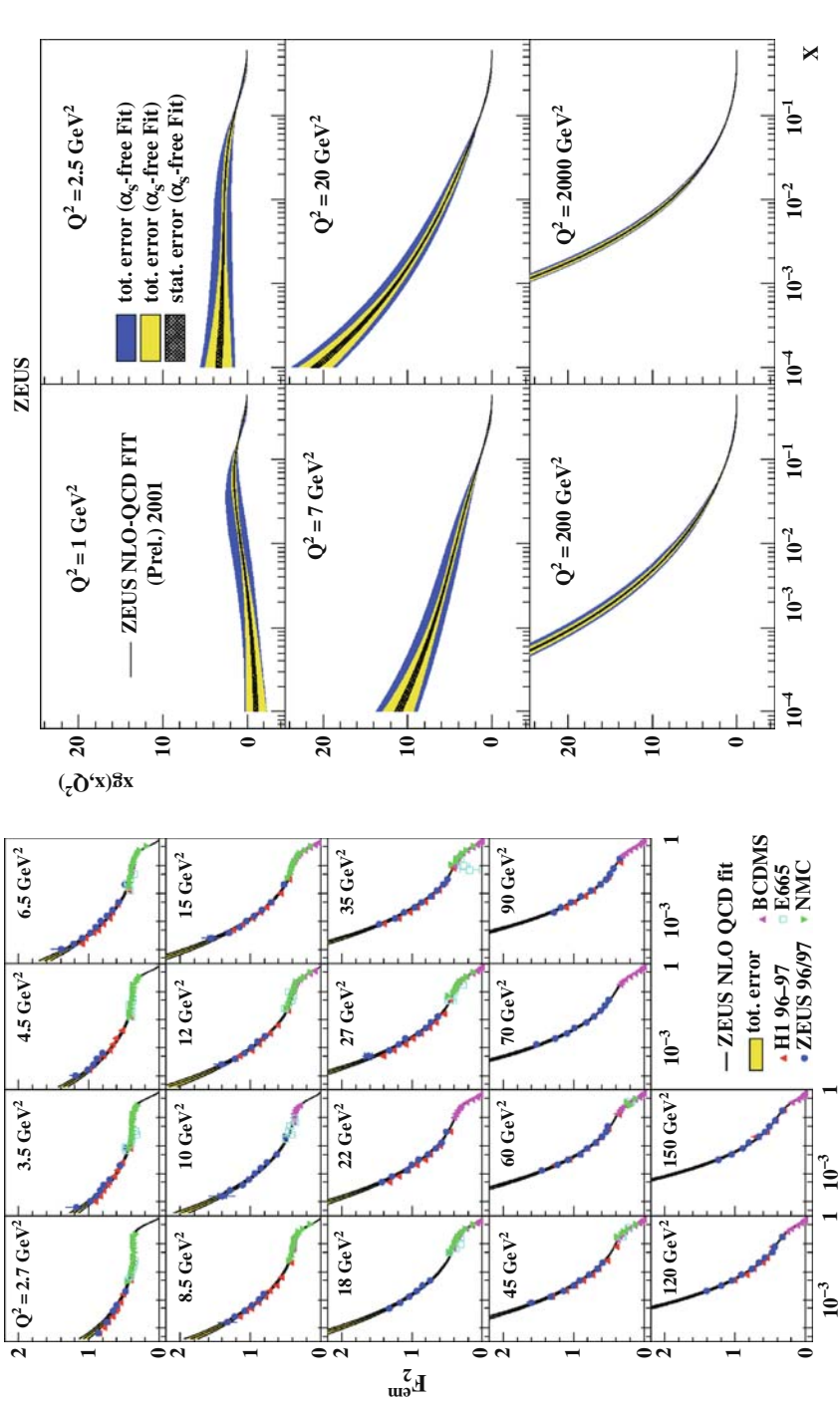

Fig. 3 Rapid growth of the structure functions at low x from the ZEUS experiment at HERA

that these diffractive events have the same dependence as the total cross section on the energy of the photon–hadron system. Within pQCD itself, it is expected that DGLAP should be supplemented by power corrections in Q^2 called "higher twist" effects, which become increasingly important as Q^2 is decreased and as one goes to smaller values of x. The higher twist formalism is however very cumbersome and not under theoretical control. It is therefore useful to take stock of the physics underlying the dynamics of partons in this kinematic region and approach the problem anew.

The physics of the small x regime is best understood in a very different asymptotic limit from the better known (and understood) Bjorken limit and goes by the name of Regge–Gribov limit in QCD. This limit corresponds to $x_{\rm Bj} \to 0$ and $s \to \infty$ with $Q^2 (\gg \Lambda^2_{\rm QCD}) =$ fixed. The Regge–Gribov limit corresponds to the regime of strong color fields in QCD. It is responsible for the bulk of multi-particle production in QCD. At sufficiently large $Q^2 \gg \Lambda^2_{\rm QCD}$, the physics of this regime, albeit non-perturbative, should be accessible in weak coupling.

In the Regge–Gribov limit, the leading logarithms in $x, \alpha_S \ln(1/x)$ dominate over the leading logs $\alpha_S \ln(Q^2/\Lambda^2_{\rm QCD})$ – the converse is true of course in the Bjorken limit. The renormalization group equation that resum these leading logs of x is called the Balitsky–Fadin–Kuraev–Lipatov (BFKL) equation [23–25]. The BFKL equation leads to a rapid power law growth in the gluon distribution with decreasing x. A schematic diagram of the parton content of the hadron in the two asymptotic limits is shown in Fig. 4. The physics issues at small x have a simple intuition. Both theory and experiments show that the gluon and the sea quark densities grow very rapidly in low x. As parton distributions grow, for fixed Q^2, the occupation number of gluons in the hadron wavefunction becomes increasingly large and it is no longer possible to neglect their mutual interactions. In terms of Feynman diagrams, these

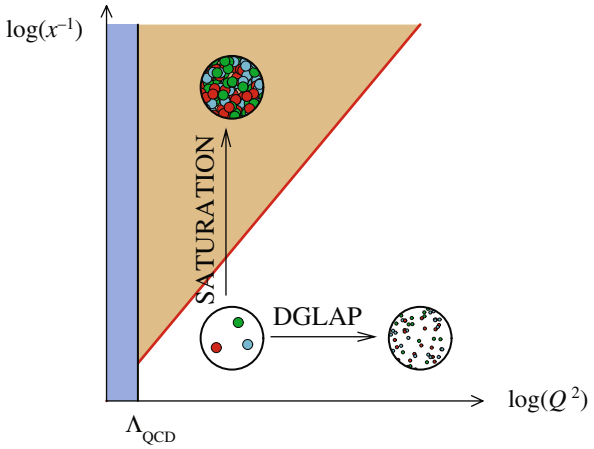

Fig. 4 The horizontal and vertical directions correspond, respectively, to the DGLAP and BFKL regimes of QCD. The *diagonal line* corresponds to the saturation boundary. The *thin vertical region* to the left is the non-perturbative region

interactions involve gluon recombination and screening which deplete the gluon density relative to the bremsstrahlung diagrams that are responsible for the rapid growth of the parton distributions. The net effect of the competition between these two effects is that the occupation number of partons "saturates" at the maximum possible value of $1/\alpha_s$ in QCD. The dynamics of QCD in this regime is fully nonlinear corresponding to the strongest electric and magnetic fields in nature. Each mode in the wavefunction, because it has a different occupation number, will saturate at a different value of x – the momentum scale Q_s at which it saturates is called the saturation scale [26, 27]. In terms of the gluon distribution, the maximal phase space density is reached when

$$\frac{1}{2(N_c^2-1)}\,\frac{xG(x,Q_s^2)}{\pi R^2 Q_s^2} = \frac{1}{\alpha_S(Q_s^2)}\,, \tag{7}$$

where πR^2 is the hadron area in the impact parameter space which is only well defined if the wavelength of the probe is small compared to R, which we will assume throughout in the future discussions. As suggested by Eq. (7), the growth of the gluon distribution functions with decreasing x implies a growth of the saturation scale as well. The saturation scale is the typical momentum of gluons in the high-energy hadron wavefunction, and when x is small, $Q_s^2 \gg \Lambda^2_{\rm QCD}$ is a semi-hard scale in QCD. Thus $\alpha_s(Q_s^2) \ll 1$, suggesting that weak coupling techniques can be applied to study the saturation regime in the Regge–Gribov limit of QCD. The use of weak coupling techniques does not necessarily mean that the physics is perturbative; in this case, the many-particle interactions are responsible for the non-perturbative nature of saturation, because, although individual interactions are small, the large number of gluons amplifies the effect necessitating a resummation of high parton density effects.

To summarize, saturation is a natural consequence of QCD in the Regge–Gribov limit of the theory because gluon occupation numbers cannot be arbitrarily large in the theory. Because saturation is achieved for different modes at different values of x, this also naturally suggests a dynamical scale that characterizes the onset of the nonlinear saturation dynamics in QCD. If this scale is large compared to the QCD confining scale $\sim \Lambda_{\rm QCD}$, the physics of saturation can be described using a weak coupling formalism. Because occupation numbers are large in this regime, the appropriate degrees of freedom here are classical fields. One is therefore, on very general grounds, led to postulate the existence of a weak coupling effective theory that captures the physics of this intensely nonlinear regime of QCD. This is the color glass condensate (CGC), and as we shall discuss, its name captures the properties of the matter in the hadron wavefunctions at high energies.

2.3 The Color Glass Condensate

One way to approach the small-x problem is to appreciate that there is a formal Born–Oppenheimer separation between large-x and small-x modes [28] for

quantum field theories on the light cone. These are, respectively, the slow and fast modes in the effective theory. Thus on the timescale of the "wee" parton small-x fields, the large-x partons can be viewed as static charges. Since these are color charges, they cannot be integrated out of the theory but must be viewed as sources of color charge for the dynamical wee fields. With this dynamical principle in mind, one can write down an effective action for wee partons in QCD at high energies [29–34]. The generating functional of wee partons has the form

$$\mathcal{Z}[j] = \int [d\rho]\, W_{\Lambda^+}[\rho] \left\{ \frac{\int^{\Lambda^+} [dA]\delta(A^+) e^{iS[A,\rho]-j\cdot A}}{\int^{\Lambda^+} [dA]\delta(A^+) e^{iS[A,\rho]}} \right\}, \tag{8}$$

where the wee parton action has the form

$$S[A,\rho] = \frac{-1}{4}\int d^4x\, F_{\mu\nu}^2 + \frac{i}{N_c}\int d^2x_\perp dx^- \delta(x^-) \times \mathrm{Tr}\left(\rho(x_\perp) U_{-\infty,\infty}[A^-]\right). \tag{9}$$

In Eqs. (8 and 9), we have the time-ordered exponential $U_{-\infty,\infty}[A^-] = T\exp\left(\int_{-\infty}^{\infty} dz^+ A^-(z^+)\right)$, ρ is a classical color charge density of the static sources and $W[\rho]$ is a weight functional of sources (which sit at momenta $k^+ > \Lambda^+$: note, $x = k^+/P^+_{\mathrm{hadron}}$). The sources are coupled to the dynamical wee gluon fields (which in turn sit at $k^+ < \Lambda^+$) via the gauge-invariant term[1] which is the second term on the RHS of Eq. 9. The first term in Eq. 9 is the QCD field strength tensor squared – the wee gluons are treated in full generality in this effective theory, formulated in the light cone gauge $A^+ = 0$. The source j is an external source – derivatives taken with respect to this source (with this source then put to zero) generate correlation functions in the effective theory.

The argument for why the sources are classical is subtle and follows from a coarse graining of the effective action to only include modes of interest. For large nuclei, or at small x, wee partons couple to a large number of sources. For a large nucleus, it can be shown explicitly that this source density is classical [36, 37]. Further, it was conjectured that the weight functional for a large nucleus was a Gaussian in the source density (corresponding to the quadratic Casimir operator) [29–34, 38]. This was shown explicitly later to be correct – albeit with a small but interesting correction, proportional to the cubic Casimir operator, that generates Odderon excitations in the effective theory [36, 37]. For a large nucleus, the variance of the Gaussian distribution, the color charge squared per unit area μ_A^2, proportional to $A^{1/3}$, is a large scale and is the only scale in the effective action.[2] Thus for $Q_s^2 \gg \Lambda^2_{\mathrm{QCD}}$, $\alpha_S(\mu_A^2) \ll 1$, and one can compute the properties of the theory in Eq. (8) in weak coupling.

[1] An alternative gauge-invariant form of the coupling of sources and fields is obtained in [35] – it reproduces the BFKL equation more efficiently.

[2] μ_A is simply related to Q_s: $Q_s \sim 0.6\mu_A$. For a detailed discussion, see [39].

The Yang–Mills equations can be solved analytically to obtain the classical field of the nucleus as a function of ρ: $A_{\rm cl.}(\rho)$ [29–34]. From the generating functional in Eq. (8), one obtains for the two-point correlator,

$$< AA >= \int [d\rho]\, W_{\Lambda^+}[\rho]\, A_{\rm cl.}(\rho)\, A_{\rm cl.}(\rho)\,. \tag{10}$$

From this expression, one can determine (for Gaussian sources) the occupation number $\phi = dN/\pi R^2/dk_\perp^2 dy$ of wee partons in the classical field of the nucleus. For $k_\perp \gg Q_s^2$, one has the Weizsäcker–Williams spectrum $\phi \sim Q_s^2/k_\perp^2$, while for $k_\perp \leq Q_s$, one has a resummation to all orders in $k_\perp$, which gives $\phi \sim \frac{1}{\alpha_S} \ln(Q_s/k_\perp)$. (The behavior at low $k_\perp$ can, more accurately, be represented as $\frac{1}{\alpha_S}\Gamma(0, z)$ where Γ is the incomplete gamma function and $z = k_\perp^2/Q_s^2$.) A nice expression for the classical field of the nucleus containing these two limits is given in [40].

We are now in a position to discuss why a high-energy hadron behaves like a color glass condensate [14]. The "color" is obvious since the degrees of freedom, the partons, are colored. It is a glass because the stochastic sources (frozen on timescales much larger than the wee parton timescales) induce a stochastic (space–time-dependent) coupling between the partons under quantum evolution (to be discussed in the next section) – this is analogous to a spin glass in condensed matter physics. Finally, the matter is a condensate since the wee partons have large occupation numbers (of order $1/\alpha_S$) and have momenta peaked about Q_s. Just as in actual condensates, the number of gluons, for a fixed configuration of sources, has a non-zero value and has a magnitude of order $1/\alpha_S$. Gauge-invariant observables are computed by averaging over all possible configurations. As we will discuss, these properties are enhanced by quantum evolution in x. The classical field retains its structure while the saturation scale grows: $Q_s(x') > Q_s(x)$ for $x' < x$.

The problem of small fluctuations about the effective action in Eq. (9) was first addressed in [41, 42] and it was noted that these gave large corrections of order $\alpha_S \ln(1/x)$ to the classical action; this implies that the Gaussian weight functional is fragile under quantum evolution of the sources. A Wilsonian renormalization group (RG) approach was later developed that systematically treated these corrections [43–48]. The basic recipe is as follows. Begin with the generating functional in Eq. (8) at some Λ^+, with an initial source distribution $W[\rho]$. Perform small fluctuations about the classical saddle point of the effective action, integrating out momentum modes in the region $\Lambda'^+ < k^+ < \Lambda^+$, ensuring that Λ'^+ is such that $\alpha_S \ln(\Lambda^+/\Lambda'^+) \ll 1$. The action reproduces itself at the new scale Λ'^+, albeit with a charge density $\rho' = \rho + \delta\rho$, where $\delta\rho$ has support only in the window $\Lambda'^+ < k^+ < \Lambda^+$, and $W_{\Lambda^+}[\rho] \longrightarrow W_{\Lambda'^+}[\rho']$. The change of the weight functional $W[\rho]$ with x is described by the JIMWLK- nonlinear RG equation [43–47] which we shall not write explicitly here – it can be found for instance in [14, 15]. The JIMWLK equation has been re-derived subsequently by several authors. We will discuss briefly in the next lecture, one such derivation by one of us and collaborators, in the context of nucleus–nucleus collisions.

The JIMWLK equations form an infinite hierarchy (analogous to the BBGKY hierarchy in statistical mechanics) of ordinary differential equations for the gluon correlators $< A_1 A_2 \cdots A_n >_Y$, where $Y = \ln(1/x)$ is the rapidity. The expectation value of such an operator $\mathcal{O}$ is defined to be

$$\langle \mathcal{O} \rangle_Y = \int [d\alpha] \mathcal{O}[\alpha] W_Y[\alpha] \,, \tag{11}$$

where $\alpha = \frac{1}{\nabla_\perp^2} \rho$. The corresponding JIMWLK equation for this operator is

$$\frac{\partial \langle \mathcal{O}[\alpha] \rangle_Y}{\partial Y} = \langle \frac{1}{2} \int_{x_\perp, y_\perp} \frac{\delta}{\delta \alpha_Y^a(x_\perp)} \chi^{ab}_{x_\perp, y_\perp}[\alpha] \frac{\delta}{\delta \alpha_Y^b(y_\perp)} \mathcal{O}[\alpha] \rangle_Y \,. \tag{12}$$

Here χ here is a nonlocal object expressed in terms of path-ordered (in rapidity) Wilson lines of α [14]. This equation is analogous to a (generalized) functional Fokker–Planck equation, where Y is the "time" and χ is a generalized diffusion coefficient. This equation illustrates the stochastic properties of operators in the space of gauge fields at high energies. For the gluon density, which is proportional to a two-point function $< \alpha^a(x_\perp) \alpha^b(y_\perp) >$, one recovers the BFKL equation in the limit of low parton densities.

For large N_c and large A ($\alpha_S^2 A^{1/3} \gg 1$), the expectation value of the product of traces of Wilson lines factorizes into the product of the expectation values of the traces:

$$< \mathrm{Tr}(V_x V_z^\dagger) \mathrm{Tr}(V_z V_y^\dagger) > \longrightarrow < \mathrm{Tr}(V_x V_z^\dagger) > < \mathrm{Tr}(V_z V_y^\dagger) > \,, \tag{13}$$

where $V_x = \mathcal{P} \exp\left(\int dz^- \alpha^a(z^-, x_\perp) T^a \right)$. Here $\mathcal{P}$ denotes path ordering in x^- and T^a is the SU(3) generator in the adjoint representation. In the dipole picture, the cross section for a dipole scattering off a target P can be expressed in terms of these two-point dipole operators as [77–79]

$$\sigma_{q\bar{q}P}(x, r_\perp) = 2 \int d^2b \, \mathcal{N}_Y(x, r_\perp, b) \,, \tag{14}$$

where $\mathcal{N}_Y$, the imaginary part of the forward scattering amplitude, is defined to be $\mathcal{N}_Y = 1 - \frac{1}{N_c} \langle \mathrm{Tr}(V_x V_y^\dagger) \rangle_Y$. Note that the size of the dipole, $\boldsymbol{r}_\perp = \boldsymbol{x}_\perp - \boldsymbol{y}_\perp$ and $\boldsymbol{b} = (\boldsymbol{x}_\perp + \boldsymbol{y}_\perp)/2$. The JIMWLK equation for the two-point Wilson correlator is identical in this large A, large N_c mean field limit to an equation derived independently by Balitsky and Kovchegov – the BK equation [49–51], which has the operator form

$$\frac{\partial \mathcal{N}_Y}{\partial Y} = \bar{\alpha}_S \, \mathcal{K}_{\mathrm{BFKL}} \otimes \left\{ \mathcal{N}_Y - \mathcal{N}_Y^2 \right\} \,. \tag{15}$$

Here $\mathcal{K}_{\mathrm{BFKL}}$ is the well-known BFKL kernel. When $\mathcal{N} \ll 1$, the quadratic term is small and one has BFKL growth of the number of dipoles; when $\mathcal{N}$ is close to

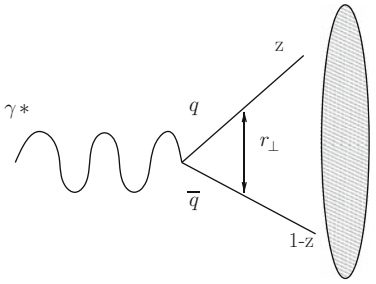

Fig. 5 Interaction of the color dipole with the nuclei

unity, the growth saturates. The approach to unity can be computed analytically [52, 53]. The BK equation is the simplest equation including both the Bremsstrahlung responsible for the rapid growth of amplitudes at small x as well as the repulsive many-body effects that lead to a saturation of this growth.

In this framework, a saturation condition, say $\mathcal{N} = 1/2$, determines the saturation scale. One obtains $Q_s^2 = Q_0^2 \exp(\lambda Y)$, where $\lambda = c\alpha_S$ with $c \approx 4.8$. As we shall discuss further in the next subsection, the (arbitrary) choice of this saturation condition affects the overall normalization of this scale but does not affect the power λ. In fixed coupling, the power λ is large and there are large pre-asymptotic corrections to this relation which die off only slowly as a function of Y. BFKL running coupling effects change the behavior of the saturation scale completely – one goes smoothly at large Y to $Q_s^2 = Q_0^2 \exp(\sqrt{2b_0 c(Y + Y_0)})$ where b_0 is the coefficient of the one-loop QCD β-function. An impressive computation of Q_s is the work of Triantafyllopoulos, who obtained Q_s by solving NLO-resummed BFKL in the presence of an absorptive boundary (which approximates the CGC) [54]. The pre-asymptotic effects are much smaller in this case and the coefficient $\lambda \approx 0.25$ is very close to the value extracted from saturation model fits to the HERA data. There is currently an intense, ongoing effort to directly compute the NLO corrections to the leading order kernels of the BK equation [55–60]. No analytical solution of the leading order BK equation exists in the entire kinematic region but there have been several numerical studies at both fixed and running coupling [61–65]. These studies suggest that the solutions have a soliton-like structure and that the saturation scale has the behavior discussed here.

The soliton-like structure of the numerical solutions is not accidental, as was discovered by Munier and Peschanski [66–68]. They noticed that the BK equation, in a diffusion approximation, bore a formal analogy to the FKPP equation describing the propagation of unstable nonlinear wavefronts in statistical mechanics [69, 70]. In addition, the full BK equation lies in the universality class of the FKPP equation. This enables one to extract the universal properties such as the leading pre-asymptotic terms in the expression for the saturation scale. It was realized [71] that a stochastic generalization of the FKPP equation – the sFKPP equation – could provide insights into impact parameter-dependent fluctuations [72] in high-energy QCD beyond the BK – equation. We shall not discuss further efforts in that direction

here except to note that there are many open ends (and opportunities) here which are still not satisfactorily resolved and require new ideas.

2.4 Color Dipole CGC Models in DIS and Hadronic Scattering

In the previous subsection, we discussed the formalism of the CGC and the JIMWL K/BK RG equations. We will discuss here phenomenological applications of these ideas to DIS and (more briefly) to hadronic collisions. The next lecture will discuss more at length the application of these ideas to heavy-ion collisions. A strong hint that semi-hard scales may play a role in small-x dynamics came from "geometrical scaling" of the HERA data [13]. The inclusive virtual photon+proton cross section for $x \leq 0.01$ and all available Q^2 scales[3] as a function of $\tau \equiv Q^2/Q_s^2$, where $Q_s^2(x) = \exp(\lambda Y)$ GeV^2. Here $Y = \ln(x_0/x)$ is the rapidity; $x_0 = 3 \cdot 10^{-4}$ and $\lambda = 0.288$ are parameters fit to the data [13, 73]. Geometrical scaling of the e+p data is shown in Fig. 6, which demonstrates that the inclusive diffractive, vector meson, and DVCS cross sections at HERA, with a slight modification[4] in the definition of τ, also appear to show geometrical scaling [73]. A recent "quality factor" statistical analysis [74] indicates that this scaling is robust; it is however unable to distinguish between the above fixed coupling energy dependence of Q_s and the running coupling $Q_s(x) \propto \exp(\sqrt{Y})$ dependence of the saturation scale. Geometrical scaling is only asymptotic in both fixed and running coupling evolution equations. However, recent analyses [75, 76] suggest that the onset of the scaling asymptotics may be precocious. Geometrical scaling alone is not sufficient evidence of saturation effects and it is important to look at the data in greater detail in saturation/CGC models.

All saturation models [77–79] express the inclusive virtual photon+proton cross section as

$$\sigma_{L,T}^{\gamma^* p} = \int \mathrm{d}^2 r_\perp \int_0^1 \mathrm{d}z \left|\Psi_{L,T}^{\gamma^*}(r_\perp, Q, z)\,.\right|^2 \sigma_{q\bar{q}P}(r_\perp, x_{\mathrm{Bj}}, b_\perp). \tag{16}$$

Here $\left|\Psi_{L,T}^{\gamma^*}(r_\perp, z, Q)\right|^2$ represents the probability for a virtual photon to produce a quark–anti-quark pair of size $r = |r_\perp|$ (Fig. 5) and $\hat{\sigma}(r_\perp, x_{\mathrm{Bj}}, b_\perp)$ denotes the *dipole cross section* for this pair to scatter off the target at an impact parameter $b_\perp$. The former is well known from QED, while the latter represents the dynamics of QCD scattering at small x – see Eq. (14). A simple saturation model (known as the GBW model [80, 81]) of the dipole cross section, parameterized as $\sigma_{q\bar{q}P} = 2(1 - e^{-r^2 Q_{s,p}(x)}/4)$ where $Q_{s,p}(x) = (x_0/x)^\lambda$ GeV^2, gives a good qualitative fit to the HERA inclusive cross-section data for $x_0 = 3 \cdot 10^{-4}$ and $\lambda = 0.288$. Though this model captures the qualitative features of saturation, it does not contain the

[3] The E665 data are a notable exception.

[4] $\tau_{D,VM} = (Q^2 + M^2)/Q_s^2$, where M denotes the mass of the diffractive/vector meson final state.

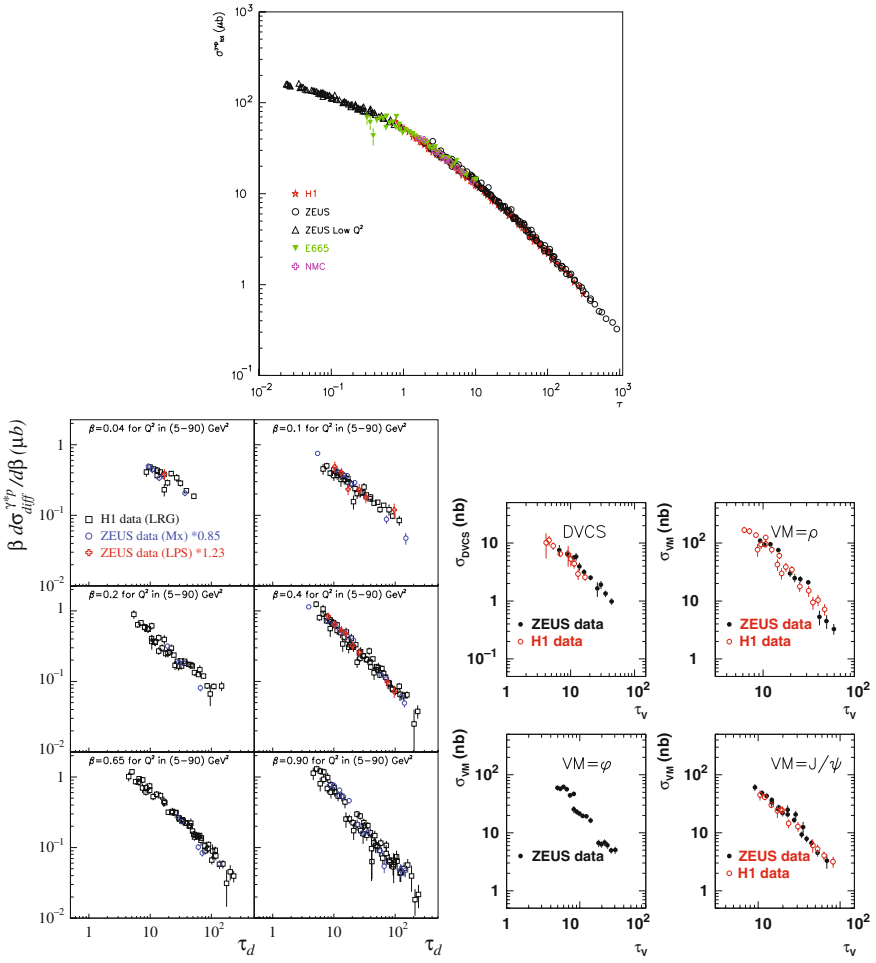

Fig. 6 The top plot shows the total DIS cross section at different Q^2. One observes that the cross section scales as a function of a single variable $\tau = Q^2/Q_s^2(x)$. The lower figures demonstrate that a nearly identical scaling holds for other less inclusive observables such as (i) inclusive diffractive cross section for different invariant masses, (ii) deeply virtual compton scattering (DVCS), and (iii) exclusive vector meson production (ρ, J/ψ, and ϕ mesons). In all cases, the saturation scale is identical. From [73]

bremsstrahlung limit of perturbative QCD (pQCD) that applies to small dipoles of size $r \ll 1/Q_{s,p}(x)$.

In the classical effective theory of the CGC, one can derive, to leading logarithmic accuracy, the dipole cross section [82, 83] containing the right small r limit. This dipole cross section can be represented as [84]

$$\sigma_{q\bar{q}P}(r_\perp, x_{\rm Bj}, b_\perp) = 2\left[1 - \exp\left(-r^2 F(x_{\rm Bj}, r_\perp) T_p(b_\perp)\right)\right], \tag{17}$$

where $T_p(b_\perp)$ is the impact parameter profile function in the proton, normalized as $\int d^2\boldsymbol{b}\, T_p(b_\perp) = 1$ and F is proportional to the gluon distribution [85]:

$$F(x_{\rm Bj}, r_\perp^2) = \pi^2 \alpha_S \left(\mu_0^2 + 4/r_\perp^2\right) x_{\rm Bj} g\left(x_{\rm Bj}, \mu_0^2 + 4/r_\perp^2\right)/(2N_c)\,, \qquad (18)$$

evolved from the initial scale μ_0 by the DGLAP equations. The dipole cross section in Eq. (17) was implemented in the impact parameter saturation model (IPsat) [84] where the parameters are fit to reproduce the HERA data on the inclusive structure function F_2. Here $Q_{s,p}$ is defined[5] as the solution of $\sigma_{q\bar{q}P}(r_\perp, x_{\rm Bj}, b_\perp) = 1/Q_{s,p}(x_{\rm Bj}, b_\perp)) = 2(1 - e^{-1/4})$.

The IPsat dipole cross section in Eq. (17) is valid when leading logarithms in x in pQCD are not dominant over leading logs in Q^2. At very small x, where logs in x dominate, quantum evolution in the CGC describes both the BFKL limit of linear small x evolution as well as the nonlinear JIMWLK/BK evolution at high parton densities [43–47, 49–51]. These asymptotics are combined with a more realistic b-dependence in the b-CGC model [86, 87]. Both the IPsat model and the b-CGC model provide excellent fits to HERA data for $x \leq 0.01$ [87, 88]. The saturation scale extracted from the fit in the IPsat model is shown in Fig. 7. The important point to note is that the energy dependence of the extracted $Q_{s,p}$ is significantly stronger than those predicted in non-perturbative models [89].

The strong field dynamics of small x partons is universal and should be manifest in large nuclei at lower energies than that in the proton. In Fig. 8 (left), we show the well-known shadowing of F_2^A in the fixed target e+A E665 and NMC experiments. Expressed in terms of $\tau \equiv Q^2/Q_s^2$ (Fig. 8 (right)), the data

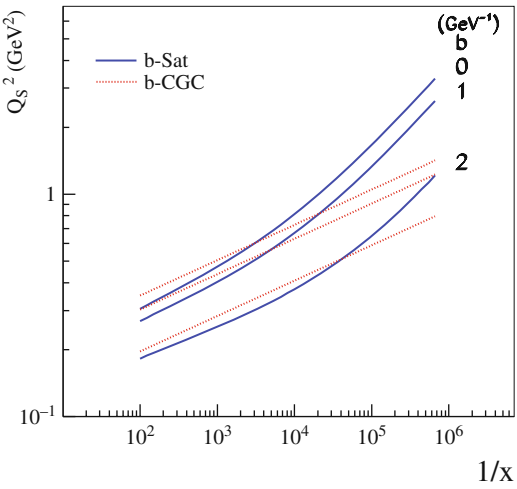

Fig. 7 The saturation scale vs. $1/x$ in the IPsat and b-CGC models [87]

[5] This choice of is equivalent to the saturation scale in the GBW model for the case of a Gaussian dipole cross section.

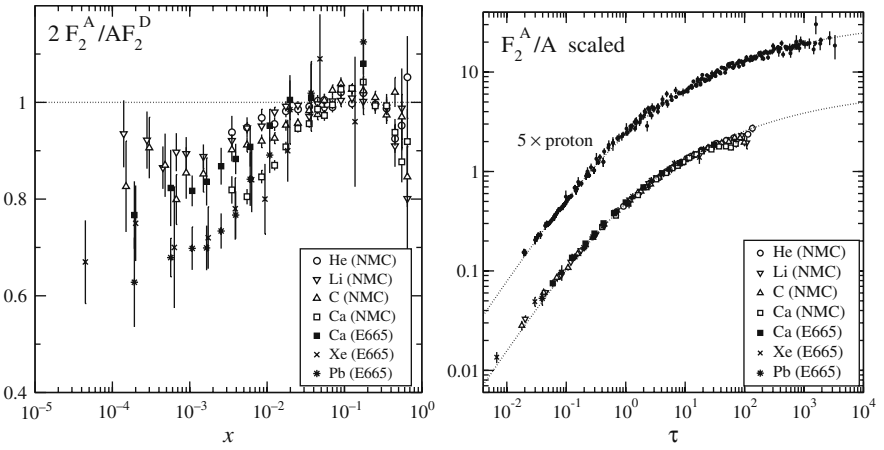

Fig. 8 *Left:* Shadowing of F_2 from the NMC and E665 fixed target experiments. *Right:* The data scaled as a function of $\tau \equiv Q^2/Q_{s,A}^2$ [90]

show geometrical scaling [90]. A careful study of nuclear DIS in the IPsat CGC framework was performed in [84, 91, 92]. The average differential dipole cross section is well approximated by $\left\langle \frac{d\sigma_A}{d^2b_\perp} \right\rangle_N \approx 2\left[1 - \left(1 - \frac{T_A(b_\perp)}{2}\sigma_p\right)^A\right]$, where $T_A(b_\perp)$ is the well-known Woods Saxon distribution. The average is defined as $\langle \mathcal{O} \rangle_N \equiv \int \prod_{i=1}^{A} d^2b_{\perp,i}\, T_A(b_{\perp,i}) \mathcal{O}(\{b_{\perp,i}\})$. Here σ_p is determined from the IPsat fits to the e+p data; no additional parameters are introduced for eA collisions. In Fig. 9 (left), the model is compared to NMC data on carbon and calcium nuclei – the agreement is reasonably good. The fit for calcium data is not as good as that for the carbon data. This may be because the calcium data shown are for larger values of x where one expects to see a breakdown in the formalism. Indeed, one sees a systematic deviation with increasing x. We note however that the largest deviation is of the order of 5% – the theoretical uncertainties, especially at larger x values, are likely significantly larger.

In Fig. 9 (right), we show the extracted saturation scale in nuclei for both central and median impact parameters. To a good approximation, the saturation scale in nuclei scales as $Q_{s,A}^2(x, b_{\text{med.}}) \approx Q_{s,p}^2(x, b_{\text{med.}}) \cdot (A/x)^{1/3}$. The factor of $200^{1/3} \approx 6$ gives a huge "oomph" in the parton density of a nucleus relative to that of a proton at the same x. *Indeed, one would require a center of mass energy* ~ 14 *times larger in the proton case*. At extremely high energies, this statement must be qualified to account for the effects of QCD evolution [93].

We now turn to a discussion of CGC effects in hadronic collisions. A systematic treatment of the scattering of two strong color sources (such as two high-energy nuclei) is discussed in the next lecture. To leading order, the problem reduces to the solution of the classical Yang–Mills (CYM) equations averaged over color sources for each nucleus [94–99]; the variance of this distribution of sources is proportional to $Q_{s,A}^2$. Besides the nuclear radius, it is the only scale in the problem, and the $Q_{s,A}^2 \sim Q_{s,}^2 \cdot (A/x)^{0.3}$ expression for the saturation scale was used in CGC

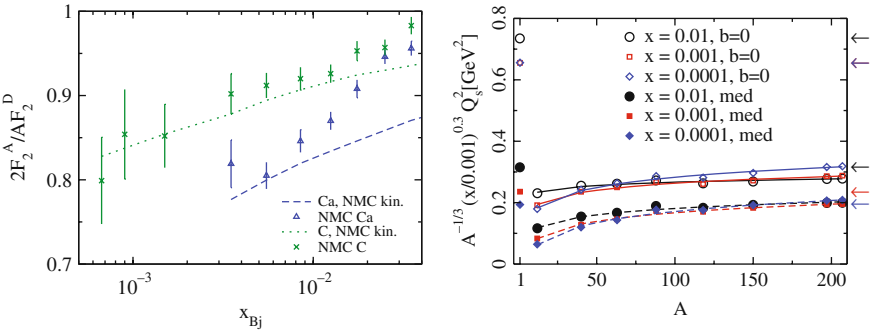

Fig. 9 *Left*: Comparison of the IPsat model (with no adjustable parameters) to the NMC data. *Right*: The A and x dependence of the saturation scale in the IPsat model [91, 92]

models of nuclear collisions to successfully predict the multiplicity [97–99] and the centrality dependence of the multiplicity [139, 140] dependence in gold+gold collisions at RHIC. The universality of the saturation scale also has a bearing on the hydrodynamics of the quark–gluon plasma (QGP); the universal form leads to a lower eccentricity [100] (and therefore lower viscosity) than a nonuniversal form that generates a larger eccentricity [101, 102] (leaving room for a larger viscosity) of the QGP[6]

For asymmetric (off-central rapidity) nuclear collisions, or proton/deuteron + heavy nucleus collisions, $k_\perp$ factorization can be derived systematically for gluon production, at leading order, in the CGC framework [103–106]. Limiting fragmentation [107] and deviations thereof are described by solutions of the BK-equation. Predictions for the multiplicity distribution in A+A collisions at the LHC [108] for both Golec–Biernat–Wusthoff (GBW) and classical CGC (MV) dipole initial conditions[7] give a charged particle multiplicity of 1000–1400 in central lead+lead collisions at the LHC.[8] The results are shown in Fig. 10.

In deuteron + gold collisions at RHIC, data on the inclusive hadron spectra[9] can be directly compared to model predictions [111]. The result is shown in Fig. 11. For a comprehensive review of applications of CGC picture to RHIC phenomenology, we refer the reader to [112]. There are a couple of caveats to this picture. Firstly, $k_\perp$ factorization is very fragile. It does not hold for quark production even at leading order in the parton density [113–118], albeit it may be a good approximation for large masses and transverse momenta [119]. For gluon production, it does not hold beyond leading order in the parton density [120–122, 97–99]. Secondly, a combined comprehensive analysis of HERA and RHIC data is still lacking though there have been first attempts in this direction [123].

---

[6] We shall present yet another take on this issue in lecture II.

[7] The MV initial condition has the same form as the IPsat dipole cross section discussed earlier.

[8] See [109] for other model predictions.

[9] The same analysis also gives good agreement for the forward p+p spectrum at RHIC [110].

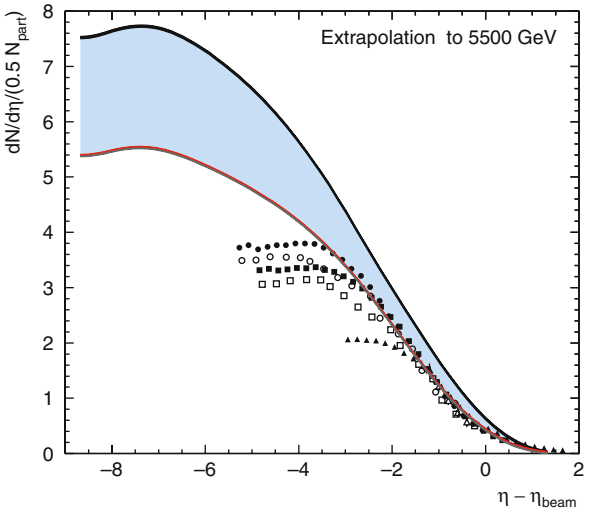

Fig. 10 Prediction for limiting fragmentation and deviations away from it at LHC energies. The bands denote the range in the predictions for GBW and MV models. From [108]

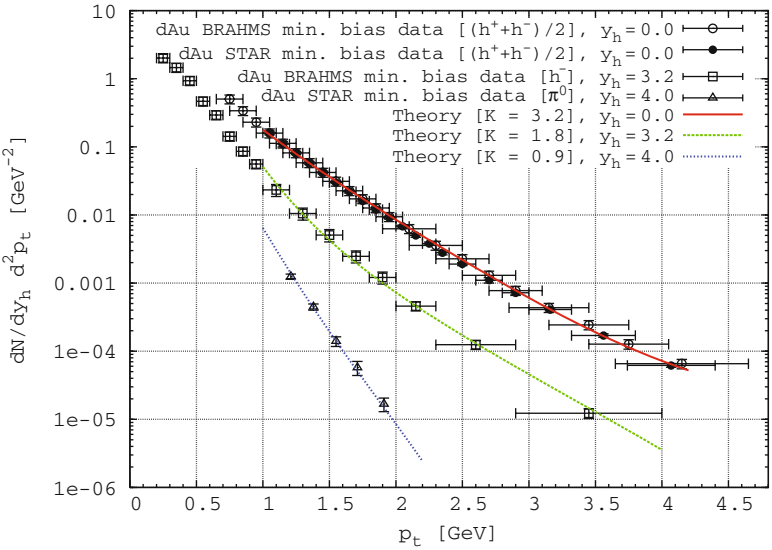

Fig. 11 The inclusive $k_\perp$ distributions in deuteron+gold collisions compared to theory curves for different rapidities. From [111]

2.5 The Future of Small x Physics at Hadron Colliders and DIS

The LHC is the ultimate small x machine in terms of reach in x for large Q^2. A plot from [124] illustrating this reach is shown in Fig. 12 (left). For a recent review

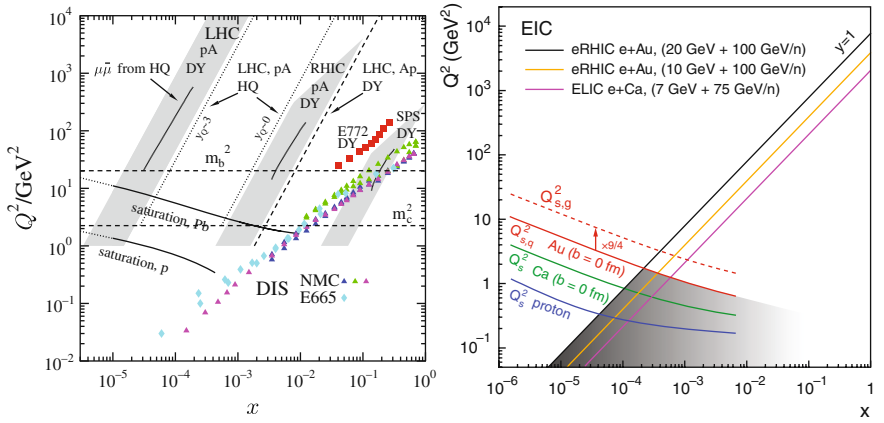

Fig. 12 *Left*: Kinematic x–Q^2 reach of different final states at the LHC compared to other experiments with nuclei . From [124]. *Right*: The saturation scale in the proton, calcium, and gold in the kinematic acceptance of the EIC

of the small x opportunities at the LHC, see [125]. The LHC will provide further, more extensive tests of the hints for the CGC seen at RHIC. The universality of parton distributions is often taken for granted but factorization theorems proving this universality have been proven only for a limited number of inclusive final states. However, as we have discussed, small x is the domain of rich multi-parton correlations. These are more sensitive to more exclusive final states for which universality is not proven [126]. Therefore, while the LHC will have unprecedented reach in x, precision studies of high-energy QCD and clean theoretical interpretations of these motivate future DIS projects. Two such projects are the EIC project in the United States [127] and the LHeC project in Europe [128]. As we discussed previously, strong color fields may be more easily accessible in DIS off nuclei relative to the proton due to the "oomph" factor. In Fig. 12 (right), we show the saturation scale $Q_{s,A}(x)$ overlaid on the x–Q^2 kinematic domain spanned by the EIC. As suggested by the figure, the EIC (and clearly the higher energy LHeC) will cleanly probe the crossover regime from linear to nonlinear dynamics in QCD. For further discussion of the physics of an electron ion collider, see [129, 130].

3 Heavy-Ion Collisions

In the first lecture, we discussed the physics of high parton densities in QCD. We motivated a description of the high-energy structure of hadrons and nuclei as a color glass condensate. We discussed the phenomenological application of CGC-based models to describe data on DIS and hadronic collisions. In this lecture, we will focus our attention on heavy-ion collisions and try and understand ab initio the properties of the QCD matter that is formed when two high-energy nuclear wavefunctions –

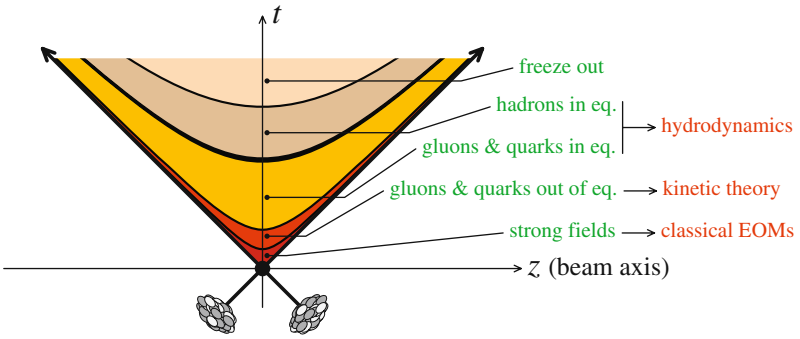

Fig. 13 The various stages of a heavy-ion collision

sheets of colored glass – collide. A schematic space–time picture of the evolution of a heavy-ion collision is shown in Fig. 13.

We shall not attempt to describe all features of a heavy-ion collision but merely focus on the very early initial dynamics for its intrinsic interest but also because it is important to understand to determine whether the matter thermalizes and can be subsequently described by hydrodynamics. The QCD matter that is formed at very early times is a coherent classical field, which expands, decays into nearly on-shell partons, and may eventually thermalize to form a quark–gluon plasma (QGP). Because it is formed by melting the frozen CGC degrees of freedom, and because it is the non-equilibrium matter preceding the QGP, this matter is called the glasma [131, 132].

4 From CGC to Glasma

We will first discuss the classical picture of the glasma that emerges from solutions of classical Yang–Mills equations. We will then discuss the role of quantum corrections in the glasma.

4.1 The Classical Solution

Let us begin by setting up the kinematics involved for the problem of two ultra-relativistic nuclei approaching each other. They are highly Lorentz contracted and can be considered to be sitting at $x^{\pm} = 0$ for $t < 0$ in the light cone coordinates. They collide at $x = t = 0$. At $t \geq 0$ it is convenient to introduce the proper time $\tau = \sqrt{t^2 - z^2}$ which is invariant under Lorentz boosts and the space–time rapidity

$$\eta = \frac{1}{2} \ln \left(\frac{t+z}{t-z} \right). \tag{19}$$

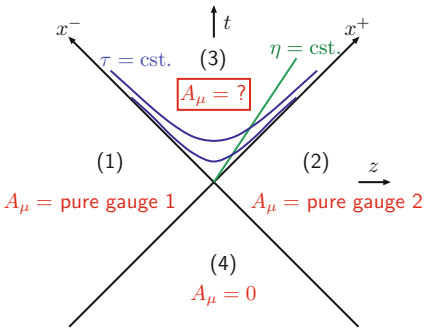

Fig. 14 The space–time distribution of gauge fields before and after the collision

For free streaming particles $z = vt = p_z t/E$ and the space–time rapidity equals the momentum space rapidity y, namely $\eta = y$.

Let us make some approximations to get to the solutions without sacrificing any essential physics. The collisions are considered to be at very high energy so that the nuclei are static light cone currents that are delta functions in $x^{\mp}$, respectively, for nuclei whose large momentum component is given by $P^{\pm}$. A consequence is that the solutions of the classical Yang–Mills equations, for this source distribution, are boost invariant. This leads to a considerable simplification since the equations now depend only on the two transverse directions and the proper time. The initial conditions for the evolution of the classical gauge fields in the forward light cone is illustrated in Fig. 14. The fields of the nuclei before the collision are the Liénard–Wiechert potentials associated with the respective color charge densities. Both the charge densities and the fields exist only on the sheets, and for each source of charge the electric field $\boldsymbol{E}$ and the magnetic field $\boldsymbol{B}$ are orthogonal to each other and to the beam direction. The situation before the collision is depicted in Fig 15. However the vector potentials lie outside the sheets but possess a discontinuity across the sheet according to Gauss law. This is where the small x gluons are located having a large longitudinal extent and coupling with a host of color sources. As has been argued before they are represented by the classical color fields, have very small lifetime, and see the color sources to be static during their lifetime. As noted previously, the infinitesimal nature of the sheets is intended to simplify the problem. A finite size can be taken care of using RG arguments. Figure 14 shows that the fields vanish in the backward light cone and are two-dimensional pure gauge transforms of vacuum in both nuclei before the collision.

In the forward light cone, a pure gauge solution of the Yang–Mills (YM) equations of motion cannot be found – the sum of two pure gauges in QCD is not a pure gauge. Solving the YM equations near the light cone [97–99, 136–138, 133, 134], with the pure gauge initial conditions from the two nuclei before the collision, one finds that the transverse color $\boldsymbol{E}$ and $\boldsymbol{B}$ fields vanish as $\tau \to 0$ but the longitudinal fields are non-vanishing. The results of a numerical simulation [133, 134] are shown in Fig. 16. We note that the nonzero $\boldsymbol{E}$ and $\boldsymbol{B}$ fields imply that the initial condi-

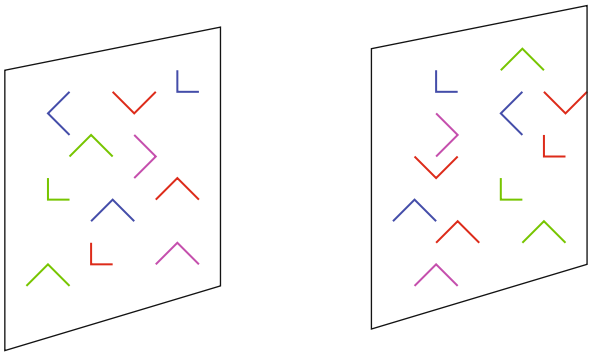

Fig. 15 The color electric and magnetic fields lying on the sheets of the charge distribution. They are perpendicular to each other and to the beam direction

tions [135] may have a large density of topological charge $F^{\mu\nu}\tilde{F}_{\mu\nu}$. The LO picture of the glasma that emerges is one of color flux tubes carrying nontrivial topological charge, localized in the transverse plane and of transverse size $1/Q_s^2$, stretching between the valence color degrees of freedom. As we shall soon see, this picture provides a plausible explanation of the near side ridge in heavy-ion collisions.

For the inclusive gluon distribution, the leading-order (LO) classical contribution is of order $O(\frac{1}{g^2})$ but all orders in $g\rho_{1,2}$, where $\rho_{1,2}$ are the local color charge densities of the two nuclei. It can be expressed as

$$E_p \frac{dN}{d^3p} = \frac{1}{16\pi^3} \lim_{x_0, y_0 \to +\infty} \int d^3x d^3y \; e^{ip\cdot(x-y)} \; (\partial_x^0 - iE_p)(\partial_y^0 + iE_p) \times \sum_\lambda \epsilon_\lambda^\mu(p)\epsilon_\lambda^\nu(p) \left\langle A_\mu(x) A_\nu(y) \right\rangle . \tag{20}$$

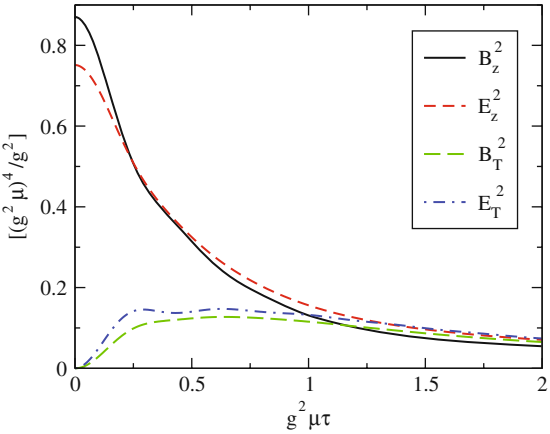

Fig. 16 The longitudinal and transverse components of the chromoelectric and chromomagnetic fields computed numerically on a 512^2 lattice with $g^2\mu R_A = 67.7$

The gauge fields on the right-hand side are computed numerically for proper times $\tau \geq 0$ [136–138, 133, 134] by solving the classical Yang–Mills (CYM) equations in the presence of the light cone current $J^{\mu,a} = \delta^{\mu+}\delta(x^-)\rho_1(x_\perp) + \delta^{\mu-}\delta(x^+)\rho_2(x_\perp)$. The expectation value $\langle \cdots \rangle$ for any inclusive operator $\mathcal{O}$ denotes[10]

$$\langle \mathcal{O} \rangle = \int [D\widetilde{\rho}_1][D\widetilde{\rho}_2]\; W_{Y_{\text{beam}}-Y}[\widetilde{\rho}_1]\, W_{Y_{\text{beam}}+Y}[\widetilde{\rho}_2]\; \mathcal{O}\,[\widetilde{\rho}_1, \widetilde{\rho}_2]\;. \tag{21}$$

We will justify the validity of this formula shortly. For central rapidity RHIC heavy-ion collisions, as discussed in the previous lecture, evolution effects are not important, and $W[\widetilde{\rho}]$ is a Gaussian functional in $\tilde{\rho}$ with the variance μ_A^2. Recall that $Q_s \sim 0.6\mu_A$. So, for these Gaussian distributions, performing the average in Eq. (21) over the solutions to the Yang–Mills equations in Eq. (20), one can compute the number (and energy distributions) of produced gluons in terms of Q_s. For the energy density, one obtains $\varepsilon \sim$ 20–40 GeV/fm^3 for the values of Q_s we mentioned – obtained by extrapolating from fits to the HERA and fixed target e+A data.

This LO formalism was applied to successfully predict the RHIC multiplicity at $y \sim 0$ [136–138, 133, 134] as well as the rapidity and centrality distribution of the multiplicities [139, 140]. At LO, the initial transverse energy is $E_T \sim Q_S$, which is about three times larger than the final measured E_T, while (assuming parton hadron duality) $N_{\text{CGC}} \sim N_{\text{had.}}$. The two conditions are consistent if one assumes nearly isentropic flow which reduces E_T due to PdV work while conserving entropy. This assumption has been implemented directly in ideal hydrodynamic simulations [141].

As discussed previously, CGC-based models give values for the initial eccentricity ϵ that are large than those in Glauber model because the energy and number density locally are sensitive to the lower of the two saturation scales (or local participant density) in the former and the average of the two in the latter. Naively, CGC initial conditions would have more flow then and have more room for dissipative effects relative to Glauber. This conclusion is turned on its head in a simple parameterization of incompletely thermalized flow [142]: $v_2/\epsilon = \dfrac{(v_2/\epsilon)_{\text{hydro}}}{(1 + K/K_0)}$, where $K = \frac{1}{S_\perp}\sigma \frac{dN}{dy} c_s$ the Knudsen number, σ the cross section, c_s the sound speed, and $S_\perp$ the transverse overlap area. K_0 is a number of order unity. If thermalization were complete, $K \to 0$ and one approaches the hydro bound. Computing ϵ with different initial conditions, and plotting the LHS ratio vs $\frac{1}{S_\perp}\frac{dN}{dy}$, one has a two-parameter fit to σ and c_s. The greater CGC eccentricity forces v_2/ϵ to be lower for more central collisions thereby leading to lower c_s; quicker saturation of v_2/ϵ forces larger σ and therefore lower η in the CGC relative to Glauber [143]. While it is conceivable,

[10] Here $\widetilde{\rho}$ is the local color charge density in Lorentz gauge, which is related by a simple gauge transformation to the corresponding color charge density ρ in light cone gauge. We note that $W[\rho]$ is gauge invariant. The light cone gauge classical fields are expressed most simply in terms of color charge densities in Lorentz gauge.

however, that this result may not prove robust against more detailed modeling, it is clear that the results are very sensitive to the initial conditions.

How much flow is generated in the glasma before thermalization? The primordial glasma has occupation numbers $f \sim \frac{1}{\alpha_S}$ and can be described as a classical field. As the glasma expands, higher momentum modes increasingly become particle like and eventually the modes have occupation numbers $f < 1$, which may be described by a thermal spectrum. A first computation of elliptic flow of the glasma found only about half the observed elliptic flow [144] albeit the computation did not properly treat the interaction between hard and soft modes in the glasma. Formulating a kinetic theory that describes this evolution is a challenging problem in heavy-ion collisions – for a preliminary discussion, see [145–148].

The LO field configurations are unstable and lead to very anisotropic momentum distributions at later times. Such distributions can trigger an instability analogous to the Weibel instability in QED plasmas [149]. It is observed in 3+1-D numerical solutions of CYM equations [150–152] that small rapidity-dependent quantum fluctuations in the initial conditions generate transverse E and B fields that grow rapidly as $\exp(\sqrt{Q_S \tau})$. They are the same size as the rapidly diluting longitudinal E and B fields on timescales of order $\frac{1}{Q_S} \ln^2(\frac{C}{\alpha_S})$. The transverse E and B fields may cause large angle deflections of colored particles leading to $p_\perp$ broadening and energy loss of jets – recent numerical simulations by the Frankfurt group appear to confirm this picture [153, 154]. These interactions of colored high momentum particle like modes with the soft coherent classical field modes may also generate a small "anomalous viscosity" whose effects on transport in the glasma may mask a larger kinetic viscosity [155]. The same underlying physics may cause "turbulent isotropization" by rapidly transferring momentum from soft "infrared" longitudinal modes to ultraviolet modes [156–158]. Finally, albeit the LO result demonstrated that one could have nontrivial Chern–Simons charge in heavy-ion collisions, the boost invariance of CYM equations disallows sphaleron transitions that permit large changes in the Chern–Simons number [135].[11] With rapidity-dependent quantum fluctuations, sphaleron transitions can go. These may have important consequences – in particular P and CP odd metastable transitions that cause a novel "chiral magnetic effect" [159, 160] in heavy-ion collisions. Numerical CYM results for Chern–Simons charge and (square root) exponential growth of instabilities are shown in Fig. 17.

4.2 QCD Factorization and the Glasma Instability

The discussion at the end of the last subsection strongly suggests that next-to-leading order (NLO) quantum fluctuations in the glasma, while parametrically suppressed, may alter our understanding of heavy-ion collisions in a fundamental way.

[11] Sphaleron transitions are dynamical real-time processes corresponding to non-trivial large gauge transformations.

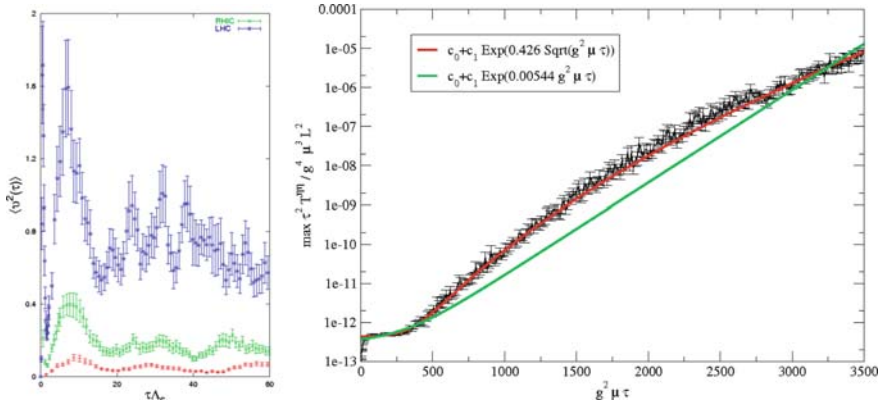

Fig. 17 *Left*: Chern–Simons mean squared charge as a function of proper time (in units of $\Lambda_s \sim 0.6Q_S$), generated in the LO boost-invariant 2+1-D glasma [135]. *Red*, *green*, and *blue* points denote the results for $\Lambda_s L = 74.2,\ 148.4$, and 297, respectively. $\Lambda_s L$ is the key dimensionless parameter for this observable; the latter two values correspond to RHIC and LHC energies, respectively. *Right*: Quantum fluctuations, albeit suppressed by α_S, grow as $\alpha_S \exp(\sqrt{Q_S\tau})$. The figure plots the amplitude of the maximal Fourier mode of the longitudinal pressure with proper time (τ). Functional forms of $\exp\tau$ and $\exp\sqrt{\tau}$ are also plotted. The former is ruled out by the numerical data. [150–152]

To cosmologists, this will not come as a surprise – quantum fluctuations play a central role there as well. In recent papers, it was shown for a scalar theory that moments of the multiplicity distribution at NLO in A+A collisions could be computed as an initial value problem with retarded boundary conditions [161–163]; this framework has now been extended to QCD [164, 165]. In QCD, the problem is subtle because some quantum fluctuations occur in the nuclear wavefunctions and are responsible for how the wavefunctions evolve with energy; others contribute to particle production at NLO. Figure 18 illustrates particle production in field theories with strong sources and the non-factorizable quantum fluctuations that are suppressed in the leading log framework.

In writing Eq. (21), its scope of validity was not specified. A factorization theorem organizing quantum fluctuations shows that all order leading logarithmic contributions to an inclusive gluon operator $\mathcal{O}$ in the glasma can be expressed as [164, 165]

$$\langle\mathcal{O}\rangle_{\rm LLog} = \int [D\widetilde{\rho}_1][D\widetilde{\rho}_2]\; W_{Y_{\rm beam}-Y}[\widetilde{\rho}_1]\, W_{Y_{\rm beam}+Y}[\widetilde{\rho}_2]\; \mathcal{O}_{\rm LO}\,[\widetilde{\rho}_1, \widetilde{\rho}_2]\ , \qquad (22)$$

where $\mathcal{O}_{\rm LO}$ is the same operator evaluated at LO by solving classical Yang–Mills equations and $W_{Y_{\rm beam}\mp Y}[\widetilde{\rho}_{1,2}]$ are the weight functionals that obey the JIMWLK Hamiltonians describing the rapidity evolution of the projectile and target wavefunctions, respectively. This theorem is valid[12] if the rapidity interval corresponding

[12] Recent work suggests that this factorization theorem is valid even when the rapidity restriction is relaxed.

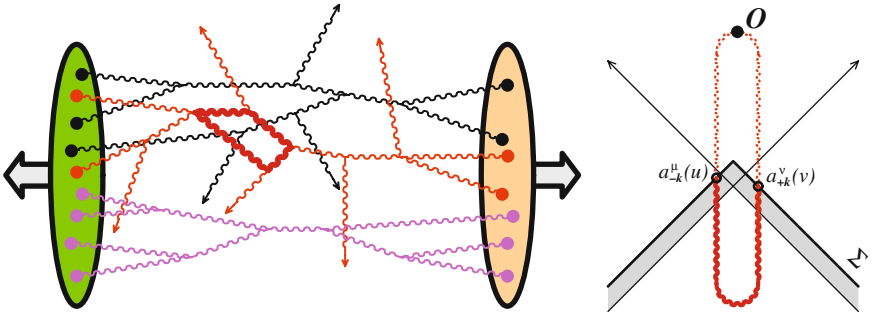

Fig. 18 *Left*: Illustration of particle production in a field theory with strong time-dependent sources. *Right*: Quantum fluctuations, where the nuclei talk to each other before the collision, are suppressed; this is responsible for high-energy factorization of inclusive gluon operators $\mathcal{O}$ in A+A collisions [164, 165]

to the production of the final state, $\Delta Y \leq \frac{1}{\alpha_S}$. The W's are analogous to the parton distribution functions in collinear factorization; determined non-perturbatively at some initial scale Y_0, their evolution with Y is given by the JIMWLK Hamiltonian.

This factorization theorem is a necessary first step before a full NLO computation of gluon production in the glasma. Equation (22) includes only the NLO terms that are enhanced by a large logarithm of $1/x_{1,2}$, while the complete NLO calculation would also include non-enhanced terms. These would be of the same order in α_S as the production of quark–antiquark pairs [166, 167] from the classical field. To be really useful, this complete NLO calculation likely has to be promoted to a next-to-leading log (NLL) result by resumming all the terms in $\alpha_S(\alpha_S \ln(1/x_{1,2}))^n$. Now that evolution equations in the dense regime are becoming available at NLO, work in this direction is a promising prospect. In addressing the role of instabilities at NLO, note that small field fluctuations fall into three classes: (i) Zero modes ($p_\eta = 0$) that generate the leading logs resummed in Eq. (22); the coefficients of the leading logs do not depend on $x^{\pm}$. (ii) Zero modes that do not contribute at leading log because they are less singular than the leading log contributions. These become relevant in resumming NLL corrections to the factorization result. Because they are zero modes, they do not trigger plasma instabilities. (iii) Nonzero modes ($p_\eta \neq 0$) that do not contribute large logarithms of $1/x_{1,2}$, but grow exponentially as $\exp(\sqrt{Q_S \tau})$. While these boost non-invariant terms are suppressed by α_S, they are enhanced by exponentials of the proper time after the collision. These leading temporal divergences can be resummed and the expression for inclusive gluon operators in the glasma revised to read

$$\langle \mathcal{O} \rangle_{\text{LLog+LInst}} = \int [D\widetilde{\rho}_1][D\widetilde{\rho}_2]\; W_{Y_{\text{beam}}-Y}[\widetilde{\rho}_1]\, W_{Y_{\text{beam}}+Y}[\widetilde{\rho}_2] \times \int \left[Da(\boldsymbol{u})\right] \widetilde{Z}[a(\boldsymbol{u})]\; \mathcal{O}_{\text{LO}}[\widetilde{\mathcal{A}}_1^{+} + a, \widetilde{\mathcal{A}}_2^{-} + a], \tag{23}$$

where $\widetilde{\mathcal{A}}_1^+(x) = -\frac{1}{\partial_\perp^2}\widetilde{\rho}_1(x_\perp, x^-)$ and $\widetilde{\mathcal{A}}_2^-(x) = -\frac{1}{\partial_\perp^2}\widetilde{\rho}_2(x_\perp, x^+)$. The effect of the resummation of instabilities is therefore to add fluctuations to the initial conditions of the classical field, with a distribution that depends on the outcome of the resummation. This spectrum $\widetilde{Z}[a(\boldsymbol{u})]$ is the final incomplete step in determining all the leading singular contributions to particle production in the glasma – see however [168]. The stress-energy tensor $T^{\mu\nu}$ can then be determined ab initio and matched smoothly to kinetic theory or hydrodynamics at late times.

4.3 Two-Particle Correlations in the Glasma and the Ridge

Striking "ridge" events were revealed in studies of the near side spectrum of correlated pairs of hadrons at RHIC [169–173]. One observes that the spectrum of correlated pairs on the near side of the STAR detector extends across the entire detector acceptance in pseudo-rapidity of order $\Delta\eta \sim 2$ units but is strongly collimated in the relative azimuthal angle between the pairs. These events are called "ridge" events because the particle correlations have the visual appearance of a mountain ridge when plotted in the η–ϕ plane for the specified $\Delta\eta$ and $\Delta\phi$ ranges. Preliminary analysis of measurements by the PHENIX and PHOBOS collaborations corroborates the STAR results. In the latter case, the ridge is observed to span the PHOBOS acceptance in pseudo-rapidity of $\Delta\eta \sim 4$ units.

Causality dictates (in strong analogy to CMB superhorizon fluctuations) that long-range rapidity correlations causing the ridge must have occurred at proper times $\tau \leq \tau_{\text{freezeout}}\ e^{-\frac{1}{2}|y_A - y_B|}$, where y_A and y_B are the rapidities of the correlated particles. If the ridge span in psuedo-rapidity is large, these correlations must have originated in the glasma. The PHOBOS data suggest correlations at times as early as a fermi. As noted previously, particles produced from glasma flux tubes are boost invariant. See Fig. 19. The correlated two gluon production in the glasma flux tube is independent of rapidity [174, 175] – thereby allowing long-range correlations. Remarkably, the result shown in Fig. 19 (right), that "classical" disconnected graphs give the leading contribution to two-particle correlations, holds true even when one includes leading logarithmic contributions to all orders in perturbation theory [165]. When the separation in rapidity between pairs $\Delta y \gg 1/\alpha_S$, particle emission between the triggered pairs will modify this result. This rapidity dependence can be computed and tested at the LHC.

Ours is the only dynamical model with this feature-for other models, see [176]. The particles produced in a flux tube are isotropic locally in the rest frame but are collimated in azimuthal angle when boosted by transverse flow [177–179]. Combining our dynamical calculation of two-particle correlations with a simple "blast wave" model of transverse flow, we obtained reasonable agreement with 200 GeV STAR data on the amplitude of the correlated two-particle spectrum relative to the number of binary collisions per participant pair. A more sophisticated recent treatment of the flow of glasma flux tubes shows excellent agreement of the amplitude of the ridge with centrality and energy, and likewise of the angular width of the

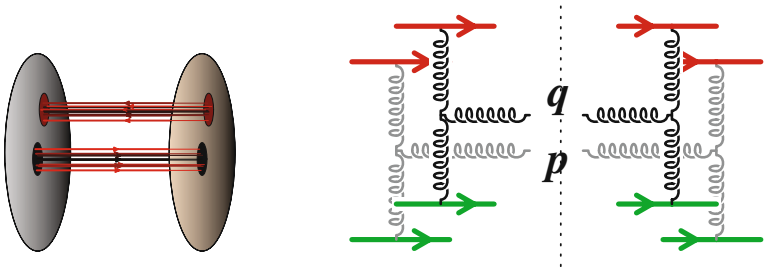

Fig. 19 *Left*:Glasma flux tubes of transverse size $\frac{1}{Q_s} < \frac{1}{\Lambda_{\rm QCD}}$. The field lines correspond to parallel E and B fields, which carry topological charge. *Right*: The leading two-particle contribution. Superficially disconnected, they are connected by averaging over the large-x color sources. Systematic power counting shows these graphs dominate over usual "pQCD" graphs at high energies

ridge with centrality and energy [180]. Three-particle correlations can further help distinguish the glasma explanation for the ridge from other mechanisms.

Acknowledgments R.V's work on this manuscript was supported by DOE Contract No. #DE-AC02-98CH10886. R.V. would like to thank Sourav Sarkar, Helmut Satz, and Bikash Sinha or their kind invitation to lecture at the QGP winter school in Jaipur and for the excellent atmosphere and hospitality at the school. D. B and R.V. would also like to thank the Center for Theoretical Sciences (CTS) of the Tata Institute for Fundamental Research (TIFR) for their support of the program and school on "Initial Conditions in Heavy Ion Collisions" at Dona Paula, Goa, where some of this work was performed.

References

1. S. Chekanov et al. [ZEUS Collaboration]: Eur. Phys. J. **C 21**, 443 (2001) 105
2. C. Adloff et al. [H1 Collaboration]: Eur. Phys. J. **C12**,595 (2000) 105
3. G.J Alner et al.: Z. Phys. **C33**, 1 (1986) 106
4. J.E. Elias et al.: Phys. Rev. **D 22**, 13 (1980)
5. I.G. Bearden et al. [BRAHMS Collaboration]: Phys. Lett. **B 523**, 227 (2001)
6. I.G. Bearden et al. [BRAHMS Collaboration]: Phys. Rev. Lett. **88**, 20230 (2002)
7. B.B. Back et al. [PHOBOS Collaboration]: Phys. Rev. Lett. **91**, 052303 (2003)
8. B.B. Back et al. [PHOBOS Collaboration]: nucl-ex/0509034
9. J. Adams et al. [STAR Collaboration]: Phys. Rev. Lett. **95**, 062301 (2005)
10. J. Adams et al. [STAR Collaboration]: Phys. Rev. **C73**, 034906 (2006) 106
11. M. Derrick et al. [ZEUS Collaboration]: Phys. Lett. **B 315**, 481 (1993) 106
12. T. Ahmed et al. [H1 Collaboration]: Nucl. Phys. **B 429**, 477 (1994) 106
13. A.M. Stasto, K. Golec-Biernat and J. Kwiecinski: Phys. Rev. Lett. **86**, 596 (2001) 106, 118
14. E. Iancu and R. Venugopalan: The Color Glass Condensate and High Energy Scattering in QCD. In: R.C. Hwa and X.-N. Wang (eds.) *Quark-Gluon Plasma 3*, World Scientific, Singapore 106, 115, 116
15. H. Weigert: Prog. Part. Nucl. Phys. **55**, 461 (2005) 106, 115
16. R.P. Feynman: *Photon-Hadron Interactions*. W.A. Benjamin, Reading, MA (1972) 109
17. R.P. Feynman: Phys. Rev. Lett. **23**, 1415 (1969)
18. J.D. Bjorken and E.A. Paschos: Phys. Rev. **185**, 1975 (1969) 109
19. G. Altarelli and G. Parisi: Nucl. Phys. **B126**, 298 (1977) 110
20. Y. Dokshitser; Sov. Phys. JETP **46**, 641 (1977)

21. L.N. Lipatov: Sov. J. Nucl. Phys. **20**, 95 (1975)
22. V.N. Gribov and L.N. Lipatov: Sov. J. Nucl. Phys. **15**, 438 (1972) 110
23. L.N. Lipatov: Sov. J. Nucl. Phys. **23**, 338 (1976) 112
24. E.A. Kuraev, L.N. Lipatov and V.S. Fadin: Sov. Phys. JETP **45**, 199 (1977)
25. Ya.Ya. Balitsky and L.N. Lipatov: Sov. J. Nucl. Phys. **28**, 822 (1978) 112
26. L.V. Gribov, E.M. Levin and M.G. Ryskin, Phys. Rep. **100**, 1 (1983) 113
27. A.H. Mueller and J.-W. Qiu: Nucl. Phys. **B268**, 427 (1986) 113
28. L. Susskind: Phys. Rev. **165**, 1535 (1968) 113
29. L.D. McLerran and R. Venugopalan, Phys. Rev. **D 49**, 2233 (1994) 114, 115
30. L.D. McLerran and R. Venugopalan, Phys. Rev. **D 49**, 3352 (1994)
31. L.D. McLerran, R. Venugopalan, Phys. Rev. **D 50**, 2225 (1994)
32. Yu.V. Kovchegov: Phys. Rev. **D 54**, 5463 (1996)
33. J. Jalilian-Marian, A. Kovner, L.D. McLerran and H. Weigert: Phys. Rev. **D 55**, 5414 (1997)
34. E. Iancu, A. Leonidov and L.D. McLerran: Nucl. Phys. **A 692**, 583 (2001) 114, 115
35. J. Jalilian-Marian, S. Jeon and R. Venugopalan: Phys. Rev. **D 63**, 036004 (2001) 114
36. S. Jeon, R. Venugopalan: Phys. Rev. **D 70**, 105012 (2004) 114
37. Jeon, R. Venugopalan: Phys. Rev. **D 71**, 125003 (2005) 114
38. Yu.V. Kovchegov: Phys. Rev. **D 54**, 5463 (1996) 114
39. T. Lappi: Eur. Phys. J. **C 55**, 285 (2008) 114
40. D. Triantafyllopoulos: hep-ph/0502114 115
41. A. Ayala, J. Jalilian-Marian, L.D. McLerran and R. Venugopalan: Phys. Rev. **D 52**, 2935 (1995) 115
42. A. Ayala, J. Jalilian-Marian, L.D. McLerran and R. Venugopalan: Phys. Rev. **D 53**, 458 (1996) 115
43. J. Jalilian-Marian, A. Kovner, A. Leonidov and H. Weigert: Nucl. Phys. **B504**, 415 (1997) 115, 120
44. J. Jalilian-Marian, A. Kovner, A. Leonidov and H. Weigert: Phys. Rev. **D59**, 014014 (1999)
45. E. Iancu, A. Leonidov and L. McLerran: Nucl. Phys. **A692**, 583 (2001)
46. E. Iancu, A. Leonidov and L. McLerran: Phys. Lett. **B510**, 133 (2001)
47. E. Ferreiro, E. Iancu, A. Leonidov and L. McLerran: Nucl. Phys. **A703**, 489 (2002) 115, 120
48. K. Rummukainen and H. Weigert, Nucl. Phys. **A 739**, 183 (2004) 115
49. I. Balitsky: Nucl. Phys. **B463**, 99 (1996) 116, 120
50. Yu.V. Kovchegov: Phys. Rev. **D60**, 034008 (1999)
51. Yu.V. Kovchegov: Phys. Rev. **D61**, 074018 (2000) 116, 120
52. E. Levin and K. Tuchin: Nucl. Phys. **B573**, 833 (2000) 117
53. E. Levin and K. Tuchin: Nucl. Phys. **A691**, 779 (2001) 117
54. D.N. Triantafyllopoulos: Nucl. Phys. **B 648**, 293 (2003) 117
55. I. Balitsky, Phys. Rev. **D 75**, 014001 (2007) 117
56. I. Balitsky and G.A. Chirilli: Phys. Rev. **D 77**, 014019 (2008)
57. E. Gardi, J. Kuokkanen, K. Rummukainen and H. Weigert: Nucl. Phys. **A 784**, 282 (2007)
58. Yu.V. Kovchegov and H. Weigert: Nucl. Phys. **A 784**, 188 (2007)
59. Yu.V. Kovchegov and H. Weigert: Nucl. Phys. **A 789**, 260 (2007)
60. J.L. Albacete and Y. Kovchegov: Phys. Rev. **D 75**, 125021 (2007) 117
61. K. Golec-Biernat, L. Motyka and A.M. Stasto: Phys. Rev. **D 65**, 074037 (2002) 117
62. M.A. Braun: hep-ph/0101070
63. N. Armesto and M.A. Braun: Eur. Phys. J. **C 20**, 517 (2001)
64. J.L. Albacete, N. Armesto, A. Kovner, C.A. Salgado and U.A. Wiedemann: Phys. Rev. Lett. **92**, 082001 (2004)
65. J.L. Albacete, N. Armesto, A. Kovner, C.A. Salgado and U.A. Wiedemann: arXiv:hep-ph/0408216 117
66. S. Munier and R. Peschanski: Phys. Rev. Lett. **91**, 232001 (2003) 117
67. S. Munier and R. Peschanski: Phys. Rev. **D 69**, 034008 (2004)
68. S. Munier and R. Peschanski: Phys. Rev. **D 70**, 077503 (2004) 117
69. R.A. Fischer: Ann. Eugen. **7**, 355 (1937) 117

70. A. Kolmogorov, I. Petrovsky and N. Piscounov: Moscow Univ. Bull. Math. **A1**, 1 (1937) 117
71. E. Iancu, A.H. Mueller and S. Munier: arXiv:hep-ph/0410018 117
72. A.H. Mueller and A.I. Shoshi: Nucl. Phys. **B 692**, 175 (2004) 117
73. C. Marquet and L. Schoeffel: Phys. Lett. **B 639**, 471 (2006) 118, 119
74. F. Gelis, R. Peschanski, G. Soyez and L. Schoeffel: Phys. Lett. **B 647**, 376 (2007) 118
75. J.L. Albacete and Y.V. Kovchegov: Phys. Rev. **D 75**, 125021 (2007) 118
76. C. Marquet, R. Peschanski and G. Soyez: Phys. Lett. **B 628**, 239 (2005) 118
77. A.H. Mueller: Nucl. Phys. **B335**, 115 (1990) 116, 118
78. N.N. Nikolaev and B.G. Zakharov: Phys. Lett. **B260**, 414 (1991)
79. N.N. Nikolaev and B.G. Zakharov: Z. Phys. **C53**, 331 (1992) 116, 118
80. K. Golec-Biernat and M. Wusthoff: Phys. Rev. **D59**, 014017 (1999) 118
81. K. Golec-Biernat and M. Wusthoff: Phys. Rev. **D60**, 114023 (1999) 118
82. L.D. McLerran and R. Venugopalan: Phys. Rev. **D59**, 094002 (1999) 119
83. R. Venugopalan: Acta Phys. Pol. **B30**, 3731 (1999) 119
84. H. Kowalski and D. Teaney: Phys. Rev. **D68**, 114005 (2003) 119, 120, 121
85. J. Bartels, K. Golec-Biernat and H. Kowalski: Phys. Rev. **D66**, 014001 (2002) 120
86. E. Iancu, K. Itakura and S. Munier: Phys. Lett. **B590**, 199 (2004) 120
87. H. Kowalski, L. Motyka and G. Watt: Phys.Rev. **D74**, 074016 (2006) 120
88. R. Forshaw, R. Sandapen and G. Shaw: JHEP **11**, 025 (2006) 120
89. A. Donnachie and P.V. Landshoff: Phys. Lett. **B 437**, 408 (1998) 120
90. A. Freund, K. Rummukainen, H. Weigert and A. Schafer: Phys. Rev. Lett. **90**, 222002 (2003) 121
91. H. Kowalski, T. Lappi and R. Venugopalan: Phys. Rev. Lett. **100**, 022303 (2008) 121, 122
92. H. Kowalski, T. Lappi, C. Marquet and R. Venugopalan: arXiv:0805.4071 [hep-ph] 121, 122
93. A.H. Mueller, Nucl. Phys. **A724**, 223 (2003) 121
94. A. Kovner, L.D. McLerran and H. Weigert: Phys. Rev. **D 52**, 3809 (1995) 121
95. A. Kovner, L.D. McLerran and H. Weigert: Phys. Rev. **D 52**, 6231 (1995)
96. Yu.V. Kovchegov and D.H. Rischke: Phys. Rev. **C 56**, 1084 (1997)
97. A. Krasnitz and R. Venugopalan: Nucl. Phys. **B 557**, 237 (1999) 122, 126
98. A. Krasnitz and R. Venugopalan: Phys. Rev. Lett. **84**, 4309 (2000)
99. A. Krasnitz and R. Venugopalan: Phys. Rev. Lett. **86**, 1717 (2001) 121, 122, 126
100. T. Lappi and R. Venugopalan: Phys. Rev. **C 74**, 054905 (2006) 122
101. T. Hirano, U.W. Heinz, D. Kharzeev, R. Lacey and Y. Nara: Phys. Lett. **B 636**, 299 (2006) 122
102. H.-J. Drescher, A. Dumitru, A. Hayashigaki and Y. Nara: Phys. Rev. **C 74**, 044905 (2006) 122
103. Y.V. Kovchegov and A. H. Mueller: Nucl. Phys. **B 529**, 451 (1998) 122
104. A. Dumitru and L.D. McLerran: Nucl. Phys. **A 700**, 492 (2002)
105. J.P. Blaizot, F. Gelis and R. Venugopalan: Nucl. Phys. **A 743**, 13 (2004)
106. F. Gelis and Y. Mehtar-Tani: Phys. Rev. **D 73**, 034019 (2006) 122
107. J. Jalilian-Marian: Phys. Rev. **C 70**, 027902 (2004) 122
108. F. Gelis, A. M. Stasto and R. Venugopalan: Eur. Phys. J. **C 48**, 489 (2006) 122, 123
109. N. Armesto: arXiv:0804.4158 [hep-ph] 122
110. D. Boer, A. Dumitru and A. Hayashigaki: Phys. Rev. **D 74**, 074018 (2006) 122
111. A. Dumitru, A. Hayashigaki and J. Jalilian-Marian: Nucl. Phys. **A 770**, 57 (2006) 122, 123
112. J. Jalilian-Marian and Y. Kovchegov, Prog. Part. Nucl. Phys. **56**, 104 (2006) 122
113. J.P. Blaizot, F. Gelis and R. Venugopalan: Nucl. Phys. **A 743**, 57 (2004) 122
114. H. Fujii, F. Gelis and R. Venugopalan: Phys. Rev. Lett. **95**, 162002 (2005)
115. H. Fujii, F. Gelis and R. Venugopalan: Nucl. Phys. **A 780**, 146 (2006)
116. K. Tuchin: Phys. Lett. **B 593**, 66 (2004)
117. N.N. Nikolaev and W. Schafer: Phys. Rev. **D 71**, 014023 (2005)
118. N.N. Nikolaev, W. Schafer and B.G. Zakharov: Phys. Rev. Lett. **95**, 221803 (2005) 122
119. F. Gelis and R. Venugopalan: Phys. Rev. **D 69**, 014019 (2004) 122
120. I. Balitsky: Phys. Rev. **D 72**, 074027 (2005) 122
121. J. Jalilian-Marian and Y.V. Kovchegov: Phys. Rev. **D 70**, 114017 (2004)
122. J. Jalilian-Marian and Y.V. Kovchegov: Phys. Rev. **D 71**, 079901 (2005) [Erratum] 122

123. V.P. Goncalves, M.S. Kugeratski, M.V.T. Machado and F.S. Navarra: Phys. Lett. **B643**, 273 (2006) 122
124. D. d'Enterria: Eur. Phys. J. **A 31**, 816 (2007) 123, 124
125. L. Frankfurt, M. Strikman and C. Weiss: Ann. Rev. Nucl. Part. Sci. **55**, 403 (2005) 124
126. J. Collins and J. W. Qiu: Phys. Rev. **D 75**, 114014 (2007) 124
127. B. Surrow, J. Phys. Conf. Ser. **110**, 022049 (2008) 124
128. J.B. Dainton, M. Klein, P. Newman, E. Perez and F.Willeke: JINST **1**, P10001 (2006) [arXiv:hep-ex/0603016] 124
129. A. Deshpande, R. Milner, R. Venugopalan and W. Vogelsang: Ann. Rev. Nucl. Part. Sci. **55**, 165 (2005) 124
130. T. Ullrich: J. Phys. **G 35**, 104041 (2008) 124
131. T. Lappi and L. McLerran, Nucl. Phys. **A 772**, 200 (2006) 125
132. F. Gelis and R. Venugopalan: Acta Phys. Pol. **B 37**, 3253 (2006) 125
133. T. Lappi: Phys. Rev. **C 67**, 054903 (2003) 126, 128
134. T. Lappi: Phys. Lett. **B 643**, 11 (2006) 126, 128
135. D. Kharzeev, A. Krasnitz and R. Venugopalan: Phys. Lett. **B 545**, 298 (2002) 127, 129, 130
136. A. Krasnitz, Y. Nara, R. Venugopalan: Phys. Rev. Lett. **87**, 192302 (2001) 126, 128
137. A. Krasnitz, Y. Nara, R. Venugopalan: Nucl. Phys. **A 717**, 268 (2003)
138. A. Krasnitz, Y. Nara, R. Venugopalan: Nucl. Phys. **A 727**, 427 (2003) 126, 128
139. D. Kharzeev and M. Nardi: Phys. Lett. **B 507**, 121 (2001) 122, 128
140. D. Kharzeev and E. Levin: Phys. Lett. **B 523**, 79 (2001) 122, 128
141. T. Hirano and Y. Nara: Nucl. Phys. **A 743**, 305 (2004) 128
142. R.S. Bhalerao, J.P. Blaizot, N. Borghini and J.Y. Ollitrault: Phys. Lett. **B 627**, 49 (2005) 128
143. H.J. Drescher, A. Dumitru, C. Gombeaud and J.Y. Ollitrault: Phys. Rev. **C 76**, 024905 (2007) 128
144. A. Krasnitz, Y. Nara and R. Venugopalan: Phys. Lett. **B 554**, 21 (2003) 129
145. A.H. Mueller and D.T. Son: Phys. Lett. **B 582**, 279 (2004) 129
146. S. Jeon: Phys. Rev. **C 72**, 014907 (2005)
147. F. Gelis, S. Jeon and R. Venugopalan: arXiv:0706.3775 [hep-ph]
148. S.V. Akkelin: arXiv:0801.1628 [nucl-th] 129
149. S. Mrowczynski and M.H. Thoma: Ann. Rev. Nucl. Part. Sci. **57**, 61 (2007) 129
150. P. Romatschke and R. Venugopalan: Phys. Rev. Lett. **96**, 062302 (2006) 129, 130
151. P. Romatschke and R. Venugopalan: Eur. Phys. J. **A 29**, 71 (2006)
152. P. Romatschke and R. Venugopalan: Phys. Rev. D **D 7**4, 045011 (2006). 129, 130
153. A. Dumitru, Y. Nara, B. Schenke and M. Strickland: arXiv:0710.1223 [hep-ph] 129
154. B. Schenke, M. Strickland, C. Greiner and M.H. Thoma, Phys. Rev. **D 73**, 125004 (2006) 129
155. M. Asakawa, S.A. Bass and B. Muller: Phys. Rev. Lett. **96**, 252301 (2006) 129
156. P. Arnold and G.D. Moore: Phys. Rev. **D 73**, 025006 (2006) 129
157. A.H. Mueller, A.I. Shoshi and S.M.H. Wong: Nucl. Phys. **B 760**, 145 (2007)
158. V. Khachatryan: arXiv:0803.1356 [hep-ph] 129
159. H.J. Warringa: arXiv:0805.1384 [hep-ph] 129
160. D.E. Kharzeev, L.D. McLerran and H.J. Warringa: Nucl. Phys. **A 803**, 227 (2008) 129
161. F. Gelis and R. Venugopalan: Nucl. Phys. **A 776**, 135 (2006) 130
162. F. Gelis and R. Venugopalan: Nucl. Phys. **A 779**, 177 (2006)
163. F. Gelis, T. Lappi and R. Venugopalan: Int. J. Mod. Phys. **E 16**, 2595 (2007) 130
164. F. Gelis, T. Lappi and R. Venugopalan: arXiv:0804.2630 [hep-ph] 130, 131
165. F. Gelis, T. Lappi and R. Venugopalan: arXiv:0807.1306 [hep-ph] 130, 131, 132
166. F. Gelis, K. Kajantie and T. Lappi: Phys. Rev.**C 71**,024904 (2005) 131
167. F. Gelis, K. Kajantie and T. Lappi: Phys. Rev. Lett. **96**, 032304 (2006) 131
168. K. Fukushima, F. Gelis and L. McLerran: Nucl. Phys. **A 786**, 107 (2007) 132
169. J. Adams et al. [STAR Collaboration]: Phys. Rev. Lett. **95**, 152301 (2005) 132
170. Fuqiang Wang [STAR Collaboration]: talk at Quark Matter 2004, J. Phys. **G 30**, S1299–S1304 (2004)
171. J. Adams et al. [STAR Collaboration]: Phys. Rev. **C 73**, 064907 (2006)

172. A. Adare et al. [PHENIX Collaboration]: arXiv:0801.4545 [nucl-ex]
173. B. Alver et al. [PHOBOS Collaboration]: J. Phys. **G 35**, 104005 (2008) 132
174. A. Dumitru, F. Gelis, L. McLerran and R. Venugopalan: Nucl. Phys. **A 810**, 91 (2008) 132
175. A. Dumitru, F. Gelis, L. McLerran and R. Venugopalan: arXiv:0804.3858 [hep-ph] 132
176. R.C. Hwa: J. Phys. **G 35**, 104017 (2008) 132
177. S.A. Voloshin: Phys. Lett. **B 632**, 490 (2006) 132
178. E.V. Shuryak: Phys. Rev. **C 76**, 047901 (2007)
179. C.A. Pruneau, S. Gavin, S.A. Voloshin: Nucl. Phys. **A 802**, 107 (2008) 132
180. S. Gavin, L. McLerran and G. Moschelli: arXiv:0806.4718 [nucl-th] 133

Hydrodynamics and Flow

Tetsufumi Hirano, Naomi van der Kolk, and Ante Bilandzic

1 Introduction and Disclaimer

The main purpose of the lecture was to lead students and young postdocs to the frontier of the hydrodynamic description of relativistic heavy-ion collisions (H.I.C.) in order for them to understand talks and posters presented in the Quark Matter 2008 (QM08) conference in Jaipur, India [1]. So the most recent studies were not addressed in this lecture as they would be presented during the QM08 conference itself. Also, we try to give a very pedagogical lecture here. For the readers who may want to study relativistic hydrodynamics and its application to H.I.C. as an advanced course, we strongly recommend them to consult the references.

This lecture note is divided into three parts. In the first part we give a brief introduction to relativistic hydrodynamics in the context of H.I.C. In the second part we present the formalism and some fundamental aspects of relativistic ideal and viscous hydrodynamics. In the third part, we start with some basic checks of the fundamental observables followed by discussion of collective flow, in particular *elliptic flow*, which is one of the most exciting phenomena in H.I.C. at relativistic energies. Next we discuss how to formulate the hydrodynamic model to describe dynamics of H.I.C. Finally, we conclude the third part of the lecture note by showing some results from ideal hydrodynamic calculations and by comparing them with the experimental data.

We use the natural units $c = \hbar = k_B = 1$ and the Minkowski metric $g^{\mu\nu} = \mathrm{diag}(1, -1, -1, -1)$ throughout the lecture note.

T. Hirano (✉)
Department of Physics, The University of Tokyo, Tokyo 113-0033, Japan,
hirano@phys.s.u-tokyo.ac.jp

N. van der Kolk
Nikhef, Kruislaan 409, 1098 SJ Amsterdam, The Netherlands,
kolk@nikhef.nl

A. Bilandzic
Nikhef, Kruislaan 409, 1098 SJ Amsterdam, The Netherlands,
anteb@nikhef.nl

Hirano, T. et al.: *Hydrodynamics and Flow*. Lect. Notes Phys. **785**, 139–178 (2010)
DOI 10.1007/978-3-642-02286-9_4

2 Introduction to Hydrodynamics in Relativistic Heavy-Ion Collisions

The excitement raised by the announcement of the discovery of the "perfect" liquid at Relativistic Heavy Ion Collider (RHIC) in Brookhaven National Laboratory (BNL) [2] is based on an agreement between predictions from *ideal* hydrodynamic models with the experimental data. While this agreement was certainly a large boost for various groups around the world doing research in hydrodynamics (and even in string theory!), there are also other reasons why the usage of hydrodynamics is strongly needed in H.I.C. Needless to say, the main goals of the physics of H.I.C. are to discover the deconfined nuclear matter under equilibrium, namely the Quark–gluon plasma (QGP), and to understand its properties such as equation of state (EoS), temperature and order of phase transition, transport coefficients, and so on. However, the system produced in H.I.C. dynamically evolves within time duration of the order of 10–100 fm/c. Hence one has to describe space–time evolution of thermodynamic variables to fill a large gap between the static aspects of QGP properties and dynamical aspects of H.I.C. It is the hydrodynamics that plays an important role in connecting them. Various stages of H.I.C. are depicted in Fig. 1. Two energetic nuclei are coming along light cone and collide with each other to create a multi-parton system. Through secondary collisions the system may reach thermal equilibrium and the QGP can be formed. This is a transient state: After further expansion and cooling the system hadronizes again. Eventually, expansion leads to a free-streaming stage through freezeout and particle spectra at this moment are seen by the detector. Hydrodynamics is applied to matter under local equilibrium in the intermediate stage. Of course, it is nontrivial a priori whether one can always apply hydrodynamics to the dynamics of H.I.C. Nevertheless it is not a bad idea to

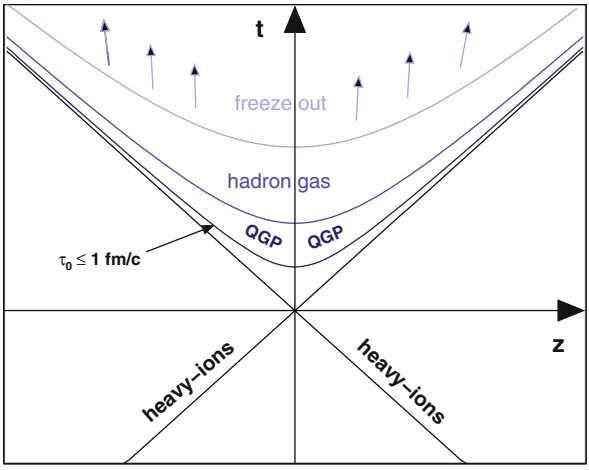

Fig. 1 A schematic view of dynamics of a heavy-ion collision along the collision axis

dare to apply it since we are eager to understand the matter under equilibrium in terms of H.I.C.

There is also another good reason to apply hydrodynamics to H.I.C. A lot of experimental data have been published so far at various collision energies. Ideally, one may want to describe these data from the first principle, i.e., quantum chromodynamics (QCD). The QCD Lagrangian density reads

$$\mathcal{L} = \bar{\psi}_i \left(i\gamma_\mu D^\mu_{ij} - m\delta_{ij} \right) \psi_j - \frac{1}{4} F_{\mu\nu\alpha} F^{\mu\nu\alpha}, \tag{1}$$

where ψ_i is a quark field, $i(= 1\text{–}3)$ is a color index for quarks, D^μ is a covariant derivative, m is a quark mass, $F^{\mu\nu}_\alpha$ is a field strength of gluons, and $\alpha(= 1, \ldots, 8)$ is a color index for gluons. However, in spite of its simple-looking Lagrangian, it is very difficult to make any predictions directly from QCD in H.I.C. due to its complexity which mainly arises from nonlinearity of interactions of gluons, strong coupling, dynamical many body system, and color confinement. One promising strategy to connect the first principle with phenomena is to introduce hydrodynamics as a phenomenological theory. We call this strategy a bottom-up approach to H.I.C. An input to this phenomenological theory comprises the equation of state,

$$P = P(e, n), \tag{2}$$

which expresses the pressure P as a function of energy density e and baryon density n. This can be obtained by exploiting lattice numerical simulations of QCD.[1] In the case of viscous hydrodynamics we need additionally the transport coefficients such as shear viscosity η, bulk viscosity ζ, heat conductivity λ.[2]

Once hydrodynamics turns out to work quite well in the description of dynamics, one can utilize its outputs such as local temperature or energy density for other observables. In the current formalism of jet quenching, one needs an information of parton density or energy density along a trajectory of an energetic parton [3, 4]. If one assumes J/ψ melts away above some temperature [5], one needs local temperature at the position of J/ψ. In the case of electromagnetic probes [6, 7], one convolutes emission rate (the number of produced particles per unit space–time volume at temperature T) of thermal photons and dileptons over the space–time volume under equilibrium. Hydrodynamics provides us with the information of the bulk matter. Therefore we can say that, in the context of H.I.C., hydrodynamics is the heart of the dynamical modeling: It not only describes expansion and collective flow of matter but also provides important information in the intermediate stage for other phenomena.

---

[1] From lattice calculations, pressure as a function of temperature rather than energy density is obtained. Note also that, due to sign problem, thermodynamic variables are available only near the region of vanishing chemical potential.

[2] In principle, the information about these quantities can be obtained also from the lattice QCD simulations although it is much harder than the EoS.

3 Formalism of the Relativistic Ideal/Viscous Hydrodynamics

The second part of the lecture note is more formal with many equations, but we try as much as possible to provide the intuitive picture behind the equations. The following references might be very helpful to complement this section [8–24].

3.1 The Basic Equations

The basic hydrodynamical equations are energy–momentum conservation

$$\partial_\mu T^{\mu\nu} = 0\,, \tag{3}$$

where $T^{\mu\nu}$ is the energy–momentum tensor and the current conservation

$$\partial_\mu N_i^\mu = 0\,, \tag{4}$$

where N_i^μ is the ith conserved current. In H.I.C., there are some conserved charges such as baryon number, strangeness, electric charges, and so on. We mainly assume the net baryon current N_B^μ as an example of N_i^μ in the following. In the first step we decompose the energy–momentum tensor and the conserved current as follows:

$$T^{\mu\nu} = eu^\mu u^\nu - P\Delta^{\mu\nu} + W^\mu u^\nu + W^\nu u^\mu + \pi^{\mu\nu}\,, \tag{5}$$

$$N_i^\mu = n_i u^\mu + V_i^\mu\,. \tag{6}$$

All the terms in the above expansion will be discussed one by one later. Now we indicate that u^μ is the time-like, normalized four-vector

$$u_\mu u^\mu = 1\,, \tag{7}$$

while the tensor $\Delta^{\mu\nu}$ is defined in the following way:

$$\Delta^{\mu\nu} = g^{\mu\nu} - u^\mu u^\nu\,, \tag{8}$$

where $g^{\mu\nu}$ is the Minkowski metric. We refer to u^μ and $\Delta^{\mu\nu}$ as the "projection" vector and tensor operators, respectively. In particular, u^μ is the local flow four-velocity, but a more precise meaning will be given later. u^μ is perpendicular to $\Delta^{\mu\nu}$, as can easily be seen from the definition of $\Delta^{\mu\nu}$ given in Eq. (8) and from the fact that u^μ is normalized,

$$u_\mu \Delta^{\mu\nu} = u_\mu (g^{\mu\nu} - u^\mu u^\nu) = u^\nu - 1 \cdot u^\nu = 0\,. \tag{9}$$

Next we define the local rest frame (LRF) as the frame in which u^μ has only the time-like component nonvanishing and in which $\Delta^{\mu\nu}$ has only the space-like components nonvanishing, i.e.,

$$u^\mu_{\rm LRF} = (1, 0, 0, 0)\,, \tag{10}$$
$$\Delta^{\mu\nu}_{\rm LRF} = {\rm diag}(0, -1, -1, -1)\,. \tag{11}$$

As is easily understood from the above equations, one can say that $u^\mu(\Delta^{\mu\nu})$ picks up the time-(space-)like component(s) when acting on some Lorentz vector/tensor.

We now discuss the physical meaning of each term in the expansion of the energy–momentum tensor (5) and the conserved current (6).

3.1.1 Decomposition of $T^{\mu\nu}$

The new quantities which appear on the RHS in the decomposition (5) are defined in the following way:

$$e = u_\mu T^{\mu\nu} u_\nu \quad \text{(energy density)}\,, \tag{12}$$
$$P = P_s + \Pi = -\frac{1}{3}\Delta_{\mu\nu} T^{\mu\nu} \quad \text{(hydrostatic + bulk pressure)}\,, \tag{13}$$
$$W^\mu = \Delta^\mu{}_\alpha T^{\alpha\beta} u_\beta \quad \text{(energy (or heat) current)}\,, \tag{14}$$
$$\pi^{\mu\nu} = \langle T^{\mu\nu} \rangle \quad \text{(shear stress tensor)}\,. \tag{15}$$

Each term corresponds to projection of the energy–momentum tensor by one or two projection operator(s), u^μ and $\Delta^{\mu\nu}$. The first two equalities imply that the energy density e can be obtained from the time-like components of the energy–momentum tensor, while the pressure P is obtained from the space-like components. Contracting the energy–momentum tensor simultaneously with u^μ and $\Delta^{\mu\nu}$ gives the energy (heat) current W^μ. Finally, the angular brackets in the definition of the shear stress tensor $\pi^{\mu\nu}$ stand for the following operation:

$$\langle A^{\mu\nu} \rangle = \left[\frac{1}{2}(\Delta^\mu{}_\alpha \Delta^\nu{}_\beta + \Delta^\mu{}_\beta \Delta^\nu{}_\alpha) - \frac{1}{3}\Delta^{\mu\nu}\Delta_{\alpha\beta} \right] A^{\alpha\beta}\,. \tag{16}$$

This means that $\langle A^{\mu\nu} \rangle$ is a symmetric and traceless tensor which is transverse to u^μ and u^ν. More concretely, one can first decompose the energy–momentum tensor by two projection tensors symmetrically

$$\tilde{\pi}^{\mu\nu} = \frac{1}{2}(\Delta^\mu{}_\alpha T^{\alpha\beta} \Delta_\beta{}^\nu + \Delta^\nu{}_\alpha T^{\alpha\beta} \Delta_\beta{}^\mu) \tag{17}$$

and then decompose it once more into the shear stress tensor (traceless) and the pressure (non-traceless)

$$\tilde{\pi}^{\mu\nu} = \pi^{\mu\nu} - P\Delta^{\mu\nu}. \tag{18}$$

3.1.2 Decomposition of N^μ

In the decomposition (6) we have introduced the following quantities:

$$n_i = u_\mu N_i^\mu \quad \text{(charge density)}\,, \tag{19}$$
$$V_i^\mu = \Delta^\mu{}_\nu N_i^\nu \quad \text{(charge current)}\,. \tag{20}$$

The physical meaning of n_i and V_i^μ is self-evident from the properties of projection operators.

QUESTION 1: *Count the number of unknowns in the above decompositions and confirm that it is* $10(T^{\mu\nu}) + 4k(N_i^\mu)$. *Here* k *is the number of independent currents.*[3]

The various terms appearing in the decompositions (5) and (6) can be grouped into two distinctive parts, which we call ideal and dissipative. In particular, for the energy–momentum tensor we have

$$T^{\mu\nu} = T_0^{\mu\nu} + \delta T^{\mu\nu}\,, \tag{21}$$
$$T_0^{\mu\nu} = eu^\mu u^\nu - P_s\Delta^{\mu\nu}\,, \tag{22}$$
$$\delta T^{\mu\nu} = -\Pi\Delta^{\mu\nu} + W^\mu u^\nu + W^\nu u^\mu + \pi^{\mu\nu}\,, \tag{23}$$

while for one charge current we have,

$$N^\mu = N_0^\mu + \delta N^\mu\,, \tag{24}$$
$$N_0^\mu = nu^\mu\,, \tag{25}$$
$$\delta N^\mu = V^\mu\,. \tag{26}$$

In the above relations $T_0^{\mu\nu}(N_0^\mu)$ denote the ideal part, while the $\delta T^{\mu\nu}(\delta N^\mu)$ denote the dissipative part of the $T^{\mu\nu}(N^\mu)$.

3.2 The Meaning of u^μ

As we have already mentioned in Sect. 3.1, u^μ is the four-velocity of "flow." Now we would like to clarify what kind of flow we have in mind in this description. In literature two definitions of flow can be found

[3] If you consider u^μ as independent variables, you need additional constraint for them since these are redundant ones. If you also consider P_s as an independent variable, you need the equation of state $P_s = P_s(e, n)$.

1. flow of energy (Landau) [10]:

$$u_L^\mu = \frac{T^\mu{}_\nu\, u_L^\nu}{\sqrt{u_L^\alpha T_\alpha{}^\beta T_{\beta\gamma} u_L^\gamma}} = \frac{1}{e} T^\mu{}_\nu\, u_L^\nu\,, \tag{27}$$

2. flow of conserved charge (Eckart) [8]:

$$u_E^\mu = \frac{N^\mu}{\sqrt{N_\nu N^\nu}} \tag{28}$$

(see Fig. 2).[4] In the first definition, u_L^μ also appears on the RHS of Eq. (27). So it should be understood as an equation with respect to u_L^μ. One may solve an eigenvalue problem for a given energy–momentum tensor $T^\mu{}_\nu \cdot u_L^\mu$ is a normalized time-like eigenvector and the corresponding positive eigenvalue is energy density e. If the dissipative currents are small enough, one can show the following relation between these two definitions of flow:

$$u_L^\mu \approx u_E^\mu + \frac{W^\mu}{e + P_s}, \quad u_E^\mu \approx u_L^\mu + \frac{V^\mu}{n}. \tag{29}$$

Equation (29) can be shown by assuming that both two definitions of flow can be connected by infinitesimal proper Lorentz transformation

$$u_E^\mu = a^\mu{}_\nu u_L^\nu \tag{30}$$

$$\approx (\delta^\mu{}_\nu + \epsilon^\mu{}_\nu) u_L^\nu, \tag{31}$$

where $\epsilon^\mu{}_\nu$ is infinitesimal anti-symmetric tensor, and by neglecting the higher orders of dissipative currents. Obviously, $W^\mu = 0$ ($V^\mu = 0$) in the Landau (Eckart) frame. In the case of vanishing dissipative currents, both definitions represent a common

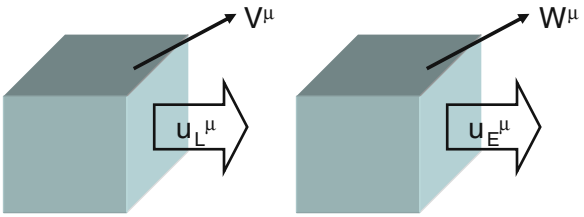

Fig. 2 A sketch of Landau and Eckart definitions of flow. Two boxes are fluid elements. There is a "leak" current W^μ or V^μ according to the definition of flow

[4] Other definitions can be made. The situation here is quite similar to the gauge fixing condition in gauge theories to eliminate the redundant variables. An essential point is to choose some "gauge" for later convenience.

flow. In other words, flow is uniquely determined in the case of ideal hydrodynamics. We should emphasize that Landau definition is more relevant in the context of H.I.C. at ultrarelativistic energies since we expect that a small baryon number is deposited near the midrapidity region.

3.3 Entropy

We start this subsection by briefly discussing the entropy conservation in "ideal hydrodynamics." By "ideal hydrodynamics" we mean the case when entropy is not produced during the evolution.[5] Neglecting the dissipative parts, the energy–momentum conservation (3) and the current conservation (4) reduce to

$$\partial_\mu T_0^{\mu\nu} = 0\,, \tag{32}$$

$$\partial_\mu N_0^{\mu} = 0\,, \tag{33}$$

where $T_0^{\mu\nu}$ and N_0^{μ} are the ideal parts introduced in Eqs. (22) and (25). Equations (32) and (33) are the basic equations of "ideal hydrodynamics."

By contracting Eq. (32) with u_ν it follows

$$\begin{aligned} 0 &= u_\nu \partial_\mu T_0^{\mu\nu} \\ &= \dots \\ &= T(u^\mu \partial_\mu s + s\partial_\mu u^\mu) + \mu(u^\mu \partial_\mu n + n\partial_\mu u^\mu)\,. \end{aligned} \tag{34}$$

We have introduced here the temperature T, entropy density s, and chemical potential μ through the first law of thermodynamics $de = Tds + \mu dn$. Here it is assumed that thermalization is maintained locally. The second term on the RHS in Eq. (34) vanishes due to Eq. (33). If we now introduce the entropy current as

$$S^\mu = su^\mu\,, \tag{35}$$

it follows from Eq. (34) that

$$\partial_\mu S^\mu = \partial_\mu(su^\mu) = u^\mu \partial_\mu s + s\partial_\mu u^\mu = 0\,. \tag{36}$$

Hence the entropy is conserved in ideal hydrodynamics.

QUESTION 2: *Go through all steps in the above derivations.*

Now we go back to viscous hydrodynamics. Hereafter we consider only the Landau frame and omit the subscript L. For simplicity, we further assume that there is no charge in the system although in the realistic case a small amount of charge might

[5] Note that, if discontinuities exist in the solution, entropy is produced even in ideal hydrodynamics.

exist in the system. What we are constructing here is the so-called first-order theory of viscous hydrodynamics. The main assumption is that the nonequilibrium entropy current vector S^μ has linear dissipative term(s) constructed from V^μ, Π, and $\pi^{\mu\nu}$ and can be written as

$$S^\mu = su^\mu + \alpha V^\mu \,. \tag{37}$$

The first term on the RHS is the ideal part and the second term is the correction due to the dissipative part. It is impossible to construct a term which would form a Lorentz vector from $\pi^{\mu\nu}$ on the RHS in the above equation because $\pi^{\mu\nu}$ is perpendicular to u^μ by definition.[6] Since we have also assumed that there is no charge in the system, i.e., $N^\mu = 0$, it follows that αV^μ vanishes.

We now calculate the product of the temperature T and the divergence of the entropy current (37). It follows

$$\begin{aligned} T\partial_\mu S^\mu &= T(u^\mu \partial_\mu s + s\partial_\mu u^\mu) \\ &= u_\nu \partial_\mu T_0^{\mu\nu} \\ &= -u_\nu \partial_\mu \delta T^{\mu\nu} \\ &= \dots \\ &= \pi_{\mu\nu} \langle \nabla^\mu u^\nu \rangle - \Pi \partial_\mu u^\mu \,, \end{aligned} \tag{38}$$

where $\nabla^\mu = \Delta^{\mu\nu}\partial_\nu$. In transferring from the second to third line in the above calculation we have used the energy–momentum conservation, $\partial_\mu T^{\mu\nu} = 0$. It is very important to note that due to the assumption that there is no charge in the system we could neglect the dissipative part of entropy current (37), but the dissipative part of energy–momentum tensor (23) does not vanish. The nonvanishing dissipative part of energy–momentum tensor gives a contribution which yields a difference between the equations characterizing the first-order theory of viscous hydrodynamics and the equations of ideal hydrodynamics derived before.

QUESTION 3: *Check the above calculation.*

In order to solve the hydrodynamic equations we must first define the dissipative current. We introduce the following two phenomenological definitions, so-called *constitutive equations*, for the shear stress tensor $\pi^{\mu\nu}$ and the bulk pressure Π:

$$\pi^{\mu\nu} = 2\eta \langle \nabla^\mu u^\nu \rangle \,, \tag{39}$$

$$\Pi = -\zeta \partial_\mu u^\mu = -\zeta \nabla_\mu u^\mu \,. \tag{40}$$

[6] Also remember $W^\mu = 0$ in the Landau definition. One may think that Πu^μ is a possible candidate in the entropy current S^μ. However, the second law of thermodynamics is not ensured in this case. See also discussion in [21].

In Table 1 we outline the new variables and terminology used in the above equations. Notice that, within our approximation $N^\mu = 0$, there is no vector component of thermodynamic force.

Table 1 New variables and terminology

Thermodynamic force	Transport coefficient	Current
$X^{\mu\nu} = \langle \nabla^\mu u^\nu \rangle$	η	$\pi_{\mu\nu}$
tensor	shear viscosity	
$X = -\partial_\mu u^\mu$	ζ	Π
scalar	bulk viscosity	

After inserting the definitions (39) and (40) in the last line of (38), we arrive at, for positive transport coefficients,

$$\begin{aligned} T\,\partial_\mu S^\mu &= \frac{\pi_{\mu\nu}\pi^{\mu\nu}}{2\eta} + \frac{\Pi^2}{\zeta} \\ &= 2\eta\,\langle \nabla^\mu u^\nu \rangle^2 + \zeta\left(-\partial_\mu u^\mu\right)^2 \geq 0\,. \end{aligned} \tag{41}$$

This ensures the second law of thermodynamics

$$\partial_\mu S^\mu \geq 0\,. \tag{42}$$

In the case of viscous hydrodynamics, entropy is not decreasing.

3.4 The Equations of Motion

In order to derive the equations of motion, we use again energy–momentum conservation (3). After contracting Eq. (3) with u_ν we have

$$u_\nu \partial_\mu T^{\mu\nu} = 0\,, \tag{43}$$

from which one can obtain the first equation of motion,

$$\dot{e} = -(e + P_s + \Pi)\theta + \pi_{\mu\nu}\,\langle \nabla^\mu u^\nu \rangle\ . \tag{44}$$

On the other hand, after contracting Eq. (3) with $\Delta_{\mu\alpha}$ it follows

$$\Delta_{\mu\alpha}\partial_\beta T^{\alpha\beta} = 0\,, \tag{45}$$

from which one can obtain the second equation of motion,

$$(e + P_s + \Pi)\dot{u}^\mu = \nabla^\mu(P_s + \Pi) - \Delta^{\mu\alpha}\nabla^\beta \pi_{\alpha\beta} + \pi^{\mu\alpha}\dot{u}_\alpha\,. \tag{46}$$

This is exactly the relativistic extension of the Navier–Stokes equation. In writing the above equations we have introduced

$$\theta = \partial_\mu u^\mu \qquad \text{expansion scalar (divergence of flow)}, \tag{47}$$

$$\text{“dot”} = D = u_\mu \partial^\mu \qquad \text{substantial time derivative}\,. \tag{48}$$

QUESTION 4: *Starting from the energy–momentum conservation* (3) *derive Eqs.* (44) *and* (46).

To get some intuitive interpretation of the first equation of motion, we insert expressions (39) and (40) for the shear stress tensor and bulk pressure into Eq. (44):

$$\begin{aligned}\dot{e} &= -e\theta - P_s\theta + \frac{\Pi^2}{\zeta} + \frac{\pi_{\mu\nu}\pi^{\mu\nu}}{2\eta} \\ &= -e\theta - P_s\theta + \zeta(-\theta)^2 + 2\eta\,\langle\nabla^\mu u^\nu\rangle^2\,.\end{aligned} \tag{49}$$

The above equation determines the time evolution of energy density e in the comoving system. The first term on the RHS describes dilution/compression of energy density due to the change of volume because θ can be expressed in terms of volume of a fluid element V as

$$\theta \approx \frac{\dot{V}}{V}\,. \tag{50}$$

In ideal hydrodynamics, this relation holds exactly. If the system expands ($\theta > 0$), the energy density is diluted. So the effect of expansion appears as negative source term $-e\theta$ in Eq. (49). If we move along with a fluid element, the internal energy in the fluid element is not conserved due to the work done by pressure, which is described by the second term on the RHS in (49). Finally, the last two positive definite terms in (49) represent the production of entropy which heats up the system.

Now we comment on the second equation of motion (46). But before doing that, we recall the nonrelativistic Navier–Stokes equation,

$$D\boldsymbol{v} = -\frac{1}{\rho}\boldsymbol{\nabla} P_s + \frac{\eta}{\rho}\boldsymbol{\nabla}^2\boldsymbol{v}\,. \tag{51}$$

Here ρ is the mass density, η is shear viscosity, and $D = \frac{\partial}{\partial t} + \boldsymbol{v}\cdot\boldsymbol{\nabla}$ is the nonrelativistic version of substantial time derivative. The above version of the nonrelativistic Navier–Stokes equation applies to the case of incompressible fluids such that $\boldsymbol{\nabla}\cdot\boldsymbol{v} = 0$ is valid. On the LHS we have the time derivative of velocity, which is nothing but acceleration. The first term on the RHS is the source of the flow and it is solely due to the pressure gradient $\boldsymbol{\nabla} P_s$, while the second term represents the diffusion of the flow. The final flow velocity comes from the interplay between these two terms: The first term generates the flow while the second term dilutes it. The ratio η/ρ is called kinetic viscosity and plays a role of diffusion constant

in the Navier–Stokes equation (51). The diffusion term in Eq. (51) requires more detailed treatment. For an illustrative purpose, consider first the heat equation in (N+1)-dimensional space–time

$$\frac{\partial T(t,\{x_i\})}{\partial t} = \kappa \sum_i^N \frac{\partial^2}{\partial x_i^2} T(t,\{x_i\}), \tag{52}$$

where T is temperature and constant κ is heat conductivity in some unit. One can discretize the heat equation (52) in $(2+1)$-dimensional space–time as follows:

$$\begin{aligned} T_{i,j}^{n+1} &= T_{i,j}^n + \frac{4\kappa\Delta t}{(\Delta x)^2}\left[\frac{T_{i-1,j}^n + T_{i,j-1}^n + T_{i+1,j}^n + T_{i,j+1}^n}{4} - T_{i,j}^n\right] \\ &= T_{i,j}^n + \frac{4\kappa\Delta t}{(\Delta x)^2}\left(\bar{T}_{i,j}^n - T_{i,j}^n\right), \end{aligned} \tag{53}$$

where i and j are indices of the site and n is the time step. The first term in the brackets in Eq. (53), $\bar{T}_{i,j}$, indicates an average of temperature around the cell under consideration. If temperature at (i, j) is smaller (larger) than the averaged one $\bar{T}_{i,j} > T_{i,j}$ ($\bar{T}_{i,j} < T_{i,j}$), the second term in Eq. (53) becomes positive (negative) and, consequently, temperature increases (decreases) in the next time step. Repeating this procedure, temperature becomes flat even if starting from a bumpy initial condition. Thus, generally speaking, the second derivative with respect to coordinates describes averaging/smoothening/diffusion of given distributions and a coefficient in front of it describes how quick the distribution diffuses. Now going back to the Navier–Stokes equation (51), it is obvious from the above discussion that the second term describes diffusion of flow and that kinetic viscosity η/ρ plays a role of a diffusion constant. The relativistic version of the Navier–Stokes equation (46) has a similar form to Eq. (51) if one plugs in constitutive equations (39) and (40) and assumes the fluid is incompressible, $\theta = 0$.

3.4.1 Bjorken's Equation in the First-Order Theory

Now we rewrite again the first equation of motion by making use of Bjorken's ansatz [16]

$$u_{\rm Bj}^\mu = \frac{\tilde{x}^\mu}{\tau} = \frac{t}{\tau}\left(1, 0, 0, \frac{z}{t}\right), \tag{54}$$

where $\tau = \sqrt{t^2 - z^2}$ is the proper time. This is a boost-invariant Bjorken's solution which is also called one-dimensional Hubble flow since velocity in the z-direction, v_z, is proportional to z, which is an analogy to three-dimensional Hubble flow of the universe. After inserting this solution into the constitutive equations (39) and (40)

$$\pi^{\mu\nu} = \frac{2\eta}{\tau}\left(\tilde{\Delta}^{\mu\nu} - \frac{1}{3}\Delta^{\mu\nu}\right), \tag{55}$$

$$\tilde{\Delta}^{\mu\nu} = \tilde{g}^{\mu\nu} - u^{\mu}_{\mathrm{Bj}} u^{\nu}_{\mathrm{Bj}}, \quad \tilde{g}^{\mu\nu} = \mathrm{diag}(1, 0, 0, -1), \tag{56}$$

$$\Pi = -\frac{\zeta}{\tau}, \tag{57}$$

we arrive at the following equation of motion:

$$\frac{de}{d\tau} = -\frac{e + P_s}{\tau}\left(1 - \frac{4}{3\tau T}\frac{\eta}{s} - \frac{1}{\tau T}\frac{\zeta}{s}\right). \tag{58}$$

This equation determines the time evolution of energy density in the first-order theory in one-dimensional expansion.

QUESTION 5: *Derive Eq.* (58).

On the RHS of (58) we have three terms in the bracket. If we neglect the last two terms this equation reduces to the famous Bjorken equation [16] which states that in ideal hydrodynamics the energy density evolution is determined by the sum of energy density e and the hydrostatic pressure P_s, divided by the proper time τ. The last two terms on the RHS in (58) represent the viscous correction to ideal hydrodynamics. The first one is the viscous correction originating from the shear viscosity in compressible fluids while the second one comes from the bulk viscosity. We remark that both terms are proportional to $1/\tau$ which is due to the fact that the expansion scalar θ in the Bjorken scaling solution can be written as

$$\theta = \frac{1}{\tau}. \tag{59}$$

Two transport coefficients in the viscous correction, η/s and ζ/s, turn out to be very important. They are the dimensionless quantities in natural units and reflect the intrinsic properties of the fluids.[7]

Recently progress has been made in obtaining the values of the transport coefficients from microscopic theories. Here we summarize the most important results and conclusions as follows:

- $\eta/s = 1/4\pi$ and $\zeta/s = 0$ are obtained from $\mathcal{N} = 4$ SUSY Yang–Mills theory [25]. The latter one is automatically obtained from the conformal nature of the theory;
- $\eta/s = \mathcal{O}(0.1 - 1)$ for gluonic matter is obtained from the lattice calculations of pure SU(3) gauge theory [26];

[7] We stress that in the context of H.I.C. the statement which is often used, "viscosity is small," is not precise. From the equations we have derived, we see that the correct statement should be "viscous coefficients are small in comparison with entropy density."

- bulk viscosity has a prominent peak around T_c resulting from trace anomaly of QCD [27, 28] (see also a phenomenological approach in [29]).

3.5 The Second-Order Theory and Its Application to Bjorken's Equation

There is an important issue in the first-order theory which is the violation of causality. We can trace back the origin of the violation of causality to our phenomenological definitions (39) and (40) for the shear stress tensor and the bulk pressure, respectively, and to the fact that the Navier–Stokes equation is a parabolic equation, namely the time derivative is of first order while the space derivative is of second order. The same arguments hold also for the violation of causality in relativistic hydrodynamics: It is known that, under linear perturbations on the moving background equilibrium state, the solutions are unstable and acausal [30] (for a more detailed discussion, see also a recent study in [31]). For an illustrative purpose, we continue this discussion by analyzing the heat equation as an example of the parabolic equation in three-dimensional space,[8]

$$\frac{\partial T}{\partial t} = \kappa \sum_i^3 \frac{\partial^2}{\partial x_i^2} T \,. \tag{60}$$

The heat equation can be easily derived by combining the balance equation,

$$\frac{\partial T}{\partial t} = -\frac{\partial q^i}{\partial x^i} \,, \tag{61}$$

together with the constitutive equation,

$$q^i = -\kappa \frac{\partial T}{\partial x_i} \qquad \text{Fourier's law.} \tag{62}$$

In the above equations T is the temperature, q^i is the heat current, and κ is the heat conductivity. The above constitutive equation is purely phenomenological. Although here we are considering the nonrelativistic equations, the general arguments and conclusions we write down are valid in the relativistic case as well. The heat equation (60) violates causality. It can be easily confirmed that Green's function of the heat equation (60), sometimes called heat kernel, is Gaussian

$$G(x^i, t; x_0^i, t_0) = \frac{1}{[4\pi\kappa(t-t_0)]^{\frac{3}{2}}} \exp\left[-\frac{(x^i - x_0^i)^2}{4\kappa(t-t_0)}\right] \tag{63}$$

[8] Again, we choose some units to simplify the following equations:

and the "long tail" of this Gauss function causes the violation of causality in the heat equation. This issue was heuristically resolved by Cattaneo in 1948 [9] after an additional term on the LHS of the constitutive equation (62) was introduced "by hand,"

$$\tau_r \frac{\partial q^i}{\partial t} + q^i = -\kappa \frac{\partial T}{\partial x_i} \,. \tag{64}$$

In the modified constitutive equation we have a new constant τ_r which is often called the "relaxation time." Correspondingly, the heat equation (60) is also modified,

$$\tau_r \frac{\partial^2 T}{\partial t^2} + \frac{\partial T}{\partial t} = \kappa \frac{\partial^2 T}{\partial x_i^2} \,, \qquad c_s = \sqrt{\kappa/\tau_r} \,. \tag{65}$$

In the literature the above equation is known as a telegraph equation. While the original heat equation can be classified as a parabolic equation, the telegraph equation belongs to the family of hyperbolic equations. Causality is not violated in Eq. (65) simply because we can now, by choosing the relaxation time τ_r to be large, reduce the signal velocity c_s to values smaller than the speed of light c.

In relativistic hydrodynamics the relaxation terms introduced above can be obtained by modifying the entropy current in the following way:

$$S^\mu = s u^\mu + \mathcal{O}(\delta T^{\mu\nu}) + \mathcal{O}\left((\delta T^{\mu\nu})^2\right) \,. \tag{66}$$

By including the quadratic dissipative terms we are starting to work within the framework of second-order theory. The nonequilibrium entropy current vector S^μ in the second-order theory has linear + quadratic dissipative term(s) constructed from $(V^\mu, \Pi, \pi^{\mu\nu})$. Again, we demand the second law of thermodynamics, $\partial_\mu S^\mu > 0$. Thus, quadratic dissipative terms modify the constitutive equations which now read as

$$\tau_\pi \Delta^{\mu\alpha} \Delta^{\nu\beta} \dot{\pi}_{\alpha\beta} + \pi^{\mu\nu} = 2\eta \langle \nabla^\mu u^\nu \rangle + \cdots \,, \tag{67}$$

$$\tau_\Pi \dot{\Pi} + \Pi = -\zeta \partial_\mu u^\mu + \cdots \,. \tag{68}$$

When compared to the constitutive equations of the first-order theory, (39) and (40), we see that in the second-order theory in each constitutive equation a relaxation term appears. Relaxation terms include τ_π and τ_Π, which are the relaxation times. It is important to note that in the second-order theory the constitutive equations are no longer algebraic equations. As a consequence, dissipative currents become dynamical quantities like thermodynamic variables. The constitutive equations with relaxation terms have been employed in recent viscous fluid simulations [32–45].[9]

[9] Some of the references here do not employ the same equations as mentioned here. There are still some hot debates how to formulate the correct *relativistic* equation of viscous fluids or which terms in the constitutive equations of the second-order theory should be kept in the simulations.

Finally, we outline Bjorken's equation in the second-order theory,

$$\frac{de}{d\tau} = -\frac{e+P_s}{\tau}\left(1 - \frac{\pi}{sT} + \frac{\Pi}{sT}\right), \tag{69}$$

$$\tau_\pi \frac{d\pi}{d\tau} + \pi = \frac{4\eta}{3\tau} - \frac{\pi\tau_\pi}{2\tau} - \frac{\pi\eta T}{2}\frac{d}{d\tau}\frac{\tau_\pi}{\eta T}, \tag{70}$$

$$\tau_\Pi \frac{d\Pi}{d\tau} + \Pi = -\frac{\zeta}{\tau} - \frac{\Pi\tau_\Pi}{\tau} - \frac{\Pi\zeta T}{2}\frac{d}{d\tau}\frac{\tau_\Pi}{\zeta T}, \tag{71}$$

where

$$\pi = \pi^{00} - \pi^{zz}. \tag{72}$$

It is easy to show that the above formulas reduce to the ones in the first-order theory if one takes $\tau_\pi \to 0$ and $\tau_\Pi \to 0$. We remark here that, contrary to the first-order theory, one needs to specify initial conditions for dissipative currents in the second-order theory.

3.6 Summary

Let us summarize the main points so far as follows:

- hydrodynamics is a framework to describe the space–time evolution of matter under local thermal equilibrium;
- a naïve extension of the Navier–Stokes equation to its relativistic version, which is called the first-order theory, has problems on instabilities and causality;
- relaxation terms are needed in the constitutive equations to resolve the above issues;
- these terms naturally arise in the constitutive equations when the second-order corrections of dissipative currents are considered in the entropy current.

4 Applications

In this section we apply the formalism of hydrodynamics to heavy-ion collisions. As already noted in Sect. 1, we do not argue recent analyses in terms of viscous hydrodynamics. We show only results from ideal hydrodynamic models. One can also consult recent other reviews of hydrodynamic models at RHIC which complement the present lecture note [46–53]. We start by discussing some basic tests of whether the system produced in H.I.C. can be described by thermodynamic quantities. Then we discuss collective flow and introduce ideal hydrodynamic models to describe the flow phenomena in H.I.C. Finally we show results from ideal hydrodynamic models and compare them with experimental data.

4.1 Basic Checks of Observables at RHIC

Recent lattice QCD results show [54] that the energy density as a function of the temperature suddenly increases by ~ 1 GeV/fm^3 at the (pseudo-)critical temperature $T_c \sim 190$ MeV.[10] Above this temperature, the system is supposed to be in the deconfined QGP. The first check is whether the energy density produced in H.I.C. is sufficient to form a QGP. Phenomenologically, the energy density in H.I.C. can be estimated through Bjorken's formula [16][11]

$$\epsilon_{\mathrm{Bj}}(\tau) = \frac{\langle m_T \rangle}{\tau \pi R^2} \frac{dN}{dy} \,. \tag{73}$$

Here $\langle m_T \rangle$ is the mean transverse mass, $y = \frac{1}{2} \ln \frac{E+p_z}{E-p_z}$ is the rapidity, $\frac{dN}{dy}$ is the number of particles per unit rapidity, $\tau = \sqrt{t^2 - z^2}$ is the proper time, and R is an effective transverse radius. The energy density obtained above depends on the proper time since the system is supposed to expand in the longitudinal direction with the expansion scalar $\theta = 1/\tau$. One can compare Bjorken's energy density to the energy density from lattice QCD simulations to see whether it is sufficient energy density to form a QGP. Figure 3 shows the PHENIX data on $\varepsilon_{\mathrm{Bj}}\tau$ versus the number of participants at three collision energies [57, 58]. If τ is taken to be 1 fm/c, Bjorken's energy densities at $\sqrt{s_{NN}} = 130$ and 200 GeV are well above the energy density at the transition region $\sim 1\,\mathrm{GeV/fm}^3$. Therefore, sufficient energy is deposited in the central rapidity region in H.I.C. at RHIC. However, attention

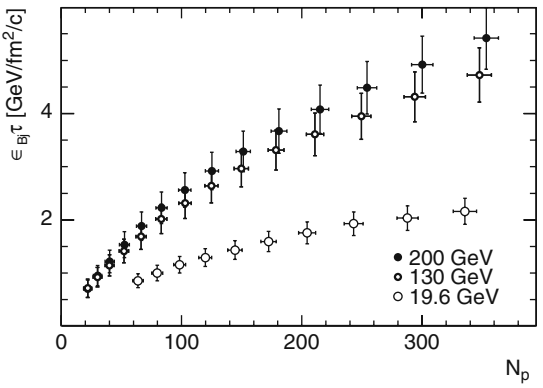

Fig. 3 $\varepsilon_{\mathrm{Bj}}\tau$ versus the number of participants at three collision energies [57, 58]

[10] Energy density increases with temperature rapidly but smoothly. So this is not a phase transition but a crossover in a thermodynamically strict sense. This is the reason why we call it pseudo-critical temperature here.

[11] This formula neglects the effect of pdV work. If the system is kinetically equilibrated, the energy density should be larger than the value obtained by this formula [55, 56].

should be paid to the interpretation. The above formula just counts the total measured energy divided by the volume of a cylinder. So the system is not necessarily thermalized. In this sense, this is a necessary condition, not a sufficient condition, to form a QGP.

The next basic check is whether the matter in H.I.C. reaches chemical equilibrium. Assuming thermal and chemical equilibria, we can calculate the number density of a certain particle species

$$n_i(T,\mu) = \frac{g}{2\pi^2}\int_0^\infty \frac{p^2 dp}{\exp\left[(E_i-\mu_i)/T\right]\pm 1}\,. \tag{74}$$

n_i gives the number density of particle species i as a function of the temperature T and chemical potential μ_i. g is the degeneracy of the particle, p is the momentum, and E is the energy. We further assume that the measured particle number is fixed at a certain temperature and chemical potential, which is called chemical freezeout. Then the average number of particles, $\langle N_i\rangle$, can be estimated by summing contribution from particles directly emitted from the system with volume V and contribution from resonance decays

$$\langle N_i\rangle = V\left[n_i^{\rm th}(T,\mu) + \sum_R \Gamma_{R\to i} n_R(T,\mu)\right]. \tag{75}$$

Here $n_i^{\rm th}$ and n_R are the number density of directly emitted particle i and resonance R, respectively. $\Gamma_{R\to i}$ is the branching ratio of the resonance R decaying into species i. When one looks at ratios of two particle numbers, the volume V is canceled out. Thus the particle ratios depend only on two parameters: the temperature T and the baryonic chemical potential μ_B. In Fig. 4, various combinations of the particle ratio observed at RHIC are fitted by two parameters [59]. We find a remarkably good fit

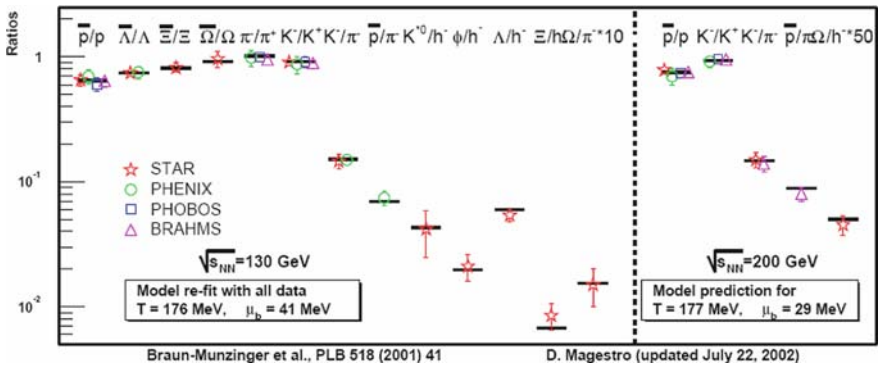

Fig. 4 Ratios of particle numbers produced at RHIC [59]

to data with only these two parameters.[12] At $\sqrt{s_{NN}} = 130$ GeV, the temperature is fitted to be 176 MeV which is close to the critical temperature from lattice QCD calculations. At the temperature, which we call chemical freezeout temperature T^{ch}, the system ceases to be in chemical equilibrium. So we expect that the system reaches chemical equilibrium above T^{ch}. Again, one has to keep in mind that this is a necessary condition since even in e^+e^- or pp collisions observed particle ratios are fitted reasonably well by using statistical models [60, 61]. See also discussions in, e.g., [62, 63]. The last basic check is whether the matter reaches kinetic equilibrium. If we suppose a system in H.I.C. is in kinetic equilibrium, the pressure is built inside the system. The matter is surrounded by vacuum, so pressure gradient in outward directions generates collective flow and, in turn, the system expands radially. The momentum distribution in kinetically equilibrated matter is isotropic. On the other hand, when the matter is moving at a finite velocity the momentum distribution is Lorentz boosted. This is illustrated in Fig. 5. If this kind of distortion in momentum distribution can be observed experimentally, one can obtain some information about kinetic equilibrium. Assuming each fluid element expands radially at radial flow velocity v_T, the p_T spectra for pions and protons can be calculated by convoluting these distorted momentum distributions over azimuthal direction (blast wave model [64, 65]). Here p_T is the transverse momentum which is perpendicular to the collision axis. The green curves are results with $T = 100$ MeV and radial flow velocity $v_T = 0.5$. On the other hand, the red curves are results with $T = 160$ MeV and vanishing flow $v_T = 0$. For light particles like pions, there is almost no sensitivity to

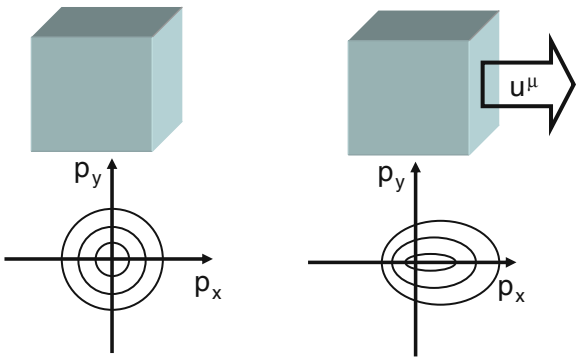

(a) Isotropic case (b) Lorentz boosted in positive x direction

Fig. 5 Fluid elements at rest and at a finite velocity in x-direction. Momentum distribution in the latter case is distorted by Lorentz boost along x-axis

[12] There are some additional parameters in the recent statistical models such as excluded volume correction, strangeness suppression factor, and so on for a better description of the data.

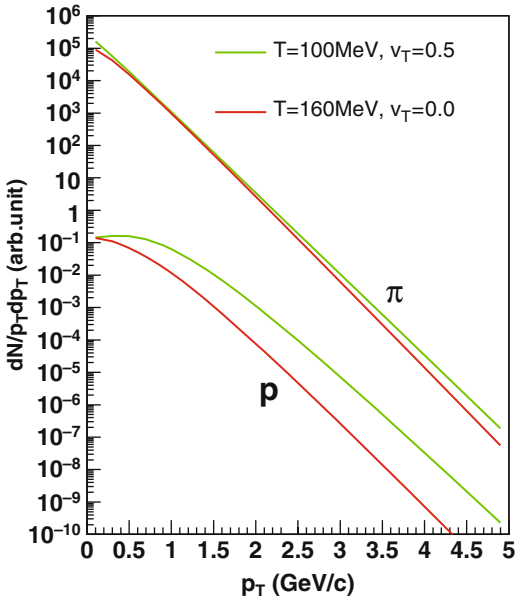

Fig. 6 p_T spectra for pions and protons from a thermal plus boost picture. See text for details

distinguish the two cases: Reduction of temperature is almost compensated by radial flow. However, in the case of heavier particles like protons, a clear difference can be seen between these two cases: There is a shoulder structure at low p_T resulting from radial flow. This kind of spectral change is observed in H.I.C., as can be seen in Fig. 7. It shows the proton p_T spectra for p+p (black), d+Au (pink), and Au+Au (red) collisions obtained by STAR Collaboration [66]. For p+p and d+Au collisions the spectra have just a power law shape. However, in Au+Au collisions, one sees a shoulder structure at low p_T (< 1 GeV/c). This is consistent with a thermal plus boost picture and suggests that a large pressure could be built up in Au+Au collisions. One can fit the p_T spectrum using a blast wave parametrization [64, 65] and obtains decoupling temperature T^{dec} and the mean collective flow velocity as a function of the centrality. Even for pp collisions these parameters are finite (see Fig. 8) [67], which indicates that a more sophisticated model would be needed to interpret the data. This kind of spectral change can also be seen in results from kinetic theories in which kinetic equilibrium is not fully achieved. Therefore it is indispensable to perform a systematic study based on a more sophisticated dynamical framework.

We have obtained the necessary conditions for studying the QGP: (1) The energy density can be well above the critical value which is predicted from lattice QCD simulations; (2) A chemical freezeout temperature extracted from particle ratios is close to pseudo-critical temperature which is again from lattice QCD simulations; (3) High pressure can be built up in H.I.C., which suggests the system reaches

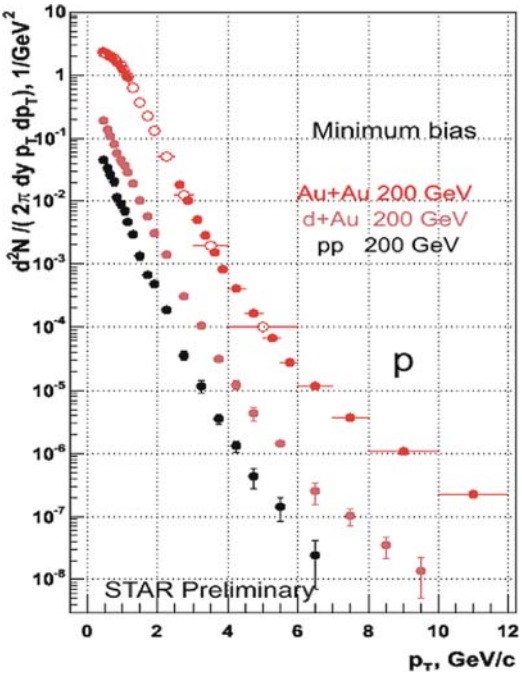

Fig. 7 Proton spectrum for pp (*black*), dAu (*pink*), and Au+Au (*red*) collisions. Adopted from a presentation file by O. Barannikova at Quark Matter 2005, Budapest, Hungary [66]

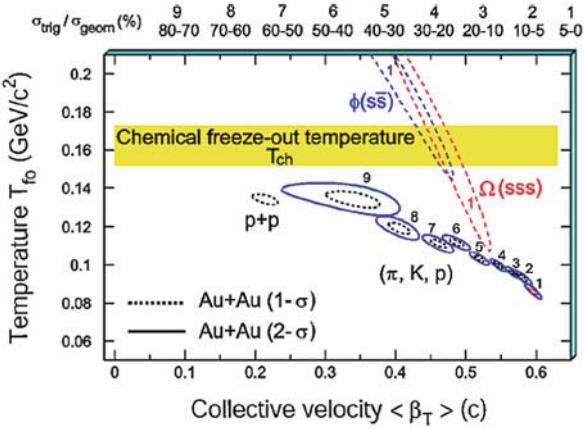

Fig. 8 Fitted parameters in blast wave model calculations [67]

kinetic equilibrium. If one of them was not confirmed through these basic checks, one would not need to go to the next steps toward detailed studies of the QGP in H.I.C.

4.2 Elliptic Flow

Before going to a detailed discussion on the hydrodynamic models, we discuss collective flow, in particular, anisotropic transverse flow. Here "collective flow" is meant by the correlation between position of matter and direction of flow, which is not necessary to be hydrodynamically evolving matter. A good example has already appeared in the previous subsection. In the case of radial flow, velocity of expanding matter has a component parallel to the radial coordinate. Figure 9 shows a heavy-ion collision in the reaction plane (left) and transverse plane (right). In such a collision a region of the locally equilibrated state can be created. In the transverse plane the overlap region has an almond-like shape, so the region is anisotropic with respect to the azimuthal angle. The azimuthal momentum distribution can be expanded into a Fourier series[13]

$$\frac{dN}{d\phi} = \frac{N}{2\pi}\left[1 + 2v_1\cos(\phi) + 2v_2\cos(2\phi) + \cdots\right], \tag{76}$$

$$v_n = \frac{\int d\phi \cos(n\phi)\frac{dN}{d\phi}}{\int d\phi \frac{dN}{d\phi}} = \langle\cos(n\phi)\rangle, \tag{77}$$

where ϕ is the azimuthal angle of momentum and v_n are the Fourier coefficients of nth harmonics [68]. Because of the symmetry around the y-axis the sine terms vanish. The first and second harmonics, v_1 and v_2, are called directed and elliptic flow parameters, respectively. The first harmonic, v_1, is illustrated in Fig. 10a. Particles are emitted preferably, e.g., in the direction of the large arrows in the reaction plane.

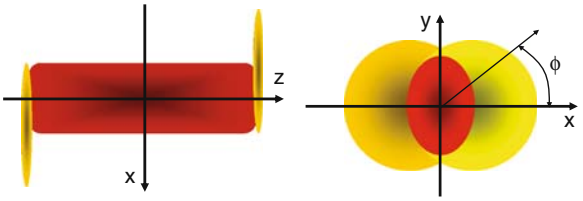

(a) In the reaction plane (b) In the transverse plane

Fig. 9 Illustration of a H.I.C.

[13] Here we suppose azimuthal angle is measured from reaction plane. Of course, in the experimental situations, the reaction plane is not known a priori. We will not go into details of how to find reaction plane experimentally.

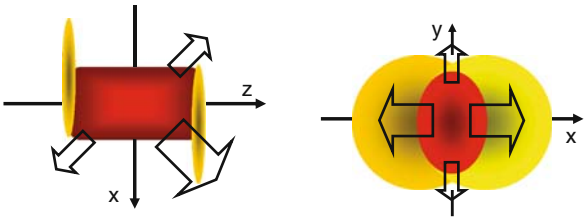

(a) First harmonic v_1 (b) Second harmonic v_2

Fig. 10 Anisotropic transverse flow

Directed flow is significantly seen near the beam rapidity region but vanishes near midrapidity due to symmetry of the collision geometry. The second harmonic, v_2, is much more relevant for studying matter around midrapidity in H.I.C. at relativistic energies since spectators already fly away [69], therefore a lot of efforts to measure v_2 have been made at RHIC so far. One of the first observables was actually v_2 measured by STAR Collaboration [70]. It is illustrated in Fig. 10b.

Elliptic flow is how the system responds to the initial spatial anisotropy [69, 71–73]. Suppose two extreme situations illustrated in Fig. 11. In the first case (see Fig. 11a) the mean free path among the produced particles is much larger than the typical size of the system. In this case the azimuthal distribution of particles does not depend on azimuthal angle on average due to the symmetry of the production process. The other extreme case is when the mean free path is very small compared to the typical system size (see Fig. 11b). In this case hydrodynamics can be applied to describe the space–time evolution of the system. The pressure gradient along the horizontal axis is much larger than that along the vertical axis due to the geometry.

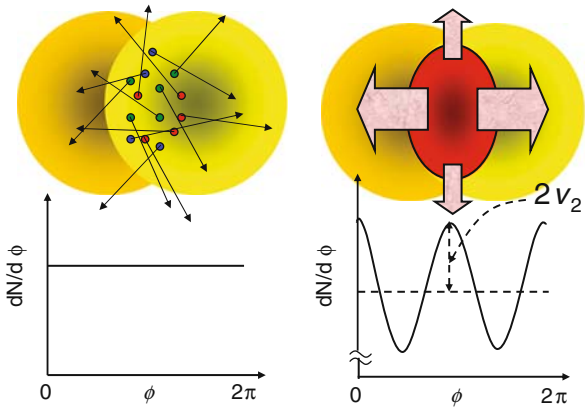

(a) Large mean free path (b) Small mean free path

Fig. 11 Normalized azimuthal distribution $dN/d\phi$ of a noncentral H.I.C.

So the collective flow is enhanced along the horizontal axis rather than along the vertical axis and, in turn, the azimuthal distribution gets oscillated. The amplitude of this oscillation in the normalized azimuthal distribution describes exactly the elliptic flow parameter. In this way, the elliptic flow is generated by the spatial anisotropy of the almond shape due to multiple interactions among the produced particles. We have good opportunities to extract some information about the mean free path from the elliptic flow analysis.

The eccentricity is a very important quantity to interpret elliptic flow phenomena. To quantify the initial almond shape, the following formula can be used:

$$\varepsilon = \frac{\langle y^2 - x^2 \rangle}{\langle y^2 + x^2 \rangle} . \tag{78}$$

The brackets denote an average over the transverse plane with the number density of participants as a weighting function

$$\langle \cdots \rangle = \int dx dy \cdots n_{\text{part}}(x, y) . \tag{79}$$

This is sometimes called the standard eccentricity. If the system is elongated along the y-axis, the eccentricity is positive. In more realistic situations, the eccentricity fluctuates from event to event. This fluctuation of the initial eccentricity [74–79] is important to understand the elliptic flow in the small system such as Cu+Cu collisions or peripheral Au+Au collisions. Figure 12 shows a sample event projected into the transverse plane from a Monte Carlo Glauber model. Participants are shown in magenta and spectators are in yellow and orange. In this case one could misidentify the tilted line as the reaction plane, while the true reaction plane is the horizontal axis (dashed line). The angle of the tilted plane with respect to the true reaction plane fluctuates event by event. Of course we cannot observe the true reaction plane from experimental data. On the other hand, an apparent reaction

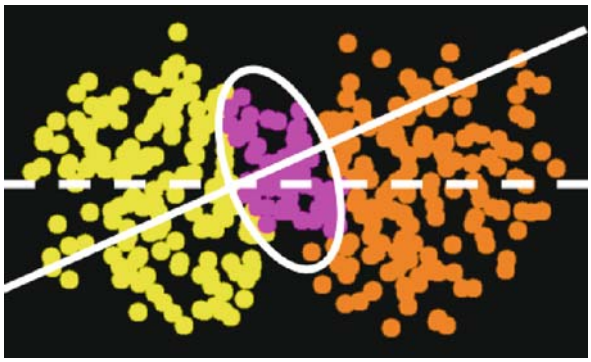

Fig. 12 An example of participants (*magenta*) and spectators (*yellow* and *orange*) in a H.I.C. from a Monte Carlo Glauber model. Adopted from a presentation file by D. Hofman at Quark Matter 2006, Shanghai, China

plane (tilted line in Fig. 12) is determined also by elliptic flow signal itself. Another definition, called the participant eccentricity, is much more relevant for quantifying the almond shape in the event-by-event basis

$$\varepsilon_{\rm part} = \frac{\sqrt{(\sigma_y^2 - \sigma_x^2)^2 + 4\sigma_{xy}^2}}{\sigma_x^2 + \sigma_y^2} , \tag{80}$$

$$\sigma_x^2 = \left\{x^2\right\} - \{x\}^2 , \tag{81}$$

$$\sigma_y^2 = \left\{y^2\right\} - \{y\}^2 , \tag{82}$$

$$\sigma_{xy} = \{xy\} - \{x\}\{y\} . \tag{83}$$

Now the average $\{\cdots\}$ is taken over in a single event generated by a Monte Carlo Glauber model.

In the following, the important properties of elliptic flow are demonstrated through hydrodynamic/transport simulations of H.I.C. In hydrodynamic simulations, the eccentricity is usually defined by weighting local energy density $e(x, y)$ or local entropy density $s(x, y)$ in the transverse plane rather than the number density of participants $n_{\rm part}(x, y)$. Figure 13 shows the eccentricity ε_x and the momentum eccentricity

$$\varepsilon_p = \frac{\int dxdy(T_0^{xx} - T_0^{yy})}{\int dxdy(T_0^{xx} + T_0^{yy})} \tag{84}$$

as a function of the proper time from a hydrodynamic simulation assuming Bjorken scaling solution in the longitudinal direction and two different sets of the EoS [46]. Details of hydrodynamic models will be discussed later. The spatial eccentricity ε_x decreases as the system expands and the momentum anisotropy rapidly increases at the same time. So the spatial anisotropy turns into the momentum anisotropy. The momentum anisotropy ε_p is created and saturates in the first several femtometers, so the observed v_2 is expected to be sensitive to the initial stage of the collision. Figure 14 shows the impact parameter dependence of the ratio of output (v_2) to input

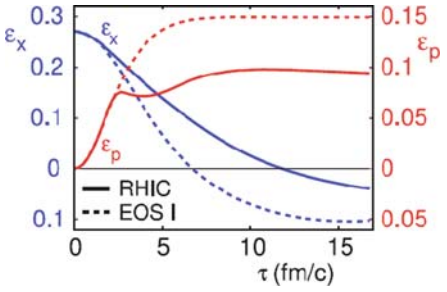

Fig. 13 The spatial eccentricity ε_x and the momentum eccentricity ε_p as a function of the proper time τ in Au+Au collisions at $b = 7$ fm [46]. *Solid* and *dashed curves* correspond to two different sets of the EoS

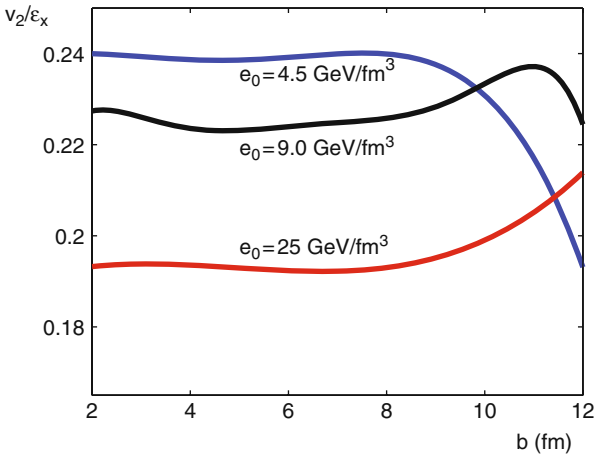

Fig. 14 v_2/ε_x as a function of impact parameter b [80]

(ε_x) [80] which can be understood as a response of the system. Ideal hydrodynamics predicts that v_2 is roughly proportional to the eccentricity

$$v_2 \approx 0.2\varepsilon\,. \tag{85}$$

Figure 15 shows a result from a kinetic approach based on the Boltzmann equation for gluons undergoing elastic scattering only [81].[14] Starting with a uniform distribution in an almond shape in coordinate space and thermal distribution in

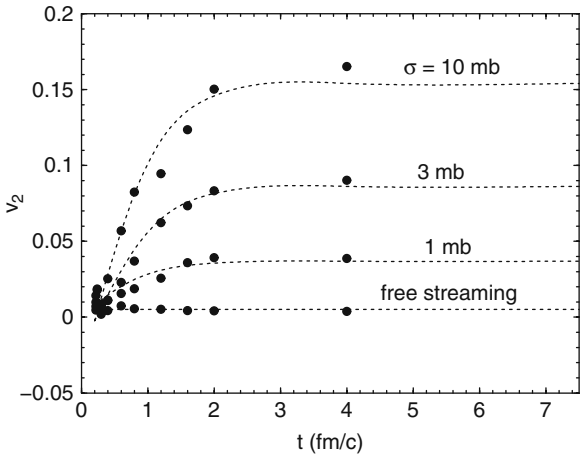

Fig. 15 v_2 as a function of proper time from Boltzmann calculations for different gluon cross sections [81]. *Curves* are guide to eyes

[14] Inelastic scattering ($gg \leftrightarrow ggg$) is implemented in a kinetic approach only recently. Although this is a higher-order process in perturbative expansion, it turns out to affect elliptic flow significantly. See [82–84]

momentum space, the multi-gluon system expands according to the Boltzmann equation with various transport cross sections.[15] From this figure we can understand several important features of the elliptic flow:

1. v_2 is not generated in the free-streaming case, so elliptic flow is generated indeed through secondary collisions;
2. elliptic flow is generated in the early stage of the collision and saturates after the first 2 to 3 fm/c;
3. the saturated value of v_2 is sensitive to the cross section among the particles

$$\sigma_{\rm tr} \propto \frac{1}{\lambda} \propto \frac{1}{\eta}\,, \tag{86}$$

   where λ is the mean free path and η is the shear viscosity calculated in the kinetic theory of gases;
4. in the limit of large transport cross sections (strongly interacting limit), the system is expected to reach the ideal hydrodynamic result[16] since $\eta \to 0$.

Through measurement of v_2 and its analysis in terms of hydrodynamic/transport models, one can extract the transport properties of the matter produced in H.I.C. In the next subsection, we discuss hydrodynamic modeling of H.I.C.

4.3 Ideal Hydrodynamic Model

Hydrodynamics introduced in Sect. 3 is a general framework to describe the space–time evolution of locally thermalized matter for a given equation of state (EoS). This framework has been applied to the intermediate stage in H.I.C. In this section, we neglect the effects of dissipation and concentrate on discussion about ideal hydrodynamic models. The main ingredient in ideal hydrodynamic models in H.I.C. is the EoS of hot and dense matter governed by QCD. In addition, one also needs to assign initial conditions to the hydrodynamic equations. Hydrodynamics can be applied to a system in which local thermalization is maintained. However, in the final state of H.I.C. the particles are freely streaming toward the detectors and their mean free path is almost infinite. This is obviously beyond the applicability of hydrodynamics. Hence we also need a description to decouple the particles from the rest of the system. To summarize, the hydrodynamic modeling of H.I.C. needs an EoS, initial conditions, and a decoupling prescription. Modeling of these ingredients in hydrodynamic simulations has been sophisticated for these years and tested against a vast body of RHIC data.

---

[15] In kinetic theories, momentum exchanges among particles are responsible for equilibration. However, forward scattering with very small scattering angle is insufficient for the system to equilibrate. So the effective (transport) cross section can be defined as $\sigma_{\rm tr} = \int d\theta_{\rm cm} \sin^2\theta_{\rm cm} \frac{d\sigma}{d\theta_{\rm cm}}$, where $\theta_{\rm cm}$ is scattering angle in the center of mass system between two scattering particles.

[16] The Boltzmann equation is applied to *dilute* gases where two-particle correlation can be ignored. So one should keep in mind the applicability condition of the kinetic theory in this case.

We first look at the EoS in more detail. The EoS is in principle calculated from lattice QCD simulations. The realistic results with (almost) physical quark masses are obtained recently [54]. However, if one wants to utilize the EoS from lattice simulations, one needs to interpret the EoS in terms of a hadron picture [85] since one calculates momentum distributions of hadrons in the final decoupling stage. For this purpose, the lattice EoS is compared with the resonance gas model below T_c. If there exists a deviation between them, it prevents one from utilizing the lattice EoS directly in hydrodynamic simulations. Instead, in hydrodynamic simulations, the models of EoS depicted in Fig. 16 are conventionally used [46]. The most simple EoS (EOS I) is $P = e/3$ for an ideal gas of relativistic massless particles.[17] A more realistic EoS (EOS Q) includes the effect of hadron masses and phase transition between hadronic matter and the QGP. At low energy density the EoS is described by a hadron resonance gas model (EOS H). This particular model includes almost all the hadrons in the Particle Data Table [86], while some models include only ground states of hadron multiplets or several low mass resonances. At high energy density, the EoS can be described by a bag model

$$P = \frac{1}{3}(e - 4B)\,. \tag{87}$$

The bag constant B is tuned to match pressure of the QGP phase to that of a hadron resonance gas at critical temperature T_c: $P_{\mathrm{QGP}}(T_c) = P_{\mathrm{hadron}}(T_c)$. As discussed in Sect. 4.1, a hadron gas in H.I.C. is not in chemical equilibrium below the chemical freezeout temperature. T^{ch} is closed to T_c, so the hadron phase may not be chemically equilibrated in H.I.C. A chemically frozen hadron resonance gas can be described by introducing the chemical potential for each hadron [87–93]. The numbers $\tilde{N}_i$ including all decay contributions from higher-lying resonances, $\tilde{N}_i = N_i + \sum_R b_{R\to iX} N_R$, are conserved during the evolution in co-moving frame

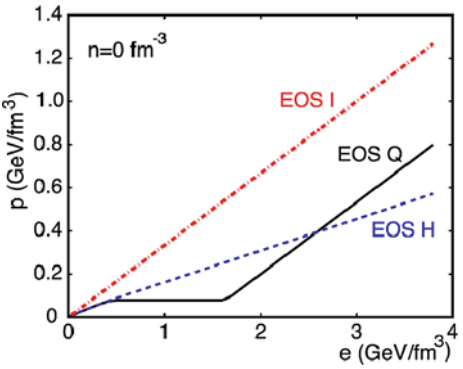

Fig. 16 Some typical EoS in hydrodynamic models [46]

[17] This EoS is always obtained in relativistic conformal field theories in which the trace of energy–momentum tensor is vanishing $T^{\mu}{}_{\mu} = e - 3P = 0$. So the particles are not necessarily "free."

of fluid elements. Here N_i is the number of the ith hadronic species in a fluid element and $b_{R\to iX}$ is the effective branching ratio (a product of branching ratio and degeneracy) of a decay process $R \to i+X$. One can calculate the chemical potential as a function of temperature from the following conditions:

$$\frac{\tilde{n}_i(T,\mu_i)}{s(T,\{\mu_i\})} = \frac{\tilde{n}_i(T_c,\mu_i=0)}{s(T_c,\{\mu_i\}=0)}\,. \tag{88}$$

Instead of solving continuity equations for each hadron, the effect of hadron number conservation can be embedded in the EoS of resonance gas through $\mu_i(T)$ obtained above. For a decoupling prescription, the Cooper–Frye formula [94] is almost a unique choice to convert the hydrodynamic picture to the particle picture

$$E\frac{dN}{d^3p} = \int_\Sigma f(x,p,t)p\cdot d\sigma(x) \tag{89}$$

$$= \frac{d}{(2\pi)^3}\int_\Sigma \frac{p\cdot d\sigma(x)}{\exp\left[(p\cdot u(x)-\mu(x))/T(x)\right]\pm 1}\,, \tag{90}$$

where E is the energy, f is the phase space distribution, d the degeneracy of the particle under consideration (e.g., $d=3$ for pions), p is the momentum, $d\sigma$ is the normal vector to the freezeout surface element, u is the four-velocity, μ is the chemical potential, and T is the decoupling temperature assuming isothermal freezeout hypersurface Σ. Contribution from resonance decays should be taken into account by applying some decay kinematics to the outcome of the Cooper–Frye formula. The decoupling temperature $T^{\rm dec}$ is fixed through *simultaneous* fitting of p_T spectra for various hadrons in the low p_T region. In the blast wave model, decoupling temperature and radial flow velocity are independent parameters to fit p_T spectra. On the other hand, there is a negative correlation between $T^{\rm dec}$ and average radial flow velocity in the hydrodynamic model: the lower decoupling temperature, the larger average radial flow velocity. This formula ensures the energy–momentum conservation on freezeout hypersurface Σ as long as the EoS is calculated using the same distribution function. If one puts resonances up to the mass of 2 GeV in the resonance gas model, one should calculate all the contribution of hadrons in the EoS. Otherwise, neglect of the contribution leads to violation of the energy momentum conservation.[18] It should be noted that $p\cdot d\sigma$ term in Eq. (90) can be negative. This means the incoming particles through Σ are counted as a negative number. Although this seems peculiar, this negative contribution is needed for global energy–momentum conservation.

The prescription to calculate the momentum distribution as above is sometimes called the sudden freezeout model since the mean free path of the particles changes from zero (ideal fluid) to infinity (free streaming) within a thin layer Σ. Although this model is too simple, it has been used in hydrodynamic calculations for a long

[18] If the lattice EoS below T_c cannot be described by a resonance gas model, the Cooper–Frye formula violates the energy–momentum conservation on Σ. This is the reason why there are only few serious attempts of lattice EoS to hydrodynamic simulations.

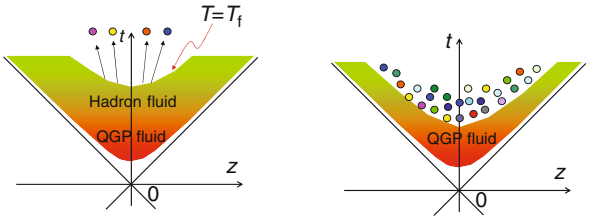

(a) Sudden freezeout (b) Gradual freezeout

Fig. 17 Two freezeout pictures in H.I.C.

time. It is illustrated in Fig. 17a. Recently one utilizes hadronic cascade models to describe the gradual freezeout [95–99]. As will be shown, this hadronic afterburner is mandatory in understanding v_2 data. Phase space distributions for hadrons are initialized below T_c by using the Cooper–Frye formula. The hadronic cascade models describe the space–time evolution of the hadron gas. This model is illustrated in Fig. 17b. This kind of hybrid approaches in which the QGP fluids are followed by hadronic cascade models automatically describes both the chemical and the thermal freezeout and is much more realistic especially for the late stage.

Initial conditions in hydrodynamic simulations are so chosen as to reproduce the centrality and rapidity dependences of multiplicity $dN_{\rm ch}/d\eta$. Initial conditions here mean energy density distribution $e(x, y, \eta_s)$ and flow velocity $u^\mu(x, y, \eta_s)$ at the initial time τ_0. Again baryon density is neglected since, at midrapidity at RHIC, the net baryon density is quite small. The pressure distribution can be obtained from the energy density distribution through the EoS. Space–time rapidity η_s, independent initial energy density distribution $e(x, y, \eta_s) = e(x, y)$, and Bjorken scaling solution $u^\mu_{\rm Bj}$ are assumed in $(2+1)$-dimensional hydrodynamic simulations. In this case, one discuss as the observables only at midrapidity. At $\eta_s = 0$, one can parametrize [100] the initial entropy density based on the Glauber model

$$s(x, y) = \frac{dS}{\tau_0 d\eta_s d^2x_\perp} \propto \alpha n_{\rm part}(x, y; b) + (1-\alpha) n_{\rm coll}(x, y; b). \tag{91}$$

The soft/hard fraction α is adjusted to reproduce the measured centrality dependence [101] of the charged hadron multiplicity at midrapidity. By using the EoS, one can calculate the initial energy density distribution from Eq. (91). For fully three-dimensional initial conditions, see [87, 97, 102]. A novel initial condition is based on the color glass condensate (CGC) picture [103]. One can calculate the local energy density of produced gluons within the CGC framework [104–106] and utilize it as an initial condition of hydrodynamic simulations. In Fig. 18, an example of the CGC initial energy density distribution for a noncentral H.I.C. in a full $(3 + 1)$-dimensional hydrodynamic simulation [107] is shown in the transverse plane (left) and in the reaction plane (right). In the right side panel the horizontal axis corresponds to the impact parameter direction and the vertical axis to the

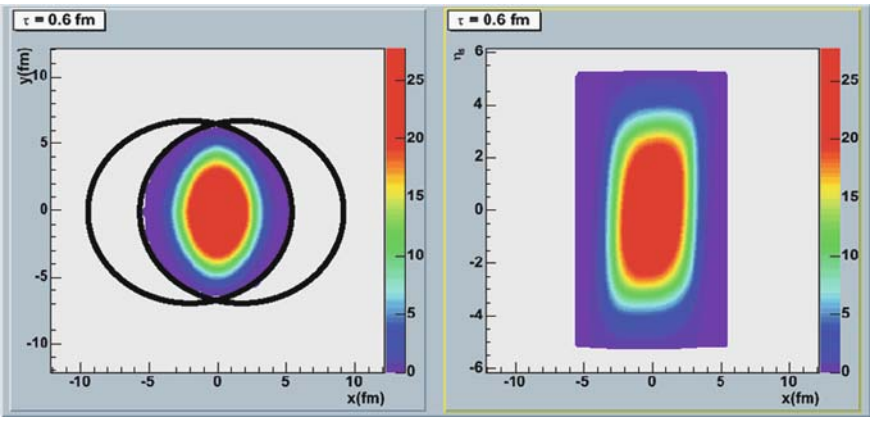

Fig. 18 Energy density distribution in a noncentral H.I.C. within a CGC initial condition in the transverse plane (*left panel*) and in the reaction plane (*right panel*). The two horizontal *thick black lines* in the right panel are the Lorentz contracted nuclei. The color gradation in the right side of each panel indicates the energy density scale in unit of GeV/fm^3

space–time rapidity η_s. Figures 19 and 20 show charged particle multiplicity from hydrodynamic simulations that are compared with the PHOBOS data [101, 108]. Figure 19 shows $dN_{\rm ch}/d\eta$ as a function of the number of participants ($N_{\rm part}$) [101]. These data are fitted by using two kinds of initial conditions: from Glauber model calculations and from color glass condensate (CGC) model calculations [97]. Both models reproduce the centrality dependence of the data. Figure 20 shows the rapidity distribution of $dN_{\rm ch}/d\eta$ for each centrality [108]. The fitting of multiplicity is the starting point of further analysis based on hydrodynamic simulations.

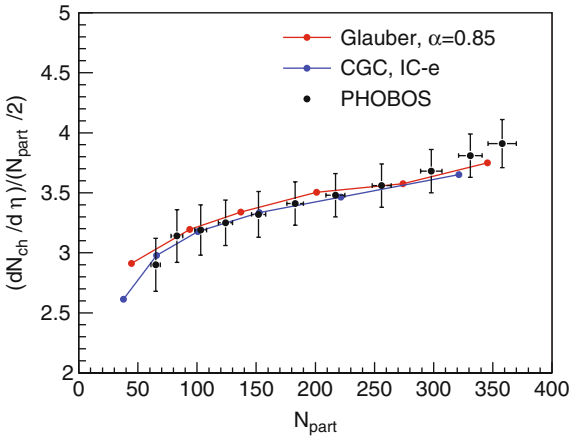

Fig. 19 Centrality dependence of multiplicity from PHOBOS [108] are fitted by hydrodynamic calculations with two different initial conditions [97, 107]

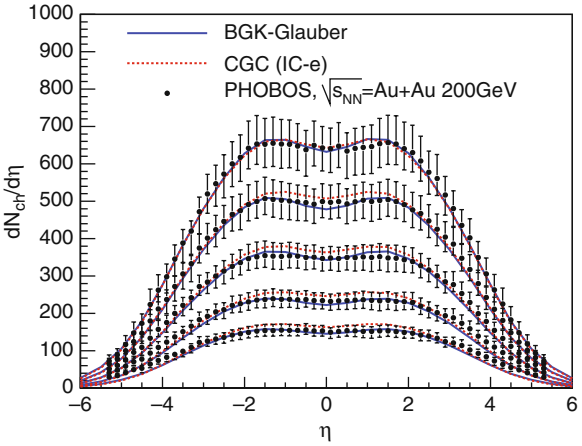

Fig. 20 Pseudorapidity dependence of multiplicity from PHOBOS [108] is fitted by hydrodynamic calculations with two different initial conditions [97, 107]

In the hydrodynamic models, various combinations of initial conditions, EoS and decoupling prescriptions, are available to analyze the experimental data in H.I.C. Of course, final results largely depend on modeling of each ingredient. So it is quite important to constrain each model and its inherent parameters through systematic analyses of the data toward a comprehensive understanding of the QGP.

4.4 Application of the Ideal Hydrodynamic Model to H.I.C.

In this subsection we analyze H.I.C. at RHIC in terms of ideal hydrodynamic models discussed in the previous subsection.

Before we start our main discussion on elliptic flow parameter v_2, we mention here that the transverse momentum distributions for pions, kaons, and protons are also important since these reflect dominant transverse flow, namely radial flow. Currently, among hydrodynamic models, yields and slopes of p_T spectra are reproduced in pure hydrodynamic calculations with early chemical freezeout or in gradual freezeout approaches. It should be noted here that simultaneous reproduction of the yields and the slopes is important. Sometimes, one only compares the slope of the p_T spectra by scaling the yields "by hand" within hydrodynamic approaches. However, chemical composition of hadronic matter does affect the transverse expansion [87]. Therefore, it does not make any sense if one compares only the slopes by keeping chemical equilibrium of hadrons.

As discussed in Sect. 4.2, v_2/ε can be interpreted as a response of the system to initial spatial eccentricity. Figure 21 shows v_2/ε as a function of the transverse multiplicity density $(1/S)dN_{\rm ch}/dy$ from AGS to RHIC energies. Hydrodynamic results in Fig. 14 are shown symbolically as horizontal lines. The experimental data monotonically increase with particle density, while ideal hydrodynamic response is

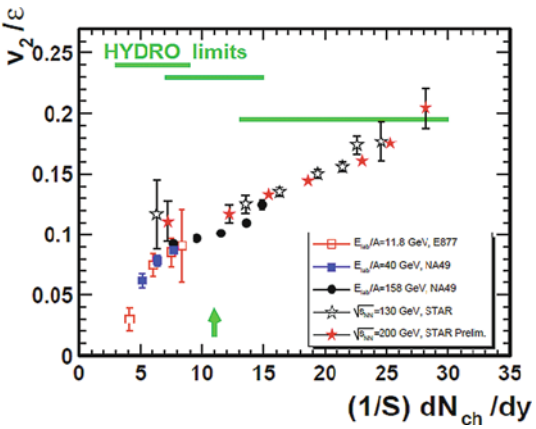

Fig. 21 v_2/ε as a function of transverse multiplicity density compiled by NA49 Collaboration [109]

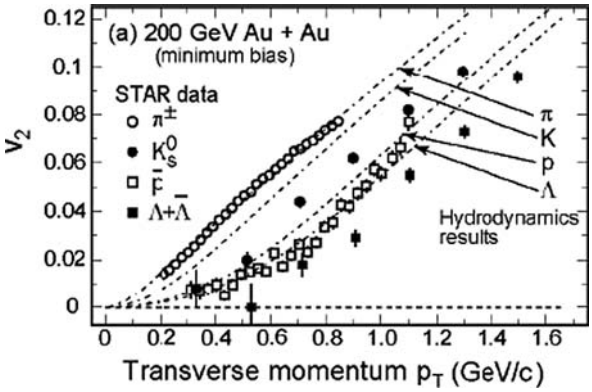

Fig. 22 Differential v_2 for pions, kaons, protons, and lambdas [67]

almost flat [80]. Ideal hydrodynamics is expected to generate the maximum response among the transport models.[19] The experimental data reach this limit for the first time at RHIC. Figure 22 shows the differential elliptic flow v_2 as a function of transverse momentum for pions, kaons, protons, and lambdas. A mass ordering pattern is seen in v_2 data, which was predicted by ideal hydrodynamic calculations [110].[20] The pseudorapidity dependence of v_2 observed by PHOBOS [111] has a triangular

[19] It should be emphasized again that the hydrodynamic results above are obtained by a particular combination of modeling, i.e., Glauber-type initial conditions, EOS Q with chemical equilibrium in the hadron phase and sudden freezeout at fixed decoupling temperature.

[20] There is a caveat to interpret the agreement since this particular hydrodynamic calculation does not reproduce particle ratios due to a lack of early chemical freezeout. The importance of hadronic viscosity and chemical freezeout in hydrodynamic calculations is recognized [112] after the announcement of the discovery of perfect fluid QGP [2].

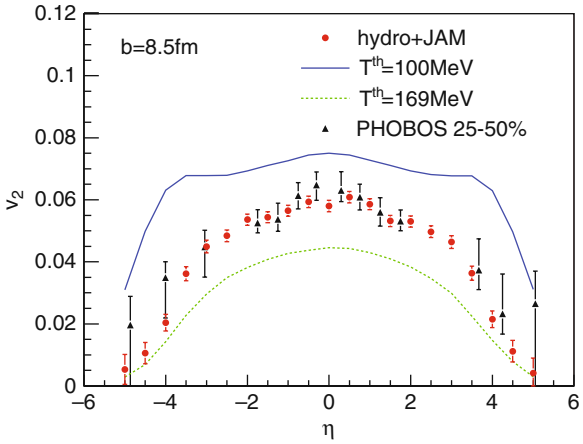

Fig. 23 Pseudorapidity dependence of v_2. PHOBOS data [111] compared to different model calculations [97]

shape as is seen in Fig. 23. In the pure ideal hydrodynamic result, hydrodynamic equations are initialized by the Glauber model and are solved all the way down to $T^{\rm dec} = 100\,{\rm MeV}$. The pure hydrodynamic model gives a comparable result with the data only at midrapidity. However, at forward and backward rapidities, it overshoots the data significantly. If we replace the hadron fluid with a hadron gas utilizing a hadron cascade, v_2 is significantly reduced in the forward and backward regions. In this hybrid model the hadrons have a finite mean free path, which results in an effective shear viscosity in the hadron phase. So dissipative hadronic "corona" effects turn out to be important in understanding the v_2 data. The model also reproduces a mass ordering pattern of v_2 for identified hadrons as a function of p_T near

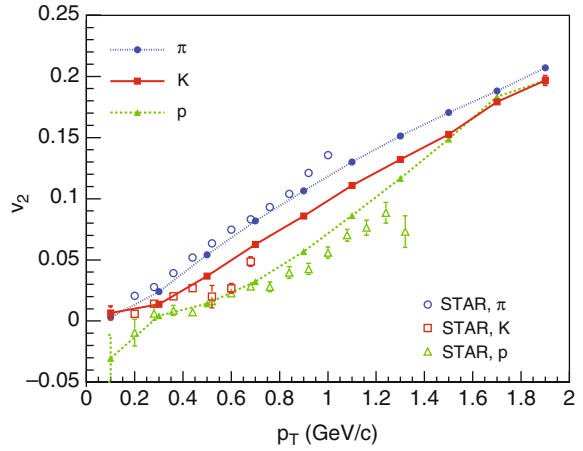

Fig. 24 Differential v_2. STAR data [67] compared to model calculations [98]

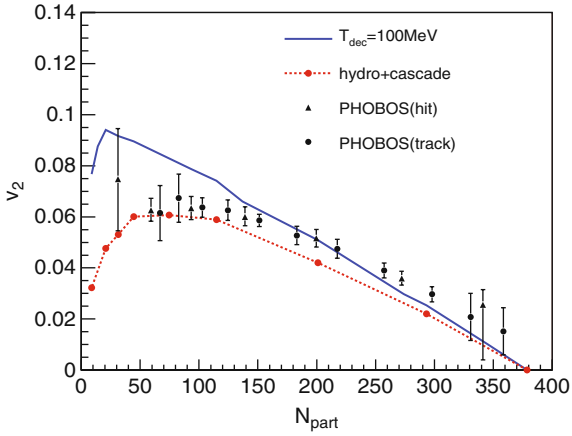

Fig. 25 v_2 as a function of centrality. PHOBOS data [111] compared to different model calculations [97]

midrapidity in Fig. 24. Figure 25 shows the centrality dependence of v_2. The solid line is the result from ideal hydrodynamic calculations while the dotted line is from the hybrid model. It is clear that for peripheral collisions, where the multiplicity is small, the hadronic viscosity plays an important role. One may notice that the result from the hybrid model is systematically and slightly smaller than the data. However, there could exist the effect of initial eccentricity fluctuations which is absent in this hydrodynamic calculations. The deviation between the results and the data can be interpreted quantitatively by this effect. Figure 26 shows $v_2(p_T)$ for pions, kaons,

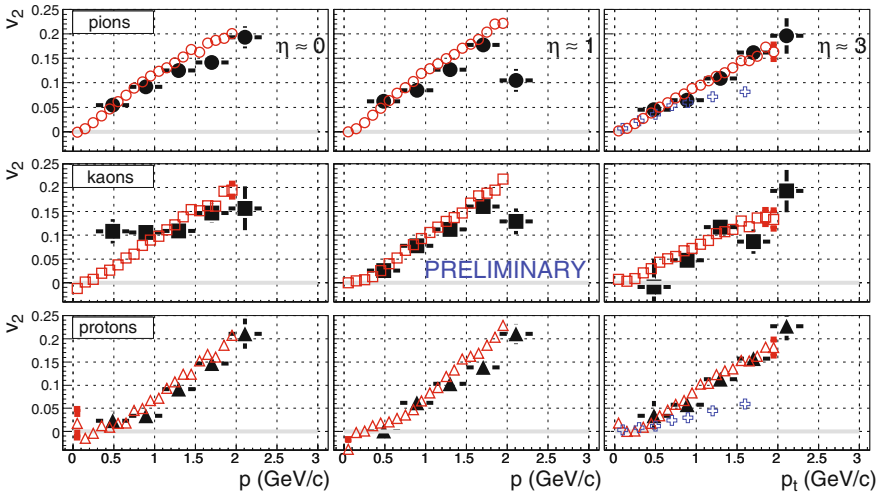

Fig. 26 Differential v_2 for pions, kaons, and protons for $\eta = 0$ (*left*), $\eta = 1$ (*middle*), and $\eta = 3$ (*right*) [113]

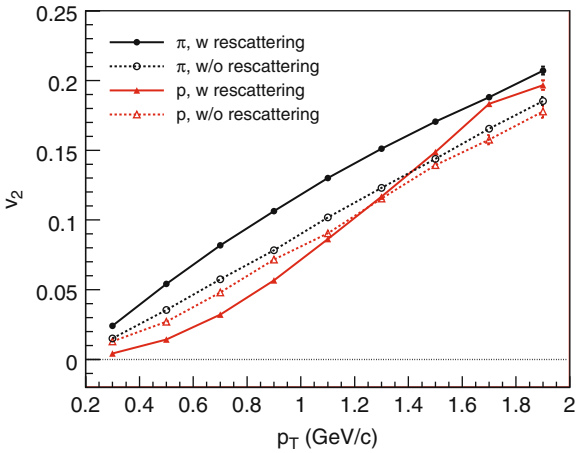

Fig. 27 Differential v_2 with and without hadronic rescattering [98]

and protons in 10–50% centrality at $\eta = 0$ (left), $\eta = 1$ (middle), and $\eta = 3$ (right) observed by BRAHMS [113]. Also here the hybrid model reproduces the p_T slope of these differential elliptic flow parameters.

We would like to point out here that the mass ordering, clearly visible in Fig. 24, is there in the final result. If one would look at the result just after the QGP phase transition, the difference between the pions and the protons would be quite small. So it turns out that the splitting patterns are caused by hadronic rescattering. This is illustrated in Fig. 27. One can conclude that the large magnitude of the integrated v_2 and the strong mass ordering of the differential $v_2(p_T)$ observed at RHIC result from a subtle interplay between perfect fluid dynamics of the early QGP stage and dissipative dynamics of the late hadronic stage: The large magnitude of v_2 is due to the large overall momentum anisotropy, generated predominantly in the early QGP stage, whereas the strong mass splitting behavior at low p_T reflects the redistribution of this momentum anisotropy among the different hadron species, driven by the continuing radial acceleration and cooling of the matter during the hadronic rescattering phase.

We have seen so far that the hydrodynamic model which includes Glauber-type initial conditions followed by a perfect fluid QGP and a dissipative hadronic gas evolution is the most successful combination for describing the RHIC data. We now go to the discussion on the initialization dependence of v_2. Two types of initial conditions, namely the Glauber-type initial conditions and the CGC initial conditions, are discussed in the previous subsection. v_2 as a function of centrality is shown again for these two initial conditions in Fig. 28. In the case of the Glauber initial conditions we can conclude early thermalization and the discovery for the perfect fluid QGP. In the case of the CGC initial conditions, we cannot, however, claim the discovery since the model initialized by CGC overshoots the data in almost the whole range. Since the hydrodynamic model calculations depend on the initial con-

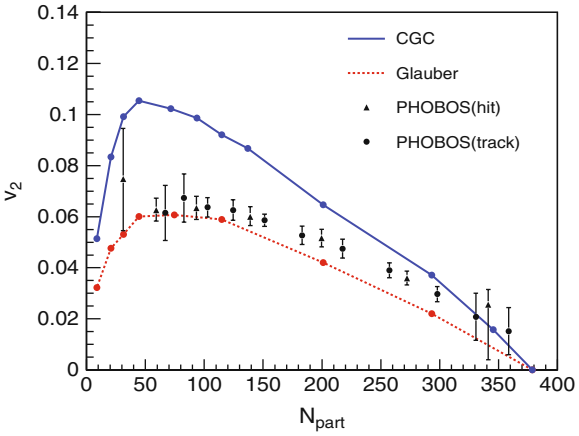

Fig. 28 v_2 as a function of centrality. PHOBOS data [111] are compared to hydrodynamic results with two different sets of initial conditions [97]

ditions, it is very important to understand them before making final conclusions. In the case of CGC initial conditions viscosity might be needed even in the QGP phase to get the model down to the data points. The effect of viscosity could therefore be quite important. The high v_2 values from the CGC initial conditions are traced back to the initial eccentricity. In Fig. 29a the energy density distribution in the impact parameter direction is plotted for different conditions. If the energy density profile has a sharp edge (no diffuseness), an integral in Eq. (78) is relatively weighted in the edge region and, consequently, eccentricity becomes maximum at a given impact parameter. If one compares the energy density profile of the CGC with the one of the Glauber model, one sees that the CGC profile has a sharper edge than the Glauber model does. The resultant eccentricity as a function of impact parameter is shown in Fig. 29b. Eccentricity from the CGC is about 20–30% larger than that from the

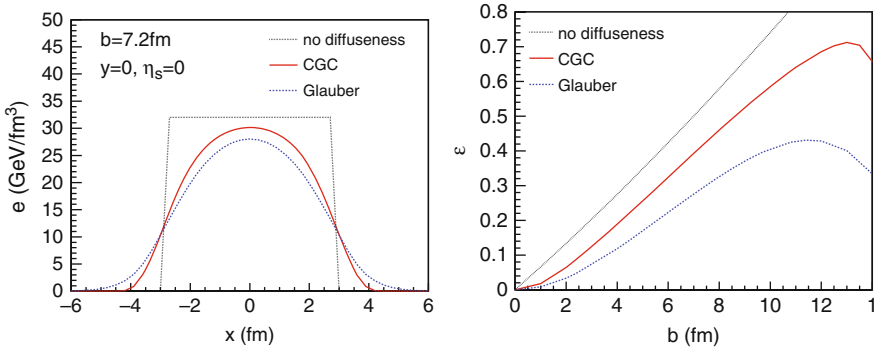

(a) Energy density distribution (b) Initial eccentricity

Fig. 29 The difference eccentricity between Glauber and CGC initial conditions

Glauber model. This is the reason why hydro + hadronic cascade approach which even includes hadronic viscosity overshoots the v_2 data.[21]

4.5 Summary

Hydrodynamics is a framework to describe the space–time evolution of matter under local equilibrium. It is applied to the intermediate stage in H.I.C. to extract the transport properties of the QGP from RHIC data. Hydrodynamic modeling includes initial conditions, EoS, and decoupling prescriptions. Final results certainly depend on combination of each modeling. So much attention should be paid to these ingredients before drawing robust conclusions from hydrodynamic analyses. Elliptic flow has played a major role in understanding the transport properties of the QGP. Glauber initial conditions, ideal hydrodynamics in the QGP phase, and dissipative gas for the hadron phase are three pillars for agreement between the model and the elliptic flow data. Whereas, if CGC initial conditions are employed, the initial eccentricity gets increased by 20–30%. If the nature chooses this kind of initial condition, viscosity might be needed even in the QGP phase.

Acknowledgments One of the authors (T.H.) is much indebted to M. Gyulassy, T. Hatsuda, U. Heinz, T. Kunihiro, S. Muroya, M. Natsuume, and Y. Nara for fruitful discussion. The work of T.H. was partly supported by Grant-in-Aid for Scientific Research No. 19740130. One of the authors (A.B.) would like to thank Despoina Evangelakou for technical support during the writing of the lecture note.

References

1. http://www.veccal.ernet.in/qm2008.html 139
2. http://www.bnl.gov/bnlweb/pubaf/pr/PR_display.asp ?prID=05–38 140, 171
3. M. Gyulassy, I. Vitev, X.N. Wang and B.W. Zhang: arXiv:nucl-th/0302077 141
4. A. Kovner and U.A. Wiedemann: arXiv:hep-ph/0304151 141
5. T. Matsui and H. Satz: Phys. Lett. **B 178**, 416 (1986) 141
6. T. Peitzmann and M.H. Thoma: Phys. Rept. **364**, 175 (2002) 141
7. D.G. d'Enterria and D. Peressounko: Eur. Phys. J. **C 46**, 451 (2006) 141
8. C. Eckart: Phys. Rev. **58**, 919 (1940) 142, 145
9. C. Cattaneo: Atti. Sem. Mat. Fis. Univ. Modena **3**, 83 (1948) 153
10. L.D. Landau, E.M. Lifshitz: *Fluid Mechanics*, pp. 133–136, Pergamon Press, New York (1959) 145
11. M. Namiki and C. Iso: Prog. Theor. Phys. **18**, 591 (1957)
12. C. Iso, K. Mori and M. Namiki: Prog. Theor. Phys. **22**, 403 (1959)
13. I. Müller: Z. Phys. **198**, 329 (1967)
14. W. Israel: Ann. Phys. **100**, 310 (1976)
15. W. Israel and J.M. Stewart: Ann. Phys. **118**, 341 (1979)
16. J.D. Bjorken: Phys. Rev. **D 27**, 140 (1983) 150, 151, 155

[21] See also recent more realistic calculations of eccentricity within a CGC framework [76].

17. A. Hosoya and K. Kajantie: Nucl. Phys. **B 250**, 666 (1985)
18. P. Danielewicz and M. Gyulassy: Phys. Rev. **D 31**, 53 (1985)
19. L.P. Csernai: *Introduction to Relativistic Heavy Ion Collisions*, John Wiley & Sons, New York (1994)
20. J.P. Blaizot and J.Y. Ollitrault: Adv. Ser. Direct. High Energy Phys. **6**, 393 (1990)
21. R. Maartens: arXiv:astro-ph/9609119 147
22. D.H. Rischke: arXiv:nucl-th/9809044
23. I. Müller: Living Rev. Rel. **2**, 1 (1999)
24. J.Y. Ollitrault: Eur. J. Phys. **29**, 275 (2008) 142
25. P. Kovtun, D.T. Son and A.O. Starinets: Phys. Rev. Lett. **94**, 111601 (2005) 151
26. A. Nakamura and S. Sakai: Phys. Rev. Lett. **94**, 072305 (2005) 151
27. D. Kharzeev and K. Tuchin: arXiv:0705.4280 [hep-ph] 152
28. F. Karsch, D. Kharzeev and K. Tuchin: Phys. Lett. **B 663**, 217 (2008) 152
29. M. Mizutani, S. Muroya and M. Namiki: Phys. Rev. **D 37**, 3033 (1988) 152
30. W.A. Hiscock and L. Lindblom: Phys. Rev. **D 31**, 725 (1985) 152
31. G.S. Denicol, T. Kodama, T. Koide and Ph. Mota: arXiv:0807.3120 [hep-ph] 152
32. A. Muronga: Phys. Rev. Lett. **88**, 062302 (2002) 153
33. A. Muronga: Phys. Rev. Lett. **89**, 159901 (2002) [Erratum]
34. A. Muronga: Phys. Rev. **C 69**, 034903 (2004)
35. A. Muronga: Phys. Rev. **C 76**, 014909 (2007)
36. A. Muronga: Phys. Rev. **C 76**, 014910 (2007)
37. U.W. Heinz, H. Song and A.K. Chaudhuri: Phys. Rev. **C 73**, 034904 (2006)
38. H. Song and U.W. Heinz: Phys. Lett. **B 658**, 279 (2008)
39. R. Baier, P. Romatschke and U.A. Wiedemann: Phys. Rev. **C 73**, 064903 (2006)
40. R. Baier, P. Romatschke and U.A. Wiedemann: Nucl. Phys. **A 782**, 313 (2007)
41. R. Baier and P. Romatschke: Eur. Phys. J. **C 51**, 677 (2007)
42. P. Romatschke: Eur. Phys. J. **C 52**, 203 (2007)
43. P. Romatschke and U. Romatschke: Phys. Rev. Lett. **99**, 172301 (2007)
44. K. Dusling and D. Teaney: Phys. Rev. **C 77**, 034905 (2008)
45. T. Koide, G.S. Denicol, Ph. Mota and T. Kodama: Phys. Rev. **C 75**, 034909 (2007) 153
46. P.F. Kolb and U.W. Heinz: arXiv:nucl-th/0305084 154, 163, 166
47. P. Huovinen: arXiv:nucl-th/0305064
48. P. Huovinen and P.V. Ruuskanen: Ann. Rev. Nucl. Part. Sci. **56**, 163 (2006)
49. T. Hirano: Acta Phys. Pol. **B 36**, 187 (2005)
50. T. Hirano: Prog. Theor. Phys. Suppl. **168**, 347 (2007)
51. Y. Hama, T. Kodama and O. Socolowski Jr.: Braz. J. Phys. **35**, 24 (2005)
52. F. Grassi: Braz. J. Phys. **35**, 52 (2005)
53. C. Nonaka: J. Phys. **G 34**, S313 (2007) 154
54. M. Cheng et al.: Phys. Rev. **D 77**, 014511 (2008) 155, 166
55. M. Gyulassy and T. Matsui: Phys. Rev. **D 29**, 419 (1984) 155
56. P.V. Ruuskanen: Phys. Lett. **B 147**, 465 (1984) 155
57. S.S. Adler et al. [PHENIX Collaboration]: Phys. Rev. **C 71**, 034908 (2005) 155
58. S.S. Adler et al. [PHENIX Collaboration]: Phys. Rev. **C 71**, 049901 (2005) [Erratum] 155
59. P. Braun-Munzinger, K. Redlich and J. Stachel: arXiv:nucl-th/0304013 156
60. F. Becattini and U.W. Heinz: Z. Phys. **C 76**, 269 (1997) 157
61. F. Becattini and U.W. Heinz: Z. Phys. **C 76**, 578 (1997) [Erratum] 157
62. D.H. Rischke: Nucl. Phys. **A 698**, 153 (2002) 157
63. V. Koch: Nucl. Phys. **A 715**, 108 (2003) 157
64. P.J. Siemens and J.O. Rasmussen: Phys. Rev. Lett. **42**, 880 (1979) 157, 158
65. E. Schnedermann, J. Sollfrank and U.W. Heinz: Phys. Rev. **C 48**, 2462 (1993) 157, 158
66. O. Barannikova [STAR Collaboration]: Nucl. Phys. **A 774**, 465 (2006) 158, 159
67. J. Adams et al. [STAR Collaboration]: Nucl. Phys. **A 757**, 102 (2005) 158, 159, 171, 172
68. A.M. Poskanzer and S.A. Voloshin: Phys. Rev. **C 58**, 1671 (1998) 160

69. J.Y. Ollitrault: Phys. Rev. **D 46**, 229 (1992) 161
70. K.H. Ackermann et al. [STAR Collaboration]: Phys. Rev. Lett. **86**, 402 (2001) 161
71. H. Heiselberg and A.M. Levy: Phys. Rev. **C 59**, 2716 (1999) 161
72. H. Sorge: Phys. Rev. Lett. **82**, 2048 (1999)
73. S.A. Voloshin and A.M. Poskanzer: Phys. Lett. **B 474**, 27 (2000) 161
74. M. Miller and R. Snellings: arXiv:nucl-ex/0312008 162
75. X.I. Zhu, M. Bleicher and H. Stoecker: Phys. Rev. **C 72**, 064911 (2005)
76. H.J. Drescher and Y. Nara: Phys. Rev. **C 75**, 034905 (2007) 176
77. R. Andrade, F. Grassi, Y. Hama, T. Kodama and O. Socolowski Jr.: Phys. Rev. Lett. **97**, 202302 (2006)
78. W. Broniowski, P. Bozek and M. Rybczynski: Phys. Rev. **C 76**, 054905 (2007)
79. B. Alver et al.: Phys. Rev. **C 77**, 014906 (2008) 162
80. P.F. Kolb, J. Sollfrank and U.W. Heinz: Phys. Rev. **C 62**, 054909 (2000) 164, 171
81. B. Zhang, M. Gyulassy and C.M. Ko: Phys. Lett. **B 455**, 45 (1999) 164
82. Z. Xu and C. Greiner: Phys. Rev. **C 71**, 064901 (2005) 164
83. Z. Xu and C. Greiner: Phys. Rev. **C 76**, 024911 (2007)
84. Z. Xu and C. Greiner: Phys. Rev. Lett. **100**, 172301 (2008) 164
85. F. Karsch, K. Redlich and A. Tawfik: Eur. Phys. J. **C 29**, 549 (2003) 166
86. C. Amsler et al.: Phys. Lett. **B 667**, 1 (2008) 166
87. T. Hirano and K. Tsuda: Phys. Rev. **C 6**6, 054905 (2002) 166, 168, 170
88. H. Bebie, P. Gerber, J.L. Goity and H. Leutwyler: Nucl. Phys. **B 378**, 95 (1992)
89. N. Arbex, F. Grassi, Y. Hama and O. Socolowski Jr.: Phys. Rev. **C 64**, 064906 (2001)
90. W.L. Qian, R. Andrade, F. Grassi, Y. Hama and T. Kodama: arXiv:0709.0845 [nucl-th]
91. D. Teaney: nucl-th/0204023
92. P.F. Kolb and R. Rapp: Phys. Rev. **C 67**, 044903 (2003)
93. P. Huovinen: arXiv:0710.4379 [nucl-th] 166
94. F. Cooper and G. Frye: Phys. Rev. **D 10**, 186 (1974) 167
95. S.A. Bass and A. Dumitru: Phys. Rev. **C 61**, 064909 (2000) 168
96. D. Teaney, J. Lauret and E.V. Shuryak: Phys. Rev. Lett. **86**, 4783 (2001)
97. T. Hirano, U.W. Heinz, D. Kharzeev, R. Lacey and Y. Nara: Phys. Lett. **B 636**, 299 (2006) 168, 169, 170, 172, 173, 175
98. T. Hirano, U.W. Heinz, D. Kharzeev, R. Lacey and Y. Nara: Phys. Rev. **C 77**, 044909 (2008) 172, 174
99. C. Nonaka and S.A. Bass: Phys. Rev. **C 75**, 014902 (2007) 168
100. T. Hirano: Phys. Rev. **C 65**, 011901 (2002) 168
101. P.F. Kolb, U.W. Heinz, P. Huovinen, K.J. Eskola and K. Tuominen: Nucl. Phys. **A 696**, 197 (2001) 168, 169
102. B.B. Back et al. [PHOBOS Collaboration]: Phys. Rev. **C 65**, 061901 (2002) 168
103. E. Iancu and R. Venugopalan: arXiv:hep-ph/0303204 168
104. D. Kharzeev and E. Levin: Phys. Lett. **B 523**, 79 (2001) 168
105. D. Kharzeev, E. Levin and M. Nardi: Nucl. Phys. **A 730**, 448 (2004)
106. D. Kharzeev, E. Levin and M. Nardi: Nucl. Phys. **A 743**, 329 (2004) [Erratum] 168
107. T. Hirano and Y. Nara: Nucl. Phys. **A 743**, 305 (2004) 168, 169, 170
108. B.B. Back et al.: Phys. Rev. Lett. **91**, 052303 (2003) 169, 170
109. C. Alt et al. [NA49 Collaboration]: Phys. Rev. **C 68**, 034903 (2003) 171
110. P. Huovinen, P.F. Kolb, U.W. Heinz, P.V. Ruuskanen and S.A. Voloshin: Phys. Lett. **B 503**, 58 (2001) 171
111. B.B. Back et al. [PHOBOS Collaboration]: Phys. Rev. **C 72**, 051901 (2005) 171, 172, 173, 175
112. T. Hirano and M. Gyulassy: Nucl. Phys. **A 769**, 71 (2006) 171
113. S.J. Sanders: J. Phys. **G 34**, S1083 (2007) 173, 174

An Introduction to the Spectral Analysis of the QGP

P. P. Bhaduri, P. Hegde, H. Satz, and P. Tribedy

Abstract This is an introduction to the study of the in-medium behavior of quarkonia and its application to the quark–gluon plasma search in high-energy nuclear collisions.

1 What Are Quarkonia?

The bound states of a heavy quark and its antiquark which are stable with respect to strong decay into open charm or bottom are collectively called *quarkonia*. We denote by Q either of the heavy quarks, charm (c) or bottom (b); the corresponding bound states are known as *charmonia* or *bottomonia*, respectively.

Among the vector (spin-one) charmonium states, the lightest (ground state) is the famous J/ψ; the excited states are the χ_c and the ψ'. For the bottom quark, the lightest quarkonium is the Υ, while the excited states include the χ_b, Υ', χ_b', and the Υ''. The stability of the $c\bar{c}/b\bar{b}$ quarkonium states implies that their masses satisfy $M_{c\bar{c}} < 2M_D$ and $M_{b\bar{b}} < 2M_B$, where $D = c\bar{u}$ and $B = b\bar{u}$ are the corresponding "open" mesons. A specific characteristic of quarkonia is their small size. While the typical hadron radius is $\sim$1 fm, the radii of charmonia and bottomonia range from 0.1 to 0.3 fm, as we shall see.

P. P. Bhaduri (✉)
Variable Energy Cyclotron centre, Kolkata-700 064, India,
partha.bhaduri@veccal.ernet.in

P. Hegde
Department of Physics and Astronomy, SUNY, Stony Brook, NY 11794-3800, USA,
phegde@grad.Physics.sunysb.edu

H. Satz
Fakultät für Physik, Universität Bielefeld, D-33501 Bielefeld, Germany,
satz@physik.uni-bielefeld.de

P. Tribedy
Variable Energy Cyclotron centre, Kolkata-700 064, India,
ptribedy@veccal.ernet.in

Bhaduri, P. P. et al.: *An Introduction to the Spectral Analysis of the QGP*. Lect. Notes Phys. **785**, 179–197 (2010)
DOI 10.1007/978-3-642-02286-9_5

Since c and b quarks are very heavy ($m_Q \ll \Lambda_{QCD} \sim 200$ MeV), the binding of the $Q\bar{Q}$ system may be treated non-relativistically. The governing equation is the non-relativistic Schrödinger equation,

$$-\frac{1}{m}\left\{\nabla^2(r) + V(r)\right\}\Psi_i(r) = (M_i - 2m)\Psi_i(r), \tag{1}$$

where $\Psi(r)$ denotes the wavefunction of the system, r the quark–antiquark separation, and m the quark mass.[1] Since Eq. (1) is a non-relativistic description of the binding, the total rest mass must be subtracted from the masses M_i of the bound states. Once we find the eigenvalues M_i of the system, we can also define the "binding energy" ΔE of each quarkonium state, $\Delta E = 2M_{D,B} - M_i$.

Lattice and spectroscopic studies suggest for the potential $V(r)$ the form [1, 2]

$$V(r) = \sigma r - \frac{\alpha}{r}, \tag{2}$$

generally known as the "Cornell potential." It is spherically symmetric and consists of two parts. The linearly rising part represents the confining force, given in terms of the *string tension* σ; lattice studies put its value at around 0.2 (GeV)^2. The second part is an effective Coulomb potential, including transverse string oscillations; string theory suggests $\alpha = \pi/12$.

Having solved the Schrödinger equation, we may determine the bound-state radii through

$$\langle r_i^2 \rangle = \frac{\int d^3r r^2 |\Psi_i(r)|^2}{\int d^3r |\Psi_i(r)|^2}. \tag{3}$$

A fair estimate can already be obtained by means of a semi-classical formulation. The energy of the system is then given by

$$E = \frac{p^2}{m} + V(r), \tag{4}$$

and from the uncertainty relation, we have $pr \simeq c$; the constant c can be fixed by requiring the correct J/ψ mass, giving $c \simeq 1.25$. Minimizing the energy determines the lowest bound-state radius r_0,

$$\sigma + \frac{\alpha}{r_0^2} = \frac{3}{mr_0^3}. \tag{5}$$

With $\sigma \simeq 0.2(\text{GeV})^2$ and $\alpha \simeq \pi/12$, together with $m_c \simeq 1.3$ GeV, we obtain a J/ψ size ($Q\bar{Q}$ separation, i.e., twice the radius) of about 0.5 fm. For the $\alpha' = 0$

[1] We work in the center-of-mass system, with a reduced mass $m/2$, so that we have $-\nabla^2/m$ instead of the usual $-\nabla^2/2m$.

Table 1 Masses, binding energies, and radii of the lowest $c\bar{c}$ and $b\bar{b}$ bound states [3]; the listed radii are $1/2\sqrt{\langle r_i^2 \rangle}$, given by Eq. (3)

State	J/ψ	χ_c	ψ'	Υ	χ_b	Υ'	χ_b'	Υ''
Mass (GeV)	3.10	3.53	3.68	9.46	9.99	10.02	10.36	10.36
ΔE (GeV)	0.64	0.20	0.05	1.10	0.67	0.54	0.31	0.20
Radius (fm)	0.25	0.36	0.45	0.14	0.22	0.28	0.34	0.39

value, we have $r_0 \sim (1/m\sigma)^{1/3} \approx 0.3$ fm; on the other hand, for $\sigma = 0$, we get $r_0 \sim (1/m\alpha) \approx 0.6$ fm. We thus see that a major contribution to the radius comes from the string tension. At $T = 0$, the radius of the J/ψ is thus to a considerable extent still determined by the confining part of the potential. We summarize some of the characteristics of the spin-averaged quarkonia in Table 1 [3].

Next, we turn to the question of the dissociation and decay of quarkonia. We have already noted that these mesons cannot decay via strong channels because their masses are smaller than the open thresholds. It is also known that quarkonia do not dissociate significantly in nuclear collisions; we shall discuss this in greater detail in Sect. 3.

How then do quarkonia dissociate? Three mechanisms have been identified, corresponding to the behavior for $T = 0$, $0 < T < T_c$, and $T \geq T_c$, where T_c is the critical temperature of deconfinement. We shall consider each of them in turn.

1.1 String Breaking

The potential in Eq. (2) is correct only in the limit $M_Q \to \infty$. If light quarks exist in the theory, then the string connecting the heavy quarks can break as soon as the overall energy in the system is greater than $2M_D$ or $2M_B$, depending on whether $Q = c$ or b (Fig. 1). Light quark–antiquark pairs appear at the broken ends of the string, and new "heavy-light" $Q\bar{q}$ or $q\bar{Q}$ mesons are formed. This behavior of the quark potential has been observed in lattice studies with dynamical quarks, as we shall show below.

We may estimate the string-breaking energy F_0. For the charm quark, $F_0 = 2(M_D - m_c) \simeq 1.2$ GeV, while for the bottom quark, $F_0 = 2(M_B - m_b) \simeq 1.2$ GeV.

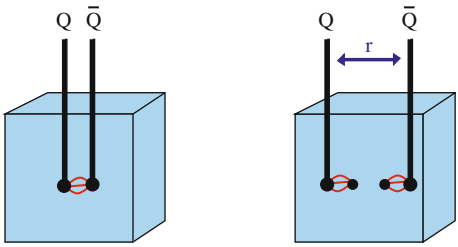

Fig. 1 Cartoon of string-breaking

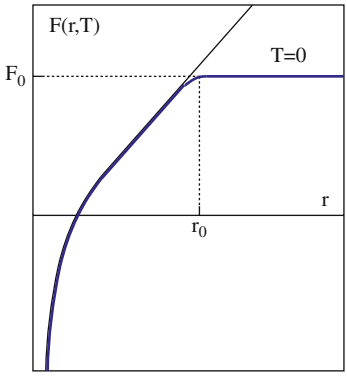

Fig. 2 String-breaking energy as a function of $Q\bar{Q}$ separation

From this, we deduce $r_0 = (1.2\ \text{GeV})/\sigma \simeq 1.5$ fm. That this value is the same for both quark species leads us to conclude that the energy required for string breaking is a property of the vacuum itself, as a medium at $T = 0$, containing virtual $q\bar{q}$ pairs which are brought on-shell by the field between the heavy quarks. The effect of string-breaking on the Cornell potential is shown in Fig. 2.

1.2 Recombination

In nuclear collisions not sufficiently energetic to create a quark–gluon plasma, there will nevertheless be abundant hadron production. These newly formed light hadrons can through a switch in bonding (recombination) turn a $Q\bar{Q}$ meson into two heavy-light mesons. This mechanism is schematically depicted in Fig. 3: when two or more hadrons overlap, their quarks can recouple to form new pairs.

If the temperature is increased, the hadron density also increases, and this in turn increases the recombination probability. As a consequence, the distance up to which the heavy quarks still bind also becomes shorter and the potential will break earlier (see Fig. 4). We thus have something like "effective screening," even though all color charges are still bound.

What happens as we get close to T_c? The density of produced hadrons will then increase strongly, and lattice studies show that in accord with our picture, both the free energy and the string-breaking radius r_T decrease rapidly near T_c, as shown in Fig. 5.

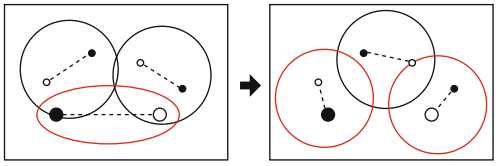

Fig. 3 A schematic view of recombination

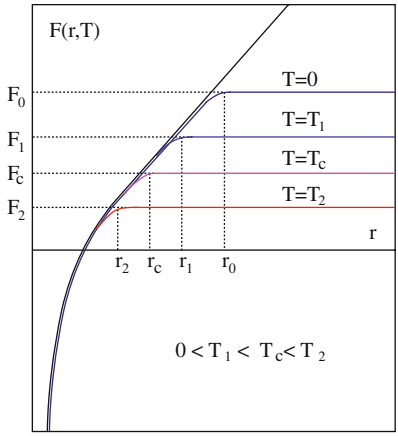

Fig. 4 Schematic dependence of the string-breaking radius with temperature

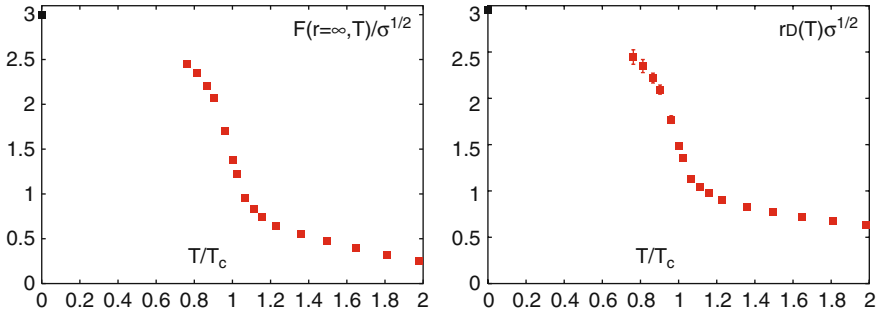

Fig. 5 Lattice results for free energy and screening radius as a function of T

1.3 Color Screening

Above $T = T_c$, we have a medium of unbound color charges and an entirely different mechanism takes over. At all temperatures T above zero, quarks and gluons are *screened*, just as electric charges experience Debye screening in an electromagnetic plasma. This screening occurs with a characteristic radius, which we denote by r_D. It decreases with increasing temperature, as the medium increases in density. Deconfinement is expected to occur when this radius becomes comparable to the average hadron size of 1 fm. Then a given quark can no longer see its former partner in a hadron; instead, it sees many other quarks and antiquarks and therefore can move around freely, without encountering any confinement limit, since it is never 1 fm away from an antiquark.

We would like to use the behavior of the J/ψ to probe if a quark–gluon plasma was formed in the collision [4]. However, as we have seen, the J/ψ and its heavier counterparts have smaller radii than the usual hadrons. Thus, charmonia and bottomonia may be expected to survive beyond the QGP phase transition up to some

higher temperature, at which they will become dissociated. Thus, if we know their sizes as well as the behavior of r_D as a function of T, we can use their dissociation points to determine the temperature and the energy density ϵ of the QGP medium [5], as illustrated in Fig. 6.

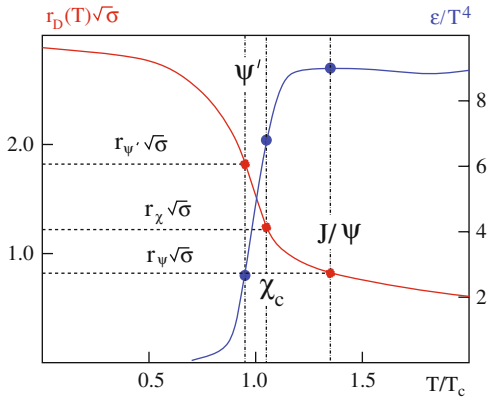

Fig. 6 Quarkonium dissociation as "thermometer" for the quark–gluon plasma

2 Studying Charmonium Dissociation

We now turn to the question of how to determine quantitatively the quarkonium dissociation points in a quark–gluon plasma. Two different approaches were used to address this problem.

- Solve the Schrödinger equation with a temperature-dependent potential $V(r, T)$ or
- calculate the quarkonium spectrum directly in finite temperature lattice QCD.

We shall look at each of these approaches in turn.

2.1 Potential Models for Quarkonium Dissociation

2.1.1 The Schwinger Model

One generalizes the Cornell potential, Eq. (2), to non-zero temperature in the form

$$V(r, T) = \sigma r \left\{ \frac{1 - e^{-\mu r}}{\mu r} \right\} - \frac{\alpha}{r} e^{-\mu r}. \tag{6}$$

The T-dependence of the above equation is in the "screening mass" $\mu(T) = 1/r_D(T)$[6]. Equation (6) gives the correct zero-temperature limit, Eq. (2), for $\mu(T) \to 0$ as $T \to 0$.

To determine the dissociation points, one solves the Schrödinger equation and determines the bound-state energies $M_i(\mu)$. With increasing temperature, the bound state i disappears at some $\mu = \mu_i$. One then uses the temperature dependence of the screening mass from lattice estimates, $\mu(T) \simeq 4\ T$, to determine the T_i. The result of this model is

- the ψ' and χ_c become dissociated around $T \simeq T_c$,
- the J/ψ survives up to about $T \simeq 1.2T_c$.

In both cases, at the dissociation point the binding energy vanishes, while the binding radius diverges.

2.1.2 Lattice Potential Models

Alternatively, one may use lattice results for the temperature dependence of the potential felt by a static quark–antiquark pair to determine the needed potential [7–13]. The static $Q\bar{Q}$ studies start from the partition function Z, which is related to the free energy by $Z = \exp(-\beta F)$; this in turn gives the thermodynamic potentials

$$\begin{aligned} F &= U - TS \\ S &= -\left(\frac{\partial F}{\partial T}\right)_V \\ U(r,T) &= F(r,T) - T\left(\frac{\partial F(r,T)}{\partial T}\right)_V . \end{aligned} \tag{7}$$

Assuming that the internal energy $U(r,T)$ provides the temperature dependence of the heavy quark potential, we use results from $N_f = 2$ lattice QCD and solve the Schrödinger equation. The results obtained from such studies indicate that

- the ψ' and χ_c are dissociated around a temperature $T \simeq 1.1T_c$,
- J/ψ survives up to a temperature $T \simeq 2\ T_c$.

Comparing these results to the ones from the Schwinger model, we see that while there is agreement in the case of the higher excited states, lattice potential models predict a considerably higher dissociation temperature for the J/ψ. The reason for this is that the internal energy $U(r,T)$ leads to much stronger binding than the Schwinger model potential.

It should be noted here that there still is some ambiguity as to whether U or F is the correct potential to be used in the Schrödinger equation. Hence there exist approaches with potentials of the form $aU + (1-a)F$, with $0 \le a \le 1$. Such potentials tend to reduce binding and lower the dissociation temperature as a is decreased.

2.2 *Lattice Studies of Charmonium Survival*

The ideal way to resolve the above ambiguity would be to calculate the $c\bar{c}$ spectrum directly on the lattice, and this is indeed what lattice studies aim to do [14–20]. More specifically, they calculate the $c\bar{c}$ spectrum $\sigma(\omega, T)$ in the appropriate quantum channel, as a function of the temperature T and the $c\bar{c}$ energy ω. Bound states show up as resonances in a plot of σ versus ω. By performing simulations at different temperatures, one can determine the temperature at which a particular peak disappears, i.e., a bound state dissolves. A schematic illustration is shown in Fig. 7. The results presently indicate that

- χ_c is dissociated for $T \geq 1.1T_c$.
- J/ψ persists upto $1.5 < T/T_c < 2.3$.

Thus, on the basis of lattice studies, the following picture emerges: The higher excited states dissociate around $T = T_c$, while the J/ψ survives up to much higher temperature, in accord with the potential model studies based on the internal energy $U(r, T)$.

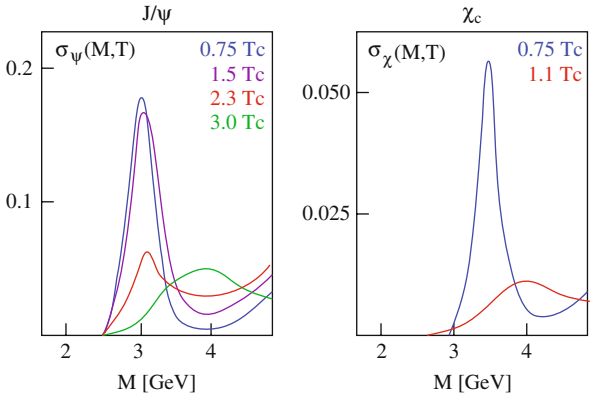

Fig. 7 Schematic view of lattice results for charmonium dissociation

There is, however, a caveat to these calculations. The discretization introduced by the lattice limits the resolution of the peak. Lattice methods are thus useful in determining the position and to some extent the amplitude of the peaks, but determining the peak *widths* remains a challenge, nor is it easy to study the spectrum in the continuum region ($\omega > 4$ GeV).

3 Dynamics of Quarkonium Dissociation

We have seen in the previous discussion that the J/ψ, the vector ground state of charmonium family, is very tightly bound. Its binding energy, i.e., the energy difference between J/ψ mass and open charm threshold, $\Delta E_{J/\psi}$, is considerably larger than the typical non-perturbative hadronic scale Λ_{QCD},

$$\Delta E_{J/\psi} = 2M_D - M_{J/\psi} = 0.6\ \text{GeV} \gg \Lambda_{QCD}.\sim 0.2\ \text{GeV}. \tag{8}$$

Consequently the size of J/ψ is much smaller than that of typical hadron,

$$r_{J/\psi}\ \sim\ 0.25\ \text{fm} \ll \Lambda_{QCD}^{-1}\ \sim\ 1\ \text{fm}. \tag{9}$$

We now want to consider by what kind of dynamical interaction such a state can be dissociated. Because of the small spatial size, the J/ψ can only be resolved by a sufficiently hard probe. Moreover, because of its high binding energy, only a sufficiently energetic projectile can break the binding. The previous study of global medium effects had led to the conclusion that only a hot deconfined medium, consisting of colored quarks and gluons, is capable of dissociating the charmonium vector ground state. We now want to study this on a microscopic level.

In a deconfined medium, the constituents are unbound partons, whereas in a confined medium the constituents are hadrons. Such thermal hadrons are incapable of causing collisional dissociation of J/ψ. Let us illustrate this point.

Consider the collision of a J/ψ with a normal hadron. Because of the small characteristic J/ψ size, only a hard partonic constituent of the hadron can see the J/ψ and interact with it. In other words, J/ψ collisions with ordinary hadrons probe the local partonic structure of these "light" hadrons, not their global aspects such as mass, size, or overall momentum. The parton nature of the interaction is illustrated in Fig. 8.

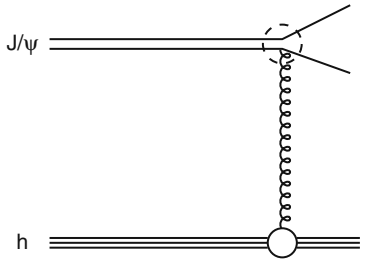

Fig. 8 Schematic view of the interaction of a normal hadron with a J/ψ

To see the effect of this more quantitatively [21], we take an ideal pion gas as the confined medium. The momentum distribution of the pions at a temperature T follows $f(p) \sim \exp(-|p|/T)$, giving the pions an average momentum $\langle p\rangle \sim 3T$. Now the gluon momentum distribution inside a hadron as determined by deep inelastic lepton–hadron scattering is given by the parton distribution function $g(x)$; here $x = 2k_g/\sqrt{s}$, with k_g for the gluon momentum, so that x may be thought of as the fraction of the incident hadron's momentum carried by the gluon. For the pionic gluon it takes the form

$$g(x)\ \sim\ (1-x)^3. \tag{10}$$

The resulting average gluon momentum in the hadron thus becomes

$$\langle k_g \rangle = p_h \cdot \frac{\int_0^1 dx\ x\ g(x)}{\int_0^1 dx\ g(x)}. \tag{11}$$

With Eq. (10) and $p_h = 3T$ for the momentum of the incident hadron, we obtain

$$\langle k_g \rangle_h = \frac{p_h}{5} = \frac{3T}{5} \leq 0.1\ \text{GeV}, \tag{12}$$

where we have assumed $T < 175\,\text{MeV}$ for the temperature of the hadronic medium. Thus gluons bound inside the hadronic constituents of confined matter are much too soft to cause the dissociation of a J/ψ.

On the other hand, in a deconfined medium, such as an ideal QGP, the gluons are free and distributed according to a thermal distribution $f(k_g) \sim \exp(-k_g/T)$, which gives

$$\langle k_g \rangle \ \sim\ 3T, \tag{13}$$

so that for $T \ \geq\ 1.2\ T_c \simeq 0.63\,\text{GeV}$, the gluons are hard enough to overcome the J/ψ binding.

We have thus noticed that deconfinement results in a hardening of the relevant gluon momentum distributions. More generally speaking, the onset of deconfinement will lead to parton distribution functions which are different from those for free hadrons, as determined by DIS experiments. Since hard gluons are needed to resolve and dissociate J/ψs, one can use J/ψs to probe the in-medium gluon hardness and hence the confinement status of the medium.

This qualitative picture can be made quantitative by short distance QCD calculations [21–23]. One has to calculate first the cross section for gluon dissociation of J/ψ, a QCD analogue of the photo-effect. This can be carried out using the operator product expansion, which is essentially a multipole expansion for the charmonium quark–antiquark system. Figure 8 shows the relevant diagram for the calculation of inelastic J/ψ–hadron cross section. The upper part of the figure corresponds to J/ψ dissociation by gluon interaction. The cross section for this process has the form

$$\sigma_{g-J/\psi}\ \sim\ \frac{1}{m_c^2}\frac{(k/\Delta E_\psi - 1)^{3/2}}{(k/\Delta E_\psi)^5}, \tag{14}$$

with $\Delta E_{J/\psi} = 2M_D - M_{J/\psi}$. The corresponding cross section for the hadron dissociation is obtained by convoluting this gluon dissociation cross section with the gluon distribution function $g(x)$ of the incident hadron. For J/ψ–meson interactions, this leads to the form

$$\sigma_{h-J/\psi}\ \simeq\ \sigma_{\text{geom}}\left(1 - \frac{\lambda_0}{\lambda}\right)^{5.5}, \tag{15}$$

with $\lambda \simeq (s - M_\psi^2)/M_\psi$ and $\lambda_0 \simeq (M_h + \Delta E_\psi)$, where $\sqrt{s}$ is the CMS energy of the J/ψ–hadron system. Here $\sigma_{\rm geom} \simeq \pi r_{J/\psi}^2 \simeq$ 2 mb is the geometric J/ψ cross section and M_h denotes the mass of the incident meson. Figure 9 compares the two dissociation cross sections, J/ψ dissociation by gluons (gluo-effect) and by pions, as a function of projectile momentum k incident on stationary J/ψ, as given by Eqs. (14) and (15). The gluon cross section shows the typical photo-effect form, vanishing until the gluon momentum k_g reaches the binding energy $\Delta E_{J/\psi}$; it peaks just a little later ($\lambda_g \sim r_{J/\psi}$) and then vanishes again when sufficiently hard gluons just pass through the (comparatively larger) charmonium bound states ($\lambda_g \ll r_{J/\psi}$). In contrast, the J/ψ–hadron inelastic cross section remains negligibly small until rather high hadron momenta (3–4 GeV). In a thermal medium such momenta correspond to temperatures of more than 1 GeV. In other words, in a confined medium in the temperature range of the order of a few hundred MeV the J/ψ should survive, but it should become dissociated in a hot deconfined medium. Confined media in the temperature range of few hundred MeV are thus essentially transparent to a J/ψ, while a deconfined medium of the same temperature is opaque to J/ψ's and very efficiently dissociates them.

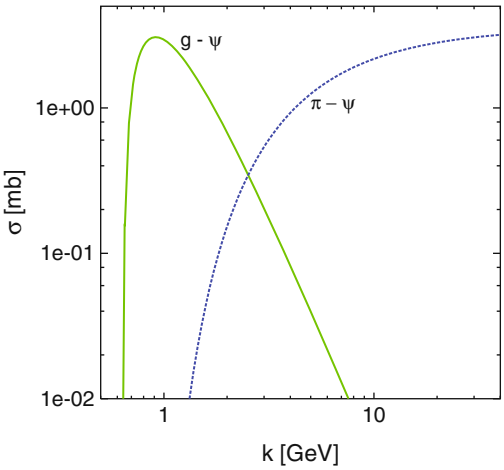

Fig. 9 Cross sections for J/ψ dissociation by gluons versus pions

4 Quarkonium Production in Nuclear Collisions

The aim of ultra-relativistic nuclear collisions is to study color deconfinement and the resulting quark–gluon plasma in the laboratory. We want to use quarkonia produced in the collision as a probe to study the medium produced in the collision. Both the quarkonium states and the medium to be probed require a "finite formation time," so we have to look at the evolution aspects in both cases. Let us first consider

the issue of charmonium production in hadron–hadron collisions and then turn to nuclear targets.

4.1 Quarkonium Production in Hadronic Collisions

Quarkonium production in hadron–hadron collisions occurs in three stages. The first stage is the production of $c\bar{c}$ pair. Because of the large quark mass ($m_c \sim 1.3\,\text{GeV}$) this process can be treated as a hard process and is well described by perturbative QCD. A parton from the projectile interacts with one from the target; the (non-perturbative) parton distributions within the hadrons are determined empirically in other reactions, e.g., by deep inelastic lepton–hadron scattering. At high energy the process of c$\bar{c}$ production dominantly occurs by gluon fusion, $gg \rightarrow c\bar{c}$ (see Fig. 10).

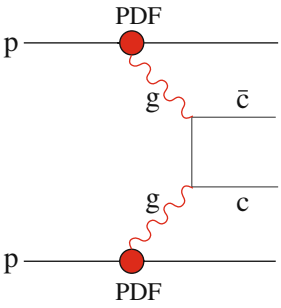

Fig. 10 Lowest order Feynman diagram for $c\bar{c}$ production through gluon fusion

The $c\bar{c}$ in general is in a color-octet state. It has to neutralize its color in order to leave the interaction zone and form a physical resonance like J/ψ or ψ'. In the second stage, color neutralization occurs by interaction with the surrounding color field. This results finally in the third stage of a physical bound state. Both the second and third stages are non-perturbative in nature.

On a fundamental theoretical level, color neutralization is not yet fully understood, but there are several models, color singlet [24], color octet [25, 26], and color evaporation [27–30]. The color evaporation model provides a particularly simple and experimentally well-supported phenomenological approach. In the evaporation process, the $c\bar{c}$ can either combine with light quarks to form open charm mesons (D and $\bar{D}$) or bind with each other to form a hidden charm (charmonium) state. A fixed fraction of the subthreshold $c\bar{c}$ production is used in charmonium production. The basic quantity in this picture is the total subthreshold charm cross section $S_{c\bar{c}}$, obtained by integrating the perturbative $c\bar{c}$ production cross section σ over the mass window from $2m_c$ to $2m_D$. Since at high energy, the dominant part of $S_{c\bar{c}}$ comes from gluon fusion (Fig. 10), we can write

$$S_{c\bar{c}}(s) \simeq \int_{2m_c}^{2m_D} d\hat{s} \int dx_1\, dx_2\, g_p(x_1)\, g_t(x_2)\, \sigma(\hat{s})\, \delta(\hat{s} - x_1 x_2 s), \qquad (16)$$

with $g_p(x)$ and $g_t(x)$ denoting the gluon densities and x_1 and x_2 the fractional momenta of the gluons from projectile and target, respectively; σ is the $gg \to c\bar{c}$ cross section.

As mentioned, the basic assumption of the color evaporation model is that the production cross section for any particular charmonium state is a fixed fraction of the subthreshold charm cross section,

$$\sigma_i(s) = f_i \; S_{c\bar{c}}(s), \tag{17}$$

where f_i is an energy-independent constant to be determined empirically. It follows that the energy dependence of the production cross section for any charmonium state is predicted to be that of the perturbatively calculated subthreshold charm cross section. As a further consequence the production ratios of different charmonium states

$$\frac{\sigma_i(s)}{\sigma_j(s)} = \frac{f_i}{f_j} = \text{constant} \tag{18}$$

must be energy independent. Both these predictions have been compared in detail to charmonium hadroproduction data over a wide range of energies [31, 32]. They are found to be well supported, both in the energy dependence of the cross sections and in the constancy of the relative species abundances.

Before turning to the topic of quarkonium production in hadron–nucleus collisions, let us consider the relevant timescales for the J/ψ formation.

The formation of a $c\bar{c}$ pair requires a time $\tau_{c\bar{c}} = 1/2m_c = 0.05$ fm. The produced $c\bar{c}$ pair is in a color-octet state. To form a physical resonance state, it has to neutralize its color. The color-octet model [25, 26] proposes that the color-octet $c\bar{c}$ combines with a soft collinear gluon to from a color-singlet $(c\bar{c} - g)$ state. After a short relaxation time τ_8 this pre-resonance $(c\bar{c} - g)$ turns into physical resonance by absorbing the accompanying gluon, with similar formation processes for the other resonances, such as χ_c and ψ' production. The color-octet model encounters difficulties if the collinear gluons are treated perturbatively, indicating once more that color neutralization seems to require non-perturbative elements. However it does provide a conceptual basis for the evolution of the formation process.

The color neutralization time τ_8 of the pre-resonant state can be estimated by the lowest momentum possible for the confined gluons $\tau_8 \simeq \left(2m_c \Lambda_{QCD}\right)^{-1/2} \simeq 0.25$ fm. The resulting scales of J/ψ formation are illustrated in Fig. 11. The formation time for the actual physical ground state J/ψ is presumably somewhat larger

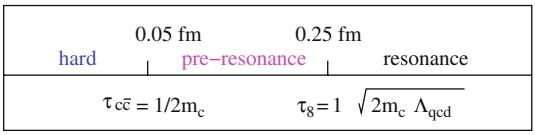

Fig. 11 Evolution of J/ψ formation in a hadron–hadron collision

than τ_8, although $r_{J/\psi} \simeq \tau_8$, the heavy c quarks move non-relativistically. For the larger higher excited states, the formation time will then be correspondingly still larger.

4.2 Quarkonium Production in p–A and A–A Collisions

Let us now turn to nuclear collisions. Both in p–A and A–A interactions there will be pre-resonant absorption in nuclear matter. In nucleus–nucleus collisions, however, there can be in addition a substantial amount of a produced "secondary medium," and testing this medium is in fact our main objective.

The creation of the medium and production of the probe lead to two distinct formation scales. In p–A collision there is no formation time for the medium, so that such collisions provide a tool to probe charmonium production, evolution, and absorption in confined matter.

Nuclear effects can arise in all the evolution stages of J/ψ production, and a number of different phenomena have to be taken into account.

- The presence of other nucleons in the nucleus can modify the initial state parton distribution functions, which enter in the perturbative $c\bar{c}$ production process, as shown in Fig. 10. This can lead to a decrease (shadowing) or to an increase (antishadowing) of the production rate.
- Once it is produced, the $c\bar{c}$ pair in its evolution will traverse the nuclear matter; it can suffer absorption both in the pre-resonance and in the resonance stage caused by successive interactions with the target nucleons.

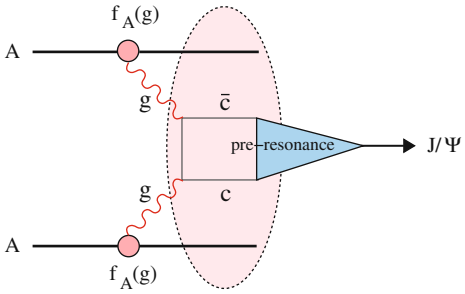

Fig. 12 J/ψ production in a nuclear medium

Hence J/ψ production in a nuclear medium is modified as compared to hadronic collisions. The modification occurs before any QGP formation and is thus independent of the effects due to a deconfined medium having free quarks and gluons. If we want to use J/ψ production and its suppression in a nuclear collision as a potential signature of the QGP formation, all normal nuclear effects must first be taken into account. Only then can charmonium suppression serve as a probe to test the confining status of the produced "secondary medium" in nuclear collisions.

So an essential question is how to account for the effects of the nuclear medium initially present on the production. The basis for this, both in theory and in experiment, is the measurement of dilepton, open charm, and charmonium production in p–A or d–A collisions. These collisions thus provide a crucial tool to understand quarkonium production in nuclear collisions.

The procedure to be used for such studies is the following:

- The initial state parton distribution functions in nuclear matter are determined by open charm and dilepton production in p–A/d–A collisions in the relevant kinematic region.
- The Glauber model then is used to determine the pre-resonance absorption of the J/ψ and ψ' by the target nucleon in p–A/d–A in the relevant kinematic region.

It is thus clear that p–A or d–A collision experiments are an absolutely essential tool for the analyis of quarkonium production in nuclear collisions.

4.3 Sequential Quarkonium Suppression

There is a further important and, as it turns out, crucial feature observed in J/ψ hadroproduction. The J/ψ actually measured in hadron–hadron collisions are not all directly produced $1S$ charmonium states; rather, they have three distinct origins. About 60% of them are indeed directly produced 1S charmonium states, but the rest are feed-down from higher excited states. About 30% come from the decay $\chi_c(1P) \rightarrow J/\psi +$ anything and the remaining 10% from $\psi'(2S) \rightarrow J/\psi +$ anything. In both cases, the decay widths of the involved higher excited states are extremely small ($< 1\,\mathrm{MeV}$), so that their lifetimes are very long and the decay occurs long after the interaction. The presence of any medium in nuclear collisions would therefore affect these excited states themselves and not their products, and we had seen above that excited states are dissociated before the ground state. This has a direct consequence on the nature of J/ψ suppression by deconfinement. In a thermal QCD medium, we should expect that with increasing temperature or energy density, first the J/ψ originating from ψ' decay and then those from χ_c decay will disappear. Only a considerably higher temperature would be able to remove the directly produced J/ψs. Such a stepwise onset of suppression with specified threshold temperatures is perhaps the most characteristic feature predicted for charmonium production in nuclear collisions. It is illustrated schematically in Fig. 13, where we have defined the J/ψ survival probability to be unity if the production rate suffers only the estimated normal nuclear suppression. The generic suppression pattern shown here will of course be softened by nuclear profile effects, impact parameter uncertainties, etc. On the other hand, this could be partially compensated if there is a discontinuous onset of deconfinement as a function of energy density of the medium.

We had seen above how to calculate the quarkonium dissociation points which specify the temperature and thus also the energy density of the medium, thereby

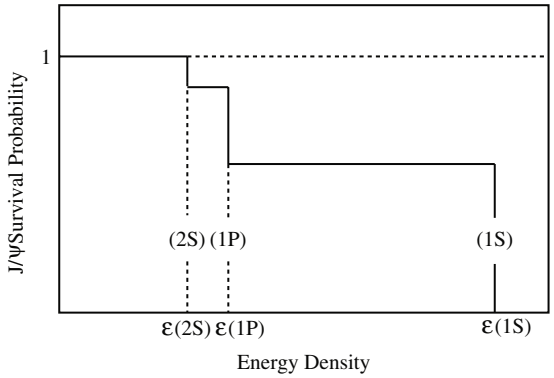

Fig. 13 Sequential J/ψ suppression

serving as a QGP thermometer. Potential model studies based on the heavy quark internal energy, as well as direct lattice QCD calculations gave as dissociation temperatures $T \simeq 1.1\, T_c$ for ψ' and χ_c and $T \geq 1.5$–$2\, T_c$ for J/ψ. If this is correct, then the direct $J/\psi(1S)$ survives up to about $\epsilon \geq 10 - 20\ \mathrm{GeV/fm^3}$. Consequently, all anomalous suppression observed at SPS and RHIC must be due to the dissociation of higher excited states χ_c and ψ' [33]. The suppression onset for this is predicted to lie around $\epsilon \simeq 1\ \mathrm{GeV/fm^3}$, and once these are gone, only the unaffected J/ψ (1S) production remains. Hence the J/ψ survival probability (once normal nuclear effects are taken into account) should be same for central Au–Au at RHIC as for central Pb–Pb collisions at SPS.

4.4 Charmonium Regeneration

In this section we want to investigate the possibility that the medium produced in high-energy nuclear collision differs from the deconfined state of matter studied in finite temperature QCD. The basic idea here is that nuclear collisions initially produce more than the thermally expected charm and this excess, if it survives, may lead to a new form of combinatorial charmonium production at hadronization [34–36].

In the QGP argumentation, a crucial aspect was that the charmonia, once dissociated, cannot be recreated at the hadronization stage, because of the extremely low thermal abundance of charm quarks in an equilibrium QGP. The thermal production rate for a $c\bar{c}$ pair relative to a pair of light quarks is

$$\begin{aligned} \frac{n_{c\bar{c}}}{n_{q\bar{q}}} &\simeq \exp -(2m_c - 2m_q/T_c\,) \\ &\simeq \exp(-2m_c/T_c) \simeq 3.5 \times 10^{-7}, \end{aligned} \tag{19}$$

with $m_c = 1.3\,\text{GeV}$ for charm quark mass and $T_c = 175\,\text{MeV}$ for the transition temperature. The initial charm production in high-energy hadronic collisions is, however, a hard non-thermal process, and the resulting rates calculated from perturbative QCD are considerably larger than the thermal rate. Moreover, in A–A interactions the resulting $c/\bar{c}$ production rate grows with the number of binary collision N_{coll}, while the light quark production rate, being a soft process, grows as the number of participant nucleons, i.e., much slower. At high collision energies, the initial charm abundance in A–A collisions is thus very much higher than the thermal value. Now the question is, what happens to this in course of the collision evolution?

The basic assumption of the regeneration approach is that the initial charm excess is maintained throughout subsequent evolution, i.e., the initial chemical non-equilibrium will persist up to the hadronization point. In charmonium hadroproduction, J/ψ are formed because some of the $c\bar{c}$ pairs produced in a given collision form the corresponding bound state. In a collective medium formed through the superposition of many nucleon–nucleon (N–N) collisions, such as a quark–gluon plasma, a c quark from one N–N collision can in principle also bind with a $\bar{c}$ from another N–N collision ("new" pairs) to create a J/ψ. This pairing provides an "exogamous" charmonium production mechanism, in which the c and $\bar{c}$ in a charmonium state have different parents, in contrast to "endogamous" production in p–p collision. At sufficiently high energies this can lead to an enhancement in J/ψ production in A–A collisions compared to scaled p–p rates [34–36], provided the overall charm density is sufficiently high at hadronization and provided the binding probability between charm quarks from different sources is large enough.

Whether or not such enhancement becomes significant depends on two factors. On one hand, the initial charm oversaturation must be preserved so that the total charm abundance is non-thermal. On the other hand, it is necessary that the recombination between charm quarks from different parents to charmonium (J/ψ) is strong enough. Here it is generally assumed that the final hadronization occurs according to the available phase space. Thus the number of statistically recombined J/ψ has the form $N_{J/\psi} \sim N^2_{c\bar{c}}$, growing quadratically in the number of $c\bar{c}$ pairs. This implies

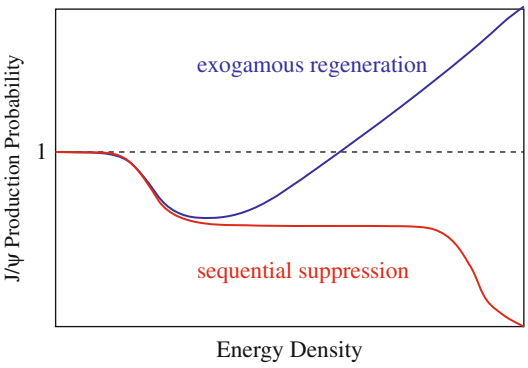

Fig. 14 Statistical J/ψ regeneration versus sequential J/ψ suppression

that the hidden to open charm ratio, e.g., $N_{J/\psi}/N_D \sim N_{c\bar{c}}/N_h$, increases with energy, in contrast to the energy-independent form obtained for the fully equilibrated QGP, or to the decrease predicted by color screening. The prediction for J/ψ production by regeneration is compared in Fig. 14 to that from sequential suppression.

5 Conclusion

Statistical QCD predicts the existence of a new state of nuclear matter, the quark–gluon plasma (QGP), at very high temperatures and/or densities. This medium, in contrast to hadronic matter, is capable of dissociating quarkonia, so that *quarkonium suppression* may be taken as a sign of QGP formation in nuclear collisions [4]. Furthermore, different quarkonia dissociate at different temperatures; the dissociation pattern thus serves as a "thermometer" for the QGP. It is therefore important to obtain precise predictions for these dissociation points, and for this, one can turn to either of two approaches: potential models or lattice studies. The former have the problem that the results are dependent on the type of potential chosen, while the latter so far suffer from the fact that lattice spacing and statistics limit the resolution of peak widths in the spectrum. It is also not easy to identify the continuum region of the spectrum on the lattice.

But what happens in case of relativistic nuclear collisions in the laboratory? If there is no regeneration of the dissociated charmonia, J/ψ remains as an external probe, and the sequential suppression pattern of the J/ψ can then serve as a tool to determine the energy density and the temperature of the produced medium. On the other hand, if there is J/ψ production through statistical combination of c and $\bar{c}$ from different collisions, leading to an overall J/ψ enhancement, this would clearly indicate the thermalization of the produced medium on a pre-hadronic level. However, charmonia could then no longer serve as a thermometer to charaterize the primordial medium. Data from LHC, soon to come, will certainly play a decisive role in settling the issue.

References

1. E. Eichten et al.: Phys. Rev. **D17**, 3090 (1978) 180
2. E. Eichten et al.: Phys. Rev. **D 21**, 203 (1980) 180
3. For a recent review, see H. Satz: J. Phys. **G 32**, R25 (2006) 181
4. T. Matsui and H. Satz: Phys. Lett. **B 178**, 416 (1986) 183, 196
5. For a recent review, see H. Satz: Nucl. Phys. **A 783**, 249c (2007) 184
6. F. Karsch, M.-T. Mehr and H. Satz: Z. Phys. **C 37**, 617 (1988) 185
7. S. Digal, P. Petreczky and H. Satz: Phys. Lett. **B 514**, 57 (2001) 185
8. E. Shuryak and I. Zahed: Phys. Rev. **D 70**, 054507 (2004)
9. C.-Y. Wong: Phys. Rev. **C 72**, 034906 (2004)
10. C.-Y. Wong: hep-ph/0509088
11. C.-Y. Wong: Phys. Rev. **C 76**, 014902 (2007)
12. W. Alberico et al.: Phys. Rev. **D 72**, 114011 (2005)
13. S. Digal et al.: Eur. Phys. J. **C 43**, 71 (2005) 185

14. T. Umeda et al.: Int. J. Mod. Phys. **A16**, 2215 (2001) 186
15. M. Asakawa and T. Hatsuda: Phys. Rev. Lett. **92**, 012001 (2004)
16. S. Datta et al.: Phys. Rev. **D 69**, 094507 (2004)
17. H. Iida et al.: PoS LAT2005, 184 (2006)
18. A. Jacovac et al.: Phys. Rev. **D 75**, 014506 (2007)
19. R. Morrin et al.: PoS LAT2005, 176 (2006)
20. G. Aarts et al.: Nucl. Phys. **A 785**, 198 (2007) 186
21. D. Kharzeev and H. Satz: Phys. Lett. **B334**, 155 (1994) 187, 188
22. M.E. Peskin: Nucl. Phys. **B 156**, 365 (1979)
23. G. Bhanot and M.E. Peskin: Nucl. Phys. **B 156**, 391 (1979) 188
24. R. Baier and R. Rückl: Z. Phys. **C 19**, 251 (1983) 190
25. G.T. Bodwin, E. Braaten and G.P. Lepage: Phys. Rev. **D 51**, 1125 (1995) 190, 191
26. E. Braaten and S. Fleming: Phys. Rev. Lett. **74**, 3327 (1995) 190, 191
27. M.B. Einhorn and S.D. Ellis: Phys. Rev. **D12**, 2007 (1975) 190
28. H. Fritzsch: Phys. Lett. **67B**, 217 (1977)
29. M. Glück, J.F. Owens and E. Reya: Phys. Rev. **D17**, 2324 (1978)
30. J. Babcock, D. Sivers and S. Wolfram: Phys. Rev. **D18**, 162 (1978) 190
31. H. Satz and X.-N. Wang (eds.): *Hard Processes in Hadronic Interactions*, Int. J. Mod. Phys. **A 10**, 2881 (1995) 191
32. M. Mangano et al. (Eds.): *Hard Probes in Heavy-Ion Collisions at the LHC*, CERN Yellow Report 2004–09, Geneva (2004) 191
33. D. Kharzeev, F. Karsch and H. Satz: Phys. Lett. **B 637**, 75 (2006) 194
34. P. Braun-Munzinger and J. Stachel: Nucl. Phys. **A690**, 119 (2001) 194, 195
35. R.L. Thews et al.: Phys. Rev. **C 63**, 054905 (2001)
36. L. Grandchamp and R. Rapp: Nucl. Phys. **A 709**, 415 (2002) 194, 195

Quarkonium Production and Absorption in Proton–Nucleus Collisions

Carlos Lourenço, Pietro Faccioli and Hermine K. Wöhri

1 Introduction

Lattice QCD calculations [1] predict that, at sufficiently large energy densities, hadronic matter undergoes a phase transition to a "plasma" of deconfined quarks and gluons (QGP). Considerable efforts have been invested since 1986 in the study of high-energy heavy-ion collisions to reveal the existence of this phase transition and to study the properties of strongly interacting matter in the new phase, in view of improving our understanding of confinement, a crucial feature of QCD. The study of quarkonium production and suppression is among the most interesting investigations in this field, because the calculations indicate that the QCD binding potential is screened in the QGP phase, the screening level increasing with the energy density of the system. Given the existence of several quarkonium states, of different binding energies, it is expected that they will be consecutively "dissolved" (into open charm or beauty mesons) above certain energy density thresholds [2, 3]. The experimental observation of such successive "thresholds" in quarkonium melting, with the ψ' and χ_c states being suppressed more easily than the more strongly bound J/ψ state, is considered a "smoking gun" signature of deconfinement.

Until now, such a "spectral analysis" of the quarkonium production yields has been performed in several collision systems (from light to heavy nuclei) and in several collision centralities (from peripheral to central), but has been limited to the J/ψ and ψ' states. The Upsilon states have too small production cross sections to be studied at the relatively low energies currently available (this situation will change once the LHC will start providing Pb–Pb collisions). On the other hand, the experimental detection of the χ_c meson has not been feasible in heavy-ion

C. Lourenço (✉)
CERN, CH-1211 Geneva 23, Switzerland, carlos.lourenco@cern.ch

P. Faccioli
LIP, Av. Elias Garcia 14, 1000-149 Lisbon, Portugal, pietro.faccioli@cern.ch

H.K. Wöhri
LIP, Av. Elias Garcia 14, 1000-149 Lisbon, Portugal, hermine.woehri@cern.ch

Lourenço, C. et al.: *Quarkonium Production and Absorption in Proton–Nucleus Collisions*. Lect. Notes Phys. **785**, 199–218 (2010)
DOI 10.1007/978-3-642-02286-9_6

collisions, in particular given the difficulty in detecting the photon emitted in the $\chi_c \rightarrow J/\psi + \gamma$ radiative decay, among the large yield of photons from π^0 decays.

Most of the experimental information on quarkonium production and suppression in heavy-ion collisions has been provided, so far, by NA38, NA50, and NA60 at the SPS (J/ψ and ψ'), and by PHENIX at RHIC (only J/ψ). For the purpose of this chapter, let us mention two of the observations made so far. First, it has been seen [4] that the J/ψ production yield, relative to the yield of high-mass Drell–Yan dimuons, is significantly suppressed in central Pb–Pb collisions, with respect to the "normal nuclear absorption reference", established on the basis of proton–nucleus measurements, which successfully describes the most peripheral Pb–Pb measurements and the S-U J/ψ suppression pattern. Second, it has been observed [5] that the suppression happens mostly at low transverse momentum, p_{T}; the high-p_{T} J/ψ's (per Drell–Yan dimuon) do not show any clear drop from peripheral to central Pb–Pb collisions.

In the remaining of this chapter, we will discuss three issues that should be seriously taken into consideration before we can consider the aforementioned observations as convincing evidence showing, beyond reasonable doubt, that a quark–gluon plasma is formed in heavy-ion collisions at SPS energies. We will start by reminding that the observed J/ψ yield, and its suppression, cannot be immediately interpreted as due to the production or absorption of J/ψ mesons in the nucleus–nucleus collisions; a large fraction of the production yield results from decays of ψ' and (more importantly) χ_c mesons, which are surely affected by the nuclear medium in different ways than the directly produced J/ψ. We will then show evidence that the J/ψ is *not unpolarized*, as currently assumed in the studies of J/ψ suppression. This is an important issue because the polarization seems to significantly change with p_{T}, from longitudinal at low p_{T} to transverse at high p_{T}. This means that the previously reported p_{T} distributions, the average p_{T} vs. nuclear target in p-nucleus collisions, and the p_{T} dependence of the J/ψ suppression in heavy-ion collisions, might be biased by an incorrect p_{T}-dependent acceptance correction and would change if the analysis would be redone with acceptances derived from a Monte Carlo simulation based on a more realistic polarization scenario. Finally, we will address the question of the energy dependence of the J/ψ break-up cross section, by analysing proton–nucleus measurements provided by several experiments, using the Glauber formalism and incorporating nuclear modifications in the parton densities. We will show that there is no reason to assume that the "J/ψ absorption cross section" derived from p-nucleus data collected at 450 GeV is suitable to calculate the normal nuclear absorption baseline in the studies of the heavy-ion data collected at 158 GeV. Several other issues could and should be studied in detail; we only selected these three specific topics because there has been recent progress in their study. They are examples of the kind of work we must perform to place on more solid ground the "anomalous observations" derived from the heavy-ion measurements.

2 J/ψ Feed-Down Fractions

It is known since long that a significant fraction of the J/ψ mesons observed in elementary collisions are, in fact, produced by χ_c radiative decays and ψ' hadronic decays. Given the larger sizes of the χ_c and ψ' charmonium states, it is natural to expect that they suffer a stronger absorption than the 1S state when traversing nuclear matter, as indeed has been experimentally observed in the ψ' case. However, the detailed implications of these feed-down contributions in the understanding of the "normal nuclear absorption" of the J/ψ have not really been studied until now. Furthermore, it has been predicted that the ψ' and χ_c states are easier to "melt" than the more strongly bound J/ψ state, when immersed in a QGP of a certain energy density. Then, it is quite conceivable that the J/ψ production yield measured in heavy-ion collisions shows a significant level of suppression even if the produced matter under scrutiny has not reached high enough energy densities to melt the directly produced J/ψ state. In particular, the J/ψ suppression pattern measured at the SPS and at RHIC might be exclusively due to the melting of the ψ' and χ_c states [6].

While the existence of these elements and the recognition of their crucial importance has been frequently mentioned in the relevant literature, until very recently there were no solid numbers concerning the J/ψ feed-down fractions, often assumed to be 10 % for the ψ' and 30 or 40 % for the χ_c, usually without mentioning experimental measurements or their uncertainties. The situation became even less clear when the HERA-B collaboration reported a J/ψ feed-down fraction from χ_c decays of around 20 %, considerably lower than the previously assumed values. A significant clarification has been provided by a recent study of all available measurements [7], which we briefly summarize here. This should not be seen as "the final word" but represents a major step forward with respect to the previous confusing status.

We start by defining the "feed-down fractions". The fraction of indirectly produced J/ψ's from ψ' decays is defined with respect to the total (inclusive) J/ψ yield as follows:

$$R(\psi') = \frac{N(J/\psi \text{ from } \psi')}{N_{\text{incl}}(J/\psi)} = \frac{\sigma(\psi') \cdot B(\psi' \to J/\psi X)}{\sigma(J/\psi)} \quad . \tag{1}$$

Most experiments measure the J/ψ and ψ' dilepton decays, reporting results for the yield ratio

$$\rho(\psi') = \frac{\sigma(\psi') \cdot B(\psi' \to l^+l^-)}{\sigma(J/\psi) \cdot B(J/\psi \to l^+l^-)} \quad . \tag{2}$$

This quantity is directly related to the ψ'-to-J/ψ feed-down fraction, $R(\psi')$, through a simple combination of branching ratios,

$$R(\psi') = \left[\frac{B(J/\psi \to l^+l^-)}{B(\psi' \to l^+l^-)} \, B(\psi' \to J/\psi \; X) \right] \rho(\psi') \quad , \tag{3}$$

the value in parentheses being 4.53 ± 0.13 [8].

$R(\chi_c)$ is defined analogously to Eq. (1), dividing the number of J/ψ's resulting from the $\chi_c \to J/\psi \; \gamma$ radiative decays by the total J/ψ yield.

2.1 Selected Measurements

The experiments mentioned in Table 1 provided the ψ' and χ_c hadroproduction measurements we used to evaluate the corresponding fractions of indirectly produced J/ψ's. More measurements exist but we decided to restrict our analysis to a sub-sample of results, for reasons explained in detail in [7]. Essentially, we only analysed measurements performed "at midrapidity", given that the forward data, collected with nuclear targets, exhibit a much stronger nuclear absorption than the corresponding midrapidity values. This means, in particular, that the data obtained in pion–nucleus collisions, mostly collected at high x_F, were excluded from our analysis. A broader analysis of the existing measurements, taking into account possible kinematic dependences induced by nuclear effects, remains to be done.

The current experimental knowledge concerning the ψ'-to-J/ψ cross-section ratio and its nuclear dependence in proton–nucleus collisions is essentially determined by the measurements performed by NA50 and NA51 at the CERN-SPS, and by E866 at Fermilab, using several target nuclei. The J/ψ and ψ' results of E866 were reported as ratios between the yields obtained with heavy and light targets (W/Be and Fe/Be), as a function of x_F. These measurements provide heavy-over-light *ratios* of $\rho(\psi')$, which do not help determining the feed-down fraction value but constrain the difference between the nuclear absorption rates of the two charmonium states, a factor that has to be taken into account when using data collected with nuclear targets. The HERA-B 2003 $R(\chi_c)$ results [15] include a systematic uncertainty (of around 10 %) due to the dependence of the detector's acceptance on the assumed J/ψ polarization, taking into account that J/ψ's from χ_c decays

Table 1 Global features of the measurements we considered in our study of the $R(\psi')$ and $R(\chi_c)$ feed-down fractions

Experiment	Collision system	E_{beam} [GeV]	Phase space	$\langle x_F \rangle$
NA51 [9]	p-H/D	450	$-0.4 < y_{\text{cm}} < 0.6$	$\simeq 0$
NA50 96/98 [10]	p-(5 nuclei)	450	$-0.5 < y_{\text{cm}} < 0.5$	$\simeq 0$
NA50 2000 [11]	p-(6 nuclei)	400	$-0.425 < y_{\text{cm}} < 0.575$	$\simeq 0$
E866 [12]	p-Be/Fe/W	800	$-0.1 < x_F < 0.8$	$\simeq 0.3$
E705 [13]	p-Li	300	$-0.1 < x_F < 0.5$	$\simeq 0.2$
HERA-B 2000 [14]	p-C/Ti	920	$-0.25 < x_F < 0.15$	-0.035
HERA-B 2003 [15]	p-C/W	920	$-0.35 < x_F < 0.15$	-0.065
ISR [16–18]	pp	$\sqrt{s} \approx 58$ (avg.)	$y_{\text{cm}} \simeq 0$	0
CDF [19]	$p\bar{p}$	$\sqrt{s} = 1800$	$\lvert y_{\text{cm}} \rvert < 0.6$	0

should have a polarization different from the directly produced ones. This effect was not considered by the previous experiments, given the poor statistical accuracy of their measurements.

2.2 J/ψ Feed-Down from ψ' Decays

The experimental points selected for the determination of the J/ψ feed-down contribution from ψ' decays are shown in Fig. 1. It is worth remarking that the ψ' is much more strongly absorbed by the nuclear medium than the J/ψ.

In order to determine the ψ'-to-J/ψ feed-down fraction in pp collisions, $R^0(\psi')$, all measurements were simultaneously fitted within the framework of the Glauber formalism [20], using the so-called ρL parametrization:

$$\sigma(pA \to \psi) \,/\, A\,\sigma(pN \to \psi) \;=\; \exp(-\sigma_{\text{abs}}\,\rho\,L) \quad ,$$

where ρ is the nuclear density and L is the nuclear path length traversed by the charmonium state of absorption cross section σ_{abs}. The $\rho\,L$ values were determined through a Glauber calculation, for each nuclear target, taking into account the appropriate nuclear density profiles, as described in [11], corresponding to an average nuclear density of 0.17 fm^{-3}. The fit provides two parameters: the $R^0(\psi')$ "reference" feed-down fraction (corresponding to $L = 0$) and the difference between the ψ' and J/ψ absorption cross sections, where the J/ψ term does not include the ψ' decay contribution (to remove auto-correlation effects). A global fit to all data points leads to the dashed lines in Fig. 1, with a chi-square probability of only 1 %, clearly indicating that the model is unable to properly reproduce the NA51 measurements, performed with hydrogen and deuterium targets (the two leftmost points in Fig. 1-left). Maybe the fact that protons and deuterons are exceptionally

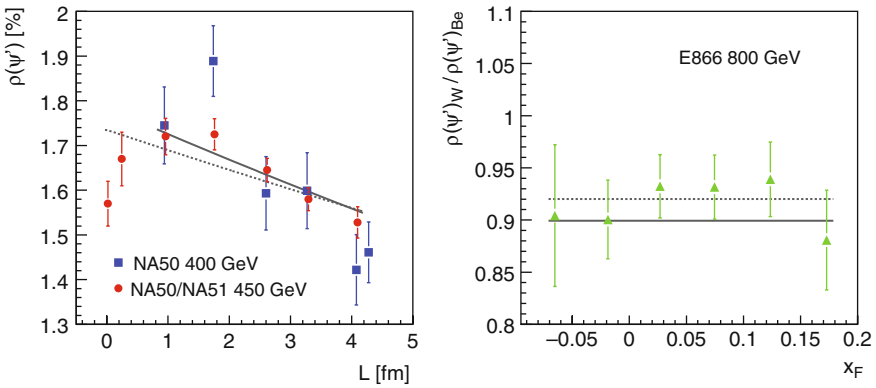

Fig. 1 $\rho(\psi')$ vs. L as measured by NA50/51 at 400 and 450 GeV (*left*), and $\rho(\psi')_{\text{W}}$ / $\rho(\psi')_{\text{Be}}$ vs. x_{F} as measured by E866 (*right*). The curves are the result of the global fit described in the text, including (*dashed lines*) or excluding (*solid lines*) the NA51 points

light nuclei places them out of the domain of applicability of the model we are using because they are not large enough to be traversed by fully formed charmonium states. It should also be noted that the use of "nuclear density profiles" in the Glauber calculation of the proton and deuteron ρL values is not as reliable as in the case of the heavier nuclei. Without the pp and p-D points, the best description of the data is represented by the solid lines, with a chi-square probability of 27 %, reflecting a much better compatibility between the data and the model used in the fit. The corresponding feed-down fraction is

$$R^0(\psi') = (8.1 \pm 0.3)\,\% \quad . \tag{4}$$

Including the NA51 points leads to $(7.9 \pm 0.3)\,\%$, a negligible change despite the visible degradation of the fit quality.

2.3 J/ψ Feed-Down from χ_c Decays

The $R(\chi_c)$ values are shown in Fig. 2-left as a function of L. The curve is the result of a fit analogous to the one explained in the previous section, using the "ρL parametrization" and leaving free the difference between the effective absorption cross sections of the χ_c mesons and of the J/ψ mesons not coming from χ_c decays. Given the conjecture, suggested by the ψ' analysis, that measurements performed with very light nuclei are not accountable within the simple absorption model we adopted, the pp point is excluded from the fit. The resulting feed-down fraction (for $L = 0$) is

$$R^0(\chi_c) = (25 \pm 5)\,\% \quad , \tag{5}$$

with a fit χ^2 probability of 25%.

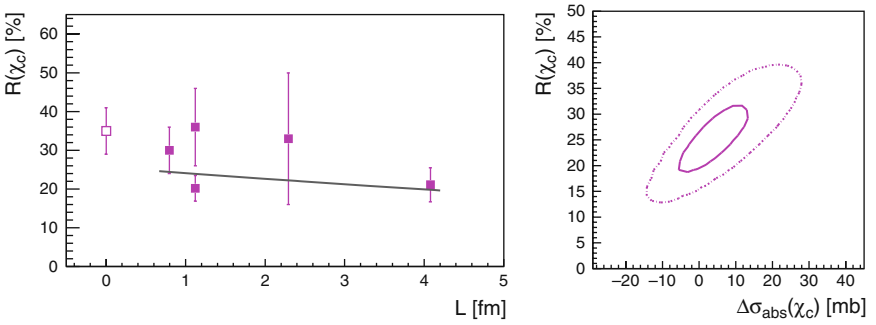

Fig. 2 *Left*: $R(\chi_c)$ versus L; the curve is the result of the fit described in the text (excluding the first point). *Right*: 68 and 99 % confidence-level contours for the bi-dimensional probability distribution of the fit parameters $R^0(\chi_c)$ and $\sigma_{\rm abs}(\chi_c) - \sigma_{\rm abs}(J/\psi)$, where the J/ψ term does not include the χ_c decay contribution

The $R^0(\chi_c)$ value considerably depends on the difference between the absorption cross sections of the two charmonium states (see Fig. 2-right). Therefore, a more precise $R^0(\chi_c)$ value can be obtained if an improved understanding of charmonium absorption in nuclear targets significantly reduces the allowed range of $\sigma_{\rm abs}(\chi_c) - \sigma_{\rm abs}(J/\psi)$.

3 J/ψ Polarization Revisited

It is well known that the $p_{\rm T}$ distribution of the J/ψ broadens from light to heavy nuclear targets in p–nucleus collisions. In particular, describing the nuclear dependence of the $p_{\rm T}$ distributions using the "α parametrization", we know that α significantly increases with $p_{\rm T}$ ("Cronin effect"), especially at low $p_{\rm T}$, seemingly saturating at high $p_{\rm T}$. However, the exact functional dependence of the observed behaviour depends on the J/ψ polarization scenario assumed in the analysis of the experimental data. For instance, the dimuon spectrometer used in the NA38, NA50, NA51 and NA60 experiments has essentially no acceptance for J/ψ dimuons outside of the window $|\cos\theta_{\rm CS}| < 0.5$, where $\theta_{\rm CS}$ is the Collins–Soper decay angle. All the results reported by these experiments are integrated in this window, assuming that the J/ψ is unpolarized. In other words, the J/ψ is assumed to have a flat $\cos\theta_{\rm CS}$ distribution, the window $|\cos\theta_{\rm CS}| < 0.5$ covering 50 % of the phase space.

A recent global analysis of the available J/ψ polarization measurements [21] indicates, however, that the J/ψ is significantly polarized, changing from longitudinal to transverse polarization from low to high momentum. This means that the window $|\cos\theta_{\rm CS}| < 0.5$ should cover *more* than 50 % of the phase space at low $p_{\rm T}$ and *less* at high $p_{\rm T}$, unlike the assumption made in the NA50 data analyses, and others. If the acceptance function were recalculated with this non-uniform polarization scenario, the acceptance-corrected $p_{\rm T}$ distributions should look flatter, with a smaller low-$p_{\rm T}$ J/ψ cross section than currently assumed. The importance of this effect should be stronger in collision systems leading mostly to low-$p_{\rm T}$ J/ψ's, where the nuclear dependence effects are more strongly $p_{\rm T}$ dependent. In particular, a reanalysis of the data might lead to flatter J/ψ $p_{\rm T}$ distributions in peripheral heavy-ion collisions, resulting in a weaker low-$p_{\rm T}$ J/ψ suppression, as compared to what is currently assumed.

3.1 Definition of Polarization Frames

There is a widespread misjudgement about the influence that the choice of the system of axes in the quarkonium rest frame has on the measurement of the angular distribution of the decay leptons. In fact, different analyses of *the same* two-body angular decay distribution may give qualitatively and quantitatively different results depending on the definition of the axes.

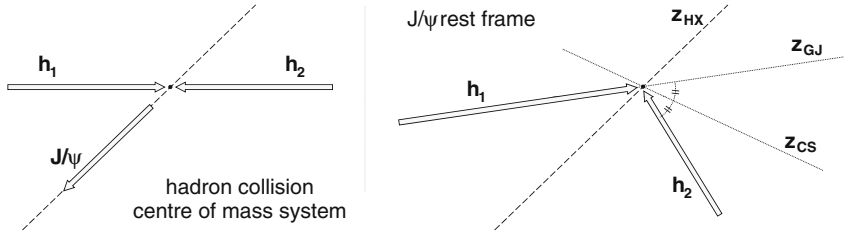

Fig. 3 Illustration of the definitions of the polarization axis, z, in the Collins–Soper (CS), Gottfried–Jackson (GJ) and helicity (HX) reference frames, with respect to the directions of motion of the colliding hadrons (h_1 and h_2) and of the J/ψ

The dilepton decay of a J/ψ with a given momentum is a two-degrees-of-freedom process, fully characterized by the angular distribution of one decay lepton in the rest frame of the mother particle. The lepton direction is expressed in a coordinate system built taking as a reference the flight lines of the two colliding hadrons, which are not collinear in the J/ψ rest frame. The actual definition of the axes of this system requires the adoption of a convention. Figure 3 gives a pedagogical illustration of how the orientation of the polar axis, z, is defined in the three different conventions we will consider.

In the helicity reference frame the polar axis is calculated as the direction of the vector $-(\boldsymbol{p}_{h_1} + \boldsymbol{p}_{h_2})$, where $\boldsymbol{p}_{h_1}$ and $\boldsymbol{p}_{h_2}$ are the momenta of the two hadrons in the J/ψ rest frame. This direction coincides with the flight direction of the J/ψ itself as seen in the centre-of-mass frame of the colliding hadrons. The choice of the helicity frame corresponds to the assumption that the polarization is acquired by the produced particle as an effectively intrinsic kinematic property. An opposite physical approach to the description of the polarization process is implicit in the definitions of the Gottfried–Jackson [22] and Collins–Soper [23] frames, where the polar axis reflects a direction established by the hard-scattering interaction. The Gottfried–Jackson frame, in particular, is defined by having the polar axis along the direction of the momentum of one of the two colliding hadrons ($\boldsymbol{p}_{h_1}$ or $\boldsymbol{p}_{h_2}$), while the Collins–Soper frame takes the bisector of the two ($\boldsymbol{p}_{h_1}/|\boldsymbol{p}_{h_1}| - \boldsymbol{p}_{h_2}/|\boldsymbol{p}_{h_2}|$). In general, the z-axis of the Collins–Soper frame is closely aligned with the direction of the relative velocity of the colliding partons, the approximation being especially good if we can neglect the parton intrinsic transverse momentum (and corresponding "smearing" effects). The Collins–Soper and helicity frames are orthogonal to each other at midrapidity (and $p_T > p_L$). All definitions become equivalent in the limit of zero J/ψ p_T, when $\boldsymbol{p}_{h_1}$ and $\boldsymbol{p}_{h_2}$ tend to be collinear.

We denote by ϑ the angle between the direction of the positive lepton and the chosen polar axis, and by φ the azimuthal angle, measured with respect to the plane formed by the vectors $\boldsymbol{p}_{h_1}$ and $\boldsymbol{p}_{h_2}$ ("production plane"). The angular distribution contains three possible terms of angular dependence [22]:

$$\frac{dN}{d(\cos\vartheta)\,d\varphi} \propto 1 + \lambda_\vartheta \cos^2\vartheta + \lambda_{\vartheta\varphi} \sin 2\vartheta \cos\varphi + \lambda_\varphi \sin^2\vartheta \cos 2\varphi \quad . \quad (6)$$

Non-zero values of the coefficients λ_ϑ, $\lambda_{\vartheta\varphi}$ and λ_φ indicate an anisotropic emission of the decay leptons, meaning that the J/ψ is polarized.

If the J/ψ is observed in a fixed kinematic configuration, any two definitions of the polarization frame only differ by a rotation around the axis perpendicular to the production plane (the "y-axis"). The functional dependence of the decay distribution on the angles ϑ and φ is invariant with respect to such a rotation, while the numerical values of the parameters λ_ϑ, $\lambda_{\vartheta\varphi}$ and λ_φ change in a correlated way. Indicating by δ a generic clockwise rotation angle around the y-axis, those changes are described by

$$\lambda'_\vartheta = \frac{\lambda_\vartheta - 3\Lambda}{1+\Lambda} \quad , \quad \lambda'_\varphi = \frac{\lambda_\varphi + \Lambda}{1+\Lambda}$$

and

$$\lambda'_{\vartheta\varphi} = \frac{\lambda_{\vartheta\varphi}\,\cos 2\delta + \frac{1}{2}\,(\lambda_\vartheta - \lambda_\varphi)\,\sin 2\delta}{1+\Lambda} \quad , \tag{7}$$

with

$$\Lambda = \frac{1}{2}\,\lambda_{\vartheta\varphi}\,\sin 2\delta + \frac{1}{2}\,(\lambda_\vartheta - \lambda_\varphi)\,\sin^2\delta \quad .$$

In particular, the coefficient $\lambda_{\vartheta\varphi}$ can always be set to zero through a suitable rotation of the reference frame around the y-axis by an angle

$$\delta_{\text{tilt}} = \frac{1}{2}\arctan\left(\frac{2\,\lambda_{\vartheta\varphi}}{\lambda_\varphi - \lambda_\vartheta}\right) \quad . \tag{8}$$

Having $\lambda_{\vartheta\varphi} = 0$ means that the frame being used has its axes along the principal axes of symmetry of the polarized angular distribution. The measurement of $\lambda_{\vartheta\varphi}$, therefore, provides a criterium for the choice of a particularly convenient reference frame for the description of the angular distribution.

It should now be clear that all three coefficients provide interesting and independent information, whatever the frame chosen for the analysis of the experimental data. Unfortunately, the majority of the available measurements of J/ψ polarization are limited to the coefficient λ_ϑ. The lack of an important part of the physical information contained in the data drastically limits the possible interpretations of the results and, furthermore, forces us to rely on model-dependent assumptions in order to compare results obtained by experiments using different reference frames. Even the seemingly simple classification of "transverse" or "longitudinal" polarization is, in fact, dependent on the reference frame. This is particularly evident when the decaying particle is produced with small longitudinal momentum ($x_{\text{F}} \approx 0$ or $y_{\text{cm}} \approx 0$), in which case the Collins–Soper and helicity polar axes are perpendicular to each other ($\delta = 90^\circ$ in Eq. 7). Assuming, for simplicity, $\lambda_\varphi = \lambda_{\vartheta\varphi} = 0$, if in one of the two frames a polarization λ_ϑ is observed, in the second frame the polarization

has smaller magnitude and opposite sign, while an azimuthal anisotropy appears:

$$\lambda'_\vartheta = -\frac{\lambda_\vartheta}{2}\,\frac{1}{1+\lambda_\vartheta/2} \quad , \quad \lambda'_\varphi = \frac{\lambda_\vartheta}{2}\,\frac{1}{1+\lambda_\vartheta/2} \quad , \quad \lambda'_{\vartheta\varphi} = 0 \quad . \tag{9}$$

There is another reason justifying that the experimental analyses should be performed in more than one reference frame. The J/ψ acquires its polarization with respect to a "natural" polarization axis which is, a priori, unknown and not necessarily definable event by event in terms of observable quantities. In practice, a fine-grained scan of the multidimensional phase space of the J/ψ production process is made impossible by the limited sample of collected events, forcing the decay distribution to be measured as an average over a wide spectrum of kinematic configurations. This means that the orientation of the polar axis of the chosen frame with respect to the "natural axis" changes from event to event, depending on the momentum of the produced J/ψ. Therefore, the decay distribution measured in a given kinematic interval is the superposition of many distributions, equal in shape but randomly rotated with respect to one another. The resulting distribution is still described by the rotation-invariant Eq. 6, but has been "smeared" into a more spherically symmetric shape and the measured absolute values of λ_ϑ and λ_φ are somewhat smaller than if measured in a fixed kinematic configuration and in the "natural frame". This shows that the reference frame providing the largest value of $|\lambda_\vartheta|$ is the one closest to the natural frame.

In summary, we have criteria that allow us to judge the quality of the reference frames used in the measurement of the angular distribution, independently of any prior theoretical expectation. The best frame is the one providing the smallest δ_{tilt} angle and the largest significance of $|\lambda_\vartheta|$. Since the direction of the polarization axis in the Gottfried–Jackson frame is always intermediate with respect to the other two cases, the Collins–Soper and helicity definitions represent a good minimal set of frames to be adopted in a measurement. It should be clear that a data-driven choice of the best reference frame is crucial not only to measure the polarization with a better significance but also to understand its origin.

3.2 Hierarchy of Polarization Frames

The HERA-B experiment reported [24] all the three parameters determining the angular distribution and in three reference frames (Collins–Soper, Gottfried–Jackson and helicity), providing a clear picture of how the shape of the distribution changes from frame to frame. As seen in Fig. 4, the λ_ϑ, λ_φ and δ_{tilt} results (integrated in the phase space covered by HERA-B) show a clear frame hierarchy, better judged from the differences in the central values since the errors are strongly correlated from one frame to another.

Giving the largest magnitude of the polarization parameter, $|\lambda_\vartheta|$, and the smallest $|\lambda_\varphi|$ and δ_{tilt}, the Collins–Soper frame clearly provides the simplest angular distribution. In the helicity frame, λ_ϑ has a smaller magnitude, λ_φ becomes significantly

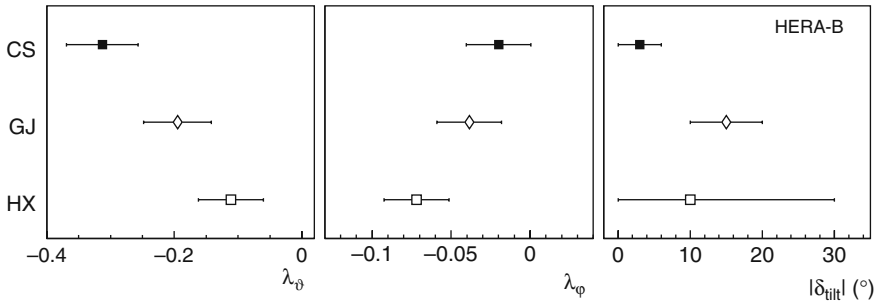

Fig. 4 The average values of λ_ϑ, λ_φ and $\delta_{\rm tilt}$ measured by HERA-B ($\sqrt{s} = 41.6$ GeV, $-0.34 < x_{\rm F} < 0.14$) in three reference frames [24]. The errors include statistical and systematic uncertainties, combined in quadrature

different from zero and, furthermore, $\delta_{\rm tilt}$ acquires a very large error, reflecting the poor precision with which the "tilt" of an almost spherically symmetric shape can be determined. The much lower significance of the polarization measurement indicates that the helicity axis is not aligned event after event with the "natural" polarization axis, the decay distribution being smeared by the varying J/ψ kinematics. The Gottfried–Jackson results are intermediate and the distribution is significantly tilted. In summary, the HERA-B measurements clearly indicate that the Collins–Soper frame is the closest to the natural polarization frame, meaning that the interaction which produces the J/ψ establishes a more correct reference direction for the description of the polarization process than the J/ψ direction itself.

3.3 Kinematical Dependence of J/ψ Polarization

We will now turn to the kinematical dependence of the J/ψ polarization measurements as reported, in the Collins–Soper frame, by the HERA-B [24] and E866 [25, 26] fixed-target experiments. As seen in Fig. 5 *left*, E866 observed a small J/ψ transverse[1] polarization ($\lambda_\vartheta \approx 0.1$) while the HERA-B pattern indicates a longitudinal polarization of decreasing magnitude with increasing $p_{\rm T}$. These measurements are not necessarily in mutual contradiction given that they cover significantly different $x_{\rm F}$ windows, as illustrated in Fig. 5 right. The average J/ψ longitudinal momentum, in the centre of mass of the collision system, is 7 and -1.4 GeV/c for E866 and HERA-B, respectively.

A consistent description of these measurements can be obtained assuming that the natural polarization frame ($\lambda_\varphi = 0$, $\lambda_{\vartheta\varphi} = 0$) coincides with the Collins–Soper frame and that λ_ϑ is a monotonically increasing function of the *total* J/ψ momentum, p, being -1 at zero momentum and $+1$ at asymptotically high momentum. We

[1] Following a common (even if misleading) practice, we qualify the polarization as transverse (longitudinal) when $\lambda_\vartheta > 0$ ($\lambda_\vartheta < 0$).

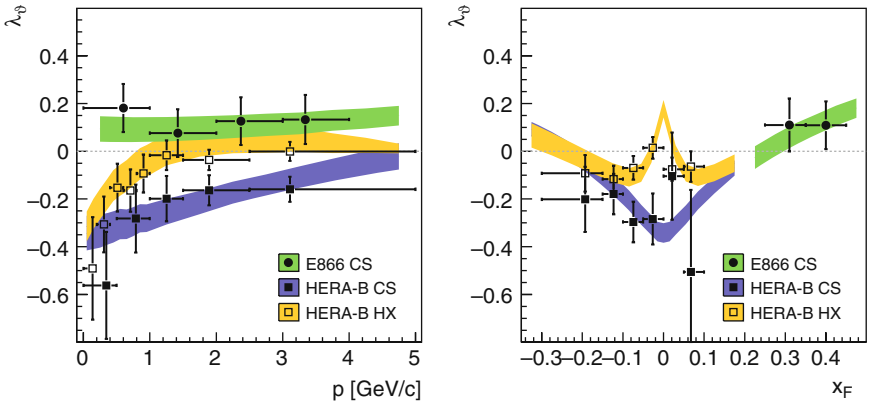

Fig. 5 λ_ϑ versus p_T (*left*) and x_F (*right*), as reported by HERA-B and E866 in the Collins–Soper (*closed symbols*) and helicity (*open symbols, not fitted*) frames. See text for the meaning of the bands

have chosen the simple parametrization

$$\lambda_\vartheta = 1 - 2^{1-(p/p_0)^\kappa} \quad , \tag{10}$$

with p_0 and κ determined by the (Collins–Soper) E866 and HERA-B patterns.

As discussed in Sect. 2, the J/ψ polarization measurements integrate a significant fraction, 0.33 ± 0.05, of J/ψ events resulting from χ_c and ψ' decays. Irrespectively of the possible χ_c and ψ' polarizations, the strong kinematical smearing induced by the varying kinematics of their decays results in a negligible *observable* polarization of the resulting J/ψ's. Also the feed-down contribution from b-hadron decays can be neglected (very small at fixed-target energies and experimentally subtracted in the CDF analysis). Therefore, we can assume that all the observed polarization stems from the directly produced J/ψ's. In this framework, and accounting for the specific kinematical and acceptance conditions of the experiments, the E866 and HERA-B data sets lead to $p_0 = 5.0 \pm 0.3$ GeV/c and $\kappa = 0.60 \pm 0.06$. The quality of the data description can be judged from Fig. 5, where the width of the bands correspond to $\pm 1\sigma$ variations in these parameters, as well as in the J/ψ feed-down fraction.

Fixing the p_0 and κ parameters from the E866 and HERA-B data, as reported in the Collins–Soper frame, we can *derive* the λ_ϑ and λ_φ coefficients in the helicity frame. We do such calculations using a Monte Carlo procedure, so as to easily incorporate the "kinematical smearing" induced by the decays. Figure 6 shows the calculated λ_ϑ and λ_φ bands, in the helicity frame and as a function of p_T, for the HERA-B [24] and CDF [27] kinematical conditions, compared to the corresponding data points. The significant decrease of λ_ϑ with p_T reported by CDF in the helicity frame is remarkably well reproduced by our assumption that, in the Collins–Soper frame, λ_ϑ grows monotonically with p_T. We remind that the CDF data do not contribute to the fit of the p_0 and κ parameters.

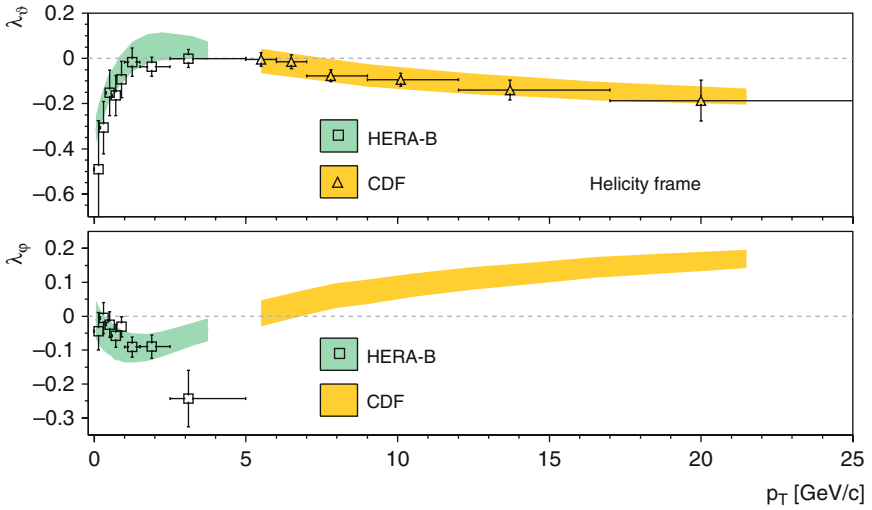

Fig. 6 λ_ϑ (*top*) and λ_φ (*bottom*) versus p_T, in the helicity frame, for the HERA-B and CDF kinematical conditions. The bands were exclusively determined by the E866 and HERA-B Collins–Soper patterns, as described in the text

It is important to note that, so far, CDF has not reported any results in the Collins–Soper frame and, furthermore, no information has been made available regarding the azimuthal part of the decay angular distribution. In the narrow rapidity window of CDF, where the maximum J/ψ longitudinal momentum (~ 4 GeV/c) is always smaller than the minimum p_T (5 GeV/c), the helicity and Collins–Soper

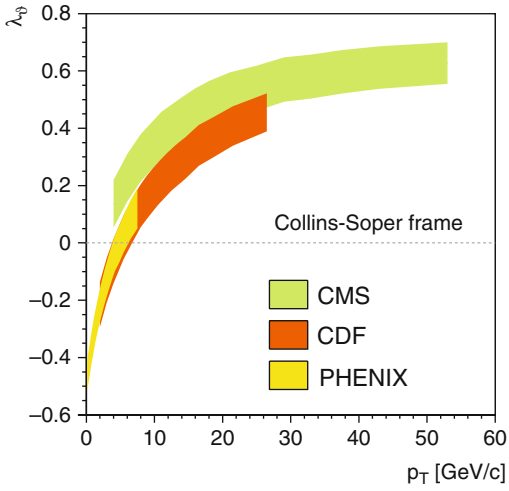

Fig. 7 p_T dependence of λ_ϑ, in the Collins–Soper frame, as calculated for the energy and rapidity windows of the PHENIX, CDF and CMS experiments

frames are essentially orthogonal to each other. The hypothesis (emerging from the E866 and HERA-B data) that the decay distribution has a purely polar anisotropy in the Collins–Soper frame implies that, in this frame, CDF should observe λ_ϑ increasing from zero to about $+0.4$, as illustrated in Fig. 7. This figure also shows the corresponding calculations for the kinematical conditions of the PHENIX ($\sqrt{s} = 200$ GeV, $|\eta| < 0.35$) and CMS ($\sqrt{s} = 14$ TeV, $|\eta| < 2.4$) experiments. If our model, inspired on the fixed-target data, holds up to the much higher energies of the LHC, we should see λ_ϑ saturating for p_T values higher than those probed by CDF, with a magnitude determined by the fraction of directly produced J/ψ mesons.

4 Energy Dependence of the J/ψ Break-Up Cross Section

We will now briefly address some "cold nuclear matter effects" affecting charmonium production in proton–nucleus collisions and their dependence on the collision energy. A detailed study of J/ψ and ψ' production in proton–nucleus collisions was made by NA50, with proton beams of 400 and 450 GeV, and up to six different nuclear targets (Be, Al, Cu, Ag, W and Pb), in the rapidity window $|y_\mathrm{cms}| < 0.5$ [10, 11]. Comparing the 400 and 450 GeV J/ψ / DY cross-section *ratios*, where Drell–Yan dimuons are used as reference, to calculations based on the Glauber formalism (neglecting nuclear modifications of the parton densities), the J/ψ "absorption cross section" was determined to be $\sigma_\mathrm{abs}^{\mathrm{J}/\psi} = 4.2 \pm 0.5$ mb [11]. This value has been used by NA50 [4] and NA60 [28] in the studies of the SPS heavy-ion data, collected at 158 GeV in the rapidity window $0 < y_\mathrm{cms} < 1$, assuming that the initial and final state "normal nuclear effects" do not change between the two energies and rapidity windows. This assumption, however, lacks supportive experimental evidence. As can be seen in Fig. 8, where the J/ψ nuclear dependence is expressed in terms of the "α parametrization", E866 [12] and HERA-B [29] observed a very strong dependence of α with x_F, and a smaller midrapidity J/ψ absorption at 800–920 GeV than NA50 saw at 450 GeV.

Recognizing the crucial importance of the normal nuclear absorption baseline in the interpretation of the J/ψ suppression seen in the heavy-ion data and knowing that the charmonium absorption processes may very well depend on collision energy [30], the NA60 experiment collected (in 2004) proton–nucleus data (with seven different nuclear targets: Be, Al, Cu, In, W, Pb and U) in the energy and kinematical conditions of the NA50 and NA60 heavy-ion data. The forthcoming results should significantly contribute to improve our understanding of the mechanisms causing the observed nuclear effects in charmonium production. In this section we analyse the J/ψ production cross sections measured in proton–nucleus collisions in several fixed-target experiments, with proton beam energies from 200 to 920 GeV. We evaluate the corresponding J/ψ break-up cross section, $\sigma_\mathrm{abs}^{J/\psi}$, by comparing the data to calculations of the charmonium production cross sections. The calculations are performed with the colour evaporation model [31], using "free proton" PDFs

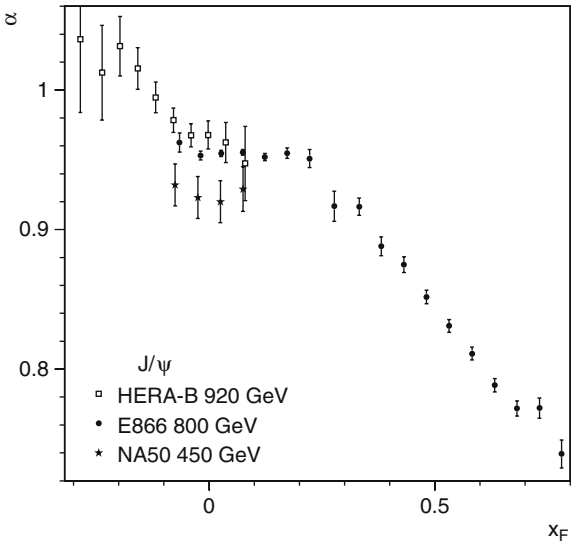

Fig. 8 Nuclear dependence of the J/ψ production cross sections, expressed in terms of α, as derived from NA50, E866 and HERA-B data

and also PDFs modified by the nuclear environment, following several parametrizations of the nuclear modifications: EKS98, nDSg and EPS08 [32–34]. The survival probability of the charmonium states traversing the nuclear matter is evaluated in the framework of the Glauber model [20], with Woods–Saxon nuclear density profiles [35, 36]. More details are given in [37]. We concentrate on the "midrapidity region" and neglect nuclear effects other than initial-state modifications of the parton densities and final-state charmonium absorption. As in most previous studies of charmonium absorption in nuclear matter, we treat the J/ψ as a single meson passing through the nuclear medium, without trying to disentangle contributions due to ψ' and χ_c decays.

Figure 9 *left* shows the $x_{\rm F}$ dependence of the J/ψ break-up cross section, $\sigma_{\rm abs}^{J/\psi}$, determined from the ratio between the p-W and the p-Be J/ψ cross sections measured by E866 at 800 GeV [12]. We clearly see that the extracted $\sigma_{\rm abs}^{J/\psi}$ values are very sensitive to the assumed initial-state nuclear effects on the PDFs. In particular, the use of nuclear parton distributions with strong antishadowing leads to $\sigma_{\rm abs}^{J/\psi}$ values significantly larger at $x_{\rm F} = -0.1$ than at $+0.2$. Another observation can be made from the $x_{\rm F}$ dependence of the E866 data. If we assume that nuclear absorption effects on the J/ψ can be effectively described by the Glauber formalism with a single $\sigma_{\rm abs}^{J/\psi}$ (ignoring formation times, feed-down contributions, energy loss, etc), we see a rather striking *increase* of $\sigma_{\rm abs}^{J/\psi}$ at forward $x_{\rm F}$, explicitly shown in Fig. 9 *right* for the EKS98 N-PDFs (this behaviour is equally seen with other N-PDFs).

These observations show that it is not straightforward to probe the existence of changes of the "midrapidity J/ψ break-up cross section" as a function of collision energy. In reality, there is no single "midrapidity" $\sigma_{\rm abs}^{J/\psi}$ value. The E866 data, in

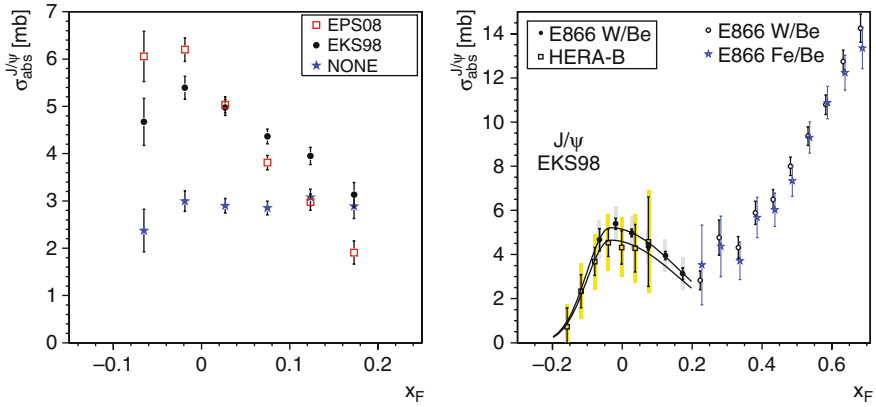

Fig. 9 *Left*: $\sigma_{abs}^{J/\psi}$ derived from the midrapidity E866 data, using different nuclear PDFs. *Right*: x_F dependence of $\sigma_{abs}^{J/\psi}$ from E866 [12] and HERA-B [15, 29] data, with EKS98 N-PDFs

particular, indicate that $\sigma_{abs}^{J/\psi}$ drops by a factor of 2 or 3 in the range $0 < x_F < 0.25$, corresponding to the centre-of-mass rapidity range $0 < y_{cms} < 1$. Therefore, when comparing measurements made at different energies, we must carefully consider the covered x_F or rapidity ranges.

Figure 10 shows $\sigma_{abs}^{J/\psi}$ as a function of y_{cms}, as obtained from the p-A data of NA3 [38, 39], NA50 [10, 11], E866 [12] and HERA-B [15, 29], with free proton PDFs ("NONE", left) and PDFs modified by the nuclear medium according to the EKS98 model (right). While the patterns derived neglecting nuclear effects on the PDFs can be considered flat in the midrapidity range $-0.3 < y_{cms} < 1.0$, the nuclear modifications of the PDFs considerably affect the $\sigma_{abs}^{J/\psi}(y_{cms})$ dependence and a

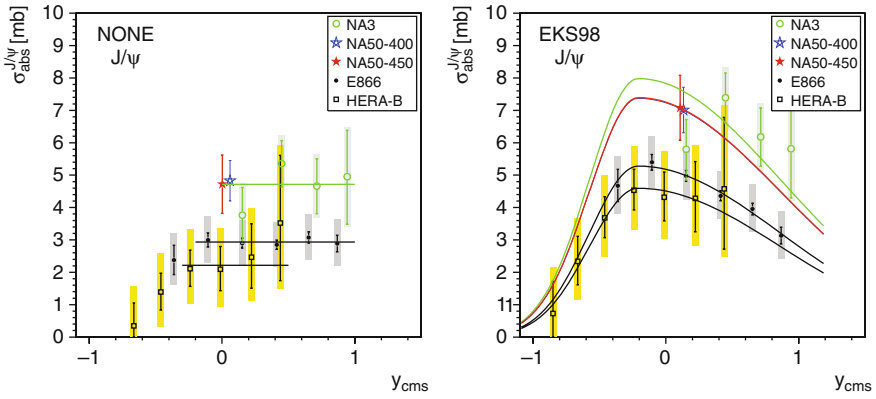

Fig. 10 $\sigma_{abs}^{J/\psi}$ as a function of y_{cms}, obtained without (*left*) and with (*right*) nuclear effects on the PDFs (using the EKS98 model). The boxes represent the total errors. When nuclear PDFs are used, the E866 and HERA-B absorption patterns clearly depend on y_{cms}

non-trivial function is needed to evaluate the $\sigma_{\rm abs}^{J/\psi}(y_{\rm cms}{=}0)$ values for the various data sets. In the EKS98 case, for example, the E866 and HERA-B data sets suggest the use of an asymmetric Gaussian function with $\mu \approx -0.21$ mb, $\sigma_{_L} \approx 0.37$ mb and $\sigma_{_R} \approx 1.1$ mb.

The change of $\sigma_{\rm abs}^{J/\psi}(y_{\rm cms}{=}0)$ with collision energy, $\sqrt{s_{_{NN}}}$, can be observed in Fig. 11, for free proton PDFs and three nuclear PDFs. The corresponding numerical values are collected in Table 2.

To determine the $\sigma_{\rm abs}^{J/\psi}$ relevant for the analysis of the SPS heavy-ion results, we must extrapolate $\sigma_{\rm abs}^{J/\psi}(y_{\rm cms}{=}0)$ down to $\sqrt{s_{_{NN}}} = 17.2$ GeV (dotted vertical line in Fig. 11). We can do the extrapolation using simple functions, like an exponential or a power law. A linear function is not suitable because it leads to negative $\sigma_{\rm abs}^{J/\psi}(y_{\rm cms}{=}0)$ values for energies not much higher than those probed by the data sets we analysed. The $\sigma_{\rm abs}^{J/\psi}(y_{\rm cms}{=}0)$ values extrapolated to 158 GeV with the exponential function are collected in Table 3, which also gives the corresponding values

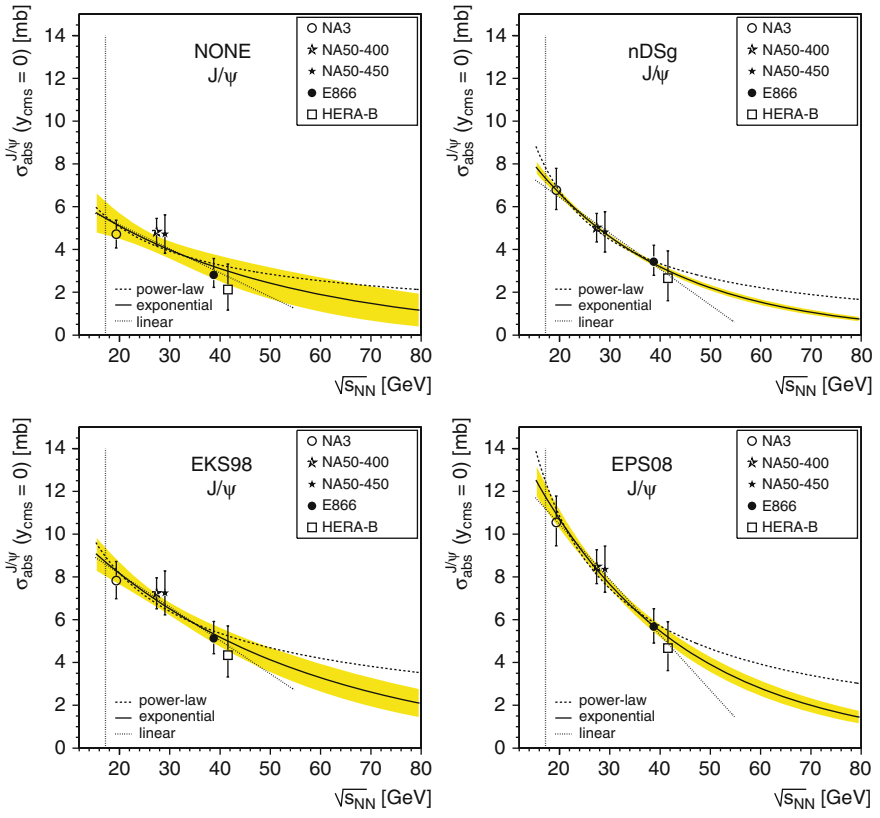

Fig. 11 Dependence of $\sigma_{\rm abs}^{J/\psi}(y_{\rm cms} = 0)$ on the nucleon–nucleon centre-of-mass energy. The curves represent fits with different functions: exponential (*solid line with error band*), power-law (*dashed line*) and linear (*dotted line*)

Table 2 $\sigma_{\rm abs}^{J/\psi}(y_{\rm cms}=0)$ values extracted from the five analysed data sets and for the nuclear PDFs we have considered, including the free protons case

Exp.	$\sigma_{\rm abs}^{J/\psi}(y_{\rm cms}=0)$ [mb]			
	NONE	nDSg	EKS98	EPS08
NA3	4.71 ± 0.66	$6.78^{+1.01}_{-0.91}$	$7.82^{+0.90}_{-0.84}$	$10.55^{+1.24}_{-1.10}$
NA50-400	4.82 ± 0.63	5.02 ± 0.67	7.24 ± 0.73	8.48 ± 0.79
NA50-450	4.72 ± 0.90	4.82 ± 0.95	7.25 ± 1.03	8.36 ± 1.08
E866	$2.82^{+0.76}_{-0.59}$	$3.43^{+0.77}_{-0.64}$	$5.13^{+0.79}_{-0.72}$	$5.68^{+0.84}_{-0.77}$
HERA-B	$2.13^{+1.19}_{-0.96}$	$2.66^{+1.28}_{-1.05}$	$4.35^{+1.37}_{-1.03}$	$4.67^{+1.24}_{-1.05}$

integrated in the NA50 heavy-ion rapidity window, $0 < y_{\rm cms} < 1$, weighted by the rapidity distribution of the J/ψ dimuons measured in Pb–Pb collisions (before acceptance corrections) [40]. The dependence of $\sigma_{\rm abs}^{J/\psi}$ on $y_{\rm cms}$ at $\sqrt{s_{NN}} = 17.2$ GeV is shown in Fig. 12-left, for several nuclear PDFs.

As shown in Table 3, if we neglect nuclear modifications on the PDFs we derive $\sigma_{\rm abs}^{J/\psi}(0 < y_{\rm cms} < 1) = 5.5 \pm 0.8$ mb, higher than the value used so far in the analyses of the SPS heavy-ion measurements (4.2 ± 0.5 mb, also using free-proton PDFs). If we use the EKS98 parametrization to model the nuclear modifications of the PDFs,

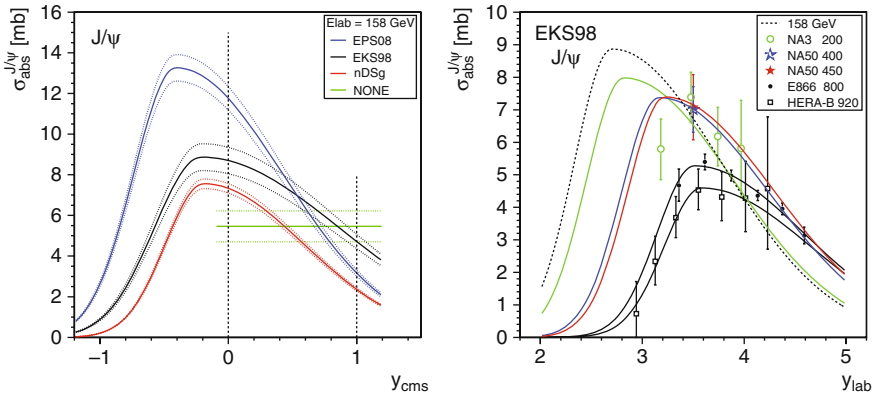

Fig. 12 *Left*: $\sigma_{\rm abs}^{J/\psi}$ as a function of $y_{\rm cms}$, extrapolated to 158 GeV considering four alternative parametrizations of the nuclear PDFs. *Right*: $\sigma_{\rm abs}^{J/\psi}$ as a function of $y_{\rm lab}$, for the several energies considered using EKS98 N-PDFs

Table 3 The $\sigma_{\rm abs}^{J/\psi}(y_{\rm cms}=0)$ and $\sigma_{\rm abs}^{J/\psi}(0 < y_{\rm cms} < 1)$ values evaluated at 158 GeV by extrapolating with an exponential function the values derived from measurements made at higher energies by NA3, NA50, E866 and HERA-B

N-PDFs	$\sigma_{\rm abs}^{J/\psi}(y_{\rm cms}=0)$ [mb]	$\sigma_{\rm abs}^{J/\psi}(0 < y_{\rm cms} < 1)$ [mb]
NONE	5.5 ± 0.8	5.5 ± 0.8
nDSg	7.3 ± 0.2	5.2 ± 0.2
EKS98	8.7 ± 0.7	7.2 ± 0.5
EPS08	11.8 ± 0.6	7.5 ± 0.4

we obtain $\sigma_{\rm abs}^{J/\psi}(0 < y_{\rm cms} < 1) = 7.2 \pm 0.5$ mb. It is interesting to notice that this is essentially equal to the values obtained by NA50 at 400–450 GeV, in rapidity windows centred at midrapidity. The drop of $\sigma_{\rm abs}^{J/\psi}$ from $y_{\rm cms} = 0$ to $y_{\rm cms} = 1$, in the EKS98 case, compensates the increase in $\sigma_{\rm abs}^{J/\psi}$ from $E_{\rm lab} = 400$–450 to 158 GeV, as is illustrated in Fig. 12-*right*.

5 Summary

One of the most important "discoveries" in the field of "heavy-ion physics" is that it is extremely important, indeed crucial, to have very robust data collected in more elementary collision systems, such as proton–proton and proton–nucleus interactions, by the same experiments, at the same collision energies, and in the same phase–space acceptance windows as the heavy-ion measurements. Only after having a solid "expected baseline", provided by a good understanding of the relevant physics processes and based, in particular, on detailed analyses of p-A data, we can realistically hope to identify patterns in the high-energy heavy-ion data that will clearly and convincingly signal the presence of "new physics" in the matter produced in those interactions.

In this chapter we have addressed a few data-driven recent developments aimed at reaching a better understanding of the basics of quarkonium production and absorption, in proton–nucleus collisions, in the absence of high-density QCD effects. Such studies need to be continued and strengthened to establish the centrality-dependent quarkonium production baseline in heavy-ion collisions, with respect to which we can extract and study signals of QGP formation, gluon saturation, etc. Clearly, such baselines are crucial to correctly interpret the charmonium "anomalous" suppressions seen at the SPS and RHIC and to analyse the quarkonium production data soon to be collected in Pb–Pb collisions at the LHC, where a solid understanding of the basics is even more important, given the lack of p-nucleus measurements and the very different energies of the pp and Pb–Pb runs.

Acknowledgments The studies reported in this chapter were made in collaboration with Ramona Vogt and João Seixas. They also reflect discussions, over many years, with Helmut Satz and several other people. We acknowledge fruitful discussions with Gonçalo Borges and Helena Santos (NA50), Mike Leitch (E866), Philippe Charpentier (NA3) and Roberto Spighi (HERA-B). The work of P.F. and H.K.W. was supported by the Fundação para a Ciência e a Tecnologia, Portugal, under contracts SFRH/BPD/42343/2007 and 42138/2007.

References

1. F. Karsch: Lattice QCD at High Temperature and Density, In: W. Plessas and L. Mathelitsch (eds.) *Lectures on Quark Matter*, p. 209, Springer, Berlin/Heidelberg (2002) 199
2. T. Matsui and H. Satz: Phys. Lett. **B 178**, 416 (1986) 199
3. F. Karsch, M.-T. Mehr and H. Satz: Z. Phys. **C 37**, 617 (1988) 199
4. B. Alessandro et al. [NA50 Collaboration]: Eur. Phys. J. **C39**, 335 (2005) 200, 212

5. L. Kluberg: Eur. Phys. J. **C 43**, 145 (2005), and references therein 200
6. F. Karsch, D. Kharzeev and H. Satz: Phys. Lett. **B 637**, 75 (2006) 201
7. P. Faccioli, C. Lourenço, J. Seixas and H.K. Wöhri: J. High Energy Phys. **10**, 004 (2008) 201, 202
8. C. Amsler et al. [Particle Data Group]: Phys. Lett. **B 667**, 1 (2008) 202
9. M.C. Abreu et al. [NA51 Collaboration]: Phys. Lett. **B 438**, 35 (1998) 202
10. B. Alessandro et al. [NA50 Collaboration]: Eur. Phys. J. **C 33**, 31 (2004) 202, 212, 214
11. B. Alessandro et al. [NA50 Collaboration]: Eur. Phys. J. **C 48**, 329 (2006) 202, 203, 212, 214
12. M.J. Leitch et al. [E866 Collaboration]: Phys. Rev. Lett. **84**, 3256 (2000), http://p25ext.lanl.gov/e866/papers/e866prlj/ratiosc.txt 202, 212, 213, 214
13. L. Antoniazzi et al. [E705 Collaboration]: Phys. Rev. Lett. **70**, 383 (1993) 202
14. I. Abt et al. [HERA-B Collaboration]: Phys. Lett. **B 561**, 61 (2003) 202
15. P. Faccioli et al. [HERA-B Collaboration]: International Workshop on Heavy Quarkonium, DESY, Hamburg, Germany (2007) 202, 214
16. A.G. Clark et al. [R702 Collaboration]: Nucl. Phys. **B 142**, 29 (1978) 202
17. J.H. Cobb et al.: Phys. Lett. **B 72**, 497 (1978)
18. C. Kourkoumelis et al.: Phys. Lett. **B 81**, 405 (1979) 202
19. F. Abe et al. [CDF Collaboration]: Phys. Rev. Lett. **79**, 578 (2003) 202
20. D. Kharzeev, C. Lourenço, M. Nardi and H. Satz: Z. Phys. **C74**, 307 (1997) 203, 213
21. P. Faccioli et al.: International Workshop on Heavy Quarkonium, Nara, Japan (2008) 205
22. K. Gottfried and J.D. Jackson: Nuovo Cim. **33**, 309 (1964) 206
23. J.C. Collins and D.E. Soper: Phys. Rev. **D 16**, 2219 (1977) 206
24. I. Abt et al. [HERA-B Collaboration]: Eur. Phys. J. **C60**, 517 (2009) 208, 209, 210
25. T.H. Chang et al. [E866 Collaboration]: Phys. Rev. Lett. **91**, 211801 (2003) 209
26. T.H. Chang: PhD thesis, New Mexico State University (1999) 209
27. A. Abulencia et al. [CDF Collaboration]: Phys. Rev. Lett. **99**, 132001 (2007) 210
28. R. Arnaldi et al. [NA60 Collaboration]: Phys. Rev. Lett. **99**, 132302 (2007) 212
29. I. Abt et al. [HERA-B Collaboration]: Eur. Phys. J. **C60**, 525 (2009), 212, 214
30. C. Lourenço et al. [NA60 Collaboration]: CERN-SPSC-2004–012, SPSC-M-715 (2004) 212
31. R.V. Gavai et al.: Int. J. Mod. Phys. **A 10**, 3043 (1995) 212
32. K.J. Eskola, V.J. Kolhinen and C. Salgado: Eur. Phys. J. **C 9**, 61 (1999) 213
33. D. de Florian and R. Sassot: Phys. Rev. **D 69**, 074028 (2004)
34. K.J. Eskola, H. Paukkunen and C. Salgado: J. High Energy Phys. **07**, 102 (2008) 213
35. C.W. De Jager et al.: Atomic Data and Nuclear Data Tables **14**, 479 (1974) 213
36. H. De Vries et al.: Atomic Data and Nuclear Data Tables **36**, 495 (1987) 213
37. C. Lourenço, R. Vogt and H.K. Wöhri: *Energy Dependence of J/ψ Absorption in Proton-Nucleus Collisions*, J. High Energy Phys. **02**, 014 (2009) 213
38. J. Badier et al. [NA3 Collaboration]: Z. Phys. **C 20**, 101 (1983) 214
39. Ph. Charpentier: private communication and PhD thesis, Université Paris-Sud (1983) 214
40. H. Santos: PhD thesis, Universidade Técnica de Lisboa (2004), http://cern.ch/NA50/theses.html 216

Electromagnetic Probes

Rupa Chatterjee, Lusaka Bhattacharya, and Dinesh K. Srivastava

Abstract We introduce the seminal developments in the theory and experiments of electromagnetic probes for the study of the dynamics of relativistic heavy-ion collisions and quark–gluon plasma.

1 Introduction

Collision of heavy nuclei at relativistic energies is expected to lead to formation of a deconfined state of matter known as quark–gluon plasma (QGP) [1], where quarks and gluons are the effective degrees of freedom rather than nucleons or hadrons [2, 3]. It is now well accepted that a few microseconds after the "Big Bang," the whole universe was in the state of QGP [4].

Several experiments performed at the super proton synchrotron (SPS) at CERN and relativistic heavy-ion collider (RHIC) at Brookhaven National Laboratory, New York, have provided a significant evidence of the formation of this novel state of matter. A giant accelerator known as large hadron collider (LHC) at CERN will be in operation very soon and will provide many new insights about the properties of QGP and the theory of strong interactions.

Heavy-ion collisions at relativistic energies produce extremely high temperatures and energy densities within a very small volume. As a result, quarks and gluons (also known as partons) no longer remain confined within the nucleonic volume and create a deconfined state of partons due to multiple scatterings and production of secondaries due to gluon multiplications. The system (or the fireball) may reach a state of local thermal equilibrium. It cools by expansion and below a certain critical temperature ($T_c \sim 180\,\mathrm{MeV}$) or energy density, the partons are confined to form

R. Chatterjee (✉)
Variable Energy Cyclotron Centre, Kolkata 700064, India, rupa@veccal.ernet.in

L. Bhattacharya
Saha Institute of Nuclear Physics, Kolkata 700064, India,
lusaka.bhattacharya@saha.ac.in

D.K. Srivastava
Variable Energy Cyclotron Centre, Kolkata 700064, India, dinesh@veccal.ernet.in

Chatterjee, R. et al.: *Electromagnetic Probes*. Lect. Notes Phys. **785**, 219–264 (2010)
DOI 10.1007/978-3-642-02286-9_7

hadrons and the system reaches a hadronic state. It may undergo a further expansion and cooling before the freeze-out takes place.

Radiation of photons and dileptons has been proposed as the most promising and efficient tool to characterize the initial state of heavy-ion collisions. Unlike hadrons, which are emitted from the freeze-out surface after undergoing intense re-scatterings, photons come out from each and every phase of the expanding fireball. Being electromagnetic in nature, they interact only weakly and their mean free path is larger than the typical system size ($\sim$10 fm). As a result once produced, they do not suffer further interaction with the medium ($\alpha \ll \alpha_s$) and carry undistorted information about the circumstances of their production to the detector [5].

Initially, photons (real as well as virtual) were studied in order to get only the temperature of the plasma. Several other possibilities, e.g., (i) evolution of the system size by intensity interferometry [6–9], (ii) momentum anisotropy of the initial partons [10, 11] as well as formation time of quark–gluon plasma [12] using elliptic flow of thermal photons, (iii) an accurate check on jet quenching and other aspects of the collision dynamics by photons due to passage of high-energy jets through plasma [13], have come to the fore. Of course dileptons are considered as the most reliable messengers of the medium modification of vector mesons [14].

2 Sources of Photons

In order to proceed, it is useful to identify various sources of photons from relativistic heavy-ion collisions. Their production is a result of convolution of the emissions from the entire history of the nuclear collision. Photons are emitted from the pre-equilibrium stage, from QGP phase, from hadronic phase, and also from the decay

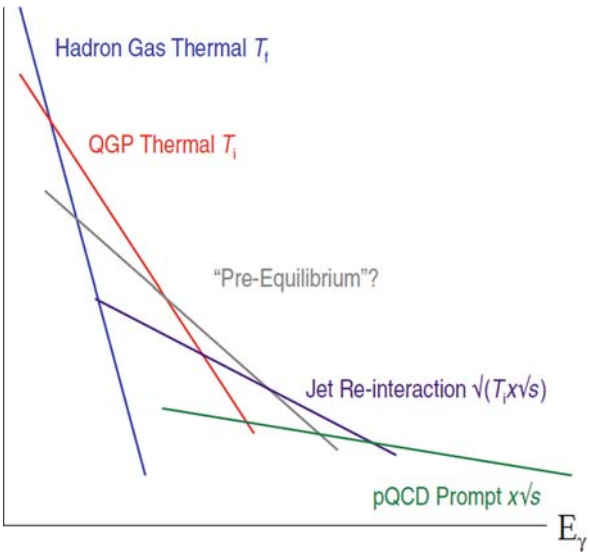

Fig. 1 Schematic diagram of different sources of photons and their relative p_T spectra

of hadrons produced at the time of freeze-out. An ideal situation would ensue if the contributions from different stages dominate different parts of the p_T spectrum. A schematic diagram of the different sources of photons and their slopes is shown in Fig. 1. We, thus, need rates and models to study the evolution from different sources. Hydrodynamics, cascade, fireball, cascade+hydrodynamics are the vastly used models for this purpose.

2.1 Direct Photons

The term "direct photons" stands for the photons which emerge directly from a particle collision. In a heavy-ion collision experiment, the detector captures all the emitted photons including those from decay of final state hadrons. The resultant spectrum is the inclusive photon spectrum. However, more than 90% of the photons in this spectrum are from hadron decay. One can subdivide this broad category of "direct photons" into "prompt," "pre-equilibrium," "thermal" (from QGP as well as hadronic phase), and "jet conversion" depending on their origin. Before we come to the different sub-categories of direct photons, we start our discussion with decay photons and their subtraction from the inclusive photon spectrum.

2.2 Decay Photons

As mentioned earlier, most of the decay photons are from 2-γ decay of π^0 and η mesons. ω, η', etc., also contribute to the decay photon spectrum, marginally. Subtraction of the decay background from inclusive photon spectrum is a very challenging task. WA98 Collaboration [15] used the subtraction method using invariant mass analysis for decay background and later PHENIX Collaboration [16] has developed this method to a much higher level of sophistication.

2.2.1 Invariant Mass Analysis

Extraction of direct photon spectrum from the inclusive photon spectrum is done using invariant mass analysis as the primary step. First, all the detected photons are listed on an event-by-event basis. Then by selecting two photons randomly from an event, invariant mass of the pair is calculated. If E_1, E_2 are the energies and $\mathbf{p_1}$, $\mathbf{p_2}$ are the three momenta of the photons respectively, then the invariant mass of the pair is

$$M_{\gamma\gamma} = [(E_1 + E_2)^2 - (\mathbf{p_1} + \mathbf{p_2})^2]^{1/2}. \tag{1}$$

If the value of $M_{\gamma\gamma}$ is close to m_{π^0}, it is assumed that they are the decay products from the same pion and a π^0 spectrum is obtained. Similarly the η spectrum is obtained. These two spectra are then used to determine the decay photon spectrum

using kinematics and the subtraction of this spectrum from the inclusive spectrum gives the direct photon spectrum.

However, in an event having N number of photons, the total number of photon pairs that can be formed is ${}^{N}C_2$. For large values of N, this number gets very large. Thus, there is a very high probability of getting a pair of photons having an invariant mass m_{π^0} or m_η, which are not decay products of the same pion or η meson.

Several other issues also need to be accounted for: (i) the detector resolution is finite, (ii) the opening angle between the decay photons can get very small, especially if the energy of the pion is large, (iii) the photons may not deposit all their energy in the detector, and (iv) one of the photons may be outside the coverage of the detector.

2.2.2 Mixed-Event Analysis

Thus, the major problem of invariant mass analysis is that the accidental (false) photon pairs can also give rise to pion mass and it is not possible to distinguish them from the correlated pairs. To overcome this problem, a mixed-event analysis [17] procedure has been used successfully. The basic idea of mixed-event technique is

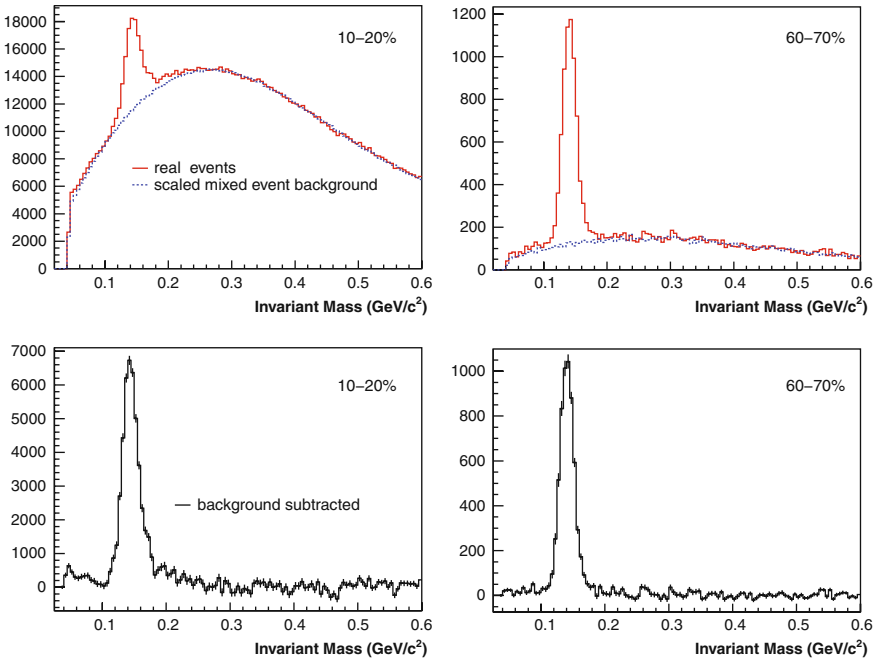

Fig. 2 Invariant mass distributions of pairs of electromagnetic clusters passing photon selection cuts for pair transverse momenta satisfying $3.0 < p_T < 3.5$ GeV. Top panels: $m_{\gamma\gamma}$ distributions in Au+Au events compared to a normalized mixed-event sample representing the combinatoric background. Bottom panels: The $m_{\gamma\gamma}$ distributions after subtraction of the combinatoric background for 10–20 and 60–70% centrality bins [17]

to compare particle spectrum from one event to the result for particle combinations from different events, which are a priori not correlated. As a first step, properly normalized mixed events are constructed by randomly sampling photons from different events. The difference of the invariant mass spectra (see Fig. 2) of the real events and the mixed events then gives the pion and η distributions. Once again, the decay photon spectrum is subtracted from the inclusive photon spectrum to get the direct photons.

2.2.3 Internal Conversion and Tagging of Decay Photons

An alternative approach of separating direct photons from decay background is by measuring the "quasi-real" virtual photons which appear as low mass electron–positron pair. It is assumed that any source of real photons also produces low mass virtual photons which decay into e^+e^- pair. This method is known as internal conversion method [18, 19] and is based on two assumptions. The first assumption is that the ratio of direct to inclusive photons is the same for real as well as virtual photons having $m_\gamma < 30$ MeV, i.e, $\gamma^*_{\rm dir}/\gamma^*_{\rm incl} = \gamma_{\rm dir}/\gamma_{\rm incl}$. Second, the mass distribution follows the Kroll–Wada formula [20]:

$$\frac{d^2n_{ee}}{dm_{ee}} = \frac{2\alpha}{3\pi}\frac{1}{m_{ee}}\sqrt{1-\frac{4m_e^2}{m_{ee}^2}}\left(1+\frac{2m_e^2}{m_{ee}^2}\right)Sdn_\gamma. \tag{2}$$

Here, m_e and m_{ee} are the masses of electron and e^+e^- pair, respectively, and α is the fine structure constant. This method is used for Compton scattering ($q + g \rightarrow q + \gamma^* \rightarrow q + e^+ + e^-$), Dalitz decay ($\pi^0, \eta \rightarrow e^+e^-\gamma$, $\omega \rightarrow e^+e^-\pi^0$), and also for two γ decay of several other hadrons. The factor S in Eq. (2) is process dependent and for π^0 ($\rightarrow \gamma\gamma^* \rightarrow \gamma e^+e^-$) decay it is expressed as [21]

$$S = |F(m_{ee}^2)|^2\left(1-\frac{m_{ee}^2}{M_h^2}\right)^3, \tag{3}$$

where M_h is the hadron mass and $F(m_{ee}^2)$ is the form factor. The factor S is 0 for $m_{ee} > M_h$ and goes to 1 as $m_{ee} \rightarrow 0$ or $m_{ee} \ll p_T$. The key advantage of this method is the greatly improved signal to background ratio which is achieved by elimination of the contribution of Dalitz (π^0) decay. The experimentally measured quantity is the ratio of e^+e^- pairs in a particular invariant mass bin and the direct photon spectrum is obtained by multiplying $\gamma^*_{\rm dir}/\gamma^*_{\rm incl}$ to the measured inclusive photon spectrum (left panel of Fig 3).

Due to the excellent resolution of the PHENIX detector to measure charged particles at low momenta, another powerful technique known as "tagging of decay photons" [22, 23] is used to eliminate the π^0 decay background. This method is very useful in the low and intermediate p_T range ($1 < p_T < 5$ GeV) as the systematic uncertainties introduced by detector efficiency, acceptance, etc., cancel out for measuring γ/γ_{π^0} directly in place of conventional double ratio

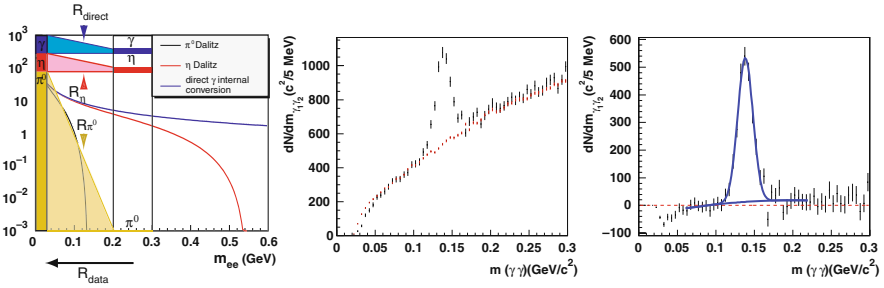

Fig. 3 *Left panel*: Invariant mass distribution of virtual photons from π^0 and η Dalitz decay as well as from direct photons [18, 19]. *Middle* and *right panels*: Invariant mass spectrum in "tagging" of decay photon method [22, 23]

$(R = (\gamma/\pi^0)_{\text{measured}}/(\gamma/\pi^0)_{\text{decay}})$ technique. In this method, the invariant mass $(m_{\gamma e^+e^-})$ distribution of the π^0 ($\rightarrow \gamma\gamma^* \rightarrow \gamma e^+e^-$) decay products is constructed and then mixed-event analysis is used for the final subtraction (middle and right panel of Fig. 3).

2.3 Sources of Direct Photons

Direct photons can be classified into different categories depending on their origin from different stages of the expanding fireball formed after the collision. These are (1) prompt photons, which originate from initial hard scatterings, (2) pre-equilibrium photons, produced before the medium gets thermalized, (3) thermal photons from quark–gluon plasma as well as by hadronic reactions in the hadronic phase, and (4) photons from passage of jets through plasma. It is not possible experimentally to distinguish between the different sources. Thus, theory can be used with a great advantage to identify these sources of direct photons and their relative importance in the spectrum [24].

2.3.1 Partonic Processes for Production of Prompt Photons

In relativistic heavy-ion collisions, prompt photons are produced due to quark–gluon Compton scattering $(q + g \rightarrow q + \gamma)$, quark–antiquark annihilation process $(q + \bar{q} \rightarrow g + \gamma)$, and quark fragmentation ($q \rightarrow q + \gamma$) following scattering of partons of the nucleons in the colliding nuclei (see Fig. 4). At lowest order in $\alpha\alpha_s$, quark–gluon Compton scattering and quark–antiquark annihilation processes dominate the photon production. In next-to-leading order (NLO) calculation, many more complicated scattering processes appear in the photon production cross section and the total contribution can be written as addition of two different terms as [25]

$$\frac{d\sigma}{d\vec{p}_T d\eta} = \frac{d\sigma^{(D)}}{d\vec{p}_T d\eta} + \frac{d\sigma^{(F)}}{d\vec{p}_T d\eta}. \tag{4}$$

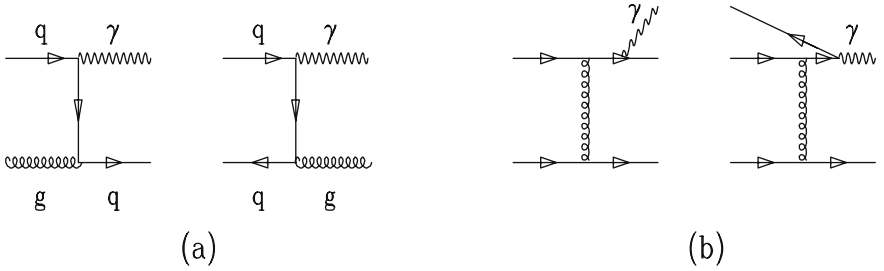

Fig. 4 Partonic processes for production of photons from (a) quark–gluon Compton scattering, quark–antiquark annihilation process, and (b) quark fragmentation

In the above equation "D" stands for "direct" or the total Compton scattering and annihilation contribution while the photons from fragmentation are denoted by "F". It is clear that the "D" photons are well separated from hadrons. The "F" photons, on the other hand, have their origin in collinear fragmentation of colored high-p_T partons and are accompanied by hadrons. This can be used with advantage as the produced photons can be separated out by employing useful isolation cuts. The two terms in Eq. (4) can be written explicitly as [26]

$$\frac{d\sigma^{(D)}}{d\overrightarrow{p}_T d\eta} = \sum_{i,j=q,\bar{q},g} \int dx_1 dx_2 \; F_{i/h_1}(x_1, M)\; F_{j/h_2}(x_2, M) \frac{\alpha_s(\mu_R)}{2\pi} \times \left(\frac{d\hat{\sigma}_{ij}}{d\overrightarrow{p}_T d\eta} + \frac{\alpha_s(\mu_R)}{2\pi} K_{ij}^{(D)}(\mu_R, M, M_F) \right) \tag{5}$$

and

$$\frac{d\sigma^{(F)}}{d\overrightarrow{p}_T d\eta} = \sum_{i,j,k=q,\bar{q},g} \int dx_1 dx_2 \frac{dz}{z^2} \; F_{i/h_1}(x_1, M)\; F_{j/h_2}(x_2, M)\; D_{\gamma/k}(z, M_F) \times \left(\frac{\alpha_s(\mu_R)}{2\pi} \right)^2 \left(\frac{d\hat{\sigma}_{ij}^k}{d\overrightarrow{p}_T d\eta} + \frac{\alpha_s(\mu_R)}{2\pi} K_{ij,k}^{(F)}(\mu_R, M, M_F) \right). \tag{6}$$

Here, $F_{i/h_{1,2}}(x, M)$ are the parton distribution functions and $\alpha_s(\mu_R)$ is the strong coupling defined in the $\overline{MS}$ renormalization scheme at the renormalization scale μ_R; for details see [25]. As mentioned earlier, in a complete and consistent NLO pQCD [$O(\alpha\alpha_s^2)$] calculation, important contribution to prompt photon result arises from various possible $2 \to 3$ processes like $ab \to \gamma cd$ for the direct as well as for the fragmentation processes [26, 27].

In case of photons from fragmentation, the higher order correction is very important at low x_T ($= 2p_T/\sqrt{s}$). By choosing a scale for factorization, renormalization, and fragmentation, all equal to $p_T/2$, a very good quantitative description is obtained for all the available pp and $p\overline{p}$ data without introduction of any intrinsic

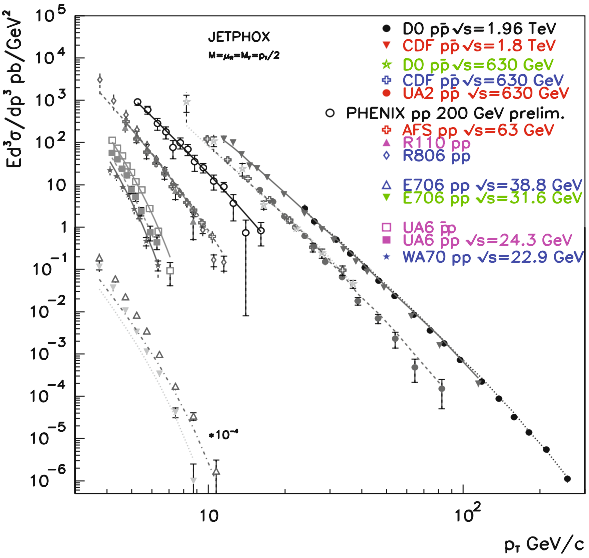

Fig. 5 World's inclusive and isolated direct photon production cross sections measured in pp and $p\bar{p}$ collisions compared to JETPHOX NLO predictions, using BFG II(CTEQ6M) for fragmentation (structure) functions and a common scale $p_T/2$ [25]

k_T. Results spanning over two orders of magnitude in energy and over nine orders of magnitude in cross sections are shown in Fig. 5.

It should be mentioned though that a similar exercise for pions requires a scale of $p_T/3$ [28].

In the early calculations, the results for nucleus–nucleus scatterings were often obtained by multiplying the pp results for some $\sqrt{s}$ with corresponding scaling factor N_{coll} ($= \sigma_{NN} T_{AB}$; where σ_{NN} is the nucleon–nucleon cross section and T_{AB} is the nuclear overlapping function for nuclei A and B) or number of binary collisions. In actual practice, often enough, σ_{NN} was replaced by σ_{pp}. However, as the valence quark structures of protons (uud) and neutrons (udd) are different, one needs to correctly account for the iso-spin of the nucleons to calculate the prompt contribution. This correction will strongly affect the results in the p_T range, where the valence quark contribution is significant. Also, remember that there is no direct measurement for pn and nn cross sections, though they can be estimated by comparing results of scatterings involving deuterons. The effect of shadowing on structure function and energy loss of final state quarks before they fragment into hadrons are two other corrections [29, 30] which need to be accounted for.

In order to clearly see this point we show the results for prompt photons for nn and pn collisions normalized to those for pp collisions at $\sqrt{s} = 200$ GeV in the left panel of Fig. 6. It is clear that at low x_T (where processes involving gluons dominate) the effect is not very significant, however with larger values of x_T (where the processes involving valence quarks dominate), the production of photons decreases by a large factor for the case of pn and nn collisions.

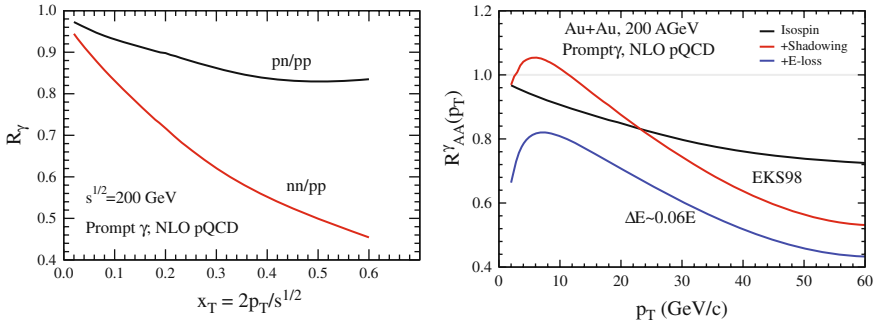

Fig. 6 *Left panel*: Prompt photons for *pn* and *nn* collisions normalized to those for *pp* collisions at $\sqrt{s} = 200$ GeV. *Right panel*: Iso-spin, shadowing, and energy loss corrected R_{AA} for prompt photons at 200*A* GeV Au+Au collisions using NLO pQCD

The transverse momentum-dependent nuclear modification factor R_{AA} defined as

$$R_{AA}(p_T) = \frac{1}{N_{\text{coll}}} \frac{d\sigma_\gamma^{AA}(p_T)/dyd^2p_T}{d\sigma_\gamma^{pp}(p_T)/dyd^2p_T} \tag{7}$$

for prompt photons using NLO pQCD and considering iso-spin, shadowing, and energy loss effects for 200*A* GeV Au+Au collisions at RHIC is shown in the right panel of Fig. 6. We note that, for $p_T < 10$ GeV, the iso-spin and shadowing corrected result shows an enhancement in the prompt photon production compared to the situation when only the iso-spin correction is incorporated [31]. This is due to anti-shadowing for larger values of Bjorken x or large x_T. The inclusion of the energy loss pushes down the value of R_{AA} to less than 1 for all p_T. We also give a comparison with the PHENIX [32] experimental data in the bottom lower panel of Fig. 8.

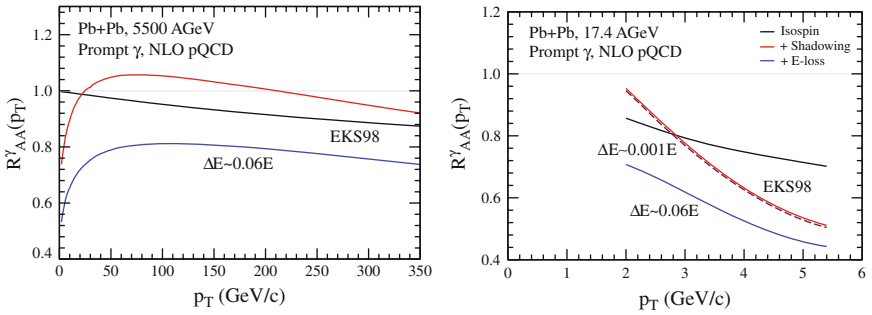

Fig. 7 Iso-spin, shadowing, and energy loss corrected R_{AA} for prompt photons at LHC (*left panel*) and SPS (*right panel*) energies using NLO pQCD

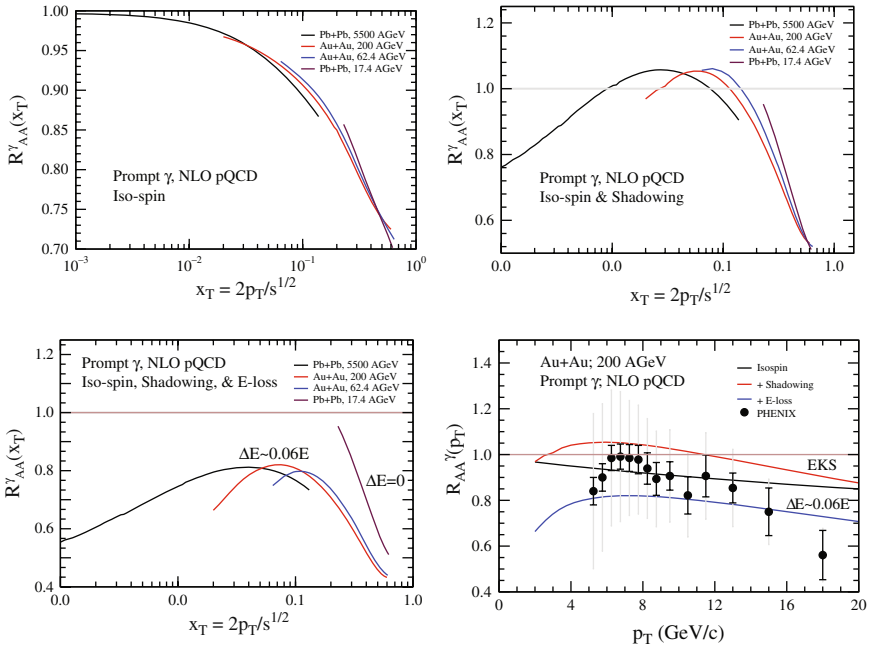

Fig. 8 Iso-spin, shadowing, and fragmentation energy-loss-corrected NLO pQCD results at different collider energies with different target projectile combination and comparison of the RHIC results with PHENIX [32] data

NLO results at LHC (Pb+Pb@5.5A TeV) and SPS (Pb+Pb@17.4A GeV) are shown in Fig. 7. To clearly demonstrate the relative features of iso-spin, shadowing, and energy-loss-corrected prompt photons at different collider energies, results for R_{AA} as function of x_T are shown in Fig. 8.

2.4 Photon Production from Quark–Gluon Plasma

The thermal emission rate of photons with energy E and momentum p from a small system (compared to the photon mean free path) is related to the imaginary part of the photon self-energy by the following relation:

$$E\frac{dR}{d^3p} = \frac{-2}{(2\pi)^3} Im\Pi_{\mu}{}^{R,\mu} \frac{1}{e^{E/T}-1}, \tag{8}$$

where $\Pi_{\mu}{}^{R,\mu}$ is the retarded photon self-energy at a finite temperature T. This relation is valid in the perturbative [33, 34] as well as non-perturbative [35] limits. It is also valid to all orders in the strong interactions and to order e^2 in the electromagnetic interactions. If the photon self-energy is approximated by carrying out a

loop expansion to some finite order, then the formulation of Eq. (8) is equivalent to relativistic kinetic theory. In order to illustrate this, we closely follow the treatment of [36, 37].

Thus using relativistic kinetic theory formulation, the contribution of these processes to the rate can be written as [36–38]

$$\mathcal{R}_i = \mathcal{N} \int \frac{d^3p_1}{2E_1(2\pi)^3} \frac{d^3p_2}{2E_2(2\pi)^3} f_1(E_1) f_2(E_2) (2\pi)^4 \delta({p_1}^\mu + {p_2}^\mu - {p_3}^\mu - p^\mu) \times |\mathcal{M}_i|^2 \frac{d^3p_3}{2E_3(2\pi)^3} \frac{d^3p}{2E(2\pi)^3} [1 \pm f_3(E_3)], \tag{9}$$

where $\mathcal{M}_i$ represents the amplitude for one of these processes and the $f's$ are the Fermi–Dirac or Bose–Einstein distribution functions as appropriate. Positive and negative signs in the last part of Eq. (9) correspond to Bose enhancement and Pauli suppression, respectively.

The integral above can be simplified by introducing Mandelstam variables $s = (p_1 + p_2)^2$, $t = (p_1 - p_3)^2$, and $u = (p_1 - p)^2$. Now the differential photon rate can be written as

$$E\frac{d\mathcal{R}_i}{d^3p} = \frac{\mathcal{N}}{(2\pi)^7} \frac{1}{16E} \int ds dt \, |\mathcal{M}_i(s,t)|^2 \int dE_1 dE_2 f_1(E_1) f_2(E_2) \times [1 \pm f_3(E_1 + E_2 - E)] \theta(E_1 + E_2 - E)(a{E_1}^2 + bE_1 + c)^{-1/2}, \tag{10}$$

where

$$\begin{aligned} a &= -(s+t)^2, \\ b &= 2(s+t)(Es - E_2 t), \\ c &= st(s+t) - (Es + E_2 t)^2. \end{aligned} \tag{11}$$

Considering the photon energy to be large, one can consider $f_1(E_1) f_2(E_2) \approx \mathrm{e}^{-(E_1+E_2)/T}$ and simplify the above as

$$E\frac{d\mathcal{R}_i}{d^3p} = \frac{\mathcal{N}}{(2\pi)^6} \frac{T}{32E} \mathrm{e}^{-E/T} \int \frac{ds}{s} \, \ln(1 \pm \mathrm{e}^{-s/4ET})^{\pm 1} \int dt |\mathcal{M}_i(s,t)|^2. \tag{12}$$

In the above equation, positive and negative signs stand for fermions (q) and bosons (g) in the final state, respectively.

The relation between the amplitude and differential cross section for mass less particles can be written as

$$\frac{d\sigma}{dt} = \frac{|\mathcal{M}|^2}{16\pi s^2}. \tag{13}$$

And thus, the differential cross sections for annihilation process and Compton scattering are

$$\frac{d\sigma^{\text{annihilation}}}{dt} = \frac{8\pi\alpha\alpha_s}{9s^2}\frac{u^2+t^2}{ut} \tag{14}$$

and

$$\frac{d\sigma^{\text{Compton}}}{dt} = \frac{-\pi\alpha\alpha_s}{3s^2}\frac{u^2+s^2}{us}. \tag{15}$$

For annihilation process, $\mathcal{N} = 20$ when summing over u and d quarks and for Compton scattering, $\mathcal{N} = 320/3$. The total cross section can be obtained after integrating over t. These differential cross sections have a singularity at t and/or $u = 0$ and the total cross section is infinite as the processes involve exchange of massless particle.

To screen this divergence many-body effects are necessary. This approach will be discussed later. As a first step let us isolate the region of phase space causing the divergences. The integration is done over

$$-s + {k_c}^2 \le t \le -{k_c}^2, \quad 2{k_c}^2 \le s \le \infty, \tag{16}$$

where $T^2 \gg {k_c}^2 > 0$ is an infrared cutoff.

This treats u and t symmetrically and maintains the identity $s + t + u = 0$ appropriate for all massless particles.

In the limit that ${k_c}^2 \to 0$,

$$E\frac{d\mathcal{R}^{\text{Compton}}}{d^3p} = \frac{5}{9}\frac{\alpha\alpha_s}{6\pi^2}T^2e^{-E/T}[\ln(4ET/{k_c}^2) + C_F], \tag{17}$$

$$E\frac{d\mathcal{R}^{\text{annihilation}}}{\mathrm{d}^3p} = \frac{5}{9}\frac{\alpha\alpha_s}{3\pi^2}T^2e^{-E/T}[\ln(4ET/{k_c}^2) + C_B], \tag{18}$$

where

$$C_F = \frac{1}{2} - C_{\text{Euler}} + \frac{12}{\pi^2}\sum_{n=2}^{\infty}\frac{(-1)^n}{n^2}\ln\, n = 0.0460\ldots, \tag{19}$$

$$C_B = -1 - C_{\text{Euler}} - \frac{6}{\pi^2}\sum_{n=2}^{\infty}\frac{1}{n^2}\ln\, n = -2.1472\ldots. \tag{20}$$

These expressions use the full Fermi–Dirac or Bose–Einstein distribution functions in the final state.

These results have a very interesting structure. Thus, the factor 5/9 arises from the sum of the squares of the electric charges of the u and d quarks, the factor $\alpha\alpha_s$ comes from the topological structure of the diagrams, a factor T^2 comes from phase

space which gives the overall dimension of the rate, and we have the Boltzmann factor $e^{-E/T}$ for photons of energy E. The logarithm arises due to the infrared behavior.

2.4.1 Infrared Contribution

The infrared divergence in the photon production rate [36, 37] discussed above is caused by a diverging differential cross section when the momentum transfer goes to zero. Oftentimes long-ranged forces can be screened by many-body effects at finite temperatures. Braaten and Pisarski have analyzed problems such as this one in QCD [39–41]. They have argued that a cure can be found in reordering perturbation theory by expanding correlation functions in terms of effective propagators and vertices instead of bare ones. These effective propagators and vertices are just the bare ones plus one-loop corrections, with the caveat that the one-loop corrections are evaluated in the high-temperature limit. This makes them relatively simple functions.

The analysis of Braaten and Pisarski shows that a propagator must be dressed if the momentum flowing through it is soft (small compared to T). This is because propagation of soft momenta is connected with infrared divergences in loops. Dressing of propagators are necessary, otherwise corrections due to these are also infinite.

Using the one-loop corrected propagators and vertices and the contribution to the rate coming from the infrared-sensitive part of phase space can be written as

$$E\frac{d\mathcal{R}^{\mathrm{BP}}}{d^3p} = \frac{5}{9}\frac{\alpha\alpha_s}{2\pi^2}T^2 e^{-E/T}\ln\left(\frac{{k_c}^2}{2{m_q}^2}\right), \tag{21}$$

where $2{m_q}^2 = \frac{1}{3}g^2T^2$.

Adding this contribution to those given by Eqs. (19) and (20), the final result can be written as

$$E\frac{d\mathcal{R}}{d^3p} = \frac{5}{9}\frac{\alpha\alpha_s}{2\pi^2}T^2 e^{-E/T}\ln\left(\frac{2.912}{g^2}\frac{E}{T}\right). \tag{22}$$

This is independent of the cutoff k_c. Thus, the Braaten–Pisarski method has worked beautifully to shield the singularity encountered above. We also note that in kinetic theory calculation, the effective infrared cutoff is ${k_c}^2 = 2{m_q}^2$. In earlier works an infrared cutoff was often imposed by giving the exchanged quark an effective temperature-dependent mass.

These early results have been brought to a high degree of sophistication and results complete to leading order in α_s with inclusion of LPM effects are now available, which should be used for detailed calculation [42].

2.4.2 Photons from Passage of Jets Through QGP

The relativistic heavy-ion collisions at RHIC (and LHC) energies are marked by a large production of high-energy quark and gluon jets which lose energy while

passing through the QGP due to collision and radiation of gluons. This is the celebrated phenomenon of jet quenching. A quark jet having a transverse momentum p_T would be formed within $\tau \sim 1/p_T$ which can be much smaller than τ_0, when QGP is formed, for large p_T. This quark (or antiquark) jet, while passing through QGP may annihilate with a thermal antiquark (or quark) or undergo a Compton scattering with a thermal gluon and lead to production of a high-energy photon. This process is called the jet-photon conversion [13].

We have seen that the kinematics of the annihilation of a quark–antiquark pair ($q + \bar{q} \rightarrow \gamma + g$) is expressed in terms of the Mandelstam variables $s = (p_q + p_{\bar{q}})^2$, $t = (p_q - p_\gamma)^2$, and $u = (p_{\bar{q}} - p_\gamma)^2$. We also recall that the largest contribution to the production of photons arises from small values of t or u, corresponding to $p_\gamma \sim p_q$ or $p_\gamma \sim p_{\bar{q}}$ [2, 13, 43].

The phase–space distribution of the quarks and gluons produced in a nuclear collision can be approximately decomposed into two components, a thermal component $f_{\rm th}$ characterized by a temperature T and a hard component $f_{\rm jet}$ given by hard scattering of the partons and limited to transverse momenta $p_T \gg 1$ GeV: $f(\mathbf{p}) = f_{\rm th}(\mathbf{p}) + f_{\rm jet}(\mathbf{p})$. $f_{\rm jet}$ dominates for large momenta, while at small momenta f is completely given by the thermal part.

The phase–space distribution for the quark jets propagating through the QGP is given by the perturbative QCD result for the jet yield [13]:

$$f_{\rm jet}(\mathbf{p}) = \frac{1}{g_q} \frac{(2\pi)^3}{\pi R_\perp^2 \tau p_T} \frac{dN_{\rm jet}}{d^2 p_T dy} R(r) \delta(\eta - y) \Theta(\tau_{\rm max} - \tau_i) \Theta(R_\perp - r), \tag{23}$$

where $g_q = 2 \times 3$ is the spin and color degeneracy of the quarks, $R_\perp$ is the transverse dimension of the system, and the η is the space–time rapidity. $R(r)$ is a transverse profile function. $\tau_{\rm max}$ is the smaller of the lifetime τ_f of the QGP and the time $\tau_{\rm d}$ taken by the jet produced at position $\mathbf{r}$ to reach the surface of the plasma.

One can approximate the invariant photon differential cross sections for the annihilation process and Compton scattering as [2, 13]

$$E_\gamma \frac{d\sigma^{(a)}}{d^3 p_\gamma} \sim \sigma^{(a)}(s) \frac{1}{2} E_\gamma [\delta(\mathbf{p}_\gamma - \mathbf{p}_q) + \delta(\mathbf{p}_\gamma - \mathbf{p}_{\bar{q}})] \tag{24}$$

and

$$E_\gamma \frac{d\sigma^{(C)}}{d^3 p_\gamma} \sim \sigma^{(C)}(s) E_\gamma \delta(\mathbf{p}_\gamma - \mathbf{p}_q). \tag{25}$$

Here, $\sigma^{(a)}(s)$ and $\sigma^{(C)}(s)$ are the corresponding total cross sections.

Using Eqs. (24) and (25), the rate of production of photons due to annihilation and Compton scattering is given by [2]

$$E_\gamma \frac{dN^{(a)}}{d^4x d^3p_\gamma} = \frac{16E_\gamma}{2(2\pi)^6} \sum_{q=1}^{N_f} f_q(\mathbf{p}_\gamma) \int d^3p f_{\bar{q}}(\mathbf{p})[1 + f_g(\mathbf{p})]\sigma^{(a)}(s) \times \frac{\sqrt{s(s-4m^2)}}{2E_\gamma E} + (q \leftrightarrow \bar{q}) \tag{26}$$

and

$$E_\gamma \frac{dN^{(C)}}{d^4x d^3p_\gamma} = \frac{16E_\gamma}{(2\pi)^6} \sum_{q=1}^{N_f} f_q(\mathbf{p}_\gamma) \int d^3p f_g(\mathbf{p})[1 - f_q(\mathbf{p})]\sigma^{(C)}(s) \times \frac{(s-m^2)}{2EE_\gamma} + (q \to \bar{q}). \tag{27}$$

The $f's$ are the distribution functions for the quarks, antiquarks, and gluons. Inserting thermal distributions for the gluons and quarks one can obtain an analytical expression for these emission rates for an equilibrated medium [2, 36–38].

In order to estimate the jet-photon conversion contribution, we first note that the integrals over **p** in Eqs. (26) and (27) are dominated by small momenta. Therefore dropping the jet part in the distributions, $f(\mathbf{p})$ in the integrands is approximated by the thermal part. Now performing the integrals and identifying the quark and antiquark distributions outside the integrals with the jet distributions, results for Compton and annihilation scatterings due to jet conversions are given as

$$E_\gamma \frac{dN_\gamma{}^{(a)}}{d^3p_\gamma d^4x} = E_\gamma \frac{dN_\gamma{}^{(C)}}{d^3p_\gamma d^4x} = \frac{\alpha\alpha_s}{8\pi^2} \sum_{f=1}^{\mathcal{N}_f} (\frac{e_{q_f}}{e})^2 [f_q(\mathbf{p}_\gamma) + f_{\bar{q}}(\mathbf{p}_\gamma)]T^2[\ln(\frac{4E_\gamma T}{m^2}) + C]. \tag{28}$$

Here, $C = -1.916$. If we include three lightest quark flavors, then $\sum_f {e_{q_f}}^2/e^2 = 2/3$. We also assume that the mass m introduced here to shield the infrared divergence can be identified with the thermal quark mass m_{th}.

These pioneering works have now been corrected for energy loss and flavor change suffered by the jets, as they pass through the plasma [44] as well as bremsstrahlung induced by the passage of the jets through the plasma [45].

2.4.3 Equilibration Time for Photons

It is of interest to get an idea about the equilibration time of photons in the medium. Following the treatment of [36, 37], we note that the six-dimensional phase–space distribution $dn/d^3p(= dN/d^3xd^3p)$ for the photons satisfies the rate equation:

$$\frac{d}{dt}\left(\frac{dn}{d^3p}\right) = \frac{dR}{d^3p}\left(1 - \frac{dn/d^3p}{dn_{\rm eq}/d^3p}\right). \tag{29}$$

In the above equation, $dn_{\rm eq}/d^3p$ is the equilibrium distribution and is expressed as Planck's distribution,

$$\frac{dn^{\rm eq}}{d^3p} = \frac{2}{(2\pi)^3}\frac{1}{{\rm e}^{E/T} - 1}. \tag{30}$$

Considering $\tau_{\rm eq}$ $(= \frac{dn_\gamma^{\rm eq}}{d^3p}/\frac{dR}{d^3p})$ as the time for equilibration and assuming zero photons at the beginning we can write

$$\frac{dn}{d^3p} = \frac{dn^{\rm eq}}{d^3p}\left(1 - {\rm e}^{t/\tau_{\rm eq}}\right). \tag{31}$$

Using the rate equation, the thermalization time can be expressed in a simplified form (considering $E > 2T$) as

$$\tau_{\rm eq} = \frac{9E}{10\pi\alpha\alpha_s T^2}\frac{1}{\ln(\frac{2.9}{g^2}\frac{E}{T} + 1)}. \tag{32}$$

For energy values $E = 0.5, 1, 2, 3$ GeV, corresponding values for $\tau_{\rm eq}$ will be about 270, 356, 505, 639 fm/c, respectively, when the temperature is 200 MeV. As the lifetime of the system is very short, of the order of few tens of fm/c, it is very clear that the high-energy photons will never reach the equilibrium state in heavy-ion collisions. This is an important confirmation for the validity of the assumption made in all such studies that photons, once produced in the collision, leave the system without any further re-interaction.

2.5 Photons from Hot Hadronic Matter

Hot hadronic matter produced after the hadronization of the quark–gluon plasma will also lead to production of photons due to hadronic reactions. These photons will dominate the spectrum at lower p_T ($<$ 1 GeV). The first ever calculation of production of thermal photons from hadronic matter was performed by Kapusta et al. [36, 37].

In a hot hadronic gas (having temperature of the order of pion mass), the most important hadronic constituents for photon production are π and ρ mesons (see Fig. 9). The low mass of pions and the large spin–iso-spin degeneracy of ρ mesons make them the most easily accessible particles in the medium. In order to illustrate the photon production from these two mesons, we closely follow the treatment of KLS [36, 37]. In a hadronic reaction involving charged π and ρ meson, the typical Lagrangian describing the interaction can be written as

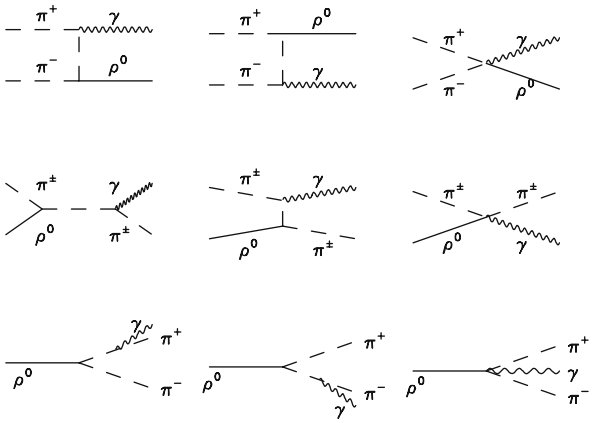

Fig. 9 Typical hadronic reactions for photon production

$$\mathcal{L} = \mid D_\mu \Phi \mid^2 - m_\pi^2 \mid \Phi \mid^2 - \frac{1}{4}\rho_{\mu\nu}\rho^{\mu\nu} + \frac{1}{2}m_\rho^2 \rho_\mu \rho^\mu - \frac{1}{4}F_{\mu\nu}F^{\mu\nu}, \tag{33}$$

where $D_\mu = \partial_\mu - ieA_\mu - ig_\rho \rho_\mu$, Φ is the complex pion field, $\rho_{\mu\nu}$ is the ρ field strength, and $F_{\mu\nu}$ is the photon field tensor. The differential cross sections for the dominating photon-producing process ($\pi\rho \rightarrow \pi\gamma$) in the hadronic phase are expressed as [36, 37],

$$\begin{aligned}\frac{d\sigma}{dt}(\pi^+\rho^0 \longrightarrow \pi^+\gamma) &= \frac{d\sigma}{dt}(\pi^-\rho^0 \longrightarrow \pi^-\gamma) \\ &= \frac{\alpha g_\rho^2}{12 s p_{\text{c.m.}}^2}\left[2 - \frac{(m_\rho^2 - 4m_\pi^2)s}{(s-m_\pi^2)^2} - (m_\rho^2 - 4m_\pi^2)\right. \\ &\left.\times\left(\frac{s - m_\rho^2 + m_\pi^2}{s - m_\pi^2}\frac{1}{u - m_\pi^2} + \frac{m_\pi^2}{(u-m_\pi^2)^2}\right)\right].\end{aligned} \tag{34}$$

Similarly for

$$\begin{aligned}\frac{d\sigma}{dt}(\pi^-\rho^+ \longrightarrow \pi^0\gamma) &= \frac{d\sigma}{dt}(\pi^+\rho^- \longrightarrow \pi^0\gamma) \\ &= -\frac{\alpha g_\rho^2}{48 s p_{\text{c.m.}}^2}\left[4(m_\rho^2 - 4m_\pi^2)\left[\frac{u}{(u-m_\pi^2)^2} + \frac{t}{(t-m_\rho^2)^2}\right.\right. \\ &\left. - \frac{m_\rho^2}{s - m_\pi^2}\left(\frac{1}{u-m_\pi^2} + \frac{1}{t-m_\rho^2}\right)\right] + \left[\left(3 + \frac{s-m_\pi^2}{m_\rho^2}\right)\right. \\ &\left.\left.\times \frac{s-m_\pi^2}{t-m_\rho^2}\right] - \frac{1}{2} + \frac{s}{m_\rho^2} - \left(\frac{s-m_\pi^2}{t-m_\rho^2}\right)^2\right]\end{aligned} \tag{35}$$

and also

$$\frac{d\sigma}{dt}(\pi^0\rho^+ \longrightarrow \pi^+\gamma) = \frac{d\sigma}{dt}(\pi^0\rho^- \longrightarrow \pi^-\gamma)$$
$$= \frac{\alpha g_\rho^2}{48 s p_{\text{c.m.}}^2}\left[\frac{9}{2} - \frac{s}{m_\rho^2} - \frac{4(m_\rho^2 - 4m_\pi^2)s}{(s-m_\pi^2)^2}\right.$$
$$+ \frac{(s-m_\pi^2)^2 - 4m_\rho^2(m_\rho^2 - 4m_\pi^2)}{(t-m_\rho^2)^2}$$
$$+ \frac{1}{t-m_\rho^2}\left(5(s-m_\pi^2) - \frac{(s-m_\pi^2)^2}{m_\rho^2}\right.$$
$$\left.\left. - \frac{4(m_\rho^2 - 4m_\pi^2)}{s-m_\pi^2}(s - m_\pi^2 + m_\rho^2)\right)\right]. \tag{36}$$

In the above set of equations, s, t, u are the Mandelstam variables and $p_{\text{c.m.}}$ is the three momentum of the interacting particles in their center-of-mass frame. Typical results are shown in Fig. 10.

Xiong et al. [46] and Song [47] first introduced the $\pi\rho \rightarrow a_1 \rightarrow \pi\gamma$ channel for photon production in hadronic phase, whereas baryonic processes and medium modification were included by Alam et al. [48, 49]. Several refinements, e.g., inclusion of strange sector, use of massive Yang–Mills theory, and t-channel exchange of ω mesons, were incorporated by Turbide et al. [50]. The last calculation is essentially the state-of the-art result at the moment. Photon spectra considering a complete leading rate from QGP [42] and exhaustive reactions in hadronic matter [36, 37, 50] are shown in Fig. 11.

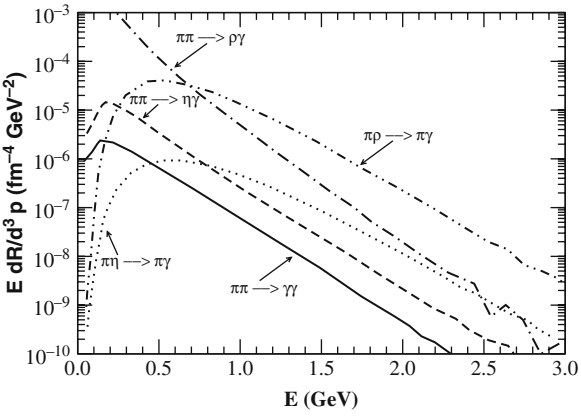

Fig. 10 *Left panel*: Yield of photons from different hadronic channels (taken from [36, 37])

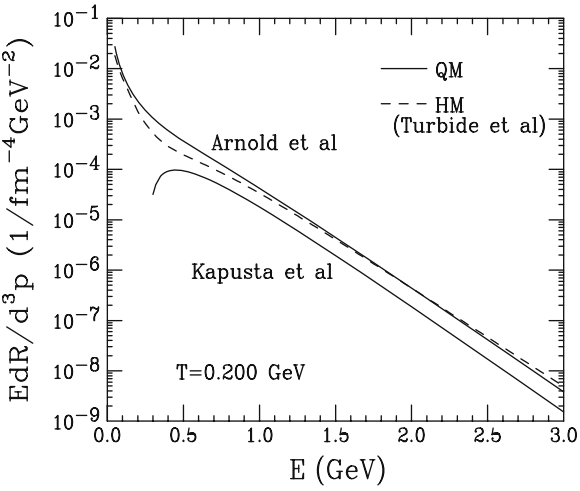

Fig. 11 Complete leading order rates from QGP and exhaustive reactions in hadronic matter [36, 37, 42, 50]

3 Photons from Pb+Pb@SPS to Au+Au@RHIC

3.1 SPS

In order to get an idea of greatly increased insights provided by single photon production, let us briefly recall some of the important results from the SPS era, many of which preceded the large strides made in our theoretical understanding mentioned above. The first hint of single photon production, which later turned out to be the upper limit of their production, came from the $S + \mathrm{Au}$ collisions studied at the SPS energies [51].

These results were analyzed in two different scenarios by authors of [52]. In the first scenario, a thermally and chemically equilibrated quark–gluon plasma was assumed to be formed at some initial time ($\tau_0 \approx 1$ fm/c), which expanded [53], cooled, and converted into a mixed phase of hadrons and QGP at a phase-transition temperature, $T_C \approx 160$ MeV. When all the quark matter was converted into a hadronic matter, the hot hadronic gas continued to cool and expand, and underwent a freeze-out at a temperature of about 140 MeV. The hadronic gas was assumed to consist of π, ρ, ω, and η mesons, again in thermal and chemical equilibrium. This was motivated by the fact that the included hadronic reactions involved [36, 37] these mesons. This was already a considerable improvement over a gas of massless pions used in the literature at that time. In the second scenario, the collision was assumed to lead to a hot hadronic gas of the same composition. The initial temperature was determined by demanding that the entropy of the system be determined from the measured particle rapidity density [54]. It was found that the scenario which did not involve a formation of QGP led to a much larger initial temperature and a production of photons which was considerably larger than the upper limit of

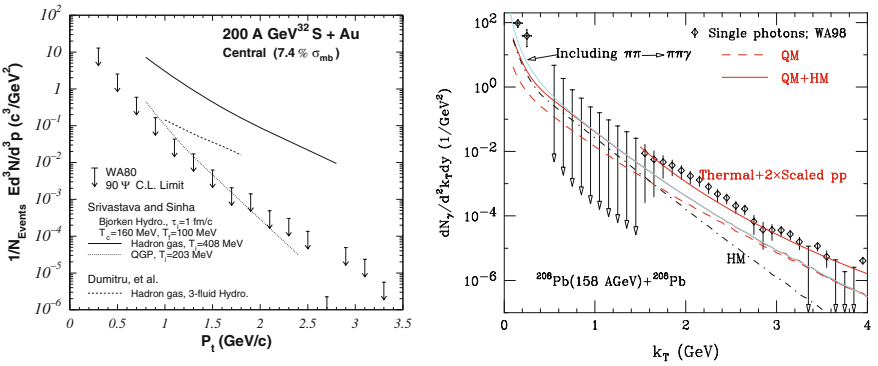

Fig. 12 *Left panel*: Upper limits at the 90% confidence level on the invariant excess photon yield for the 7.4% σ_{mb} most central collisions of 200A GeV ^{32}S + Au [51]. The *solid and the dashed curves* give the thermal photon production expected from hot hadron gas calculation [52], while the *dotted curve* is the calculated thermal photon production expected in the case of a QGP formation. *Right panel*: Single photon production in Pb+Pb collision at CERN SPS. Prompt photons are estimated using pQCD (with a K-factor estimated using NLO calculation) and intrinsic k_T of partons [55]

the photon production, and could be ruled out. The calculation assuming a quark–hadron phase transition yielded results which were consistent with the upper limit of the photon production. These results were confirmed [56–62] by several calculations exploring different models of expansion (see left panel of Fig. 12).

It was soon realized that one may not limit the hadronic gas to contain just π, ρ, ω, and η mesons, as there was increasing evidence that perhaps all the mesons and baryons were being produced in a thermal and chemical equilibrium in such collisions. Thus authors of [63] explored the consequences of using a hadronic gas consisting of essentially all the hadrons in the Particle Data Book, in a thermal and chemical equilibrium. This led to an interesting result for the Pb+Pb collision at SPS energies, for which experiments were in progress. It was found that with the rich hadronic gas, the results for the production of photons in the phase-transition and no-phase-transition models discussed above were quite similar, suggesting that measurement of photons at the SPS energy could perhaps not distinguish between the two cases. However, in a very important observation, it was also noted that the calculations involving hot hadronic gas at the initial time would lead to hadronic densities of several hadrons/fm^3, and while those involving a quark–gluon plasma in the initial state would be free from this malady. Thus, it was concluded that the calculations involving a phase transition to QGP offered a more natural description.

The WA98 experiment [15] reported the first observation of direct photons in central 158A GeV Pb+Pb collisions studied at the CERN SPS. This was explained [64] in terms of formation of quark–gluon plasma in the initial state (at $\tau_0 \approx 0.2$ fm/c), which expanded, cooled, and hadronized as in [63] (see right panel of Fig. 12). An independent confirmation of this approach was provided by an accurate

description [65] of excess dilepton spectrum measured by the NA60 experiment for the same system.

Once again the results for single photons were analyzed by several authors using varying models of expansion as well as rates for production of photons; viz., with or without medium modification of hadronic properties (see, e.g., [50, 66–69]). The outcome of all these efforts can be summarized as follows: the single photon production in Pb+Pb collisions at SPS energies can be described either by assuming a formation of QGP in the initial state or by assuming the formation of a hot hadronic gas whose constituents have massively modified properties. The later description, however, involved a hadronic density of several hadrons/fm^3, which raises doubts about the applicability of a description in terms of hadrons, as suggested by [63].

3.2 RHIC

The first experimental photon result obtained from the relativistic heavy-ion collider was the centrality dependent single photon data for 200*A* GeV Au+Au collisions by PHENIX collaboration [16], where single photons were identified clearly for $p_T > 4$ GeV. For central collisions, the lower bound on photon transverse momenta was even much lower, upto 2 GeV (Fig. 13). Those data were in good agreement with NLO pQCD results for pp collisions, scaled by number of binary collisions (without considering the iso-spin effect).

Thermal radiation dominates the direct photon spectrum at lower values of p_T ($\leq$3 GeV) and the measured slope of the thermal photon spectrum can be related to the temperature of the system.

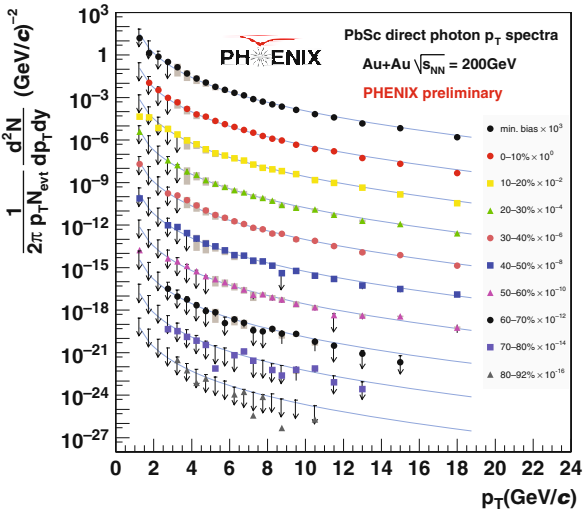

Fig. 13 Direct photon results for Au+Au collisions (*left panel*) and $p + p$ collisions (*right panel*) at $\sqrt{s_{NN}} = 200A$ GeV [16]

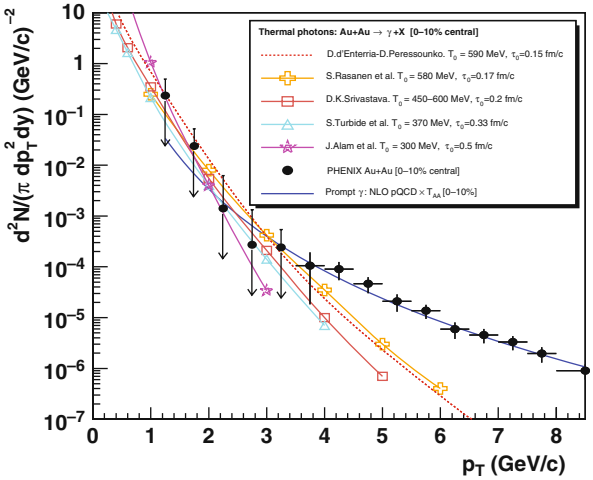

Fig. 14 Thermal photon spectra for central 200*A* GeV Au+Au collision computed within different models [71] compared to the expected pQCD prompt photon yield and to the experimental total direct photon spectrum measured by PHENIX [32]

In Fig. 14 results from several theoretical models based on hydrodynamics for thermal photon production at RHIC are shown. The initial temperature and thermalization time for Au+Au collision at 200*A* GeV quoted by several theoretical groups [50, 64, 66–71] are in the range of 450–650 MeV and about 0.2 fm/*c*, respectively.

All these calculations are comparable to the experimental data and with each others within a factor of 2 and also confirm the dominance of thermal radiation in the direct photon spectrum in low and intermediate p_T range.

3.2.1 Indications for Jet Conversion Photons

We have already discussed the procedure for calculating the high-energy photons due to passage of jets through the quark–gluon plasma.

The parametrized p_T distribution of jets (quarks, antiquarks, and gluons) obtained by using CTEQ5L parton distribution function and EKS98 nuclear modification factor is given by

$$\frac{dN^{\text{jet}}}{d^2p_T dy}|_{y=0} = T_{AA}\frac{d\sigma^{\text{jet}}}{d^2p_T dy}|_{y=0} = K\frac{a}{(1+p_T/b)^c}. \tag{37}$$

Here, $T_{\text{AA}} = 9A^2/8\pi {R_\perp}^2$ is the nuclear thickness for a head-on collision and to include the higher order effects a K-factor of 2.5 is introduced. Numerical values for the parameters for quarks, antiquarks, and gluons can be found in [13].

Now as a first step, let us ignore the transverse expansion of the plasma and assume that a thermally and chemically equilibrated plasma is produced in the collision at an initial time τ_0 at temperature T_0. In an isentropic longitudinal expansion,

T_0 and τ_0 are related by the observed particle rapidity density (dN/dy) by

$$T_0{}^3\tau_0 = \frac{2\pi^4}{45\zeta(3)}\frac{1}{4a\pi R_\perp^2}\frac{dN}{dy}, \tag{38}$$

where $a = 42.25\pi^2/90$, for QGP consisting of u, d, and s quarks and gluons. dN/dy can be taken as $\simeq$1260, based on the charge particle pseudorapidity density measured by PHOBOS experiment [72] for central collision of Au nuclei at $\sqrt{s}_{NN} = 200$ GeV. For central collision of Pb nuclei at LHC energies $dN/dy \simeq 5625$ was used by Fries et al. [13] as in [73].

Further assuming a rapid thermalization, initial conditions can then be estimated as [73] $T_0 = 446$ MeV and $\tau_0 = 0.147$ fm/c for the RHIC and $T_0 = 897$ MeV and $\tau_0 = 0.073$ fm/c for the LHC. Now, taking the nuclei to be uniform spheres, the transverse profile for initial temperature is given by $T(r) = T_0[2(1 - r^2/R_\perp{}^2)]^{1/4}$, where $R_\perp = 1.2A^{1/3}$ fm. The same profile $R(r) = 2(1 - r^2/R_\perp{}^2)$ is used for the jet production.

The jet traverses the QGP medium until it reaches the surface or until the temperature drops to the transition temperature T_c ($\sim$160 MeV).

First estimates for the jet conversion photons at RHIC and LHC energies along with other sources of photons having large transverse momentum are given in Fig. 15. We see that the jet conversion photons make a fairly large contribution in the p_T range of 4–10 GeV.

The centrality dependence of jet conversion photons was also studied by Fries et al. [74] (see Fig. 16), which indicates a small but clear contribution of photons due to passages of jets through the plasma. These early calculations have been brought to a high degree of sophistication by the McGill group [75] (see Fig. 17), where jet quenching and jet-photon conversion along with bremsstrahlung is treated in a single framework. The details can be seen in [75].

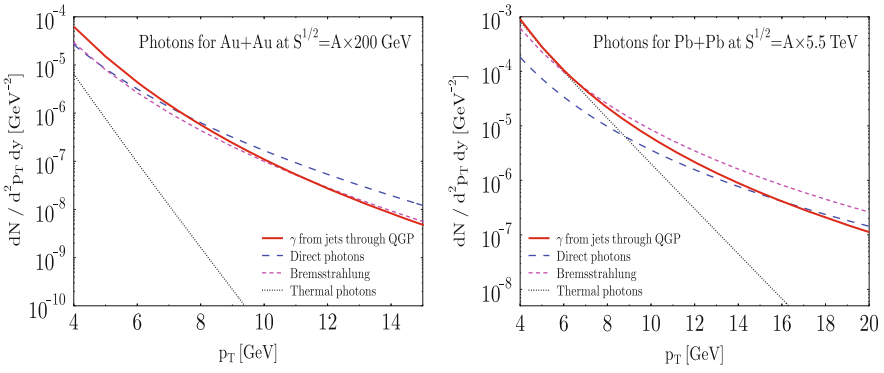

Fig. 15 Jet conversion photons at RHIC [*left panel*] and LHC [*right panel*] energies (taken from [13])

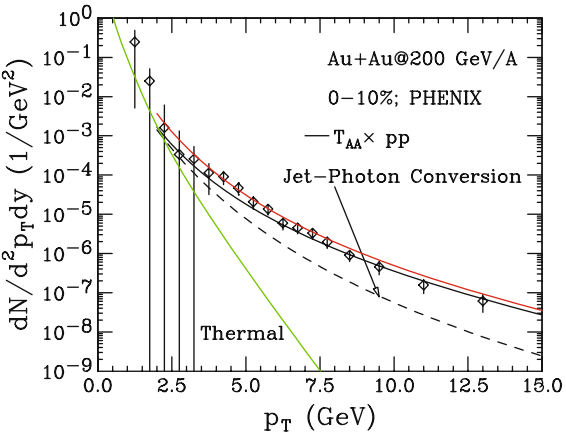

Fig. 16 Photon yield as a function of p_T in central (0–10%) Au+Au collisions at 200A GeV. Results of jet-photon conversion (*solid* and *labeled*), primary hard photons (*dashed*), and the sum of the two (*upper-most solid curve*) along with thermal photons are shown separately. Data are from the PHENIX collaboration [32]

In Fig. 17, the results for thermal photons, direct photons due to primary processes, bremsstrahlung photons, and the photons coming from jets passing through the QGP in central collision of gold nuclei at RHIC energies are plotted. The quark jets passing through the QGP give rise to a large yield of high-energy photons. For RHIC this contribution is a dominant source of photons up to $p_T \simeq 6$ GeV. Due to multiple scattering suffered by the fragmenting partons a suppression of the bremsstrahlung contribution is found. This will further enhance the importance of the jet-photon conversion process.

Obviously a high statistics data at several centralities and energies will go a long way in clearly establishing the presence of jet conversion photons at RHIC and

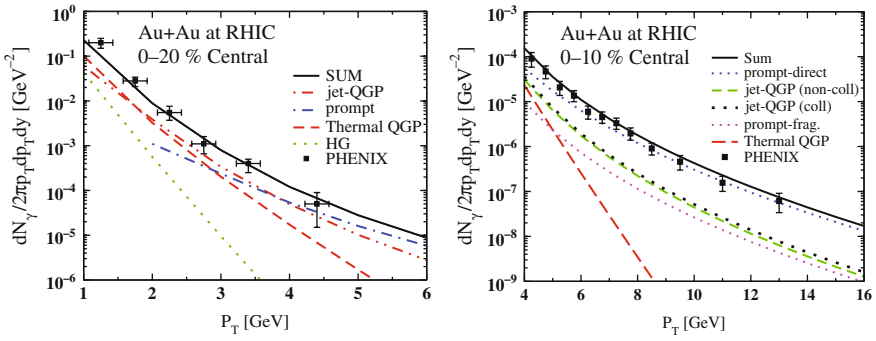

Fig. 17 Yield of photons in Au+Au collisions at RHIC, for centrality classes 0–10% (*left panel*) and 0–10% (*right panel*). See [75] for details. The data sets are from [76] and [32], respectively

LHC energies. This is also of importance, as there are indications that these photons measure the initial spatial anisotropy of the system [75].

4 Dileptons

Virtual photons or dileptons are also very powerful and efficient probes like the real photons to study the dynamics of heavy-ion collisions and the properties of the medium created in the collisions. Real photons are massless, whereas dileptons are massive. Thus, invariant mass M and the transverse momentum p_T are the two parameters available for dileptons, which can be tuned to investigate the different stages of the expanding fireball. Dileptons having large invariant mass and high p_T are emitted very early, soon after the collision when the temperature of the system is very high. On the other hand, those having lower invariant masses come out later from a relatively cooler stages and at low temperatures.

Similar to the real photons, dileptons are also emitted from every stage of heavy-ion collisions [2]. In the QGP phase, a quark can interact with an antiquark to form a virtual photon γ^*, which subsequently decays in to a lepton (l^-) and an anti-lepton (l^+) pair, together known as dilepton. In the hadronic phase, dileptons are produced from interactions of charged hadrons with their anti-particles by processes like ($\pi^+ + \pi^- \rightarrow l^+ + l^-$) (see Fig. 18). They are also produced from decay of hadronic resonances like ρ, ω, ϕ, and J/Ψ as well as from Drell–Yan process. In the Drell–Yan process, a valence quark from a nucleon in the projectile nucleus interacts with a sea antiquark from a nucleon in the target nucleus to form a virtual photon, which decays into a lepton pair. The dilepton emissions can be classified into three distinct regimes in a rough estimation, depending on the invariant mass M of the emitted lepton pairs. These are

(a) Low mass region (LMR): $M \leq M_\phi (= 1.024\,\text{GeV})$: In this mass range, vector meson decays are the dominating source of dilepton production and medium-modified spectral density is one of the key issues which needs to be addressed.

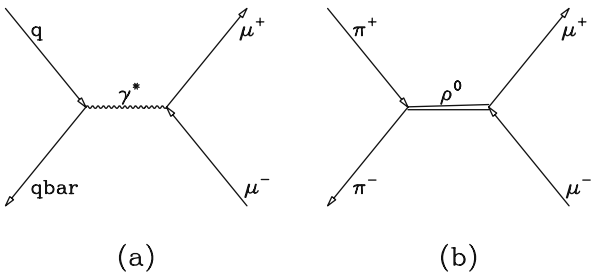

Fig. 18 Dilepton production from (a) quark–antiquark annihilation and (b) $\pi^+\pi^-$ annihilation through ρ channel

(b) Intermediate mass region (IMR): $M_\phi < M < M_{J/\Psi}(=3.1\,\text{GeV})$: In intermediate mass region, continuum radiation from QGP dominates the dilepton mass spectrum and thus this region is important for getting a pure QGP signature.
(c) High mass region (HMR): $M \geq M_{J/\Psi}$: In the HMR, the most interesting phenomenon is the primordial emission and heavy quarkonia like J/Ψ and Υ suppression.

A schematic diagram of continuous dilepton mass spectrum is shown in Fig. 19.

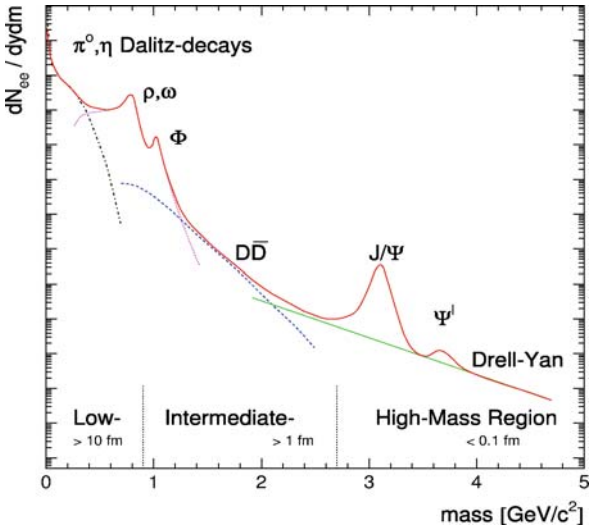

Fig. 19 Expected sources of dilepton production as a function of invariant mass in relativistic heavy-ion collisions (schematic)

4.1 Dileptons from QGP and Hadronic Phase

Dilepton production by quark–antiquark annihilation process or by $\pi^+\,\pi^-$ annihilation process can be expressed in a general form as

$$a^+ + a^- \rightarrow l^+ + l^- \tag{39}$$

where the particle "a" can be either a quark or a π meson. We closely follow the treatment of [14] for calculation of dilepton spectra in this section. From quantum electrodynamics (QED), the cross section for $e^+e^- \rightarrow \mu^+\mu^-$ can be written as

$$\tilde{\sigma}(M) = \frac{4\pi}{3}\frac{\alpha^2}{M^2}\left[1 + \frac{2m_l^2}{M^2}\right]\left[1 - \frac{4m_l^2}{M^2}\right]^{1/2}. \tag{40}$$

In the above equation, α is the fine structure constant ($\approx 1/137$), m_l is the mass of μ, and M is the dilepton-invariant mass. For the quark–antiquark annihilation process, this cross section is modified by inclusion of a color factor $N_c(=3)$ and the fractional charges of the up(u) and down(d) quarks. Thus, the new cross section takes the form as

$$\sigma_q(M) = F_q \tilde{\sigma}(M), \tag{41}$$

$$F_q = N_c(2s+1)^2 \sum_f e_f^2, \tag{42}$$

where s is the spin of quarks, e_f is the fractional charge, and the sum is over different quark flavor "f." If we consider only u and d quarks having fractional charges 1/3 and 2/3, respectively, then the factor F_q is 20/3.

In the hadronic phase, the $\pi^+\pi^-$ annihilation from vector meson dominance model can be expressed as

$$\pi^+ + \pi^- \rightarrow \rho \rightarrow l^+ + l^-. \tag{43}$$

For this case, the QED cross section is multiplied by form factor $F_\pi(M)$ which is of Breit–Wigner form as

$$F_\pi(M) = \frac{m_\rho^4}{(m_\rho^2 - M^2)^2 + m_\rho^2 \Gamma_\rho^2}. \tag{44}$$

Here, M_ρ is the mass of the ρ meson ($\sim$ 770 MeV) and Γ_ρ ($\sim$ 155 MeV) is the decay width. Thus, the total pion cross section as a function of M becomes

$$\sigma_\pi(M) = F_\pi \tilde{\sigma}(M)(1 - 4m_\pi^2/M^2)^{1/2}. \tag{45}$$

The reaction rate "R" can be obtained from the kinetic theory:

$$R(a^+a^- \rightarrow l^+l^-) = \int \frac{d^3p_1}{(2\pi)^3} f(\mathbf{p_1}) \int \frac{d^3p_2}{(2\pi)^3} f(\mathbf{p_2}) \sigma(a^+a^- \rightarrow l^+l^-; \mathbf{p_1}\mathbf{p_2}) v_{\text{rel}} \tag{46}$$

where

$$v_{rel} = \frac{[(p_1.p_2)^2 - m_a^4]^{1/2}}{E_1 E_2}, \tag{47}$$

$f(\mathbf{p})$ is the occupation probability at momentum $\mathbf{p}$, and energy $E = \sqrt{\mathbf{p}^2 + m_a^2}$. Now, using the distribution function $f(\mathbf{p}) \sim e^{-E/T}$ and integrating over five out of the six variables, the reaction rate takes a simplified form as

$$R(T) = \frac{T^6}{(2\pi)^4} \int_{z_0}^{\infty} \sigma(z) z^2 (z^2 - 4z_a^2) K_1(z) dz. \tag{48}$$

Here, $z = M/T$, $z_a = m_a/T$, and K_1 is the modified Bessel function of the first kind. The value of the parameter z_0 is taken as the larger of $2m_a/T$ and $2m_l/T$. Now, for massless u and d quarks (as $m_u, m_d \ll T$), the e^+e^- emission rate takes a simple form of T^4 law,

$$R = \frac{10}{9\pi^3}\alpha^2 T^4. \tag{49}$$

One can also estimate the relaxation time for lepton pairs to come to equilibrium with the QGP:

$$t_{\rm rel} = \frac{n^l_{\rm eq}}{2R} = \frac{9\pi}{10\alpha^2 T}. \tag{50}$$

For a temperature range of 200–500 MeV, the value of $t_{\rm rel}$ varies from 20 to 60×10^3 fm/c. We know that the lifetime of the QGP phase is only ~ 10 fm/c, which is more than three order of magnitude smaller than $t_{\rm rel}$. Thus, like the real photons, the produced lepton pairs also escape the system without suffering significant absorption in the medium.

Now, the dilepton emission rate R is actually defined as the total number of lepton pairs emitted from a 4-volume element d^4x ($= \mathrm{d}^2x_T\ \mathrm{d}\eta\ \tau\ \mathrm{d}\tau$) at a particular temperature T is given by

$$R = \mathrm{d}N/\mathrm{d}^4x. \tag{51}$$

Thus, the rate of production of dileptons having invariant mass M can be expressed using Eq. (46) as

$$\frac{dN}{d^4x dM^2} = \frac{\sigma(M)}{2(2\pi)^4} M^3 T K_1(M/T)\left[1 - \frac{4m_a^2}{M^2}\right]. \tag{52}$$

From the last equation and using properties of the modified Bessel's functions, the production rate per unit 4-volume for total energy E, momentum p, and invariant mass M (where $E = \sqrt{p^2 + M^2}$) can be written as

$$E\frac{dN}{d^4x dM^2 d^3p} = \frac{\sigma(M)}{4(2\pi)^5} M^2 e^{-E/T}\left[1 - \frac{4m_a^2}{M^2}\right]. \tag{53}$$

Integrating the rate of emission over the entire 4-volume from QGP and hadronic phase, one can obtain the p_T spectra at a particular M as

$$\frac{dN}{dM^2 d^2 p_T dy} = \int \tau \, d\tau \, r \, dr \, d\eta \, d\phi \left[\left[E \frac{dR}{dM^2 d^3 p} \right]_{\mathrm{QGP}} f_{\mathrm{QGP}}(r, \tau) + \left[E \frac{dR}{dM^2 d^3 p} \right]_{\mathrm{HM}} f_{\mathrm{HM}}(r, \tau) \right], \tag{54}$$

where η is the space–time rapidity. In the above equation, the temperature T, QGP, and hadronic matter (HM) distribution functions ($f_{\mathrm{QGP}}, f_{\mathrm{HM}}$) all are functions of space $\mathbf{r}\,(x, y)$, transverse velocity v_T, and proper time τ. Equation (54) can be solved numerically by using any appropriate model [e.g., [77]] with a proper equation of state (EOS). One can also get the invariant mass spectrum by integrating out the variable p_T from Eq. (54). The invariant mass spectrum of thermal dilepton is dominated by QGP radiation above ϕ mass and hadronic radiation outshines the QGP contribution for $M \leq M_\phi$.

4.2 Medium Modification

As mentioned earlier, in the low-mass region, dilepton emission is largely mediated by $\rho(770)$, a broad vector meson, as a result of its strong coupling to the $\pi\pi$ channel and a short lifetime, which is about 1.3 fm/c. In-medium properties of vector mesons, like change in medium mass and width, have long been considered as prime signatures of a hot and dense hadronic medium. CERES/NA45 [78, 79] started the pioneering experiment on dilepton measurement during the period 1989–1992 at CERN SPS. For $p+$Be and $p+$Au collisions, the theoretical estimates, considering only hadron decay (as source of dilepton production), were in excellent agreement with the experimental data points. However, the CERES/NA45 experimental data for S + Au and Pb + Au at 200A GeV and 158A GeV, respectively, exhibit excess radiation beyond the electromagnetic final state decay of produced hadrons below the ϕ mass. From these observations, it was concluded that the theoretical models based on $\pi\pi$ annihilation can reproduce the experimental data, only if the properties of the intermediate ρ meson are modified in the medium. This was an exciting discovery and a genuine consequence of many-body physics. However, the resolution and statistical accuracy of the data were insufficient to distinguish between models suggesting a drop in the mass of ρ mesons [80] and those which suggest an increase in their decay width [81] and thus, determine the in-medium spectral properties of the ρ meson.

Shortly after this, an excess dimuon (over the sources expected from pA measurement) was identified experimentally by Helios/3 [82, 83] (measured both e^+e^- and $\mu^+\mu^-$) and NA38/NA50 [84] collaborations.

Rapp and Shuryak [85] and Kvasnikova et al. [65] showed that the excess dimuon observed by NA50 in the mass region $1.5 < M < 2.5$ GeV can be explained by thermal signal without invoking any anomalous enhancement in the charm production. Kvasnikova et al. studied the NA50 intermediate mass dimuon result using hydrodynamic model and a detailed analysis of the rates of dilepton production from

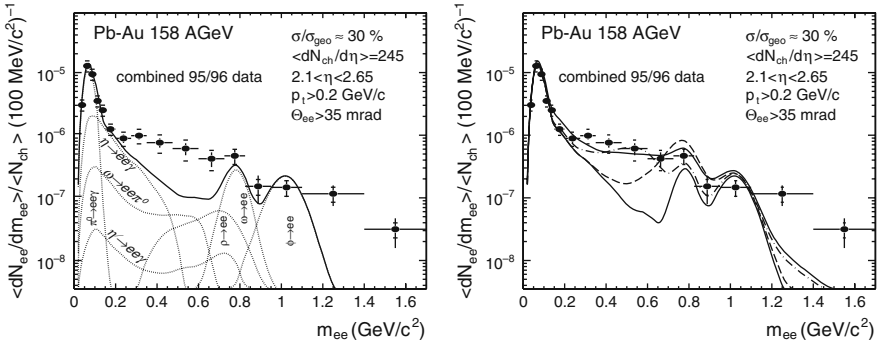

Fig. 20 *Left panel*: Invariant mass spectrum of e^+e^- pairs emitted in 158A GeV Pb+Au collisions from the combined analysis of 1995 and 1996 data by CERES/NA45 [78, 79]. The *solid line* shows expected yield from hadron decay and *dashed lines* indicate the individual contribution to the total yield. *Right panel*: Comparison of the experimental data to (i) free hadron decays without ρ decays (*thin solid line*), (ii) model calculations with a vacuum ρ spectral function (*thick dashed line*), (iii) with dropping in-medium ρ mass (*thick dash-dotted line*), and (iv) with a medium-modified ρ spectral function (*thick solid line*)

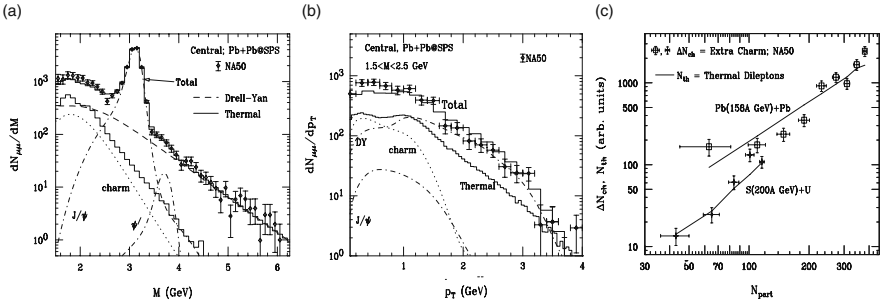

Fig. 21 (a) The dimuon invariant mass spectrum after correcting for detector acceptance and resolution and NA50 data. The Drell–Yan and thermal contributions are shown separately along with correlated charm decay and direct decays of the J/Ψ and $\bar{J}/\Psi$. (b) The dimuon transverse momentum spectrum. (c) Centrality dependent results from [65] and NA50 data [84]

hadronic phase [65]. Detector resolution and acceptance were accurately modeled in their calculation and the normalization was determined by a fit to the Drell–Yan data using the MRSA parton distribution function as done in the experimental NA50 analysis. The results are shown in Fig. 21. They also studied the centrality dependence of the NA50 data using hydrodynamics by incorporating azimuthal anisotropy in the calculation. The results were in fairly good agreement with the measured excess dilepton data, as can be seen in the third panel of Fig. 21.

4.2.1 Dropping m_ρ vs. Increasing Γ_ρ

The CERES data were unable to distinguish between the models suggesting drop in the mass of ρ meson and those suggesting an increase in its width, as seen in Fig. 20.

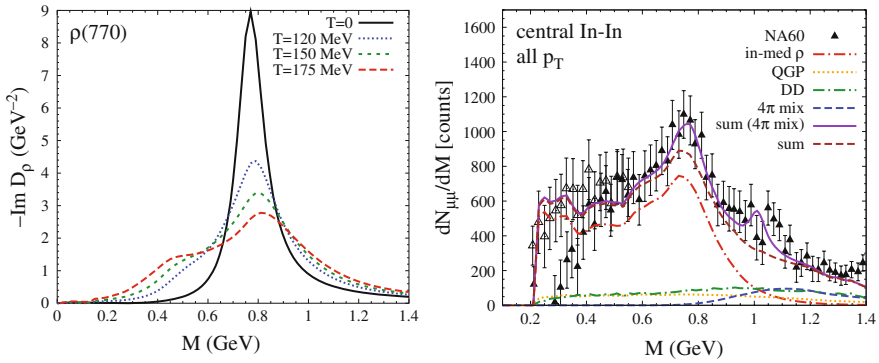

Fig. 22 *Left panel*: In-medium vector meson spectral functions from hadronic many-body theory. The ρ in cold nuclear matter at several densities proportional to the saturation density $\rho_0 = 0.16$ fm^{-3}. *Right panel*: NA60 [86] excess dimuons in central In + In collisions at SPS compared to thermal dimuon radiation using in-medium electromagnetic rates [87]

The high statistics data obtained by the NA60 Collaboration for In + In collisions at SPS energies for the dimuon excess rather clearly ruled out the models advocating the dropping mass scenarios. They rather firmly establish the models advocating the substantial broadening of the decay width of the ρ meson due to many-body effects (see Fig. 22).

5 Elliptic Flow

Elliptic flow is one of the key observables in relativistic collisions of heavy nuclei, which confirms the collectivity and early thermalization in the created hot and dense matter. For a non-central collision (impact parameter $b \neq 0$) of two spherical nuclei, the overlapping zone between the nuclei no longer remains circular in shape, rather it takes an almond shape. This initial spatial anisotropy of the overlapping zone is converted into momentum space anisotropy of particle distribution via the action of azimuthally anisotropic pressure gradient, which gives rise to elliptic flow [88]. Note that, this anisotropic flow or elliptic flow can also be produced in central collisions of deformed nuclei, such as U + U collisions [89]. The driving force for momentum anisotropy is the initial spatial eccentricity ϵ_x ($=< y^2 - x^2 > / < y^2 + x^2 >$) and the momentum anisotropy can grow as long as $\epsilon_x > 0$ [90]. Elliptic flow coefficient v_2 is quantified as the second Fourier coefficient of particle distribution in the p_T space, which is of the form:

$$\frac{dN(b)}{p_T dp_T\, dy\, d\phi} = \frac{dN(b)}{2\pi p_T\, dp_T\, dy}(b) \times [1 + 2v_1(p_T, b)\cos(\phi) + 2v_2(p_T, b)\cos(2\phi) + 2v_3(p_T, b)\cos(3\phi) + \ldots]. \quad (55)$$

At midrapidity ($y = 0$) and for collisions of identical nuclei, only the even cosine terms survive in the above Fourier series and v_2 is the lowest non-vanishing anisotropic flow coefficient. Now, the value of v_2 depends on the impact parameter b, transverse momentum p_T, as well as on the particle species through their rest masses m. For massless real photons, v_2 depends on the elliptic flow of parent particles.

5.1 Thermal Photon v_2

Elliptic flow coefficient v_2 for photons is a much more powerful tool than the v_2 of hadrons to study the evolution history of the system depending on the different emission time and production mechanism of photons compared to hadrons. Photons are emitted from all stages and throughout the evolution of the system, whereas hadrons are emitted only from the freeze-out surface at a relatively much cooler temperature ($\sim$ 100 MeV). The interplay of the photon contributions from fluid elements at different temperatures with varying radial flow pattern gives the photon v_2 a richness, which is not possible for hadrons. Also, photons emitted from QGP phase as a result of $q\bar{q}$ annihilation and quark–gluon Compton scattering carry the momenta of the parent quarks or antiquarks, which makes them an unique tool for QGP study.

Ideal hydrodynamic model has successfully predicted the elliptic flow for different hadronic species upto a p_T value of 1.5(2.3) GeV for mesons (baryons) [90] at RHIC. Experimental data show that $v_2(p_T)$ for hadrons saturate beyond that p_T range. However, ideal hydrodynamics predicted $v_2(p_T)$ rises monotonically with p_T. The saturation at higher p_T is often explained as due to viscosity, neglected in the discussion here.

Figure 23 shows the p_T-dependent v_2 for thermal photons [10, 11] for a typical impact parameter $b = 7$ fm. Contributions from quark matter (QM) and hadronic matter (HM) along with the sum of the two are shown separately (left panel of

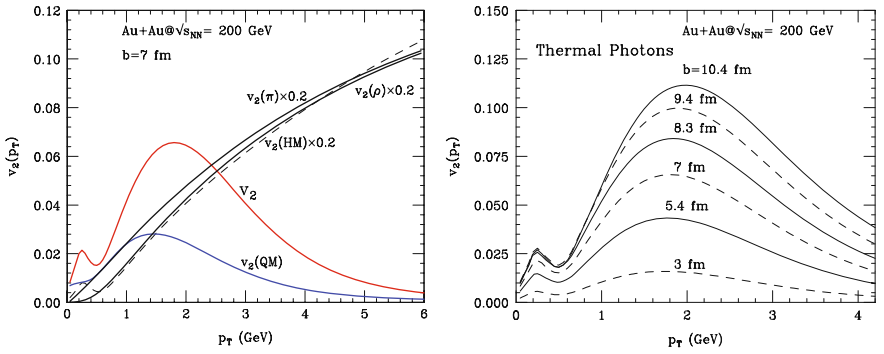

Fig. 23 *Left panel*: $v_2(p_T)$ for thermal photons along with the v_2 for π and ρ mesons. Contributions from the quark matter and the hadronic matter are shown separately with the sum contribution. *Right panel*: Thermal photon v_2 for different centrality bins (taken from [10, 11])

Fig. 23). One can see that $v_2(HM)$ rises monotonically with p_T, similar to the hadronic v_2 predicted by hydrodynamics. On the other hand, $v_2(QM)$ is very small at high p_T or early times, as very little flow is generated by that time. $v_2(QM)$ rises for smaller values of p_T and after attaining a peak value around 1.5–2.0 GeV, it tends to 0 as $p_T \to 0$. The total flow or v_2(QM+HM) tracks the $v_2(QM)$ at high p_T in spite of very large $v_2(HM)$, as the yield of photons from hadronic phase is very small at high p_T. It is well known and mentioned earlier that, for photon energy larger than the rest masses of the photon-emitting particles, the photon production cross section peaks when the photon momentum and momentum of photon-emitting particles become almost identical [2]. Thus, at high p_T photon v_2 reflects the anisotropies of the quarks and antiquarks at early times. Also, the collision-induced conversion of vector mesons (ρ) starts dominating the photon production for $p_T \geq 0.4$ GeV, which gives rise to a structure at the transition point in the photon v_2 curve [10, 11]. As HM contribution dominates the p_T spectrum and hydrodynamics is well applicable around that p_T range, the structure is expected to survive in the experimental result also.

Recently Turbide et al. [75] have shown that total contribution to photon v_2 from prompt fragmentation (small $+ve$ v_2) and jet-conversion (small $-ve$ v_2) photons is very small, almost equal to zero. Also, we know that the prompt photons from Compton and annihilation processes do not contribute to elliptic flow as their emission is not subjected to collectivity and has azimuthal symmetry. Thus, at low and intermediate p_T range, v_2 from thermal photons plays a dominant role in deciding the nature of the direct photon v_2.

For central collision of two spherical nuclei, the spatial eccentricity (ϵ) of the overlapping zone is zero, thus the flow coefficient v_2 is also zero. The $v_2(p_T)$ for thermal photons for different centrality bins are shown in the right panel of Fig. 23, where the value of v_2 rises from central toward peripheral collisions. Now, the elliptic flow as well as spatial eccentricity both rise with higher values of impact parameter. However, the ratio of the two remains independent of impact parameter

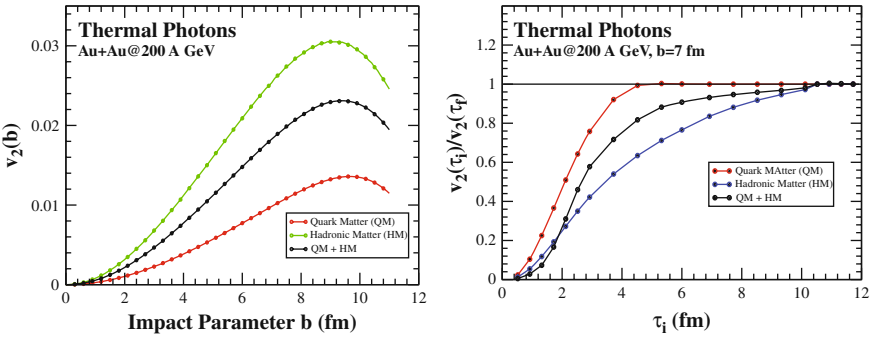

Fig. 24 *Left panel*: p_T integrated elliptic flow of thermal photons from different phases at RHIC. *Right panel*: Time evolution of elliptic flow from different phases, normalized by the final value at the time of freeze-out (taken from [91, 92])

up to a very large value of b [91, 92]. The p_T integrated v_2 for thermal photons from different phases as a function of collision centrality shows an interesting behavior (left panel of Fig. 24). The $v_2(b)$ rises with b until for very peripheral collisions. For these, the system size itself becomes very small to generate enough pressure gradient and elliptic flow, and as a result $v_2(b)$ decreases. The p_T-dependent as well as p_T-integrated time evolution results [91, 92] of thermal photon spectra and elliptic flow show explicitly the gradual buildup of spectra and v_2 with time very well. The photon v_2 from QGP phase saturates within about 4–5 fm/c (right panel of Fig. 24), whereas v_2 from hadronic phase is not very significant at early times and it saturates much later.

5.2 Thermal Dilepton v_2

Elliptic flow of thermal dileptons is another very interesting and illustrative observable which gives information of the different stages of heavy ion collision depending on invariant mass M and transverse momentum p_T [93]. At the ρ and ϕ masses, the p_T spectra and $v_2(p_T)$ show complete dominance of hadronic phase. At these resonance masses, radiation from quark matter becomes significant only for very large $p_T(\geq 4)$ GeV (left panel of Fig. 25). The $v_2(p_T)$ at $M = m_\rho$ also shows similar nature as spectra and the total v_2 is almost similar to hadronic v_2 upto a large p_T. Right panel of Fig. 25 shows dilepton v_2 at ρ mass along with v_2 of ρ meson where $v_2(HM)$ tracks $v_2(\rho)$. Also, the hadronic v_2 is little smaller than the $v_2(HM)$ for dileptons. The effective temperature of dilepton emission is a little larger than for hadrons, thus the spectra of the later are boosted by a somewhat larger radial flow [93], which results in smaller elliptic flow.

A totally different situation emerges for the p_T spectrum and v_2 for dilepton invariant mass $M > M_\phi$. For $M = 2$ GeV, the dilepton v_2 is similar to $v_2(QM)$ in spite of the 20 times larger $v_2(HM)$, as hadronic dileptons are very few compared to QGP radiation at this M value (Fig. 26).

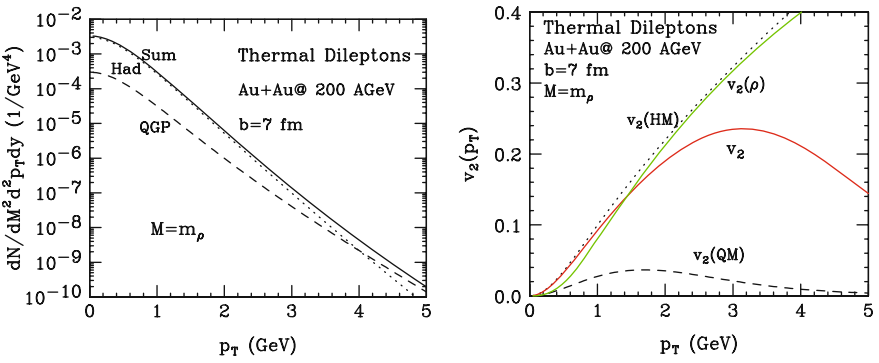

Fig. 25 p_T spectra (*left panel*) and v_2 (*right panel*) for thermal dileptons at $M = m_\rho$. $v_2(\rho)$ is also plotted in the v_2 curve for comparison [93]

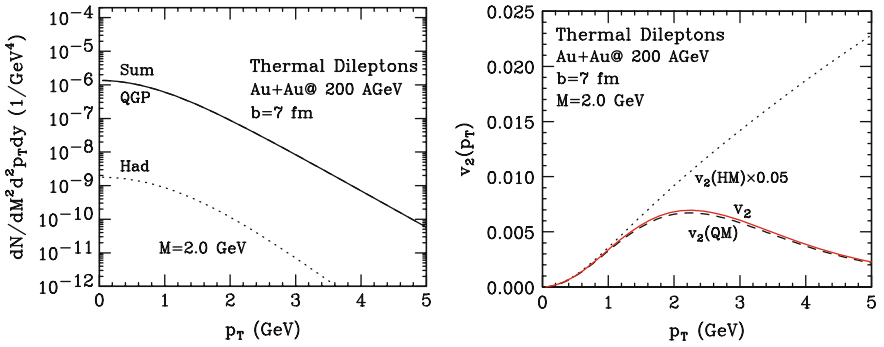

Fig. 26 p_T spectra (*left panel*) and v_2 (*right panel*) for thermal dileptons at $M = 2$ GeV [93]

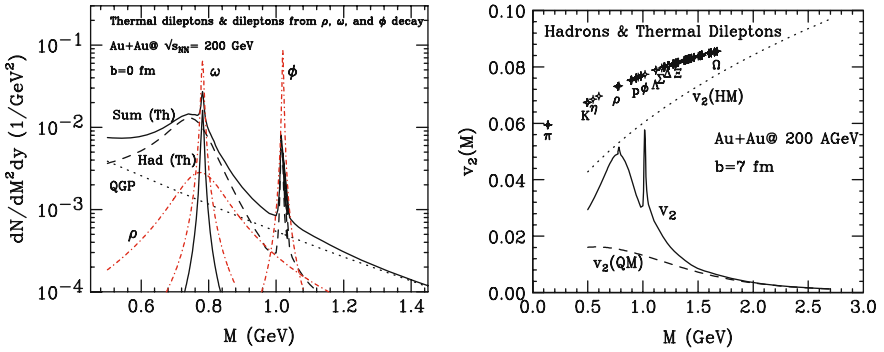

Fig. 27 *Left panel*: The mass spectra of thermal dileptons from a hydrodynamical simulation of central 200A GeV Au + Au collision. Quark and hadronic matter contributions are shown separately. *Right panel*: p_T-integrated elliptic flow parameter for dileptons and various hadrons [93]

The p_T-integrated spectra and v_2 as a function of invariant mass M show well-defined peaks at the resonance masses (ρ, ω, and ϕ), as can be seen Fig. 27. For $M \leq M_\phi$, the dilepton spectrum is totally dominated by hadronic phase and above that it is dominated by contribution from QGP. $v_2(QM)$ is very small at large M and rises for smaller M. It shows a nature similar to the thermal photon v_2. The M-dependent $v_2(HM)$ is significant only at the resonance masses and beyond ϕ mass its contribution to total v_2 is negligible. Thus, for large values of M or at early times flow comes from QGP phase and its value is very small, whereas at later times or at low M values it is from HM, which is very strong. The measurement of flow parameter at high M and/or high p_T values can be very useful to reveal a pure QGP signature.

5.3 Elliptic Flow of Decay Photons

We have already discussed that most of the produced photons in heavy-ion collisions are from the 2-γ decay of π^0 and η mesons and the direct photons contain a small fraction of the inclusive photon spectrum. Thus it is very interesting to know the

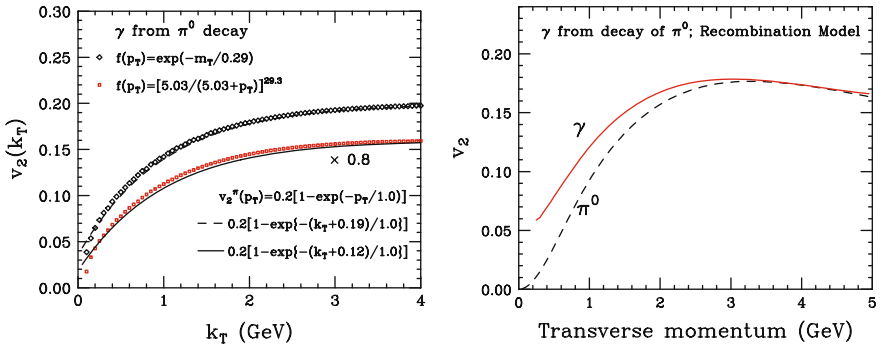

Fig. 28 *Left panel*: Elliptic flow of photons from π^0 decay at midrapidity. $f(p_T)$ stands for the momentum distribution of the π^0. *Right panel*: Elliptic flow parameters for photons from decay of π^0 obtained using the recombination model (taken from [96])

nature of v_2 of decay photons from pion and η decays. The momentum distribution of decay photons from π^0 decay in an invariant form can be expressed as [94, 95]

$$k_0 \frac{dN}{d^3k}(p,k) = \frac{1}{\pi}\,\delta(p\cdot k - \frac{1}{2}m^2)\,, \tag{56}$$

where p and k are the 4-momentum of the pion and photons and m is the pion mass. Thus the Lorentz invariant cross section of the decay photons using the decay kinematics from Eq. (56) is

$$k_0 \frac{d\sigma}{d^3k} = \int \frac{d^3p}{E}\left(E\frac{d\sigma}{d^3p}\right)\frac{1}{\pi}\delta(p\cdot k - \frac{1}{2}m^2)\,. \tag{57}$$

Layek et al. [74] have calculated elliptic flow of decay photons considering several azimuthally asymmetric pion distributions (Fig. 28). They have shown that k_T-dependent v_2 of decay photons closely follows the $v_2(p_T)$ of π^0 evaluated at $p_T \sim k_T + \delta$ (where $\delta \sim$ 0.1–0.2 GeV). Similar results were obtained for decay photons from η mesons also. This study could be useful in identifying additional sources of photons as the v_2 of π^0 is similar to that of π^+ and π^-. Also by using the property of quark number scaling or the recombination model, the decay photon v_2 can help to estimate the v_2 of constituent partons in the π^0 or η mesons (right panel of Fig. 28). See [96] for details.

5.3.1 Experimental Measurement of Direct Photon v_2

PHENIX has measured direct photons and its v_2 by subtracting v_2 of decay photons (2-γ decay of π^0 and η mesons) from inclusive photon v_2 using appropriate weight factor [97]. The procedure followed by them to estimate direct photon v_2 is as follows:

$$v_2^{\text{dir.}} = \frac{R \times v_2^{\text{incl.}} - v_2^{\text{bkgd.}}}{R - 1}, \tag{58}$$

where R is the direct photon excess over hadron decays defined as

$$R = \frac{(\gamma/\pi^0)_{\text{incl.}}}{(\gamma/\pi^0)_{\text{bkgd.}}}. \tag{59}$$

The factor R is measured from spectral analysis. The inclusive and hadron decay v_2 are measured using reaction plane method where the background photons are measured using a Monte Carlo simulation. We have already seen that the photon v_2 shows different signs and/or magnitude depending on the production procedure of photons in heavy-ion collisions. Thus experimental measurement of photon v_2 can be a very powerful tool to disentangle the intermix contributions from different sources in different p_T ranges. However, the experimentally measured preliminary PHENIX data still contain a large systematic error (Fig. 29), which need to be reduced before making any specific conclusion about direct photon v_2.

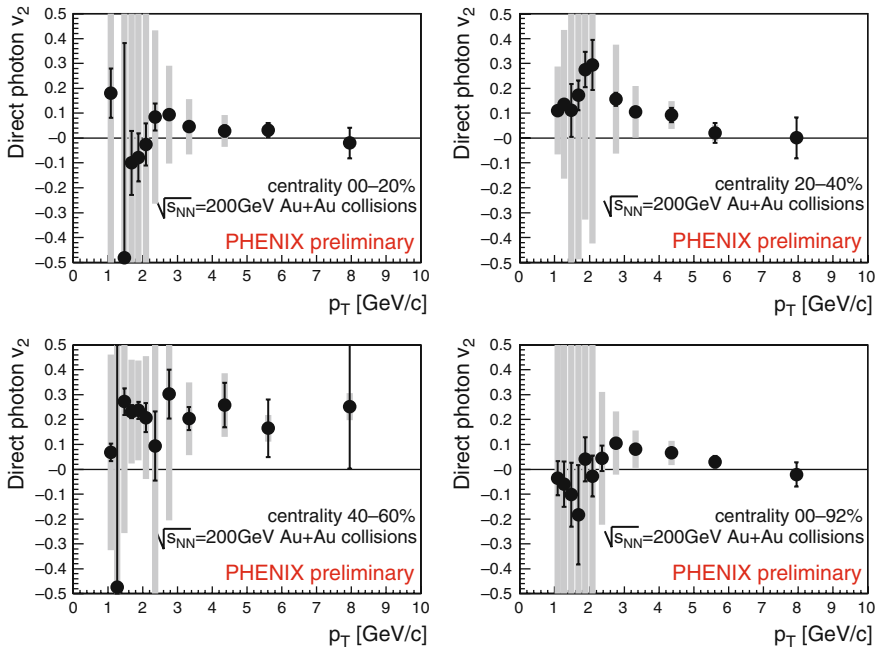

Fig. 29 Elliptic flow of direct photons from 200A GeV Au + Au collision at RHIC [98]

6 Photon-Tagged Jets

Jets are hard phenomenon characterized by a large momentum transfer between partons and are characterized by several hadrons in a small angle around a leading particle as a result of jet fragmentation. The hadrons surrounding a jet are known as associated particles of the jet.

One of the key observables at RHIC energy is the strong suppression of leading hadron yield at high values of transverse momentum compared to expectations based on $p + p$ or $d + A$ collisions at same collision energy. This is the celebrated phenomenon of "jet quenching." It is assumed that the hard partons lose a large fraction of their energy when passing through the strongly interacting medium. A variety of qualitatively different models are available using collisional energy loss and radiative energy loss mechanisms to describe the nuclear modification factor R_{AA} defined as

$$R_{AA}(p_T, y) = \frac{d^2N_{AA}/dp_T dy}{T_{AA}(b)d^2\sigma^{NN}/dp_T dy}. \tag{60}$$

Here, T_{AA} is the nuclear overlap function and σ_{NN} is the nucleon–nucleon cross section. The major problem for studying jet properties arises from the fact that conventional calorimetric study cannot measure the jet energy loss very accurately. Also it is very difficult to directly measure the modification of jet fragmentation function and jet production cross section.

The "jet quenching" in heavy-ion collisions can be studied by measuring the p_T distributions of charged hadrons in opposite direction of a tagged direct photon. Quark–gluon Compton scattering and quark–antiquark annihilation process are the main mechanisms by which direct photons are produced at very high p_T, and jets are produced in the opposite direction of these photons. From momentum conservation law, the initial transverse energy of the produced jets are equal to that of the produced photons, i.e, $E_\gamma = E_{\text{jet}}$. Thus uncertainties regarding the jet cross section can be avoided by tagging a direct photon in the direction opposite to the jet (see [99]).

Medium-modified parton fragmentation function $D_{h/a}(z)$ (z is fractional momenta of the hadrons) is used to study the jet energy loss. The differential p_T distribution of hadrons from jet fragmentation in the kinematical region $(\Delta\phi, \Delta y)$ using $D_{h/a}(z)$ can be written as

$$\frac{dN_{\text{ch}}^{\text{jet}}}{dyd^2p_T} = \sum_{r,h} r_a(E_T^\gamma)\frac{D_{h/a}(p_T/E_T)}{p_T E_T}\frac{C(\Delta y\Delta\phi)}{\Delta y\Delta\phi}, \tag{61}$$

where $C(\Delta y\Delta\phi) = \int_{|y|\le\Delta y/2} dy \int_{|\phi-\bar{\phi}_\gamma|\le\Delta\phi/2} d\phi f(y - |\phi - \bar{\phi}_\gamma|)$ is an overall factor and $f(y, \phi)$ is the hadron profile around the jet axis and $r_a(E_T^\gamma)$ is the fractional production cross section of a typical jet associated with the direct photons. Thus, comparison between extracted fragmentation function in AA and pp collisions can

be used to determine the jet energy loss as well as the interaction mean free path in the dense matter produced in high-energy heavy-ion collisions. Thorston Renk [100] has shown that by γ hadron correlation measurement, the averaged probability distributions for quarks are accessible experimentally and he has also explained an analysis procedure capable of distinguishing between different energy-loss scenarios leading to the same nuclear suppression factor (see Fig. 30).

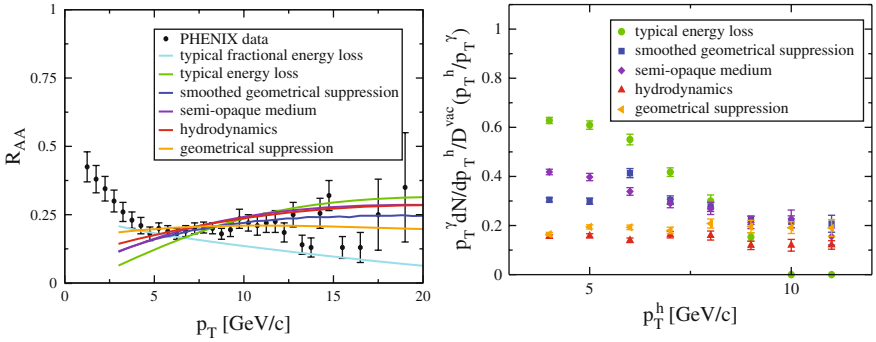

Fig. 30 *Left panel*: Nuclear suppression factor R_{AA} for different toy models and hydrodynamical simulation compared with PHENIX data. *Right panel*: Momentum spectrum of hard hadrons correlated back to back with a photon trigger normalized to the expectation of geometrical absorption (taken from [100])

6.1 Isolating the Bremsstrahlung Photons

In order to measure direct photon cross section by suppressing the hadron decay background or in particular to isolate bremsstrahlung photons from accompanying hadrons, an interesting method known as "isolation cut" can be used successfully. The basic assumption for performing the cut is that the hadronic energy in a cone around the photon is less than a certain fraction of the photon energy, i.e., a photon is considered as isolated if the combined energy of the accompanying hadrons is less than ϵE_γ (where E_γ is the photon energy) inside a cone of half-opening angle δ around the photon. The parameter ϵ is very small (~ 0.1) and is called the energy resolution parameter. The cone around the tagged photon is known as isolation cone. The cone opening can be related to the radius R of a circle centered around the photon in the center of mass system, where R is defined in terms of rapidity η and azimuthal angle ϕ as

$$R \geq \sqrt{\Delta\eta^2 + \Delta\phi^2}. \tag{62}$$

For small rapidities, the half-opening angle δ equals the radius R. This method was successfully implemented into the theoretical study of isolated prompt photon production considering fragmentation contribution also in next-to-leading order (NLO)

by Gordon and Vogelsang [28]. A very good accuracy of this method over a wide range of isolation parameters for prompt photon production was demonstrated in their calculation. Results from RHIC and LHC for this would be very valuable.

6.2 Dilepton-Tagged Jets

In the study of photon-tagged jets, the main problem arises from the jet pair production background, where a leading π^0 in the jet is misidentified as a photon. For an event having a huge background "isolation cut" is not a very efficient mechanism in the low p_T range to study photon-tagged jets in heavy-ion collisions and it is useful only for pp collisions. In the high p_T range although the background contribution related problems are reduced, a substantial problem in photon isolation is created by small opening angle. On the contrary jets tagged by dileptons are not affected by background and can be used to observe p_T imbalance, a signal of medium-induced partonic energy loss. As we have mentioned earlier, for dileptons not only p_T but also invariant mass M is another equally important parameter which can be used accordingly to study dilepton-tagged jets in the medium. At high p_T and high M, the dilepton yield is much lower compared to low p_T and low M range; however, the relative background contribution is also lower in that range.

At very high transverse momentum Drell–Yan process ($h_1 + h_2 \rightarrow l^+l^- + X$) dominates the dilepton production from QGP phase. Srivastava et al. [101] have estimated the results for dilepton-tagged jets by studying Drell–Yan process at NLO in relativistic heavy-ion collisions at RHIC and LHC energies. They have also shown that correlated charm and bottom decay are unimportant as background for dileptons having large transverse momentum or in the kinematical region of interest for jet quenching. Lokhtin et al. [102] have studied the dimuon + jet production (including both $\gamma^*/Z \rightarrow \mu^+\mu^-$ modes) at LHC energy and have shown the p_T imbalance between $\mu^+\mu^-$ pair and a leading particle in a jet is clearly visible even for moderate energy loss. It is directly related to absolute value of partonic energy loss and almost insensitive to the angular spectrum of emitted gluons and to experimental jet energy resolution.

7 Intensity Interferometry of Thermal Photons

The quantum statistical interference between identical particles emitted in relativistic heavy-ion collisions provide valuable insight about the shape and size of the particle emitting source. We know that direct photons emitted from different stages of the collision dominate the p_T spectra depending on the range of transverse momentum range. Thus, one can extract space–time dimension of the system at different stages of the collision by measuring the correlation radii for photons at different transverse momentum.

Two particle correlation function $C(\boldsymbol{q}, \boldsymbol{K})$ for photons having momenta $\boldsymbol{k_1}$ and $\boldsymbol{k_2}$ emitted from a completely chaotic source can be written as

$$C(\boldsymbol{q}, \boldsymbol{K}) = 1 + \frac{1}{2} \frac{|\int d^4x S(x, \boldsymbol{K}) e^{iq.x}|^2}{\int d^4x S(x, \boldsymbol{k_1}) \int d^4x S(x, \boldsymbol{k_2})}. \tag{63}$$

In the above equation, the factor 1/2 appears for averaging over spin and $S(x, \boldsymbol{K})$ is the space–time density function defined as

$$E \frac{dN}{d^3K} = \int d^4x S(x, \boldsymbol{K}), \tag{64}$$

$$\text{where } \boldsymbol{q} = \boldsymbol{k_1} - \boldsymbol{k_2}, \boldsymbol{K} = (\boldsymbol{k_1} + \boldsymbol{k_2})/2. \tag{65}$$

The correlation function $C(\boldsymbol{q}, \boldsymbol{K})$ can be expressed in terms of outward, sideward, and longitudinal momentum difference and radii (q_{out}, q_{side}, q_{long}, and R_{out}, R_{side}, R_{long}, respectively) as

$$C(q_{\text{out}}, q_{\text{side}}, q_{\text{long}}) \sim 1 + \frac{1}{2} \exp[-(q_{\text{out}}^2 R_{\text{out}}^2 + q_{\text{side}}^2 R_{\text{side}}^2 + q_{\text{long}}^2 R_{\text{long}}^2)/2]. \tag{66}$$

Photon 4-momentum in terms of transverse momentum k_T, rapidity y, and azimuthal angle ψ can be expressed as

$$k^\mu = (k_T \cosh y, k_T \cos\psi, k_T \sin\psi, k_T \sinh y) \tag{67}$$

and

$$\begin{aligned} q_{\text{long}} &= |k_{1z} - k_{2z}| = |k_{1T} \sinh y_1 - k_{2T} \sinh y_2| \\ q_{\text{out}} &= \mathbf{q_T}.\mathbf{k_T}/k_T, \\ q_{\text{side}} &= |\mathbf{q_T} - q_{\text{out}}\mathbf{k_T}/k_T|. \end{aligned}$$

Photon interferometry in the QGP phase has been investigated by several theoretical groups and the first experimental results on direct photon were obtained by WA98 [103] collaboration. Bass, Müller, Srivastava [6–9] have calculated two-body quantum correlation of high-energy photon using parton cascade model (PCM) and ideal hydrodynamic model for central 200A GeV Au + Au collision at RHIC. They have shown that one can differentiate between the direct photons from early pre-equilibrium stage and the same from later QGP and hadronic gas stages depending on features of the correlation function. Left panel of Fig. 31 shows that about 88% of the total photons having transverse momenta (1 ± 0.1) GeV (produced by hard parton scattering in PCM [104]) are emitted within a time period of 0.3 fm/c at rapidity $y = 0$. Right panel of the same figure shows that at $k_T = 1$ GeV, the contribution of pre-equilibrium phase and thermal photons is similar to the total photon yield, whereas at $k_T = 2$ GeV hard photons from PCM outshine the thermal ones by an order of magnitude. The emission time in PCM is very small and hydrodynamic calculation with $\tau_0 = 0.3$ fm/c allows a smooth continuation of the emission rate. Intensity correlation for $k_T \geq 2$ GeV (Fig. 31) reveals a pre-thermal photon

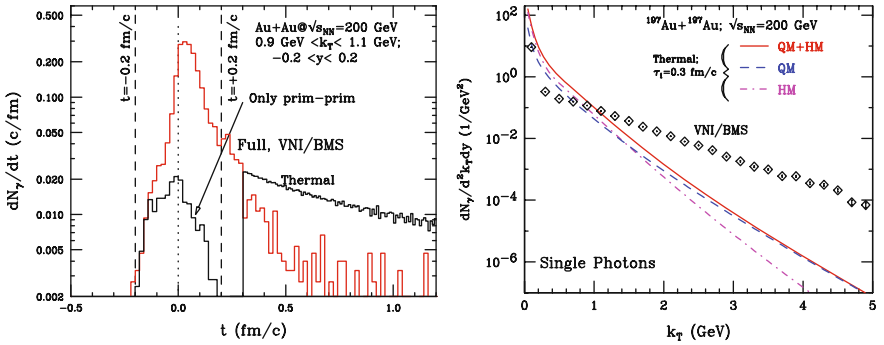

Fig. 31 *Left panel*: The production rate (per event) of hard photons in a central collision of gold nuclei at $\sqrt{s_{NN}} = 200$ GeV as a function of time in the centre of mass system. *Right panel*: Spectrum of photons from various sources. QM and HM denote quark matter and hadronic matter contribution respectively (figures are from [6–9]

dominated small size source of brief duration. On the contrary, for $k_T = 1$ GeV we can see much larger radii for an extended source and suppression of pre-thermal contribution over thermal (Fig. 32).

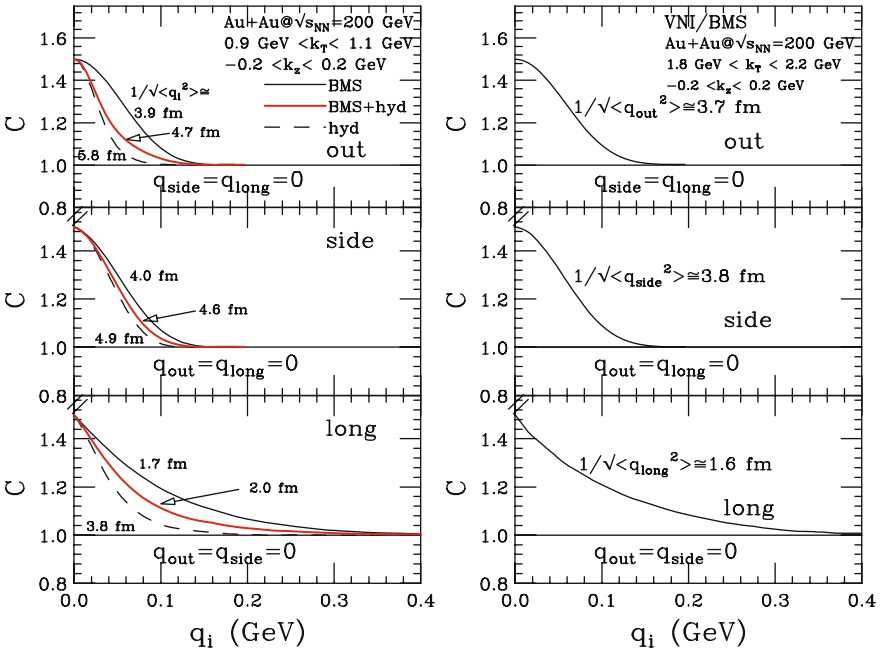

Fig. 32 *Left panel*: Intensity correlation of photons at 1 GeV, considering only PCM(BMS), only thermal (hyd), and all PCM + thermal photons (BMS+hyd) (See [6]). *Right panel*: The outward, sideward, and longitudinal correlations of direct photon predicted by PCM at $K_T = 2$ GeV, inclusion of thermal photons changes the results only marginally

Intensity interferometry of thermal photons having transverse momentum $k_T \sim 0.1 - 2.0$ GeV [55] provides an accurate information about the temporal and spatial structure of the interacting medium.

In reference [55] WA98 data are compared with theoretical results and prediction are given for RHIC and LHC energies. One-dimensional correlation function in terms of q_{inv} (invariant momentum difference) for different k_T and rapidity windows along with WA98 data is shown in Fig. 33. Theoretical results are well fitted in the form $C = 1 + 0.5\, a \exp[-q_{\mathrm{inv}}^2 R_{\mathrm{inv}}^2/2]$ and are in reasonable agreement with the experimental data. At RHIC energy, contribution from quark matter increases and as a result the two-source aspect in the outward correlation radii becomes more clear. Similar results are obtained for LHC energies. It is found that the transverse momentum dependence of the different radii are quite different from the corresponding results for pions and do not decrease as $1/\sqrt{m_T}$. For SPS, RHIC, and LHC energies the longitudinal correlations show similar values, which can be explained as a result of boost invariance of the flow pattern.

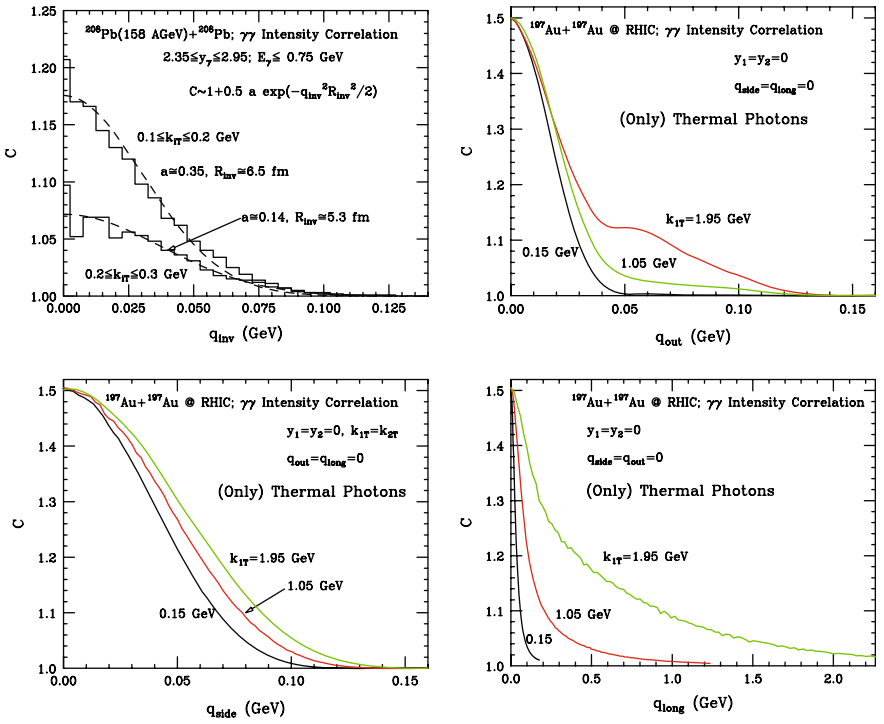

Fig. 33 One-dimensional correlation function for the kinematic window used in WA98 experiment, assuming a fully source and emitting only a single photon. Outward, sideward, and longitudinal correlation function for thermal photons in central collision at RHIC energy (taken from [55])

8 Epilogue

We have tried to give a reasonably complete introduction to the exciting possibilities provided by radiation of direct photons and dileptons for the study of the dynamics of relativistic heavy-ion collisions.

While low-mass dileptons provide insights into the medium modification of vector mesons, those having intermediate masses carry signatures of thermal radiation from the quark–gluon plasma. We have, due to lack of space, left out the discussion of correlated decay of charm and bottom mesons which give a large contribution to dileptons. These are also important as they carry valuable information about the extent of thermalization, elliptic flow, and energy loss exhibited by heavy quarks.

We have discussed sources of direct photons, consisting of prompt photons, thermal radiation from quark and hadronic matter, and those due to passage of jets through QGP. We have also seen that photons carry information about the initial temperature, evolution of elliptic flow, and size of the system. High statistics data at RHIC and LHC along with photon or dilepton-tagged jets will go a long way in seeing that we realize the full potential of electromagnetic probes of quark–gluon plasma.

Acknowledgments This write-up is based on the notes taken by RC and LB from the lectures given by DKS at the QGP Winter School 2008 at Jaipur. We thank the organizers for their warm hospitality. The work discussed here has benefited from discussions and collaborations with colleagues over many years and from many countries, and we take this opportunity to thank all of them and also to apologize to those whose work may not have found mention in these introductory lectures as this write-up is not intended to be a review.

Finally, we thank the organizers for their patience and for giving us extra time to complete this write-up.

References

1. B. Müller: *The Physics of Quark Gluon Plasma*, Springer, Heidelberg (1985) 219
2. C.Y. Wong: *Introduction of High Energy Heavy Ion Collisions*, World Scientific, Singapore (1994) 219, 232, 233, 243, 251
3. R.C. Hwa (ed.): *Quark Gluon Plasma*, vols. I and II, World Scientific, Singapore (1990 and 1995) 219
4. U. Heinz: CERN Yellow Report CERN-2004–001, arXiv: 0407360 [hep-ph] 219
5. E.L. Feinberg: Nuovo Cim. **A 34**, 391 (1976) 220
6. S.A. Bass, B. Müller and D.K. Srivastava: Phys. Rev. Lett. **93**, 162301 (2004) 220, 259, 260
7. S.A. Bass, B. Müller and D.K. Srivastava: Phys. Rev. Lett. **90**, 082301 (2003)
8. S.A. Bass, B. Müller and D.K. Srivastava: Phys. Rev. **C 66**, 061902 (2002)
9. T. Renk, S.A. Bass and D.K. Srivastava: Phys. Lett. **B 632**, 632 (2006) 220, 259, 260
10. R. Chatterjee, E. Frodermann, U. Heinz and D.K. Srivastava: Phys. Rev. Lett. **96**, 202302 (2006) 220, 250, 251
11. U. Heinz, R. Chatterjee, E. Frodermann, C. Gale and D.K. Srivastava: Nucl. Phys. **A 783**, 379 (2007) 220, 250, 251
12. R. Chatterjee and D.K. Srivastava: Phys. Rev. **C 79**, 021901 (2009) 220
13. R.J. Fries, B. Müller and D.K. Srivastava: Phys. Rev. Lett. **90**, 132301 (2003) 220, 232, 240, 241

14. K. Kajantie, J. Kapusta, L. McLerran and A. Mekijan: Phys. Rev. **D 34**, 2746 (1986) 220, 244
15. M.M. Aggarwal et al. [WA98 Collaboration]: Phys. Rev. Lett. **85**, 3595 (2000) 221, 238
16. S.S. Adler et al. [PHENIX Collaboration]: Phys. Rev. Lett. **94**, 232301 (2005) 221, 239
17. S.S. Adler et al. [PHENIX Collaboration]: Phys. Rev. **C 76**, 034904 (2007) 222
18. A. Adare et al. [PHENIX Collaboration]: arXiv: 0804.4168 [nucl-ex] 223, 224
19. S. Bathe [PHENIX Collaboration]: Eur. Phys. J. **C 49**, 225 (2007) 223, 224
20. N.M. Kroll and W. Wada: Phys. Rev. **98**, 1355 (1955) 223
21. L.G. Landsberg: Phys. Rep. **128**, 301 (1985) 223
22. H. Gong [PHENIX Collaboration]: Proceedings of 19th International Conference on Ultra-Relativistic Nucleus-Nucleus Collisions: Quark Matter 2006 (QM2006), Shanghai, China, 14–20 Nov 2006, arXiv:0705.1133 [nucl-ex] 223, 224
23. T. Dahms et al.: Eur. Phys. J. **C 49**, 249 (2007) 223, 224
24. D.K. Srivastava: J. Phys. **G 35**, 104026 (2008) 224
25. P. Aurenche, J.-P. Guillet, E. Pilon and M. Werlen: Phys. Rev. **D 73**, 094007 (2006) 224, 225, 226
26. P. Aurenche, M. Fontannaz, J.-P. Guillet, B. Kniehl, E. Pilon and M. Werlen: Eur. Phys. J. **C 9**, 107 (1999) 225
27. L.E. Gordon and W. Vogelsang: Phys. Rev. **D 50**, 1901 (1994) 225
28. P. Aurenche, R. Basu, M. Fontannaz and R.M. Godbole: Eur. Phys. J. **C 42**, 43 (2005) 226, 258
29. S. Jeon, J. Jalilian-Marian and I. Sarcevic: Nucl. Phys. **A 715**, 795 (2003) 226
30. F. Arleo: JHEP **0609**, 015 (2006) 226
31. R. Chatterjee, D.K. Srivastava and S. Jeon: Phys. Rev. **C 79**, 034906 (2009) 227
32. T. Isobe [PHENIX Collaboration]: J. Phys. **G 34**, S1015 (2007) 227, 228, 240, 242
33. L.D. McLerran and T. Toimela: Phys. Rev. **D 31**, 545 (1985) 228
34. H.A. Weldon: Phys. Rev. **D 42**, 2384 (1990) 228
35. C. Gale and J. Kapusta: Nucl. Phys. **B 357**, 65 (1991) 228
36. J. Kapusta, P. Lichard and D. Seibert: Phys. Rev. **D 44**, 2774 (1991) 229, 231, 233, 234, 235, 236, 237
37. J. Kapusta, P. Lichard and D. Seibert: Phys. Rev. **D 47**, 4171 (1993) [Erratum] 229, 231, 233, 234, 235, 236
38. R. Baier, H. Nakkagawa, A. Niegawa and K. Redlich: Z. Phys. **C 53**, 433 (1992) 229, 233
39. R.D. Pisarski: Nucl. Phys. **B 309**, 476 (1988) 231
40. R.D. Pisarski: Phys. Rev. Lett. **63**, 1129 (1989)
41. E. Braaten and R.D. Pisarski: Nucl. Phys. **B 337**, 569 (1990) 231
42. P. Arnold, G.D. Moore and L.G. Yaffe: JHEP **0112**, 009 (2001) 231, 236, 237
43. H. Nadeau: Phys. Rev. **D 48**, 3182 (1993) 232
44. S. Turbide, C. Gale, S. Jeon and G.D. Moore: Phys. Rev. **C 72**, 014906 (2005) 233
45. B.G. Zakharov: JETP Lett. **80**, 1 (2004) 233
46. L. Xiong, E.V. Shuryak and G.E. Brown: Phys. Rev. **D 46**, 3798 (1992) 236
47. C. Song: Phys. Rev. **C 47**, 2861 (1993) 236
48. J. Alam, P. Roy and S. Sarkar: Phys. Rev. **C 68**, 031901 (2003) 236
49. J. Alam, S. Sarkar, P. Roy, T. Hatsuda and B. Sinha: Ann. Phys. **286**, 159 (2001) 236
50. S. Turbide, R. Rapp and C. Gale: Phys. Rev. **C 69**, 014903 (2004) 236, 237, 239, 240
51. R. Albrecht et al. [WA80 Collaboration]: Phys. Rev. Lett. **76**, 3506 (1996) 237, 238
52. D.K. Srivastava and B. Sinha: Phys. Rev. Lett. **73**, 2421 (1994) 237, 238
53. J. Alam, D.K. Srivastava, B. Sinha and D.N. Basu: Phys. Rev. **D 48**, 1117 (1993) 237
54. R.C. Hwa and K. Kajantie: Phys. Rev. **D 32**, 1109 (1985) 237
55. D.K. Srivastava: Phys. Rev. **C 71**, 034905 (2005) 238, 261
56. A. Dumitru, U. Katscher, J.A. Maruhn, H. Stöecker, W. Greiner and D.H. Rischke: Phys. Rev. **C 51**, 2166 (1995) 238
57. N. Arbex, U. Ornik, M. Plümer, A. Timmermann and R.M. Weiner: Phys. Lett. **B 345**, 307 (1995)
58. J. Sollfrank, P. Huovinen, M. Kataja, P.V. Ruuskanen, M. Prakash and R. Venugopalan: Phys. Rev. **C 55**, 392 (1997)
59. J.V. Steele, H. Yamagishi and I. Zahed: Phys. Rev. **D 56**, 5605 (1997)
60. T. Hirano, S. Muroya and M. Namiki: Prog. Theor. Phys. **98**, 129 (1997)

61. D.K. Srivastava and B.C. Sinha: Eur. Phys. J. **C 12**, 109 (2000)
62. D.K. Srivastava and B.C. Sinha: Eur. Phys. J. **C 20**, 397 (2001) [Erratum] 238
63. J. Cleymans, K. Redlich and D.K. Srivastava: Phys. Rev. **C 55**, 1431 (1997) 238, 239
64. D.K. Srivastava and B. Sinha: Phys. Rev. **C 64**, 034902 (2001) 238, 240
65. I. Kvasnikova, C. Gale and D.K. Srivastava: Phys. Rev. **C 65**, 064903 (2002) 239, 247, 248
66. J. Alam, S. Sarkar, T. Hatsuda, T.K. Nayak and B. Sinha: Phys. Rev. **C 63**, 021901 (2001) 239, 240
67. P. Huovinen, P.V. Ruuskanen and S.S. Rasanen: Phys. Lett. **B 535**, 109 (2002)
68. S.S. Rasanen: Nucl. Phys. **A 715**, 717 (2003)
69. H. Niemi, S.S. Rasanen and P.V. Ruuskanen: CERN Yellow Report, CERN-2004–009, arXiv:0311131 [hep-ph] 239
70. J. Alam, J.K. Nayak, P. Roy, A.K. Dutta-Mazumder and B. Sinha: J. Phys. **G 34**, 871 (2007)
71. D.G. d'Enterria and D. Peressounko: Eur. Phys. J. **C 46**, 451(2006) 240
72. B.B. Back et al. [PHOBOS Collaboration]: Phys. Rev. **C 65**, 061901 (2002) 241
73. J. Kapusta, L.D. McLerran and D.K. Srivastava: Phys. Lett. **B 283**, 145 (1992) 241
74. R.J. Fries, B. Müller and D.K. Srivastava: Phys. Rev. **C 72** 041902(R) (2005) 241, 254
75. S. Turbide, C. Gale, E. Frodermann and U. Heinz: Phys. Rev. **C 77**, 024909 (2008) 241, 242, 243, 251
76. H. Busching [PHENIX Collaboration]: Nucl. Phys. **A 774**, 103 (2006) 242
77. K. Kajantie, M. Kataja, L. McLerran and P.V. Ruuskanen: Phys. Rev. **D 34**, 811 (1986) 247
78. G. Agakichiev et al. [CERES Collaboration]: Eur. Phys. J. **C 41**, 475 (2005) 247, 248
79. D. Adamova et al. [CERES/NA45 Collaboration]: Phys. Rev. Lett. **91**, 042301 (2003) 247, 248
80. G.E. Brown and M. Rho: Phys. Rep. **269**, 333 (1996) 247
81. R. Rapp and J. Wambach: Eur. Phys. J. **A 6**, 415 (1999) 247
82. M. Masera et al.: Nucl. Phys. **A 590**, 93c (1995) 247
83. A.L.S. Angelis et al.: Eur. Phys. J. **C 13**, 433 (2000) 247
84. M.C. Abreu et al. [NA38/NA50 Collaboration]: Eur. Phys. J. **C 14**, 443 (2000) 247, 248
85. R. Rapp and E.V. Shuryak: Phys. Lett. **B 473**, 13 (2000) 247
86. R. Arnaldi et al. [NA60 Collaboration]: Phys. Rev. Lett. **96**, 162302 (2006) 249
87. H. van Hees and R. Rapp: Phys. Rev. Lett. **97**, 102301 (2006) 249
88. J. -Y. Ollitrault: Phys. Rev. **D 46**, 229 (1992) 249
89. U.W. Heinz and A. Kuhlman: Phys. Rev. Lett. **94**, 132301 (2005) 249
90. P.F. Kolb and U. Heinz: In: R.C. Hwa and X.-N. Wang (eds.) *Quark-Gluon Plasma 3*, World Scientific, Singapore (2004), arXiv: 0305084 [nucl-th] 249, 250
91. R. Chatterjee, D.K. Srivastava and U. Heinz: Proceedings of 20th International Conference on Ultra-Relativistic Nucleus-Nucleus Collisions: Quark Matter 2008 (QM2008), Jaipur, India, 4–10 Feb 2008 251, 252
92. R. Chatterjee, D.K. Srivastava and U. Heinz: Proceedings of International Conference on Particle and Nuclei (PANIC08), Eilat, Israel, 9–14 Nov 2008, arXiv: 0901.3270 [nucl-th] 251, 252
93. R. Chatterjee, D.K. Srivastava, U. Heinz and C. Gale: Phys. Rev. **C 75**, 054909 (2007) 252, 253
94. R.N. Cahn: Phys. Rev. **D 7**, 247 (1973) 254
95. C. Gale and J. Kapusta: University of Minnesota Report No. 88/2 (1988) [unpublished] 254
96. B. Layek, R. Chatterjee and D.K. Srivastava: Phys. Rev. **C 74**, 044901 (2006) 254
97. T. Sakaguchi [PHENIX Collaboration]: arXive: 0705.1711 [nucl-ex] 254
98. Kentaro Miki: Proceedings of 19th International Conference on Ultra-Relativistic Nucleus-Nucleus Collisions: Quark Matter 2006 (QM2006), Shanghai, China, 14–20 Nov 2006 255
99. X. -N. Wang, Z. Huang and I. Sarcevic: Phys. Rev. Lett. **77**, 231 (1996) 256
100. T. Renk: Phys. Rev. **C 74**, 034906 (2006) 257
101. D.K. Srivastava, C. Gale and T.C. Awes: Phys. Rev. **C 67**, 054904 (2003) 258
102. I.P. Lokhtin, A.V. Sherstnev and A.M. Snigirev: Phys. Lett. **B 599**, 260 (2004) 258
103. M.M. Aggarwal et al. [WA98 Collaboration]: Phys. Rev. Lett. **93**, 022301 (2004) 259
104. S. Turbide, C. Gale and R.J. Fries: Phys. Rev. Lett. **96**, 032303 (2006) 259

Measuring Dimuons Produced in Proton–Nucleus Collisions with the NA60 Experiment at the SPS

Carlos Lourenço and Hermine K. Wöhri

1 Introduction

Considerable efforts are currently being invested in the study of high-energy heavy-ion collisions. The main goals of this experimental programme are the discovery of the phase transition from confined hadronic matter to deconfined partonic matter, predicted by lattice QCD calculations to occur when the system reaches sufficiently high energy densities or temperatures [1] and the study of the physical properties of the new phase. Both goals are fundamental for the understanding of confinement, a crucial feature of QCD.

The measurement of dimuon production allows us to access several different physics processes that are expected to provide crucial information regarding the formation and the properties of the high density and temperature QCD medium presumably produced in high-energy nuclear collisions. Measuring dimuons is particularly suitable to access the production yields of heavy quarkonium states (J/ψ, ψ' and the Υ family), which are expected to be considerably suppressed by "colour screening" if a QCD medium with deconfined quarks and gluons is formed in heavy-ion collisions [2]. Other interesting signals that can be studied through the measurements of dimuon production include the modifications of the spectral properties of the low-mass vector mesons, the enhancement of strangeness production through the study of the ϕ yields, the search for prompt dimuons (virtual photons) radiated from a thermal medium, etc.

However, the search for "new physics" in the patterns observed in the data collected in high-energy heavy-ion collisions requires a good understanding of what happens to the corresponding signatures in the case of proton–nucleus collisions, where such "anomalies" should be absent. The extraction of robust signals also requires an accurate control of the corresponding backgrounds; it is easy to "create" a large signal enhancement, or suppression, with respect to the "well-known"

C. Lourenço (✉)
CERN, CH-1211 Geneva 23, Switzerland, carlos.lourenco@cern.ch

H.K. Wöhri
LIP, Av. Elias Garcia 14, 1000-149 Lisbon, Portugal, hermine.woehri@cern.ch

Lourenço, C., Wöhri, H.K.: *Measuring Dimuons Produced in Proton–Nucleus Collisions with the NA60 Experiment at the SPS*. Lect. Notes Phys. **785**, 265–284 (2010)
DOI 10.1007/978-3-642-02286-9_8

expected processes when the yield of the expected signal is only $\sim 1\%$ of the (estimated) background. Spurious anomalies can also be faked by the lack of a solid understanding of measurement efficiencies, acceptances, phase space windows, etc.

In the next sections we consider several issues that play important roles in a typical analysis of dimuon measurements. We will use the NA60 detector and procedures, as used in the running period of year 2002, as a concrete example for illustrating some concepts, difficulties, methods, etc. To start with, the capabilities and limitations of the detector used to collect the measurements should be understood. Then, we will go through the treatment of the raw data, a procedure involving data reconstruction, track matching, vertexing, event selection, background subtraction, etc. Finally, before physics results can be extracted, a Monte Carlo simulation needs to be made, generating the physics sources expected to contribute to the event sample under scrutiny, to define the phase space window where the results are obtained and to evaluate the acceptances and efficiencies for each physics process in the conditions of each data set.

2 Detector Design and Operation

The purpose of the NA60 experiment was to accurately study dimuon production in proton–nucleus and heavy-ion collisions, by triggering on and reconstructing two muon tracks in a magnetic spectrometer (as previously done by NA10, NA38 and NA50), and by remeasuring their momenta and angles with improved accuracy in a silicon vertex tracker placed just after the target.

The muon spectrometer, initially built for the NA10 experiment in the late 1970s and schematically illustrated in Fig. 1, consisted of a hadron absorber, eight multiwire proportional chambers (MWPC), four trigger hodoscopes (R1–R4) and an air-core magnet (ACM). The toroidal field of the ACM magnet was generated by circulating current in coils mounted on six radial iron poles, each 4 m long and covering 18° in azimuth (see Fig. 2). The hexagonal geometry of the magnet determined the shape of the detector elements, organised in sextants. The muons were not deflected

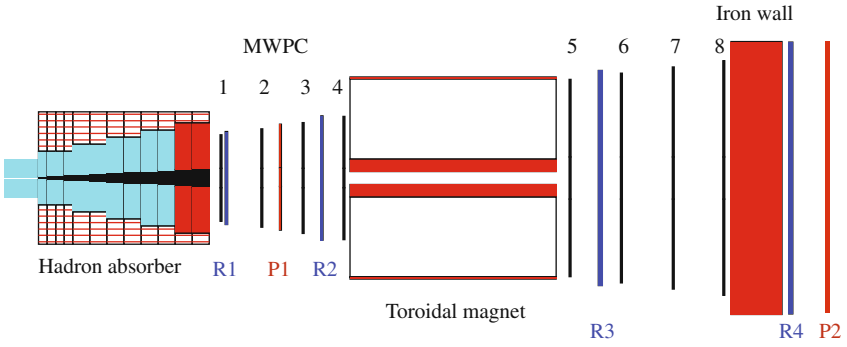

Fig. 1 Schematic representation of the 17 m long muon spectrometer. The beam comes from the left side

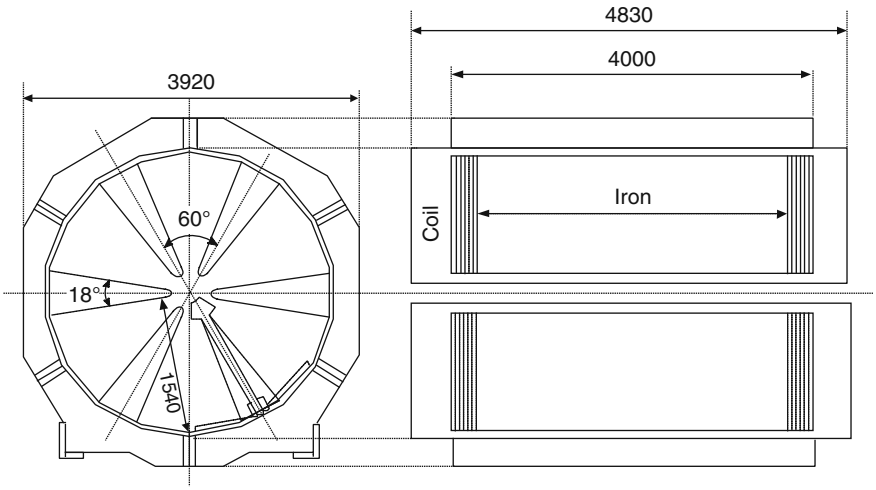

Fig. 2 Front and longitudinal views of the toroidal magnet of the muon spectrometer (dimensions in mm)

in azimuth by the toroidal field and suffered a polar angle deflection inversely proportional to their *transverse* momentum. The magnet's air gap extended between an inner radius of 29.5 cm and an outer radius of 154 cm, defining the angular coverage of the spectrometer, 35–120 mrad. For a beam energy around 400 GeV this corresponds roughly to one unit of rapidity at mid-rapidity. The ACM magnet, with its "air core", was quite a significant improvement with respect to most earlier experiments, where the muons would have to traverse large amounts of iron and, hence, would suffer from multiple scattering and energy loss effects, resulting in a degraded dimuon mass resolution. In the data-taking period of 2002, the operating current was ± 4000 A, resulting in an azimuthal field with a bending power decreasing from ~ 3.1 Tm at a radial distance of 30 cm to ~ 0.6 Tm at 150 cm.

The 5.5 m long main hadron absorber was placed immediately after the vertex tracker, as close as possible to the target, in order to minimise the fraction of pions and kaons decaying into muons. It was made of materials with a low atomic number, to minimise the multiple scattering induced on the traversing muons, and with high densities, so as to stop the hadrons in a relatively small distance. The non-interacting beam was stopped in a beam dump made of uranium. The MWPC chambers consisted of three wire planes, rotated by 60° with respect to each other, to allow a good measurement of one space point. The four "R" trigger hodoscopes were made of scintillator slabs with a time resolution of around 2 ns, arranged in six independent sextants and oriented parallel to the outer edges. The width of the slabs of the R1 and R2 hodoscopes increased with the distance from the beam line, such that a muon produced in the target and passing through slab i in R1 would also hit slab i in R2. In order to accommodate the spatial extent of the target and multiple scattering for low energetic muons, the coincidence $\mathrm{R}_1^i \times \mathrm{R}_2^{i-1}$ was also allowed in the trigger logic. This "R1–R2 coincidence", which ensured that the muons came from the

target region, was then combined with the R3–R4 information. A dimuon trigger occurred when the hits in the four hodoscopes formed one of the pre-defined "road patterns" and if the two muons passed through different sextants. This requirement imposes a minimum opening angle between the two muons, strongly suppressing the acceptance of low-mass and low-p_T dimuons, a crucial feature for the NA10 experiment, which was aimed at studying high-mass dimuon production and had a limited data acquisition bandwidth. It is important to understand this trigger condition and the bias it imposes on the measured event samples, in particular in the context of the background subtraction procedure, as will be mentioned later on. Two additional trigger hodoscopes (P1 and P2) were used in special data-taking periods to evaluate the efficiency of the R1–R4 trigger system. A 120 cm thick iron wall was placed after the tracking chambers and before the last trigger hodoscope, increasing to around 21 interaction lengths the thickness of the material that must be crossed by a particle to give a trigger signal, ensuring that no punch-through hadrons would give fake triggers. While preventing hadrons from triggering the experiment, this material also absorbs low-energy muons, strongly reducing the detection probability of low-mass dimuons. The material thickness before the muon chambers is only 13.4 interaction lengths, to limit the degradation of the tracking due to the multiple scattering undergone by the muons when traversing the hadron absorbers. To improve the dimuon mass resolution, among other things, NA60 remeasured the muons *before* the hadron absorbers, with a silicon tracker placed immediately after the targets. The muon tracks were found among the many charged particle tracks by matching them to the tracks reconstructed in the muon spectrometer, using the information on both angles and momenta.

Figure 3 illustrates the overall layout of the target region, as used in 2002, with the silicon telescope placed in the 104 mm vertical gap of the dipole magnet, between the targets and the first elements of the hadron absorber. The dipole magnet was operated at a current of ± 900 A, providing a very homogeneous field of 2.5 T at the centre of the gap and a field integral of 0.95 Tm between the centre of the target system and the last silicon tracking plane. To evaluate possible systematic effects, the polarities of both magnets were reversed every few hours, leading to data samples with four polarity combinations.

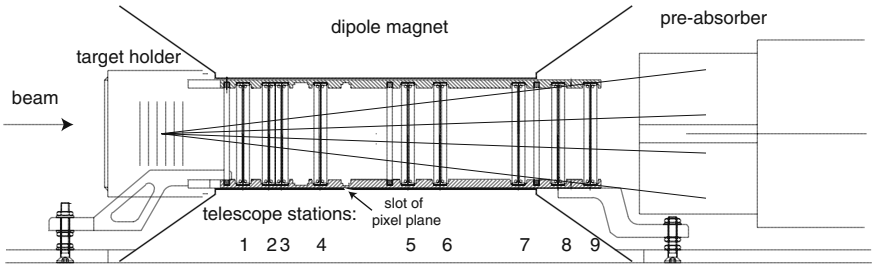

Fig. 3 The silicon tracking telescope, placed in the magnet gap, between the targets and the hadron pre-absorber. The muon spectrometer's angular acceptance (around 35–120 mrad) is also indicated

To study the nuclear dependence of the production cross section of various particles, three different nuclear targets, with significantly different mass numbers, were used in the 2002 run of NA60: Be, In and Pb. They had a diameter of 12 mm, completely intercepting the transverse profile of the proton beam, around 300–400 μm full width half-maximum in both transverse directions. The Be target was made of four disks, 2 mm thick each, to minimise reinteractions inside the target. To reduce the systematic uncertainties in the extraction of the nuclear dependence of the production cross sections, all targets were *simultaneously* exposed to the beam. They were placed every 8 mm along the beam line, to minimise the probability that the particles produced in one target would interact on the next one. Their thicknesses were $4 \times 0.45\%$ (Be), 0.88% (In) and 1.15% (Pb) nuclear interaction lengths. There was no extra material between the targets and the silicon tracker.

Immediately upstream of the target system was placed a beam tracker, with the purpose of providing the flight path of the incident beam particle in order to calculate the transverse coordinates of the interaction vertex. It was made of two tracking stations, placed 10 and 30 cm upstream of the target's centre, each one composed of two single-sided silicon micro-strip sensors, rotated by 90°. The four 400 μm thick silicon sensors had 24 strips of 50 μm pitch, were placed in a vacuum box and were operated at a temperature of 130 K, to minimise the degradation of the charge collection efficiency induced by the accumulated radiation damage. The two 100 μm thick stainless steel windows of the vacuum cryostat plus the four silicon sensors were as thick (0.46% of an interaction length) as a Be disk.

The vertex telescope used during the 2002 proton run was composed of 14 silicon micro-strip sensors, designed with variable strip length and pitch (between 60 and 227 μm), so as to match the highly inhomogeneous track density across the sensor surface and to keep the occupancy below 3%, even in the area closest to the beam axis and in p–Pb interactions [3]. The number of strips per sensor, $2 \times 6 \times 128$, was determined by the used read-out chips (12 per sensor) [4–6]. Each sensor was produced from a single silicon wafer, 10 cm. in diameter and 300 μm thick. This was the only material on the way of the particles to be tracked. They had a central hole of 3.6 mm diameter, for the non-interacting beam protons to pass through. Bi-dimensional information about the transverse position of the particles required that two sensors were assembled back to back, forming a "station". The strips of the sensors of a tracking station had an inclination angle of $\pm 25^\circ$ with respect to the vertical axis. This value leads to similar resolutions in the x and y coordinates while simultaneously optimising the curvature (inverse momentum) resolution, given the presence of the dipole field.

The measurement of production cross sections requires knowing how many protons interacted during the data collection period, which depends on the intensity of the beam. The proton beam intensity was redundantly measured, for each burst, by three independent multi-foil ionisation chambers, filled with argon, placed upstream of the target. They measured identical values, within 1%. In 2002, the beam intensity was kept at around 2×10^8 protons per burst, with a spill length of 4.8 s and a SPS cycle of 16.8 s, so that the interaction pile-up rate would not exceed 20% in the 100 ns window of the micro-strip tracker [7].

3 Data Reconstruction

3.1 Track and Vertex Reconstruction

Several steps need to be followed to convert the measured "raw data" in information that can be used for the extraction of physics results. Here we will mention the procedure used in the reconstruction of the data collected by NA60 in 2002 [8]. The tracks in the muon spectrometer were reconstructed first. Many of the triggered events were discarded in this step, mostly because at least one of the muons traversed one of the 4 m long iron poles of the ACM magnet. Such events, if kept, would lead to a degradation of the dimuon mass resolution. The tracking in the vertex telescope was performed only when at least two muons were reconstructed in the muon spectrometer and had their origin in the target region. Figure 4 shows a typical event, where the tracks produced in the Pb target are reconstructed with the information provided by the silicon micro-strip stations (and by a small pixel detector under test in this running period).

If at least two tracks were reconstructed in the vertex telescope, the event reconstruction proceeded to the vertexing step. Only tracks consisting of at least 10 clusters and having a good fit quality contributed to the vertex fitting, made with a "robust method", which assigns a weight to each of the contributing tracks, decreasing the influence of the outliers. A Monte Carlo study showed that only $\sim 2\%$ of the generated events had the collision vertex reconstructed in a wrong target.

Figure 5 shows that the six targets can clearly be distinguished in the distribution of the z coordinate (along the beam axis) of the reconstructed vertices. The peak at around -4.2 cm corresponds to the exit window of the beam tracker's vacuum cryostat. Deconvoluting the target thicknesses from the measured distribution, the z-vertex resolution is seen to be between 600 and 900 μm, depending on the target position. The resolution is better for the most downstream targets because the reconstructed tracks are extrapolated over a smaller distance and do not traverse the other targets, undergoing less multiple scattering. The resolution also depends on

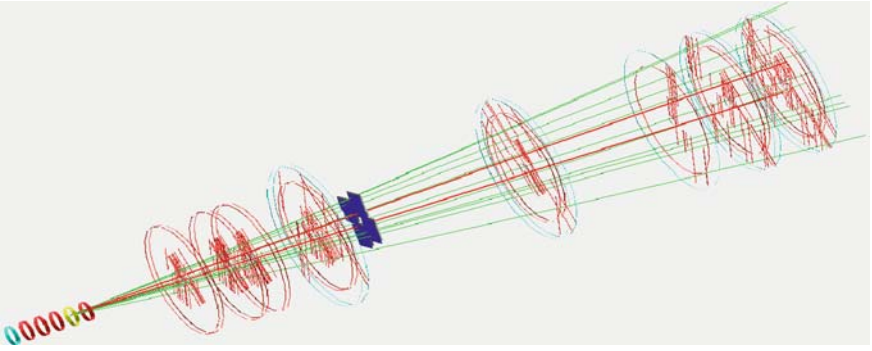

Fig. 4 Example of an event reconstructed in the vertex tracker. The two *red tracks* represent the muons

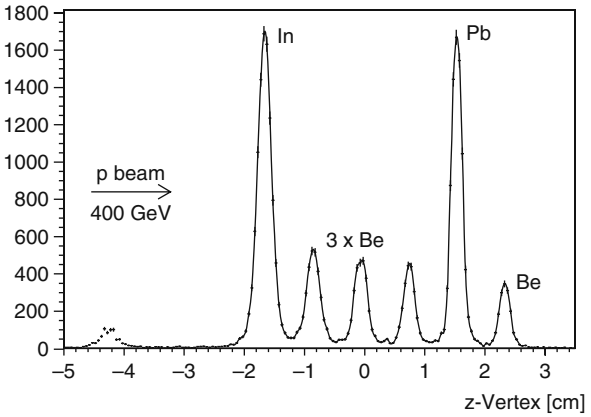

Fig. 5 Distribution of the z coordinate of the reconstructed vertices, for events with both muons matched to tracks in the vertex region

the number of tracks attached to the vertex; on average, between four and six tracks were attached to the reconstructed vertices, slightly depending on the target.

3.2 Track Matching

The matching procedure was performed, independently for each muon, using the angles and momentum information, accounting for the multiple scattering and the (average) energy lost by the muons in the hadron absorber [9, 10]. Only vertex tracks with the same charge and similar kinematics as the muon track were considered as track matching candidates. When there were several track candidates, the one giving the best matching χ^2 was selected. Once two matched muons were found, their kinematics were recalculated imposing a common (dimuon) origin, to further improve the dimuon mass resolution.

Figure 6 shows the distribution of the z coordinate of the common origin of the matched opposite-sign muon pairs, in the mass region of the ϕ meson. The resolution is around 1.6 mm for dimuons at the ϕ mass and remains better than 2 mm for the ω dimuons. For dimuons of mass below 500 MeV/c^2 the resolution of the dimuon origin degrades to values in the range 2.5–6.5 mm (depending on the target position), showing that low-mass dimuons cannot be used to identify the target where they were produced.

The rate of matches where the muon is combined with a vertex track that does not correspond to the real muon (fake matches) is completely negligible in p–A collisions, given the small particle multiplicities. A significant number of muons is lost in the matching procedure because the acceptance of the vertex telescope does not cover the full angular acceptance of the muon spectrometer. Forward tracks produced in downstream targets are particularly affected by the limited geometrical coverage of the silicon sensors, given the presence of their beam holes. Nevertheless,

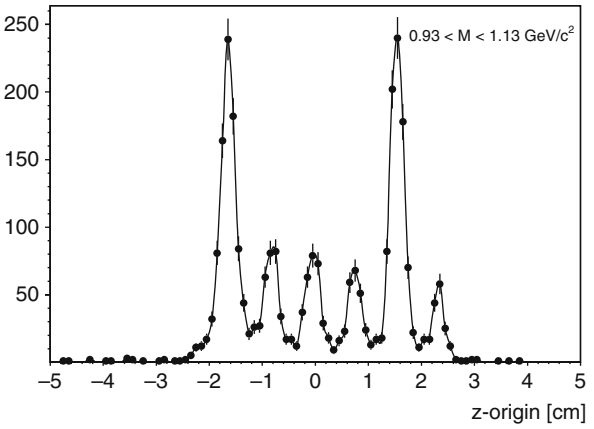

Fig. 6 Distribution of the z-origin of the dimuons in the mass range of the ϕ meson, after track matching

the loss in dimuon statistics when selecting only matched dimuons is largely compensated by the very significant improvement in terms of dimuon mass resolution, as can be appreciated in Fig. 7. This figure shows the *opposite-sign* dimuon mass distribution as measured at the level of the muon spectrometer (left) and after the improvements provided by the vertex tracker information. Before the matching, the ϕ is barely visible as a shoulder on the ρ/ω peak; after the matching we see two prominent peaks, with dimuon mass resolutions of 29 ± 1 and 32 ± 1 MeV/c^2, for the ω and ϕ resonances, respectively. The improvement in dimuon mass resolution is less pronounced for the J/ψ, the more energetic muons being less affected by the multiple scattering.

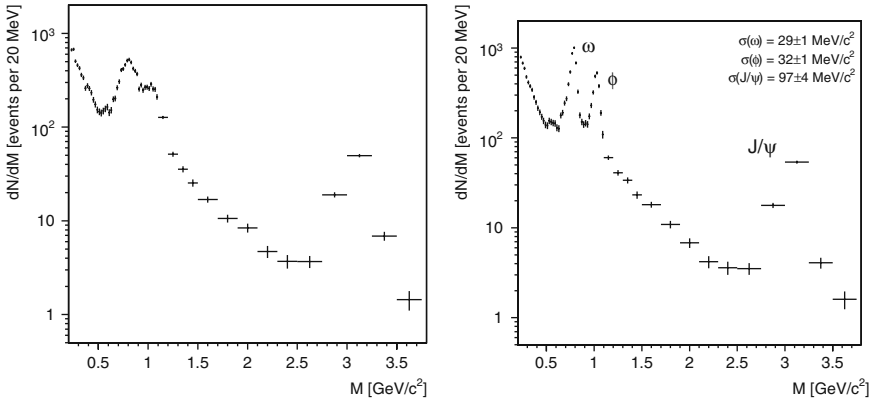

Fig. 7 Mass distributions of the opposite-sign dimuons kept in the physics analysis event sample (all targets together), at the muon spectrometer level (*left*) and after the muon track-matching step (*right*)

3.3 Combinatorial Background

All dimuon measurements include a certain level of events where the muon pair is not really a "signal dimuon" but rather a spurious combination of two muons of uncorrelated origin, mostly due to decays of pions and kaons. This kind of "combinatorial background" leads to muon pairs of the same charge just as well as to pairs of opposite charges. Therefore, its level in the opposite-sign sample can be estimated through a mixed-event technique, in which single muons from different like-sign events are combined to form muon pairs of all charge combinations. This procedure works well at SPS energies, where two muons of the same sign cannot result from the decay of a single particle. Muon pairs also result from simultaneous semi-muonic decays of charmed hadrons. At SPS energies the number of D meson pairs produced in each collision is never higher than one and, therefore, open charm decays contribute only to the (correlated) opposite-sign dimuon event sample, being treated in the analysis as a "signal contribution" (discussed later). However, at the much higher LHC energies, for instance, charm decays will be as "combinatorial" as pion and kaon decays.

In the case of the NA60 experiment the measured single muons cannot simply be combined with each other, because the samples of positive and negative single muons were obtained from *dimuon* triggers and are, therefore, *biased* by the trigger condition requiring the two muons to be in different sextants. This bias distorts in different ways the muon azimuthal distributions of the $+-$, $++$ and $--$ samples, mostly because of the anisotropy introduced by the vertex dipole field. Therefore, before combining the single muons in muon pairs, we must evaluate what would be their distribution among the six sextants in the absence of azimuthal angle correlations imposed by the dimuon trigger logic [4, 9, 10]. This event-mixing procedure was developed for the analysis of the intermediate mass dimuons collected by NA60 in In–In collisions, where the overwhelming fraction of combinatorial background muon pairs imposes a very accurate evaluation of this contribution. As shown in [4, 9, 10], where the whole procedure is described in detail, the measured like-sign muon pairs kinematical distributions are reproduced by the generated mixed-event samples, in shape and in normalisation, without any free parameters to be adjusted, with a precision around 1%.

By construction, the $+-$ sample generated by event mixing reproduces only the *uncorrelated* background contribution to the measured opposite-sign dimuon spectra. In the case of proton–nucleus collisions, given the low charged particle multiplicities, there is also a non-negligible *correlated* background contribution due, for instance, to charge correlations. The total opposite-sign background, needed to derive the signal from the measured opposite-sign data, can be obtained by scaling up the estimated uncorrelated part by the so-called R factor [8, 11, 12]. Starting from an R factor of 1.19 ± 0.04, measured by NA38 for p–W collisions at 200 GeV [11], the values 1.31, 1.19 and 1.17 are derived for p–Be, p–In and p–Pb, respectively, at 400 GeV, assuming that the value by which R exceeds unity is inversely proportional to the charged particle multiplicity, which increases with collision energy as $\log \sqrt{s}$ and with the mass number of the target nucleus as $A^{0.2}$.

In any case, the fraction of background in the opposite-sign dimuon data is relatively small in the dimuon sample collected by NA60 in 2002, given the low particle multiplicities of the proton–nucleus collisions and the relatively low beam intensity used (only one collision takes place within the 20 ns time window of the muon spectrometer). It decreases from around 30% to around 10% after the muon track matching step, because pion and kaon tracks seen in the vertex telescope are often not matched to the corresponding decay muon. The signal over background ratio is 10 in the ω and ϕ mass regions, and 1.5 in the continuum mass window 1.2–2.1 GeV/c^2.

3.4 Luminosity

The determination of production cross sections requires knowing the integrated luminosity corresponding to the analysed sample of events. In the case of fixed-target experiments, the integrated luminosity can be calculated as $\mathcal{L} = N_{\mathrm{inc}} \cdot N_{\mathrm{tgt}}$, where N_{inc} is the integrated number of protons incident on the target and N_{tgt} is the number of nuclei per unit transverse area in that target. N_{tgt} can be calculated as $N_A \cdot \rho \cdot l_{\mathrm{eff}}/\mathrm{A}$, where N_A is Avogadro's constant, ρ is the density, A is the atomic weight and l_{eff} is the effective target length, λ_{I} $(1 - \exp(-L/\lambda_{\mathrm{I}}))$, where λ_{I} is the nuclear interaction length and L is the target thickness. The relevant properties of the targets and beam tracker used by NA60 in 2002 are collected in Table 1 [13]. The beam tracker materials (sensors plus windows) should roughly generate as many collisions as a single Be target. The resulting values for N_{tgt} are 0.0240, 0.0075 and 0.0064 b^{-1} for the Be (each of the four), In and Pb targets, respectively.

The number of protons integrated during the bursts selected for the physics analysis is 1.74×10^{12} protons, as calculated from the measurements provided by the three independent ionisation chambers. Not all the collisions corresponding to the measured luminosity will be seen by the experiment, however, because the trigger system is not 100% efficient and because the data acquisition system, after receiving a trigger, is unable to process a new event during the "dead time" it takes to read out the data. In the case of the 2002 running period, given the low number of triggers per burst and the relatively small data volume per event, the DAQ lifetime was very high, 99.2% (measured by comparing the beam intensity integrated irrespective of the DAQ operation with the value measured when the scalers are vetoed during the periods when the DAQ is busy [8]). The trigger efficiency was estimated to be

Table 1 Properties of the targets and of the beam tracker materials placed on the beam line

Material	A	ρ [g/cm^3]	λ_{I} [cm]	L [mm]	L [% λ_{I}]
Beryllium (Be)	9.012	1.848	43.30	1.95	0.45
Indium (In)	114.818	7.310	22.40	1.97	0.88
Lead (Pb)	207.2	11.350	17.03	1.95	1.15
Inox (Fe/Cr/Ni)	55.183	7.870	16.93	0.2	0.12
Silicon (Si)	28.086	2.329	47.31	1.6	0.34

0.87 ± 0.03, from measurements made in the year 2000 [14, 15] with the same trigger system.

4 Simulation of the Expected Dimuon Sources

Several sources contribute to the dimuon mass spectrum, resulting in several pronounced resonances on the top of a continuously falling shape. The mass continuum processes are the Drell–Yan dimuons, which dominate at large dimuon masses (above the ψ' peak) and the simultaneous semi-muonic decays from two (correlated) D mesons. At the lower end of the dimuon mass spectrum, the electromagnetic decays of the light pseudo-scalar and vector mesons (η, η', ρ, ω and ϕ) are the dominating processes, via their Dalitz decays or $\mu^+\mu^-$ decays. To evaluate how the measurements are affected by experimental effects, such as the geometrical coverage of the detectors, the track reconstruction efficiencies, the vertexing, the track-matching rates, the smearing due to the limited resolution, a detailed Monte Carlo simulation needs to be performed, convoluting the generated physics processes with the performance of the experiment.

The Drell–Yan and open charm contributions can be simulated with the Pythia event generator [16], for instance. At SPS energies, the p–A charm cross sections are expected to exceed a linear scaling from pp collisions because the gluon distribution function is "anti-shadowed". This nuclear effect can be taken into account through the use of the EKS98 parameterisation [17], or others. The "hadronic decay cocktail" can be generated with the "Genesis" code [18], after being specifically tuned for proton–nucleus collisions [8]. It gives the $\mu^+\mu^-$ decays of the η, ω, ρ and ϕ mesons, and the Dalitz decays $\eta \to \mu^+\mu^-\gamma$, $\eta' \to \mu^+\mu^-\gamma$ and $\omega \to \mu^+\mu^-\pi^0$.

For the extraction of physics quantities, the measured distributions are compared to the result of a full detector simulation chain. In particular, the generated events must satisfy the trigger conditions and are subject to the same reconstruction procedure (with the same settings) as the real data. All the charged particles produced in the collisions and within the acceptance of the vertex tracker need to be reconstructed, to find suitable match candidates for the two tracks seen in the muon spectrometer and to identify the target where the interaction took place. Clearly, the number of clusters in the vertex telescope influences the track reconstruction efficiencies, while the number of reconstructed tracks influences the vertexing and the track-matching efficiencies. In order to have a Monte Carlo simulation as realistic as possible (including effects such as noisy micro-strip channels), before the reconstruction step the two generated muons should be immersed in a measured event, from which the information corresponding to its own muons was previously removed. In the analysis of the 2002 NA60 data, the simulated muon tracks were generated at the vertex of the measured event and the probability that they leave a hit in each micro-strip detector plane was given by the strip efficiency maps, previously measured [8] for each sensor. The tracking of the events through the NA60 apparatus was done using the GEANT transport code [19]. This detailed procedure should ensure that the detector's acceptance and smearing effects (due to multiple

scattering and to the finite resolution of the detectors), as well as the reconstruction efficiencies, are applied to the simulated events in a way that closely reproduces what happens to the measured data. To verify that the Monte Carlo simulation procedure properly describes the physics processes and the effects introduced by the detector, the reconstructed Monte Carlo events must be compared to the measured events, using several variables, such as the dimuon rapidity, transverse momentum, etc. This is a very important step because it often happens that the Monte Carlo simulations are "too good" with respect to the real data. This might be due to misalignments in the detector geometry not accounted for in the simulation, or because the measured events are collected over a long running period, including days when some detectors could not be operated, while the simulation is done for a single "setup", etc.

5 Acceptances, Phase Space Window and Efficiencies

5.1 Acceptances and Phase Space Window

The angular coverage of the NA60 muon spectrometer, which can be translated into an acceptance window in dimuon rapidity, is determined by the aperture of the toroidal magnet. Even if both muons are emitted in the angular region covered by the detectors, the event will be rejected if one of the muons (or both) does not have enough energy to reach the last trigger hodoscope, if both muons are emitted into the same sextant of the R trigger hodoscopes, or if one of the muons (or both) traverses one of the six 4 m long iron poles of the ACM magnet. Understanding and computing these detection probabilities ("acceptances") is very important to extract the real (physics) information from the measured (and distorted) information.

As an example, Fig. 8 shows the differential acceptances of the ω and ϕ mesons, at the level of the muon spectrometer, as a function of the rapidity and $\cos\theta_{\mathrm{CS}}$ kinematical variables, where θ_{CS} is the polar angle of the muons in the Collins–Soper reference frame. While the probability that a dimuon is detected in the muon spectrometer does not depend on the target where it was produced, this is no longer the case when the vertex tracker information is used. In particular, the beam hole of the silicon sensors reduces the angular coverage of the (low-p_{T}) muons produced in the most downstream targets. This means that, for instance, the final event sample contains fewer forward rapidity ω dimuons from the Pb target than from the In target. Clearly, such limitations of the detector capabilities must be carefully evaluated before deriving the nuclear dependence of particle production. Furthermore, the phase space window where the physics results are obtained must be chosen such that all the targets are properly covered. We cannot derive a nuclear dependence by comparing forward rapidity ω dimuons produced in the Be targets to backward rapidity ones produced in the Pb target, for instance.

For dimuon masses above 400 MeV/c^2 the NA60 apparatus has good acceptance down to zero p_{T}, while for lower masses the acceptance starts being reasonable for dimuons of p_{T} larger than $\sim$400 MeV/c. Figure 9 (left) shows the ω and ϕ

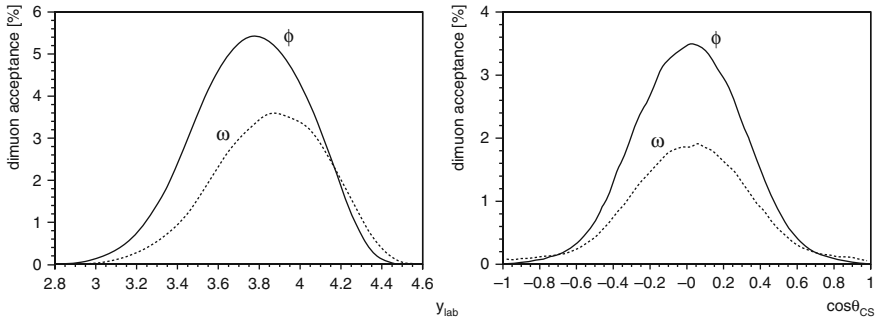

Fig. 8 Rapidity and $\cos\theta_{CS}$ differential acceptances for the ω and ϕ dimuons, before matching the muons to tracks in the vertex region

acceptances as a function of p_T. Since the p_T acceptance for low-mass dimuons depends also on rapidity, a rapidity-dependent transverse mass (m_T) cut has been included in the definition of the phase space window, graphically shown in Fig. 9 (right). It is important to underline that the presence of the vertex dipole magnet largely increases the NA60 acceptance for *opposite-sign* low-mass and low-p_T dimuons, with respect to previous dimuon experiments. In particular, many of the accepted events would be lost without the dipole field because both muons would go into the same sextant of the trigger hodoscopes, not passing the trigger condition requiring that the two muons must be in different sextants. Besides, some dimuons would also be lost in the dead area immediately surrounding the beam line, if it were not for the dipole field which deflects them into the angular acceptance of the muon spectrometer. This exceptional improvement can be appreciated in Fig. 10, where the raw-level p_T distributions obtained by NA60, in two different mass windows, are

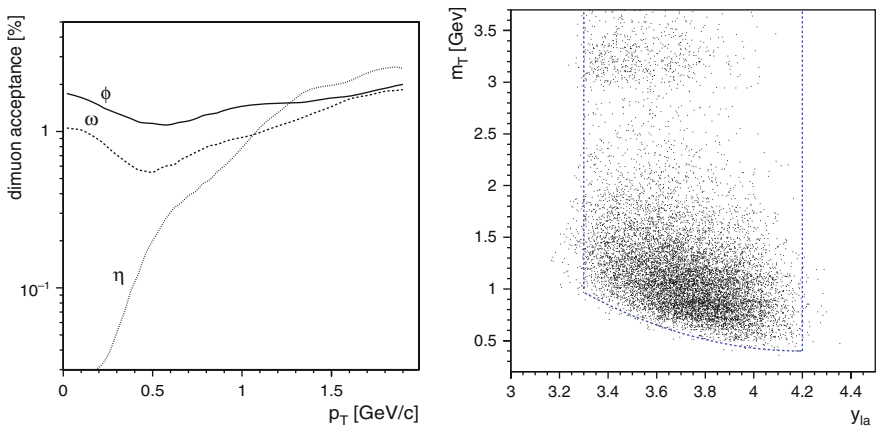

Fig. 9 *Left*: p_T differential acceptances for the ω, ϕ and η dimuons, before matching them to tracks in the vertex region. *Right*: Correlation between the transverse mass and the rapidity of the dimuons measured in the muon spectrometer. The *lines* indicate the selected phase space window

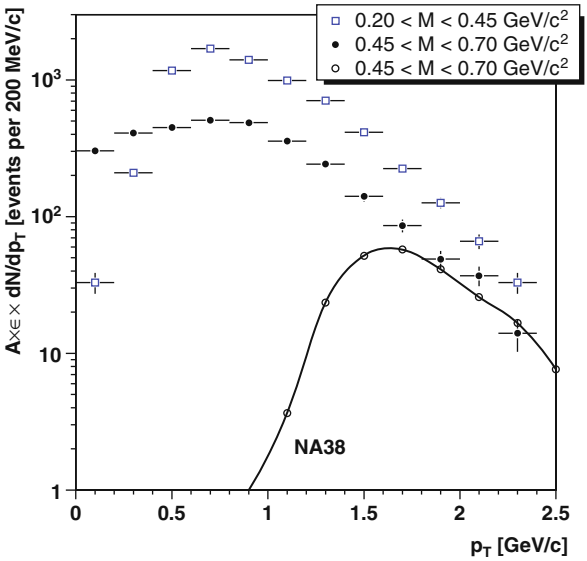

Fig. 10 Measured p_{T} distributions for two mass windows, compared to NA38's distribution for its lowest dimuon mass window

compared with the p_{T} distribution of the lowest mass dimuons detected by NA38, a predecessor experiment using the same muon spectrometer but without vertex dipole magnet.

The phase space window where the analysis of the 2002 NA60 data was made is defined by the ranges $3.3 < y_{\mathrm{lab}}^{\mu\mu} < 4.2$, $|\cos\theta_{\mathrm{CS}}| < 0.5$, $\eta_\mu < 4.2$ and $m_{\mathrm{T}} > 0.4 + 0.7 \cdot (y_{\mathrm{lab}} - 4.2)^2$ GeV. In this window, the acceptances vary by less than a factor 10 between any two selected events. Events collected outside of this window have a very small probability of being accepted and their study would be quite sensitive to possible differences between the simulated experiment and the real one. The effective thickness of the hadron absorber, the magnitudes of the magnetic fields and the alignment of the silicon tracking planes are only a few examples of the many elements that are needed to calculate the detection acceptances, and which might be inaccurately known.

5.2 Efficiencies

Besides the global efficiencies already mentioned in Sect. 3.4, i.e. the dimuon trigger efficiency and the DAQ lifetime, there are further efficiencies that need to be considered when extracting production cross sections from the measured yields: the track reconstruction efficiency, the track-matching efficiency, the vertexing efficiency, etc. The efficiency with which the tracks are reconstructed in the muon spectrometer basically depends on the hit occupancy of the chambers and, therefore, on the beam

intensity and effective thickness of the hadron absorber. Given the relatively low beam intensity of the 2002 running period and the small multiplicity of charged particles produced per proton–nucleus collision, the dimuon reconstruction efficiency was essentially 100%. The efficiency of the track reconstruction in the vertex tracker (VT) depends primarily on the efficiency maps of each sensor (which were measured and incorporated in the Monte Carlo simulation) and on the number of clusters present in the event. Simulating the dimuons on the top of measured events (after removing from the data the clusters previously assigned to the muon tracks), the simulated distribution of the number of silicon clusters is identical to the measured one, by construction. The "VT reconstruction efficiency" drops from 100% for very clean events to around 80% for events with a very high number of clusters in the silicon sensors.

Even if the muon track is within the geometrical coverage of the vertex telescope, and is reconstructed, the event may still be lost because the track is not recognised as a muon in the "track-matching" step. It turns out, however, that the track-matching efficiency is quite high, $\sim 98\%$, and almost independent of the number of reconstructed tracks, given that the matching uses the momenta of the tracks, and the number of "high-momentum" tracks is relatively small in proton–nucleus collisions. The number of fake matches is negligible; in the rare cases when the matching does not work, the muon is not matched rather than being matched to a wrong track.

The left panel of Fig. 11 shows how the convolution of the single muon reconstruction and matching efficiencies decreases as the number of clusters increases, in the case of p–In collisions (the other targets give very similar patterns). The right panel shows the measured distribution of the number of clusters seen in the full vertex tracker, for the In target.

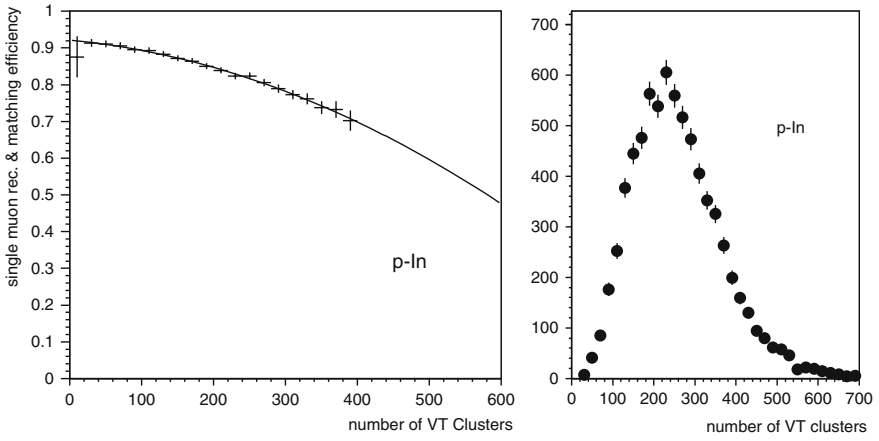

Fig. 11 *Left*: Single muon reconstruction and matching efficiency as a function of the number of clusters, for the In target. *Right*: Distribution of the number of clusters in the vertex tracker, as seen in the measured data, for the In target

5.3 Comments on Event Selection

Requiring that both muons must be matched to tracks in the vertex tracker rejects a large fraction of the collected events. It is important to realise, however, that many of the rejected events are due to background sources and, therefore, their loss improves the quality of the physics analysis event sample. Of the 75 000 like-sign muon pairs (due to pion and kaon decays) reconstructed in the muon spectrometer, only 2500 (i.e. 3.3%) survive the matching step, while the signal dimuons have a much higher survival rate: 25%. Besides, some of the rejected dimuons were produced in collisions downstream of the target region (in the beam dump or in the hadron absorber, for instance). Some of the signal dimuons produced in the targets are also rejected in the matching procedure, essentially because the vertex tracker does not cover the full geometrical acceptance of the muon spectrometer (mostly because of the beam hole of the silicon sensors). However, this loss of statistics is largely compensated by the significant improvement in dimuon mass resolution, which allows us to clearly distinguish the ω and ϕ resonances, as was shown in Fig. 7. Out of 35 000 opposite-sign matched dimuons, 76% were produced in one of the six targets; the others had their vertices in the sensors of the beam tracker (10%) or had no identified vertex (14%).

6 Target Identification

Having all the nuclear targets simultaneously exposed to the beam should, in principle, lead to smaller systematic uncertainties in the extraction of the nuclear dependences of particle production cross sections than having each different nuclear target independently exposed to the beam in a different running period. This is due to the fact that some sources of systematic errors, such as beam counting, trigger efficiencies, etc., are common to all the data samples and, hence, cancel out in *relative* studies, from light to heavy targets. However, having all the targets on the beam line introduces other problems, such as having acceptances that depend on rapidity in different ways for each target, as we saw before. Furthermore, it is crucial to identify the specific target where the collision occurred and the dimuon was produced, something not done with the same efficiency for all the targets and all dimuons. This is a very important issue and deserves some detailed discussion.

There are two alternative ways of identifying the target where the dimuon was produced. The first one, illustrated in Fig. 5, consists in calculating the interaction vertex by using all the charged tracks measured in the silicon vertex tracker. To first order, this method is insensitive to the kinematics of the dimuons, given that the algorithm ignores which tracks are the muons. However, it is $\sim 20\%$ more efficient (according to Monte Carlo simulations) at finding the correct interaction vertex in the case of p–In and p–Pb collisions than in the case of p–Be collisions, because the more tracks are produced the easier it is to find their common origin. The other alternative consists in using the point of closest approach between the

two muon tracks (after matching) to identify the target where they were produced. This method, illustrated in Fig. 6, has the advantage of treating in the same way the collisions produced in the different targets (light or heavy) but is limited by the resolution with which the origin of the dimuon can be determined. In the case of the "soft" muons from very low-mass dimuons, below ~ 500 MeV/c^2, this method is not good enough to accurately discriminate between two neighbouring targets.

The best way to ensure that the physics results are not biased by the procedure used to identify the interaction target is to perform two "analyses" in parallel. In the first one, the vertexing exclusively relies on the tracks of the vertex tracker, completely ignoring the dimuon information. If no vertex is found in the target region, the event is rejected. In the second one, the dimuon information is used to "validate" the vertex found from the charged tracks; if the dimuon origin is not compatible with the vertex, taking into account both uncertainties, the event is rejected. Besides, events where no vertex was found from the reconstructed tracks are recovered by taking the dimuon origin to identify the target, except if its uncertainty is too large to significantly discriminate between two consecutive targets. The physics results cannot depend on the vertexing procedure used; any differences should be taken as a contribution to the systematic error.

The average number of identified vertices in the NA60 2002 data was 1.04, to be compared with the 1.2 interactions per trigger expected from interaction pile-up, given the beam intensity and target thicknesses used [7]. These two numbers are in good agreement, considering that the vertexing algorithm fails to identify a vertex in 14% of the events with two matched muons. In the events with two vertices, the one with the largest number of associated tracks is upstream of the other one in exactly 50% of the cases, indicating that the events with two vertices are due to interaction pile-up and not to cases where a particle produced in one collision interacts in a downstream target, producing a second interaction. If such events would occur, they should be rejected if the dimuon was produced in the downstream vertex, since that dimuon would not be produced in a 400 GeV proton–nucleus collision.

Of the events with a well-identified vertex, 10% result from collisions upstream of the target region, as expected considering the effective thickness of the beam tracker materials. These events must be rejected from the final analysis event sample, and the integrated luminosity correspondingly decreased. Almost no events (with matched muons) have their vertex located downstream of the target region.

7 Summary and Final Remarks

In the previous sections we presented several issues that need to be considered when extracting a physics result from dimuon measurements. As a concrete example, we described the measurements made by the NA60 experiment in 2002 and reviewed the procedure leading to the understanding of the dimuon mass distributions produced in interactions of 400 GeV protons on beryllium, indium and lead targets. The next step would be, for instance, to determine the production cross sections of the ω

and ϕ mesons, and their ratios, for each of the p–A studied collision systems, as well as their nuclear dependences. This can be done by fitting the opposite-sign dimuon mass distributions to the superposition of the several expected sources. The background contributions can be fixed to the opposite-sign dimuon mass distributions obtained from the mixed-event procedure, scaled up by the appropriate R factors, as described in Sect. 3.3. The Drell–Yan and open charm contributions can also be kept fixed in the fits, with the shapes resulting from the reconstructed Monte Carlo events (incorporating the acceptance and efficiency effects) and the normalisations determined from the expected cross sections and branching ratios, scaled by the integrated luminosity. The sum of these three fixed contributions leads to a broad continuum which should reproduce the window 1.2–2.4 GeV/c^2 of the measured opposite-sign dimuon mass distributions. This is indeed the case, as shown in Fig. 12.

The mass window between the dimuon threshold and 1.1 GeV/c^2 can be described by the contributions from the light meson decays, fitting the production cross sections of the η, ω and ϕ mesons. The result is illustrated by Fig. 12, where the normalisations of the Dalitz and dimuon decay contributions of the ω (and also of the η) are bound to each other through the corresponding branching ratios [20], and the yields of the η' and ρ were fixed through $\sigma_{\mathrm{pA}}^{\eta'} = 0.15 \cdot \sigma_{\mathrm{pA}}^{\eta}$ and $\sigma_{\mathrm{pA}}^{\rho} = 1.0 \cdot \sigma_{\mathrm{pA}}^{\omega}$. It is worth emphasising that what is really extracted from the data is the product of the production cross section and the branching ratio of the dimuon decay channel.

The next step consists in evaluating the systematic uncertainties affecting the result. In the case of the ω and ϕ production cross sections, besides being affected by the luminosity determination and by the acceptance calculations, they are also affected by the vertexing uncertainties, which are larger for the Be targets than for the In and Pb targets, as seen by comparing the values obtained with the two different vertex determination methods previously described. The results are also affected by uncertainties related to the fitting procedure, which can be evaluated by redoing the fits several times, each time changing one of the inputs. For instance, it is reasonable to change the background contribution by $\pm 10\%$, the ρ/ω ratio by

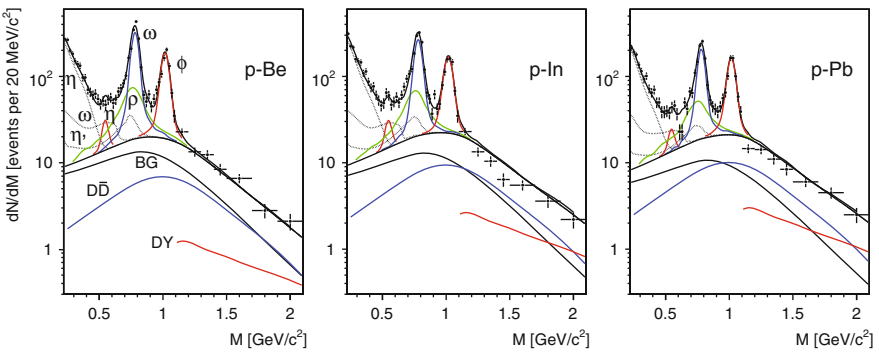

Fig. 12 Dimuon mass spectra collected in p–Be, p–In and p–Pb interactions fitted to the superposition of expected sources. The background, Drell–Yan and open charm contributions are fixed

$\pm 10\%$, the η'/η ratio by $\pm 50\%$, and the charm normalisation by $\pm 25\%$. It should also be seen how the results depend on the assumptions used in the calculation of the "hadron decay cocktail".

Cross-section *ratios* are more robust than absolute values, because they are not affected by the luminosity evaluation and are less sensitive to the acceptance uncertainties. Changing the vertexing identification procedure should also have a minor effect. For such results, hence, the biggest source of systematic uncertainty is the fitting procedure.

Clearly, many other points would need to be addressed in a "course on how to measure dimuons in proton–nucleus and nucleus–nucleus collisions". In this chapter we ignored several problems that affect the measurements made with nuclear beams. For instance, how to distinguish a dimuon produced in a central collision from one produced in a peripheral collision followed by an interaction of a beam fragment on another target, resulting in very similar information (number of emitted tracks, etc.) as a central collision. The background subtraction is also much more challenging in the case of heavy-ion collisions. We could also have discussed in more detail the advantages and disadvantages of measuring the nuclear dependence of particle production using several targets simultaneously on the beam line (as done by NA60) or using one target each time (as done by NA50). The validation of the Monte Carlo simulation by looking at the real data also deserves a much more detailed discussion, exposing some difficulties related to the isolation of the signal in the data sample, etc. Another limitation of this chapter is that some of the issues mentioned here would be different at much lower or higher collision energies. For instance, the like-sign muon pair sample is no longer exclusively due to uncorrelated sources in the very high energy collisions soon to be probed at the LHC, given the high production cross sections of beauty mesons. Much more could have been said about the evaluation of systematic uncertainties. The list of items not addressed in this chapter is, indeed, quite long. Clearly, there is room for a broader review of the many issues that need to be considered when studying dimuon measurements. We hope, nevertheless, that this chapter can be useful as a concrete and pedagogical illustration of some specific points.

Acknowledgments The work described in this chapter is based on the PhD thesis of H.K. Wöhri, made possible thanks to the financial support of the Austrian government (Bundesministerium für Bildung, Wissenschaft und Kultur), of CERN, and of CFIF/IST-Lisbon (scholarship from Fundação para a Ciência e a Tecnologia, Portugal, contract POCTI/FP/FNU/50173/2003). We acknowledge useful discussions with many NA60 collaborators.

The NA60 notes can be found at: http://na60.cern.ch/www/experiment/notes
The PhD theses of C. Lourenço (NA38), G. Borges and H. Santos (NA50), and H.K. Wöhri and A. David (NA60), can be found through the web pages of these experiments: http://cern.ch/NA38/, http://cern.ch/NA50/, http://cern.ch/NA60/.

References

1. F. Karsch: *Lattice QCD at High Temperature and Density*, Lecture Notes in Physics **583**, 209 (2002) 265
2. T. Matsui and H. Satz: Phys. Lett. **B178**, 416 (1986) 265
3. J. Buytaert et al.: The NA60 Silicon Tracking Telescope for Proton Running, NA60 Note 2001–5, Jul 2001 269
4. A. David: PhD Thesis, IST, Lisbon, Portugal (2006) 269, 273
5. A. David: Commissioning of NA60's Silicon Micro-Strip Telescope Readout Chain, NA60 Note 2002–2, Mar 2002
6. A. David et al. [NA60 Collaboration]: Nucl. Instrum. Methods **A509**, 118 (2003) 269
7. C. Lourenço: Measuring Absolute Production Cross Sections from the Proton-Nucleus Data Collected by NA60, NA60 Note 2007–1, Apr 2007 269, 281
8. H.K. Wöhri: PhD Thesis, TU Wien, Vienna, Austria (2004) 270, 273, 274, 275
9. R. Shahoyan et al. [NA60 Collaboration]: Eur. Phys. J. **C43**, 209 (2005) 271, 273
10. R. Shahoyan et al. [NA60 Collaboration]: Nucl. Phys. **A774**, 677 (2006) 271, 273
11. C. Lourenço: PhD Thesis, IST, Lisbon, Portugal (1995) 273
12. M.C. Abreu et al. [NA50 Collaboration]: Eur. Phys. J. **C14**, 443 (2000) 273
13. The atomic weights and the densities were taken from the Particle Data Group tables (http://pdg.lbl.gov/2006/AtomicNuclearProperties/index.html). The interaction lengths were calculated by the expression $\lambda_{\mathrm{int,A}} \frac{\mathrm{A}}{\sigma_{\mathrm{inel,p-A}} \cdot N_{\mathrm{Av}} \cdot \rho}$, where $\sigma_{\mathrm{inel,p-A}} = \sigma_0 \cdot \mathrm{A}^{\alpha}$, with $\sigma_0 = 38.53 \pm 1.10\,\mathrm{mb}$ and $\alpha = 0.719 \pm 0.007$; see Appendix C of G. Borges, PhD Thesis, IST, Lisbon, Portugal (2005) 274
14. B. Alessandro et al. [NA50 Collaboration]: Eur. Phys. J. **C48**, 329 (2006) 275
15. H. Santos: PhD Thesis, IST, Lisbon, Portugal (2004) 275
16. T. Sjöstrand et al.: Comp. Phys. Comm. **135**, 238 (2001) 275
17. K.J. Eskola et al.: Eur. Phys. J. **C9**, 61 (1999) 275
18. H. Sako [CERES Collaboration]: GSI Tech. Report 03–24 275
19. R. Brun et al. [Geant, version 3.21]: CERN DD/EE/84–1 275
20. S. Eidelman et al. [Particle Data Group]: Phys. Lett. **B592**, 1 (2004) 282

High-p_T Hadron Suppression and Jet Quenching

David d'Enterria and Barbara Betz

Abstract In these introductory lectures, we present a broad overview of the physics of hadron and jet production at large transverse momenta in high-energy nucleus–nucleus collisions. Emphasis is put on experimental and theoretical "jet quenching" observables that provide direct information on the (thermo)dynamical properties of hot and dense QCD matter.

1 Introduction

The research programme of high-energy nucleus–nucleus physics is focused on the study of the fundamental theory of the strong interaction – quantum chromodynamics (QCD) – in extreme conditions of temperature, density, and small parton momentum fraction (low-x) – see, e.g., [1] for a recent review. By colliding two heavy nuclei at relativistic energies one expects to form a hot and dense deconfined medium whose collective (colour) dynamics can be studied experimentally. Lattice QCD calculations [2] predict a new form of matter at energy densities (well) above $\varepsilon_{\rm crit} \approx 1\,{\rm GeV/fm}^3$ consisting of an extended volume of deconfined and bare-mass quarks and gluons: the quark–gluon plasma (QGP) [3–6].

Direct information on the thermodynamical properties (like temperature, energy, or particle densities) and transport properties (such as viscosities, diffusivities, conductivities) of the QGP is commonly obtained by comparing the results for a given observable Φ_{AA} measured in nucleus–nucleus (AA, "QCD medium") to those measured in proton–proton (pp, "QCD vacuum") collisions as a function of

D. d'Enterria (✉)
CERN, PH-EP, CH-1211 Geneva 23, Switzerland LNS, MIT, Cambridge, MA 02139-4307, USA,
david.d'enterria@cern.ch

B. Betz
Institut für Theoretische Physik, Johann Wolfgang Goethe-Universität,
Max–von–Laue–Str. 1, 60438 Frankfurt am Main, Germany,
betz@th.physik.uni-frankfurt.de

d'Enterria, D., Betz, B.: *High-*$\rm p_T$ *Hadron Suppression and Jet Quenching*. Lect. Notes Phys. **785**, 285–339 (2010)
DOI 10.1007/978-3-642-02286-9_9

centre-of-mass (c.m.) energy $\sqrt{s_{NN}}$, transverse momentum p_T, rapidity y, reaction centrality (impact parameter b), and particle type (mass m). Schematically

$$R_{AA}(\sqrt{s_{NN}}, p_T, y, m; b) = \frac{\text{"hot/dense QCD medium"}}{\text{"QCD vacuum"}} \propto \frac{\Phi_{AA}(\sqrt{s_{NN}}, p_T, y, m; b)}{\Phi_{pp}(\sqrt{s}, p_T, y, m)}. \quad (1)$$

Any observed *enhancements* and/or *suppressions* in the $R_{AA}(\sqrt{s_{NN}}, p_T, y, m; b)$ ratios can then be directly linked to the properties of strongly interacting matter after accounting for a realistic hydrodynamical modelling of the space–time evolution of the expanding system of quarks and gluons (globally called partons) produced in the collision.

2 Jet Quenching and Parton Energy Loss in QCD Matter

2.1 Hard Probes of Hot and Dense QCD Matter

Among all available observables in high-energy nuclear collisions, particles with large transverse momentum and/or high mass, $p_T, m \gtrsim 2$ GeV $\gg \Lambda_{\rm QCD}$ (where $\Lambda_{\rm QCD} \approx 0.2$ GeV is the QCD scale) constitute very useful tools to "tomographically" study the hottest and densest phases of the reaction (Fig. 1). Indeed, such

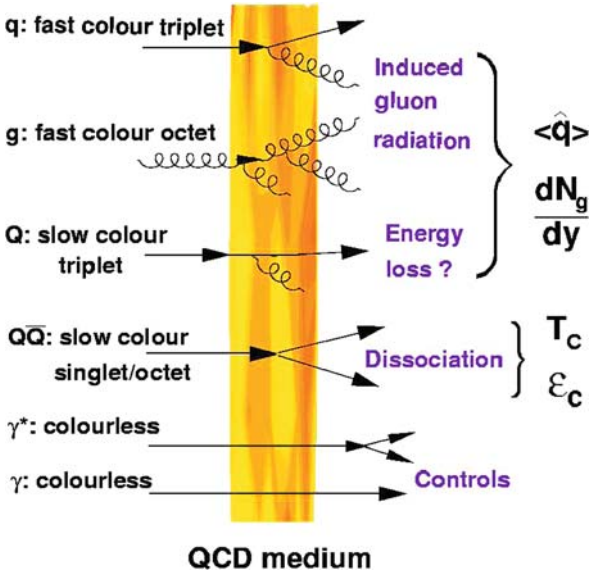

Fig. 1 Examples of hard probes whose modifications in high-energy AA collisions provide direct information on properties of QCD matter such as the transport coefficient $\hat{q}$, the initial gluon rapidity density dN^g/dy, the critical temperature $T_{\rm crit}$, and energy density $\varepsilon_{\rm crit}$ [1]

"hard probes" [7] (i) originate from partonic scatterings with large momentum transfer Q^2 and thus are directly coupled to the fundamental QCD degrees of freedom, (ii) are produced in very short timescales, $\tau \approx 1/p_T \lesssim 0.1$ fm/c, allowing them to propagate through (and be potentially affected by) the medium, and (iii) their cross sections can be theoretically predicted using the perturbative QCD (pQCD) framework.

Jet production in hadronic collisions is an archetypical hard QCD process. An elastic ($2 \to 2$) or inelastic ($2 \to 2 + X$) scattering of two partons from each of the colliding hadrons (or nuclei) results in the production of two or more partons in the final state. The two outgoing partons have a large virtuality Q which they reduce by subsequently radiating gluons and/or splitting into quark–antiquark pairs. Such a parton branching evolution is governed by the QCD radiation probabilities given by the Dokshitzer–Gribov–Lipatov–Altarelli–Parisi (DGLAP) equations [8–12] down to virtualities $\mathcal{O}(1\ \mathrm{GeV}^2)$. At this point, the produced partons fragment non-perturbatively into a set of final-state hadrons. The characteristic collimated spray of hadrons resulting from the fragmentation of an outgoing parton is called a "jet".

One of the first proposed "smoking guns" of QGP formation was "jet quenching" [13], i.e. the attenuation or disappearance of the spray of hadrons resulting from the fragmentation of a parton due to energy loss in the dense plasma produced in the reaction (Fig. 2). The energy lost by a particle in a medium, ΔE, provides fundamental information on its properties. In a general way, ΔE depends both on the particle characteristics (energy E and mass m) and on the plasma properties (temperature T, particle–medium interaction coupling α, and thickness L), i.e.

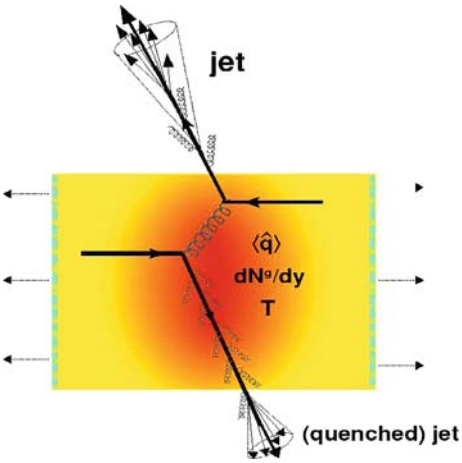

Fig. 2 "Jet quenching" in a head-on nucleus–nucleus collision. Two quarks suffer a hard scattering: one goes out directly to the vacuum, radiates a few gluons, and hadronises; the other goes through the dense plasma formed in the collision (characterised by transport coefficient $\hat{q}$ and gluon density dN^g/dy), suffers energy loss due to medium-induced gluonstrahlung, and finally fragments outside into a (quenched) jet

$\Delta E(E, m, T, \alpha, L)$. The following (closely related) variables are extremely useful to characterise the energy loss in a medium:

- the *mean free path* $\lambda = 1/(\rho\sigma)$, where ρ is the medium density ($\rho \propto T^3$ for an ideal gas) and σ the integrated cross section of the particle–medium interaction,[1]
- the *opacity* $N = L/\lambda$ or number of scattering centres in a medium of thickness L,
- the *Debye mass* $m_D(T) \sim g\,T$ (where g is the coupling parameter, i.e. $m_D \sim e\,T$, $\alpha_s^{1/2}\,T$ in QED, QCD) is the inverse of the screening length of the (chromo) electric fields in the plasma. m_D characterises the lowest momentum exchanges with the medium: the effective masses of the plasma constituents are $\mathcal{O}(m_D)$,
- the *transport coefficient* $\hat{q} \equiv m_D^2/\lambda$ encodes the "scattering power" of the medium through the average transverse momentum squared transferred to the traversing particle per unit path length. $\hat{q}$ combines both thermodynamical (m_D, ρ) and dynamical (σ) properties of the medium [14–16]:

$$\hat{q} \equiv m_D^2/\lambda = m_D^2\,\rho\,\sigma\,. \tag{2}$$

  As a numerical example,[2] let us consider an equilibrated *gluon* plasma at $T = 0.4$ GeV and a strong coupling $\alpha_s \approx 0.5$ [17]. At this temperature, the particle (energy) density is $\rho_g = 16/\pi^2\ \zeta(3)\cdot T^3 \approx 15$ fm^{-3} ($\epsilon_g = 8\pi^2/15\cdot T^4 \approx 17$ GeV/fm^3), i.e. 100 times denser than normal nuclear matter ($\rho = 0.15$ fm^{-3}). At leading order (LO), the Debye mass is $m_D = (4\pi\alpha_s)^{1/2}T \approx 1$ GeV. The (transport) gluon–gluon cross section is to LO accuracy: $\sigma_{gg} \simeq 9\pi\alpha_s^2/(2m_D^2) \approx 1.5$ mb. The gluon mean free path in such a medium is $\lambda_g = 1/(\rho_g\sigma_{gg}) \simeq (18/\pi^2\ \zeta(3)\alpha_s T)^{-1} \simeq 0.45$ fm (the mean free path for a quark is $\lambda_q = 9/4\,\lambda_g \approx 1$ fm). The transport coefficient is therefore $\hat{q} \simeq m_D^2/\lambda_g \simeq 2.2$ GeV^2/fm. Note that such a numerical value has been obtained with a LO expression for the parton-medium cross section. Higher order scatterings can well account for a factor $K = 2$–3 larger $\hat{q}$.
- the *diffusion constant* D, characterising the dynamics of *heavy* non-relativistic particles (mass M and speed v) traversing the plasma, is connected, via the Einstein relations

$$D = 2T^2/\kappa = T/(M\,\eta_D) \tag{3}$$

  to the *momentum diffusion coefficient* κ – the average momentum gained by the particle per unit time (related to the transport coefficient as $\kappa \approx \hat{q}\,v$) – and the *momentum drag coefficient* η_D.

[1] One has $\lambda \sim (\alpha T)^{-1}$ since the QED (QCD) Coulomb (Yukawa) scattering is $\sigma_{el} \propto \alpha/T^2$.

[2] Natural units used ($c = \hbar = 1$). For unit conversion, multiply by powers of $\hbar c = 0.197$ GeV fm.

2.2 Mechanisms of In-Medium Energy Loss

In the most general case, the total energy loss of a particle traversing a medium is the sum of collisional and radiative terms: $\Delta E = \Delta E_{\rm coll} + \Delta E_{\rm rad}$. Depending on the kinematic region, a (colour) charge can lose energy[3] in a plasma with temperature T mainly[4] by two mechanisms:

- **Collisional energy loss** through *elastic* scatterings with the medium constituents (Fig. 3, left), dominates at low particle momentum. The *average* energy loss in one scattering (with cross section $d\sigma/dt$, where t is the momentum transfer) is

$$\left\langle \Delta E_{\rm coll}^{\rm 1scat} \right\rangle = \frac{1}{\sigma\, T} \int_{m_D^2}^{t_{\rm max}} t\, \frac{d\sigma}{dt}\, dt \quad . \tag{4}$$

- **Radiative energy loss** through *inelastic* scatterings within the medium (Fig. 3, *right*) dominates at higher momenta. This loss can be determined from the corresponding single- or double-differential photon/gluon *Bremsstrahlung spectrum* ($\omega\, dI_{\rm rad}/d\omega$ or $\omega\, d^2 I_{\rm rad}/d\omega\, dk_\perp^2$, where $\omega, k_\perp$ are the energy, transverse momentum of the radiated photon/gluon):

$$\Delta E_{\rm rad}^{\rm 1scat} = \int^{E} \omega\, \frac{dI_{\rm rad}}{d\omega}\, d\omega \quad \text{or} \quad \Delta E_{\rm rad}^{\rm 1scat} = \int^{E} \int^{k_{T,\rm max}} \omega\, \frac{d^2 I_{\rm rad}}{d\omega\, dk_\perp^2}\, d\omega\, dk_\perp^2 \; . \tag{5}$$

For incoherent scatterings one has simply $\Delta E^{\rm tot} = N \cdot \Delta E^{\rm 1scat}$, where $N = L/\lambda$ is the opacity. The energy loss per unit length or *stopping power*[5] is:

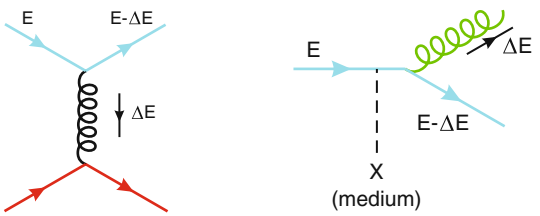

Fig. 3 Diagrams for collisional (*left*) and radiative (*right*) energy losses of a quark of energy E traversing a quark–gluon medium

[3] Note that if the energy of the particle is similar to the plasma temperature ($E \approx T$) the particle can also *gain* energy while traversing it.

[4] In addition, synchrotron-, Čerenkov-, and transition-radiation energy losses can take place, respectively, if the particle interacts with the medium magnetic field, if its velocity is greater than the local phase velocity of light, or if it crosses suddenly from one medium to another. Yet those effects are usually less important in terms of the amount of $E_{\rm loss}$.

[5] By "stopping power", one means a property of the matter, while "energy loss per unit length" describes what happens to the particle. The numerical value and units are identical (and both are usually written with a minus sign in front).

$$-\frac{dE}{dl} = \frac{\left\langle \Delta E^{\text{tot}} \right\rangle}{L}\,, \tag{6}$$

which for incoherent scatterings reduces to $-dE/dl = \left\langle \Delta E^{1\text{scat}} \right\rangle / \lambda$. As an example, we show in Fig. 4 the stopping power of muons in copper. At low and high energies, the collisional (aka "Bethe–Bloch") and the radiative energy losses dominate, respectively.

Yet the hot and dense plasma environment that one encounters in "jet quenching" scenarios is not directly comparable to the QED energy loss in *cold* matter represented in Fig. 4. A recent review by Peigné and Smilga [18] presents the parametric dependences of the energy loss of a lepton traversing a *hot* QED plasma with temperature T and Debye-mass m_D. In a simplified manner, inserting the Coulomb (lepton–lepton) and Compton (lepton–photon) scattering cross sections in Eq. (4) and using Eq. (6), one obtains

- Light lepton ($M^2 \ll ET$): $-\frac{dE_{\text{coll}}}{dl} \approx \frac{\pi}{3}\alpha^2 T^2 \ \ln\left(\frac{ET}{m_D^2}\right) \approx \frac{\pi}{3}\alpha \ m_D^2 \ \ln\left(\frac{ET}{m_D^2}\right)$
- Heavy lepton ($M^2 \gg ET$): $-\frac{dE_{\text{coll}}}{dl} \approx \frac{2\pi}{3}\alpha^2 T^2 \ \ln\left(\frac{ET}{m_D\, M}\right) \approx \frac{2\pi}{3}\alpha \ m_D^2 \ \ln\left(\frac{ET}{m_D\, M}\right)$

For *radiative* losses, the amount of photon emission depends chiefly on the thickness of the plasma.[6] For thin media ($L \ll \lambda$), the traversing particle suffers at most one single scattering and the QED radiation spectrum is just given by the Bethe–Heitler

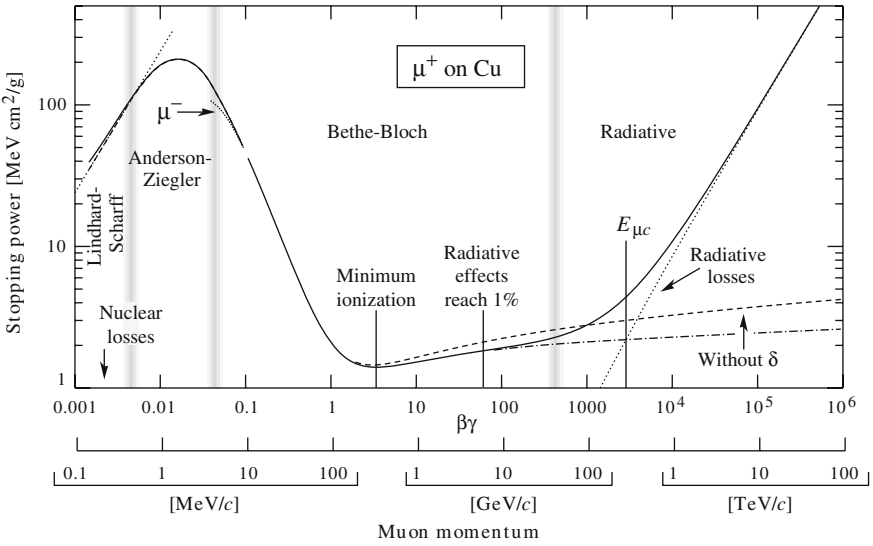

Fig. 4 Stopping power, $-dE/dl$, for positive muons in copper as a function of $\beta\gamma = p/Mc$ (or momentum p). The *solid curve* indicates the total stopping power [19]

[6] We consider here the formulas where the charged particle is produced *inside* the plasma, as this is the typical situation encountered in a QGP.

(BH) Bremsstrahlung expression. On the contrary, for thick media ($L \gg \lambda$) there are N(=opacity) scatterings and the Landau–Pomeranchuk–Migdal (LPM) [20] coherence effect[7] reduces the amount of radiation compared to N times the BH spectrum. Making use of Eq. (5) one can obtain [18]:

- BH photon spectrum ($L \ll \lambda$)[8]: $\omega \frac{dI_{\rm rad}}{d\omega} \approx \alpha\ (L^2 m_D^2/\lambda) \cdot \omega/E^2 \approx \alpha\ \hat{q}\ L \cdot \omega/E^2$

$$\Delta E_{\rm rad}^{\rm BH} \approx \alpha\ \hat{q}\ L^2 \approx \alpha^3\, T^3\, L^2 \implies -\frac{dE_{\rm rad}}{dl} = \frac{\Delta E_{\rm rad}}{L} \approx \alpha^3\, T^3\, L\ . \qquad (7)$$

- LPM photon spectrum ($L \gg \lambda$): $\omega \frac{dI_{\rm rad}}{d\omega} \approx \alpha^2\, L \sqrt{T^3\, \frac{\omega}{E^2}\, \ln\left(E^2/(\omega T)\right)}$

$$\Delta E_{\rm rad}^{\rm LPM} \approx \alpha^2\, L\, \sqrt{ET^3\, \ln(E/T)} \implies -\frac{dE_{\rm rad}}{dl} \approx \alpha^2 \sqrt{ET^3\, \ln(E/T)}. \qquad (8)$$

In general, the radiative energy losses of an energetic lepton crossing a hot QED plasma are much larger than their collisional losses. Yet, if the particle is heavy, the amount of radiation at angles within a cone $\theta < M/E$ is suppressed by a factor m_D^2/M^2 ("dead cone" effect, see later) resulting in a reduction of the Bremsstrahlung emission by a factor $m_D^2/M^2 = \alpha\, T^2/M^2$.

The main differences from QED and QCD result from the non-Abelian nature of QCD: the fact that gluons can also interact with themselves (at variance with photons in QED) introduces several important changes. First, the QCD coupling α_s runs more rapidly than α_{em} (at least for not asymptotically high temperatures), and the scale Q at which $\alpha_s(Q)$ is evaluated needs to be explicitly considered in all calculations of *collisional* energy losses [21, 22]. Second, for *radiative* losses it is crucial to take into account the different couplings between quarks and gluons. The relative strengths of the three distinct QCD vertices, $\alpha_s C_F$ for $q \to qg$, $\alpha_s C_A$ for $g \to gg$, and $\alpha_s T_F$ for $g \to q\bar{q}$, are completely determined by the structure (Casimir factors C_R) of the gauge group describing the strong force [23]. For $SU(N_c)$ where N_c is the number of colours, $C_A = N_c$, $C_F = (N_c^2 - 1)/2N_c$, and $T_F = 1/2$. The probability for a gluon (quark) to radiate a gluon is proportional to the colour factor $C_A = 3$ ($C_F = 4/3$). In the asymptotic limit, and neglecting the gluon splitting into quark–antiquark pairs (proportional to the smaller factor $T_R = 1/2$), the average number of gluons radiated by a gluon is $C_A/C_F = 9/4$ times higher than that radiated by a quark. That is the reason why gluon jets have a larger (and softer) hadron multiplicity than quark jets.

---

[7] The LPM effect describes the fact that, since it takes a finite time to emit a photon, neighbouring scattering centres interfere coherently and act as one effective scattering centre, inducing *single* photon radiation.

[8] This spectrum is often written as $\omega \frac{dI_{\rm rad}}{d\omega} \approx \alpha\, \omega_c\, \omega/E^2$, where $\omega_c \approx \hat{q}\, L^2$ is the characteristic frequency of the radiated photons.

2.2.1 QCD Collisional Energy Loss

The collisional energy loss due to elastic scattering of a parton of energy E inside a QGP of temperature T was originally estimated by Bjorken [13] and Braaten–Thoma [24] and later improved (including running coupling, finite energy kinematics, and quark mass effects) by various authors [21, 22, 25]. Using Eq. (4) with the momentum-transfer integral limits given by (i) the QGP Debye mass squared $t_{\min} = m_D^2(T) \simeq 4\pi\alpha_s T^2(1 + N_f/6)$ and (ii) $t_{\max} = s \simeq ET$ and taking the dominant contribution to the parton–parton t-differential elastic cross section

$$\frac{d\sigma}{dt} \approx C_i \, \frac{4\pi \, \alpha_s^2(t)}{t^2} \, , \quad \text{with } \alpha_s(t) = \frac{12\pi}{(33 - 2n_f) \ln\left(t/\Lambda^2_{\rm QCD}\right)}, \tag{9}$$

where $C_i = 9/4, 1, 4/9$ are the colour factors for gg, gq, and qq scatterings respectively, one finally obtains [22]

- Light quark, gluon: $-\frac{dE_{\rm coll}}{dl}\big|_{q,g} = \frac{1}{4} \, C_R \, \alpha_s(ET) \, m_D^2 \, \ln\left(\frac{ET}{m_D^2}\right)$,
- Heavy quark: $-\frac{dE_{\rm coll}}{dl}\big|_{Q} = -\frac{dE_{\rm coll}}{dl}\big|_{q} - \frac{2}{9} \, C_R \, \pi \, T^2 \, \left[\alpha_s(M^2)\alpha_s(ET) \, \ln\left(\frac{ET}{M^2}\right)\right]$,

with C_R = 4/3 (3) being the quark (gluon) colour charge. The amount of $\Delta E_{\rm coll}$ is linear with the medium thickness, and it depends only logarithmically on the initial parton energy. As a numerical example, taking $T = 0.4$ GeV, $E = 20$ GeV, $M = 1.3$ GeV (charm quark), and $\alpha_S = 0.5$ (which yields $m_D = 1$ GeV), the elastic energy loss per unit length is $-dE_{\rm coll}/dl\big|_q = 2.3$ GeV/fm and $-dE_{\rm coll}/dl\big|_Q = 2.6$ GeV/fm.

2.2.2 QCD Radiative Energy Loss

The dominant mechanism of energy loss of a fast parton in a QCD environment is of radiative nature ("gluonstrahlung") [26–32]: a parton traversing a QGP loses energy mainly by medium-induced multiple gluon emission. The radiated gluon spectrum, $\omega \, dI(\omega, l)/d\omega$, has been computed by diverse groups under various approximations (see Sect. 3.2). The starting point is the QCD radiation probabilities given by DGLAP splitting functions ($P_{q,g\to g}$): $\omega \, dI(\omega)/d\omega \propto P_{q,g\to g}(\omega/E)$, modified to take into account the enhanced medium-induced radiation. All medium modifications are often encoded into the "transport coefficient" parameter, $\hat{q}$, introduced previously, Eq. (2). For thin (thick) media, one deals with the Bethe–Heitler (Landau–Pomeranchuk–Migdal) gluonstrahlung spectrum. In the LPM case, one further differentiates between the soft and hard gluon emission cases with respect to the characteristic gluonstrahlung energy[9] $\omega_c = \frac{1}{2}\hat{q} \, L^2$. Making use of Eq. (5), the basic QCD radiative energy loss formulas read [12]

[9] Up to prefactors, ω_c is the average energy lost in the medium: $\omega_c \simeq 2 \, \langle \Delta E_{\rm rad} \rangle \, / (\alpha_s C_R)$.

- Bethe–Heitler (BH) regime ($L \ll \lambda$):

$$\omega \frac{dI_{\rm rad}}{d\omega} \approx \alpha_s\, C_R\, \hat{q}\, L^2/\omega \implies \Delta E^{\rm BH}_{\rm rad} \approx \alpha_s\, C_R\, \hat{q}\, L^2 \ln(E/(m_D^2\, L)). \qquad (10)$$

- Landau–Pomeranchuk–Migdal (LPM) regime ($L \gg \lambda$):

$$\omega \frac{dI_{\rm rad}}{d\omega} \approx \alpha_s\, C_R \begin{cases} \sqrt{\hat{q}\, L^2/\omega} \\ \hat{q}\, L^2/\omega \end{cases} \implies \Delta E^{\rm LPM}_{\rm rad} \approx \alpha_s\, C_R \begin{cases} \hat{q}\, L^2 & (\omega < \omega_c) \\ \hat{q}\, L^2\, \ln(E/(\hat{q} L^2)) & (\omega > \omega_c). \end{cases} \qquad (11)$$

The main differences between the energy loss in a QCD and QED plasma are the colour factors (C_R) and the extra logarithmic dependence of $\Delta E_{\rm rad}$ on the energy E of the traversing particle. As a numerical example, taking $E = 20$ GeV, $L = 6$ fm, and a medium with $\hat{q} = 2$ GeV^2/fm, the LPM radiative energy losses per unit length $dE_{\rm rad}/dl$ are $\mathcal{O}(10$ GeV/fm), to be compared with the elastic losses of $\mathcal{O}(2$ GeV/fm) estimated before. As we see in Fig. 5, $\Delta E_{\rm coll}$ is in general a small correction compared to $\Delta E_{\rm rad}$ for light quarks and gluons but it can be an important contribution for slower heavy quarks (see next).

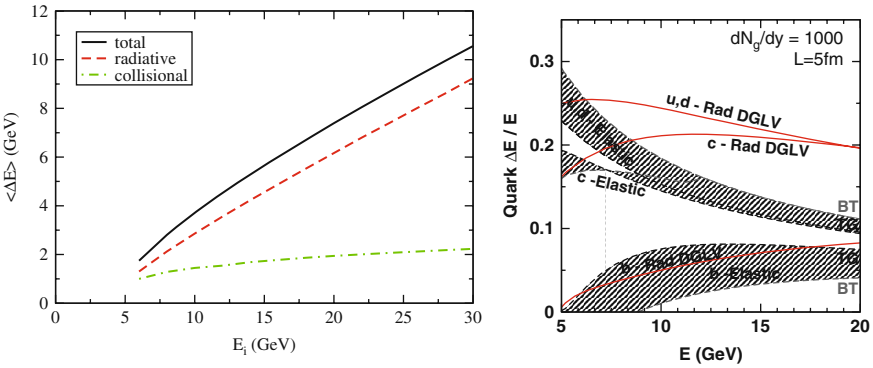

Fig. 5 Comparison of the average radiative and elastic energy losses of light quarks (*left*) and light and heavy quarks (*right*) passing through the medium produced in central AuAu collisions at RHIC energies as obtained by the AMY [34] and DGLV [35] models (see later)

2.2.3 Heavy-Quark Radiative Energy Loss ("Dead Cone" Effect)

Gluon bremsstrahlung off a heavy quark differs from that of a massless parton. Due to kinematics constraints, the radiation is suppressed at angles smaller than the ratio of the quark mass M to its energy E. The double-differential distribution of gluons of transverse momentum $k_\perp$ and energy ω radiated by a heavy quark at small angles ($k_\perp \approx \omega\,\theta$) differs from the standard bremsstrahlung spectrum by the factor

$$\omega \frac{dI_{\mathrm{rad},Q}}{d\omega\, dk_\perp^2} = \frac{\alpha_s\, C_F}{\pi}\, \frac{k_\perp^2}{(k_\perp^2 + \omega^2\theta_0^2)^2} \;\approx\; \omega \frac{dI_{\mathrm{rad}}}{d\omega\, dk_\perp^2} \cdot \left(1 + \frac{\theta_0^2}{\theta^2}\right)^{-2}, \quad \theta_0 \equiv \frac{M}{E} = \frac{1}{\gamma}\,. \tag{12}$$

This effect, known as the "dead cone" [33], results in a reduction of the total gluon radiation emitted off heavy quarks. In the medium, the total amount of reduction depends on a non-trivial way on the various kinematics scales (E, M, L) of the problem [18]. In a simplified way, the reduction is $\mathcal{O}(m_D/M)$ (compared to $\mathcal{O}(m_D^2/M^2)$ in the QED case). For a plasma with Debye mass $m_D = 1$ GeV/c^2, the reduction of radiative energy loss for a charm (bottom) quark of mass 1.3 (4.2) GeV/c^2 is a factor $\sim$25% (75%).

2.3 Phenomenological Consequences of Parton Energy Loss

Medium-induced parton energy loss in AA reactions results in various observable experimental consequences compared to the same measurements in proton–proton (pp) collisions in "free space". The presence of jet quenching manifests itself via

(i) a suppression of the spectrum (dN_{AA}/dp_T) of high-p_T hadrons [26, 27],
(ii) unbalanced back-to-back high-p_T di-hadron azimuthal correlations ($dN_{\mathrm{pair}}/d\phi$) [36, 37],
(iii) modified energy–particle flow (softer hadron spectra, larger multiplicity, increased angular broadening, etc.) within the final jets [38–43].

Due to the aforementioned hierarchy of flavour-dependent radiative energy losses

$$\Delta E_{\mathrm{rad}}(g) > \Delta E_{\mathrm{rad}}(q) > \Delta E_{\mathrm{rad}}(c) > \Delta E_{\mathrm{rad}}(b)\,, \tag{13}$$

all these medium effects are expected to be larger for gluons and u, d, s quarks than for c or b quarks (the top quark decays into $W\,b$ immediately, $\tau < 0.1$ fm/c, after production).

(i) High-p_T leading hadron spectra

The *leading hadron* of a jet is the hadron that carries the largest fraction of the energy of the fragmenting parton.[10] In a heavy-ion collision, if the parent parton suffers energy loss, the energy available for such hadrons is reduced and consequently their spectrum is depleted compared to pp. From the measured suppression factor one can determine ΔE_{loss} and estimate properties of the produced plasma (expanding with original transverse area $A_\perp = \pi\, R_A^2 \approx 150$ fm^2 and thickness L) such as

[10] The high-p_T part of hadron spectra is dominated by particles with $\langle z \rangle = p_{\mathrm{hadron}}/p_{\mathrm{parton}} \approx$ 0.4–0.7 [43].

- the average *transport coefficient* $\langle\hat{q}\rangle$, from Eq. (10): $\langle\Delta E\rangle \propto \alpha_s\, C_R\, \langle\hat{q}\rangle\, L^2$,
- the initial *gluon density* $\mathrm{dN}^g/\mathrm{dy}$ from [30, 31]:

$$\Delta E \propto \alpha_s^3\, C_R\, \frac{1}{A_\perp} \frac{dN^g}{dy}\, L\ . \tag{14}$$

(ii) High-p_T di-hadron correlations

Parton–parton $2 \to 2$ scatterings are balanced in p_T, i.e. they are back-to-back in azimuthal angle ($\Delta\phi \approx \pi$). Such azimuthal correlation is smeared out if one or both partons suffer rescatterings in a dense plasma.

- The φ-broadening arising from the interactions of a parton in an expanding QGP $\langle k_T^2\rangle_{\mathrm{med}} \propto m_D^2/\lambda \ln(L/\tau_0)$, is $\langle k_T^2\rangle_{\varphi} = \langle k_T^2\rangle_{\varphi,\mathrm{vac}} + \frac{1}{2}\langle k_T^2\rangle_{\mathrm{med}}$. The azimuthal correlations between the hadrons issuing from quenched partons will show a dependence on the $\hat{q}$ and thickness of the medium: $d^2N_{\mathrm{pair}}/d\Delta\phi = f(\hat{q}, L)$.

In addition, it has been proposed that a fast parton propagating through a QGP with supersonic ($\beta > c_s$) or "superluminal" ($\beta > 1/n$) velocities can generate a wake of lower energy gluons with either Mach- [44–48] or Čerenkov-like [48–51] conical angular patterns. After hadronisation those secondary gluons can show up in the final azimuthal correlations of the measured hadrons with respect to the original jet axis:

- In the first case, the *speed of sound* of the traversed matter, [11] $c_s^2 = \partial P/\partial\varepsilon$, can be determined from the characteristic Mach angle θ_M of the secondary hadrons:

$$\cos(\theta_M) = \frac{c_s}{\beta}. \tag{15}$$

- In the second scenario, the *refractive index* of the medium, $n \approx \sqrt{\varepsilon_r}$ where ε_r is the gluon dielectric constant, can be estimated from the Čerenkov angle of emission θ_c of the hadrons:

$$\cos(\theta_c) = \frac{1}{n\,\beta} = \frac{1}{\sqrt{\varepsilon_r}\,\beta}. \tag{16}$$

(iii) Jet spectra and jet shapes

The measurements of fully reconstructed (di)jets or of jets tagged by an away-side photon or Z-boson [52, 53] in heavy-ion collisions allow one to investigate the mechanisms of in-medium parton radiation and to characterise the medium properties via

[11] The speed of sound – namely the speed of a small disturbance through the medium – for an *ideal* QGP (with $\varepsilon = 3P$, where P is the pressure) is simply $c_s = 1/\sqrt{3}$.

- Medium-modified jet profiles and multiplicities [38, 54], through the differential $\rho^{\rm med}(r;\hat{q})$ and integrated $\Psi^{\rm med}(r;\hat{q})$ jet shapes, which provide a sensitive probe of the mechanisms of energy loss in a QCD plasma.
- Medium-modified fragmentation functions [55], $D^{\rm med}_{\rm parton\to hadron}(z)$ where $z = p_{\rm hadron}/p_{\rm parton}$ is the fractional energy carried by a hadron in the jet, are a sensitive probe of the plasma properties ($\hat{q}$ for a given L) [39, 56, 57, 40]. Medium effects enter, e.g. as an additive correction to the DGLAP splitting functions:

$$P_{\rm med}(z) = P_{\rm vac}(z) + \Delta P(z, Q^2, E; \hat{q}, L) \,, \tag{17}$$

where $\Delta P(z, Q^2) \simeq 2\pi Q^2/\alpha_s \; dI_{\rm rad}(\hat{q}, L)/dz dQ^2$ is directly derivable from the medium-induced gluon radiation spectrum, Eq. (11).

3 Parton Energy Loss Phenomenology

The use of fast partons as a calibrated tomographic probes of hot and dense QCD matter in heavy-ion collisions relies on the possibility to compute theoretically (i) their perturbative production cross sections and (ii) their modifications suffered while propagating through a strongly interacting medium. We discuss here the basic pQCD principles used to compute high-p_T hadron (and jet) cross sections, and we outline the various existing parton energy loss schemes.

3.1 High-$\mathbf{p_T}$ Hadroproduction: QCD Factorisation in AA Collisions

Because of asymptotic freedom, the QCD coupling α_s is small for high-energy (short distance) parton interactions: $\alpha_s(Q^2 \to \infty) \to 0$. The single inclusive[12] production of a high-p_T parton c in a parton–parton collision, $ab \to c + X$, can be thus computed using perturbation theory techniques. Over short distances, the infinite number of Feynman diagrams that would theoretically result in the production of the outgoing parton c can be approximated accurately by a much more manageable number of terms. In high-energy *hadron–hadron* collisions, the production of high-p_T particles can be computed from the underlying *parton–parton* processes using the QCD "factorisation theorem" [58]. The production cross section of a high-p_T hadron h can be written, to order $\mathcal{O}(1/Q^2)$, as the product

$$d\sigma^{\rm hard}_{AB\to h} = f_{a/A}(x_1, Q^2) \otimes f_{b/B}(x_2, Q^2) \otimes d\sigma^{\rm hard}_{ab\to c}(x_1, x_2, Q^2) \otimes D_{c\to h}(z, Q^2) \,, \tag{18}$$

where $\sigma_{ab\to c}(x_1, x_2, Q^2)$ is the perturbative partonic cross section computable up to a given order in α_s, and there are two non-perturbative terms:

[12] *Inclusive* refers to the consideration of *all* possible channels that result in the production of a given particle c, without any particular selection of the final state X.

- $f_{a/A}(x, Q^2)$: parton distribution functions (PDF), encoding the probability of finding a parton of flavour a and momentum fraction $x = p_{\text{parton}}/p_{\text{nucleus}}$ inside the nucleus A,
- $D_{c\to h}(z, Q^2)$: fragmentation function (FF), describing the probability that the outgoing parton c fragments into the observed hadron h with fractional momentum $z = p_{\text{hadron}}/p_{\text{parton}}$,

that are universal objects that can be determined experimentally, e.g. in deep-inelastic $e^{\pm}$ nucleus and e^+e^- collisions, respectively. In Eq. (18), one sets $D_{c\to h} = \delta(1-z)$ if interested in the total parton (i.e. jet) cross section.

The basic assumption underlying the factorised form of Eq. (18) is that the characteristic time of the parton–parton interaction is much shorter than any long-distance interaction occurring before (among partons belonging to the same PDF) or after (during the evolution of the struck partons into their hadronic final state) the hard collision itself (see sketch in Fig. 6). The validity of Eq. (18) holds thus on the possibility to separate long- and short-distance effects with independent QCD time- (length-) scales, as well as on the "leading-twist"[13] assumption of *incoherent* parton–parton scatterings. Since partons are effectively "frozen" during the hard scattering, one can treat each nucleus as a collection of free partons. Thus, *with regard to high-p_T production*, the density of partons in a nucleus with mass number A is expected to be simply equivalent to that of a superposition of A independent nucleons: $f_{a/A}(x, Q^2) = A \cdot f_{a/N}(x, Q^2)$. Thus,

$$d\sigma^{\text{hard}}_{AB\to h} \approx A \cdot B \cdot f_{a/p}(x, Q^2) \otimes f_{b/p}(x, Q^2) \otimes d\sigma^{\text{hard}}_{ab\to c} \otimes D_{c\to h}(z, Q^2). \quad (19)$$

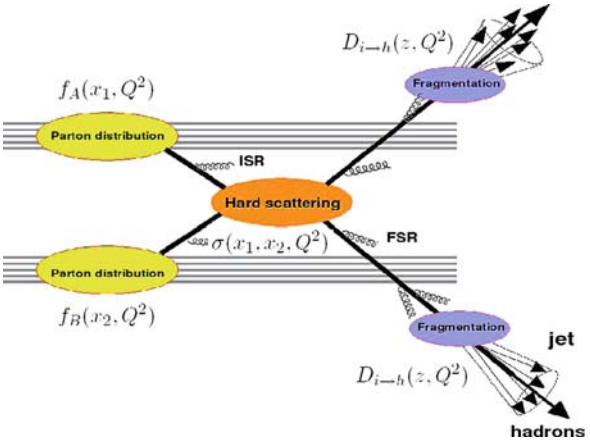

Fig. 6 Sketch of dijet production and pQCD factorisation in hadronic collisions

[13] Processes in which more than one parton from the same hadron/nucleus interact coherently, are called "higher twist" processes.

From (18), it is clear that QCD factorisation implies that total hard inclusive cross sections in a AB reaction scale simply as $A \cdot B$ times the corresponding pp cross sections:

$$d\sigma_{AB}^{\text{hard}} = A \cdot B \cdot d\sigma_{pp}^{\text{hard}}. \tag{20}$$

Since nucleus–nucleus experiments usually measure invariant *yields* for a given centrality bin (or impact parameter b), one writes instead

$$dN_{AB}^{\text{hard}}(b) = \langle T_{AB}(b) \rangle \cdot d\sigma_{pp}^{\text{hard}}, \tag{21}$$

where the nuclear overlap function at b, $T_{AB}(b)$, is determined within a geometric Glauber eikonal model from the measured Woods–Saxon distribution for the interacting nuclei [59]. Intuitively, one can think of the nuclear overlap $T_{AA}(b)$ as a function that characterises the surface profile of two "beams" of nucleons colliding at a distance b. The [area]$^{-1}$ units of T_{AA} indicate that it represents somehow the effective "parton (integrated) luminosity" of the collision. Since the number of inelastic nucleon–nucleon (NN) collisions at b, $N_{\text{coll}}(b)$, is proportional to $T_{AB}(b)$: $N_{\text{coll}}(b) = T_{AB}(b) \cdot \sigma_{NN}^{\text{inel}}$, one also writes often Eq. (21) as

$$dN_{AB}^{\text{hard}}(b) = \langle N_{\text{coll}}(b) \rangle \cdot dN_{pp}^{\text{hard}}. \tag{22}$$

For minimum-bias[14] $A\,B$ collisions, the average nuclear overlap and number of NN collisions take a simple form[15]: $\langle T_{AB} \rangle = A\,B\,/\sigma_{AB}^{\text{geo}}$ and $\langle N_{\text{coll}} \rangle = A\,B \cdot \sigma_{NN}/\sigma_{AB}^{\text{geo}}$. The standard method to quantify the effects of the medium on the yield of a hard probe in a AA reaction is thus given by the *nuclear modification factor*:

$$R_{AA}(p_T, y; b) = \frac{d^2N_{AA}/dydp_T}{\langle T_{AA}(b) \rangle \times d^2\sigma_{pp}/dydp_T}. \tag{23}$$

This factor, which is a quantitative version of the ratio (1), measures the deviation of AA at b from an incoherent superposition of NN collisions ($R_{AA} = 1$). This normalisation is often known as "binary collision scaling".

3.2 Jet Quenching Models

The energy loss formulas presented in Sect. 2.2 refer to an idealistic situation with an infinite-energy parton traversing a *static* and *uniform* QGP with an ideal-gas

[14] *Minimum-bias* collisions are those where there is no specific selection of the final state (e.g. in particular no centrality selection for heavy ions).

[15] For example, for AuAu at $\sqrt{s_{NN}} = 200\,\text{GeV}$ ($\sigma_{NN}^{\text{inel}} = 41\,\text{mb}$, $\sigma_{\text{AuAu}}^{\text{geo}} = 7000\,\text{mb}$): $\langle T_{\text{AuAu}} \rangle = 5.5\ (23.3)\ \text{mb}^{-1}$ and $\langle N_{\text{coll}} \rangle = 230\ (955)$ for minimum-bias (0–10% most central) collisions, respectively.

equation-of-state (EoS). Experimentally, the situation that one encounters with *realistic* plasmas in heavy-ion collisions is more complex:

- first, there is no direct measurement of the traversing parton but (in the best case) only of the final-state *hadrons* issuing from its fragmentation,
- the traversing partons can be produced at any point of the fireball and their energy spectrum is steeply (power law) falling,
- the temperature and density of the plasma, and correspondingly its Debye mass and transport coefficient, are position dependent: $m_D(\mathbf{r})$, $\hat{q}(\mathbf{r})$,
- the produced plasma is expanding with large longitudinal (transversal) velocities, $\beta \approx 1$ (0.7),
- the finite size of the plasma and associated energy loss fluctuations have to be taken into account.

All those effects can result in potentially significant deviations from the analytical formulas of Sect. 2.2 (e.g. in an expanding plasma the dependence of $\Delta E_{\rm rad}$ on the medium thickness L becomes effectively *linear* rather than quadratic). Four major phenomenological approaches have been developed [60] to connect the QCD energy loss calculations with the experimental observables mentioned in Sect. 2.3:

- Path-integral approach to the opacity expansion (BDMPS–LCPI/ASW) [61–67, 32, 68, 69]
- Reaction operator approach to the opacity expansion (DGLV) [70–73, 35]
- Higher twist (HT) [74–79]
- Finite temperature field theory approach (AMY) [80–83]

The models differ in their assumptions about the relationships between the relevant scales (parton energy E and virtuality Q^2, and medium typical momentum $\mu \approx m_D$ and spatial extent L), as well as by how they treat or approximate the structure of the medium. In practical terms, all schemes are based on a pQCD factorised approach, i.e. on Eq. (18), where the *entire* effect of energy loss is concentrated on the calculation of the medium-modified parton fragmentation functions into final hadrons: $D^{\rm vac}_{c\to h}(z) \to D^{\rm med}_{c\to h}(z', \hat{q})$. The final hadronisation of the hard parton is always assumed to occur in the vacuum after the parton, with degraded energy ($z' < z$), has escaped from the medium (Fig. 7).

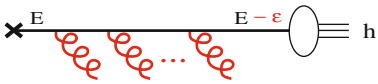

Fig. 7 Schematic representation of parton energy loss implemented via energy rescaling of the fragmentation function [55]

3.2.1 BDMPS–LCPI and ASW

The approaches of Baier, Dokshitzer, Müller, Peigné, and Schiffer (BDMPS) [65, 66, 84, 85] and the light-cone path integral (LCPI) by Zakharov [61] compute

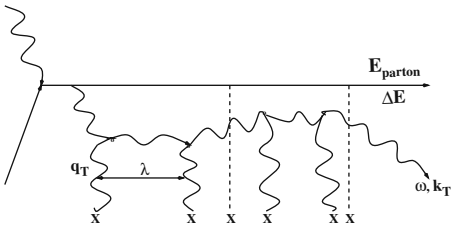

Fig. 8 Typical gluon radiation diagram in the BDMPS approach [66]

energy loss in a coloured medium in a multiple soft-scatterings approximation. A hard parton traversing the medium interacts with various scattering centres and splits into an outgoing parton as well as a radiated gluon (Fig. 8). The propagation of the traversing parton and radiated gluons is expressed using Green's functions which are obtained by a path integral over the fields. The final outcome of the approach is a complex analytical expression for the radiated gluon energy distribution $\omega\, dI/d\omega$ as a function of the transport coefficient $\hat{q}$ defined perturbatively as [86]

$$\hat{q} \equiv \rho \int d^2k_\perp \, k_\perp^2 \, \frac{d\sigma}{d^2k_\perp} \, . \tag{24}$$

Here ρ is the density of scattering centres (mainly gluons) in the medium, $k_\perp$ is the transverse momentum of the radiated gluon, and $d\sigma$ is the differential parton-medium cross section. The medium-modified parton-to-hadron fragmentation functions are modelled as

$$D_{i\to h}^{\text{med}}(z',\, Q^2) = P_E(\varepsilon;\hat{q}) \otimes D_{i\to h}^{\text{vac}}(z,\, Q^2), \tag{25}$$

where the *quenching weights* $P_E(\varepsilon;\hat{q})$ – computed by Armesto, Salgado, and Wiedemann (ASW) [32, 87, 69, 88] – encode the probability (assumed Poissonian) that the propagating parton loses a fraction of energy $\varepsilon = \Delta E/E$ due to gluon emission in N (=opacity) scatterings

$$P_E(\varepsilon;\hat{q}) = \sum_{N=0}^{\infty} \frac{1}{N!} \left[\prod_{i=1}^{N} \int d\omega_i \frac{dI^{\text{med}}(\hat{q})}{d\omega} \right] \delta\left(\varepsilon; -\sum_{i=1}^{N} \frac{\omega_i}{E} \right) \exp\left[-\int d\omega \frac{dI^{\text{med}}}{d\omega} \right]. \tag{26}$$

The quenching weights have been implemented in a Monte Carlo model, the parton quenching model (PQM) [89, 90] accounting for a realistic description of the parton production points in heavy-ion collisions. The transport coefficient $\hat{q}$ is used as the fit parameter for the data. The longitudinal expansion of the plasma is taken into account by rescaling the transport coefficient according to the following law [68]:

$$\langle \hat{q} \rangle = \frac{2}{L^2} \int_{\tau_0}^{\tau_0+L} d\tau \; (\tau - \tau_0) \; \hat{q}(\tau), \tag{27}$$

where $\hat{q}(\tau) = \hat{q}(\tau_0)\,(\tau_0/\tau)^\alpha$ and α characterises the time dependence of the plasma density: $n(\tau) \propto \tau^{-\alpha}$. A purely longitudinal (or Bjorken) expansion corresponds to $\alpha = 1$ and is often assumed in phenomenological applications. When $\tau_0 \ll L$, Eq. (27) reduces to $\langle \hat{q} \rangle \simeq 2\,\hat{q}(\tau_0)\,\tau_0/L$ [86].

3.2.2 GLV

The Gyulassy–Levai–Vitev (GLV) [91, 70, 92, 71, 72] (aka DGLV [73, 35]) approach calculates the parton energy loss in a dense deconfined medium consisting, as in the BDMPS approach, of almost static (i.e. heavy) scattering centres (Fig. 9) producing a screened Yukawa potential. At variance with the BDMPS *multiple-soft* bremsstrahlung, GLV starts from the *single-hard* radiation spectrum which is then expanded to account for gluon emission from multiple scatterings via a recursive diagrammatic procedure [71]. The traversing parton gains a transverse momentum $\mathbf{q}_\perp$ and radiates (before or after the scattering) a gluon with a certain momentum $\mathbf{k} = (xE, \frac{k_\perp^2}{xE}\mathbf{k}_\perp)$. The gluon differential distribution at first order in opacity [70] is

$$x\frac{dI^{(1)}}{dxdk_\perp^2} = x\frac{dI^{(0)}}{dxdk_\perp^2}\frac{L}{\lambda_g}\int_0^{q_{\max}^2} d^2q_\perp \frac{\mu_D^2}{\pi(q_\perp^2+\mu_D^2)^2}\frac{2k_\perp\cdot q_\perp(k-q_1)^2L^2}{16x^2E^2+(k-q)_\perp^2L^2}, \quad (28)$$

where λ_g is the mean free path of the radiated gluon. Applying the aforementioned recursive procedure, one obtains the gluon distribution to finite order ($N \geq 1$) in opacity. Each emission at a given opacity is assumed independent and a probabilistic scheme is set up, wherein, the parton loses an energy fraction ε in N tries with a Poisson distribution [72],

$$P_N(\epsilon, E) = \frac{\mathrm{e}^{-\langle N^g\rangle}}{N!}\Pi_{i=1}^N\left[\int dx_i\frac{dN^g}{dx_i}\right]\delta\left(\varepsilon - \sum_{i=1}^n x_i\right), \quad (29)$$

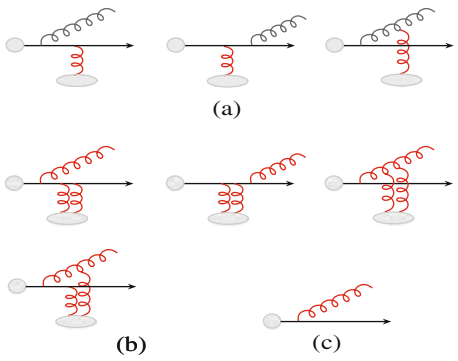

Fig. 9 Diagrams contributing to the lowest order in the opacity energy loss expansion [93]

where $\langle N^g \rangle$ is the mean number of gluons radiated per coherent interaction set. Summing over N gives the probability $P(\varepsilon)$ for an incident parton to lose a momentum fraction ε due to its passage through the medium. This is then used to model a medium-modified FF, by shifting the energy fraction available to produce a hadron in a similar way as Eq. (25). The key medium property to be obtained from the fits to the experimental data is the initial gluon density dN^g/dy, after accounting for longitudinal expansion. Note that the density of colour charges of a cylinder of plasma with "length" τ and surface $A_\perp$ is $\rho \approx dN^g/dy/(\tau A_\perp)$.

3.2.3 Higher Twist (HT)

The higher twist approximation [94–96, 74–76] describes the multiple scattering of a parton as power corrections to the leading-twist cross section (Fig. 10). These corrections are enhanced by the medium length L and suppressed by the power of the hard scale Q^2. Originally, this approach was applied to calculate the medium corrections to the total cross section in nuclear deep-inelastic $e\,A$ scattering.

The scheme allows one to compute multiple Feynman diagrams such as those in Fig. 10 which are then combined coherently to calculate the modification of the fragmentation function directly as a medium-dependent *additive* contribution, $D_{i\to h}^{\text{med}} = D_{i\to h}^{\text{vac}} + \Delta D_{i\to h}^{\text{med}}$,

$$\Delta D_{i\to h}^{\text{med}}(z, Q^2) = \int_0^{Q^2} \frac{dk_\perp^2}{k_\perp^2} \frac{\alpha_s}{2\pi} \left[\int_{z_h}^1 \frac{dx}{x} \sum_{j=q,g} \left\{ \Delta P_{i\to j}^{\text{med}}\, D_{j\to h}\left(\frac{z_h}{x}\right) \right\} \right]. \quad (30)$$

Here, $\Delta P_{i\to j} \propto P_{i\to j}\; C_A \alpha_s T_{qg}^A$ represents the medium-modified splitting function of parton i into j (a momentum fraction x is left in parton j and the radiated gluon or quark carries away a transverse momentum $k_\perp$). The entire medium effects are incorporated in the nuclear quark–gluon correlation T_{qg}^A term. The normalisation C of this correlator is set by fitting to one data point from which one can directly calculate the medium-modified FFs and then the final hadron spectrum. The parameter C can also be used to calculate the average energy loss suffered by the parton.

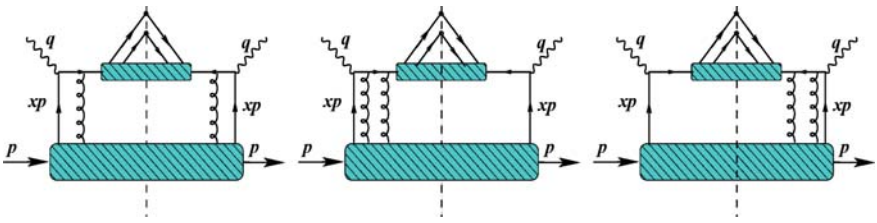

Fig. 10 Leading and next-to-leading order twist contribution to quark scattering in a medium (hatched area) [97]

3.2.4 AMY

The Arnold–Moore–Yaffe (AMY) [80, 98, 99, 82, 83] approach describes parton energy loss in a hot equilibrated QGP, where the hierarchy $T \gg gT \gg g^2T$ can be introduced. The hard parton scatters off other partons in the medium, leading to momentum transfers of $\mathcal{O}(gT)$ and inducing collinear radiation. Multiple scatterings of the incoming (outgoing) parton and the radiated gluon are combined to get the leading-order gluon radiation rate. One essentially calculates the imaginary parts of ladder diagrams such as those shown in Fig. 11 by means of integral equations which yield the $1 \to 2$ transition rates Γ^a_{bg} of a hard parton (a) into a radiated gluon g and another parton (b). These rates, with T-dependent Bose (for gluons) and Fermi (for quarks) exponential factors for the medium partons, are then used to evolve the original distributions over the medium length by means of a Fokker–Planck-like equation [82]:

$$\frac{dP_a(p)}{dt} = \int dk \sum_{b,c} \left[P_b(p+k) \frac{d\Gamma^b_{ac}(p+k,\, p)}{dk dt} - P_a(p) \frac{d\Gamma^a_{bc}(p,k)}{dk dt} \right]. \quad (31)$$

The medium-modified FF is obtained from the convolution of the vacuum FF with the hard parton distributions when exiting the plasma [83]:

$$D^{\text{med}}_{a\to h}(z) = \int dp_f \frac{z'}{z} \sum_a P_a(p_f; p_i) D^{\text{vac}}_{a\to h}(z')\,, \quad (32)$$

where $z = p_h/p_i$ and $z' = p_h/p_f$, with p_i and p_f the momenta of the hard partons immediately after the hard scattering and prior to exit from the medium. The model of the medium is essentially contained in the space–time profile chosen for the initial temperature appearing in the transition rates.

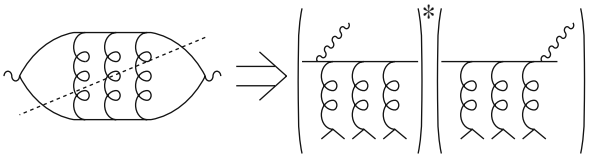

Fig. 11 A typical ladder diagram in the AMY formalism [99]

3.2.5 Models Comparison

The four energy loss formalisms discussed above can be roughly divided into two groups: those calculating the radiated gluon spectrum, i.e. the energy lost by the initial parton (GLV and BDMPS/ASW) and those determining directly the change in the final distribution of the traversing partons (higher twist and AMY). Each approach has its advantages and disadvantages:

- *ASW*: It is applicable to both thin and thick media, but so far lacks an implementation of elastic energy loss.
- *GLV*: It can be applied in confined and deconfined media, but it does not account for the energy flow *into* the medium.
- *Higher twist*: It can directly compute the medium-modified fragmentation functions and allows the study of multi-hadron correlations, but the formalism is more appropriate for thin than thick media.
- *AMY*: It is the only framework that accounts for processes where a thermal gluon or quark can be absorbed by a hard parton, elastic energy loss can be included in a straightforward way, but its application to non-thermalised media is questionable.

All four schemes have independently made successful comparisons to the available data (see Fig. 12 and forthcoming sections). The outcome of the models is one parameter tuned to ideally fit all experimental observables: $\hat{q}$ in the BDMPS/ASW scheme, the initial dN^g/dy density in GLV, the energy loss ε_0 in HT, and the temperature T in AMY. All jet quenching observables in AuAu collisions at 200 GeV can only be reproduced with medium parameters consistent with a QGP at temperatures above the QCD phase transition. The analytical results of the different schemes under "controlled" situations are in principle equivalent, see, e.g., [14]. Yet the detailed comparison of the models is not always straightforward as they

- use different approximations in their calculations,
- do not always include the same list of physics processes (e.g. $\Delta E_{\rm coll}$ is neglected in some cases),
- choose a different fitting parameter to characterise the medium, and
- the space–time profile of the quenching medium is not always equivalent.

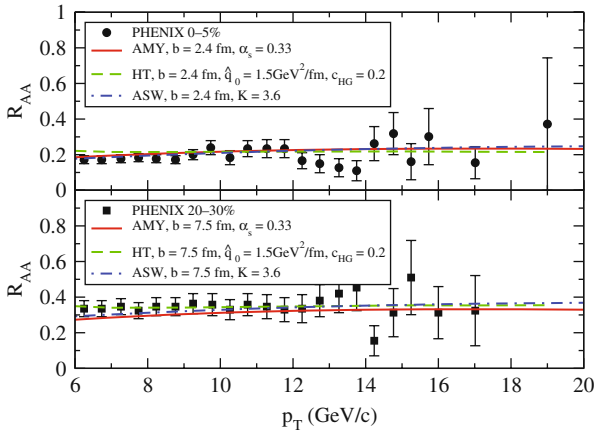

Fig. 12 Suppression factor for high-p_T pions in central (*top*) and semicentral (*bottom*) AuAu collisions at RHIC [100] compared to AMY, HT, and ASW energy loss calculations [101]

The quantitative consistency of the different schemes has been investigated within a 3-dimensional hydrodynamics approach (Fig. 12) [101] linking the various medium properties via thermodynamical relations and using the same space–time evolution. Yet the extracted $\hat{q}$ values still differ by factors of 2–3 (see Sect. 4.2). At least part of the uncertainty is due to the relative insensitivity of the $\hat{q}$ parameter to the irreducible presence of (unquenched) partons emitted from the surface of the plasma [102]. Additional constraints on $\hat{q}$ can be placed by requiring also the reproduction of the suppressed *di-hadron* azimuthal correlations (see Sect. 5.1).

3.3 Jet Quenching Monte Carlos

Ultimately, the discussed energy loss schemes are all based on a final energy rescaling of the vacuum parton-to-hadron fragmentation functions (Fig. 7). Recently, attempts to reformulate parton energy loss as a medium modification of the perturbative *evolution* of the fragmentation functions have been implemented in Monte Carlo (MC) models [56, 103–105]. Such MC approaches allow one to address more detailed experimental observables such as the particle and energy flows within a jet. The DGLAP scale-dependence (Q^2-evolution) equation of the FFs reads

$$\frac{\partial D_{i\to h}(x,\, Q^2)}{\partial \log Q^2} = \sum_j \int_x^1 \frac{dz}{z} \frac{\alpha_s}{2\pi} \;\; P_{i\to j}(z)\; D_{j\to h}(x/z,\, Q^2)\;, \tag{33}$$

with splitting functions $P_{i\to j}(z)$. The probabilistic nature of parton showering – the "Sudakov factor" $\exp[-\int dQ/Q^2 \;\; \int dz\, \alpha_s/2\pi \;\; P_{i\to j}(z,\, Q^2)]$ gives the probability that a parton evolves from times t_1 to t_2 without branching – can be easily implemented in MC codes by calculating the virtuality and energy fraction of a parton at each branching point with proper energy-momentum conservation. Parton showers are a basic ingredient of event generators such as PYTHIA [106] or HERWIG [107] which are often used to compare the experimental jet data to the details of the underlying QCD radiation pattern. Medium effects can be easily included by, e.g. modifying the splitting functions in Eq. (33). HYDJET [108, 109] was the first MC code which incorporated medium effects via a PYQUEN routine which modifies the standard PYTHIA branching algorithm to include radiative and elastic energy losses. More recent developments like Q-PYTHIA and Q-HERWIG [40] modify the DGLAP evolution of these two parton-shower MCs. The JEWEL MC [103] implements elastic scattering in DGLAP evolution plus radiative energy loss through a multiplicative constant in the collinear part of the splitting functions [39].

3.4 Parton Energy Loss in AdS/CFT

So far, we have discussed perturbative calculations of parton energy loss in an ideal QGP. Yet the medium produced at RHIC has temperatures $\mathcal{O}(2\,T_{crit})$ in a domain

where lattice QCD [2] still predicts large deviations with respect to the asymptotic ideal-gas behaviour. Many experimental signals at RHIC are consistent with the formation of a *strongly coupled* plasma (sQGP) [110–112]. Such a regime is theoretically treatable via the anti-de-Sitter/conformal-field-theory (AdS/CFT) correspondence between weakly coupled gravity and strongly coupled gauge theories [113–115].

The AdS/CFT correspondence conjectures that string theories described in an anti-de-Sitter space[16] times a 5-dimensional sphere ($AdS_5 \times S_5$) are equivalent to a conformal field theory (CFT), defined on the 4-dimensional boundary of this space. A particularly useful case is $\mathcal{N} = 4$ supersymmetric Yang-Mills (SYM)[17] at strong coupling g_{YM} and large number of colours N_c (i.e. at large 't Hooft coupling $\lambda = g^2_{\rm YM} N_c \gg 1$) which is dual to supergravity in a curved space–time. The string coupling g_s, the curvature radius R of the AdS metric, and the tension $(2\pi\alpha')^{-1}$ of the string are related to the SYM quantities via $R^2/\alpha' = \sqrt{\lambda}$ and $4\pi\, g_s = g^2_{YM} = \lambda/N_c$. Essentially, taking the large N_c limit at fixed λ (i.e. weakly coupled gravity: $g_s \to 0$) and the large λ limit (i.e. weakly curved space and large string tension), the SYM theory can be described by classical gravity in a 5-dimensional space. By virtue of such a duality, one can carry out analytical calculations of gravity, which can then be mapped out "holographically" to the *non-perturbative* dynamics of the gauge sector.

One can further exploit the AdS/CFT correspondence for theories at *finite temperature*, by replacing the AdS_5 space by an AdS Schwarzschild black hole. The temperature of the gauge theory is then equal to the black hole Hawking temperature, $T = r_0/(\pi\, R^2)$, where r_0 is the coordinate of the black hole horizon. Recent applications of this formalism in the context of heavy-ion physics have led to the determination of transport properties of strongly coupled (SYM) plasmas – such as its viscosity [117], the $\hat{q}$ parameter [118], and the heavy-quark diffusion coefficients [119–122] – from simpler black hole thermodynamics calculations.

In the case of jet quenching calculations [123, 124], one expresses the propagation of a parton through a medium in terms of Wilson lines. The $\hat{q}$ parameter can be identified with the coefficient in the exponential of an adjoint Wilson loop averaged over the medium length: $\left\langle W^A(C)\right\rangle \equiv \exp\left[(-1/4\sqrt{2})\hat{q}\, L^- L^2\right]$ [118]. One then evaluates the gravity dual of this Wilson loop given by the classical action of a string stretching in an $AdS_5 \times S_5$ space with a Schwarzschild black hole background. After solving the equations of motion of the string, the transport coefficient $\hat{q}$ is determined to be

$$\hat{q}_{\rm sym} = \frac{\pi^{3/2}\Gamma(\frac{3}{4})}{\Gamma(\frac{5}{4})}\,\sqrt{g^2 N_c}\, T^3. \tag{34}$$

---

[16] AdS_5 is a 5-dimensional space with constant and negative curvature.

[17] SYM is a quantum-field $SU(N_c)$ theory like QCD ($\mathcal{N} = 4$ indicates four additional supercharges) but dissimilar from QCD in many aspects: extra SUSY degrees of freedom, no running coupling, no confinement, etc. Yet such differences "wash out" at finite T [116].

Though this result is computed in the infinite coupling and number of colours limits, typical values of $\alpha_s = 0.5$ and $N_c = 3$ lead to $\hat{q} = 4.5 - 20.7$ GeV^2/fm for $T = 300$–500 MeV [124], consistent with phenomenological fits of the RHIC data [102].

There have also been AdS/CFT-based calculations [119–122] of the diffusion properties of heavy quarks, described by a semiclassical string in the gravity theory, such as the diffusion constant in a $\mathcal{N} = 4$ SYM plasma [120]

$$D \approx \frac{0.9}{2\pi T}\left(\frac{1.5}{\alpha_s N_c}\right)^{1/2}, \tag{35}$$

which agrees with the drag coefficient, see Eq. (3), computed independently.

4 High-p_T Leading Hadron Suppression: Data vs. Theory

The most simple empirically testable (and theoretically computable) consequence of jet quenching is the suppression of the single inclusive high-p_T hadron spectrum relative to that in proton–proton collisions. Since most of the energy of the fragmenting parton goes into a single *leading* hadron, QCD energy loss was predicted to result in a significantly suppressed production of high-p_T hadrons ($R_{AA} \ll 1$) [26, 27]. We compare in this section the existing measurements of large-p_T hadroproduction in pp and AA collisions and discuss their agreement with jet quenching models.

4.1 High-p_T Hadron Spectra in Proton–Proton and Proton–Nucleus Collisions

Figure 13 collects several p_T-differential inclusive cross sections measured at RHIC in pp collisions at $\sqrt{s}$ = 200 GeV: jets [125], charged hadrons [126], neutral pions [127], direct photons [128], and D, B mesons (indirectly measured via inclusive $e^{\pm}$ from their semileptonic decays) [129] at central rapidities ($y = 0$) and negative hadrons at forward pseudorapidities (η = 3.2) [130]. The existing measurements cover nine orders of magnitude in cross section (from 10 mb down to 1 pb) and broad ranges in transverse momentum (from zero for D, B mesons up to 45 GeV/c, a half of the kinematical limit, for jets) and rapidity (η = 0–3.2).

Standard next-to-leading-order (NLO) [131–138] or resummed next-to-leading log (NLL) [139] pQCD calculations (yellow bands in Fig. 13) with recent proton PDFs [140], fragmentation functions [141, 142], and with varying factorisation-renormalisation scales ($\mu = p_T/2 - 2p_T$) reproduce well the pp data. This is true even in the semi-hard range $p_T \approx 1 - 4$ GeV/c, where a perturbative description would be expected to give a poorer description of the spectra. These results indicate that the hard QCD cross sections at RHIC energies are well under control both experimentally and theoretically in their full kinematic domain.

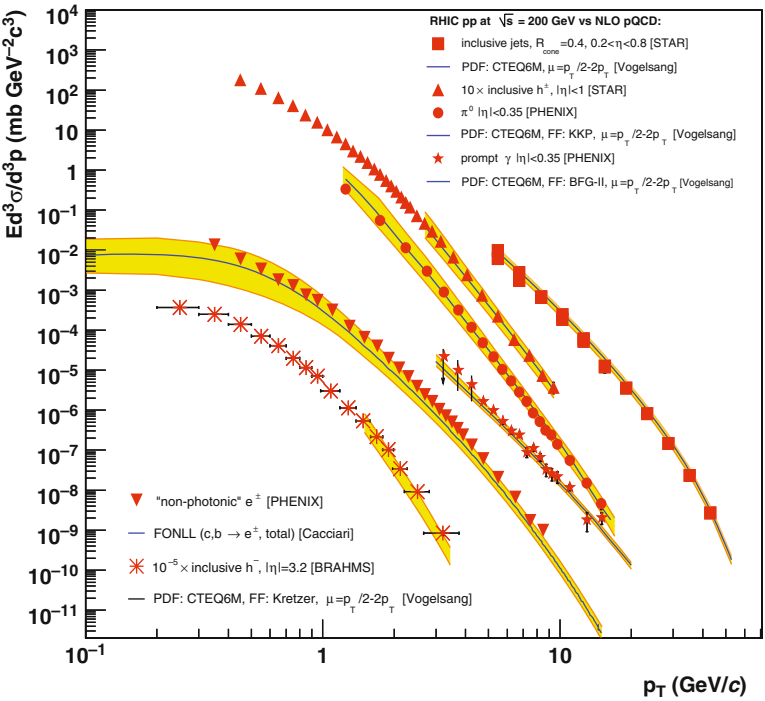

Fig. 13 Compilation of hard cross sections in pp at $\sqrt{s}$ = 200 GeV measured by STAR [125, 126], PHENIX [127–129], and BRAHMS [130] (10–30% syst. uncertainties not shown for clarity) compared to NLO [131–138] and NLL [139] pQCD predictions (*yellow bands*)

Not only the proton–proton hard cross sections are well under theoretical control at RHIC but the hard yields measured in deuteron–gold collisions do not show any significant deviation from the perturbative expectations. Figure 14 shows the nuclear modification factors measured in dAu collisions at $\sqrt{s_{NN}}$ = 200 GeV for high-p_T π^0 at $y = 0$ [143, 144]. The maximum deviation from the $R_{d\mathrm{Au}} = 1$ expectation is of the order of ∼10%, well accounted for by standard pQCD calculations [145, 146] that include DGLAP-based parametrisations of nuclear shadowing [147] and/or a mild amount of initial-state p_T broadening [148] to account for a modest "Cronin enhancement" [149, 150]. [The only exception to this is baryon (in particular, proton) production which shows a large Cronin enhancement: $R_{d\mathrm{Au}}$ = 1.5–2.0 [151].] These data clearly confirm that at RHIC *midrapidities*, the parton flux of the incident gold nucleus can be basically obtained by geometric superposition of the nucleon PDFs and that the nuclear (x, Q^2) modifications of the PDFs are very modest. Since no dense and hot system is expected to be produced in dAu collisions, such results indicate that any deviations from R_{AA} = 1 larger than $1 - R^2_{d\mathrm{Au}}$ ∼20% potentially observed for hard probes in AuAu collisions (at central rapidities) can only be due to *final-state* effects in the medium produced in the latter reactions.

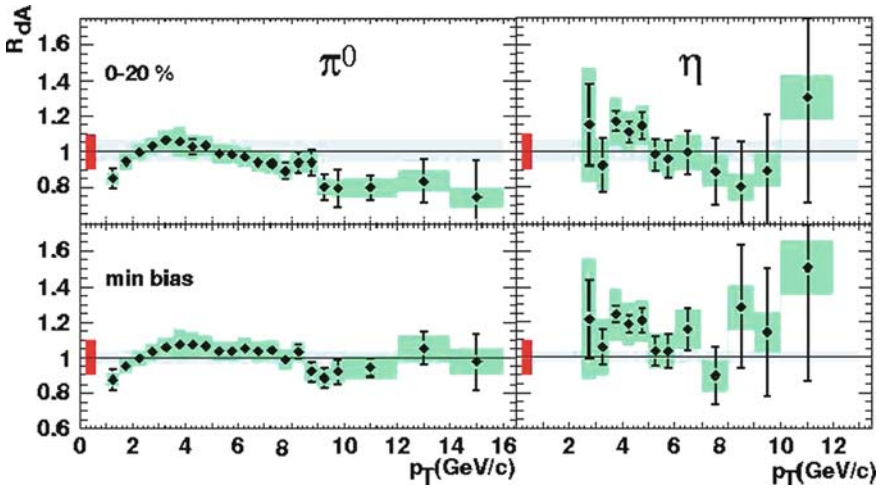

Fig. 14 Nuclear modification factors for high-p_T π^0 (*left*) and η (*right*) mesons at midrapidity in dAu collisions at $\sqrt{s_{NN}}$ = 200 GeV [143, 144] compared to pQCD calculations [145, 146] with EKS98 [147] nuclear PDFs

4.2 High-p_T Hadron Spectra in Nucleus–Nucleus Collisions

Among the most exciting results from RHIC is the large high-p_T hadron suppression ($R_{AA} \ll 1$) observed in central AuAu compared to pp or dAu reactions. We discuss here the properties of the measured suppression factor and compare it to detailed predictions of parton energy loss models.

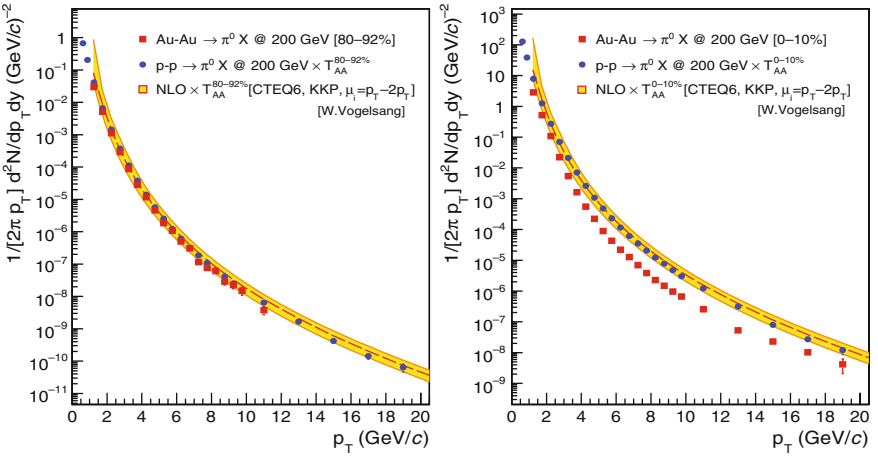

Fig. 15 Invariant π^0 yields measured by PHENIX in peripheral (*left*) and central (*right*) AuAu collisions (*squares*) [100] compared to the (T_{AA}-scaled) pp π^0 cross section (*circles*) [152] and to a NLO pQCD calculation (*curves* and *yellow band*) [131–133]

(a) Magnitude of the suppression: medium properties

Figure 15 shows the π^0 spectrum measured in pp collisions [152] compared to peripheral (*left*) and central (*right*) AuAu spectra [100] at 200 GeV, as well as to NLO pQCD calculations [131–133]. Whereas the peripheral AuAu spectrum is consistent with a simple superposition of individual NN collisions, the data in central AuAu show a suppression factor of 4–5 with respect to this expectation.

The amount of suppression is better quantified taking the ratio of both spectra in the nuclear modification factor, Eq. (23). Figure 16 compiles the measured $R_{AA}(p_T)$ for various hadron species and for direct γ in central AuAu collisions at $\sqrt{s_{NN}}$ = 200 GeV. Above $p_T \approx 5$ GeV/c, π^0 [153], η [154], and charged hadrons [126, 155] (dominated by $\pi^{\pm}$ [155]) all show a common factor of ∼5 suppression relative to the $R_{AA} = 1$ expectation that holds for hard probes, such as direct photons, which do not interact with the medium [156]. The fact that $R_{AA} \approx 0.2$ irrespective of the nature of the finally produced hadron is consistent with a scenario where final-state energy loss of the *parent* parton takes place *prior* to its fragmentation into hadrons in the vacuum according to *universal* (but energy-rescaled) FFs. The suppression factor at top RHIC energies is very close to the "participant scaling", $(N_{\rm part}/2)/N_{\rm coll} \approx 0.17$, expected in the strong quenching limit where only hadrons produced at the *surface* of the medium reach the detector without modifications [157]. From the R_{AA} one can approximately obtain the fraction of energy lost, $\varepsilon_{\rm loss} = \Delta p_T/p_T$, via

$$\varepsilon_{\rm loss} \approx 1 - R_{AA}^{1/(n-2)} \,, \tag{36}$$

when both the AuAu and *pp-invariant* spectra are power laws with exponent n, i.e. $1/p_T\, dN/dp_T \propto p_T^{-n}$ [158].

The high-p_T AuAu suppression can be well reproduced by parton energy loss models that assume the formation of a very dense system with initial gluon rapidity densities $dN^g/dy \approx 1400$ (yellow line in Fig. 16) [160, 161], transport coefficients $\langle\hat{q}\rangle \approx 13$ GeV^2/fm (red line in Fig. 17, left) [89], or plasma temperatures $T \approx 400$ MeV [83]. The quality of agreement between the theory and data has been studied in detail in [162, 100] taking into account the experimental (though not theoretical) uncertainties. The PHENIX π^0 suppression constrains the PQM model [89] transport coefficient $\langle\hat{q}\rangle$ as $13.2\ ^{+2.1}_{-3.2}$ and $^{+6.3}_{-5.2}$ GeV^2/fm at the one and two standard deviation levels (Fig. 17).

The consistency between the extracted $\hat{q}$, dN^g/dy, and T values in the various models can be cross-checked considering the simple case of a gluon traversing a thermalised gluon plasma. The transport coefficient, Eq. (2), is the product of the particle density, the medium Debye mass, and the parton-medium cross section. Taking $\sigma_{gg} = 9\pi\alpha_s^2/(2\,m_D^2)$ with $\alpha_s = 0.5$ for the latter, one has a simple relation[18] between $\hat{q}$ and ρ:

[18] Conversion between units is done multiplying by suitable powers of $\hbar c = 0.197$ GeV fm.

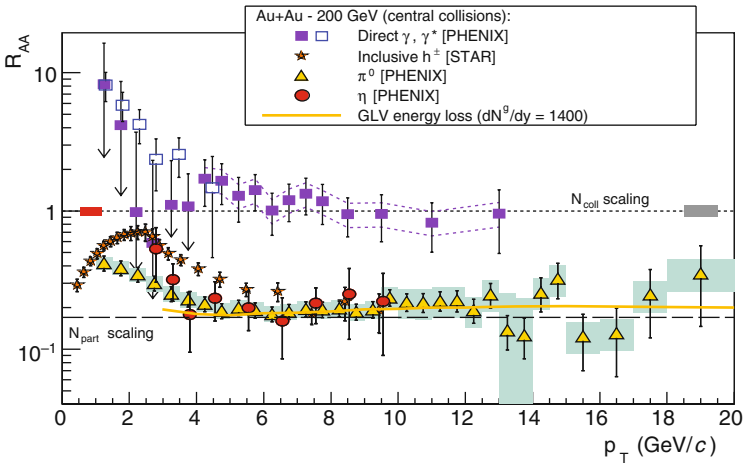

Fig. 16 $R_{AA}(p_T)$ measured in central AuAu at 200 GeV for π^0 [100] and η [154] mesons, charged hadrons [126], and direct photons [156, 159] compared to theoretical predictions for parton energy loss in a dense medium with $dN^g/dy = 1400$ (*yellow curve*) [160, 161]

$$\hat{q}[\mathrm{GeV}^2/\mathrm{fm}] = m_D^2 \times \sigma \times \rho = m_D^2 \times 9\pi\alpha_s^2/(2\,m_D^2) \times \rho \approx 0.14\,K\ \rho[\mathrm{fm}^{-3}], \quad (37)$$

where we introduce the K factor to account for possible higher order scatterings not included in the LO perturbative cross section. For an ideal ultrarelativistic gas, the particle density scales with the cube of the temperature as $\rho \approx \mathrm{ndf}/9 \cdot T^3$. For a pure gluon plasma, with ndf = 16, $\rho[\mathrm{fm}^{-3}] \approx 260 \cdot (T[\mathrm{GeV}])^3$, and one can write Eq. (37) as

$$\hat{q}[\mathrm{GeV}^2/\mathrm{fm}] \approx 36\,K \cdot (T[\mathrm{GeV}])^3. \quad (38)$$

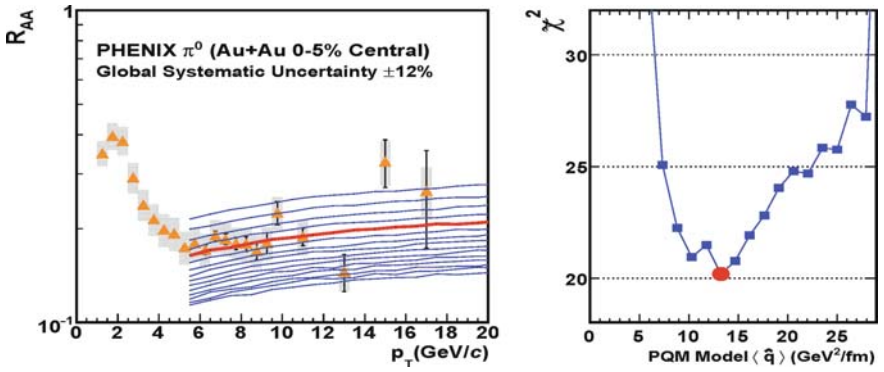

Fig. 17 *Left*: $R_{AA}(p_T)$ for neutral pions in central AuAu collisions [100] compared to PQM model calculations [89] for varying values of the $\hat{q}$ coefficient (*red curve*, best fit). *Right*: Corresponding (data vs. theory) χ^2 values for the fitted PQM $\hat{q}$ parameter [162]

In addition, as particle and energy densities are related by $\rho[\mathrm{fm}^{-3}] \approx 1.9 \cdot (\varepsilon[\mathrm{GeV/fm}^3])^{3/4}$, one can express Eq. (37) also as $\hat{q}[\mathrm{GeV}^2/\mathrm{fm}] \approx 0.27\, K \cdot (\varepsilon[\mathrm{GeV/fm}^3])^{3/4}$. In an expanding plasma, the density follows a power law evolution as a function of time, $\rho = \rho_0\,(\tau_0/\tau)^\alpha$, and thus so does the transport coefficient (37):

$$\hat{q}(\tau)[\mathrm{GeV}^2/\mathrm{fm}] \approx 0.14\, K \cdot \rho_0 \left(\frac{\tau_0}{\tau}\right)^\alpha = 0.14\, K \cdot \frac{dN^g}{dV}\left(\frac{\tau_0}{\tau}\right) \approx 0.14\, K \cdot \frac{1}{A_T}\,\frac{dN^g}{dy}\,\frac{1}{\tau}\,, \tag{39}$$

where for the two last equalities we have assumed a 1-dimensional (aka Bjorken) longitudinal expansion, i.e. $\alpha = 1$ and $dV = A_T\,\tau_0\,dy$, where $A_T[\mathrm{fm}^2]$ is the transverse area of the system. Combining Eq. (39) with Eq. (27) that relates the *time-averaged* $\hat{q}(\tau)$ to that of a static medium with effective length L_{eff}, we finally get

$$\langle\hat{q}\rangle\,[\mathrm{GeV}^2/\mathrm{fm}] \approx 0.14\, K \cdot \frac{2}{L_{\mathrm{eff}}[\mathrm{fm}]\,A_T[\mathrm{fm}^2]}\,\frac{dN^g}{dy} \approx 1.4\,10^{-3} \cdot K \cdot \frac{dN^g}{dy}\,, \tag{40}$$

where, for the last equality, we use $L_{\mathrm{eff}} \approx 2$ fm and $\langle A_T\rangle \approx 100\ \mathrm{fm}^2$ for the overlap area in 0–10% most central AuAu. This approximate relation between the average transport coefficient and the original gluon density is only well fulfilled by the data (see Table 2 below) for a very large $K \approx 7$ factor. The fact that the jet quenching data favour an effective elastic parton-medium cross section much larger than the LO perturbative estimate ($\sigma_{gg} \approx 1.5$ mb) has been discussed many times in the literature – e.g. in the context of the strong partonic elliptic flow seen in the data [163, 164] – and supports the strongly coupled nature of the QGP produced at RHIC.

A more detailed comparison of different energy loss schemes within a realistic 3-dimensional hydrodynamics evolution has been carried out in [165]. The extraction of a common $\hat{q}$ parameter from the different model predictions relies on additional assumptions about the (thermo)dynamical state of the produced matter. The results for ASW, AMY, and HT are shown in Table 1 (last two rows). The ASW calculations consistently predict a higher $\hat{q}_0$ than AMY or HT. These differences can be traced to uncertainties of the thermodynamical scaling choice ($\hat{q} \propto T^3$ or $\varepsilon^{3/4}$) and to the initial time where the medium is supposed to start to quench (hydro

Table 1 Medium parameters derived in various parton energy loss schemes that reproduce the high-p_T π^0 suppression in central AuAu [100]. The last two rows are from a 3-dimensional hydro simulation with two choices of $\hat{q}(\mathbf{r}, \tau)$ scaling with the local thermal properties of the plasma (T_0, ε_0) [165]

Medium parameter	ASW	HT	AMY
$\langle\hat{q}\rangle$	13 GeV^2/fm (PQM)	–	–
T_0	–	–	0.4 GeV
$\hat{q}_0 \propto \varepsilon_0^{3/4}(\mathbf{r}, \tau)$	18.5 GeV^2/fm	4.5 GeV^2/fm	–
$\hat{q}_0 \propto T_0^3(\mathbf{r}, \tau)$	10 GeV^2/fm	2.3 GeV^2/fm	4.1 GeV^2/fm

calculations at RHIC often start at $\tau_0 = 0.6\,\mathrm{fm}/c$). In addition, AMY accounts for collisional loses which are neglected in the purely radiative ASW approach.

(b) Centre-of-mass energy dependence

As one increases the centre-of-mass energy in nucleus–nucleus collisions, the produced plasma reaches higher energy and particle densities and the system stays longer in the QGP phase. Since $\Delta E_{\mathrm{loss}} \propto dN^g/dy \propto dN_{ch}/d\eta$, and since the charged particle multiplicity in AA at midrapidity increases with collision energy as [166, 167]

$$dN_{ch}/d\eta \approx 0.75 \cdot (N_{part}/2) \cdot \ln(\sqrt{s_{NN}}\,[\mathrm{GeV}]/1.5), \tag{41}$$

one naturally expects the hadron quenching to increase accordingly with $\sqrt{s_{NN}}$. The actual "excitation function" of the suppression factor is only approximately given by Eq. (41) because for increasing energies other factors play competing roles: (i) the lifetime of the quenching medium becomes longer, (ii) the parton spectrum becomes flatter leading to a comparatively smaller suppression for the same value of ΔE_{loss} (see next), and (iii) the fraction of quarks and gluons produced at a fixed p_T changes (see Fig. 22 below and the associated colour factor discussion).

Figure 18 compiles the measured $R_{AA}(p_T)$ for high-p_T π^0 in central AA collisions in the range $\sqrt{s_{NN}} \approx 20$ – $200\,\mathrm{GeV}$ compared to parton energy loss calculations that assume the formation of systems with initial gluon densities per unit rapidity in the range $dN^g/dy \approx 400$ – 1400 [160, 161, 171] or, equivalently, averaged transport coefficients $\langle\hat{q}\rangle \approx 3.5$ – $13\ \mathrm{GeV}^2/\mathrm{fm}$ [74] (Table 2). As can be seen from Eq. (36), R_{AA} depends not only on ΔE_{loss} but also on the steepness (power law exponent n) of the parton p_T spectrum. With decreasing $\sqrt{s_{NN}}$, the p_T spectra become steeper effectively leading to a larger suppression (i.e. smaller R_{AA}) for the

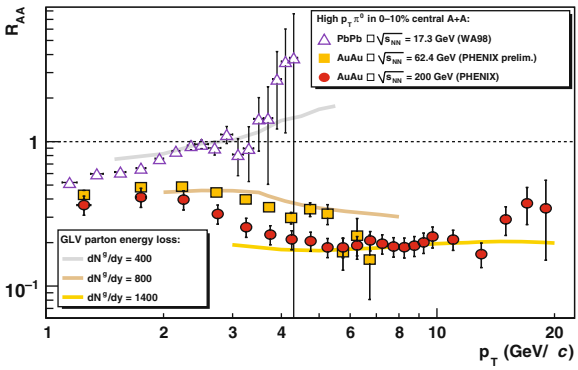

Fig. 18 Nuclear modification factor, $R_{AA}(p_T)$, for neutral pions in central PbPb at $\sqrt{s_{NN}} = 17.3$ GeV [168, 169] and AuAu at $\sqrt{s_{NN}} = 62.4$ GeV [170], 200 GeV [153]; compared to GLV energy loss calculations for initial gluon densities: $dN^g/dy = 400$, 800, 1400 [160, 161, 171], respectively. Experimental normalisation errors, $\mathcal{O}(10$–$25\%)$, not shown

same $\Delta E_{\rm loss}$. The SPS data show an R_{AA} for central PbPb which, though consistent with unity [169], is significantly suppressed compared to the "Cronin enhancement" observed for peripheral PbPb and for pPb collisions [172].

For each collision energy, the derived values for dN^g/dy are consistent with the final charged hadron density $dN_{\rm ch}/d\eta$ measured in the reactions. Indeed, assuming an isentropic[19] expansion process, all the hadrons produced at midrapidity in a AA collision come directly from the original gluons released[20]:

$$\frac{dN^g}{dy} \approx \frac{N_{\rm tot}}{N_{\rm ch}} \left|\frac{d\eta}{dy}\right| \frac{dN_{\rm ch}}{d\eta} \approx 1.8 \cdot \frac{dN_{\rm ch}}{d\eta}. \tag{42}$$

This relation is relatively well fulfilled by the data as can be seen by comparing the fourth and fifth columns of Table 2.

Table 2 Initial gluon densities dN^g/dy [160, 161, 171], and transport coefficients $\langle\hat{q}\rangle$ [89] for the dense media produced in central AA collisions at SPS and RHIC energies obtained from parton energy loss calculations reproducing the observed high-p_T π^0 suppression at each $\sqrt{s_{NN}}$. The measured charged particle densities at midrapidity, $dN_{\rm ch}^{\rm exp}/d\eta$ [166, 167], are also quoted

	$\sqrt{s_{NN}}$ (GeV)	$\langle\hat{q}\rangle$ (GeV^2/fm)	dN^g/dy	$dN_{\rm ch}^{\rm exp}/d\eta$
SPS	17.3	3.5	400	312 ± 21
RHIC	62.4	7.	800	475 ± 33
RHIC	130.	$\sim$11	$\sim$1000	602 ± 28
RHIC	200.	13	1400	687 ± 37

(c) p_T-dependence of the suppression

At RHIC top energies, the quenching factor remains constant from 5 GeV/c up to the highest transverse momenta measured so far, $p_T \approx 20$ GeV/c (Fig. 16). The flatness of $R_{AA}(p_T)$ was not expected since many original analytical calculations based on the LPM effect (see, e.g., [173]) predicted an R_{AA} slowly (logarithmically) increasing with p_T. However, the combined effect of (i) kinematics constraints (which modify the asymptotic $\Delta E_{\rm loss}$ formulas), (ii) the steeply falling p_T spectrum of the scattered partons, and (iii) $\mathcal{O}(20\%)$ p_T-dependent (anti)shadowing differences between the proton and nuclear PDFs included in the various models [160, 161, 171, 82, 102] results in an effectively flat $R_{AA}(p_T)$ as found in the data.

The much larger kinematical range opened at LHC energies will allow to test the p_T-dependence of parton energy loss over a much wider domain than at RHIC. The GLV and PQM predictions for the charged hadron suppression in PbPb at 5.5 TeV are shown in Fig. 19. Apart from differences in the absolute quenching factor, PQM

[19] Namely, expanding at constant entropy, i.e. without extra particle production.

[20] We use $N_{\rm tot}/N_{\rm ch}$ = 3/2 and the Jacobian $|d\eta/dy| = E/m_T \approx 1.2$ for a mostly pionic system.

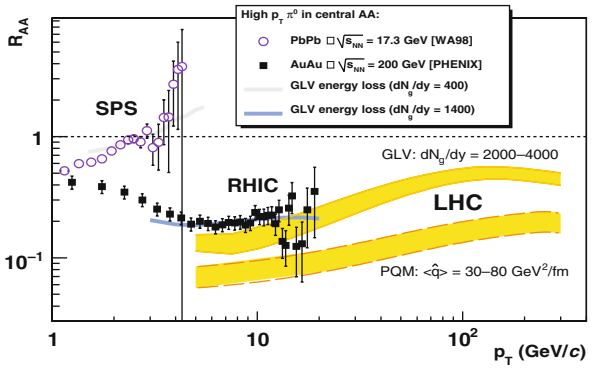

Fig. 19 $R_{AA}(p_T)$ for neutral pions at SPS [168, 169] and RHIC [100] compared to the expected suppression of charged hadrons in central PbPb at the LHC ($\sqrt{s_{NN}}$ = 5.5 TeV) by the GLV ($dN^g/dy = 2000$–4000) [160, 161] and PQM ($\langle\hat{q}\rangle \approx 30$–$80\,\mathrm{GeV}^2/\mathrm{fm}$) [89, 90] models

seemingly predicts a slower rise of $R_{AA}(p_T)$ than GLV. The large p_T reaches of the ALICE [174], ATLAS [175], and CMS [176] experiments (up to 300 GeV/c for the nominal luminosities) will allow them to test such level of model details.

(d) Centrality (system-size) dependence

The volume of the overlap zone in a heavy-ion collision can be "dialed" either by selecting a given impact parameter b – i.e. by choosing more central or peripheral reactions – or by colliding larger or smaller nuclei. From Eq. (14), the relative amount of suppression depends[21] on the effective mass number A_{eff} or, equivalently, on the number of participant nucleons N_{part} as $\varepsilon = \Delta E/E \propto A_{\mathrm{eff}}^{2/3} \propto N_{\mathrm{part}}^{2/3}$. Combining this expression with Eq. (36) yields [177]

$$R_{AA} = \left(1 - \kappa\, N_{\mathrm{part}}^{\alpha}\right)^{n-2}, \quad \text{with } \alpha \approx 2/3 \text{ and } \kappa \text{ an arbitrary constant.} \tag{43}$$

Figure 20 (*left*) compares the measured high-p_T pion suppression in CuCu and AuAu at $\sqrt{s_{NN}}$ = 200 GeV [178, 179]. Because of the large difference in the Cu (A = 63) and Au (A = 197) atomic masses, the same N_{part} value (same overlap volume) implies very different collision geometries: a thin, elongated collision zone in AuAu and a thicker, more spherical one in the CuCu case. Yet interestingly the average suppression in the two systems depends only on N_{part}. Fitting this dependence with expression (43) yields $\alpha = 0.56 \pm 0.10$, consistent with $\alpha \approx 0.6$ expected in parton energy loss scenarios [100, 177].

[21] Since $dN^g/dy \propto dN_{\mathrm{ch}}/dy \propto A_{\mathrm{eff}} \propto N_{\mathrm{part}}$, $L \propto A_{\mathrm{eff}}^{1/3} \propto N_{\mathrm{part}}^{1/3}$, and $A_{\perp} \propto A_{\mathrm{eff}}^{2/3} \propto N_{\mathrm{part}}^{2/3}$.

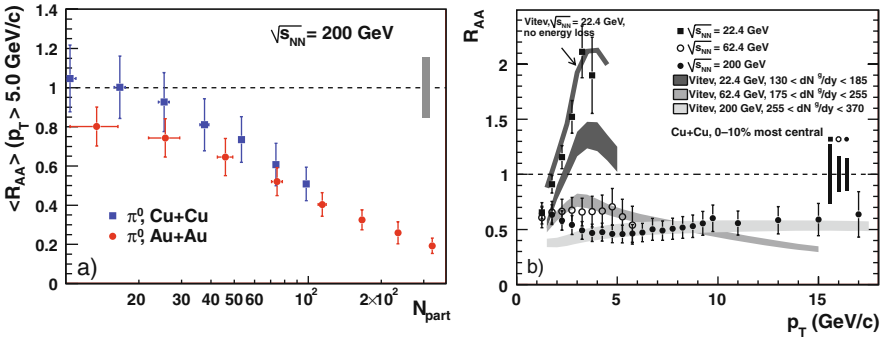

Fig. 20 *Left*: Centrality ($N_{\rm part}$) dependence of the high-p_T π^0 suppression in CuCu and AuAu at 200 GeV [179]. *Right*: $R_{AA}(p_T)$ for π^0 in central CuCu collisions at 22.4, 62.4, and 200 GeV compared to GLV calculations with initial gluon densities $dN^g/dy \approx 100$–370 [178]

Figure 20 (*right*) shows the $R_{AA}(p_T)$ measured in CuCu at 22.4, 62.4, and 200 GeV. The amount of suppression observed is roughly a factor $(A_{\rm Au}/A_{\rm Cu})^{2/3} \approx 2$ lower than in AuAu at the same energies (Fig. 18). The $R_{AA}(p_T)$ can be described by GLV with initial gluon densities $dN^g/dy \approx 100$–370 (the CuCu enhancement at 22.4 GeV is actually consistent with a scenario *without* parton energy loss).

(e) Path-length dependence

The *quadratic* dependence of the energy loss on the thickness of the medium L, Eq. (11), becomes a *linear* dependence on the *initial* value of L when one takes into account the expansion of the plasma. Experimentally, one can test the L-dependence of parton suppression by exploiting the spatial asymmetry of the system produced in non-central nuclear collisions (Fig. 21, *left*). Partons produced "in plane" ("out of

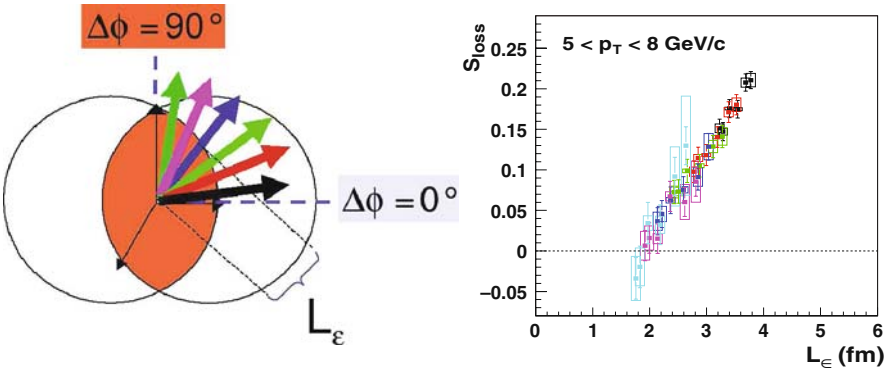

Fig. 21 *Left*: Effective thicknesses along various azimuthal directions with respect to the reaction plane in the overlap region of two heavy ions. *Right*: Fraction of energy loss $S_{\rm loss}$ vs. effective path-length L_ε measured for high-$p_{\rm T}$ neutral pions in AuAu at 200 GeV [158]

plane"), i.e. along the short (long) direction of the ellipsoid matter with eccentricity ε will comparatively traverse a shorter (longer) thickness.

PHENIX [158] has measured the high-p_T neutral pion suppression as a function of the angle with respect to the reaction plane, $R_{AA}(p_T, \phi)$. Each azimuthal angle ϕ can be associated with an average medium path-length L_ϵ via a Glauber model. Figure 21 (*right*) shows the measured fractional energy loss $S_{\rm loss}(\phi)$, obtained via Eq. (36), as a function of L_ε for pions in the range $p_T = 5$–$8\,{\rm GeV}/c$ (markers of different colours correspond to varying centralities, i.e. eccentricities ε). The energy loss is found to satisfy the expected $\Delta E_{\rm loss} \propto L$ dependence above a minimum length of $L \approx 2$ fm. The absence of suppression in the surface of the medium is explained as due to a geometric "corona" effect [180].

(f) Non-Abelian (colour factor) dependence

The amount of energy lost by a parton in a medium is proportional to its colour Casimir factor C_R (i.e. $C_A = 3$ for gluons, $C_F = 4/3$ for quarks). Asymptotically, the probability for a gluon to radiate another gluon is $C_A/C_F = 9/4$ times larger than for a quark and, thus, g-jets are expected to be more quenched than q-jets in a QGP. One can test such a genuine *non-Abelian* property of QCD energy loss in two ways:

(1) by measuring hadron suppression at a *fixed* p_T for *increasing* $\sqrt{s}$ [181, 182],
(2) by comparing the suppression of high-p_T *(anti)protons* (coming mostly from gluon fragmentation) to that of *pions* (which come from both g and $q, \bar{q}$).

The motivation for (1) is based on the fact that the fraction of quarks and gluons scattered at midrapidity in a pp or AA collision at a *fixed* p_T varies with $\sqrt{s_{NN}}$ in a proportion given[22] by the relative density of $q, \bar{q}$, and g at the corresponding Bjorken $x = 2p_T/\sqrt{s}$ in the proton/nucleus. At large (small) x, hadroproduction is dominated by quark (gluon) scatterings. A full NLO calculation [131–133] (Fig. 22, *left*) predicts that hadrons with $p_T \approx 5$ GeV/c at SPS (LHC) energies are ∼100% produced by valence quarks (gluons), whereas at RHIC they come 50–50% from both species.

Figure 22 (*right*) shows the R_{AA} for 4-GeV/c pions measured at SPS and RHIC compared to two parton energy loss curves, both normalised at the $R_{AA} \approx 1$ measured at SPS and extrapolated all the way up to LHC energies [182]. The lower curve shows the expected R_{AA} assuming the normal non-Abelian behaviour ($\Delta E_g/\Delta E_q = 9/4$). The upper (dotted) curve shows an arbitrary prescription in which quarks and gluons lose the same energy ($\Delta E_g = \Delta E_q$). Above $\sqrt{s_{NN}} \approx 100$ GeV, gluons take over as the dominant parent parton of hadrons with $p_T \approx 5\,{\rm GeV}/c$ and, consequently, the R_{AA} values drop faster in the canonical non-Abelian scenario.

[22] The different "hardness" of quarks and gluons fragmenting into a given hadron at the corresponding $z = p_{\rm hadron}/p_{\rm parton}$ plays also a (smaller) role.

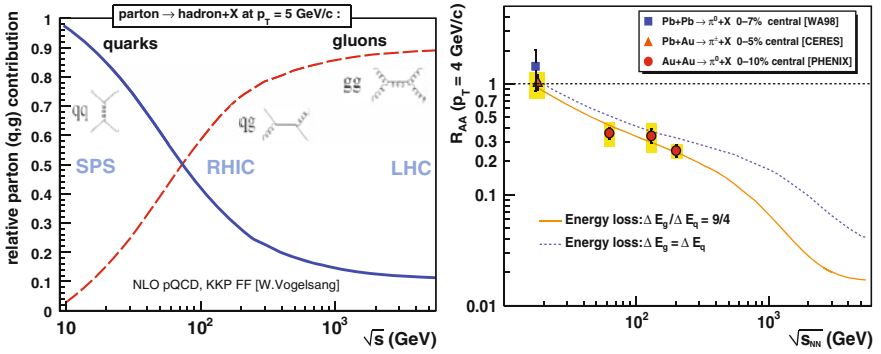

Fig. 22 *Left*: Relative fraction of quarks and gluons fragmenting into a hadron at $p_T = 5$ GeV/c in pp collisions in the range $\sqrt{s} = 10$–5500 GeV given by NLO pQCD [131–133]. *Right*: $R_{AA}(p_T = 4$ GeV/c) for π^0 in central AA collisions as a function of collision energy compared to non-Abelian (*solid*) and "non-QCD" (*dotted*) energy loss curves [181, 182]

The experimental high-p_T π^0 data supports the expected colour factor dependence of $R_{AA}(\sqrt{s_{NN}})$ [181].

The second test of the colour charge dependence of hadron suppression is based on the fact that gluons fragment comparatively more into (anti)protons than quarks do. One would thus naively expect $R_{AA}^{p,\bar{p}} < R_{AA}^{\pi}$. The STAR results (Fig. 23, left) are, however, seemingly at variance with this expectation: pions appear more suppressed than protons at high-p_T [183]. The use of (anti)protons as a perturbative reference for particle production is, however, questionable: p, $\bar{p}$ are already found to be enhanced in dAu compared to pp collisions by a factor $\sim$ 50–100% for p_T's as large as 7 GeV/c [151]. It is likely that there is an extra mechanism of baryon production, based, e.g. on in-medium quark coalescence [185–187], which compensates for the energy loss suffered by the parent partons. It is also important to

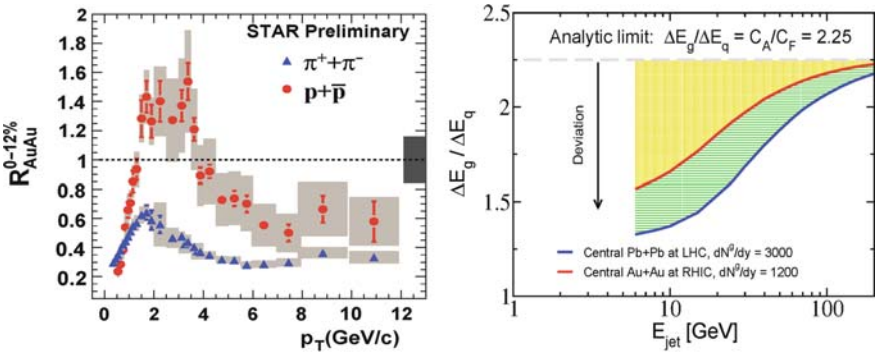

Fig. 23 *Left*: $R_{AA}(p_T)$ for pions and (anti)protons in central AuAu at $\sqrt{s_{NN}} = 200$ GeV [183]. *Right*: Comparison between ΔE_g and ΔE_q in central collisions of large nuclei at RHIC and LHC showing large deviations from $\Delta E_g = 2.25 \Delta E_q$ for finite parton energies [184]

stress that the $\Delta E_g/\Delta E_q = 9/4$ expectation holds only for asymptotic parton energies. Finite energy constraints yield values $\Delta E_g/\Delta E_q \approx 1.5$ for realistic kinematics (Fig. 23, right) [184].

(g) Heavy-quark mass dependence

A robust prediction of QCD energy loss models is the hierarchy $\Delta E_Q < \Delta E_q < \Delta E_g$. Due to the dead cone effect, the radiative energy loss for a charm (bottom) quark is ∼25% (75%) less than for a light quark (see Sect. 2.2). Surprisingly, PHENIX and STAR measurements of high-p_T electrons from the semileptonic decays of D and B mesons indicate that their suppression is comparable to that of light mesons, $R_{AA}(Q) \sim R_{AA}(q, g) \approx 0.2$ (Fig. 24, left) [188–190]. Such a low R_{AA} cannot be described by radiative energy loss calculations with the same initial gluon densities or transport coefficients needed to quench the light hadron spectra [191, 192].

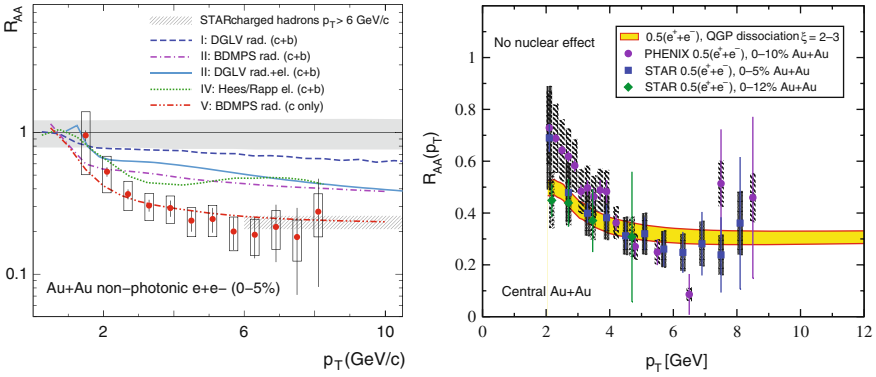

Fig. 24 $R_{AA}(p_T)$ for decay electrons from D and B mesons in central AuAu at $\sqrt{s_{NN}} = 200$ GeV [188–190] compared to various radiative+elastic energy loss models for c and b quarks (*left*) and to a model of D and B meson dissociation in the plasma [196] (*right*)

Various explanations have been proposed to solve the "heavy flavour puzzle":

- First, if only c quarks (three times more suppressed than the heavier b quarks) actually contributed to the measured high-p_T decay electron spectrum, then one would indeed expect $R_{AA}(c) \approx 0.2$ [192]. Yet indirect measurements from PHENIX [193] and STAR [194] have confirmed the similar production yields of electrons from D and B mesons above $p_T \approx 5$ GeV/c predicted by NLL pQCD [195].
- The heavy-quark suppression has revived the interest of computing *elastic* energy loss in a QGP [197, 21, 198, 22]. As discussed in Sect. 2.2, ΔE_{el} can indeed be a significant contribution for heavy quarks (see "rad+el" curves in Fig. 24, *left*).
- The strongly coupled nature of the plasma at RHIC would lead, according to AdS/CFT calculations [119–122, 199], to a larger heavy-quark momentum dif-

fusion parameter than expected in perturbative approaches [200]. This would explain the larger charm/bottom quenching observed in the data.

- Two works [201, 202] argue that the large charm-quark coalescence into Λ_c baryons (with a small semileptonic decay branching ratio) in the plasma would deplete the number of open-charm mesons and correspondingly reduce the number of decay electrons compared to pp collisions.
- The assumption of vacuum hadronisation (after in-medium radiation) implicit in all parton energy loss formalisms may well not hold in the case of a heavy quark. All existing quark-hadronisation time estimates [148] are inversely proportional to the mass m_h of the final produced hadron. The heavier the hadron, the faster the formation. In the rest frame[23] of the fragmenting heavy-Q the formation time of D and B mesons [196]

$$\tau_{\rm form} = \frac{1}{1+\beta_Q}\frac{2z(1-z)p^+}{\mathbf{k}^2+(1-z)m_h^2-z(1-z)m_Q^2}, \quad \text{where } \beta_Q = p_Q/E_Q, \tag{44}$$

is of order $\tau_{\rm form} \approx 0.4$–$1$ fm/c, respectively. Thus, theoretically, one needs to account for the energy loss of the heavy quark in the medium as well as for the dissociation rate of the heavy-quark *meson* inside the QGP. The expected amount of suppression in that case is larger and consistent with the data (Fig. 24, *right*).

5 High-p_T Di-hadron ϕ, η Correlations: Data vs. Theory

Beyond the leading hadron spectra discussed in the previous section, detailed studies of the modifications of the jet structure in heavy-ion collisions have been addressed via high-p_T multi-particle (mostly di-hadron) ϕ, η correlations. Jet-like correlations are measured on a *statistical* basis by selecting high-p_T *trigger* particles and measuring the azimuthal ($\Delta\phi = \phi - \phi_{\rm trig}$) and pseudorapidity ($\Delta\eta = \eta - \eta_{\rm trig}$) distributions of *associated* hadrons ($p_T^{\rm assoc} < p_T^{\rm trig}$) relative to the trigger:

$$C(\Delta\phi, \Delta\eta) = \frac{1}{N_{\rm trig}}\frac{d^2N_{\rm pair}}{d\Delta\phi d\Delta\eta}. \tag{45}$$

Combinatorial background contributions, corrections for finite pair acceptance, and the superimposed effects of *collective* azimuthal modulations (elliptic flow) can be taken care of with different techniques [203–205]. A commonly used $C(\Delta\phi)$ background-subtraction method is the "zero yield at minimum" (ZYAM) [206].

A schematic representation of the di-hadron azimuthal-pseudorapidity correlations $dN_{\rm pair}/d\Delta\phi d\eta$ measured in pp and central AuAu collisions is shown in Fig. 25. In the pp case, without significant initial- or final-state interactions, a dijet signal appears clearly as two distinct back-to-back Gaussian-like peaks at $\Delta\phi \approx 0$,

[23] Note that in the lab system there is an extra Lorentz boost factor: $\tau_{\rm lab} = \gamma_Q \cdot \tau_{\rm form}$.

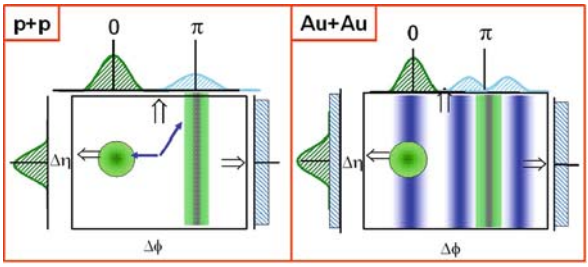

Fig. 25 Schematic illustration summarising the jet-induced di-hadron correlation signals in $\Delta\phi$ and $\Delta\eta$ observed in pp (*left*) and central AuAu (*right*) at $\sqrt{s_{NN}}$ = 200 GeV [207]

$\Delta\eta \approx 0$ (near-side), and $\Delta\phi \approx \pi$ (away-side). The away-side peak is broader in $\Delta\eta$ (up to $\Delta\eta \approx 2$) than the near-side peak due to the *longitudinal* momentum imbalance between the two colliding partons with different x_1, x_2 momentum fractions (the collision is boosted in η in the direction of the larger $x_{1,2}$). At variance with such a standard dijet topology, the di-hadron correlations in AuAu reactions at RHIC show several striking features, discussed in detail below:

- The *away-side* azimuthal peak at $\Delta\phi \approx \pi$ *disappears* with increasing centrality for hadrons with $p_T^{\text{assoc}} \lesssim 5\,\text{GeV}/c$, consistent with strong suppression of the leading fragments of the recoiling jet traversing the medium [203].
- The vanishing of the away-side peak is accompanied with an *enhanced* production of *lower* p_T hadrons ($p_T^{\text{assoc}} \lesssim 2.5\,\text{GeV}/c$) [205, 204] with a characteristic *double-peak* structure at $\Delta\phi \approx \pi \pm 1.1$–$1.3$.
- One observes a large *broadening* ("ridge"), out to $\Delta\eta \approx 4$, of the *near-side pseudorapidity* $\mathrm{d}N_{\text{pair}}/\mathrm{d}\Delta\eta$ correlations [204].

5.1 Azimuthal Correlations: Away-Side Quenching and Energy Loss

Figure 26 shows the increasingly distorted back-to-back azimuthal correlations in high-p_T triggered central AuAu events as one decreases the p_T of the associated hadrons (right to left). Whereas compared to pp the near-side peak remains unchanged for all p_T's, the away-side peak is only present for the highest partner p_T's but progressively disappears for less energetic partners [208, 209]. Early STAR results [203] showed a monojet-like topology with a complete disappearance of the opposite-side peak for $p_T^{\text{assoc}} \approx 2 - 4\,\text{GeV}/c$.

For any range of trigger p_T^{trig} and associated p_T^{assoc} intervals, the correlation strength over an azimuthal range $\Delta\phi$ between a trigger hadron h_t and a partner hadron h_a in the opposite azimuthal direction can be constructed as a function of the momentum fraction $z_T = p_T^{\text{assoc}}/p_T^{\text{trig}}$ via a "pseudo-fragmentation function" [210]:

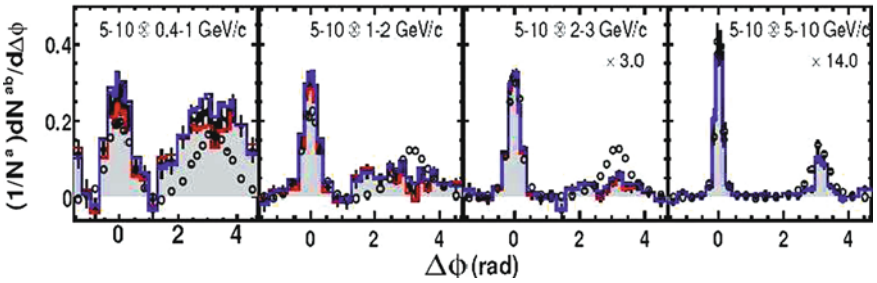

Fig. 26 Comparison of the azimuthal di-hadron correlation $\mathrm{d}N_{\mathrm{pair}}/\mathrm{d}\Delta\phi d\eta$ for pp (*open symbols*) and central AuAu (*closed symbols*) at $\sqrt{s_{NN}} = 200$ GeV for $p_T^{\mathrm{trig}} = 5$–10 GeV/c and increasingly smaller (*right to left*) values of p_T^{assoc} [209]

$$D^{\mathrm{away}}_{pp(AA)}(z_T) = \int_{p_{T,\min}^{\mathrm{trig}}}^{p_{T,\max}^{\mathrm{trig}}} dp_T^{trig} \int_{p_{T,\min}^{\mathrm{assoc}}}^{p_{T,\max}^{\mathrm{assoc}}} dp_T^{\mathrm{assoc}} \int_{\mathrm{away}} d\Delta\phi \, \frac{d^3\sigma^{h_t h_a}_{pp(AA)}/dp_T^{\mathrm{trig}} dp_T^{\mathrm{assoc}} d\Delta\phi}{d\sigma^{h_t}_{pp(AA)}/dp_T^{\mathrm{trig}}} . \tag{46}$$

Figure 27 (left) shows the measured D_{AA}^{away} distributions for pp and AuAu collisions as a function of z_T compared to predictions of the HT parton energy loss model [211] for various values of the ε_0 parameter quantifying the amount of energy loss. Similarly to $R_{AA}(p_T)$, the magnitude of the suppression of back-to-back jet-like two-particle correlations can be quantified with the ratio $I_{AA}(z_T) = D_{AA}(z_T)/D_{pp}(z_T)$. I_{AA}^{away} (bottom-left panel of Fig. 27) is found to decrease with increasing centrality, down to about 0.2–0.3 for the most central events [203, 212]. The right plot of Fig. 27 shows the best $\varepsilon_0 \approx 1.9$ GeV/fm value that fits the measured R_{AA} and I_{AA} factors. Due to the irreducible presence of (unquenched) partons emitted from the surface of the plasma, the leading hadron quenching factor $R_{AA}(p_T)$

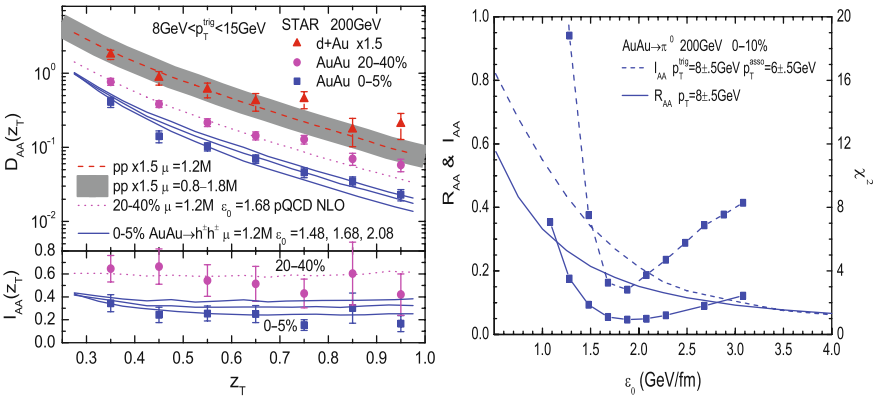

Fig. 27 *Left*: $D^{\mathrm{away}}_{pp(AA)}(z_T)$ distributions for dAu and AuAu collisions at 200 GeV and $I_{AA}(z_T)$ ratio (for central AuAu) [212], compared to HT calculations [211] for varying ϵ_0 energy loss parameter. *Right*: Corresponding (data vs. theory) χ^2 values for the fitted ε_0 parameter [211]

is in general less sensitive to the value of ε_0 than the di-hadron modification ratio $I_{AA}(z_T)$.

5.2 Azimuthal Correlations: Away-Side Broadening and "Conical" Emission

Since energy and momentum are conserved, the "missing" fragments of the away-side (quenched) parton at intermediate p_T's must be either shifted to lower energy ($p_T \lesssim 2$ GeV/c) and/or scattered into a broadened angular distribution. Both softening and broadening are seen in the data when the p_T of the away-side associated hadrons is *lowered* (see two leftmost panels of Fig. 26). Figure 28 shows in detail the di-hadron azimuthal correlations $dN_{\text{pair}}/d\Delta\phi$ in central AuAu collisions [205, 213]: the away-side hemisphere shows a very unconventional angular distribution with a "dip" at $\Delta\phi \approx \pi$ and two neighbouring local maxima at $\Delta\phi \approx \pi \pm 1.1$–$1.4$. Such a "volcano"-like profile has been interpreted as due to the preferential emission of energy from the quenched parton at a finite angle with respect to the jet axis. This could happen in a purely energy loss scenario due to large-angle radiation [214], but more intriguing explanations have been put forward based on the dissipation of the lost energy into a *collective* mode of the medium in the form of a wake of lower energy gluons with Mach- [44–48] or Čerenkov-like [48–51] angular emissions.

In the Mach cone scenario [44–48], the local maxima in central AuAu are caused by the Mach shock of the supersonic recoiling parton traversing the medium with a resulting preferential emission of secondary partons from the plasma at an angle θ_M (Fig. 29). Such a mechanism would give access, via Eq. (15), to the speed sound c_s of the traversed matter. In an expanding plasma, the speed of sound changes from $c_s = 1/\sqrt{3}$ (QGP) to $c_s \approx \sqrt{0.2}$ (hadron gas) through $c_s = 0$ (mixed phase). The

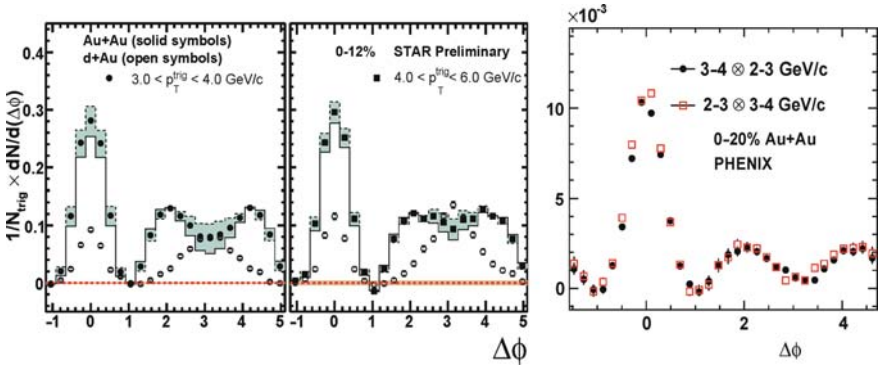

Fig. 28 Normalised azimuthal di-hadron distributions, $1/N_{\text{trig}}\, dN_{\text{pair}}/d\Delta\phi$. *Left*: STAR data in central AuAu (*squares*) and dAu (*circles*) for $p_T^{\text{assoc}} = 1.3 - 1.8$ GeV/c and two ranges of p_T^{trig} [213]. *Right*: PHENIX results in central AuAu for various $p_T^{\text{trig,assoc}}$ ranges [209]

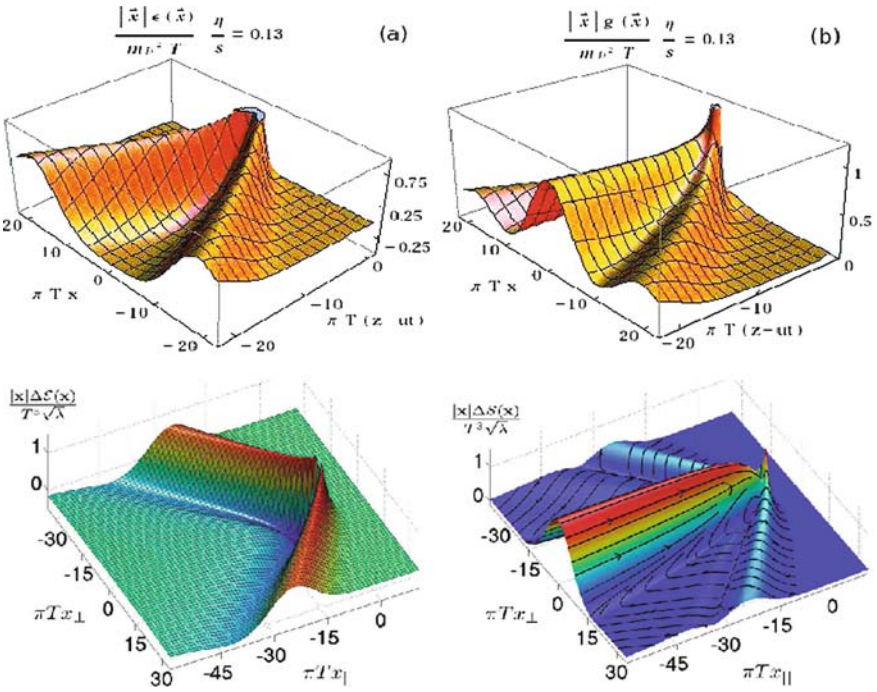

Fig. 29 *Top*: Perturbed energy (*left*) and momentum (*right*) densities for a gluon moving with $\beta = 0.99955$ in a perturbative QGP [220]. *Bottom*: Perturbed energy density (*left*) and energy flux (Pointing vector, *right*) for a jet with $\beta = 0.75$ from an AdS/CFT model [219]

time-averaged value is $\langle c_s \rangle = \frac{1}{\tau}\int_0^\tau dt\, c_s(t) \approx 0.3$ [46, 47] with a resulting Mach angle $\theta_M = \arccos(c_s) \approx 1.3$, in rough agreement with the experimental data.

In the Čerenkov picture [48–51], it is argued that the combination of the LPM gluonstrahlung interference and a medium with a *large* dielectric constant ($n \approx 2.75$ is needed in Eq. (16) to reproduce the location of the experimental peaks) should also result in the emission of QCD Čerenkov radiation with the double-hump structure observed in the data. However, at variance with the Mach angle which is constant in the fluid, the Čerenkov angle *decreases* with the momentum of the radiated gluon. Such a trend is seemingly in disagreement with the fact that the measured θ_c remains relatively constant as a function of $p_T^{\rm assoc}$ [209, 215]. In addition, STAR [216] and PHENIX [217] 3-particle correlation studies seem to clearly favour the *conical* over deflected-jets interpretation.

Theoretically, the disturbance of the energy-momentum tensor caused by a heavy quark has been studied in a $\mathcal{N} = 4$ SYM plasma [218, 219] as well as for a light quark in a perturbative plasma [220]. In both cases a clear conical structure as well as a strong flow generated along the path of the jet (diffusion wake [221–224]) are observed (Fig. 29). The results are sensitive to the viscosity of the medium. Yet, phenomenologically, it is unclear if such partonic collective wake(s) and cone survives both hadronisation and the final hadronic freeze-out [223–229]. Results for

a pQCD plasma [227] indicate that the conical signal does not survive freeze-out: a peak at $\Delta\phi = \pi$ appears due to the strong diffusion wake. More involved studies, accounting for, e.g. the plasma expansion and the hadronic phase, are needed before a final conclusion can be reached.

5.3 Pseudorapidity Correlations: Near-Side "Ridge"

Figure 30 shows the associated $\Delta\eta$–$\Delta\phi$ particle yield ($p_T^{\text{assoc}} \gtrsim 20$ MeV/c) for trigger hadrons $p_T^{\text{trig}} > 2.5$ GeV/c in pp (PYTHIA simulations) and central AuAu (PHOBOS data) at 200 GeV. Both distributions show a clear peak at $(\Delta\eta, \Delta\phi) \approx (0, 0)$ as expected from jet fragmentation, but the near-side peak in heavy-ion collisions features a wide associated yield out to $\Delta\eta \approx 4$, referred to as the "ridge" [230]. The existence of such unique long-range rapidity correlations in the near side of the *trigger* parton which is, by construction, the least affected by the medium is puzzling. The properties (particle composition, p_T slope, intra-particle correlations) of this structure are very similar to those of the soft underlying event in the collision [231], clearly suggesting that the ridge is formed from bulk matter and not from jet fragments. Though many different interpretations have been put forward (see, e.g., [232] for a summary), models that do *not* require jet triggers for the effect to appear – such as, e.g."glasma" flux tubes [233] or "trivial" modifications of the 2- and 3-particle correlations due to radial flow [232] – seem favoured.

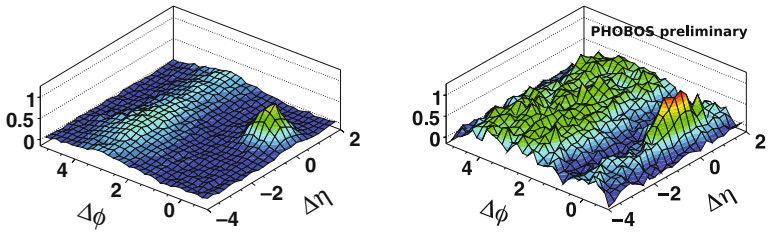

Fig. 30 Per-trigger associated hadron yield for $p_T^{\text{trig}} > 2.5$ GeV/c as a function of $\Delta\eta$ and $\Delta\phi$ for pp (PYTHIA, *left*) and 0–30% central AuAu (PHOBOS, *right*) collisions at 200 GeV [234]

6 Jet Observables in AA Collisions

The measurement of the leading fragments of a jet (single-hadron spectra and/or di-hadron azimuthal correlations at high-p_T) in AA collisions has been covered in detail in the previous sections. In this last chapter, we focus on *full jet* reconstruction in nuclear reactions. The study of the energy and particle-multiplicity distributions within a jet issuing from the fragmentation of quenched parton is a powerful tool to study the response of hot and dense QCD matter to fast quark and gluons.

6.1 Full Jet Reconstruction in AA Collisions

Experimental reconstruction of jets in hadronic and nuclear collisions is an involved exercise [235, 236] that requires at least three steps:

- *Clustering algorithm*: Hadrons belonging to a given jet are measured in the detector (usually in the cells of the hadronic and electromagnetic calorimeters) and are clustered together, according to relative "distances" in momentum and/or space, following an *infrared- and collinear-safe* procedure that can be also appropriately applied to "theoretical" (Monte Carlo) jets. The algorithm needs to be *fast* enough to be run over events with very high multiplicities. Various jet finders exist presently that fulfil all such conditions, e.g. k_T [237] and SISCone [238] as implemented in the FASTJET package [239].
- *Background subtraction*: Jets are produced on top of a large "underlying event" (UE) of hadrons coming from other (softer) parton–parton collisions in the same interaction. At LHC energies, extrapolating from $dE_T/d\eta|_{\eta=0} = 0.6$ TeV measured at RHIC [166, 167], one expects a total transverse energy of $\sim$1 TeV in 1-unit rapidity at midrapidity. Jet reconstruction is usually carried out with small cone radius $R = \sqrt{\Delta\eta^2 + \Delta\phi^2} = 0.3$–$0.5$ (or similar k_T-distances, D) to minimise the UE contributions. Indeed, at the LHC in a $R = 0.4$ cone one expects $\Delta E_T = \pi \times R^2 \times 1/(2\pi) \times dE_T/d\eta|_{\eta=0} \approx 80$ GeV with large fluctuations. This observation already indicates that it will be challenging to reconstruct jets below $E_T \approx 50$ GeV. Various UE subtraction techniques have been developed in combination with the k_T [240–242], UA1-cone [242, 243], or iterative-cone [244] algorithms.
- *Jet corrections*: The energy of the reconstructed and background-subtracted jets has to be corrected for various experimental and model-dependent uncertainties before comparing it to theoretical predictions. Experimentally, the *jet energy scale* (JES) is the most important source of systematic uncertainties in the jet yield and requires careful data-driven studies (e.g. via dijet and γ-, Z-jet balancing in proton–proton collisions). In addition, before a given "parton-level" pQCD calculation can be compared to a measured "hadron-level" jet spectrum, one needs to estimate the non-perturbative effects introduced by the underlying-event and hadronisation corrections. In pp collisions, this final step is carried out usually comparing the results from two Monte Carlos (e.g. PYTHIA and HERWIG) with different models for the UE multiparton interactions as well as for the hadronisation (string and cluster-fragmentation, respectively).

6.2 Jet Clustering Algorithms

In practical terms one usually deals with three types of "jets" (Fig. 31, left). Experimentally, a *calorimeter jet* (aka "CaloJet") is a collection of four vectors based on calorimeter towers clustered in pseudorapidity- azimuth according to a given algorithm. At the Monte Carlo generator level, a *hadron or particle jet* (aka "GenJet") is

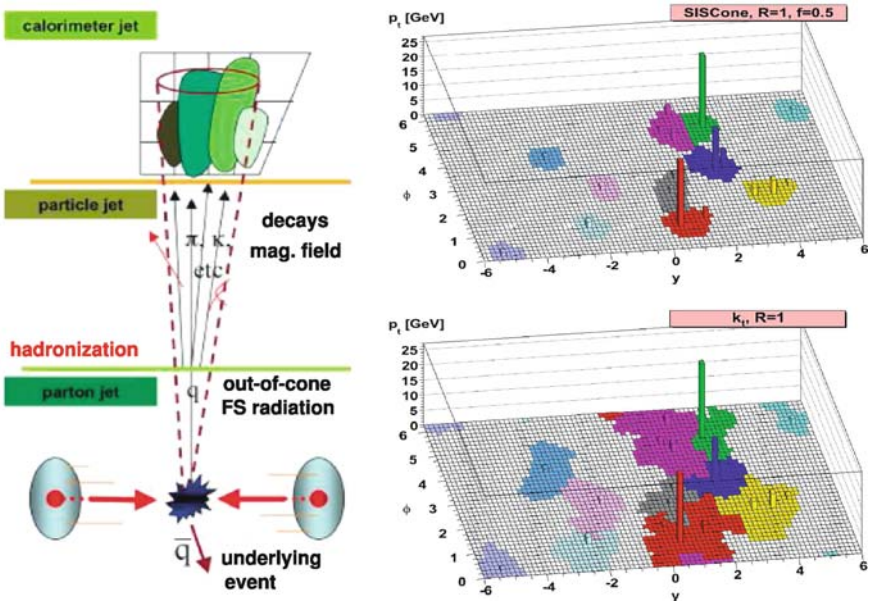

Fig. 31 *Left*: Schema of jet production and measurement [235]. *Right*: Reconstructed jets in η–ϕ space with the SISCone (*top*) and k_T (*bottom*) algorithms for a simulated pp event at the LHC [245]

a collection of hadrons issuing from the (non-perturbative) hadronisation of a given parton. Theoretically, a *parton-level jet* is what one actually calculates in pQCD. The (non-unique) method to link an initial parton to a set of final-state particles relies on a procedure known as "jet algorithm".

The goal of a clustering algorithm is to combine hadrons into jets according to a given "distance" (radius). Theoretically, such a procedure must be *infrared* and *collinear safe* – i.e. adding a soft gluon or splitting a given parton must *not* change the final number of reconstructed jets. In addition, the jet finder must not be too sensitive to non-perturbative effects – hadronisation, underlying event (and pileup in pp) – and it must be realistically applicable at detector level (e.g. not too slow). There are two broad groups of jet algorithms [235, 236]:

- *Cone-type* algorithms are "top-down" approaches, i.e. they identify energy flow into pre-defined cones of a given radius. One sums the momenta of all particles j within a cone of radius R around a seed particle i (often the particle or calorimeter tower with the largest transverse momentum) in azimuthal angle ϕ and pseudorapidity η, i.e. taking all j such that

$$\Delta_{ij}^2 = \left(\eta_i - \eta_j\right)^2 + \left(\phi_i - \phi_j\right)^2 < R^2 \,. \tag{47}$$

  The direction of the resulting sum is then used as a new seed direction, and one iterates the procedure until the direction of the resulting cone is stable

(Fig. 31, top-right). There exist many flavours of this method developed (JetClu, ILCA/MidPoint, ICone, SISCone, etc.) which have been mainly employed at hadron colliders. Their main advantages are their speed, which makes them easy to implement in triggers, and the simplicity of the UE corrections. On the other hand, their particular implementations can be messy (seeding, split–merge, dark towers, etc.) and infrared/collinear safety is not guaranteed in many cases.

- *Sequential clustering* algorithms are "bottom-up" approaches that rely on pairwise successive recombinations of the closest hadrons in momentum up to a given (predefined) distance D. One introduces distances d_{ij} between entities (particles, pseudojets) i and j, and d_{iB} between entity i and the beam (B). The clustering proceeds by identifying the smallest of the distances, and if it is a d_{ij} recombining entities i and j, while if it is d_{iB} calling i a jet and removing it from the list. The distances are recalculated and the procedure repeated until no entities are left. The distance measures for several algorithms are of the form

$$d_{ij} = \min(k_{T,i}^{2p}, k_{T,j}^{2p}) \frac{\Delta_{ij}^2}{D^2} \quad , \quad d_{iB} = k_{T,i}^{2p} \, , \tag{48}$$

where Δ_{ij}^2 is defined in Eq. (47), $k_{T,i}$ is the transverse momentum of particle i, D is the jet-radius parameter, and p parameterises the type of algorithm: k_T ($p = 1$) [246], Cambridge/Aachen ($p = 0$) [247], anti-k_T ($p = -1$) [245] (Fig. 31, bottom-right). On the positive side, these algorithms – widely used at LEP and HERA – are explicitly infrared and collinear safe and more "realistic" than the cone-based ones as they mimic (backwards) the QCD shower branching dynamics. On the other hand, they used to be slow and the UE subtraction trickier compared to the cone jet finders, making them not competitive in a heavy-ion environment with very large hadron multiplicities. Recently, the time taken to cluster N particles has been significantly improved in the FastJet [239] implementation, based on Voronoi diagrams, going down from $\mathcal{O}(N^3)$ for the default k_T jet finder to $\mathcal{O}(N \ln N)$. Jet clustering in nucleus–nucleus collisions is now routinely performed at sub-second times.

6.3 Underlying Event Subtraction

Background energy in a jet cone of size R is $\mathcal{O}(R^2)$ and background fluctuations are $\mathcal{O}(R)$. As aforementioned, the soft background from the underlying event in a cone of $R = 0.4$ in central nucleus–nucleus collisions at RHIC (LHC) is about 40 (80) GeV. Figure 32 (left) shows the (charged) jet and background energies as a function of the cone radius R in ALICE [174, 241]. Jets can only be identified if the background energy within the cone is smaller than the signal energy. This can be achieved by decreasing the cone size ($E_T^{\rm bgd} \propto R^2$) to $R = 0.3$–0.5 and by applying p_T or energy cuts on the charged hadrons or calorimeter towers. The latter option is not optimal since it also introduces potential biases in the measurement of jet

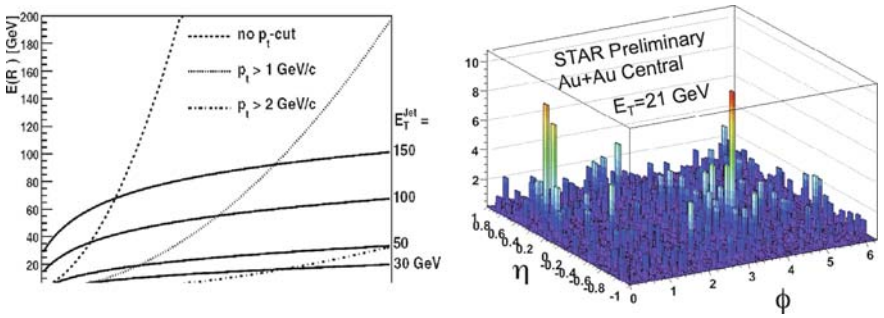

Fig. 32 *Left*: Charged jet energy in a cone of radius R (*full lines*) in ALICE compared to the background energy from a HIJING [248] simulation for different cuts in the particles p_T (*dashed lines*) [174]. *Right*: STAR AuAu dijet event after background subtraction [249, 250]

quenching effects. STAR [249, 250] (Fig. 32, right) uses a seeded-cone algorithm with $R = 0.4$ and $p_T^{cut} = 0.1 - 2$ GeV/c and estimates the UE background event by event from the average energy in cones without seeds which is then subtracted from the reconstructed jets. ALICE uses a modified version of the UA1-cone algorithm ($R = 0.4$) where the mean cell energy from cells outside a jet cone is recalculated after each iteration of the cone jet finder and subtracted from all cells [174, 241].

Similarly, CMS [244, 176] subtracts the UE on an event-by-event basis with a variant of the iterative "noise/pedestal subtraction" for pp collisions [251]. Initially, the mean value and dispersion of the energies in the calorimeter cells are calculated for rings of constant pseudorapidity, η. The value of this pedestal function, P(η), is subtracted from all cells (the cell energy is set to zero in case of negative values) and the jets are reconstructed with the default ICone finder. In a second iteration, the pedestal function is recalculated using only calorimeter cells outside the area covered by jets with $E_T > 30$ GeV. The cell energies are updated with the new pedestal function and the jets are reconstructed again, using the updated calorimeter cells.

Alternatively, FASTJET [240] proposes a background-subtraction procedure *after* running any infrared-safe algorithm. The method is based on the concept of a "jet area" A constructed by adding infinitely soft particles ("ghosts") and identifying the region in η, ϕ where those ghosts are clustered within each jet [241]. Each reconstructed jet p_T is then corrected by subtracting the median value of the noise distribution in the event, $\rho = \text{median}\,[\{p_T/A\}]$, in the jet area A, via $p_T^{\text{sub}} = p_T - A \cdot \rho$. In practical terms, one fits the measured $p_T(\eta)/A$ background distribution for each event with a parabola form, $\rho(\eta) = a + b\,\eta^2$ (which excludes any jet peak) and corrects then the jet p_T using the formula above.

6.4 Jet Corrections

The last step of any jet analysis consists in correcting the p_T of any measured *CaloJet* to match closely that of the associated *GenJet* or *parton-level* jet, so that it can be

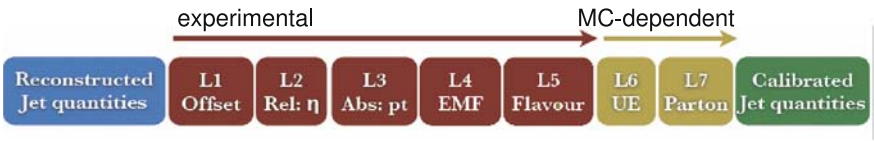

Fig. 33 List of typical factorised jet energy corrections (CMS analysis) [251]

compared to theoretical expectations. In principle, the different corrections can be decomposed as shown in Fig. 33. The experimental corrections (labelled levels 1–5 in the plot) can be extracted from the data themselves. For example, the correction L1 (noise offset) can be obtained from minimum-bias events *without* jet activity, and the L2 (flattening of relative, η-dependent, p_T responses of the calorimeters) and L3 (absolute p_T calibration) can be derived using p_T-balancing techniques in back-to-back dijet and γ-, Z-jet events in pp collisions. A precise calibration of the jet energy scale (JES) is essential. Given the steep (power law) fall-off of the jet cross section as a function of energy, an uncertainty of 10% in the JES can propagate into uncertainties as large as 50% in the jet yield at a given p_T bin. The L3 correction is thus the most important source of experimental uncertainty in any jet measurement. The two last corrections, L4 (fraction EMF of energy deposited by hadrons in the EM calorimeter) and L5 (flavour correction accounting for the different characteristics of – and therefore detector responses to – gluon, light-quark, and heavy-quark jets) can be, e.g. obtained in back-to-back γ-jet and b,c-identified dijet events in pp.

The two "theoretical" corrections (L6 – UE and L7 – parton) aim at bringing the p_T of a *CaloJet* as close as possible to that of its originating parton. They can only be obtained from MC simulations that model the effects of final-state radiation (FSR), hadronisation, and underlying event. In pp collisions, the total shift on a jet p_T can be approximated by the uncorrelated sum $\langle \delta p_T^2 \rangle \approx \langle \delta p_T \rangle^2_{\text{FSR}} + \langle \delta p_T \rangle^2_{\text{hadr}} + \langle \delta p_T \rangle^2_{\text{UE}}$. FSR and hadronisation tend to remove energy out of the jet cone, whereas the UE has the contrary "splash-in" effect [252]. The way these effects modify the jet energy as a function of the parton p_T, flavour and the used cone radius R are summarised in Table 3. Whereas the effect of FSR can be in principle computed perturbatively, the UE and hadronisation corrections rely on model-dependent descriptions of multi-parton interactions (MPI) and parton fragmentation. In pp collisions, one usually compares the result of PYTHIA and HERWIG – which have different MPI and dif-

Table 3 Main physical effects that contribute to a shift $\langle \delta p_T \rangle$ between the transverse momentum of a jet and its parent parton in pp collisions (cases with "–" do not have any dependence at LO) [252]

	Dependence of jet $\langle \delta p_T \rangle$ shift on		
	Parton p_T	Colour factor	Radius R
Final-state radiation	$\sim \alpha_s(p_T)\, p_T$	C_i	$\ln R + \mathcal{O}(1)$
Hadronisation	–	C_i	$-1/R + \mathcal{O}(R)$
Underlying event	–	–	$R^2/2 + \mathcal{O}(R^4)$

ferent (string vs. cluster) fragmentation models – to gauge the dependence of the measured jet observables on these non-perturbative phenomena.

In heavy-ion collisions, in-medium FSR and UE are significantly enhanced compared to pp jets, but, since hadronisation occurs after traversing the medium, the final parton-to-hadron fragmentation should be the same as in the vacuum. Ideally, the effects of the UE can be controlled embedding MC jets in real events, and the influence of hadronisation can be gauged, e.g. comparing the results of Q-PYTHIA and Q-HERWIG [40]. Jet quenching observables – which are the ultimate goal of our studies – can then be isolated comparing the results of different parton energy loss MCs such as, e.g. PYQUEN (with large out-of-cone elastic energy loss) and Q-PYTHIA (with its embedded BDMPS radiative energy loss).

6.5 Jet Shapes

The study of the internal structure of jets – via observables such as jet shapes and jet multiplicity distributions – in $p\bar{p}$ collisions at Tevatron has provided valuable tests of the models for parton branching and soft-gluon emission in the vacuum [253]. The energy degradation of partons traversing a dense QCD plasma will be also directly reflected in the modification of such jet observables in heavy-ion collisions. Two variables are useful in this context:

- the *differential jet shape*, $\rho(r)$, is the average fraction of the jet p_T that lies inside an annulus of radius $r \pm \delta r/2$ around the jet axis (e.g. $\delta r = 0.1$):

$$\rho(r) = \frac{1}{\delta r}\frac{1}{N_{\text{jet}}}\sum_{\text{jets}}\frac{p_T(r-\delta r/2, r+\delta r/2)}{p_T(0,R)}, \quad 0 \le r = \sqrt{\Delta y^2 + \Delta\phi^2} \le R, \tag{49}$$

- the *integrated jet shape*, $\Psi(r)$, is the average fraction of the jet p_T that lies inside a cone of radius r concentric to the jet cone (by definition, $\Psi(r = R) = 1$):

$$\Psi(r) = \frac{1}{\mathrm{N}_{\text{jet}}}\sum_{\text{jets}}\frac{p_T(0,r)}{p_T(0,R)}, \quad 0 \le r \le R. \tag{50}$$

Medium-modified jet shapes in $PbPb$ collisions at LHC energies have been analytically investigated in [38, 54]. More detailed studies using the recently available jet quenching Monte Carlos (see Sect. 3.3) are needed.

6.6 Medium-Modified Fragmentation Functions

Due to the coherence and interference of gluon radiation *inside* a jet (resulting, on average, in *angular ordering* of the sequential branching), not the softest partons but those with intermediate energies ($E_h \propto E_{\text{jet}}^{0.3-0.4}$) multiply most effectively in QCD cascades [254]. This is best seen in the approximately Gaussian distribution

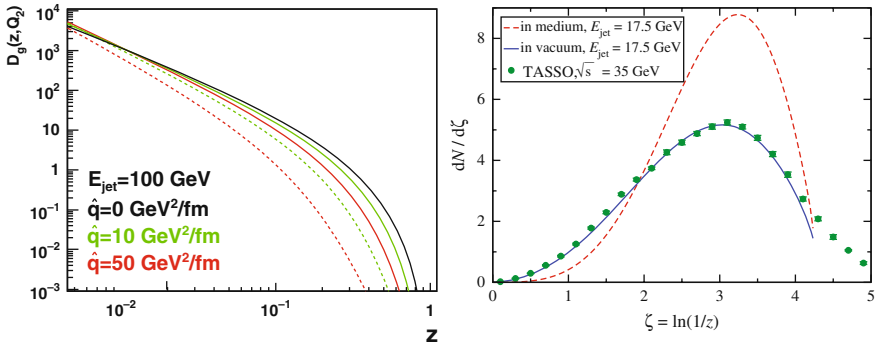

Fig. 34 *Left*: Medium-modified pion fragmentation function for a 100-GeV gluon going through a medium with increasing $\hat{q}$ parameter [56]. *Right*: Single inclusive distribution of hadrons vs. $\xi = \ln(E_{\rm jet}/p)$ for a 17.5-GeV jet in e^+e^- collisions (TASSO data) compared to MLLA predictions in the vacuum (solid curve) and in-medium (dashed curve) [39]

in the variable $\xi = \log(E_{\rm jet}/p) = \log(1/z)$ for particles with momentum p in a jet of energy $E_{\rm jet}$, which peaks at the so-called humpback plateau at intermediate $\xi \approx 3$–4 values (Fig. 34, right). As discussed previously, energy loss in a QCD medium shifts parton energy from high-z to low-z hadrons. As a result, leading hadrons are suppressed as seen in Fig. 34 (left) where, for increasing $\hat{q}$ coefficient, the fragmentation function $D_{i\to h}(z, Q^2)$ is depleted at high-z. Correspondingly, the number of low-p_T hadrons increases, as seen by the *higher* humped back in Fig. 34 (*right*).

Theoretically, the resummed (next-to) modified leading logarithmic approximation (N)MLLA approach describes well, to (next-to)-next-to-leading order $\sqrt{\alpha_s}$ accuracy, the measured distributions of hadrons $D_{i\to h}(z, Q^2)$ inside a jet (Fig. 34, right) down to non-perturbative scales $Q_{\rm eff} \approx \Lambda_{QCD} \approx 200$ MeV, provided that each parton is mapped locally onto a hadron ("Local Parton–Hadron Duality", LPHD) [255] with a proportionality factor $\kappa \approx 1$. Various recent promising applications of the (N)MLLA approach [256, 57, 41, 42] have investigated QCD radiation in the presence of a medium.

6.7 Photon-Jet Correlations

The γ-jet (and Z-jet) channel provides a very clean means to determine parton fragmentation functions (FFs) [257]. In the dominant QCD Compton process of photon production ($qg \to q\gamma$), because of momentum conservation the photon is produced back to back to the hard quark, with equal and opposite transverse momentum. Since the prompt γ is not affected by final-state interactions, its transverse energy (E_T^γ) can be used as a proxy of the away-side parton energy ($E_T^{\rm jet} \approx E_T^\gamma$) *before* any jet quenching has taken place in the medium. Once the quark fragments into a hadron h, the γ–h momentum imbalance variable [52], $z_{\gamma h} \equiv -\mathbf{p}_{\rm T,h}.\mathbf{p}_{\rm T,\gamma}/|\mathbf{p}_{\rm T,\gamma}|^2$, reduces

at LO to the fragmentation variable, $z_{\gamma h} = z$. The FF, defined as the normalised distribution of hadron momenta $1/N_{\text{jets}}\, dN/dz$ relative to that of the parent parton E_T^{jet}, can be constructed using $z_{\gamma h}$ or, similarly, $\xi = -\ln(z_{\gamma h})$, for all particles with momentum p_T associated with the jet.

ALICE [242, 258] and CMS [259] have carried out simulation studies of the γ-jet channel, where the isolated γ is identified in ECAL, the away-side jet *axis* ($\Delta\phi_{\gamma-\text{jet}} > 3$ rad) is reconstructed in the calorimeters, and the momenta of hadrons around the jet axis ($R_{\text{jet}} < 0.5$) are measured in the tracker. In the CMS acceptance and for $E_T^{\gamma} > 70$ GeV, about 4500 γ-jet events are expected according to PYTHIA (scaled by the Glauber nuclear overlap) in one PbPb year at the nominal luminosity. The obtained FFs for photon-jet events – after subtraction of the underlying-event tracks – are shown in Fig. 35 for central PbPb. Medium-modified FFs are measurable with high significance in the ranges $z < 0.7$ and $0.2 < \xi < 6$.

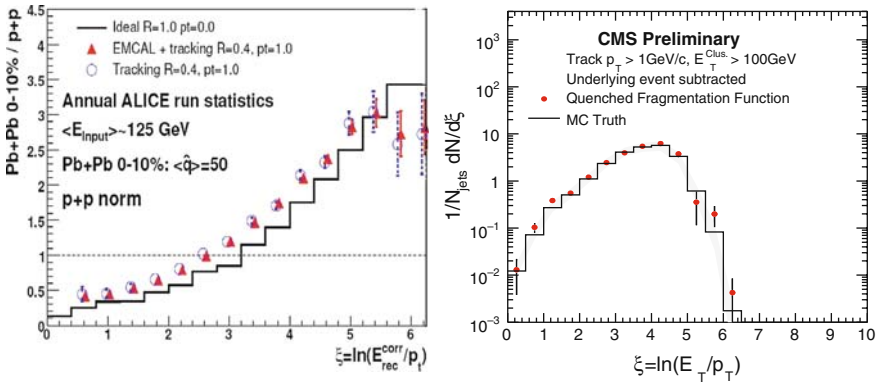

Fig. 35 Medium-modified FF (*right*) and ratio FF(med)/FF(vac) (*left*) as a function of ξ for quenched partons obtained in γ-jet simulations for central PbPb at 5.5 TeV (0.5 nb^{-1}) in ALICE (*left*) [242, 258] and CMS (*right*) [259]

7 Summary

We have reviewed the main theoretical motivations behind the experimental study of parton scattering and jet fragmentation in the hot and dense QCD matter created in high-energy nucleus–nucleus collisions. The phenomenology of parton energy loss has been summarised as well as the main experimental results on single inclusive spectra and di-hadron correlations measured at high transverse momentum, mainly in AuAu reactions at RHIC collider energies ($\sqrt{s_{NN}} = 200$ GeV). The "tomographic" analysis of jet structure modifications in AA collisions provides quantitative information on the thermodynamical and transport properties of the strongly interacting medium produced in the reactions. Two notable experimental results have been discussed in detail: (i) the observed factor ~5 suppression of

high-p_T leading hadrons and (ii) the strongly distorted azimuthal distributions of secondary hadrons emitted in the away-side hemisphere of a high-p_T trigger hadron, in central AuAu relative to pp collisions in free space. Most of the properties of the observed high-p_T single hadron and di-hadron suppression (such as its magnitude, light flavour "universality", p_T, reaction centrality, path-length, and $\sqrt{s_{NN}}$ dependences) are in quantitative agreement with the predictions of parton energy loss models. The confrontation of these models to the data permits to derive the initial gluon density $dN^g/dy \approx 1400$ and transport coefficient $\langle \hat{q} \rangle \approx 13$ GeV^2/fm of the produced medium at RHIC.

In the last section of this document, we have reviewed the details of jet reconstruction in heavy-ion collisions: jet algorithms, underlying-event background subtraction, and jet energy corrections. The analysis of jet shapes and the extraction of medium-modified parton-to-hadron fragmentation functions at low- and high-hadron momenta promise to shed more light onto the mechanisms of parton energy loss in QCD matter at the coming LHC energies. The study of jet quenching phenomena is significantly expanding our knowledge of the dynamics of the strong interaction at extreme conditions of temperature and density.

Acknowledgments DdE would like to thank Sourav Sarkar, Helmut Satz, and Bikash Sinha for their kind invitation to lecture at the 2008 Jaipur QGP Winter School and for the excellent atmosphere and hospitality at the school. DdE acknowledges support by the 6th EU Framework Programme contract MEIF-CT-2005-025073. The work of B.B. is supported by BMBF and by the Helmholtz Research School H-QM.

References

1. D. d'Enterria: J. Phys. **G 34**, S53 (2007) 285, 286
2. See e.g. F. Karsch and E. Laermann: arXiv:hep-lat/0305025 285, 306
3. E.V. Shuryak: Sov. Phys. JETP **47**, 212 (1978) 285
4. E.V. Shuryak: Zh. Eksp. Teor. Fiz. **74**, 408 (1978)
5. J.C. Collins and M.J. Perry: Phys. Rev. Lett. **34**, 1353 (1975)
6. B.A. Freedman and L.D. McLerran: Phys. Rev. **D 16**, 1169 (1977) 285
7. A. Accardi et al.: arXiv:hep-ph/0310274 287
8. V.N. Gribov and L.N. Lipatov: Sov. J. Nucl. Phys. **15**, 438 (1972) 287
9. V.N. Gribov and L.N. Lipatov: Yad. Fiz. **15**, 781 (1972)
10. G. Altarelli and G. Parisi: Nucl. Phys. **B 126**, 298 (1977)
11. Y.L. Dokshitzer: Sov. Phys. JETP **46**, 641 (1977)
12. Y.L. Dokshitzer: Zh. Eksp. Teor. Fiz. **73**, 1216 (1977) 287, 292
13. J.D. Bjorken: FERMILAB-PUB-82–059-THY (1982) 287, 292
14. P. Arnold: arXiv:0808.2767 [hep-ph] 288, 304
15. P. Arnold and W. Xiao: arXiv:0810.1026 [hep-ph]
16. R. Baier and Y. Mehtar-Tani: arXiv:0806.0954 [hep-ph] 288
17. R. Baier and D. Schiff: JHEP **0609**, 059 (2006) 288
18. S. Peigné and A.V. Smilga: arXiv:0810.5702 [hep-ph] 290, 291, 294
19. W.M. Yao et al. [Particle Data Group]: J. Phys. **G 33**, 1 (2006) 290
20. A.B. Migdal: Phys. Rev. **103**, 1811 (1956) 291
21. A. Peshier: Phys. Rev. Lett. **97**, 212301 (2006) 291, 292, 319
22. S. Peigné and A. Peshier: Phys. Rev. **D 77**, 114017 (2008) 291, 292, 319

23. R.K. Ellis, W.J. Stirling and B.R. Webber: *QCD and Collider Physics*, Camb. Monogr. Part. Phys. Nucl. Phys. Cosmol. **8**, 1 (1996) 291
24. E. Braaten and M.H. Thoma: Phys. Rev. **D 44**, 2625 (1991) 292
25. B.G. Zakharov: JETP Lett. **86**, 444 (2007) 292
26. M. Gyulassy and M. Plümer: Phys. Lett. **B243**, 432 (1990) 292, 294, 307
27. X.N. Wang, M. Gyulassy: Phys. Rev. Lett. **68**, 1480 (1992) 294, 307
28. R. Baier, Y.L. Dokshitzer, A.H. Mueller, S. Peigné and D. Schiff: Nucl. Phys. **B484**, 265 (1997)
29. R. Baier, D. Schiff and B.G. Zakharov: Ann. Rev. Nucl. Part. Sci. **50**, 37 (2000)
30. M. Gyulassy, P. Levai and I. Vitev: Phys. Rev. Lett. **85**, 5535 (2000) 295
31. M. Gyulassy, P. Levai and I. Vitev: Nucl. Phys. **B594**, 371 (2001) 295
32. U.A. Wiedemann: Nucl. Phys. **B 588**, 303 (2000) 292, 299, 300
33. Y.L. Dokshitzer and D.E. Kharzeev: Phys. Lett. **B 519**, 199 (2001) 294
34. G.Y. Qin et al.: Phys. Rev. Lett. **100**, 072301 (2008) 293
35. S. Wicks, W. Horowitz, M. Djordjevic and M. Gyulassy: Nucl. Phys. **A 784**, 426 (2007) 293, 299, 301
36. D.A. Appel: Phys. Rev. **D 33**, 717 (1986) 294
37. J.P. Blaizot and L.D. McLerran: Phys. Rev. D **34**, 2739 (1986) 294
38. C.A. Salgado and U.A. Wiedemann: Phys. Rev. Lett. **93**, 042301 (2004) 294, 296, 331
39. N. Borghini and U.A. Wiedemann: arXiv:hep-ph/0506218 296, 305, 332
40. N. Armesto, L. Cunqueiro and C.A. Salgado: arXiv:0809.4433 [hep-ph] 296, 305, 331
41. R. Perez-Ramos: arXiv:0811.2418 [hep-ph] 332
42. R. Perez-Ramos: arXiv:0811.2934 [hep-ph] 332
43. S. Kretzer: Acta Phys. Polon. **B 36**, 179 (2005) 294
44. H. Stoecker: Nucl. Phys. **A750**, 121 (2005) 295, 323
45. L.M. Satarov, H. Stoecker and I.N. Mishustin: Phys. Lett. **B 627**, 64 (2005)
46. J. Casalderrey-Solana, E.V. Shuryak and D. Teaney: J. Phys. Conf. Ser. **27**, 22 (2005) 324
47. J. Casalderrey-Solana, E.V. Shuryak and D. Teaney: Nucl. Phys. **A 774**, 577 (2006) 324
48. J. Ruppert and B. Muller: Phys. Lett. **B618**, 123 (2005) 295, 323, 324
49. I.M. Dremin: Nucl. Phys. **A 767**, 233 (2006)
50. A. Majumder and X.N.Wang: nucl-th/0507062
51. V. Koch, A. Majumder and X.N. Wang: nucl-th/0507063 295, 323, 324
52. F. Arleo, P. Aurenche, Z. Belghobsi and J.P. Guillet: JHEP **0411**, 009 (2004) 295, 332
53. I.P. Lokhtin, A.V. Sherstnev and A.M. Snigirev: Phys. Lett. **B 599**, 260 (2004) 295
54. I. Vitev, S. Wicks and B.W. Zhang: arXiv:0810.2807 [hep-ph] 296, 331
55. F. Arleo: arXiv:0810.1193 [hep-ph] 296, 299
56. N. Armesto, L. Cunqueiro, C.A. Salgado and W.C. Xiang: JHEP **0802**, 048 (2008) 296, 305, 332
57. N. Armesto, C. Pajares and P. Quiroga-Arias: arXiv:0809.4428 [hep-ph] 296, 332
58. J.C. Collins, D.E. Soper and G. Sterman: Nucl. Phys. **B 261**, 104 (1985) 296
59. See e.g. D. d'Enterria: nucl-ex/0302016 298
60. A. Majumder: J. Phys. **G 34**, S377 (2007) 299
61. B.G. Zakharov: JETP Lett. **63**, 952 (1996) 299
62. B.G. Zakharov: JETP Lett. **65**, 615 (1997)
63. B.G. Zakharov: Phys. Atom. Nucl. **61**, 838 (1998)
64. B.G. Zakharov: Yad. Fiz. **61**, 924 (1998)
65. R. Baier, Y.L. Dokshitzer, A.H. Müller, S. Peigné and D. Schiff: Nucl. Phys. **B 483**, 291 (1997) 299
66. R. Baier, Y.L. Dokshitzer, A.H. Müller, S. Peigné and D. Schiff: Nucl. Phys. **B 484**, 265 (1997) 299, 300
67. U.A. Wiedemann: Nucl. Phys. **B 582**, 409 (2000) 299
68. C.A. Salgado and U.A. Wiedemann: Phys. Rev. Lett. **89**, 092303 (2002) 299, 300
69. C.A. Salgado and U.A. Wiedemann: Phys. Rev. **D 68**, 014008 (2003) 299, 300
70. M. Gyulassy, P. Levai and I. Vitev: Nucl. Phys. **B 571**, 197 (2000) 299, 301
71. M. Gyulassy, P. Levai and I. Vitev: Nucl. Phys. **B 594**, 371 (2001) 301

72. M. Gyulassy, P. Levai and I. Vitev: Phys. Lett. **B 538**, 282 (2002) 301
73. M. Djordjevic and M. Gyulassy: Nucl. Phys. **A 733**, 265 (2004) 299, 301
74. X.F. Guo and X.N. Wang: Phys. Rev. Lett. **85**, 3591 (2000) 299, 302, 313
75. X.N. Wang and X.F. Guo: Nucl. Phys. **A 696**, 788 (2001)
76. B.W. Zhang and X.N. Wang: Nucl. Phys. **A 720**, 429 (2003) 302
77. A. Majumder, E. Wang and X.N. Wang: Phys. Rev. Lett. **99**, 152301 (2007)
78. A. Majumder and B. Muller: Phys. Rev. **C 77**, 054903 (2008)
79. A. Majumder, R.J. Fries and B. Muller: Phys. Rev. **C 77**, 065209 (2008) 299
80. P. Arnold, G.D. Moore and L.G. Yaffe: JHEP **0111**, 057 (2001) 299, 303
81. P. Arnold, G.D. Moore and L.G. Yaffe: JHEP **0011**, 001 (2000)
82. S. Jeon and G.D. Moore: Phys. Rev. **C 71**, 034901 (2005) 303, 314
83. S. Turbide, C. Gale, S. Jeon and G.D. Moore: Phys. Rev. **C 72**, 014906 (2005) 299, 303, 310
84. R. Baier, Y.L. Dokshitzer, A.H. Müller and D. Schiff: Phys. Rev. **C 58**, 1706 (1998) 299
85. R. Baier, Y.L. Dokshitzer, A.H. Müller and D. Schiff: Nucl. Phys. **B 531**, 403 (1998) 299
86. R. Baier: Nucl. Phys. **A 715**, 209 (2003) 300, 301
87. U.A. Wiedemann: Nucl. Phys. **A 690**, 731 (2001) 300
88. N. Armesto, C.A. Salgado and U.A. Wiedemann: Phys. Rev. **D 69**, 114003 (2004) 300
89. A. Dainese, C. Loizides and G. Paic: Eur. Phys. J. **C 38**, 461 (2005) 300, 310, 311, 314, 315
90. C. Loizides: Eur. Phys. J. **C 49**, 339 (2007) 300, 315
91. M. Gyulassy and X.N. Wang: Nucl. Phys. **B 420**, 583 (1994) 301
92. M. Gyulassy, P. Levai and I. Vitev: Phys. Rev. Lett. **85**, 5535 (2000) 301
93. I. Vitev: J. Phys. Conf. Ser. **50**, 119 (2006) 301
94. J.W. Qiu and G. Sterman: Nucl. Phys. **B 353**, 105 (1991) 302
95. J.W. Qiu and G. Sterman: Nucl. Phys. **B 353**, 137 (1991)
96. M. Luo, J.W. Qiu and G. Sterman: Phys. Rev. **D 50**, 1951 (1994) 302
97. A. Majumder and X.N. Wang: arXiv:0806.2653 [nucl-th] 302
98. P. Arnold, G.D. Moore and L.G. Yaffe: JHEP **0112**, 009 (2001) 303
99. P. Arnold, G.D. Moore and L.G. Yaffe: JHEP **0206**, 030 (2002) 303
100. A. Adare et al. [PHENIX Collaboration]: Phys. Rev. Lett. **101**, 232301 (2008) 304, 309, 310, 311, 312, 315
101. S.A. Bass et al.: arXiv:0805.3271 [nucl-th] 304, 305
102. K. Eskola, H. Honkanen, C. Salgado and U. Wiedemann: Nucl. Phys. **A 747**, 511 (2005) 305, 307, 314
103. K. Zapp, G. Ingelman, J. Rathsman, J. Stachel and U.A. Wiedemann: arXiv:0804.3568 305
104. S. Domdey, G. Ingelman, H.J. Pirner, J. Rathsman, J. Stachel and K. Zapp: arXiv:0802.3282 [hep-ph]
105. T. Renk: Phys. Rev. **C 78**, 034908 (2008) 305
106. T. Sjostrand, S. Mrenna and P. Skands: JHEP **0605**, 026 (2006) 305
107. G. Corcella et al.: arXiv:hep-ph/0210213 305
108. I.P. Lokhtin and A.M. Snigirev: Eur. Phys. J. **C 45**, 211 (2006) 305
109. I.P. Lokhtin, L.V. Malinina, S.V. Petrushanko, A.M. Snigirev, I. Arsene and K. Tywoniuk: arXiv:0810.2082 [hep-ph] 305
110. E. Shuryak: Prog. Part. Nucl. Phys. **53**, 273 (2004) 306
111. T.D. Lee: Nucl. Phys. **A 750**, 1 (2005)
112. M. Gyulassy and L. McLerran: Nucl. Phys. **A 750**, 30 (2005) 306
113. J.M. Maldacena: Adv. Theor. Math. Phys. **2**, 231 (1998) 306
114. J.M. Maldacena: Int. J. Theor. Phys. **38**, 1113 (1999)
115. E. Witten: Adv. Theor. Math. Phys. **2**, 505 (1998) 306
116. K. Kajantie, T. Tahkokallio and J.T. Yee: JHEP **0701**, 019 (2007) 306
117. P. Kovtun, D.T. Son and A.O. Starinets: Phys. Rev. Lett. **94**, 111601 (2005) 306
118. H. Liu, K. Rajagopal and U.A. Wiedemann: Phys. Rev. Lett. **97**, 182301 (2006) 306
119. C.P. Herzog, A. Karch, P. Kovtun, C. Kozcaz and L.G. Yaffe: JHEP **0607**, 013 (2006) 306, 307, 319
120. J. Casalderrey-Solana and D. Teaney: Phys. Rev. **D 74**, 085012 (2006) 307
121. J. Casalderrey-Solana and D. Teaney: JHEP **0704**, 039 (2007)
122. S.S. Gubser: Phys. Rev. **D 74**, 126005 (2006) 306, 307, 319

123. H. Liu, K. Rajagopal and U.A. Wiedemann: JHEP **0703**, 066 (2007) 306
124. J. Casalderrey-Solana and C.A. Salgado: Acta Phys. Polon. **B 38**, 3731 (2007) 306, 307
125. B.I. Abelev et al. [STAR Collaboration]: Phys. Rev. Lett. **97**, 252001 (2006) 307, 308
126. J. Adams et al. [STAR Collaboration]: Phys. Rev. Lett. **91**, 172302 (2003) 307, 308, 310, 311
127. S.S. Adler et al. [PHENIX Collaboration]: Phys. Rev. Lett. **91**, 241803 (2003) 307, 308
128. S.S. Adler et al. [PHENIX Collaboration]: Phys. Rev. Lett. **98**, 012002 (2007) 307
129. A. Adare et al. [PHENIX Collaboration]: Phys. Rev. Lett. **97**, 252002 (2006) 307, 308
130. I. Arsene et al. [BRAHMS Collaboration]: Phys. Rev. Lett. **93**, 242303 (2004) 307, 308
131. F. Aversa, P. Chiappetta, M. Greco and J.P. Guillet: Nucl. Phys. **B 327**, 105 (1989) 307, 308, 309, 310, 317, 318
132. B. Jager, A. Schafer, M. Stratmann and W. Vogelsang: Phys. Rev. **D 67**, 054005 (2003)
133. W. Vogelsang (private communication) 309, 310, 317, 318
134. L.E. Gordon and W. Vogelsang: Phys. Rev. **D 48**, 3136 (1993)
135. L.E. Gordon: Phys. Rev. **D 50**, 6753 (1994)
136. W. Vogelsang (private communication)
137. P. Aurenche, A. Douiri, R. Baier, M. Fontannaz and D. Schiff: Phys. Lett. **B 140**, 87 (1984)
138. P. Aurenche, R. Baier, M. Fontannaz and D. Schiff: Nucl. Phys. **B 297**, 661 (1988) 307, 308
139. M. Cacciari, P. Nason and R. Vogt: Phys. Rev. Lett. **95**, 122001 (2005) 307, 308
140. J. Pumplin, D.R. Stump, J. Huston, H.L. Lai, P.M. Nadolsky and W.K. Tung: JHEP **0207**, 012 (2002) 307
141. B.A. Kniehl, G. Kramer and B. Potter: Nucl. Phys. **B 597**, 337 (2001) 307
142. S. Kretzer: Phys. Rev. **D 62**, 054001 (2000) 307
143. S.S. Adler et al. [PHENIX Collaboration]: Phys. Rev. Lett. **91**, 072303 (2003) 308, 309
144. S.S. Adler et al. [PHENIX Collaboration]: Phys. Rev. Lett. **98**, 172302 (2007) 308, 309
145. R. Vogt: Phys. Rev. **C 71**, 054902 (2005) 308, 309
146. V. Guzey, M. Strikman and W. Vogelsang: Phys. Lett. **B 603**, 173 (2004) 308, 309
147. K.J. Eskola, V.J. Kolhinen and C.A. Salgado: Eur. Phys. J. **C 9**, 61 (1999) 308, 309
148. A. Accardi, F. Arleo, W.K. Brooks, D. d'Enterria and V. Muccifora: Riv. Nuovo Cim. (2009), to appear; arXiv:0907.3534 [nucl-th] 308, 320
149. J.W. Cronin, H.J. Frisch, M.J. Shochet, J.P. Boymond, R. Mermod, P.A. Piroue and R.L. Sumner: Phys. Rev. **D 11**, 3105 (1975) 308
150. D. Antreasyan, J.W. Cronin, H.J. Frisch, M.J. Shochet, L. Kluberg, P.A. Piroue and R.L. Sumner: Phys. Rev. **D 19**, 764 (1979) 308
151. J. Adams et al. [STAR Collaboration]: Phys. Lett. **B 637**, 161 (2006) 308, 318
152. A. Adare et al. [PHENIX Collaboration]: Phys. Rev. **D 76**, 051106 (2007) 309, 310
153. S.S. Adler et al. [PHENIX Collaboration]: Phys. Rev. Lett. **91**, 072301 (2003) 310, 313
154. S.S. Adler et al. [PHENIX Collaboration]: Phys. Rev. Lett. **96**, 202301 (2006) 310, 311
155. S.S. Adler et al. [PHENIX Collaboration]: Phys. Rev. **C69**, 034910 (2004) 310
156. S.S. Adler et al. [PHENIX Collaboration]: Phys. Rev. Lett. **94**, 232301 (2005) 310, 311
157. B. Muller: Phys. Rev. **C 67**, 061901 (2003) 310
158. S.S. Adler et al. [PHENIX Collaboration]: Phys. Rev. **C 76**, 034904 (2007) 310, 316, 317
159. A. Adare et al. [PHENIX Collaboration]: arXiv:0804.4168 [nucl-ex] 311
160. I. Vitev and M. Gyulassy: Phys. Rev. Lett. **89**, 252301 (2002) 310, 311, 313, 314, 315
161. I. Vitev: J. Phys. **G 30**, S791 (2004) 310, 311, 313, 314, 315
162. A. Adare et al. [PHENIX Collaboration]: Phys. Rev. **C 77**,064907 (2008) 310, 311
163. D. Molnar and M. Gyulassy: Nucl. Phys. **A 697**, 495 (2002) 312
164. D. Molnar and M. Gyulassy: Nucl. Phys. **A 703** (2002) 893 [Erratum] 312
165. S.A. Bass et al.: arXiv:0808.0908 [nucl-th] 312
166. S.S. Adler et al. [PHENIX Collaboration]: Phys. Rev. **C 71**, 034908 (2005) 313, 314, 326
167. S.S. Adler et al. [PHENIX Collaboration]: Phys. Rev. **C 71**, 049901 (2005) [Erratum] 313, 314, 326
168. M.M. Aggarwal et al. [WA98 Collaboration]: Eur. Phys. J. **C 23**, 225 (2002) 313, 315
169. D. d'Enterria: Phys. Lett. **B 596**, 32 (2004) 313, 314, 315

170. H. Buesching: Eur. Phys. J. **C 49**, 41 (2006) 313
171. I. Vitev: Phys. Lett. **B 606**, 303 (2005) 313, 314
172. M.M. Aggarwal et al. [WA98 Collaboration]: Phys. Rev. Lett. **100**, 242301 (2008) 314
173. S. Jeon, J. Jalilian-Marian and I. Sarcevic: Phys. Lett. **B 562**, 45 (2003) 314
174. B. Alessandro et al. [ALICE Collaboration]: J. Phys. **G 32**, 1295 (2006) 315, 328, 329
175. N. Grau [ATLAS Collaboration]: J. Phys. **G 35**, 104040 (2008) 315
176. D. d'Enterria et al. (eds.) [CMS Collaboration]: J. Phys. **G 34**, 2307 (2007) 315, 329
177. I. Vitev: Phys. Lett. **B 639**, 38 (2006) 315
178. A. Adare et al. [PHENIX Collaboration]: Phys. Rev. Lett. **101**, 162301 (2008) 315, 316
179. K. Reygers [PHENIX Collaboration]: J. Phys. **G 35**, 104045 (2008) 315, 316
180. V.S. Pantuev: JETP Lett. **85**, 104 (2007) 317
181. D. d'Enterria: Eur. Phys. J. **C43**, 295 (2005) 317, 318
182. Q. Wang and X.N. Wang: Phys. Rev. **C71**, 014903 (2005) 317, 318
183. B. Mohanty [STAR Collaboration]: J. Phys. **G 35**, 104006 (2008) 318
184. I. Vitev: J. Phys. **G 35**, 104011 (2008) 318, 319
185. R.C. Hwa and C.B. Yang: Phys. Rev. **C67**, 034902 (2003) 318
186. R.J. Fries, B. Muller, C. Nonaka and S.A. Bass: Phys. Rev. **C68**, 044902 (2003)
187. V. Greco, C.M. Ko and P. Levai: Phys. Rev. Lett. **90**, 202302 (2003) 318
188. S.S. Adler et al. [PHENIX Collaboration]: Phys. Rev. Lett. **96**, 032301 (2006) 319
189. A. Adare et al. [PHENIX Collaboration]: Phys. Rev. Lett. **98**, 172301 (2007)
190. B.I. Abelev et al. [STAR Collaboration]: Phys. Rev. Lett. **98**, 192301 (2007) 319
191. M. Djordjevic, M. Gyulassy and S. Wicks: Phys. Rev. Lett. **94**, 112301 (2005) 319
192. N. Armesto, A. Dainese, C. Salgado and U.Wiedemann: Phys. Rev. **D71**, 054027 (2005) 319
193. Y. Morino [PHENIX Collaboration]: J. Phys. **G 35**, 104116 (2008) 319
194. A. Mischke [STAR Collaboration]: J. Phys. **G 35**, 104117 (2008) 319
195. M. Cacciari, P. Nason and R. Vogt: Phys. Rev. Lett. **95**, 122001 (2005) 319
196. A. Adil and I. Vitev: Phys. Lett. **B 649**, 139 (2007) 319, 320
197. M.G. Mustafa: Phys. Rev. **C 72**, 014905 (2005) 319
198. M. Djordjevic: Phys. Rev. **C 74**, 064907 (2006) 319
199. S. Caron-Huot and G.D. Moore: JHEP **0802**, 081 (2008) 319
200. H. van Hees, M. Mannarelli, V. Greco and R. Rapp: Phys. Rev. Lett. **100**, 192301 (2008) 320
201. P.R. Sorensen and X. Dong: Phys. Rev. **C 74**, 024902 (2006) 320
202. G. Martinez-Garcia, S. Gadrat and P. Crochet: Phys. Lett. **B 663**, 55 (2008) 320
203. C. Adler et al. [STAR Collaboration]: Phys. Rev. Lett. **90**, 082302 (2003) 320, 321, 322
204. J. Adams et al. [STAR Collaboration]: Phys. Rev. Lett. **95**, 152301 (2005) 321
205. S.S. Adler et al. [PHENIX Collaboration]: Phys. Rev. Lett. **97** 052301 (2006) 320, 321, 323
206. N.N. Ajitanand et al.: Phys. Rev. **C 72**, 011902 (2005) 320
207. J. Jia: arXiv:0810.0051 [nucl-ex] 321
208. A. Adare et al. [PHENIX Collaboration]: Phys. Rev. **C 77**, 011901 (2008) 321
209. A. Adare et al. [PHENIX Collaboration]: Phys. Rev. **C 78**, 014901 (2008) 321, 322, 323, 324
210. M.J. Tannenbaum: Int. J. Mod. Phys. **E 16**, 2011 (2007) 321
211. H. Zhang, J.F. Owens, E. Wang and X.N. Wang: Phys. Rev. Lett. **98**, 212301 (2007) 322
212. J. Adams et al. [STAR Collaboration]: Phys. Rev. Lett. **97**, 162301 (2006) 322
213. M.J. Horner [STAR Collaboration]: J. Phys. **G 34**, S995 (2007) 323
214. A.D. Polosa and C.A. Salgado: Phys. Rev. **C 75**, 041901 (2007) 323
215. J.G. Ulery: J. Phys. **G 35**, 104032 (2008) 324
216. B.I. Abelev et al. [STAR Collaboration]: arXiv:0805.0622 [nucl-ex] 324
217. N.N. Ajitanand [PHENIX Collaboration]: Nucl. Phys. **A 783**, 519 (2007) 324
218. S.S. Gubser, S.S. Pufu and A. Yarom: Phys. Rev. Lett. **100**, 012301 (2008) 324
219. P.M. Chesler and L.G. Yaffe: Phys. Rev. **D 78**, 045013 (2008) 324
220. R.B. Neufeld, B. Muller and J. Ruppert: Phys. Rev. **C 78**, 041901 (2008) 324
221. H. Stoecker: Nucl. Phys. **A 750**, 121 (2005) 324
222. J. Casalderrey-Solana, E.V. Shuryak and D. Teaney: Nucl. Phys. **A 774**, 577 (2006)

223. B. Betz, M. Gyulassy, D.H. Rischke, H. Stocker and G. Torrieri: J. Phys. **G 35**, 104106 (2008) 324
224. B. Betz, J. Noronha, G. Torrieri, M. Gyulassy, I. Mishustin and D.H. Rischke: arXiv:0812.4401 [nucl-th] 324
225. J. Noronha, M. Gyulassy, and G. Torrieri: arXiv:0807.1038 [hep-ph]
226. M. Gyulassy, J. Noronha and G. Torrieri: arXiv:0807.2235 [hep-ph]
227. B. Betz, M. Gyulassy, J. Noronha and G. Torrieri: arXiv:0807.4526 [hep-ph] 325
228. R.B. Neufeld: Phys. Rev. **D 78**, 085015 (2008)
229. R.B. Neufeld: arXiv:0810.3185 [hep-ph] 324
230. J. Putschke: J. Phys. **G 34**, S679 (2007) 325
231. M. van Leeuwen [STAR collaboration]: arXiv:0808.4096 [nucl-ex] 325
232. C.A. Pruneau, S. Gavin and S.A. Voloshin: Nucl. Phys. **A 802**, 107 (2008) 325
233. A. Dumitru, F. Gelis, L. McLerran and R. Venugopalan: Nucl. Phys. **A 810**, 91 (2008) 325
234. B. Alver et al. [PHOBOS Collaboration]: J. Phys. **G 35**, 104080 (2008) 325
235. S.D. Ellis, J. Huston, K. Hatakeyama, P. Loch and M. Tonnesmann: Prog. Part. Nucl. Phys. **60**, 484 (2008) 326, 327
236. C. Buttar et al.: arXiv:0803.0678 [hep-ph] 326, 327
237. S. Catani, Y.L. Dokshitzer, M.H. Seymour and B.R. Webber: Nucl. Phys. **B 406**, 187 (1993) 326
238. G.P. Salam and G. Soyez: JHEP **0705**, 086 (2007) 326
239. M. Cacciari and G.P. Salam: Phys. Lett. **B 641**, 57 (2006) 326, 328
240. M. Cacciari and G.P. Salam: Phys. Lett. **B 659**, 119 (2008) 326, 329
241. M. Cacciari, G.P. Salam and G. Soyez: JHEP **0804**, 005 (2008) 328, 329
242. A. Morsch [ALICE Collaboration]: AIP Conf. Proc. **1026**, 72 (2008) 326, 333
243. S.L. Blyth et al.: J. Phys. **G 34**, 271 (2007) 326
244. O. Kodolova, I. Vardanian, A. Nikitenko and A. Oulianov: Eur. Phys. J. **C 50**, 117 (2007) 326, 329
245. M. Cacciari, G.P. Salam and G. Soyez: JHEP **0804**, 063 (2008) 327, 328
246. S.D. Ellis and D.E. Soper: Phys. Rev. **D 48**, 3160 (1993) 328
247. M. Wobisch and T. Wengler: arXiv:hep-ph/9907280 328
248. M. Gyulassy and X.N. Wang: Comput. Phys. Commun. **83**, 307 (1994) 329
249. J. Putschke [STAR Collaboration]: Eur. Phys. J. **C61**, 629 (2009), arXiv:0809.1419 329
250. S. Salur [STAR Collaboration]: arXiv:0810.0500 [nucl-ex] 329
251. G.L. Bayatian et al. [CMS Collaboration]: J. Phys. **G 34**, 995 (2007) 329, 330
252. M. Dasgupta, L. Magnea and G.P. Salam: JHEP **0802**, 055 (2008) 330
253. D.E. Acosta et al. [CDF Collaboration]: Phys. Rev. **D 71**, 112002 (2005) 331
254. Y.L. Dokshitzer, V.A. Khoze, A.H. Mueller and S.I. Troian: *Basics of Perturbative QCD*, p. 274, Ed. Frontières, Gif-sur-Yvette, France (1991) 331
255. Y.I. Azimov, Y.L. Dokshitzer, V.A. Khoze and S.I. Troyan: Z. Phys. **C 27**, 65 (1985) 332
256. N. Borghini: Eur. Phys. J. **C 49**, 327 (2007) 332
257. X.N. Wang, Z. Huang and I. Sarcevic: Phys. Rev. Lett. **77**, 231 (1996) 332
258. G. Conesa, H. Delagrange, J. Diaz, Y.V. Kharlov and Y. Schutz: Nucl. Instrum. Meth. **A 585**, 28 (2008) 333
259. C. Loizides [CMS Collaboration]: J. Phys. **G 35**, 104166 (2008) 333

In Search of the QCD–Gravity Correspondence

Theodor Braşoveanu, Dmitri Kharzeev, and Mauricio Martinez

Abstract Quantum chromodynamics (QCD) is the fundamental theory of strong interactions. It describes the behavior of quarks and gluons which are the smallest known constituents of nuclear matter. The difficulties in solving the theory at low energies in the strongly interacting, non-perturbative regime have left unanswered many important questions in QCD, such as the nature of confinement or the mechanism of hadronization. In these lectures oriented toward the students we introduce two classes of dualities that attempt to reproduce many of the features of QCD, while making the treatment at strong coupling more tractable: (1) the AdS/CFT correspondence between a specific class of string theories and a conformal field theory and (2) an effective low-energy theory of QCD dual to classical QCD on a curved conformal gravitational background. The hope is that by applying these dualities to the evaluation of various properties of the strongly interacting matter produced in heavy-ion collisions, one can understand how QCD behaves at strong coupling. We give an outline of the applications, with emphasis on two transport coefficients of QCD matter – shear and bulk viscosities.

1 Introduction

Recent results from the Relativistic Heavy Ion Collider (RHIC) at BNL reveal surprising dynamical properties of the strongly coupled quark–gluon plasma (sQGP). Some of these properties may be explained through two less than traditional methods that employ dualities to reformulate the underlying gauge theory in curved conformal gravitational backgrounds.

T. Braşoveanu (✉)
Department of Physics, Princeton University, Princeton, NJ 08544, USA,
tbrasove@princeton.edu

D. Kharzeev
Department of Physics, Brookhaven National Laboratory, Upton, NY 11973-5000, USA,
kharzeev@bnl.gov

M. Martinez
Helmholtz Research School and Otto Stern School, Goethe-Universität Frankfurt am Main, Germany, guerrero@fias.uni-frankfurt.de

Braşoveanu, T. et al.: *In Search of the QCD–Gravity Correspondence*. Lect. Notes Phys. **785**, 341–369 (2010)
DOI 10.1007/978-3-642-02286-9_10

The first approach is inspired by string theory and is based on the Anti de Sitter/conformal field theory (AdS/CFT) gravity/gauge theory duality [1–3]. This correspondence maps conformal strongly coupled SU(N_c) gauge theories (i.e., with large 't Hooft coupling $\lambda = g^2 N_c$) onto a weakly coupled dual gravity theory. This formalism has been applied to conformal gauge theories that share some features with QCD, such as a maximally super-symmetric $\mathcal{N} = 4$ Yang–Mills theory. This leads to interesting predictions for several classes of observables that may be related to the QGP, such as entropy production, transport properties, jet quenching, dijet-bulk correlations (for a review, see [4]).

The second approach introduces an effective low-energy Lagrangian of QCD which satisfies the constraints imposed by the renormalization group, is scale and conformally invariant in the limit of vanishing vacuum energy density, and matches the perturbative behavior at short distances (high energies) [5–7]. This theory has a dual description as classical gluodynamics on a curved conformal space–time background on one hand, and gluodynamics in flat space–time coupled to scalar glueballs (which play the role of dilatons) on the other. In this approach, one may be able to describe confinement as an event horizon for colored particles [8–10], in close analogy to what happens in the vicinity of a black hole. Recent efforts link the bulk viscosity of QCD matter and the associated entropy production to the breaking of scale invariance [11, 12].

2 QCD and Its Properties

Quantum chromodynamics (QCD) is at present universally accepted as the theory of the strong interaction. The fundamental degrees of freedom in the theory are the quarks and gluons that carry color charges. These particles cannot be directly seen in Nature because confinement binds them into the color-neutral bound states – baryons and mesons. QCD has been thoroughly tested in experiment and is known to possess the expected properties: The coupling constant weakens as the resolution scale grows (celebrated "asymptotic freedom" [13, 14]), the quarks and gluons manifest themselves through the production of jets, the partonic constituents of matter are seen in deep inelastic scattering, the corresponding structure functions exhibit scaling violation, etc.

However, in spite of these successes the behavior of the theory at low energies or large distances and the structure of its vacuum state are still poorly understood. One may hope that a progress can be achieved through the studies of thermodynamics of quarks and gluons – if history is any indication, understanding thermodynamic behavior may appear simpler than understanding the dynamics of the individual constituents. At temperatures accessible experimentally, the typical distances between the quarks and gluons in the "quark–gluon plasma" (QGP) are quite large and the coupling is strong. Achieving a progress in the understanding of QGP thus requires methods that apply in the strong coupling domain. In these lectures we will focus on two such methods, with applications to the transport coefficients of the quark–gluon plasma.

2.1 The QCD Lagrangian

QCD is formulated as a gauge theory, in analogy with QED. The structure of QED is entirely fixed by the requirement of invariance under local gauge transformations, that is, invariance with respect to the phase rotation of the electron field $\exp(i\alpha(x))$, where the phase factor α depends on the space–time coordinates. In the case of QCD, we have the constituents – quarks – that come in three different colors, $N_c = 3$. The local gauge invariance with respect to the $SU_c(N_c)$ rotations in color space introduces $N_c^2 - 1 = 8$ gauge bosons, the gluons. Quarks are spin 1/2 particles that belong to the fundamental representation of the $SU_c(3)$ whereas gluons are spin 1 particles defined in the adjoint representation of $SU_c(3)$. Since quarks can have three different colors – say, red, green, and blue – a quark state vector can be expressed as a color multiplet of three components. Interactions with gluons repaint the colors of the quarks; since color rotations do not commute (in other words, $SU_c(3)$ is a non-abelian group) gluons can also interact with each other.

Let us now formulate this mathematically. First, consider the free Lagrangian of quark fields:

$$\mathcal{L}_{\text{free}} = \sum_{q=u,d,s\ldots} \sum_{\text{colors}} \bar{q}(x) \left(\mathrm{i}\gamma_\mu \frac{\partial}{\partial x_\mu} - m_q \right) q(x) \tag{1}$$

and impose its invariance under a gauge transformation of the quark fields defined as

$$U: \qquad q^j(x) \quad \rightarrow \quad U_{jk}(x) q^k(x), \tag{2}$$

with $j, k \in 1 \ldots 3$ (we always sum over repeated indices). The fact that the Lagrangian of the theory is invariant with respect to these gauge transformations implies that all physical observables must be gauge invariant.

Note that in Eq. (2) U is a unitary complex-valued matrix, i.e., $UU^\dagger = U^\dagger U = 1$ and $\det U = 1$. In the fundamental representation of the group these matrices form the group $SU(3)$ with 3 being the number of colors N_c. This group has eight generators T^a_{ij}, $a \in 1,2,\ldots,8$ of the fundamental representation of $SU(3)$, hence the matrix U can be represented as

$$U(x) = \exp(-i\ \phi_a(x)\, T^a). \tag{3}$$

The properties of U imply that the generators T^a_{ij} are Hermitian ($T^a = T^{a\dagger}$) and traceless ($TrT^a = 0$) (check this by making an infinitesimal transformation about unity). These generators satisfy a Lie algebra:

$$[T^a, T^b] = i f_{abc} T^c, \tag{4}$$

where f_{abc} are $SU(3)$ structure constants. This means that unlike QED, QCD is a non-abelian gauge theory: different color rotations do not commute.

After we apply the local gauge transformation to the quark fields, the free Lagrangian given in Eq. (1) acquires some extra terms proportional to $\partial_\mu \phi_a(x)$. In order to keep gauge invariance, it is necessary to compensate for this extra terms. This can be achieved by introducing the gauge field (in QCD, gauge fields will be understood as gluons) A^μ_{kj} and replacing the normal derivative ∂_μ in the free Lagrangian (1) by the so-called covariant derivative:

$$\partial^\mu q^j(x) \quad \rightarrow \quad D^\mu_{kj} q^j(x) \equiv \left\{ \delta_{kj} \partial^\mu - \mathrm{i} A^\mu_{kj}(x) \right\} q^j(x). \tag{5}$$

Note that if we request for a gauge invariance, the Lagrangian written in terms of covariant derivatives is no longer free, so we now have a coupling between quark fields and gauge fields. Under gauge transformations the gauge fields should transform as

$$A^\mu(x) \rightarrow U(x) A^\mu(x) U^\dagger(x) + \mathrm{i} U(x) \partial^\mu U^\dagger(x). \tag{6}$$

So the QCD Lagrangian reads as[1]

$$\mathcal{L}_{\mathrm{QCD}} = \sum_q \bar{q}(x) \left(i \gamma_\mu D^\mu - m_q \right) q(x) - \frac{1}{4g^2} \mathrm{tr}\, G^{\mu\nu}(x) G_{\mu\nu}(x), \tag{7}$$

where

$$D_\mu = \partial_\mu - i A^a_\mu t^a; \tag{8}$$

note that we have included g in the definition of the gauge potential to reveal the dependence of the Lagrangian (7) on the coupling constant; we will need it in what follows.

The first term of Eq. (7) describes the dynamics of the interaction between the quarks and gluons while the second one describes the dynamics of the gluon field. The gluon field strength tensor is given by

$$G^{\mu\nu}(x) \equiv \mathrm{i} \left[D^\mu, D^\nu \right] = \partial^\mu A^\nu(x) - \partial^\nu A^\mu(x) - i \left[A^\mu(x), A^\nu(x) \right] \tag{9}$$

or in terms of the color components A^μ_a of the gauge field:

$$G^{\mu\nu}_a(x) = \partial^\mu A^\nu_a(x) - \partial^\nu A^\mu_a(x) + f_{abc} A^\mu_b(x) A^\nu_c(x). \tag{10}$$

The term $Tr(G^{\mu\nu}(x) G_{\mu\nu}(x))$ is also gauge invariant because $Tr\,(U G_{\mu\nu} G^{\mu\nu} U^\dagger) = Tr\,(G_{\mu\nu} G^{\mu\nu})$. Note that the term $Tr\,(G_{\mu\nu} G^{\mu\nu})$ for the given stress tensor has nonlinear couplings between the gauge fields themselves. Such self-interactions are responsible for the complexity of QCD dynamics.

[1] Hereafter we will omit color indices explicitly.

2.2 Asymptotic Freedom

One of the most remarkable properties of QCD is related to the fact that at large energies the coupling constant is small, i.e., perturbation theory is applicable. To better understand this aspect, let us first refer to what happens in QED. The electron–positron pairs screen the electric charge. Therefore, the electric charge becomes stronger at short distances. The dependence of the observed effective charge on the distance is given by

$$e^2(r) = \frac{e^2(r_0)}{1 + \dfrac{2e^2(r_0)}{3\pi} \log \dfrac{r}{r_0}}. \tag{11}$$

This result can be obtained by resumming (logarithmically divergent and regularized at the distance r_0) electron–positron loops dressing the virtual photon propagator.

The running of the coupling constant with the distance prescribed by Eq. (11) has some paradoxical consequences. Indeed, at distances $r \gg r_0$ the coupling constant is seen to be independent of the value of the coupling at renormalization scale r_0. Moreover, it vanishes as $\sim \log^{-1}(r/r_0)$ so if we require the coupling constant be finite at r_0, in the local limit of $r_0 \to 0$ the coupling will vanish. This is the so-called Moscow zero discovered by Landau and Pomeranchuk [16]. The possible ways out include the following: (a) We know that QED is not a complete theory; at the scale $r_0 \sim 1/M_Z$ it has to be extended to the electroweak theory; (b) at short distances QED is no longer weakly coupled, and so the perturbative expression (11) cannot be trusted and one should find a true non-perturbative answer.

Instead of the dependence on the distance, we can also use momentum space and consider the dependence of the coupling on the virtuality of the photon, say, $q^2 \equiv Q^2$. In terms of this variable, the expression (11) can be rewritten as

$$\alpha(Q^2) = \frac{\alpha(Q_0^2)}{1 - \dfrac{\alpha(Q_0^2)}{3\pi} \log\left(\frac{Q^2}{Q_0^2}\right)}. \tag{12}$$

The "Moscow zero" in momentum space manifests itself through the singularity at $Q^2 = Q_0^2 \exp(3\pi/\alpha)$; note that since $\alpha \ll 1$, for all particle accelerator energies this pole is very far away and so QED is an excellent effective theory.

In QCD the situation is different. Because of the gluon self-interactions, we have *anti*-screening [13, 14] – the constant coupling becomes small at short distances (high energies) but large at large distances (low energies). In Coulomb gauge, the anti-screening stems from the diagram in which the exchange of a Coulomb gluon excites from the vacuum zero modes of the transverse gluons [17–19]; for review see [20]. This diagram is purely real and leads to a Coulomb interaction that strengthens as the distance grows. As a result, the sign of $\log(Q^2/Q_0^2)$ changes. The final result is given by the expression

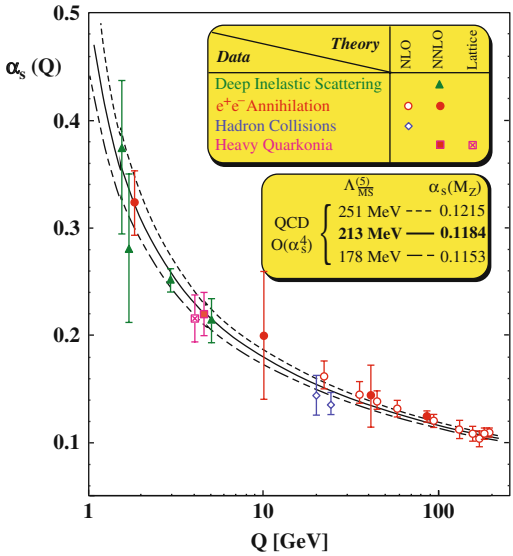

Fig. 1 The running coupling constant $\alpha_s(Q^2)$ as a function of momentum transfer Q^2 determined from a variety of processes; from [15]

$$\alpha_s(Q^2) = \frac{\alpha_s(Q_0^2)}{1 + \frac{\alpha_s(Q_0^2)}{12\pi}(11\,N_C - 2\,N_f)\,\log(Q^2/Q_0^2)}. \tag{13}$$

In Fig. 1 we show the experimental verification of this prediction. Formally speaking, the fact that the coupling constant is small at high energies is related to the negative value of the so-called β-function. We will explain this in detail in Sect. 2.3.

Note that with Eq. (13), no singularity appears in the local limit – so QCD by itself is a fully consistent field theory. However, the pole is still present at small virtuality; it thus could affect all soft processes. This problem is very likely related to confinement of quarks and gluons, and finding the right way of dealing with it is akin to discovering the Holy Grail for the QCD theorists.

2.3 Scale Invariance Breaking in QCD

Scale invariance plays an important role in many subfields of physics. In a scale-invariant theory, the physics looks the same at all scales. Suppose that the action that describes the dynamics of some theory is invariant under dilatations:

$$x \to \lambda x. \tag{14}$$

If this is the case, by Noether theorem, we have a dilatation current s^μ that is conserved and is given by

$$s^{\mu} = x_{\nu}\,\theta^{\mu\nu}, \tag{15}$$

where $\theta^{\mu\nu}$ is the energy–momentum tensor. The conservation law reads as

$$\partial_{\mu} s^{\mu} = \theta^{\mu}_{\mu}. \tag{16}$$

Therefore the divergence of the scale current corresponding to a scale transformation is equal to the trace of the energy–momentum tensor, and a scale-invariant theory will have $\theta^{\mu}_{\mu} = 0$. Deviations from this will indicate a breaking of scale invariance.

As a simple example consider classical electrodynamics without external sources:

$$\mathcal{L} = -\frac{1}{4} F_{\mu\nu} F^{\mu\nu}. \tag{17}$$

From this Lagrangian, it is straightforward to obtain the energy–momentum tensor:

$$\theta^{\mu}_{\nu} = -F^{\mu\rho} F_{\nu\rho} + \frac{1}{4} \delta^{\mu}_{\nu} F_{\rho\sigma} F^{\rho\sigma}. \tag{18}$$

Taking the trace of this tensor, we find that it will vanish in four dimensions since in that case $\delta^{\mu}_{\mu} = 4$; this shows that classical electromagnetism without sources is scale invariant. Indeed, the result is the same at classical level for non-abelian Yang–Mills theories.

However at quantum level this is not true. A simple way to understand this is the following: In quantum theory, the fluctuations can exist at all scales and thus their total energy is infinite. To obtain a finite result, we have to renormalize the theory. We do this at the cost of introducing the renormalization scale which is a dimensionful parameter. Clearly, its presence violates the original classical scale invariance of our theory.

In Sect. 2.2, we mentioned that the coupling constant in gauge theories changes as a function of the virtuality Q^2 due to quantum effects – the fluctuations of the vacuum that dress the propagator of a gauge boson. Because of this, QED and QCD lose the invariance under scaling transformations at quantum level. Indeed, once quantum correction is taken properly, the trace of the energy–momentum tensor calculated from the QCD Lagrangian (7) is [21–26]:

$$\partial^{\mu} s_{\mu} = \Theta^{\mu}_{\mu} = \sum_{q} m_q \bar{q} q + \frac{\beta(g)}{2g^3} \mathrm{tr} \mathrm{G}^{\mu\nu} \mathrm{G}_{\mu\nu}, \tag{19}$$

where $\beta(g)$ is the QCD β-function, which governs the behavior of the running coupling:

$$\mu \frac{dg(\mu)}{d\mu} = \beta(g). \tag{20}$$

As we already discussed in Sect. 2.2, the small value for the coupling α_s at high energies is related to the sign of the β-function which is negative for QCD. This means that the theory is asymptotically free. The leading term in the perturbative expansion is (cf. Eq. (13))

$$\beta(g) = -b\frac{g^3}{(4\pi)^2} + O(g^5), \qquad b = 11N_c - 2N_f, \tag{21}$$

where N_c and N_f are the numbers of colors and flavors, respectively.

The hadron masses are defined as the forward matrix elements of trace of the QCD energy–momentum tensor: $2m_h^2 = \langle h|\Theta^\mu_\mu|h\rangle$ (the factor of $2m_h$ is due to relativistic normalization of states $|h\rangle$. The sum in Eq. (19) runs over all quark flavors, and it might seem that heavy quarks can give a substantial contribution to the masses of light hadrons. However that does not happen since at small virtualities the heavy flavor contribution to the sum (19) is exactly canceled by a corresponding heavy flavor contribution to the β-function [27]. Since the light quarks are light, the dominant contribution to the masses of most light hadrons comes from the gluon term in Eq. (19) – in other words, most of the observable mass in the Universe is due to the energy of gluon interactions.

2.4 Confinement and the Broken Scale Invariance

The asymptotic freedom allows us to probe quarks and gluons at short distances when the coupling constant is small. However, the growth of the coupling at large distances leads to the binding of quarks and gluons into color-singlet hadrons of size ~ 1 fm.

In quantum field theory, the evaluation of scattering amplitudes involves the concept of asymptotic states. However, the fact that quarks and gluons are confined prevents us from using quarks and gluons as asymptotic states within the S matrix approach. An appropriate object for studying confinement of quarks is the so-called Wilson loop [28]:

$$W(R,T) = Tr\left\{P\ exp\left[i\int_C A^a_\mu T^a dx^\mu\right]\right\}, \tag{22}$$

where A^a_μ is the gluon field and T^a is the generator of $SU(3)$. Let us first choose the contour C in the integral as a rectangle with side R in one of the space dimensions and T in the time direction. With this contour we are dealing with the propagation of a heavy static quark and antiquark separated by a distance R propagating in time for a period T. One important property of the Wilson loop is its relation to the potential acting between the static quark and antiquark: when $T \to \infty$,

$$\lim_{T\to\infty} W(R,T) = \exp\left[-TV(R)\right], \tag{23}$$

where $V(R)$ is the static potential between the heavy quarks.

If we now decide to stretch the size of the rectangle in all directions by the same factor ($T \to \lambda T$ and $R \to \lambda R$ simultaneously) one can expect that the value of the Wilson loop will be modified. The only exception is the Coulomb potential, which maintains the scale invariance in the asymptotic value of the Wilson loop:

$$W(R, T) = W(\lambda R, \lambda T), \quad \texttt{if} \quad V(R) \sim 1/R. \tag{24}$$

For QCD, the quark–antiquark potential has the form

$$V(R) = -\frac{4}{3}\frac{\alpha_s(R)}{R} + \sigma R, \tag{25}$$

where σ is the tension of the string stretched between the quark and antiquark. Phenomenology tells us that its value is around $\sim$1 GeV/fm. As one can easily see, both the running coupling and the confinement are in violent contradiction with the scale invariance.

In the limit when $T \to \infty$ and large distances, the asymptotic behavior of the Wilson loop reads approximately as

$$W(R, T) \simeq \exp\left[-\sigma T R\right]. \tag{26}$$

This is the famous "area law" of the Wilson loop that signals confinement.

At finite temperature, various transport properties of QCD matter appear sensitive to confinement. In Sect. 5.3 we discuss the intriguing relation between bulk viscosity and breaking of scale invariance.

3 Black Holes

The concept of a black hole dates back to the eighteenth century, when the British geologist and astronomer Rev. John Mitchell advanced the idea of the existence of a body so massive that the escape velocity at its surface would be equal to the speed of light. In a paper he wrote to the Royal Society in 1783 he concludes that "*all light emitted would be made to return towards it, by its own proper gravity.*" This was due in part to the popularity of the "corpuscular theory" of light at the time, which made possible that light could be affected by gravity in the same way as ordinary matter [29].

The same idea of strong-gravity objects trapping light was proposed by the mathematician Pierre-Simon Laplace in his book *Exposition du Systeme du Monde* in 1796, though it did not gain much consideration throughout the nineteenth century, as the "wave theory" of light was gaining ground.

Later on, upon the advent of general relativity as a new theory of gravity in 1915 and the formulation of Einstein's field equations, relating the curvature of space–time with the matter and energy content within the space–time (via the stress–energy tensor $T_{\mu\nu}$)

$$G_{\mu\nu} = \frac{8\pi G}{c^4} T_{\mu\nu}, \tag{27}$$

the German physicist and astronomer Karl Schwarzschild gave the solution for a static, isotropic gravitational field, predicting the existence of a singularity at $r = 2GM$, the so-called Schwarzschild radius [30]. Schwarzschild introduced a metric

$$ds^2 = c^2 dt^2 (1 - \frac{2GM}{rc^2}) - \frac{dr^2}{1 - \frac{2GM}{rc^2}} - r^2 d\Omega^2, \tag{28}$$

which was proved to be the most general solution of Einstein's equations without matter ($T_{\mu\nu} = 0$) and spherical symmetry – via Birkhoof's theorem in 1923. It was later used by Oppenheimer and Volkoff in 1939 to predict the collapse of massive stars [31]. It was not until the introduction of the Eddington–Finkelstein coordinates in 1958 that the Schwarzschild surface $r = 2GM$ was interpreted as the event horizon of a black hole, acting as a perfect unidirectional membrane. That is, information from outside the boundary was allowed to cross it, but events occurring inside the boundary could in no way affect an outside observer [32].

A major breakthrough came in the 1970s, when Jacob Bekenstein proposed that a black hole should have a finite nonzero entropy and temperature, proportional to the area of its horizon. A finite entropy is in agreement with the second law of thermodynamics. By applying quantum field theory to the curved space–time around the event horizon, Stephen Hawking concluded in 1974 that black holes should emit thermal radiation [33]. He found the temperature of the emitted radiation to be proportional to the acceleration due to gravity of a near-horizon observer

$$T_{BH} = \frac{\hbar c^3}{8\pi G M k_B} \tag{29}$$

and confirmed Bekenstein's conjecture by fixing the constant of proportionality between the entropy and the area of the black hole event horizon. In the equation above, k_B is Boltzmann's constant, G is Newton's gravitational constant, h is Planck's constant, while M is the mass of the black hole.

Interestingly, in gravitational theories the black hole entropy appears to be the maximum entropy that one can squeeze within a fixed volume, and this entropy is proportional to the area A of the black hole horizon:

$$S_{BH} = \frac{k_B A c^3}{4G\hbar}. \tag{30}$$

This is in sharp contradiction to the "usual" physics when the entropy is proportional to the volume of the system. Since the entropy counts the number of degrees of freedom, one may wonder whether the "true" number of degrees of freedom in gravitational theory is smaller than naively expected and whether the dynamics

might be formulated as a dynamics of the surface modes. We will come back to this crucial question shortly.

An interesting consequence of Eq. (29) is that black holes that are less massive than the planet Mercury would become hotter than the cosmic microwave background (about 2.73 K) and would slowly evaporate with time by giving up energy through Hawking radiation. As their mass decreased, their temperature would gradually increase. Thus, small black holes will eventually undergo runaway evaporation and vanish in a burst of radiation.

During the last decade, concerns regarding the formation in high-energy particle accelerators of black holes that would accrete ordinary matter and put in danger the Earth were firmly dismissed. The reader can easily check on the basis of formulas given in this section that the energies of any existing or planned accelerator are many orders of magnitude below the one needed for the black hole formation in either classical or quantum gravitational framework. The corresponding studies have been done at both the Relativistic Heavy-Ion Collider (RHIC) [34] and more recently at the Large Hadron Collider (LHC). In the case of RHIC, the speculative disaster scenarios were to some extent due to the misinterpretation of a mathematically dual treatment of the hot QCD matter as a black hole in $AdS_5 \times S^5$ space via the AdS/CFT correspondence [35], which is the topic of Sect. 4.1.

4 Using Black Holes to Understand Gauge Theories

4.1 The AdS/CFT Correspondence

The AdS/CFT correspondence is a successfully tested conjecture about the mathematical equivalence of a string theory defined on an Anti de Sitter (AdS) space and a conformal field theory[2] defined on the boundary of the AdS space. It follows as an application of the holographic principle [36], developed by 't Hooft and Susskind, which states that the description of a volume of space can be encoded on a boundary to that region of space.[3]

Here we focus on a particular version of this equivalence, namely the duality between type IIB string theory on $AdS_5 \times S^5$ and a supersymmetric $\mathcal{N} = 4$ Yang–Mills gauge theory[4] on the four-dimensional boundary of AdS_5, as it was originally introduced by Maldacena [1] in 1997, followed by Gubser, Klebanov, Polyakov [2], and Witten [3] in 1998.

---

[2] Conformal invariance is a generalization of scale invariance.

[3] In case of a black hole, the holographic principle states that the description of all objects falling into the black hole is entirely given by surface fluctuations of the event horizon.

[4] $\mathcal{N} = 4$ supersymmetric Yang–Mills is a conformal field theory.

4.2 Anti de Sitter Space

On the gravity side, the requirement of conformal invariance fixes the metric of the fifth dimension uniquely; it is an Anti de Sitter space AdS_5 – that is, a space with Lorentzian signature $(-++\cdots+)$ and constant negative curvature [37]. The Anti de Sitter space is a maximally symmetric, vacuum solution of Einstein's field equations with negative cosmological constant $\Lambda < 0$. In d dimensions, it is defined by an embedding in $d+1$ dimensions

$$ds^2 = -dx_0^2 + \sum_{i=1}^{d-1} dx_i^2 - dx_{d+1}^2, \tag{31}$$

$$-R^2 = -x_0^2 + \sum_{i=1}^{d-1} x_i^2 - x_{d+1}^2, \tag{32}$$

which makes it the Lorentzian version of Lobachevski space. It is invariant under the group SO(2, $d-1$) that rotates the coordinates $x_\mu = (x_0, x_{d+1}, x_1, \ldots, x_{d-1})$ into $x'^\mu = \Lambda^\mu_\nu x^\nu$. In Poincaré coordinates, the metric of this space is given by

$$ds^2 = \frac{R^2}{x_0^2}\left(-dt^2 + \sum_{i=1}^{d-2} dx_i^2 + dx_0^2\right), \tag{33}$$

where $t > -\infty$, $x_i < +\infty$, and $0 < x_0 < +\infty$. Up to a conformal factor, this is just like (flat) three-dimensional Minkowski space, though not all space is covered. Thus, in these Poincaré coordinates, Anti de Sitter space can be understood as a $d-1$ dimensional Minkowski space in $(t, x_1, \ldots, x_{d-2})$ coordinates, with a *warp factor* (gravitational potential) that depends only on the additional coordinate x_0.

4.3 Supersymmetry

Now, our conformal field theory needs to be supersymmetric – that is, associate a fermion (particle with half-integer spin) to every type of boson (particle with integer spin) and a boson to every type of fermion. This can be represented by a graded Lie algebra generalization of the Poincaré + internal symmetries, with "even" generators P_a, J_{ab}, T_r and "odd" generators Q^i_α, satisfying the following commuting and anticommuting laws [37]:

$$[\text{even}, \text{even}] = \text{even};\ \{\text{odd}, \text{odd}\} = \text{even};\ [\text{even}, \text{odd}] = \text{odd}. \tag{34}$$

We note that P_a and J_{ab} are, respectively, the generators of 3+1 dimensional translation symmetries and the Lorentz generators of the SO(1, 3) Lorentz group, which together define the Poincaré symmetry, T_r correspond to internal symmetries of particle physics such as local U(1) of electromagnetism or local SU(3) of QCD or

global SU(2) of isospin, while Q^i_α are spinors satisfying the supersymmetry algebra

$$Q \text{ boson} = \text{fermion}; \; Q \text{ fermion} = \text{boson}. \tag{35}$$

Since all symmetries of the field theory should be reflected in the dual string theory, the supersymmetry requirement further constrains the 10-dimensional string theory to live in $AdS_5 \times S^5$ (that is five-dimensional AdS space times a 5-sphere) [38]. We make sense of the higher dimensions ($D > 4$) of the theory by means of Kaluza–Klein dimensional reduction, which states that the extra D – 4 dimensions are all curled up in a small space, in the form of a small sphere or torus.

4.4 D-Branes and Black Holes in String Theory

The metric commonly used in AdS/CFT calculations is the AdS_5-Schwarzschild solution, which describes the near-horizon geometry of D3-branes (see below):

$$ds_5^2 = \frac{L^2}{z^2}\left[-h(z)dt^2 + d\vec{x}^2 + \frac{dz^2}{h(z)}\right], h(z) = 1 - \frac{z_H^4}{z^4}. \tag{36}$$

Here L is the common radius of curvature of AdS_5 and S^5, $z = \frac{L^2}{r}$ and z_H is the corresponding z-coordinate of the black hole horizon.[5] This metric extremizes an action derived from type IIB string theory on S^5:

$$S = \frac{1}{16\pi G_5}\int d^5x\sqrt{-g}\left(R + \frac{12}{L^2}\right). \tag{37}$$

The relationship between gauge theories and string theory on Anti de Sitter spaces was motivated by studies of D-branes and black holes in string theory [38]. D-branes are solitons in string theory and are defined (in string perturbation theory) as surfaces where open strings can end. These open strings have massless modes

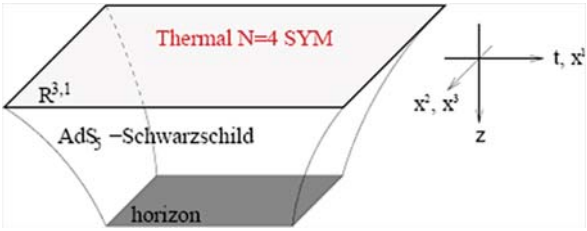

Fig. 2 The AdS–Schwarzschild solution, dual to a thermal state of $\mathcal{N} = 4$ super Yang–Mills, by Gubser

[5] z ranges from 0 to ∞ and corresponds to what we previously defined as x_0 in Eq. (32).

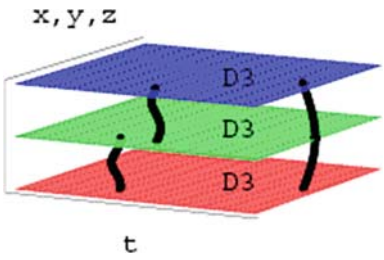

Fig. 3 D-brane representation, by Gubser

describing the oscillations of the branes, a gauge field living on the brane or their fermionic partners. Having N coincident branes on which the open strings can start and end points us toward a low-energy dynamics described by a U(N) gauge theory. Now, if one considers Dp-branes, which are charged under $p+1$-form gauge potentials, and adds to them D-branes, they generate together a flux of the corresponding field strengths associated with the gauge potentials, which contributes to the stress-energy tensor; so the geometry becomes curved. One can find solutions of the supergravity equations carrying these fluxes. These solutions are very similar to extremal charged black hole solutions in general relativity, except that in this case they are black branes with p extended spatial dimensions (which, like black holes, contain event horizons).

If one considers a set of N coincident D3-branes, the near-horizon geometry turns out to be the famed $AdS_5 \times S^5$ [38]. We also know that the low-energy dynamics on their worldvolume is governed by a U(N) gauge theory with $\mathcal{N} = 4$ supersymmetry. These two pictures of D-branes are perturbatively valid for different regimes of the coupling. While perturbative field theory is valid when $g_s N$ is small, the low-energy gravitational description is perturbatively valid when the radius of curvature is much larger than the string scale, that is when $g_s N$ becomes very large. As an object is brought closer to the black brane horizon, its energy measured by an outside observer gets redshifted by the large gravitational potential, so it becomes very small. Since low-energy excitations on the branes are governed by the Yang–Mills theory, it becomes natural to conjecture that Yang–Mills theory at strong coupling is describing the near-horizon region of the black brane, whose geometry is $AdS_5 \times S^5$!

Near $r = 0$, the extremal 3-brane geometry given in Eq. (36) is non-singular and all appropriately measured curvature components become small for large L. Thus, for L much larger than the string scale $\sqrt{\alpha'}$, the entire 3-brane geometry has small curvature everywhere and can be described by the supergravity approximation to type IIB string theory. By expressing the ADM tension (mass per unit area) of the extremal 3-brane classical solution to N times the tension of a single D3-brane, one obtains the relation [39]

$$\frac{2}{\kappa^2} L^4 \Omega_5 = N \frac{\sqrt{\pi}}{\kappa}. \tag{38}$$

In this context, $\Omega_5 = \pi^3$ is the volume of a unit 5-sphere and $\kappa = \sqrt{8\pi G}$ is the 10-dimensional gravitational constant. Since $\kappa = 8\pi^{7/2} g_s \alpha'^2$ and $g_{YM}^2 = 4\pi g_s$, Eq. (38) becomes

$$L^4 = g_{YM}^2 N \alpha'^2, \tag{39}$$

where g_s and g_{YM} are the string and Yang–Mills couplings, respectively. Thus, for large $L \gg \sqrt{\alpha'}$ a strong 't Hooft coupling $g_{YM}^2 N \gg 1$ is required. This remarkable result lies at the heart of the success of the AdS/CFT correspondence. We further point to references [37–39] for comprehensive reviews of the conjectured equivalence.

4.5 QCD and Gravity

As we discussed above, asymptotic freedom and confinement explicitly break conformal invariance in QCD, and the AdS/CFT correspondence relies on conformal symmetry in a very essential way. This is at present the main obstacle in the way of applying these ideas to QCD. We are interested in the strong coupling behavior which in QCD is encountered in the low-energy regime. It is thus natural to try and gain a physical insight on confinement by considering effective low-energy theories. In this section we will sketch the construction of one of these theories. What is interesting in this example is that it also points toward gravity: The resulting effective Lagrangian can be mathematically reformulated as classical QCD on a curved conformal gravitational background. Our discussion follows the arguments from [5, 6].

We would like to construct an effective theory that is not scale invariant but transforms under scale transformations in a well-defined way prescribed by the asymptotic freedom, i.e., is invariant under the *Renormalization Group* (RG) transformations.[6] Since as we have seen above the scale transformations are generated by the trace of the energy momentum tensor, we will begin by encoding the dynamics prescribed by the RG into a set of low-energy theorems for the correlation functions of the trace of the energy–momentum tensor. We reproduce the derivation [40] of these theorems here because they will be relevant in the construction of the effective Lagrangian.

The expectation value of an operator $\mathcal{O}$ that is invariant with respect to the change of renormalization scale M_0 can be written as

$$\langle \mathcal{O} \rangle \sim \left[M_0 \, e^{-\frac{8\pi}{b\, g^2(M_0)}} \right]^d ; \tag{40}$$

[6] Renormalization group is a field theory technique that allows one to investigate the changes of a physical system as one views it at different distance scales.

this way the expectation value does not change with the scale M_0, and there is thus no *anomalous dimension*, only the canonical dimension d.

On the other hand, we can write down this expectation value as a functional integral that will contain the exponential of the action. We have seen above (see Eq. (7)) that the action density in gluodynamics depends on the coupling constant g; it is proportional to $1/4g^2$:

$$\mathcal{L} \,=\, (-1/4g^2)\tilde{F}^{a\mu\nu}\tilde{F}^{a}_{\mu\nu} \tag{41}$$

where $\tilde{F} = gF$ is the rescaled gluon field. The derivative w.r.t. $-1/4g^2(Q^2)$ of the expectation value of $\mathcal{O}$ thus generates a zero-momentum correlation function:

$$i \int dx\, \langle T\{\, \mathcal{O}(x)\,,\; \tilde{F}^2(0)\,\}\rangle \,=\, -\frac{d}{d(-1/4g^2)}\,\langle \mathcal{O}\rangle; \tag{42}$$

this procedure is analogous to differentiating w.r.t. the inverse temperature in statistical mechanics. Combining Eqs. (40) and (42), we obtain [40] for $d = 4$

$$i \lim_{q\to 0} \int dx\, e^{i\,q\,x}\, \langle 0|T\{\, \mathcal{O}(x)\,,\; \frac{\beta(\alpha_s)}{4\,\alpha_s}\, F^2(0)\,\}|0\rangle_{\text{connected}} = \langle O\rangle\,(-4)\,. \tag{43}$$

This result can be easily generalized through an iteration method to obtain a set of relations between n-point correlation functions and an arbitrary number of operators F^2. If our operator $\mathcal{O}$ is the trace of the energy–momentum tensor itself, i.e.,

$$\mathcal{O} \equiv \theta^{\mu}_{\mu} = \frac{\beta(g)}{2\,g} F^{a}_{\mu\nu}\, F^{a\mu\nu}, \tag{44}$$

then Eq. (43) can be written as

$$i^n \int dx_1 \ldots dx_n\, \langle 0|T\{\theta^{\mu_1}_{\mu_1}(x_1), \ldots, \theta^{\mu_n}_{\mu_n}(x_n), \theta^{\mu}_{\mu}(0)\}|0\rangle_{\text{connected}} \tag{45}$$
$$= \langle \theta^{\mu}_{\mu}(x)\rangle\,(-4)^n.$$

This infinite chain of low-energy theorems determines the structure of the low-energy theory completely, and we will now construct our effective Lagrangian using the method developed in [41].

Let us consider gluodynamics in a curved conformally flat background in d dimensions, with a background described by the metric

$$g_{\mu\nu}(x) \,=\, e^{h(x)}\,\delta_{\mu\nu}. \tag{46}$$

The action of the gluon fields in this curved background is

$$S = -\frac{1}{4\,g^2}\int d^d x\,\sqrt{-g}\,g^{\mu\nu}\,g^{\lambda\sigma}\,\tilde{F}^a_{\mu\lambda}\,\tilde{F}^a_{\nu\sigma}, \tag{47}$$

with $g = \det g^{\mu\nu}$. Note that Yang–Mills theory on a curved background is scale and conformally invariant in any number of dimensions d, contrary to the case a flat space when the same theory is scale and conformally invariant only if $d = 4$, see Eq. (18). The regularization of the action brings in an extra term in Eq. (47) in $d = 4$:

$$\Delta S = -\frac{1}{4\,g^2}\int d^4 x\,e^{2h}\left[-\frac{b\,g^2}{32\,\pi^2}(\tilde{F}^a_{\mu\nu})^2\right], \tag{48}$$

where $b = 11\,N_C/3$. This new term is proportional to the second term of the right-hand side of Eq. (19). Therefore, the explicit breaking of the scale invariance of QCD manifests itself in the theory defined by the effective action given by the sum of Eqs. (47) and (48) through a term containing the auxiliary scalar field $h(x)$ [41], without any dimensionful parameters. For a theory defined on a flat space–time, the scale anomaly presents itself in the phenomenon of dimensional transmutation, which brings in a dimensionful parameter explicitly.

The kinetic part for the field $h(x)$ can be obtained in a manifestly scale and conformally invariant way using the Einstein–Hilbert Lagrangian for the one-loop effective Yang–Mills field:

$$S_{\text{eff}} = \int d^4 x\,\sqrt{-g}\left(\frac{1}{8\,\pi\,G}\,R\,-\,\frac{1}{4\,g^2}\,g^{\mu\nu}\,g^{\lambda\sigma}\,\tilde{F}^a_{\mu\lambda}\,\tilde{F}^a_{\nu\sigma}\,-\,e^{2h}\,\theta^\mu_\mu\right), \tag{49}$$

where G is some dimensionful constant and R is the Ricci scalar. Using (46) we get

$$R\sqrt{-g} \equiv R^\mu_\mu\sqrt{-g} = e^h\frac{3}{2}(\partial_\mu h)^2. \tag{50}$$

In deriving Eq. (50) we have neglected terms of higher order in derivatives and constrained ourselves to Einstein's gravity. This corresponds to an expansion in powers of the gradients for a slowly varying background field.

With this example, we have constructed an effective Lagrangian that preserves scale invariance of QCD in a classical curved background at a price of a new dilaton field $h(x)$.

4.6 Confinement as an Event Horizon for Colored Particles?

In the previous section we have constructed an effective low-energy Lagrangian that preserves the scale invariance. This effective theory is mapped mathematically onto classical QCD on a curved conformal gravitational background. It is interesting that this theory may offer a geometrical way of associating confinement with an event

horizon for colored particles [10]. In general relativity the appearance of an event horizon occurs through the modification of the underlying space–time structure by the gravitational interaction. Our effective Lagrangian $\mathcal{L}$ depends on a single background field, and the modification of the metric can be computed as follows [42]:

$$g_{\mu\nu} = \eta_{\mu\nu}\mathcal{L}' - 4\,F_{\alpha\mu}F^{\alpha}_{\nu}\mathcal{L}'', \tag{51}$$

where the primes indicate first and second derivatives with respect to $F \equiv F_{\mu\nu}F^{\mu\nu}$. The vanishing of the temporal component of the modified metric will define the compact region of the theory, i.e., the counterpart of a black hole. It is possible to write the effective Lagrangian derived from the action (49) as

$$\mathcal{L}_{\rm QCD} = \frac{1}{4}F_{\mu\nu}F^{\mu\nu}\frac{g^2(0)}{g^2(gF)} = \frac{1}{4}F_{\mu\nu}F^{\mu\nu}\epsilon(gF), \tag{52}$$

with the "dielectric" constant of the system under the presence of the background field at one loop given by

$$\epsilon(gF) \simeq 1 - \beta_0\left(\frac{g^2}{4\pi}\right)\ln\frac{\Lambda^2}{gF}. \tag{53}$$

Here $\beta_0 = (11N_c - 2N_f)/48\pi^2$, while N_c and N_f specify the number of colors and flavors, respectively. Therefore the effective metric (51) computed for the Lagrangian (52) can yield the vanishing temporal component $g_{00} = 0$ when

$$gF^* = \Lambda^2\exp\{-4\pi/\beta_0 g^2\}. \tag{54}$$

Therefore, an event horizon may be formed at $r^* \sim 1/\sqrt{gF^*}$ in our effective theory – it would take colored particles an infinite time to escape. In black hole physics there is a deep relation between the Hawking temperature and the existence of an event horizon. Consequently, the radiation emitted by a black hole and its evaporation process might be related to thermal hadron production (see [10] for details).

5 Applications: Shear and Bulk Viscosities

To exemplify the use of the two methods presented previously in Sects. 4.1 and 4.5 we will discuss the calculation of two important transport coefficients of QCD matter, which can be linked to relevant observables in studies of ultrarelativistic heavy-ion collisions.

5.1 Definitions

In finite-temperature field theory, the shear and bulk viscosities are defined as transport coefficients of the energy-momentum tensor. For this, we consider a plasma slightly out of equilibrium, such that there is local thermal equilibrium everywhere, but the temperature and average velocity are allowed to slowly vary in space. Then one can define at any point a local rest frame, where the 3-momentum density vanishes, $\theta_{i0} = 0$. In this frame, one has the following constitutive relation for the energy-momentum tensor [43, 44]:

$$\theta_{ij} = P_{eq}(\epsilon)\delta_{ij} - \eta(\partial_i u_j + \partial_j u_i - \frac{2}{3}\delta_{ij}\partial_k u_k) - \zeta\delta_{ij}\,\vec{\nabla}\cdot\vec{u}, \tag{55}$$

where $P_{eq}(\epsilon)$ is the pressure (related to the energy density of the system through an equilibrium equation of state), η is the shear viscosity, ζ the bulk viscosity, and u_i are the flow velocities. All kinetic coefficients can be expressed, via Kubo formulas, as static limits of correlation functions of the corresponding currents, namely [45]

$$\eta = \frac{1}{2}\lim_{\omega\to 0}\frac{1}{\omega}\int_0^\infty dt\int d^3r\, e^{i\omega t}\,\langle[\theta_{xy}(t,\mathbf{x}),\theta_{xy}(0,\mathbf{0})]\rangle, \tag{56}$$

$$\zeta = \frac{1}{9}\lim_{\omega\to 0}\frac{1}{\omega}\int_0^\infty dt\int d^3r\, e^{i\omega t}\,\langle[\theta_{ii}(t,\mathbf{x}),\theta_{kk}(0,\mathbf{0})]\rangle. \tag{57}$$

The shear viscosity η indicates how much entropy is produced by transformation of shape at constant volume; it is generated by translations. Correspondingly, the bulk viscosity ζ quantifies how much entropy is produced by transformation of volume at constant shape; it is generated by dilatations.

5.2 The Shear Viscosity Bound

In [46], the ratio of shear viscosity to volume density of entropy η/s is computed for a large class of strongly interacting quantum field theories which have a dual description involving black holes in Anti de Sitter space. This ratio can be used to characterize how close a given fluid is to being perfect.

A first step is to relate the shear viscosity as defined in Eq. (56) to the absorption cross section of low-energy gravitons. We consider a graviton of frequency ω, polarized in the xy direction and propagating perpendicularly to a brane. Since according to the gauge–gravity duality, the stress–energy tensor couples to the metric perturbations at the boundary [38], then in the field theory picture the absorption cross section of the graviton by the brane is proportional to the imaginary part of the retarded Green function of the operator coupled to h_{xy}, that is, θ_{xy}:

$$\sigma_{abs}(\omega) = -\frac{2\kappa^2}{\omega}ImG^R(\omega) = \frac{\kappa^2}{\omega}\int_0^\infty dt\int d^3r\, e^{i\omega t}\,\langle[\theta_{xy}(t,\mathbf{x}),\theta_{xy}(0,\mathbf{0})]\rangle, \tag{58}$$

where $\kappa = \sqrt{8\pi G}$ emerges as a result of the normalization of the graviton's action. Upon comparing Eqs. (56)–(58), one obtains immediately the shear viscosity as a function of the graviton absorption cross section:

$$\eta = \frac{\sigma_{abs}(0)}{2\kappa^2} = \frac{\sigma_{abs}(0)}{16\pi G}. \tag{59}$$

The next step is to prove that the absorption cross section of a graviton by a black hole is the same as that of a scalar, which is equal in the low-frequency limit $\omega \to 0$ to the area of the horizon, namely $\sigma_{abs}(0) = a$.

Finally, one needs to compute the volume density of entropy. Again, we use the dual holographic description and conclude that the entropy of the dual field theory is equal to the entropy of the black brane, which is proportional to the area of its event horizon, as found by Bekenstein and Hawking in Eq. (30). The entropy density is therefore

$$s = \frac{k_B a}{4G\hbar}, \tag{60}$$

which results in a shear viscosity to entropy density ratio of

$$\frac{\eta}{s} = \frac{\hbar}{4\pi k_B}. \tag{61}$$

It is remarkable that the result – which applies in the limit of strong coupling, where the gravity description is appropriate – does not depend on the specific metric chosen, the ratio being the same for various types of Dp- and Mp-branes, even if the corresponding dual theories are very different. Furthermore, according to a conjecture due to the authors of [46], this result can be viewed as a universal lower bound for all relativistic quantum field theories at finite temperature and zero chemical potential. The inequality is to be saturated by theories with gravity duals. We

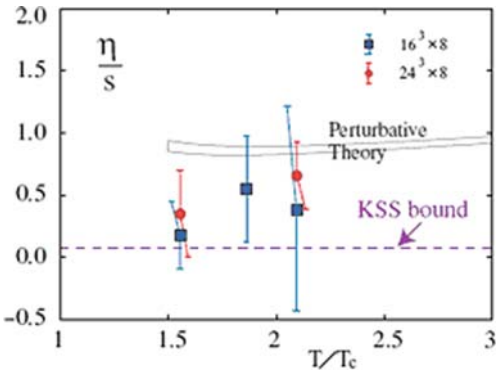

Fig. 4 The ratio of the shear viscosity to the entropy as a function of T/T_c from [50]. KSS bound is $1/4\pi$

further refer to [46] for the arguments supporting this conjecture; see also [47, 48] for a discussion of circumstances under which this bound may be violated.

Recent lattice results [49] give $\eta/s = 0.134(33)$ for $T = 1.65\,T_c$ and $\eta/s = 0.102(56)$ for $T = 1.24\,T_c$ – the values which are above, but not much above, the bound (61).

At the same time, RHIC data provide a limit for the ratio η/s by measuring the elliptic flow of particles produced in very energetic heavy-ion collisions. Results so far have pointed toward a very low-viscosity, nearly perfect fluid of quarks and gluons [51–54].

5.3 Bulk Viscosity and Hadronization

The transport coefficient of the plasma which is directly related to its conformal properties is the bulk viscosity [11]. Indeed, it is related by Kubo's formula to the correlation function of the trace of the energy-momentum tensor. It is clear from Eq. (57) that for any conformally invariant theory with $\theta^\mu_\mu = 0$ the bulk viscosity should vanish. This is the case for $\mathcal{N} = 4$ SUSY Yang–Mills theory. In contrast, a nonzero ζ can be generated by breaking the scale invariance.

A perturbative evaluation by [44] has yielded very small values for ζ, with the ratio ζ/η of the order of 10^{-3} for 3-flavor QCD with $\alpha_S \leq 0.3$, neglecting quark masses. Specifically, ζ was found to scale with α_S^2 for massless QCD, where conformal symmetry is broken by the running of the coupling $\beta(\alpha_S) \sim \alpha_S^2$:

$$\zeta \sim \frac{T^3}{\alpha_S^2 \log[1/\alpha_S]} \times (\alpha_S^2)^2 \sim \frac{\alpha_S^2 T^3}{\log[1/\alpha_S]} \text{ for } m_0 \ll \alpha_S T. \tag{62}$$

The presence of quark masses also leads to breaking conformal invariance provided that $m_0 \leq T$, and this time

$$\zeta \sim \frac{T^3}{\alpha_S^2 \log[1/\alpha_S]} \times (\frac{m_0^2}{T^2})^2 \sim \frac{m_0^4}{T\alpha_S^2 \log[1/\alpha_S]} \text{ for } \alpha_S T \ll m_0 \ll T. \tag{63}$$

Here m_0 refers to the heaviest zero-temperature quark mass which is smaller than or of the order of the temperature T. Only the case of weakly coupled QCD, with vanishing or negligible chemical potential $\mu \sim 0$ was considered. Based on the above results, we can safely conclude that bulk viscosity is negligibly small (at least with respect to shear viscosity) in the perturbative regime of QCD. Specifically

$$\frac{\zeta}{s} \sim \alpha_S^2 \text{ and } \frac{\eta}{s} \sim \frac{1}{\alpha_S^2}. \tag{64}$$

Note that the parametric dependence of the shear and bulk viscosities on the coupling constant (64) can be easily read off the Kubo formulas (56) and (57) if we

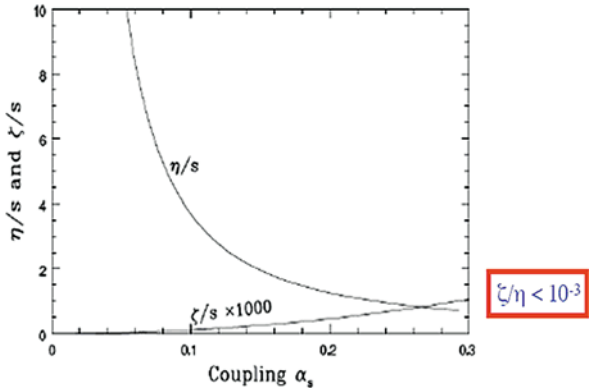

Fig. 5 Shear vs. bulk viscosity: η/s and ζ/s (s the entropy density) as a function of α_S, for $N_f = 3$ QCD, neglecting quark masses. Bulk viscosity ζ has been rescaled by a factor of 1000; from [44]

recall the dependence of the QCD action and the trace of the energy–momentum tensor on the coupling constant, see Eqs. (7) and (19).

But what happens at strong coupling, where perturbation theory is no longer applicable? Such is the regime of interest for the quark–gluon plasma. Lattice calculations [50, 49] indicate that shear viscosity gets small, with η/s not much higher than the conjectured lower bound of $1/4\pi$ (refer to Sect. 5.2). Does this mean that the bulk viscosity at strong coupling may become large?

Since the bulk viscosity is related by the Kubo formula (57) to the correlation function of the trace of the energy–momentum tensor, this quantity is intimately related to the breaking of scale invariance. In Sect. 4.5, we introduced the low-energy theorems for the correlation functions of the trace of the energy–momentum tensor which do not rely on perturbation theory. Let us see what can be said about the bulk viscosity on the basis of this approach; we will follow [11].

In this approach, bulk viscosity can be related to the "*interaction measure*", i.e., the expectation value of the trace of the energy-momentum tensor $\langle\theta\rangle = \epsilon - 3P$, where ϵ is the energy density and P is the pressure, both of which are measured with high precision on the lattice. Following the definitions and conventions of [45], we can rewrite Eq. (57) by means of the retarded Green's function as

$$\zeta = \frac{1}{9} \lim_{\omega\to 0} \frac{1}{\omega} \int_0^\infty dt \int d^3r\, e^{i\omega t}\, i\, G^R(x) = -\frac{1}{9} \lim_{\omega\to 0} \frac{1}{\omega}\, Im\, G^R(\omega, \vec{0}), \qquad (65)$$

where P-invariance was imposed to yield the last expression. Since the spectral density is defined as

$$\rho(\omega, \vec{p}) = -\frac{1}{\pi}\, Im\, G^R(\omega, \vec{p}), \qquad (66)$$

we can further express the retarded Green's function by using the Kramers–Kronig relation to yield [11]

$$G^R(\omega, \vec{p}) = \frac{1}{\pi}\int_{-\infty}^{\infty} \frac{Im\, G^R(u, \vec{p})}{u - \omega - i\epsilon} du = \int_{-\infty}^{\infty} \frac{\rho(u, \vec{p})}{\omega - u + i\epsilon} du. \tag{67}$$

Now, relate by analytic continuation the retarded Green's function for a bosonic excitation to the corresponding Euclidean Green's function

$$G^E(\omega, \vec{p}) = -G^R(i\omega, \vec{p}),\ \omega > 0 \tag{68}$$

and use Eq. (67) together with the fact that $\rho(\omega, \vec{p})$ is odd w.r.t. ω to obtain

$$G^E(0, \vec{0}) = 2\int_0^{\infty} \frac{\rho(u, \vec{0})}{u} du. \tag{69}$$

We can now use the set of low-energy theorems [40] satisfied by the correlation functions of the trace of the energy–momentum tensor θ introduced in Sect. 4.5 to relate the Euclidean Green's function to the thermal expectation value of θ. Following the generalization to the case of finite temperature of [55], we get

$$G^E(0, \vec{0}) = \int d^4x\, \langle T\theta(x), \theta(0)\rangle = (T\frac{\partial}{\partial T} - 4)\, \langle\theta\rangle\,. \tag{70}$$

As discussed before in Sect. 2.3, the scale symmetry of the QCD Lagrangian is broken by quantum fluctuations, which makes θ acquire a nonzero expectation value. We now know from Eq. (57) that a nonzero bulk viscosity is associated with $\langle\theta\rangle \neq 0$, a fact clearly observed on the lattice for SU(3) gluodynamics [56] (the same holds in the presence of quarks or at large N_c). So let us relate this thermal expectation value to the quantities computed on the lattice via

$$(\epsilon - 3P)_{LAT} = \langle\theta\rangle_T - \langle\theta\rangle_0 \ \text{ with } \ \langle\theta\rangle_0 = -4\,|\epsilon_v|\,, \tag{71}$$

where the zero-temperature expectation value of θ, related to the vacuum energy density $\epsilon_v < 0$ has to be subtracted. Using Eqs. (69), (70), and (71) we derive an exact sum rule for the spectral density ρ [11]:

$$2\int_0^{\infty} \frac{\rho(u, \vec{0})}{u} du = (T\frac{\partial}{\partial T} - 4)\, \langle\theta\rangle_T = T^5 \frac{\partial}{\partial T}\frac{(\epsilon - 3P)_{LAT}}{T^4} + 16\,|\epsilon_v|\,. \tag{72}$$

Before extracting the bulk viscosity from Eq. (72), one needs to make an ansatz for the spectral density in the low-frequency regime only – since the perturbative, divergent contribution has already been subtracted in the definition of the quantities on the r.h.s. of the sum rule (72). In order to satisfy Eqs. (65) and (66), the following ansatz has been assumed in [11]

$$\frac{\rho(\omega, \vec{0})}{\omega} = \frac{9\zeta}{\pi} \frac{\omega_0^2}{\omega_0^2 + \omega^2}. \tag{73}$$

Upon substituting Eqs. (73) into (72) one obtains the much-sought expression for the bulk viscosity

$$\zeta = \frac{1}{9\omega_0} \left\{ T^5 \frac{\partial}{\partial T} \frac{(\epsilon - 3P)_{LAT}}{T^4} + 16\,|\epsilon_v| \right\}. \tag{74}$$

We have to emphasize that our result depends crucially on the assumed spectral density. The shape of the spectral density (and in particular the presence of a $\sim \omega\delta(\omega)$ term) and the behavior of the relaxation time $\sim \omega_0^{-1}$ in the vicinity of the critical point both affect the extracted bulk viscosity.

Contrary to what Kubo's formula (57) may naively imply, ζ is linear rather than quadratic in the difference $\epsilon - 3P$, which seems to be in agreement with the strong-coupling result obtained for the nonconformal SUSY Yang–Mills gauge plasma studied by [57]. The parameter $\omega_0(T) \propto T$ is the scale at which perturbation theory becomes valid, i.e., when the lattice calculations of the running coupling coincide with the perturbative expression at a given temperature. In the region $1 < \frac{T}{T_c} < 3$ it was found that $\omega_0(T) \approx 1.4 \left(\frac{T}{T_c}\right)$ GeV.

Applying Eq. (74) to the lattice data from [56], with $|\epsilon_v| = 0.62\, T_c^4$ and $T_c = 0.28\,\text{GeV}$, the bulk viscosity can be extracted and the ratio ζ/s computed as a function of temperature. It turns out that ζ is indeed small at high T away from the critical temperature T_c – in agreement with the perturbative results of [44], but becomes very large at T close to T_c, as confirmed by recent lattice calculations of [58, 59]. A comparison between the results of [11] and [58] is given in Fig. 6.

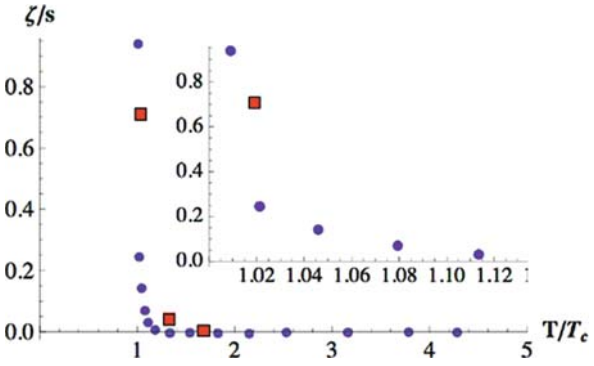

Fig. 6 ζ/s as a function of T/T_c; comparison with lattice results [58]

Corroborated with the lattice results for shear viscosity of [50, 49], the present result suggests that bulk viscosity may be the dominant correction to ideal hydrodynamics in the vicinity of the deconfinement phase transition in the plasma. Several

condensed matter systems, such as He^3 near the critical liquid–vapor point, exhibit an analogous behavior, with a large ratio of ζ/η affecting sound propagation in these media [60].

The analysis described above has been extended to the case of QCD with 2+1 quark flavors [12], with qualitatively similar results. This latter case is directly relevant for heavy-ion collision experiments, where the two light flavors "up" and "down," along with strangeness, are produced most abundantly. More recent, high statistics lattice data on the equation of state for QCD with almost physical quark masses from the RIKEN-BNL-Columbia-Bielefeld collaboration [61] are used as an input to extract the bulk viscosity.

The behavior of bulk viscosity near the critical temperature in the presence of light quarks has been discussed in the framework of the effective Lagrangians, see [62–66]. It is interesting to note that bulk viscosity can exhibit a rapid growth in the vicinity of the chiral critical point [12].

We should mention that the effects of conformal symmetry breaking on bulk viscosity have been studied before in the framework of the gauge–gravity duality, for nonconformal supersymmetric mass-deformed[7] $\mathcal{N}$=2* Yang–Mills theory in the regime of large 't Hooft coupling $g_{YM}^2 N_c \gg 1$ in [57], yielding a linear dependence of ζ in $\epsilon - 3P$ which is similar to [11]. Further progress has been made by [67] and [68] in computing bulk viscosity by considering various classes of black hole solutions, which are gravity duals of gauge theories with broken conformal invariance, via the AdS/CFT correspondence introduced in Sect. 4.1. The latter results also yield a rise of ζ in the vicinity of $T = T_c$, though much less sharp than the one predicted in [11] and [12].

5.4 Bulk Viscosity and the Mechanism of Hadronization

Let us now briefly discuss the connection between the growth of bulk viscosity near the critical temperature and an increase in entropy, manifested in abundant particle production in heavy-ion collisions. Namely, the expansion of QCD matter close to the phase transition, produced in such collisions, is accompanied by the production of many soft partons, which screen the color charges of the quarks and gluons present in the medium [12]. Such a scenario may be called "*soft statistical hadronization*," since the produced partons carry low momenta and the hadronization pattern is not expected to depend on the phase-space distributions of the original partons.

The association of inherent entropy to the hadronization process may be similar to the "*black hole hadronization*" picture that associates an event horizon to the confinement of colored particles [8–10]. Since quantum tunnelling turns out to be the only allowed means of crossing the event horizon of quarks, one could in principle relate entropy growth and hadron production to a succession of quantum

[7] Assumes the same mass for all fermions and bosons in the theory.

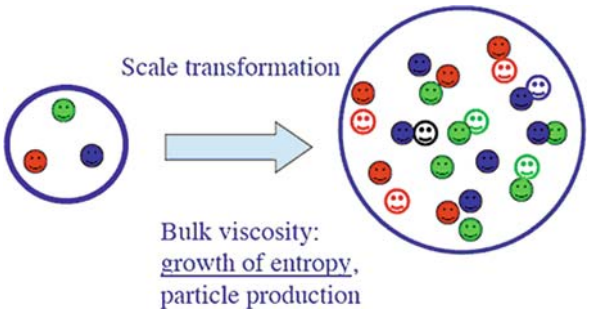

Fig. 7 The mechanism of soft statistical hadronization as an indicator of entropy growth

tunnelling processes that lead to the emission of thermal radiation, which is the QCD counterpart of the Hawking–Unruh radiation emitted by black holes.

Within this framework, the results of [11] and [58] shown in Fig. 6 point toward the ζ/s vs. T dependence as a clear indicator of confinement, as seen by the off-equilibrium thermodynamics. In heavy-ion collisions, this may be manifested through both a decrease of the average transverse momentum of the resulting particles and an increase in the total particle multiplicity. Let us also mention an interesting scenario [69] where the growth of bulk viscosity induces an instability in the hydrodynamical flow of the plasma.

6 Limitations of the Present Approaches and Outlook

In these lectures, we have introduced the two dualities relating QCD and gravity and discussed applications to the computation of the shear and bulk viscosities of strongly coupled QCD matter. However, useful and mathematically sound these dual approaches may seem, there are some serious drawbacks associated with the use of these methods which we outline below.

In the case of the AdS/CFT correspondence presented in Sect. 4.1, it relates perturbative string theory calculations to non-perturbative (strong coupling) calculations in the four-dimensional $\mathcal{N} = 4$ super Yang–Mills theory, which are otherwise very difficult to obtain. The ultimate interest is, however, to perform strong coupling calculations in the real world – in QCD, the theory of the strong interaction. $\mathcal{N} = 4$ super Yang–Mills is quite far from QCD, in particular by being supersymmetric and conformally invariant. The fact that AdS/CFT is defined for a gauge group SU(N_c) as a perturbation around $N_c = \infty$ further complicates matters.

In the case of the second method, one major but hopefully solvable problem is to include the quarks in the effective action. It may also be useful to formulate the effective action explicitly as a gravity action in five dimensions and to study the duality of solutions of the effective dilaton–gluon action on one side and of the Einstein–Hilbert gravity action on the other. The string-like confining solution of the effective dilaton–gluon action has been obtained recently in [7] where it was found

that the formation of the string is accompanied by the emergence of a massless dilaton mode.

The two approaches outlined in these lectures are at first glance completely different: It is enough to mention that one is essentially guided by conformal invariance whereas the other is driven by the pattern of conformal invariance *breaking*. Nevertheless, it is quite likely that once the breaking of scale invariance is introduced within the AdS/CFT correspondence on one hand (see [70–72, 67] for work in this direction), and the effective dilaton action is formulated in dual language as a five-dimensional gravity on the other, the two approaches may appear closer than it seems at present. In any case, even a remote prospect of finding some day a gravity dual of QCD certainly justifies giving it a try.

Acknowledgments D.K. is grateful to H. Satz and B. Sinha for the invitation to deliver these lectures and the hospitality in Jaipur. The work of D.K. was supported by the U.S. Department of Energy under Contract No. DE-AC02-98CH10886.

References

1. J. Maldacena: *The Large N Limit of Superconformal Field Theories and Supergravity*, Adv. Theor. Math. Phys. **2**, 231–252 (1998), arXiv:hep-th/9711200 342, 351
2. S. Gubser, I. Klebanov and A. Polyakov: *Gauge Theory Correlators from Non-critical String Theory*, Phys. Lett. **B 428**, 105–114 (1998), arXiv:hep-th/9802109 351
3. E. Witten: *Anti-de Sitter Space, Thermal Phase Transition, and Confinement in Gauge Theories*, Adv. Theor. Math. Phys. **2**, 505–532 (1998), arXiv:hepth/9803131 342, 351
4. E. Shuryak: *Physics of Strongly Coupled Quark-Gluon Plasma*, Prog. Part. Nucl. Phys. **62**, 48 (2009), arXiv:0807.3033 [hep-ph] 342
5. D. Kharzeev, E. Levin and K. Tuchin: *QCD in Curved Space-Time: A Conformal Bag Model*, Phys. Rev. **D 70**, 054005 (2004), arXiv:hep-ph/0403152 342, 355
6. D. Kharzeev, E. Levin and K. Tuchin: Phys. Lett. **B 547**, 21 (2002), arXiv:hep-ph/0204274 355
7. D. Kharzeev, E. Levin and K. Tuchin: *Broken Scale Invariance, Massless Dilaton and Confinement in QCD*, arXiv:0809.3794 [hep-ph] 342, 366
8. D. Kharzeev and K. Tuchin: *From Color Glass Condensate to Quark Gluon Plasma Through the Event Horizon*, Nucl. Phys. **A 753**, 316 (2005), arXiv:hepph/0501234 342, 365
9. D. Kharzeev, E. Levin and K. Tuchin: *Multi-Particle Production and Thermalization in High-Energy QCD*, Phys. Rev. **C 75**, 044903 (2007), arXiv:hepph/0602063
10. P. Castorina, D. Kharzeev and H. Satz: *Thermal Hadronization and Hawking-Unruh Radiation in QCD*, Eur. Phys. J. **C 52**, 187 (2007), arXiv:0704.1426 [hep-ph] 342, 358, 365
11. D. Kharzeev and K. Tuchin: *Bulk Viscosity of QCD Matter Near the Critical Temperature*, arXiv:0705.4280 [hep-ph] 342, 361, 362, 363, 364, 365, 366
12. F. Karsch, D. Kharzeev, K. Tuchin: *Universal Properties of Bulk Viscosity Near the QCD Phase Transition*, Phys. Lett. **B 663**, 217 (2008), arXiv:0711.0914 [hep-ph] 342, 365
13. D.J. Gross and F. Wilczek: *Ultraviolet Behavior of non-Abelian Gauge Theories*, Phys. Rev. Lett. **30**, 1343 (1973) 342, 345
14. H.D. Politzer: *Reliable Perturbative Results for Strong Interactions?*, Phys. Rev. Lett. **30**, 1346 (1973) 342, 345
15. S. Bethke: *Determination of the QCD Coupling* α_s, J. Phys. **G 26**, R27 (2000), arXiv:hep-ex/0004021 346
16. L.D. Landau and I.Y. Pomeranchuk: *On Point Interactions in Quantum Electrodynamics*, Dokl. Akad. Nauk Ser. Fiz. **102**, 489 (1955); also published in *Collected Papers of L.D. Landau*, D. Ter Haar (ed.), pp. 654–658, Pergamon Press, Oxford (1965) 345

17. I.B. Khriplovich: *Green's Functions in Theories with non-Abelian Gauge Group*, Yad. Fiz. **10**, 409 (1969) 345
18. V.N. Gribov: *Quantization of non-Abelian Gauge Theories*, Nucl. Phys. **B 139**, 1 (1978)
19. D. Zwanziger: *No Confinement Without Coulomb Confinement*, Phys. Rev. Lett. **90**, 102001 (2003), arXiv:hep-lat/0209105 345
20. Y.L. Dokshitzer and D.E. Kharzeev: *The Gribov Conception of Quantum Chromodynamics*, Ann. Rev. Nucl. Part. Sci. **54**, 487 (2004), arXiv:hep-ph/0404216 345
21. J.R. Ellis: *Aspects of Conformal Symmetry and Chirality*, Nucl. Phys. **B 22**, 478 (1970) 347
22. R.J. Crewther: *Broken Scale Invariance in the Width of a Single Dilaton*, Phys. Lett. **B 33**, 305 (1970)
23. M.S. Chanowitz and J.R. Ellis: *Canonical Anomalies and Broken Scale Invariance*, Phys. Lett. **B 40**, 397 (1972)
24. J. Schechter: *Effective Lagrangian with Two Color Singlet Gluon Fields*, Phys. Rev. **D 21**, 3393 (1980)
25. J.C. Collins, A. Duncan and S.D. Joglekar: *Trace and Dilatation Anomalies in Gauge Theories*, Phys. Rev. **D 16**, 438 (1977)
26. N.K. Nielsen: *The Energy Momentum Tensor in a Nonabelian Quark Gluon Theory*, Nucl. Phys. **B 120**, 212 (1977) 347
27. M.A. Shifman, A.I. Vainshtein and V.I. Zakharov: *QCD and Resonance Physics. Sum Rules*, Nucl. Phys. **B 147**, 385 (1979) 348
28. K. Wilson: *Confinement of Quarks*, Phys. Rev. **D 10**, 2445 (1974) 348
29. A. Ellis: *Black Holes - History*, Journal of the Astronomical Society of Edinburgh **39**, (1999) 349
30. K. Schwarzschild: *Ü ber das Gravitationsfeld eines Kugel aus inkompressibler Flüssigkeit nach der Einsteinschen Theorie*, pp. 424–434, Sitzungsber. Preuss. Akad. D. Wiss. (1916) 350
31. J. Oppenheimer and G. Volkoff: *On Massive Neutron Cores*, Phys. Rev. **55**, 374–381 (1939) 350
32. D. Finkelstein: *Past-Future Asymmetry of the Gravitational Field of a Point Particle*, Phys. Rev. **110**, 965–967 (1958) 350
33. S. Hawking: *Black Hole Explosions?*, Nature **248**, 3031 (1974) 350
34. W. Busza, R. Jaffe, J. Sandweiss and F. Wilczek: *Review of Speculative "Disaster Scenarios" at RHIC*, arXiv:hep-ph/9910333 351
35. H. Nastase: *The RHIC Fireball as a Dual Black Hole*, arXiv:hep-th/0501068 351
36. R. Bousso: *The Holographic Principle*, arXiv:hep-th/0203101 351
37. H. Nastase: *Introduction to AdS-CFT*, arXiv:0712.0689 [hep-th] 352, 355
38. O. Aharony, S. Gubser, J. Maldacena, H. Ooguri and Y. Oz: *Large N Field Theories, String Theory and Gravity*, Phys. Rept. **323**, 183–386 (2000), arXiv:hepth/9905111 353, 354, 359
39. I. Klebanov: *TASI Lectures – Introduction to the AdS/CFT Correspondence*, arXiv:hep-th/0009139 354, 355
40. V.A. Novikov, M.A. Shifman, A.I. Vainshtein and V.I. Zakharov: *Are All Hadrons Alike?*, Nucl. Phys. **B 191**, 301 (1981) 355, 356, 363
41. A.A. Migdal and M.A. Shifman: *Dilaton Effective Lagrangian in Gluodynamics*, Phys. Lett. **B 114**, 445 (1982) 356, 357
42. M. Novello, V.A. De Lorenci, J.M. Salimand R. Klippert: *Geometrical Aspects of Light Propagation in Nonlinear Electrodynamics*, Phys. Rev. **D 61**, 045001 (2000), arXiv:gr-qc/9911085 358
43. G. Policastro, D. Son and A. Starinets: *Shear Viscosity of Strongly Coupled $N = 4$ Supersymmetric Yang-Mills Plasma*, Phys. Rev. Lett. **87**, 081601 (2001), arXiv:hep-th/0104066 359
44. P. Arnold, C. Dogan and G. Moore: *The Bulk Viscosity of High-Temperature QCD*, Phys. Rev. **D 74**, 085021 (2006), arXiv:hep-ph/0608012 359, 361, 362, 364
45. E. Lifshitz and L. Pitaevskii: *Statistical Physics*, Pt. 2, Sec. 90, Pergamon Press, New York (1980) 359, 362
46. P. Kovtun, D. Son and A. Starinets: *Viscosity in Strongly Interacting Quantum Field Theories from Black Hole Physics*, Phys. Rev. Lett. **94**, 111601 (2005), arXiv:hep-th/0405231 359, 360, 361
47. Y. Kats and P. Petrov: arXiv:0712.0743 [hep-th] 361

48. A. Buchel, R.C. Myers and A. Sinha: arXiv:0812.2521 [hep-th] 361
49. H. Meyer: *A Calculation of the Shear Viscosity in SU(3) Gluodynamics*, arXiv:0704.1801 [hep-lat] 361, 362, 364
50. A. Nakamura and S. Sakai: *Transport Coefficients of Gluon Plasma*, Phys. Rev. Lett. **94**, 072305 (2005), arXiv:hep-lat/0406009 360, 362, 364
51. K. Dusling and D. Teaney: *Simulating Elliptic Flow with Viscous Hydrodynamics*, Phys. Rev. **C 77**, 034905 (2008), arXiv:0710.5932 [nucl-th] 361
52. P. Romatschke and U. Romatschke: *Viscosity Information from Relativistic Nuclear Collisions: How Perfect is the Fluid Observed at RHIC?*, Phys. Rev. Lett. **99**, 172301 (2007), arXiv:0706.1522 [nucl-th]
53. M. Luzum and P. Romatschke: *Conformal Relativistic Viscous Hydrodynamics: Applications to RHIC Results at 200 GeV*, Phys. Rev. **C 78**, 034915 (2008), arXiv:0804.4015 [nucl-th]
54. H. Song and U.W. Heinz: *Extracting the QGP Viscosity from RHIC Data – A Status Report from Viscous Hydrodynamics*, arXiv:0812.4274 [nucl-th] 361
55. P. Ellis, J. Kapusta and H. Tang: *Low-Energy Theorems for Gluodynamics at Finite Temperature*, Phys. Lett. **B 443**, 63 (1998), arXiv:nucl-th/9807071 363
56. G. Boyd, J. Engels, K. Karsch, E. Laermann, C. Legeland, M. Luetgemeier and B. Petersson: *Thermodynamics of SU(3) Lattice Gauge Theory*, Nucl. Phys. **B 469**, 419–444 (1996), arXiv:hep-lat/9602007 363, 364
57. P. Benincasa, A. Buchel and A.O. Starinets: *Sound Waves in Strongly Coupled non-Conformal Gauge Theory Plasma*, Nucl. Phys. **B 733**, 160 (2005), arXiv:hepth/0507026 364, 365
58. H. Meyer: *A Calculation of the Bulk Viscosity in SU(3) Gluodynamics*, arXiv:0710.3717 [hep-lat] 364, 366
59. A. Nakamura and S. Sakai: *Lattice Calculation of the QGP Viscosities*, arXiv:0710.3625 [hep-lat] 364
60. A. Kogan and H. Meyer: J. Low Temp. Phys. **110**, 899 (1998) 365
61. M. Cheng et al: *The QCD Equation of State with Almost Physical Quark Masses*, arXiv:0710.0354 [hep-lat] 365
62. K. Paech and S. Pratt: *Origins of Bulk Viscosity at RHIC*, Phys. Rev. **C 74**, 014901 (2006), arXiv:nucl-th/0604008 365
63. J.W. Chen and J. Wang: *Bulk Viscosity of a Gas of Massless Pions*, arXiv:0711.4824 [hep-ph]
64. D. Fernandez-Fraile and A.G. Nicola: *Bulk Viscosity and the Conformal Anomaly in the Pion Gas*, arXiv:0809.4663 [hep-ph]
65. J. Noronha-Hostler, J. Noronha and C. Greiner: *Transport Coefficients of Hadronic Matter Near T_c*, arXiv:0811.1571 [nucl-th]
66. C. Sasaki and K. Redlich: *Transport Coefficients Near Chiral Phase Transition*, arXiv:0811.4708 [hep-ph] 365
67. S. Gubser, A. Nellore, S. Pufu and F. Rocha: *Thermodynamics and Bulk Viscosity of Approximate Black Hole Duals to Finite Temperature Quantum Chromodynamics*, arXiv:0804.1950 [hep-th] 365, 367
68. S. Gubser, S. Pufu and F. Rocha: *Bulk Viscosity of Strongly Coupled Plasmas with Holographic Duals*, arXiv:0806.0407 [hep-th] 365
69. G. Torrieri and I. Mishustin, *Instability of Boost-Invariant Hydrodynamics with a QCD Inspired Bulk Viscosity*, Phys. Rev. **C 78**, 021901 (2008), arXiv:0805.0442 [hep-ph] 366
70. A. Karch, E. Katz, D.T. Son and M.A. Stephanov, *Linear Confinement and AdS/QCD*, Phys. Rev. **D 74**, 015005 (2006), arXiv:hep-ph/0602229 367
71. U. Gursoy and E. Kiritsis, *Exploring Improved Holographic Theories for QCD*, JHEP **0802**, 032 (2008), arXiv:0707.1324 [hep-th]
72. U. Gursoy and E. Kiritsis: *Exploring Improved Holographic Theories for QCD*, JHEP **0802**, 019 (2008), arXiv:0707.1349 [hep-th] 367